UNIVERSITY OF ADELAIDE
19/11/04
LIBRARY

Detecting Scene Changes Using Synthetic Aperture Radar Interferometry

Mark Preiss

Thesis submitted for the degree of

Doctor of Philosophy



THE UNIVERSITY
OF ADELAIDE
AUSTRALIA

School of Electrical and Electronic Engineering
Faculty of Engineering, Computer and Mathematical Sciences
The University of Adelaide
Adelaide, South Australia

November 2004

Contents

Abstract v

Declaration vii

Acknowledgments ix

List of Figures xi

List of Tables xxiii

Glossary xxv

Symbols xxvii

Publications xxix

1 Introduction 1
- 1.1 SAR Image Formation . . . 2
- 1.2 SAR Interferometry . . . 4
- 1.3 Thesis Outline and Contributions . . . 6
  - 1.3.1 Chapter Outlines . . . 8

2 Spotlight SAR Image Formation 11
- 2.1 Introduction . . . 11
- 2.2 Background . . . 12
  - 2.2.1 The Image Formation Problem . . . 12
  - 2.2.2 Spotlight SAR Image Formation Algorithms - A Review . . . 18
  - 2.2.3 Research Motivation . . . 22
- 2.3 The Polar Format Algorithm . . . 24
  - 2.3.1 Spotlight SAR Signal History Analysis . . . 24
  - 2.3.2 Limitations of the PFA . . . 31
- 2.4 PFA With Post Filtering - The PF2 . . . 36
  - 2.4.1 Limitations of the PF2 Algorithm . . . 39
- 2.5 Simulation Results . . . 42
- 2.6 Application to Ingara SAR Data . . . 44
- 2.7 Conclusions . . . 49

3 Autofocus Algorithms for Spotlight SAR **51**
3.1 Introduction . . . 51
3.2 Background . . . 52
3.2.1 Demodulation Phase Error Model . . . 52
3.2.2 Demodulation Errors and the PFA . . . 54
3.2.3 Autofocus Algorithms . . . 57
3.2.4 Research Motivation . . . 64
3.3 A Complete Phase Error Model . . . 65
3.3.1 Azimuth and Elevation Angle Errors in the Polar Format Algorithm . . . 65
3.4 Image Domain Defocus . . . 70
3.4.1 An Example: An Along Track Velocity Error . . . 73
3.5 Limitations of the PGA Phase Error Model . . . 75
3.5.1 Range Dependence of the Demodulation Phase Error . . . 77
3.5.2 PGA Algorithm in the Presence of Range Dependent Phase Errors . . . 80
3.5.3 Impact on Interferogram Estimation . . . 85
3.6 Conclusions . . . 88

4 SAR Interferometry **93**
4.1 Introduction . . . 93
4.2 Background . . . 94
4.3 Interferometric Spotlight SAR System Model . . . 99
4.3.1 Single Channel Spotlight SAR . . . 99
4.3.2 Interferometric Dual Channel Spotlight SAR . . . 102
4.4 Interferometric Scene Model . . . 105
4.4.1 Single Channel Homogeneous Distributed Target Model . . . 106
4.4.2 Dual Channel Homogeneous Distributed Target Model . . . 108
4.4.3 Additive Receiver Noise . . . 114
4.5 Estimating the Joint Channel Statistics . . . 115
4.5.1 Heterogeneous Distributed Target Model . . . 117
4.6 Processing Correlation - Acquisition and Processing Errors . . . 119
4.6.1 First Order Effects . . . 119
4.6.2 Higher Order Effects . . . 121
4.7 Results From a Repeat Pass Interferometric SAR Experiment . . . 123
4.7.1 The Ingara X-band SAR Interferometry Experiments . . . 123
4.7.2 The Interferometric Processor . . . 124
4.7.3 Experimental Results . . . 131
4.8 Conclusions . . . 131

5 Interferometric Change Detection **141**
5.1 Introduction . . . 141
5.2 Change Detection Using the SAR Image Intensity . . . 142
5.3 Change Detection Based on the Cross Correlation Coefficient . . . 148
5.3.1 A Temporal Decorrelation Model . . . 149
5.3.2 Sample Cross Correlation Coefficient Change Statistic . . . 156
5.4 Other Coherence Estimators . . . 162
5.4.1 Intensity Correlation . . . 162
5.4.2 The Multiple Correlation Coefficient . . . 165
5.5 Experimental Results . . . 166

5.6 Conclusions 167

6 A Log-Likelihood Interferometric Change Statistic **173**
6.1 Introduction 173
6.2 Complex Reflectivity Change Model and Hypothesis Statement 174
6.3 Likelihood Ratio Change Statistic 175
6.3.1 An Optimal Clairvoyant Detector 176
6.4 Density Functions of the Change Statistic 178
6.5 Change Statistic PDF Under Equal Channel Power 184
6.6 Change Statistic PDF Under Zero Coherence 187
6.7 Detection Performance of Clairvoyant Detector 188
6.8 A Generalised Likelihood Ratio Test 192
6.8.1 Parameter Estimates 195
6.8.2 Application to Experimental Data 197
6.9 Conclusions 197

7 Experimental Results **199**
7.1 Introduction 199
7.2 Experimental Interferometric Data 200
7.2.1 Ingara Repeat Pass SAR Experiments 203
7.2.2 Processing and Analysis Methodology 206
7.3 Coherent Image Pair 1 210
7.3.1 Experimental Description and Parameters 210
7.3.2 Interferometric Image Pair Statistics 213
7.3.3 Change Detections 220
7.4 Coherent Image Pair 2 226
7.4.1 Experimental Description and Parameters 226
7.4.2 Interferometric Image Pair Statistics 232
7.4.3 Change Detections 232
7.4.4 Detection Improvements Arising from the Modified PGA 238
7.5 Coherent Image Pair 3 243
7.5.1 Experimental Description and Parameters 243
7.5.2 Interferometric Image Pair Statistics 249
7.5.3 Change Detections 253
7.6 Conclusions 257

8 Conclusion **259**
8.1 Detailed Chapter Summaries and Contributions 260
8.2 Future Work 263

A Deramp Demodulation **265**

B The PGA Algorithmic Steps **269**
B.1 The Signal Model - Circular Shifting 270
B.2 Covariance Estimation - Filtering 272

C Dual Channel Distributed Target Model **275**

D Comparison of Theoretical PDFs and Histogram Estimates **281**

Bibliography 293

Abstract

Synthetic Aperture Radar (SAR) is a coherent standoff imaging technique capable of generating fine resolution images of the complex radar backscatter of a scene from large standoff ranges. An important application of SAR is the detection of temporal changes in a scene. Change detection is an application to which SAR is particularly well suited as SARs can consistently produce high quality, well calibrated imagery with good geolocation accuracy. In this thesis techniques for the detection of fine-scale scene changes using repeat pass Interferometric SAR (InSAR) imagery are examined. The interferometric processing of SAR imagery permits scene disturbances to be detected via changes in the mean backscatter power of the scene, as well as by identifying regions in a scene exhibiting a low complex cross correlation. The mean backscatter power of a scene is sensitive to the scene's structural and dielectric properties and may be used to detect changes such as variations in the soil and vegetation moisture content and surface roughness. The complex correlation on the other hand, is sensitive to the relative distribution of scattering elements in the resolution cell and therefore can be used to detect very subtle scene changes such as vehicle tracks in a field.

The robust, reliable detection of fine-scale scene changes, which may be spatially small and vary abruptly over the scene, requires SAR image resolutions commensurate with the size of the scene disturbances. This thesis thus firstly examines the use of wide-angle spotlight SAR to obtain fine resolution imagery suitable for use in interferometric change detection processing. Algorithms for efficient image formation of wide-angle collections are examined and a technique is proposed for generating fine resolution imagery suitable for subsequent interferometric processing. Extended aperture, wide-angle collections pose significant array calibration challenges and autofocus algorithms are generally required to recover a well focused image. The image domain effects of array miscalibration in wide-angle spotlight SAR are examined and a modification to the Phase Gradient Autofocus (PGA) algorithm is proposed to improve the image focus for a common source of array miscalibration. Given suitably focused imagery, the interferometric processing of an image pair is examined. Potential sources of relative mismatch in the formation of wide-angle spotlight mode image pairs are identified and techniques are proposed to minimise their effects on the transduced image pair complex cross correlation.

Finally, the change detection problem is addressed by formulating the problem in an hypothesis testing framework using statistical models to describe the changed and unchanged scene. Forming the log likelihood ratio gives a new change statistic that encodes both changes in the mean backscatter power and the cross correlation for discriminating between changed and unchanged areas regions of a scene. The detection performance of the statistic is derived theoretically and is shown to be significantly better than the commonly used mean backscatter power ratio and complex cross correlation coefficient change statistics. The superior performance is verified through simulations as well as extensive testing on experimental repeat pass X-band spotlight SAR data acquired with various ground truthed scene changes.

Declaration

This work contains no material that has been accepted for the award of any other degree or diploma in any university or other tertiary institution and, to the best of my knowledge and belief, contains no material previously published or written by another person, except where due reference has been made in the text.

I give consent to this copy of my thesis, when deposited in the University Library, being available for loan and photocopying.

Signature .

Date 16/11/04

Acknowledgments

I wish to thank a number of people and organisations that have greatly contributed to this thesis.

My supervisors Professor Doug Gray and Dr Nick Stacy have provided much support and encouragement throughout my candidature. Doug's ability to grasp the essence of a problem and ask the right questions invariably kept me on track. Nick's willingness to share his wealth of knowledge on imaging radar and help in overcoming the numerous obstacles and problems I encountered throughout my research was invaluable and greatly appreciated.

I would also like to thank the Defence Science and Technology Organisation for allowing me the opportunity to pursue this research. Also, the Centre for Sensor Signal and Information Processing in Adelaide and the University of Adelaide for providing the resources to carry out this research and providing a stimulating, enriching place to study.

This work would not have been possible without the assistance of the Ingara team at the Defence Science and Technology Organisation. The Ingara SAR is a world class SAR and it is a privilege to work in such a dedicated and intelligent team.

A special thanks to the gardening boys Ross Kirby, Daryl Ireland, Ian Watson and also Jason Gillespie for his expert calligraphy skills with a lawn mower.

Finally to my wife, whose patience, understanding and support made this all possible.

List of Figures

2.1 A typical spotlight SAR imaging geometry. As the radar moves past the scene the antenna is steered so as to continually illuminate the same ground patch. This allows the collection of range echo data over an extended collection aperture for processing into an image with fine azimuth resolution. The coordinates (x_a, y_a, z_a) give the radar location at a particular transmit/receive point and (x, y, z) is some scattering location in the scene. 13

2.2 Range compressed raw echo data collected for three point scatterers with compensation to a line. Each of the scatterers undergoes a hyperbolic range migration defined by the imaging geometry at each transmit/received point. 16

2.3 At each transmit/receive point along the collection aperture the radar transduces the integrated reflectivity function $f_c(r)$. The range r is the differential range $(R - R_T)$ where R is the range measured along the line of sight of the radar and R_T is the range to the scene centre. The value of $f_c(r)$ at a given range is the superposition of all scattering contributions lying along a contour of equirange from the radar transmit/receive point. 17

2.4 Range compressed raw echo data collected for three point scatterers where the demodulation reference function is the transmit chirp waveform delayed by the propagation distance to the scene centre. The point at the scene centre undergoes no range migration, while the scatterers offset in azimuth and range undergo a sinusoidal like range migration. 19

2.5 Spotlight SAR imaging geometry. The radar (point A) is a distance R_T from the scene focus point (point O) at altitude h. Angles θ_T and ψ_T are the azimuth and depression angles defined by the vector from the scene centre to the radar. A point scatterer (point C) lies a distance R from the radar at location given in cylindrical coordinates (ρ, γ, z), centred at the scene focus point. 25

2.6 Deramp demodulated echo data acquired when the radar is at location (R_T, θ_T, ψ_T) evaluates the scene reflectivity in the spatial frequency domain along the radial defined by the same azimuth and depression angles. As the radar moves past the scene the deramp echo data sweep out a sector of the plane $k_z = k_y\beta_0$. 28

2.7 In the plane wave approximation the transduced reflectivity at location (x_0, y_0) in the image formation plane $z = z_0$ is determined by the superposition of scatterers lying along the line through (x_0, y_0, z_0) and perpendicular to the radar look direction i.e. $h = \beta_0(y_0 - y) + z_0$. 29

2.8 Simulation scene consisting of four point scatterers in the ground plane. The scatterer locations have been selected to illustrate the variation in the point spread function obtained using the PFA and PF2 algorithms. 43

2.9 Point Spread function for scatterer (1) of Figure 2.8 recovered via the PFA. On the left hand side is the transduced PFA image while on the right hand side is a plot showing the associated azimuth point spread function. 45
2.10 Point Spread function for scatterer (2) of Figure 2.8 recovered via the PFA. On the left hand side is the transduced PFA image while on the right hand side is a plot showing the associated azimuth point spread function. 45
2.11 Point Spread function for scatterer (3) of Figure 2.8 recovered via the PFA. On the left hand side is the transduced PFA image while on the right hand side is a plot showing the associated azimuth point spread function. 46
2.12 Point Spread function for scatterer (4) of Figure 2.8 recovered via the PFA. On the left hand side is the transduced PFA image while on the right hand side is a plot showing the associated azimuth point spread function. 46
2.13 Point Spread function for scatterer (1) of Figure 2.8 recovered via the PF2 algorithm. On the left hand side is the transduced PFA image while on the right hand side is a plot showing the associated azimuth point spread function. 47
2.14 Point Spread function for scatterer (2) of Figure 2.8 recovered via the PF2 algorithm. On the left hand side is the transduced PFA image while on the right hand side is a plot showing the associated azimuth point spread function. 47
2.15 Point Spread function for scatterer (3) of Figure 2.8 recovered via the PF2 algorithm. On the left hand side is the transduced PFA image while on the right hand side is a plot showing the associated azimuth point spread function. 48
2.16 Point Spread function for scatterer (4) of Figure 2.8 recovered via the PF2 algorithm. On the left hand side is the transduced PFA image while on the right hand side is a plot showing the associated azimuth point spread function. 48
2.17 Ingara spotlight SAR image processed to 0.15 m azimuth and 0.5 m range resolution using the PF2 technique. The image on the right shows an overview of a portion of the total imaged scene while the images on the left show the full resolution imagery of a small image subchip recovered using the PFA and PF2. 49

3.1 Spotlight SAR imaging geometry. The radar is a distance $R_T = R_m + R_e$ from the scene centre at altitude h, where R_m is the measured distance and R_e the error in the measured distance. Angles θ_T and ψ_T are the azimuth and depression angles defined by the vector from the scene centre to the radar. A point scatterer at location (x_s, y_s, z_s) lies a distance R from the radar. 54
3.2 Ground plane projection of the polar raster grid of the collected signal history data obtained using the measured and true azimuth and depression look angles for the case of straight and level flight without squint subject to a bias in the measurement of the along track velocity. 67
3.3 At each transmit/receive position along the synthetic aperture the measurement of the radar platform location is subject displacement errors Δx, Δy and Δz. The measured location of the radar in spherical coordinates with respect to the scene centre is given by (R_m, θ_m, ψ_m) while the true radar location is (R_T, θ_T, ψ_T). 71
3.4 Range compressed history data obtained for a point scatterer located at the scene centre collected with an along track velocity error in the radar platform of 0.36 percent of the true platform along track velocity. The range point spread function is a sinc function with a resolution, given by the location of the first null, of 0.29 m. The range pixel spacing is 0.11 m. 81

3.5 Image of a point scatterer located at the scene centre obtained using the PFA where at 0.36 percent error in the along track velocity of the radar platform. The image point spread function in the absence of phase phase errors is a sinc function with a nominal resolution of 0.14 m in azimuth and 0.29 m in range. The pixel spacing is 0.095 m in azimuth and 0.11 m in range. 81

3.6 Narrow band phase error estimate obtained from a slice of the range compressed history generated using the simulation parameters described in Table 3.2. 83

3.7 Magnitude envelope of the slice of the range compressed history data used to obtain the narrow band phase error estimate for the simulation parameters described in Table 3.2. The 7 dB roll off at the band edges arises due to the uncompensated range cell migration. 83

3.8 Point spread function for a PFA plus PGA SAR processor obtained using the imaging parameters described in Table 3.2. 85

3.9 Point spread function for a PFA plus PGA SAR processor with correction of the residual range cell migration obtained using the imaging parameters described in Table 3.2. 86

3.10 Loss in interferometric coherence obtained with a uncompensated quadratic range cell migration measured as a fraction of the range resolution cell size. 87

3.11 SAR image recovered from data collected using the DSTO Ingara X-band airborne SAR and processed using PFA with post filtering and application of the PGA algorithm. The resolution of the recovered image is 0.58 m in range and 0.12 m in azimuth and has been subsequently spatially averaged for display. 89

3.12 The PGA phase error estimate obtained from the experimental Ingara X-band data as a function of the azimuth spatial frequency. The phase error shows a dominant quadratic component consistent with a 0.23 percent error in the along track velocity measurement. 90

3.13 Enlarged view of the PGA phase error estimate for a region around the aperture centre. High frequency components in the phase error estimate are evident. 90

3.14 Coherence map estimate obtained from the primary and repeat pass image where the primary image is subject to uncompensated range dependent defocus which has been compensated for in the repeat pass image. Figures (a) and (b) show the same coherence map with different scales as indicated. Ideally the coherence should be unity however the residual relative range dependent defocus has reduced the coherence to 0.939 in the open field region of the scene which is consistent with a relative range cell migration of 0.4 of a range resolution cell size. 91

3.15 Coherence map estimate obtained from the primary and repeat pass image where a range cell migration correction step has been carried out on the primary image. Figures (a) and (b) show the same coherence map with different scales as indicated. The dominant deleterious effects of the relative range dependent defocus have largely been corrected with the coherence over the open field increased to 0.987. 92

4.1 Spotlight SAR imaging geometry corresponding to straight and level flight without squint. The depression angle and standoff range at aperture centre are ψ_1 and $R_{bs_{g1}}$ respectively. The acquired range echo data are samples of the scene's complex reflectivity evaluated over an acquisition plane in the scene's spatial frequency domain given by $k_z = \tan\psi_1 k_y$. 100

4.2 Repeat pass spotlight SAR imaging geometry acquired with an across track baseline B_x and an above track baseline of B_z. The depression angles for the primary and repeat pass acquisitions at aperture centre are ψ_1 and ψ_2 respectively while the standoff ranges are $R_{bs_{g1}}$ and $R_{bs_{g2}}$ respectively. The acquired range echo data in the primary and repeat pass are samples of the scene's complex reflectivity evaluated over two offset acquisition planes in the scene's spatial frequency domain given by $k_z = \tan\psi_1 k_y$ in the case of the primary pass and $k_z = \tan\psi_2 k_y$ in the repeat pass. 103
4.3 Apertures of support in the (k_x, k_y) plane for the acquisition and image formation transfer functions for a repeat pass image pair after baseband translation. Also shown is the common overlapping aperture of support. The size and k_y offsets of the apertures of support are determined by the baseline offsets between the primary and repeat pass collections. 105
4.4 A repeat pass interferometric system model. The scene is modelled as an ensemble of stable and unstable scatterers, where the unstable contributions undergo a perturbation in the interval between collections. Noise sources m and n are additive receiver noise. The interferometric information is available in the cross correlation coefficient of the interferometric image pair. 114
4.5 Flow chart of the processing steps required to generate an image pair repeat pass SAR data suitable for applying interferometric change detection algorithms. 124
4.6 Histograms of the depression angle difference and ground range offset difference between the primary and repeat pass collections obtained at a nominal depression angle of 15 degrees. 126
4.7 Histograms of the depression angle difference and ground range offset difference between the primary and repeat pass collections obtained at a nominal depression angle of 30 degrees. 126
4.8 Azimuth and range misregistration in metres, given by equations (4.112) and (4.113) respectively, of a PFA interferometric image pair collected with a nominal depression angle of 30 degrees and standoff range 13.1 km with baseline offsets of $\Delta\psi = 0.2$ degrees and $\Delta R_{bs_g} = 200$ m. 127
4.9 Peak value of the quadratic phase difference in radians associated with a PFA interferometric image pair processed to 0.1 m unweighted azimuth resolution and collected with a nominal depression angle of 30 degrees, a standoff range of 13.1 km and a baseline offset of $\Delta\psi = 0.2$ degrees and $\Delta R_{bs_g} = 200$ m. 128
4.10 Cross correlation coefficient magnitude obtained for a PFA image pair processed to 0.1 m unweighted azimuth resolution and collected with a nominal depression angle of 30 degrees, a standoff range of 13.1 km and a baseline offset of $\Delta\psi = 0.2$ degrees and $\Delta R_{bs_g} = 200$ m. 129
4.11 Primary collection intensity image. The image has been processed to a resolution of 0.58 m (range) x 0.150 m (azimuth) with a Hamming window applied. 132
4.12 Repeat pass collection intensity image. The image has been processed to a resolution of 0.58 m (range) x 0.150 m (azimuth) with a Hamming window applied. The temporal baseline for the repeat pass interferometric pair is approximately 12 minutes 133
4.13 Magnitude image of the sample complex cross correlation coefficient obtained by spatially averaging over a sliding estimation window (2 by 6 pixels in range and azimuth respectively). 134
4.14 Phase image of the sample complex cross correlation coefficient obtained by spatially averaging over a sliding estimation window (2 by 6 pixels in range and azimuth respectively). 135

4.15 Enlarged view of the coherence map over the dirt track that appears along the top of the scene image. 136

4.16 Enlarged view of the coherence map over the low coherence random tracks appearing in middle portion of the scene. 137

4.17 Enlarged view of the coherence map as well as the primary and repeat pass intensity images over one of the track like disturbances. 138

5.1 Simulated and theoretically obtained density functions for the mean backscatter ratio change statistic corresponding to an unchanged scene and a scene with a 3 dB change in the backscatter. The number of independent averages used in the intensity estimates is $N = 9$. 145

5.2 Simulated and theoretical ROC curves for the intensity ratio change statistic obtained using an $N = 9$ and mean backscatter power changes of 1, 3, 5 and 10 dB. 147

5.3 Simulated and theoretical ROC curves for the intensity ratio change statistic for a mean backscatter power change of 3 dB and values of N of 9, 16, 25 and 36. 147

5.4 Misregistration component of the cross correlation coefficient for an interferometric image pair where the scatterers in the scene have been subject to a random Gaussian displacement in the interval between imaging collections. The standard deviation, or equivalently the RMS value, of the random displacement has been normalised to the image resolution cell size. 155

5.5 Phase component of the cross correlation coefficient of an interferometric image pair where the scatterers in the scene have been subject to a random Gaussian displacement in range and imaged with depression angles of 15 and 45 degrees. The RMS displacement has been normalised to the effective radar wavelength. 155

5.6 Expected value of the coherence estimate plotted against the underlying true coherence for a range of sample estimate sizes. 157

5.7 Simulated and theoretical probability density functions of the sample coherence corresponding to a true underlying coherence of 0 and 0.6. The sample estimate has been obtained by averaging over $N = 9$ independent pixel pairs. 159

5.8 Simulated and theoretical ROC curves for sample coherence change statistic obtained with an unchanged scene partial coherence $\gamma_{unchanged}$ = 0.45, 0.6, 0.75 and 0.9, a changed scene coherence of $\gamma_{changed}$ = 0 and an estimation window size of $N = 9$ independent pixels 161

5.9 Simulated and theoretical ROC curves for sample coherence change statistic obtained with an unchanged scene partial coherence of $\gamma_{unchanged}$ = 0.6, a changed scene coherence of $\gamma_{changed}$ = 0 and estimation window sizes of N =4, 9, 16 and 25 independent pixels 161

5.10 Simulated probability density functions for the sample intensity correlation coefficient for underlying true coherence values of 0.6 and 0.0 obtained using an estimation window size of $N = 9$ independent pixels. 164

5.11 Simulated ROC curves for the sample intensity correlation coefficient change statistic obtained using $N = 9$ and $\gamma_{changed}$ = 0.0 and $\gamma_{unchanged}$ = 0.45, 0.6, 0.75 and 0.9. . 164

5.12 Simulated ROC curves for multiple correlation coefficient change statistic obtained by averaging over $N = 9$ independent pixels and $\gamma_{changed}$=0.0 and $\gamma_{unchanged}$ = 0.45, 0.6, 0.75 and 0.9 assuming the interferometric phase is zero. 166

5.13 Scene coherence maps obtained using the multi-correlation coefficient. The top left figure shows the interferometric phase modulation applied to the repeat pass image. The remaining figures show the estimated coherency maps obtained with the phase modulation applied and underlying true coherence values of 1.0, 0.9 and 0.8. 167
5.14 Intensity ratio change statistic map obtained by spatially averaging over a sliding estimation window (2x6 pixels in range and azimuth respectively). 169
5.15 Square root of the intensity cross correlation change statistic map obtained by spatially averaging over a sliding estimation window (2x6 pixels in range and azimuth respectively). 170
5.16 Square root of the multiple cross correlation change statistic map obtained by spatially averaging over a sliding estimation window (2x6 pixels in range and azimuth respectively). 171
5.17 Sample interferometric phase obtained by spatially averaging over a sliding estimation window (2x6 pixels in range and azimuth respectively). 172

6.1 The expected value of the decision statistic z under H_1, normalised by the number of samples, as a function of the coherence γ. 178
6.2 The expected value of the decision statistic under H_0 and H_1, normalised by the number of samples, as a function of the backscatter ratio r expressed in dB. 179
6.3 Simulated and theoretical density functions of the likelihood ratio change statistic for the unchanged H_0 hypothesis and the changed H_1 hypothesis. The mean backscatter ratio of the primary and repeat pass images is 1.04 dB under H_0 and 3.77 dB under H_1, $N = 9$ and $\gamma = 0.45$. 183
6.4 Simulated and theoretical density functions of the sample coherence for the unchanged H_0 hypothesis and the changed H_1 hypothesis. Under H_0 the true underlying coherence is $\gamma = 0.45$ while under H_1 $\gamma = 0$ and $N = 9$. 183
6.5 Simulated and theoretical density functions of the ratio statistic r for the unchanged H_0 hypothesis and the changed H_1 hypothesis. The mean backscatter ratio of the primary and repeat pass images is 1.04 dB under H_0 and 3.77 dB under H_1 and $N = 9$.184
6.6 Density functions for the decision statistic under H_0 and H_1 for the case of equal backscatter powers $\sigma_f^2 = \sigma_g^2$ with a partial coherence under H_0 of $\gamma = 0.45$ and $N = 9$.187
6.7 Density functions for the decision statistic under H_0 and H_1 for the case of zero coherence $\gamma = 0$ and mean backscatter powers of $\sigma_{g_0}^2 = 1.7847e8$ and $\sigma_{g_1}^2 = 0.95067e8$ (a 2.73 dB reduction in the mean backscatter power) and $N = 9$. 188
6.8 Theoretical and simulated ROC curves for equal channel powers and coherence values of 0.45, 0.6, 0.75 and 0.9 with $N = 9$. 191
6.9 Theoretical and simulated ROC curves for equal channel powers and N = 4, 9, 16, 25 with a coherence of 0.6. 192
6.10 Theoretical and simulated ROC curves for zero coherence under H_0 and changes in the backscatter power of $\sigma_{g_1}^2/\sigma_{g_0}^2$ = 1 dB, 3 dB, 5 dB and 10 dB with $N = 9$. 193
6.11 Theoretical and simulated ROC curves for zero coherence under H_0 and N = 9, 16, 25 and 36 with a change in the backscatter power value of $\sigma_{g_1}^2/\sigma_{g_0}^2$ = 3 dB. 193
6.12 Theoretical and simulated ROC curves for a scene change scenario where the mean backscatter ratio of the primary and repeat pass images is 1.04 dB under H_0 and 3.77 under H_1, $N = 9$ and $\gamma = 0.45$. 194

6.13 Average ROC curves for the log likelihood change statistic obtained using Monte-Carlo simulation techniques. Sample window sizes of $M = 25, 64, 121$ and 400 have been used to estimate $\underline{v}_{H_0}$ and $\underline{v}_{H_1}$ and a window size of $N = 7$ has been used to compute the log likelihood statistic. The unchanged scene coherence is $\gamma = 0.62$ and it has been assumed that $\sigma^2_{g_0} = \sigma^2_{g_1}$. 198

7.1 Intensity SAR image of the scene used for the September 1999 repeat pass interferometry experiments. Superimposed on the image is a schematic showing the scene changes carried out with the rotary hoe and lawn mower. 204

7.2 Intensity SAR image of the scene used for the May 2000 repeat pass interferometry experiments. Superimposed on the image is a schematic showing the scene changes carried out with the rotary hoe and lawn mower. 205

7.3 Diagram outlining the processing steps required to generate a repeat pass SAR image pair suitable for applying interferometric change detection algorithms. 207

7.4 Intensity SAR image generated from the primary pass collection. The imagery has been processed to a resolution of 0.61 m (range) x 0.150 m (azimuth) with a Hamming window applied. Also shown is the image subchip selected for further processing and change detection analysis. 211

7.5 Intensity SAR image generated from the repeat pass collection. The imagery has been processed to a resolution of 0.61 m (range) x 0.150 m (azimuth) with a Hamming window applied. The temporal baseline between the primary and repeat pass collection is approximately 24 hours and in this period scene changes were carried out with a rotary hoe and lawn mower, see Figure 7.2. Also shown is the image subchip selected for further processing and change detection analysis. 212

7.6 Mean backscatter power ratio change statistic evaluated over the primary and repeat pass image pair using a 3 by 7 pixel spatial estimation window. The resolution of the estimate is 0.64 m by 0.22 m with a pixel spacing of 0.45 m by 0.34 m. The 20 m x 20 m area with a modified backscatter coefficient is clearly visible as a darker region in the lower left of the image. 214

7.7 Sample coherence evaluated over the repeat pass image pair using a 3 by 7 pixel spatial estimation window. The resolution of the estimate is 0.64 m by 0.22 m with a pixel spacing of 0.45 m by 0.34 m. The modified 20 m x 20 m area is clearly visible as an area of low coherence. Other regions of low coherence are visible below and above the modified area and are associated with a different vegetation type that is more susceptible to temporal change over the 24 hour revisit period. 215

7.8 Sample interferometric phase evaluated over the repeat pass image pair using a 3 by 7 pixel spatial estimation window. The resolution of the estimate is 0.64 m by 0.22 m with a pixel spacing of 0.45 m by 0.34 m. The modified 20 m x 20 m area is clearly visible as an area of rapid phase fluctuations. Other regions of random phase variation are associated with regions of low coherence in the scene. 216

7.9 Ground truth observations of the scene disturbances. Different areas of the field have different types of vegetation cover which are distinguishable by their differing coherence properties over the 24 hour revisit period. The rotary hoe has been used to clear a 20 m by 20 m area of vegetation. 217

7.10 Amplitude and phase histograms for the primary and repeat pass image subchips. Superimposed on the histograms are the theoretical Rayleigh amplitude and uniform phase density functions that are associated with complex Gaussian scattering behaviour. Also shown is the likely range (three standard deviations) in variation of the histogram estimates of the PDF that are to be expected assuming the Rayleigh amplitude and uniform phase PDFs are accurate models 219

7.11 Histogram and theoretical density function of the sample coherence. The estimated true coherence and ENL used to calculate the theoretical fit are 0.45 and 7 respectively. Also shown is the likely range in variation (three standard deviations) of the histogram estimate of the PDF that is to be expected assuming the jointly Gaussian model is correct. 219

7.12 Histograms and theoretical density functions of the sample interferometric phase obtained by partitioning the image subchips into four equally sized, non-overlapping quadrants. The estimated mean underlying phase is indicated in each subplot and the coherence and ENL used to calculate the theoretical fits are 0.45 and 7 respectively. Also shown is the likely range in variation (three standard deviations) of the histogram estimate of the PDF that is to be expected assuming the jointly Gaussian model is correct. 221

7.13 Theoretical and simulated ROC curves of the three change statistics obtained using the covariance matrix estimates given in (7.20) with an ENL=7. 222

7.14 The images on the left hand side show, from top to bottom, the mean backscatter power ratio, sample coherence and log likelihood change statistic maps evaluated over the subsampled subchip image pair using a 3 by 3 pixel sliding estimation window. Scene changes are identified as dark pixels. The images on the right hand size show the detections obtained by applying a threshold to the corresponding change maps. The threshold has been experimentally selected to give a false alarm rate of 0.05. . . 224

7.15 Experimentally obtained histogram of the log likelihood change statistic obtained using a 3 by 3 sliding estimation window over the entire image subchip pair. The histogram is thus a mixture of values obtained over both changed and unchanged areas. The theoretical density functions for the changed and unchanged hypotheses are shown along with the likely range in variation (three standard deviations) of the histogram estimate of the PDF that is to be expected under the changed and unchanged hypotheses. 225

7.16 Intensity SAR image generated from the primary pass collects. The imagery has been processed to a resolution of 0.58 m (range) x 0.150 m (azimuth) with a Hamming window applied. Also shown is the image subchip selected for further processing and change detection analysis. 227

7.17 Intensity SAR image generated from the repeat pass collection. The imagery has been processed to a resolution of 0.58 m (range) x 0.150 m (azimuth) with a Hamming window applied. The temporal baseline between the primary and repeat pass images is approximately 12 minutes. Also shown is the image subchip selected for further processing and change detection analysis. 228

7.18 Mean backscatter power ratio change statistic in dB evaluated over the primary and repeat pass image pair using a 2 by 7 pixel spatial estimation window. The resolution of the estimate is 0.595 m by 0.225 m with a pixel spacing of 0.405 m by 0.358 m. . 229

7.19 Sample coherence evaluated over the repeat pass image pair using a 2 by 7 pixel spatial estimation window. The resolution of the estimate is 0.595 m by 0.225 m with a pixel spacing of 0.405 m by 0.358 m. The track like areas of low coherence in the middle of the scene may possibly be due to the movements of grazing sheep during the 12 minute revisit period between imaging collections. 230

7.20 Sample interferometric phase evaluated over the repeat pass image pair using a 2 by 7 pixel spatial estimation window. The resolution of the estimate is 0.595 m by 0.225 m with a pixel spacing of 0.405 m by 0.358 m. Areas of low coherence manifest as regions of rapid, random phase fluctuations in the interferometric phase map. 231

7.21 Amplitude and phase histograms for the primary and repeat pass image subchips. Superimposed on the histograms are the theoretical Rayleigh amplitude and uniform phase density functions associated with complex Gaussian scattering behaviour. Also shown in the plots are the likely range in variation (three standard deviations) of the histogram estimate of the PDF that is to be expected assuming the Rayleigh and uniform PDF are correct. 233

7.22 Histogram and theoretical density function for the sample coherence obtained from the primary and repeat pass subsampled image subchips. A true coherence of 0.94 and and ENL = 7 have been used to obtain the theoretical density function of the sample coherence. Also shown is the likely range in variation (three standard deviations) of the histogram estimate of the PDF that is to be expected assuming the jointly Gaussian model is correct. 234

7.23 Histograms and theoretical density functions for the interferometric phase obtained by partitioning the subsampled image subchips into four equally size non-overlapping image quadrants. A true coherence of 0.94, an ENL = 7 and an underlying true interferometric phase of 1.95 radians have been used to obtain the theoretical density functions. Also shown is the likely range in variation (three standard deviations) of the histogram estimates of the PDF that are to be expected assuming the jointly Gaussian model is correct. 235

7.24 Theoretical and simulated ROC curves of the sample coherence and log likelihood ratio change statistics using change detection scenario described by the covariance matrices given in (7.23). 235

7.25 The images on the left hand side show, from top to bottom, the sample coherence and log likelihood change statistic maps, evaluated over the subsampled subchip image pair using a 3 by 3 pixel sliding estimation window. The images on the right hand size show the associated change detections obtained by applying a threshold to the change maps. The threshold has been experimentally selected to give a false alarm rate of 0.05. 236

7.26 Experimentally obtained histogram of the log likelihood change statistic obtained using a 3 by 3 sliding estimation window over the entire image subchip pair. The histogram is thus a mixture of values obtained over both changed and unchanged areas. Also shown are the theoretical density functions as well as the anticipated range in variation (three standard deviation) of the histogram PDF estimate under the changed and unchanged hypotheses. 237

7.27 Enlarged view of the histogram of the log likelihood change statistic obtained using a 3 by 3 sliding estimation window over the entire image subchip pair. Also shown is the theoretical density function and the anticipated range in variation (three standard deviation) of the histogram PDF estimate for the unchanged scene hypothesis. 237

7.28 Primary and repeat pass intensity SAR images. The imagery has been processed to a resolution of 0.45 m (range) and 0.12 m (azimuth) with an unweighted aperture. Also shown is the image subchip selected for further processing and change detection analysis. 239

7.29 Primary and repeat pass PGA phase error estimates. 240

7.30 Sample coherence and change detections evaluated using a 3x3 pixel sliding estimation window with and without the range cell migration correction step. The sample coherence is shown on a full scale where black denotes zero coherence and white denotes unity coherence Also shown are the detections obtained by applying a threshold of 0.8. 241

7.31 Log likelihood change statistic and change detections evaluated using a 3x3 pixel sliding estimation window with and without the range cell migration correction step. Also shown are the detections obtained by applying a threshold of 15.0. 242

7.32 Intensity SAR image generated from the primary pass imaging collection. The imagery has been processed to a resolution of 0.52 m (range) x 0.150 m (azimuth) with a Hamming window applied. 244

7.33 Intensity SAR image generated from the repeat pass imaging collection. The imagery has been processed to a resolution of 0.52 m (range) x 0.150 m (azimuth) with a Hamming window applied. The temporal baseline between the primary and repeat pass collections is approximately two hours and in this period scene changes were carried out with a rotary hoe and a lawn mower, see Figure 7.1. 245

7.34 Mean backscatter power ratio change statistic evaluated over the primary and repeat pass image pair using a 2 (range) by 6 (azimuth) pixel spatial estimation window. The resolution of the estimate is 0.57 m by 0.22 m with a pixel spacing of 0.343 m by 0.34 m. 246

7.35 Sample coherence evaluated over the repeat pass image pair using a 2 by 7 pixel spatial estimation window. The resolution of the estimate is 0.57 m by 0.22 m with a pixel spacing of 0.343 m by 0.34 m. The areas modified using the rotary hoe and lawn mower are clearly visible as areas of low coherence. 247

7.36 Sample interferometric phase evaluated over the repeat pass image pair using a 2 by 7 pixel spatial estimation window. The resolution of the estimate is 0.57 m by 0.22 m with a pixel spacing of 0.343 m by 0.34 m. The modified regions of the scene appear as areas of random phase fluctuations. 248

7.37 Thin plate spline models describing the spatial variation of the mean backscatter power of the primary pass image subchip, indicated on the left and repeat pass image subchip indicated on the right. 249

7.38 Amplitude histograms for the 100 by 100 pixel primary and repeat pass image region. Superposed on the histograms are the theoretical amplitude distributions corresponding the Gaussian and K distributions. Also shown in the plots are the the likely ranges in variation (three standard deviations) of the histogram estimates of the PDFs that are to be expected assuming the theoretical PDFs are correct. 251

7.39 Phase histograms for the 100 by 100 pixel primary and repeat pass image region. Superposed on the histograms is the theoretical uniform phase probability density function. Also shown in the plots are the the likely ranges in variation (three standard deviations) of the histogram estimates of the PDF that are to be expected assuming the theoretical PDF is correct. 252

7.40 Histogram and theoretical density functions for the sample coherence evaluated of the primary and repeat pass image subchips. The histogram has been obtained using a 3 by 3 pixel sliding spatial estimation window. A true coherence of 0.62 and an ENL = 7 have been used to specify the theoretical sample coherence density function. Also shown is the likely range in variation (three standard deviations) of the histogram estimate of the PDF that is to be expected. 252

7.41 The image on the left hand side indicates sample estimates of the interferometric phase obtained using a 3 by 3 pixel sliding estimation window applied over the image subchip pair. On the right hand side is a thin plate spline fit to the sample estimates of the interferometric phase. 253

7.42 Theoretical and simulated ROC curves of the sample coherence and log likelihood change statistics applied to the pair of image subchips using the change scenario specified by the covariance matrices given in (7.27) and (7.28). 254

7.43 The images on the left hand side show, from top to bottom, the sample coherence and log likelihood change statistic maps evaluated over the subchip image pair using a 3 by 3 pixel spatial estimation window. The images on the right hand size show the detections obtained by applying a threshold to the corresponding change maps. The thresholds have been experimentally selected to give a false alarm rate of 0.018 . . . 255

7.44 Experimentally obtained histogram of the log likelihood change statistic obtained using a 3 by 3 sliding estimation window over the entire image subchip pair. The histogram is thus a mixture of values obtained over both changed and unchanged areas. Superimposed on the histogram are the theoretical density functions as well as the likely range in variation (three standard deviations) of the histogram estimate of the PDF for the changed and unchanged hypotheses. 256

A.1 Two way propagation delay extent of chirp echoes received from the near, centre and far edges of the illuminated scene. τ_0 is the two propagation delay to the scene centre, T is the chirp duration and $\tau_p = 2R_p/c$ is the two way propagation delay extent of the image swath. 266

List of Tables

2.1 Radar system parameters and imaging geometry used in repeat pass interferometry experiments conducted using the DSTO's Ingara airborne X-band SAR. 37
2.2 PFA image patch size limitations for a variety of azimuth resolutions. The patch size limitation arises from the plane wave propagation model used in the PFA. Processing larger patch sizes than those given produces imagery with a predominantly azimuthal defocus. 37
2.3 PF2 image patch size and resolution constraints arising from the dominant uncompensated cubic phase error. 41
2.4 Analytical expressions for the PF2 image patch size limitations arising from the dominant uncompensated quadratic phase. 42
2.5 Patch size limitations corresponding to the imaging scenarios of Table 2.1 arising from the uncompensated dominant quadratic phase in PF2 imagery. 42

3.1 Relationships between the collected signal history data, the range compressed signal history and the image domain data for both continuous and sample data domains. . . 61
3.2 Simulation parameters corresponding to an imaging scenario in which the SAR motion sensor is subject to an error in the measurement of the along track component of the platform velocity. 80

4.1 The Ingara X-Band airborne SAR system configuration parameters for the repeat pass interferometric change detection experiments conducted in 1999 and 2000. 123
4.2 Maximum and minimum repeat pass collection depression angles at which the primary and repeat pass acquisition apertures of support have no common overlapping intersection for primary collection depression angles of 15, 30 and 45 degrees. . . . 125

6.1 Hypothesis statements for the unchanged scene (null) hypothesis and the changed scene (alternative) hypothesis. 174

7.1 System parameters for the Ingara airborne SAR as configured for the repeat pass interferometry experiments. 203
7.2 Experimental SAR interferometric image pairs selected for change detection analysis. 206
7.3 Theoretical threshold levels and probability of detection values of the three change statistics corresponding to a false alarm probability of 0.05. Also shown is the experimentally set threshold required to achieve the same probability of false alarm and the measured probability of detection over the 20 m by 20 m modified area. 223

Glossary

Abbreviations

ATI	Along Track Interferometry
CAT	Computerized Axial Tomography
CBP	Convolution BackProjection
CCD	Coherent Change Detection
CCRS	Canadian Centre for Remote Sensing
CSA	Chirp Scaling Algorithm
DLR	German Aerospace Research Centre
DSTO	Defence Science and Technology Organisation
ENL	Equivalent Number of Looks
ERS	European Remote Sensing satellite
GLRT	Generalised Likelihood Ratio Test
GPS	Gobal Positioning System
InSAR	Interferometric Synthetic Aperture Radar
INU	Inertial Navigation Unit
JERS	Japanese Earth Resources Satellite
ML	Maximum Likelihood
MLE	Maximum Likelihood Estimate
PDF	Probability Density Function
PF2	Polar Format Algorithm with Post Filtering
PFA	Polar Format Algorithm
PGA	Phase Gradient Autofocus
PS	Permanent Scatterer
RCMC	Range Cell Migration Correction
RCS	Radar Cross Section
RMA	Range Migration Algorithm
RMS	Root Mean Square
ROC	Receiver Operating Characteristic
SAR	Synthetic Aperture Radar

SNR Signal to Noise Ratio

SIR Shuttle Imaging Radar

UHF Ultra High Frequency

UAV Unmanned Aerial Vehicle

VHF Very High Frequency

Symbols

$\Re\{z\}$	The real part of complex number z.
$\Im\{z\}$	The imaginary part of complex number z.
$E\{z\}$	Expected value of z.
$arg\{z\}$	Argument of complex number z.
$\otimes$	Convolution operator.
$\otimes_y$	Convolution operator with respect to variable y.
$Tr\{A\}$	Trace of matrix A.
β_0	tan of the depression angle at aperture centre.
β_1	tan of the depression angle at aperture centre of primary pass.
β_2	tan of the depression angle at aperture centre of repeat pass.
θ_T	True azimuth angle from scene centre to radar.
θ_m	Measured azimuth angle from scene centre to radar.
θ_e	Error in azimuth angle.
ψ_T	True depression angle from radar to scene centre.
ψ_m	Measured depression angle from radar to scene centre.
ψ_0	Depression angle from radar to scene centre at aperture centre.
ψ_e	Error in depression from radar to scene centre at aperture centre.
$\underline{v}_T$	True unit pointing vector from scene centre to radar.
$\underline{v}_m$	Measured unit pointing vector from scene centre to radar.
$\underline{\rho}$	Vector from scene centre to a scatterer in the scene.
k_r	Propagation range spatial frequency.
k_{bw}	Spatial frequency bandwidth.
k_{bw_x}	Azimuth spatial frequency bandwidth.
k_{bw_y}	Range spatial frequency bandwidth.
k_0	Radar centre spatial frequency.
k_{0_g}	Ground plane projection of radar centre spatial frequency.
k_x	Azimuth spatial frequency.
k_y	Range spatial frequency.
k_z	Height spatial frequency.

ρ_r	Image resolution.
ρ_x	Azimuth resolution.
ρ_y	Range resolution.
R_{bs_g}	Ground range offset at aperture centre.
R_T	True range from radar to scene centre.
R_m	Measured range from radar to scene centre.
R_e	Demodulation propagation range error.
G	Acquired signal history data.
$\mathcal{G}$	Range compressed signal history data.
g	Recovered SAR image.
α	Chirp rate.
ω_0	Radar centre frequency.
λ	Radar wavelength.
$h(x, y)$	Terrain height at location (x, y).
$w(x, y, z)$	Antenna illumination footprint.
$\gamma exp(j\Phi)$	Complex cross correlation coefficient.
P_d	Probability of detection.
P_{fa}	Probability of false alarm.
Q_0	Covariance matrix of null hypothesis.
Q_1	Covariance matrix of alternate hypothesis.
H_0	Null or no change scene hypothesis.
H_1	Alternative or scene change hypothesis.

Publications

1. M. Preiss, D. Gray and N. J. S. Stacy. The effect of polar format resampling on uncompensated motion phase errors and the phase gradient autofocus algorithm. In *Proceedings of the 2001 IEEE International Geoscience and Remote Sensing Symposium*, Volume 3, 9-13 July, 2001, pages 1442-1444.

2. M. Preiss, D. Gray and N. Stacy. Estimating Scene Coherence in a Change Detection Experiment Using the DSTO Ingara SAR. In *Proceedings of 4th European Conference on Synthetic Aperture Radar*, 4-6 June 2002, pages 225-228.

3. M. Preiss, D. Gray and N. Stacy. Space Variant Filtering of Polar Format Spotlight SAR Images for Wavefront Curvature Correlation and Interferometric Processing. In *Proceedings of the 2002 IEEE International Geoscience and Remote Sensing Symposium.* Volume 1, 24-28 June 2002, pages 179-181.

4. M. Preiss, D. Gray and N. Stacy. A Change Detection Statistic for Repeat Pass Interferometric SAR. In *Proceedings of the 2003 IEEE International Conference on Acoustics, Speech and Signal Processing*, Volume 5, pages 241-244.

5. M. Preiss, D. Gray and N. Stacy. A Change Detection Technique for Repeat Pass Interferometric SAR. In *Proceedings of the 2003 IEEE International Geoscience and Remote Sensing Symposium.* Volume 2, 21-25 July 2003, pages 938-940.

6. M. Preiss, D. Gray and N. Stacy, Change Detection in Repeat Pass Interferometric Synthetic Aperture Radar. In *Proceedings of the 2003 International Conference on Radar*, 3-5 September 2003, Adelaide, Australia.

7. M. Preiss, D. Gray and N. Stacy, A Log Likelihood Statistic for Change Detection in Repeat Pass Interferometric SAR. In *Proceedings of 5th European Conference on Synthetic Aperture Radar*, 25-27 May 2004.

Chapter 1

Introduction

Since its inception in the 1950s, Synthetic Aperture Radar (SAR) has matured into an extremely capable standoff imaging technology. As SAR is an active sensor system, usually operating in the microwave region of the electromagnetic spectrum, it can operate in almost all weather, day or night, overcoming many of the shortcomings of other passive imaging technologies such as optical and infra-red imaging systems.

An important parameter influencing the interpretability and information content of an image of a scene is the image resolution. In the absence of coherent processing, image resolution is determined by the standoff range and the antenna (or aperture) size measured in terms of the sensor wavelength. Passive sensors, working in the visible and infra-red bands can achieve very fine resolution imagery from standoff ranges of hundreds of kilometres using only modest apertures owing to the small operating wavelength of these sensors. The acquisition of fine resolution imagery using "real" aperture radars operating in the microwave band on the other hand, requires exceedingly large antennas which are impractical for airborne or spaceborne platforms. Synthetic aperture radar overcomes this limitation by synthesizing a large antenna through the coherent processing of range echo data acquired as the radar platform moves past the scene. Through aperture synthesis a fine resolution, two dimensional, plan view of the scene's complex radar backscatter can be generated. Furthermore the coherent processing generates an image with azimuthal resolution that is independent of range, thus the azimuth resolution at near range is the same as that at far range in the image.

Aside from the fine resolution capabilities afforded by aperture synthesis, the coherent processing of range echo data also transduces an amplitude and phase at each resolution cell in the SAR image. The complex nature of SAR imagery permits image pairs to be processed interferometrically to deduce further information about the geophysical properties of the scene. In particular, the interferometric processing of image pairs acquired with slightly different imaging geometries can be used to deduce terrain topography [Gra74] while repeat pass interferometry may be used for target detection and scene classification [Yoc98] and also the detection of subtle scene changes [JWE+96].

The fine resolution, broad area coverage afforded by SAR, coupled with its unique interferometric capabilities make it an extremely useful tool across a broad range of civilian and military applications. SARs are commonly used for target detection, classification and tracking in military applications and many systems are in operation on a number of different platforms including the U2 [Wea98], and Joint STARS [Hay90] as well as Unmanned Aerial Vehicles (UAVs) such as Global Hawk [Off01]. SAR has also proven invaluable in many remote sensing applications such as forest biomass measurements in relation to global warming research, topographic and land use mapping and for the monitoring of natural disasters such as earthquakes, volcanoes and flooding. In these applications spaceborne SARs offer unprecedented, sustained global coverage and resolution. Indeed the growth in the availability of high quality satellite SAR imagery appears set to continue with the recent launch

of ENIVSAT [RZT+03] by the European Space Agency, ESA, as well as the pending launches of TERRASAR [BBM+03] (Germany), RADARSAT2 [BB02], (Canada), ALOS [KI00] (Japan), and COSMO-SKYMED [CSVM98] (Italy) in the coming years. There is also a plethora of airborne systems operating as commercial enterprises as well as research and development testbeds for fielding new technologies and testing new algorithms.

An important application of SAR is the detection of temporal changes in a scene. Change detection has important military applications for the automated cueing of image analysts to areas of activity in a scene and has also proven useful in remote sensing applications such as monitoring crops, soil and vegetation moisture content, glaciers, landslides and sea-ice tracking. SARs are particularly well suited to this task as multi-date, consistent high quality imagery can be readily obtained. Furthermore the precise flight track measurements necessary for synthetic aperture formation allows imagery to be acquired with good radiometric and geometric calibration, as well as good geolocation accuracy.

While change detection techniques using passive remotely sensed data have been extensively explored [Sin89], the unique characteristics of SAR imagery require careful consideration in formulating appropriate change statistics. In particular, the amplitude of a complex SAR image typically exhibits random fluctuations, commonly called speckle, while the phase may vary across the scene in a completely random way. Two forms of change detection may therefore be considered in the context of SAR imaging. Incoherent change detection based on the image amplitude and coherent change detection based on changes in the amplitude and phase of an Interferometric SAR (InSAR) image pair. Incoherent change detection is used to identify changes in the mean backscatter power of the scene by examining the image intensity (amplitude squared). Due to the random speckle fluctuations however, the image intensity must be averaged over a local area to obtain an accurate measure of the mean backscatter power and so reliably detect changes in the backscatter between images. The speckle noise however is indicative of the sub-resolution cell scattering structure. In particular any change in the relative arrangement of the scatterers within a resolution cell due to scene disturbances will cause a change in the speckle pattern as well as a change in the transduced phase. This may be detected by using coherent change detection in which the interferometric decorrelation of the complex reflectivity is used as the change statistic. Coherent change detection thus has the potential to detect very subtle scene changes that may not be identified using intensity based change detection. Coherent change detection however, requires the imagery to be acquired and processed interferometrically which necessitates very careful control of offsets between the imaging geometries as well as additional processing complexity.

In this thesis the problem of the detection of subtle, fine scale scene disturbances using interferometrically processed data will be addressed. In the following sections of this chapter the issues regarding the formation of very fine resolution imagery suitable for interferometry and the design of appropriate change statistics for coherent change detection will be described to motivate the specific research undertaken in this thesis.

1.1 SAR Image Formation

SAR transduces a fine resolution image of the complex radar backscatter of a scene using a two step process of data acquisition followed by image formation. Fine range resolution is achieved by using a wide bandwidth transmit waveform and applying pulse compression techniques on the received echoes. Indeed using stepped frequency waveforms transmit bandwidths of 1.8 GHz at X-band (fractional bandwidth of approximately 18 percent) have been demonstrated with associated range resolutions of 10 cm [BE03]. Fine azimuth resolution on the other hand, is achieved by coherently processing a series of range echoes acquired as the radar moves past the scene to, in effect,

synthesize a large aperture. In the case of airborne X-band SARs at standoff ranges of 20 km synthetic apertures of the order of 3 km (collection angle variation of approximately 10 degrees) can be readily produced yielding azimuthal resolutions of the order of decimetres. The signal processing required to achieve the aperture synthesis is computationally intensive and requires the implementation of spatially varying, two dimensional matched filters, matched to the transduced range echo response of each scattering location in the scene. While the theoretical aspects of SAR image formation are well understood, research into the design of efficient image formation processors for focusing wide-band, wide-angle range echo data remains an active area of research. Some of the key issues being addressed in the literature include:

- **Image formation with large fractional bandwidths and wide-angle collections.**
  Image resolution remains a key parameter in the interpretation of SAR imagery and in applications such as target detection and classification. Also the robust, reliable detection of fine scale scene changes requires image resolutions commensurate with the size of the scene change. Achieving fine range and azimuth resolution however, requires large transmit signal bandwidths and long synthetic apertures. The generation of large fractional bandwidths can be problematic, particularly at small wavelengths such as at X-band, and requires careful calibration as well as wideband transmitters, receivers, antennas and high sample rates. Wide angle collections on the other hand can be readily achieved using spotlight SAR in which the antenna is continually steered onto the imaged scene. Coherent processing over approximately 10 degrees at X-band gives a fractional doppler bandwidth of 20 percent and corresponding azimuthal resolutions of 10 cm. In these imaging scenarios narrow-band and small collection angle approximations, commonly employed in efficient frequency domain focusing algorithms are no longer appropriate to describe the phase relationship between the acquired range echo data. Furthermore, in these scenarios deviations and drifts of the sensor platform from the desired flight track can be significant and must be accommodated in the focusing algorithm. The design of efficient focusing algorithms for these systems is the subject of ongoing research.

- **Array Calibration.**
  The coherent processing of data acquired over a synthetic aperture requires measurements of the radar location at each transmit/receive point along the aperture. The required tolerance on the radar location measurements is of the order of a fraction of a wavelength and is usually provided by Inertial Navigation Units (INU) and GPS units on board the sensor platform. For the processing of extended collection apertures however, these systems may not provide the required accuracy and are often subject to significant drifts over the longer apertures. These measurement errors manifest in the range echo data as phase errors that cause distortion and defocus in the recovered imagery. Automatic data driven focusing algorithms for the estimation and removal of these phase errors are thus vitally important for the recovery of high quality fine resolution imagery. The performance of these algorithms however, is crucially dependent on the models used to describe the nature of the phase error function, its variation across the aperture as well as the nature of the imaged scene. Generally the phase error models used by the various autofocus algorithms employ narrow-band, small angle approximations to simplify the autofocus estimation and compensation steps. These approximations however begin to break down in wide-band and wide-angle acquisitions and so the phase models and autofocus algorithms need to be re-assessed to ensure well focused imagery is recovered in these imaging scenarios.

1.2 SAR Interferometry

As SAR is a coherent imaging system the scene backscatter, as transduced by the radar, has an amplitude and a phase that are related to the spatial distribution of scatterers in the scene, their structural and dielectric properties as well as the imaging geometry. In SAR interferometry further information about the geophysical properties of the scene are obtained by examining the amplitude and phase differences between two or more complex valued SAR images. The additional information available through the interferometric processing of an image pair is determined by the relationship between the imaging geometries used to acquire the images and also any temporal separation between the acquisitions. Where an image pair is acquired such that there is an across and/or above track offset between the synthetic apertures the phase difference between the image pair is related to the terrain topography and the interferometric baseline between the acquisition geometries. The terrain height mapping application of SAR interferometry was first demonstrated by Graham in 1974 however, it wasn't until the launch of ERS-1 by the European Space Agency in 1991 that suitable high quality data sets became widely available. This spurred intensive research into understanding the information content of a interferometric SAR image pair and a subsequent maturing of the technology and processing algorithms.

Ideally an interferometric image pair acquired for terrain mapping purposes is obtained using two receive antennas placed on the same sensor platform located so as to achieve the required baseline offset. Alternatively a single antenna SAR sensor may be flown in a repeat pass configuration where the flight tracks are defined to achieve the required baseline offset. In the repeat pass interferometer however, amplitude and phase differences between the image pair may arise from disturbances in the scene which introduce noise and bias into the measurement of the terrain height component of the interferometric phase. Indeed the dependence of the interferometric observables on the temporal baseline in the acquisitions of a repeat pass interferometer may be used to track scene changes that occur over time scales ranging from hours to days and even years.

In differential SAR interferometry and the related field of permanent scatterer analysis the movement of large scale regions of the scene in a preferred direction are quantified by changes in the interferometric phase over time (after removal of any terrain height phase component). Such scene displacements typically arise through tectonic plate activity or land subsidence due to mining, pumping of ground water or oil depletion. Alternatively where a scene disturbance has caused random displacements of the scattering contributions in a scene the transduced interferometric amplitude and phase changes are random and so the scene disturbance may be detected as a localised area of scene decorrelation. In the case of imaging using small wavelength radars such as C and X band radars, man-made disturbances, such as vehicle tracks across a field, can cause significant scatterer displacements on the scale of the radar wavelength which may be detected as areas of significant decorrelation. While the potential of interferometric change detection for detecting subtle man-made scene changes has been known since at least the mid 1970s only a few applications of the technique have been reported in the literature. In [CR98] Corr used coherent change detection to detect vehicle tracks in images acquired from the ERS satellite with a 1 day revisit period. Interferometric change detection processing of 1 m resolution airborne X-band SAR imagery was also employed in [JWE+96] to identify changes in a earthworks site.

While the techniques for interferometric processing has matured considerably in the past decade a number of key issues, especially in relation to the detection of fine scale scene changes, remain:

- **The inversion of the interferometric observables into useful geophysical parameters.** The transduced amplitude and phase in a SAR resolution cell is determined by many physical and geometric parameters of the imaged scene. Inversion of the transduced image pair to estimate a particular geophysical property of the scene thus suffers from high ambiguity and

multiple observations over time, frequency, polarisation and incidence angle are required to assist in the inversion. In SAR interferometry multiple observations are made at different times and/or different observation angles to infer further information about the scene. The recovery of this information however, requires specific models to describe the scene properties to obtain a meaningful solution. For example, in the terrain mapping application of SAR interferometry the scene is taken to be a two dimensional surface function reflectivity modulated by a terrain height. The interferometric phase between a SAR image pair can subsequently be shown to be a measure of this height function.

In the context of interferometric change detection very simple models describing a scene in a repeat pass collection have been proposed by Zebker [ZV92] and Hagberg [HUA95]. In these models the scene backscatter is decomposed into stable scattering contributions, that remain unchanged between collections and unstable scattering contributions that are subject to independent random displacements between collections. Using these models a relationship between the scene decorrelation, the variance of the random displacement, the incidence angle and the radar wavelength can be established. Regions of the scene that exhibit low correlation have relatively little stable scattering contributions and thus may be identified as areas of scene change. These models however remain speculative and have not been verified experimentally. In particular the specific form of the random displacement was chosen arbitrarily without consideration of what the sources of the physical change might be. Also, while the mutually independent scatterer displacement assumption facilitates mathematical analysis it is not necessarily an accurate assumption given the physical structure of scene scatterers and the possible sources of scene change, for example wind. Further elaboration of these models to describe the relationship between the changes in the scattering mechanisms and the interferometric observables can potentially provide a deeper understanding of the physical mechanisms that produce decorrelation and lead to improved change statistics.

- **Sources of decorrelation in an interferometric image pair.**
  Coherent change detection is based on identifying regions of a scene in which man-made scene disturbances have caused a change in the complex backscattering characteristics resulting in a loss in the scene correlation. The scene decorrelation however is not directly measured by the SAR as there are other sources of decorrelation contributing to the transduced image pair. These include decorrelation due to the presence of receiver noise in the transduced imagery, relative mismatch between the SAR acquisitions and image formation processors used to generate the image pair as well as temporal decorrelation due to other physical and environmental effects. These effects reduce the overall correlation of the transduced image pair making it difficult to distinguish between the changed and unchanged regions of the scene.

  An analysis of these sources of decorrelation in a SAR image pair has been conducted in the literature [JB94], [ZV92]. This analysis however has generally been concerned with the interferometric processing of modest resolution stripmap SAR imagery for applications such as terrain mapping, scene classification or the detection of broad scale scene changes. In these applications significant spatial averaging can be used to obtain reliable estimates of the interferometric observables. For example, in the terrain mapping application the terrain height is usually assumed to be a slowly varying function hence only modest resolution imagery is required and large spatial estimation windows may be used. As a consequence only first order effects of the decorrelation sources have generally been considered in the analysis. For the detection of subtle, fine-scale scene changes in fine resolution imagery the extent to which spatial averaging can be conducted is limited. Furthermore narrow-band, small aperture approximations in modelling the acquisition and image formation processors are no longer valid.

The analysis therefore needs to be re-examined to quantify the higher order effects and devise techniques, where appropriate, to mitigate the more serious deleterious decorrelation effects.

- **Design of appropriate change statistics.**
  Change detection using repeat pass complex interferometric SAR imagery is a challenging problem due to the unique statistical properties of the complex image pair and the manner in which the interaction of the scene disturbances and the scene scattering mechanisms manifest in the observed image amplitude and phase. The change detection techniques proposed in the literature are based on simple estimators of key statistical parameters of the image pairs. In particular, intensity based change detection identifies changes in the mean backscatter power of the scene by computing the ratio of the local mean pixel intensity of the two images. Coherent change detection using the complex cross correlation coefficient on the other hand identifies changes in the coherent combination of scattering contributions in a resolution cell by computing the spatially averaged sample cross correlation coefficient. The statistical properties of these sample statistics have been extensively studied in the context of speckle filtering and the terrain mapping application of SAR interferometry [Zel76], [PMIM76], [Lee83], [FSSH82], [QR95], [TBQ95] and [TL96]. In these applications the density function and the moments of the distribution provide useful information about the quality of the appropriate sample parameter estimates. In the context of change detection, and in particular automated change detection however, a more useful measure of performance of the change statistics that needs to be evaluated, is the probability of detection and false alarm as a function of the decision threshold and the sample size. This allows theoretical Receiver Operating Characteristic (ROC) curves to be generated so that the detection performance of the change statistics may be readily assessed and comparisons made. In applications where change detection analysis is to be carried out on large volumes of image data, the automated detection and subsequent cross cueing of analysts to areas of scene changes is cruical to managing the large data sets. The use of change statistics that achieve low false alarm rates while maintaining good detection performance are vital to achieving reliable and robust performance in such automated systems.

  The mean backscatter power and cross channel correlation coefficient are independent statistical parameters of a joint SAR image pair and hence areas of change identified by these two change statistics do not always agree [RvZ93]. As a consequence both statistics should be used to provide a more complete characterisation of scene changes. The question as to how these change statistics may be combined in an optimal way however has not been addressed. Furthermore, while the change techniques proposed in the literature have focused on identifying changes in certain statistical parameters alternative more rigorous approaches based on the framework of statistical hypothesis testing have not been explored. In these approaches change detection algorithms are developed using statistical models describing the imaged scene under a changed and unchanged hypothesis. Decision statistics may subsequently be formulated which maximise the probability of detection for a specified probability of false alarm and facilitate the design of reliable and robust algorithms for the automated detection of scene changes.

1.3 Thesis Outline and Contributions

This thesis investigates techniques for the detection of fine scale scene changes from SAR imagery acquired using repeat pass SAR interferometry.

The robust, reliable detection of fine scale scene changes requires imagery with resolution commensurate with the spatial size of the scene changes. The thesis thus firstly addresses aspects of image formation and autofocus for the processing of wide-angle spotlight SAR range echo data. A

rigorous analysis of the spotlight SAR acquisition function for extended aperture collections leads to the development of an efficient image formation processor yielding ground plane imagery suitable for subsequent interferometric processing. The analysis also quantifies the impact of measurement errors in the radar location over the synthetic aperture. It is shown that for wide-angle, extended aperture collections the measurement errors manifest as a spatially varying, two dimensional phase error function modulating the acquired range echo data.

Interferometric processing of repeat pass SAR imagery for change detection applications requires strict control of the imaging geometries used in the primary and repeat pass collections. It also requires careful consideration and compensation of the sources of acquisition and processing mismatch in the image pairs. These issues are addressed in this thesis through the design of an interferometric processor for the processing of wide-angle spotlight mode SAR. The processor is demonstrated using experimental repeat pass interferometric data acquired with the DSTO Ingara X-band airborne SAR.

Finally the problem of the detection of fine scale changes in a scene using fine resolution repeat pass interferometric spotlight SAR data is addressed. In particular the change detection problem is expressed in a hypothesis testing framework leading to the formulation of a new log likelihood ratio change statistic. The detection performance of this statistic is shown, via theoretical analysis as well as extensive simulations and application to experimental data, to be superior to the commonly used sample average intensity ratio and sample correlation coefficient change statistics. The development of the log likelihood change statistic is thus an important step in the design of an automated change detection algorithm.

The image formation processor, autofocus phase error model, interferometric processor and log likelihood change statistics are extensively tested using experimental repeat pass interferometric data containing various ground truthed scene changes acquired with the DSTO Ingara X-band airborne SAR.

The main contributions of this thesis are:

- **A rigorous analysis of the SAR signal history data acquired in wide-angle spotlight SAR collections including the effects of measurement errors in the platform location over the synthetic aperture. This leads to the development of an efficient image formation processor for focusing wide-angle spotlight SAR data yielding fine resolution imagery suitable for subsequent interferometric processing. A modification to the Phase Gradient Autofocus (PGA) algorithm is also proposed for improving the image focus in the presence of an error in the measurement of the along track velocity of the radar. This modification accounts for a subtle, higher order, range dependent image defocus that manifests in wide-angle spotlight SAR collections.**

- **The proposal of a new log likelihood change statistic for detecting man-made scene changes in repeat pass interferometric SAR imagery. This change statistic gives a single statistic encoding both coherence and mean backscatter power changes for discriminating between the unchanged and changed regions of a scene. Through theoretical analysis, extensive simulation and processing of experimental data it is demonstrated that the new statistic shows a significant improvement in detection performance over both the mean backscatter and sample coherence change statistics.**

1.3.1 Chapter Outlines

In Chapter 2 the problem of the efficient processing of wide-band, wide-angle spotlight SAR range echo data is addressed. A full three dimensional imaging geometry is considered to analyse the point target response in the acquired deramp demodulated range echo data and to derive the spotlight SAR acquisition function. The Polar Format Algorithm (PFA) is derived by applying a first order Taylor series expansion to the SAR acquisition function. This establishes a framework for the description of the acquired range echo data in terms of the scene's spatial frequency domain representation and indicates that an image may be recovered by applying an inverse Fourier transform to the deramp demodulated echo data. By considering the higher order terms in the Taylor series expansion for the SAR acquisition function it is shown that the PFA image is corrupted by distortion and defocus that varies spatially across the image. These deleterious image domain effects become increasingly significant in wide-band, wide-angle, near field imaging and must be adequately compensated for to achieve suitably focused fine resolution imagery. A spatially varying image domain filter, to be applied to the PFA image, is proposed for correcting the dominant second order defocus effects to generate a well focused ground plane image suitable for interferometric processing [PGS02b]. Use of the ground plane as the image focus plane is preferable when there is significant out-of-plane motion during the aperture formation [JWE+96], [Pay04]. The proposed filter is similar to that given by Jakowatz and Doren [JWTD97], [DJWT97] however the filter presented here specifically uses the full three dimensional imaging geometry formulation to obtain a filter appropriate for the formation of a ground plane image. Image pairs can thus be formed in a common image plane, namely the ground plane, for subsequent interferometric processing. Resolution and patch size limitations of the new filter are derived and verified through simulations of the point spread function of the new image formation algorithm. The technique is also applied to experimental data acquired with the DSTO Ingara X-band SAR to generate imagery with a resolution of 0.58 m in range and 0.15 m in azimuth.

The main contributions in this chapter are the rigorous analysis of the SAR acquisition function and the derivation of image resolution and patch size constraints. Another contribution is the development of an image formation processor for generating fine resolution ground plane imagery using very wide-angle spotlight SAR acquisitions.

In Chapter 3 a detailed analysis of the form of the SAR acquisition function in the presence of errors in the measurement of the radar platform location is presented. Using the description of the acquired range echo data in terms of the scene's spatial frequency domain representation established in Chapter 2 the image domain effects of measurement errors are considered. It is shown that, for the case of wide-angle collections, the measurement errors manifest as a spatially varying, two dimensional phase error function. In the image recovered from the deramp demodulated echo data the phase error function manifests as a distortion and defocus of the SAR point spread function and varies as a function of scattering location. For narrow-band, small-angle collections it is shown that the image domain defocus reduces to the conventional azimuthal only defocus model that is independent of scattering location. For increasing collection apertures however, subtle higher order effects become increasingly significant and the full spatially varying, two dimensional nature of the phase error function begins to manifest. The form of the phase error function that arises due to an error in the measurement of the along track velocity of the radar platform is derived and its impact on the Phase Gradient Autofocus (PGA) algorithm is considered. A simple range cell migration step is proposed for compensating for the range dependence of the phase error function that manifests in wide-angle collections [PGS01].

The main contributions in this chapter are the detailed analysis of the phase error function in the SAR acquisition function that arise due to the errors in the measurement of the radar platform location over the collection aperture. It is shown that for wide-angle collections subtle, higher order effects, become increasingly significant and the phase error manifests as a spatially varying, two dimensional image domain defocus. The simple case of an along track velocity error is analysed and a modification of the PGA is proposed to account for the dominant components of the image domain defocus that can arise in wide-angle collections.

In Chapter 4 the principles and techniques for the interferometric processing of wide-angle fine resolution spotlight mode are presented. This forms the theoretical basis for the subsequent chapters on interferometric processing for change detection. A statistical description of a joint interferometric image pair is given in terms of spotlight mode SAR acquisition and image formation processor developed in Chapter 2 and Hagberg's [HUA95] scene model in which the scene consists of an ensemble of stable and unstable scatterers. In this formulation the transduced image cross correlation coefficient may be decomposed into a component dependent on the relative mismatch between the acquisition and image formation processor of the two images and a scene correlation component determined by the relative contributions of the stable and unstable scatterers. Details of an experimental interferometric processor developed to process experimental repeat pass interferometric SAR data acquired with the DSTO Ingara X-band SAR are described. A sample cross correlation coefficient estimate map obtained from one of the Ingara repeat pass interferometric experiments is presented in which track like disturbances, possibly due to the movement of grazing animals, are observed [PGS02a]. These results highlight the sensitivity of the coherent change detection technique.

The main contribution in this chapter is a statistical description of a joint interferometric image pair in terms of the SAR acquisition and image formation processor developed in Chapter 2 and Hagberg's scene model [HUA95] in which the scene is modelled as consisting of an ensemble of stable and unstable scatterers. A sample cross correlation coefficient map obtained from an experimental repeat pass image is presented in which track like disturbances, possibly due to the movement of animals, are observed.

In Chapter 5 a review of change detection techniques based on changes in the mean backscatter power and a loss in scene cross correlation is presented. A modified form of the sample average image intensity ratio originally proposed by Touzi [TLB88] for SAR edge detection is considered for identifying changes in the mean backscatter power while the sample image coherence is used to detect regions of low scene correlation. The performance of these change statistics is quantified and compared by evaluating ROC curves describing the probability of detection and false alarm for the change statistics as a function of the detection threshold and the size of the estimation window. It is shown that for the detection of fine scale scene changes the change statistics generally suffer from high false alarm rates thereby limiting their usefulness in automated change detection algorithms. A number of alternative estimators of the scene cross correlation are also considered as change statistics. However such estimators, which do not require the full complex primary and repeat pass image data, are shown to suffer from a degraded detection performance. The change statistics for the experimental repeat pass image pair previously presented in Chapter 4 are used to assess the detectability of the track like disturbances under each change statistic.

The main contribution in this chapter is a comparison of the detection performance of a number of change statistics, suitable for detecting fine scale scene changes, proposed in the literature.

In Chapter 6 the change detection problem is formulated in an hypothesis testing framework and a new generalised log likelihood change statistic is proposed for discriminating between the changed and unchanged regions of the scene [PGS03a], [PGS03b]. In the hypothesis testing formulation models describing the scene under the null (no change) hypothesis and alternate (changed hypothesis) are postulated and are defined in terms of a number of key parameters that need to be estimated from the observed imagery. The theoretical performance of a clairvoyant log likelihood detector, obtained assuming perfect knowledge of the unknown parameters, is derived and shows significant improvement in the detection performance over both the mean backscatter power ratio and sample coherence change statistics. The log likelihood change statistic thus offers the potential for significant improvements in the reliability of automated change detection algorithms. The performance improvement of the new change statistic is verified by extensive simulations under a variety of scene change scenarios. While the clairvoyant log likelihood detector is unrealisable, it is an optimal Neyman-Pearson detector and gives an upper bound on the detection performance of any practical detector. The generalised log likelihood detector is one such practical implementation in which the unknown model parameters are replaced with their maximum likelihood estimates obtained from the observed data.

The main contribution in this chapter is the development of a new generalised log likelihood change statistic that encodes in a single statistic, changes in the mean backscatter power as well as a loss in correlation. The theoretical upper bound on the detection performance has been derived by considering a clairvoyant detector and shows a significant improvement in detection performance over both the mean backscatter power ratio and sample coherence change statistics.

In Chapter 7 Touzi's modified mean backscatter power ratio, the sample cross correlation coefficient and the new generalised log likelihood change statistic developed in Chapter 6 are applied to experimental repeat pass interferometry experiments conducted with the DSTO Ingara airborne X-band SAR. The experimental data was acquired with a variety of ground truthed scene changes carried out in the interval between repeat pass collections. The repeat pass image interferometric image pairs were processed using the image formation processor developed in Chapter 2 and the interferometric processor outlined in Chapter 4. For each experimental change scenario considered the superior detection performance of the log likelihood change statistic is demonstrated [PGS03a], [PGS03c]. Experimentally obtained values for the probability of detection and probability of false alarm for the three statistics are in broad agreement with the theoretical values obtained in Chapters 5 and 6.

The main contribution in this chapter is the experimental demonstration of the new generalised log likelihood change statistic proposed in Chapter 6. A number of different experimental change detection scenarios are considered and in each case the superior detection performance of the log likelihood change statistic is demonstrated.

Chapter 8 provides a summary of the thesis and conclusions are drawn. Areas for future research are also discussed.

Chapter 2

Spotlight SAR Image Formation

2.1 Introduction

Synthetic Aperture Radar (SAR) imaging is a two step process of coherent data acquisition and subsequent coherent processing of a series of radar range echoes to recover a fine resolution image of a scene. The resolution of the focused SAR imagery is an important parameter in determining the interpretability of the imagery and the quality of the information that may be extracted [OQ98]. In particular the performance of post processing applications such as target detection, classification [NOW99] as well as interferometry applications such as change detection [CR98], [JWE+96] are all sensitive to the image resolution.

The achievable range and azimuth resolutions of a SAR are limited by the collection constraints of the transmit waveform bandwidth and the angular extent of the collection aperture respectively. In spotlight SAR, by continually steering the antenna onto a single focus point in the scene as the radar platform moves past, range echo data can be obtained over an extended collection aperture. This permits the formation of very fine azimuth resolution imagery at the expense of broad area coverage. While the theoretical aspects of image formation are well understood, the efficient processing of wide-band, wide-angle spotlight SAR range echo data to generate very fine resolution imagery is still challenging. In particular the spatially varying, two dimensional nature of the focusing correlation kernels makes the implementation of efficient real time on-board processors problematic. In this chapter an efficient wide-angle spotlight SAR image formation processor designed to generate fine resolution imagery suitable for subsequent interferometric processing for an airborne SAR is considered.

In Section 2.2 the form of the acquired spotlight range echo data is analysed and the mechanisms by which the transduced range echo response may be resolved into a fine resolution image of the scene reflectivity are discussed. This leads to a review of image formation algorithms for processing spotlight SAR data and their ability to generate imagery suitable for subsequent interferometric processing. In Section 2.3 the Polar Format Algorithm (PFA) for focusing spotlight SAR phase history data is derived by examining the point target signal history. The analytical framework developed in Section 2.3 allows the limitations of the PFA for processing wide-angle spotlight SAR collections to be analysed. Section 2.4 considers a full three dimensional imaging geometry to derive a post PFA image domain filter that overcomes the PFA limitations. In particular, the proposed filter is used to form a ground plane image that is suitable for subsequent interferometric processing. The filter is similar to that used in the PF2 algorithm proposed in [JWTD97] and [DJWT97] however, the present formulation specifically allows the formation of a ground plane image. Image resolution and patch size limitations for the modified form of the PF2 algorithm are obtained and simulation results illustrating the point spread function of the PFA and the modified PF2 algorithm are given in Section 2.5.

Finally, in Section 2.6, the PFA post filtering technique is applied to real SAR data collected with the DSTO X-band Ingara airborne SAR.

2.2 Background

Synthetic aperture radar transduces a fine resolution image of the complex radar backscatter of a scene using a two step process of data acquisition followed by image formation. Fine range resolution is readily achieved using large bandwidth transmit pulses and pulse compression techniques. Indeed airborne radars with 1.8 GHz transmit bandwidths have been demonstrated with corresponding range resolutions of 0.1 m [BE03], [CDF03]. The transduced range echos however contain contributions from all scatterers illuminated by the antenna footprint. The range echo data thus represents an integrated scene response and the ability to resolve scatterers displaced in azimuth, without further processing, is limited by the size of the antenna footprint as determined by the antenna beamwidth and the slant range to the scene. Finer azimuth resolution may be achieved by using a spatially longer antenna to obtain a narrower azimuth beamwidth. For typical SAR standoff ranges however, the antenna size required to achieve azimuth resolutions commensurate with commonly achieved range resolutions is generally impractical.

In synthetic aperture radar fine azimuth resolution is achieved using an antenna of modest size by coherently processing a series of range echos obtained as the radar moves past the scene. The coherent processing combines the information from the series of range echoes to, in effect, synthesize a large spatial array. This permits the inversion of the integrated scene response into a fine resolution two dimensional estimate of the complex reflectivity of the scene. In spotlight SAR, in which the antenna is continually steered onto the scene as the radar moves past, very large spatial arrays may be synthesized to achieve very fine azimuth resolution imagery over a limited spatial area.

The image formation process, whereby the integrated scene response is inverted, relies on the accurate measurement of fine scale structure in the amplitude and phase response of the transduced range echoes over the coherent processing interval. In particular, through accurate measurements of the radar platform location and an appropriate model describing the propagating electromagnetic waves, a matched filter may be designed to resolve the aggregated scene response into a fine azimuth resolution image. The difficulty in designing an algorithm that applies the matched filter in an efficient and timely manner across the entire scene arises because the filter must be both two dimensional and vary spatially over the scene.

In the following section the spotlight SAR data acquisition process will be discussed and the two dimensional, spatially varying nature of the point target response will be quantified. This leads into a review of image formation algorithms that have been proposed in the literature to efficiently apply the matched filtering required to recover a focused image. This is followed by a discussion of the imaging requirements for conducting repeat pass interferometric change detection.

2.2.1 The Image Formation Problem

In the typical airborne spotlight SAR data acquisition geometry the SAR antenna is steered, nominally perpendicular to the flight path, so as to continually illuminate a ground patch using the side looking geometry shown in Figure 2.1. While moving past the scene the SAR periodically transmits a wide bandwidth electromagnetic pulse $p(t)$ of duration T at the radar centre frequency ω_0. The transmitted signal may be represented by,

$$s(t) = \Re\left\{p(t)exp(j\omega_0 t)\right\}, \tag{2.1}$$

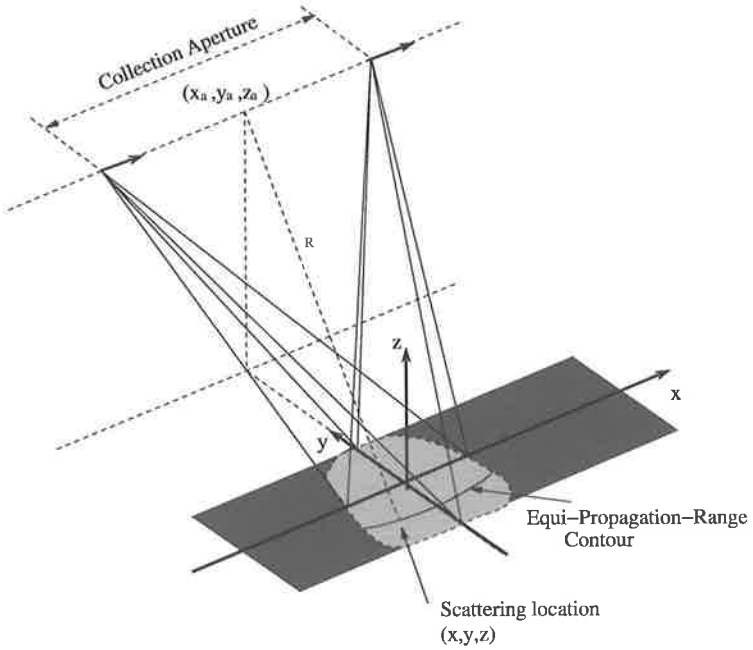


Figure 2.1: A typical spotlight SAR imaging geometry. As the radar moves past the scene the antenna is steered so as to continually illuminate the same ground patch. This allows the collection of range echo data over an extended collection aperture for processing into an image with fine azimuth resolution. The coordinates (x_a, y_a, z_a) give the radar location at a particular transmit/receive point and (x, y, z) is some scattering location in the scene.

where $s(t)$ is zero outside the interval $-T/2 \leq t \leq T/2$. A small portion of the transmitted energy, incident on the scene, is re-radiated back towards the radar. By employing an assumption of linearity, the echo received by the radar at delay τ after transmission may be considered to be the superposition of all scattering contributions lying at equi-propagation-range $R = \frac{\tau c}{2}$ from the radar, where c is the speed of light in free space. The scene reflectivity observed by the radar at range delay τ may thus be written as,

$$f(\tau) = \int_c w(x, y, z) r(x, y, z) dx dy dz, \tag{2.2}$$

where $r(x, y, z)$ is the scene complex backscatter and $w(x, y, z)$ is the antenna illumination footprint which shall be taken to be,

$$w(x, y, z) = \begin{cases} 1, & \text{Inside the antenna footprint,} \\ 0, & \text{Outside the antenna footprint.} \end{cases} \tag{2.3}$$

The range of values of τ over which $f(\tau)$ is non-zero is defined by the antenna footprint. Defining R_1 and R_2 to be the propagation ranges from the radar to the near and far edge of the illuminated scene respectively then τ takes values in the range $2R_1/c \leq \tau \leq 2R_2/c$. The integration in (2.2) is over a contour C given by the intersection of the spherically propagating transmit electromagnetic wave and the surface scattering layer such that,

$$\tau = \frac{2}{c}\sqrt{(x - x_a)^2 + (y - y_a)^2 + (z - z_a)^2}. \tag{2.4}$$

The coordinate (x_a, y_z, z_a) is the location of the antenna at the transmit/receive point and (x, y, z) is a scattering location in the scene. In this description the start/stop approximation to SAR imaging is used wherein the radar is assumed to be stationary over the transmit/receive interval.

Since the received echoes consist of a superposition of scattering contributions, with each contribution being a delayed version of the transmit waveform $s(t)$, the received range echo may be written as,

$$g_{rx}(t) = \int_{\tau_1}^{\tau_2} f(\tau)s(t-\tau)d\tau, \tag{2.5}$$

where $\tau_1 = 2R_1/c$ and $\tau_2 = 2R_2/c$ and $g_{rx}(t)$ is non-zero for values of t in the range $\tau_1 - T/2 \leq t \leq \tau_2 + T/2$. Substituting (2.1) into the expression for $g_{rx}(t)$ gives,

$$g_{rx}(t) = \int_{\tau_1}^{\tau_2} f(\tau)\Re\left\{p(t-\tau)exp(j\omega_0(t-\tau))\right\}d\tau, \tag{2.6}$$

As the radar moves past the scene a collection of range echoes are transduced each of the form of equation (2.6) where the slant range and hence propagation delay from the radar to a given scatterer in the scene varies according to the imaging geometry at each transmit/receive point.

It is the task of the SAR image formation algorithm to recover $r(x, y, z)$ from the transduced echoes $g_{rx}(t)$. The first step of the inversion process is to perform baseband demodulation followed by digital sampling and range compression to recover $f(\tau)$. In the demodulator the received waveform is mixed with a pair of reference functions $G^I_{ref}(t)$ and $G^Q_{ref}(t)$ to generate the in-phase and quadrature-phase channels respectively of the analytic signal,

$$g(t) = LPF\{G^I_{ref}(t)g_{rx}(t)\} + jLPF\{G^Q_{ref}(t)g_{rx}(t)\}, \tag{2.7}$$

where LPF is a low pass filter operator applied to remove the high frequency components that arise in the mixing process. While the principal task of the demodulator is to obtain a baseband signal for subsequent image focusing, the reference functions also provide a form of crude compensation for the slant range variation of a point scatterer response over the collection aperture. That is, the amplitude and phase variation of the demodulated response is determined by the relative variation between the received signal and the demodulation reference function. The choice of reference function will thus determine the two dimensional nature of the matched filter required in the image formation algorithm. It will also determine the sample rate of both the received signal and the synthetic aperture necessary to recover the scene response from the signal history data. Two different reference function approaches, called compensation to a line and compensation to a point, are commonly used each producing a different point scatterer response in the demodulated signal history data.

Compensation to a Line

In the compensation to a line approach a sinusoid at the carrier frequency is used as the demodulation reference function,

$$G^I_{ref}(t) = 2\cos(\omega_0 t), \tag{2.8}$$

$$G^Q_{ref}(t) = -2\sin(\omega_0 t). \tag{2.9}$$

Substituting these reference functions into (2.7) along with the expression for the received range echo in (2.6) gives the following demodulated analytic signal,

$$\begin{aligned} g(t) &= \int_{\tau_1}^{\tau_2} f(\tau)exp(-j\omega_0\tau)p(t-\tau)d\tau, \\ &= f'(t) \otimes p(t), \end{aligned} \tag{2.10}$$

where,

$$f'(t) = rect\left(\frac{t-(\tau_2+\tau_1)/2}{\tau_2-\tau_1}\right) f(t)exp(-j\omega_0 t), \tag{2.11}$$

is the integrated reflectivity function, $f(\tau)$, limited to the interval $\tau_2 \leq t \leq \tau_1$, modulated by a phase term dependent on the delay, τ and radar centre frequency ω_0. Equation (2.10) indicates that $g(t)$ is formed by the convolution of the baseband component $p(t)$ of the transmit waveform $s(t)$ with the phase modulated, integrated reflectivity function $f'(\tau)$. In the Fourier domain, the demodulated signal $g(t)$ is determined by the product of the Fourier transform of the phase modulated integrated reflectivity function and the Fourier transform of wide bandwidth waveform $p(t)$. The sample rate required to digitise $g(t)$ is thus determined by the bandwidth of $p(t)$.

An estimate of the phase modulated integrated reflectivity may be obtained by applying a matched filter, $p^*(-\tau)$ to $g(t)$, a process commonly called range compression,

$$\begin{aligned} g_{rc}(t) &= p^*(-t) \otimes g(t), \\ &= p^*(-t) \otimes p(t) \otimes f'(t), \\ &= f'(t) \otimes h_r(t), \end{aligned} \tag{2.12}$$

where $h_r(t) = p^*(-t) \otimes p(t)$ is the impulse response function along slant range after range compression. The ability to distinguish between scatterers at different propagation range delays, i.e., the range resolution is determined by the main lobe width of the range impulse response function $h_r(t)$. Using phase coded waveforms such as chirps and pulse compression, fine resolution with low peak transmit power can be readily achieved. The illuminated ground patch can thus be divided into equirange contours spaced by the range resolution and all scatterers lying within an equirange contour will be unresolvable in the range echo despite having possibly different azimuth and elevation locations.

If a series of range echo pulses are collected as the radar moves past the scene a crude unfocused image of the scene may be formed by arranging the range compressed echoes side-by-side to form a raw data matrix, as shown in Figure 2.2. In this case the response of a given scatterer is "smeared" out and unfocused with the cross range resolution of the image defined by the antenna azimuth beamwidth. From Figure 2.2 however, it can be seen that the point scatterer response in the range compressed data has a structure which is related to the variation in the imaging geometry over the synthetic aperture. Considering a point scatterer at location at $(x, y, z) = (x_s, y_s, z_s)$ the two way propagation delay is given by (2.4). Over a collection of range echo pulses τ thus varies in a hyperbolic fashion as the radar flies by the scene. In terms of the received signal, given by (2.6), the variation in τ will manifest as a variation in the location, or a migration, of the received echo across the range resolution cells of the data matrix as well as a varying phase modulation $exp(-j\omega_0\tau)$. This variation defines the minimum sample rate of the synthetic aperture that can be used to unambiguously represent the signal. It is also clear from equation (2.4) and Figure 2.2 that the nature of the hyperbolic range migration varies spatially across the illuminated scene. In particular, scatterers at near range undergo a more significant range migration than scatterers at far range.

Compensation to a point - Deramp Demodulation

Deramp demodulation is an alternative approach that may be used for the imaging of relatively small scene patches when the transmit waveform is a linear FM chirp waveform modulated onto the radar centre frequency i.e.,

$$s(t) = rect\left(\frac{t}{T}\right) exp(j\alpha t^2)exp(j\omega_0 t), \tag{2.13}$$

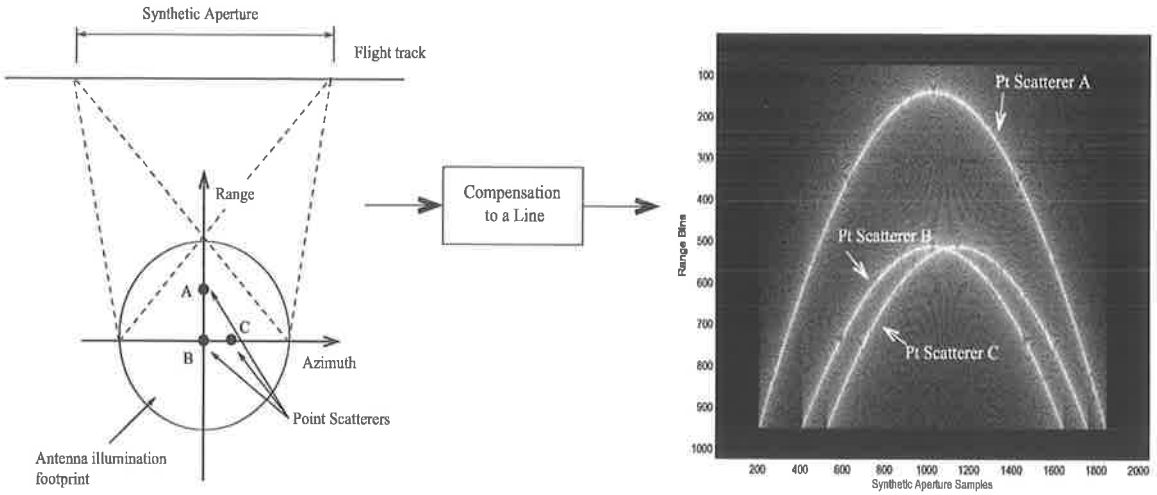


Figure 2.2: Range compressed raw echo data collected for three point scatterers with compensation to a line. Each of the scatterers undergoes a hyperbolic range migration defined by the imaging geometry at each transmit/received point.

where α is the chirp rate and T is the chirp duration. The demodulation reference functions applied in this case are delayed replicas of the transmit chirp,

$$G^I_{ref}(t) = 2\Re\{s^*(t-\tau_0)\}, \tag{2.14}$$

$$G^Q_{ref}(t) = -2\Im\{s^*(t-\tau_0)\}. \tag{2.15}$$

The delay τ_0 varies from one transmit/receive point to another and is chosen to be the propagation delay from the radar's current transmit/receive location to a particular focus point in the scene, typically chosen to be the scene centre.

Compared to compensation to a line, compensation to a point reduces the sample rate required to unambiguously sample the demodulated signal. Furthermore compensation to a point also reduces the along track spatial sample rate required to unambiguously represent the demodulated signal's pulse to pulse variation over the complete synthetic aperture. This makes the technique particularly useful in fine resolution imaging where the sampling of wide transmit bandwidths and long synthetic apertures is required. The point scatterer response in the range compressed signal history domain under deramp demodulation also differs thus necessitating a different image focusing algorithm to that of the compensation to a line method.

Provided the imaged swath width (as determined by $\tau_2 - \tau_1$) is small compared to the spatial extent of the chirp given by cT then the received, demodulated analytic signal can be shown to be, (see Appendix A),

$$G(k_r) = rect\left(\frac{k_r}{k_{bw}}\right)\int_{R_1-R_T}^{R_2-R_T} f_c(r)exp(-j(k_r+k_0)r)dr, \tag{2.16}$$

where the range variables $R_{(T,1,2)}$ in (2.16) are directly related to the corresponding time domain variables by the scale factor $c/2$, so $R_1 = \frac{cT_1}{2}$ is the range to near swath, $R_2 = \frac{cT_2}{2}$ is the range to far swath, $R_T = \frac{cT_0}{2}$ is the range to the scene focus point and $R = \frac{cT}{2}$ is the propagation delay range.

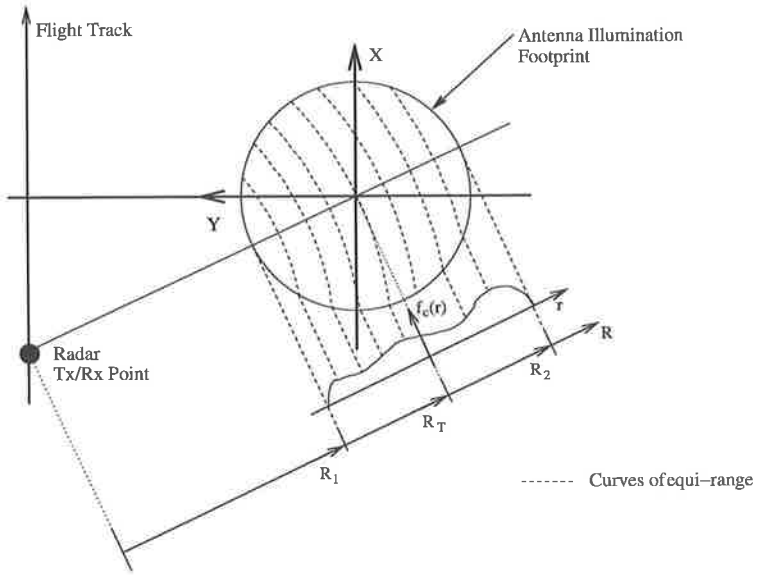


Figure 2.3: At each transmit/receive point along the collection aperture the radar transduces the integrated reflectivity function $f_c(r)$. The range r is the differential range $(R - R_T)$ where R is the range measured along the line of sight of the radar and R_T is the range to the scene centre. The value of $f_c(r)$ at a given range is the superposition of all scattering contributions lying along a contour of equirange from the radar transmit/receive point.

The variable $r = R - R_T$ is the difference between the range from the radar of a given scattering location in the scene and the range to the scene centre where positive values of r are taken to be in the direction away from the radar. The function $f_c(r) = f(\tau + \tau_0)$ is the integrated reflectivity function with origin defined as the scene focus point as illustrated in Figure 2.3. The variables in k in (2.16) are spatial frequency variables given by,

$$k_r = \frac{4\alpha}{c}\left(t - \frac{2R_T}{c}\right), \tag{2.17}$$

$$k_0 = \frac{2}{c}\omega_0, \tag{2.18}$$

$$k_{bw} = \frac{4\alpha T}{c}. \tag{2.19}$$

An examination of the integral in (2.16) shows that the deramp demodulated samples $G(k_r)$ are in fact samples of the Fourier transform of $f_c(r)$ evaluated over the unweighted aperture of support $(-k_{bw}/2 < k_r < k_{bw}/2)$, where $f_c(r)$ has been restricted to the receive window swath width $(R_1 - R_T < r < R_2 - R_T)$. Applying an inverse Fourier transform to the deramp demodulated samples yields the range compressed echo given by,

$$\begin{aligned} g(r) &= \frac{1}{2\pi}\int G(k_r)exp(jk_r r)dk_r, \\ &= \frac{k_{bw}}{2\pi}\int_{R_1-R_T}^{R_2-R_T} f_c(\alpha)exp(-jk_0\alpha)sinc\left(\frac{(r-\alpha)k_{bw}}{2\pi}\right)d\alpha, \\ &= \frac{k_{bw}}{2\pi}sinc\left(\frac{rk_{bw}}{2\pi}\right) \otimes f_c(r)exp(-jk_0 r), \end{aligned} \tag{2.20}$$

where $f_c(r)$ is limited to the range swath $[R_1 - R_T, R_2 - R_T]$. The demodulated range compressed echo is thus the integrated reflectivity function f_c convolved with a $sinc$ function and the range resolution may be defined by the distance measured from the mainlobe peak to the first null of the sinc function,

$$\rho_r = \frac{2\pi}{k_{bw}}. \tag{2.21}$$

Substituting (2.19) for k_{bw} in the expression for ρ_r gives,

$$\rho_r = \frac{c\pi}{2\alpha T}. \tag{2.22}$$

In practice, instead of the uniform weighting over k_r used in (2.16), some form of tapered window is applied to achieve a compromise between the mainlobe width of the resulting image domain convolution kernel and the size of the associated sidelobes.

Figure 2.4 shows the unfocused image obtained from a series of deramp demodulated range echo pulses collected as the radar moves past the scene. In this case the variation in the range delay $r = R - R_T$ determines the range migration and associated phase modulation of the individual scatterer responses in the range compressed signal history. It can be seen from Figure 2.4 that scatterers displaced in azimuth with respect to the focus point are subject to a sinusoidal range variation while scatterers displaced in range are subject to a co-sinusoidal response. A scatterer at the scene centre however is compensated for exactly and is subject to no pulse-to-pulse range variation over the collection aperture. Compared to the demodulation to a line method, the pulse-to-pulse range variation of the scatterer responses in the deramp demodulation method is significantly less. As a consequence the spatial sampling along the synthetic aperture required to unambiguously represent the demodulated pulse-to-pulse variation need not be as fine. In [PGR91] and [GWET94] techniques are examined to reduce the along track sampling requirement for the compensation to a line demodulation approach however, these methods introduce additional signal processing complexity to the image formation algorithms.

2.2.2 Spotlight SAR Image Formation Algorithms - A Review

During SAR data acquisition an aggregate backscatter response over all scatterers illuminated by the antenna footprint is transduced as a function of demodulation delay and position along the synthetic aperture as illustrated in Figures 2.2 and 2.4. The azimuth resolution of these images is limited by the size of the antenna illumination footprint which is determined by the antenna beamwidth and the slant range to the scene. Over the coherent processing interval however, the demodulation delay associated with each scatterer manifests as a variation in the range location of the range compressed echo as well as a varying phase modulation. The exact form of this variation is unique for each scatterer and it is this fine scale structure that provides the mechanism by which range compressed signal history data may be processed to generate a fine range and azimuth resolution image of the scene.

The phase modulation present in the range compressed integrated scene reflectivity functions given in equations (2.10) and (2.20) is a significant quantity as the transduced range echo delay is scaled by the radar centre frequency. Small variations in the transduced range echo delay from one transmit/receive point to another along the collection aperture can manifest as large changes in the transduced modulation phase. Indeed, for typical imaging geometries the phase will go through many 2π cycles across the length of the collection aperture. The modulating phase function thus carries high bandwidth information encoding the location of the scatterer and this provides the mechanism for achieving fine azimuth resolution imagery. By accurately measuring the aircraft location along

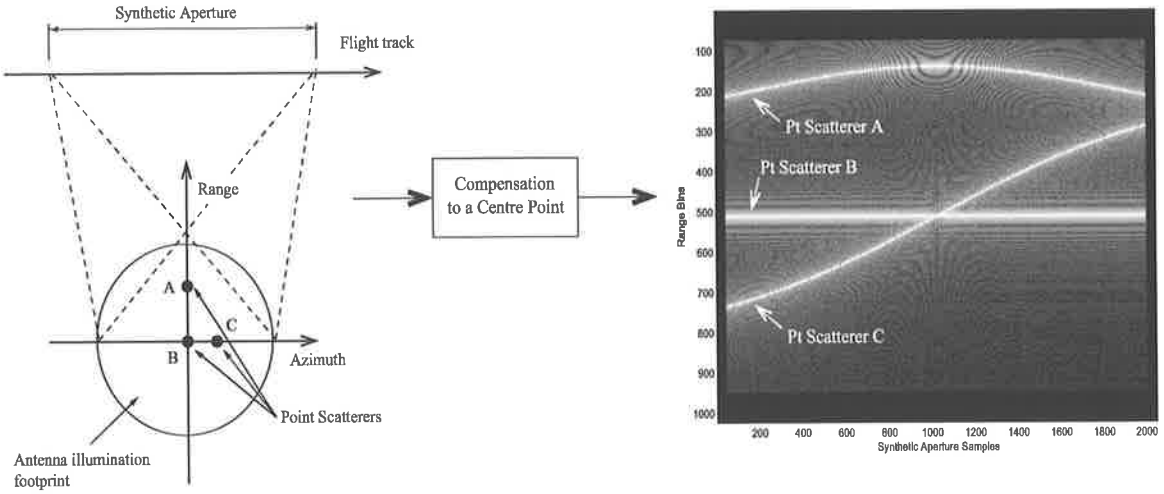


Figure 2.4: Range compressed raw echo data collected for three point scatterers where the demodulation reference function is the transmit chirp waveform delayed by the propagation distance to the scene centre. The point at the scene centre undergoes no range migration, while the scatterers offset in azimuth and range undergo a sinusoidal like range migration.

the synthetic aperture the demodulation delay and hence the modulating phase associated with a particular scattering location may be computed. An appropriate matched filter may thus be designed to spatially "compress" the "smeared" scatterer response to recover a focused image with azimuth resolution commensurate with the spatial bandwidth of the phase term. The matched filter however, must be a two dimensional filter to allow for the range migration of the scatterer response through the range compressed signal history data which may be significant in fine range resolution systems and near field imaging. Furthermore, the form of the demodulation delay is unique for each scatterer and thus the two dimensional matched filter must also vary spatially across the image.

This time domain correlation approach to image formation is optimal in the sense that it correctly accounts for the scatterers amplitude and phase response over the collection aperture. It is however, prohibitively computationally expensive and is not generally used except in the most extreme imaging scenarios, such as ultra wideband imaging [BE02], [Bre02]. Most imaging algorithms employ some degree of approximation to the scatterer's amplitude and phase response allowing an computationally efficient processor to be implemented. As these algorithms only partially compensate for the range migration and associated phase variation some residual defocusing remains in the processed imagery. The form of the defocusing depends on the level of approximation in the algorithms and it is important to select an algorithm that generates acceptably focused imagery for the given radar parameters, imaging scenarios and imaging applications to be considered. In particular, for spotlight mode SAR in which the extended collection aperture allows for the recovery of very fine resolution imagery the accurate compensation of the scatterer range migration is crucial to realising the full resolution potential of this imaging modality.

The Polar Format Algorithm - Its History

The Polar Format Algorithm (PFA) for spotlight SAR image formation is an efficient, readily implemented algorithm for the focusing of deramp demodulated echo data. The origins of the polar format technique may be traced back to research conducted by the University of Michigan in the early 1960s into fine resolution imaging of rotating objects using radar. In this research the coherent doppler filtering of fine resolution range echo data collected from targets placed on a rotating platform was found to produce poorly focused imagery. This was attributed to the pronounced scatterer migration through resolution cells as the scene rotated past the radar. In [Wal80], Walker proposed placing the range echo data in a polar grid to compensate for the observed sinusoidal variation of the range migration. This effectively compensates for the range cell migration in a simple and efficient step for all scatterers in the illuminated scene, obviating the need for a two dimensional focusing correlation kernel. Subsequent range doppler processing generates the desired fine resolution spotlight SAR imagery using simple Fourier transform techniques.

Considerable insight into the spotlight mode SAR image formation problem and the inherent polar alignment of the data was gained by the discovery that the image formation problem could be formulated as a tomographic reconstruction problem. In [MOJ83] Munson was able to demonstrate that the deramp demodulated range echo samples could be related directly to the spatial frequency domain description of the scene reflectivity via the projection-slice theorem. That is, a deramp demodulated range echo collected in a given look direction, measured from the scene focus point to the radar sensor, is approximately equal to the scene's reflectivity, in the spatial frequency domain, along a radial with the same look direction. The offset of the data samples along the frequency domain radial is proportional to the radar centre frequency while the length of support along the radial is determined by the chirp signal bandwidth. As the radar sensor moves past the scene the range echo data samples will sweep out a polar raster grid in the spatial frequency domain defined by the angular width of the synthetic aperture. Fast efficient image formation may thus proceed by direct Fourier domain reconstruction: polar to rectangular reformatting followed by a two dimensional fast Fourier transform. The projection-slice theorem thus provides a rigorous basis for the polar formatting data alignment proposed by Walker.

By demonstrating that the spotlight mode SAR image formation problem could be interpreted as a tomographic reconstruction problem Munson established a link between spotlight SAR and medical Computerized Axial Tomography (CAT) developed for the non-invasive imaging of the body. This linkage prompted investigations into the application of the Convolution Back-Projection (CBP) image formation technique, commonly found in medical CAT scanners, to spotlight SAR image formation [DJ92]. The convolution backprojection technique has a number advantages over the polar format algorithm. It only requires a one dimensional interpolation as opposed to a full two-dimensional interpolation as required by the PFA. The CBP algorithm also maps well into a parallel processing architecture for real time applications as the recovery of the complex reflectivity at a given resolution cell can be carried out independently of other resolution cells. Finally, image reconstruction via the CBP algorithm may be applied as each range echo line is collected. Unlike the PFA, which operates in a batch mode on a complete data set, the CBP can process each line as it is collected, with the incorporation of more range echo lines providing finer resolution imagery [CGM95], [DJ92]. The CBP however, is more computationally complex and it is difficult to integrate autofocus techniques into the algorithm [CGM95].

The projection-slice theorem relates the evaluation of a line integral of a two dimensional function to the Fourier transform of the function. In the context of spotlight SAR the projection-slice is applied in an approximate sense. Provided the imaged scene is sufficiently small and the radar sensor is sufficiently far away from the scene then the propagating electromagnetic waves incident on the scene

and received by the radar may be modelled as plane waves. Under this approximation the transduced reflectivity at delay τ will be given by the integral of the scene reflectivity over a line perpendicular to the direction of wave propagation. The projection-slice theorem may thus be applied to relate the transduced data to the scene's reflectivity in the spatial frequency domain and focused imagery may be recovered using the PFA. A more accurate description of the incident electromagnetic wave however, is to use a spherically propagating wave model. In this model the integrated scene response at a given demodulation delay is formed by taking an integral along an circular arc rather than along a straight line. In this case the PFA doesn't completely compensate for the range migration and the associated phase modulation of the scatterer response in the acquired signal history data. As a consequence the recovered PFA image is subject to a defocus and geometric distortion that varies spatially over image [JWE+96]. Two conditions must be satisfied if the line integral approximation is to be applied. Firstly, the range migration error due to wavefront curvature over the imaged scene must be less than the resolution cell size. Secondly, over the coherent processing interval the range error due to wavefront curvature for a particular scatterer must vary by no more than a small fraction of a wavelength. With these constraints Munson [MOJ83] derived limits on the resolution and image patch size that may be recovered using the PFA. For imaging scenarios beyond these limits image formation algorithms must address the effects of wavefront curvature on the scatterer point response in the acquired signal history data.

Wavefront Curvature Correction

A number of efficient processing algorithms have been proposed for spotlight SAR image formation that provide improved compensation for the wavefront curvature effects without the expense of carrying out a full time domain correlation. In particular the Range Migration Algorithm (RMA) [FRP89], [CPR91b], [CPR91a] and the Chirp Scaling Algorithm (CSA) [RRB+92] are commonly used to provide high quality fine resolution imagery.

The RMA operates in the wavenumber domain wherein suitably demodulated and formatted data are Fourier transformed across the collection aperture. Using the principle of stationary phase an approximation describing the transformed data may be derived indicating that a two dimensional remapping - Stolt resampling [Sto78] - of the data followed by an inverse Fourier transform will recover a focused image of the scene. The compensation for the motion through resolution cells and the associated phase modulation is thus efficiently carried out for all scatterers in the scene in the wavenumber domain by means of the Stolt mapping. In the ideal case of a perfectly straight collection flight track with no motion errors the RMA provides accurate compensation for wavefront curvature effects and low residual phase errors. Airborne sensors however typically show significant deviations from the ideal flight track due to wind and turbulence which need to be adequately accounted for and compensated by the processor. Due to the processing architecture of the RMA high precision motion compensation is difficult to incorporate into the processor and is the subject of ongoing research [PRM+02], [CPR91a].

The CSA is a computationally efficient variation to the RMA in which the Stolt mapping is approximated by means of a series of Fourier transforms and multiplicative phase factors. While this eliminates the need for a full two dimensional resampling of the phase history data the approximation effectively limits the collection aperture that may be processed and hence the resolution of the focused imagery compared to that of the RMA. The Extended Chirp Scaling (ECS) algorithm [MMS96] however provides a first and second order motion compensation strategy to allow effective imaging in airborne scenarios in which the radar platform is subject to strong deviations from the ideal straight line flight track.

The CSA and RMA algorithms are formulated with the received echo data demodulation carried

out using a fixed reference range (i.e. compensation to a line) rather than a varying range (i.e. compensation to a point) as required for the PFA. Therefore echo data collected and demodulated via deramp processing must be mixed with a suitable reference signal to remap the data into the format required for CSA and RMA processing [CGM95]. Furthermore, the remapping process must address the increased synthetic aperture sampling requirements of echo data demodulated to a line. This can be achieved using the collected data and accurate knowledge of the aircraft flight track to interpolate additional transmit/receive points over the collection aperture. From a practical point of view this is troublesome as a considerably larger quantity of phase history data must now be processed.

An alternative approach proposed by Jakowatz and Doren [JWTD97] termed PFA with post filtering PF2, simply applies an image domain filter that varies spatially over the image to correct for the dominant wavefront curvature effects present in a PFA image. In [JWE+96] Jakowatz shows that the dominant image defocus arising due to wavefront curvature is a quadratic azimuthal defocus that varies spatially over the image. With knowledge of the imaging geometry the azimuthal defocus may be computed and an appropriate matched filter applied. While the filter is specifically matched to the defocus of a scatterer at only one location, the variation in the filter coefficients over the scene is typically small and thus the same filter may be applied to focus neighbouring points thereby leading to an efficient implementation. It is shown in [JWTD97] that this method is computationally efficient compared to the RMA and has been extended by Doren [DJWT97] to include squinted imaging geometries.

Despite the plethora of available algorithms, image formation still remains an active area of research. One particularly challenging imaging problem still being addressed is the wide-band, wide-angle processing of low frequency UHF/VHF SAR [SSL94], [HUGL96]. The unique foliage penetration capabilities of electromagnetic radiation at this frequencies allows the detection of targets, such as vehicles, under forest canopies [GUMdP02]. The formation of fine resolution imagery with extremely large fractional bandwidths however, presents a particular challenging image formation problem. While the RMA and CSA provide good compensation for the deleterious effects of wavefront curvature, the approximations made in their formulations make these algorithms suboptimal. Alternative approaches based on the CBP [UHS03] have been implemented and new techniques based on inversion of the circular Radon transform [RN01], [RP03] have recently been proposed.

2.2.3 Research Motivation

From the discussion in Section 2.2.2 it is evident that a wide range of image formation algorithms are available, each having different capabilities and constraints. For a given set of radar parameters it is important to select an algorithm that generates suitably focused imagery at the desired resolution for the particular imaging application under consideration. In this thesis the problem of the detection of fine scale man-made scene changes using repeat pass SAR interferometry is to be addressed. This places a number of constraints on the radar imaging parameters, the required image resolution and thus the most appropriate image formation algorithm.

In the coherent point scattering model for homogeneous, natural scenes (see Chapter 4) the amplitude and phase transduced in a given resolution cell is dependent on the complex reflectivity of the component scatterers as well as their path length to the radar. Scene disturbances that cause a change in the relative spatial distribution of the scatterers may thus be detected by comparing the amplitude and phase of an interferometric repeat pass image pair. In forming SAR images for subsequent interferometric change detection it is therefore important that the image formation algorithm recovers an accurate estimate of both the amplitude and phase of the complex radar backscatter. For imaging algorithms based on wavenumber domain resampling, such as the RMA and PFA, this may be achieved by using sufficiently accurate, linear phase interpolation filters to minimise any phase

distortion introduced via the interpolation process.

Since the transduced amplitude and phase in a resolution cell is dependent on the contributing scatterer's path length to the radar measured in terms of the radar wavelength, higher frequency radars are more sensitive to changes in the scatterer locations. However, while higher radar frequencies offer improved detection sensitivity the significance of small errors in measurement of the radar platform location over the synthetic aperture are amplified. Location measurement errors must be kept to within a fraction of a wavelength otherwise significant phase errors arise over the synthetic aperture. This leads to significant image defocus as well as amplitude and phase differences between repeat pass image pairs which can obscure the changes that arise due to scene disturbances. For airborne systems, which are subject to turbulence, determining the radar location with sufficient accuracy can be difficult and generally some form of data driven autofocus algorithm is required to ensure adequate focusing.

The sensitivity of a change detection algorithm in detecting spatially fine scale changes in repeat pass SAR interferometry is crucially dependent on both the radar wavelength and the image resolution. In the presence of system noise, processing aberrations and image misregistration, robust reliable change detection performance may be achieved by the formation of a spatially averaged change statistic. However, unless the spatial estimation window is commensurate with the size of the area affected by the scene disturbance the sample change statistic will contain contributions from both changed and unchanged pixels, thereby reducing the contrast between changed and unchanged regions in the change statistic. For man-made scene changes, such as vehicle tracks that occur on spatial scales of decimetres, reliable change detection performance may be achieved with image resolutions of similar size. The use of coarser resolution imagery leads to a reduction in the detection performance especially in the presence of system noise, processing errors and temporal decorrelation in the scene. For X-band SARs image resolutions of this order may be readily achieved. Using a transmit bandwidth of 600 MHz and pulse compression techniques 30 cm range resolution is commonly achieved in practice, while spotlight mode imaging allows the collection of extended synthetic apertures for the generation of even finer azimuth resolutions.

From the above discussion it can be seen that for robust change detection performance using airborne repeat pass SAR relatively large fractional bandwidths are required. Furthermore in order to generate well focused imagery using high frequency SAR automatic data-driven focusing techniques must be employed. For the processing of airborne deramp demodulated spotlight mode data the PFA is a simple and efficient algorithm that addresses many of these requirements. It introduces negligible phase distortion provided sufficiently accurate polar to rectangular interpolators are used and facilitates the simple incorporation of autofocus algorithms necessary for focusing very fine resolution spotlight imagery. The PFA also allows the formation of a ground plane image which facilitates the interferometric processing of repeat pass image pairs. The relatively large fractional bandwidths and wide-angle collections indicated for robust change detection performance however are problematic for the PFA. In this thesis rather than consider the RMA or CSA and the associated complexities of transforming experimental deramp demodulated echo data into data with compensation to a line, the PF2 will be considered for the generation of fine resolution imagery for interferometric change detection. In particular, the form of the image domain filter proposed by Jakowatz and Doren [JWTD97] requires an extra transformation from the slant plane to the ground plane and in the remaining sections of this chapter a different image domain filter is considered which allows the direct formation of a ground plane image. The algorithm's suitability and limitations for generating fine resolution image interferometric image pairs is also examined.

2.3 The Polar Format Algorithm

The PFA is commonly derived in the literature using the projection-slice theorem. This method however, is based on a plane wave propagation assumption and does not provide a means of quantifying the image domain effects of wavefront curvature. An alternative approach is to consider a signal history representation of the range echo data acquired over the collection aperture. This formulation provides an accurate description of the data which allows the point spread function of the PFA to be computed in the presence of wavefront curvature.

In the following analysis a full three dimensional imaging geometry is considered to derive the deramp demodulated point scatterer signal history response over the collection aperture. Through appropriate small angle approximations the PFA is derived and analysis of the higher order terms in the approximations permits the dominant distortion and defocus effects of wavefront curvature in the PFA image to be quantified. In particular the distortion and defocus effects are derived for a ground plane PFA image.

2.3.1 Spotlight SAR Signal History Analysis

The deramp demodulated range echo data acquired at a given transmit/receive point is specified in (2.16) wherein the propagation range delay is defined in the direction from the radar to the scene centre. In the following analysis however, the propagation range delay shall be defined in the opposite direction, from the scene centre to the radar, consistent with the scene range dimension given by the Y axis in Figure 2.5. In this case the acquired deramp demodulated echo data is given by,

$$G_1(k_r) = rect\left(\frac{k_r}{k_{bw}}\right)\int_{R_T-R_2}^{R_T-R_1} f_c(-r)exp(j(k_r+k_0)r)dr, \tag{2.23}$$

and for a scene consisting of a single point scatterer with reflectivity $q_s exp(j\phi_s)$, at location (ρ,γ,z) given in cylindrical coordinates, as shown in Figure 2.5, $G_1(k_r)$ becomes,

$$G_2(k,\theta_T,\psi_T) = q_s exp(j\phi_s) rect\left(\frac{k-k_0}{k_{bw}}\right) e^{jk(R-R_T)}, \tag{2.24}$$

where $k = k_r + k_0$. The variables R_T and R in (2.24) are the distances from the radar to the scene centre and the radar to the point scatterer respectively and vary as a function of radar location along the synthetic aperture. The angles (θ_T,ψ_T) indicate the azimuth and elevation look direction from the scene centre to the radar position along the sensor flight track. The range difference $(R-R_T)$ appearing in the phase term of the deramp demodulated echo may be written in terms of the point target location (ρ,γ,z) and the radar location (R_T,θ_T,ψ_T) as follows. From the geometry in Figure 2.5 the distance from the radar to the point scatterer is given by (cosine rule to triangle ABC),

$$R^2 = R_{AB}^2 + z^2 - 2zR_{AB}\cos\chi, \tag{2.25}$$

where,

$$\cos\chi = \frac{h}{R_{AB}}. \tag{2.26}$$

From the geometry of Figure 2.5 the following relations also exist,

$$R_{DB}^2 = R_{AB}^2 - h^2, \tag{2.27}$$
$$R_T^2 = R_{DO}^2 + h^2, \tag{2.28}$$
$$R_{DO} = R_T\cos\psi_T. \tag{2.29}$$

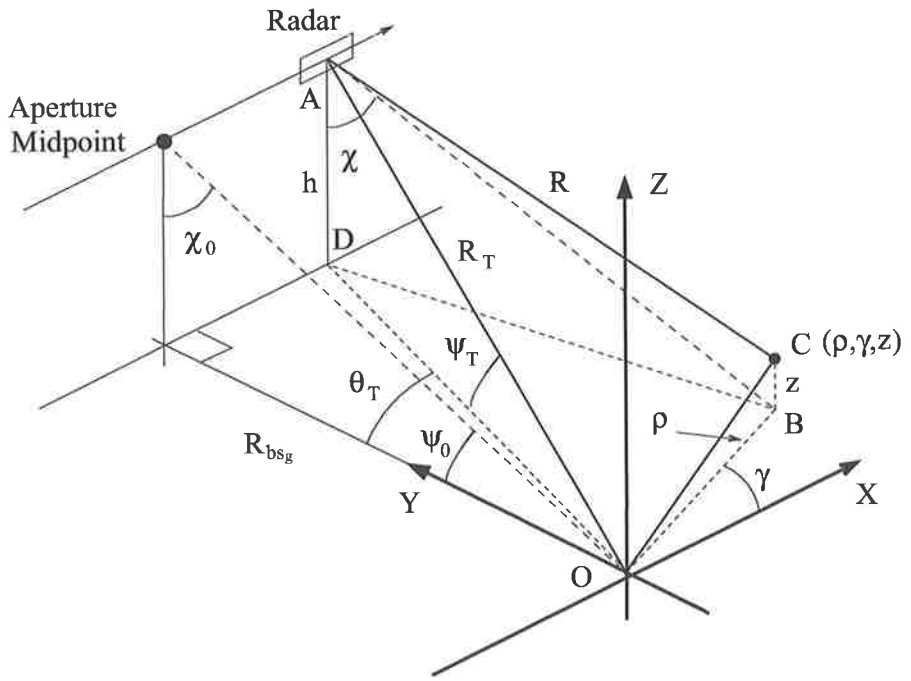


Figure 2.5: Spotlight SAR imaging geometry. The radar (point A) is a distance R_T from the scene focus point (point O) at altitude h. Angles θ_T and ψ_T are the azimuth and depression angles defined by the vector from the scene centre to the radar. A point scatterer (point C) lies a distance R from the radar at location given in cylindrical coordinates (ρ, γ, z), centred at the scene focus point.

Applying the cosine rule to triangle DBO gives,

$$R_{DB}^2 = R_{DO}^2 + \rho^2 - 2\rho R_{DO}\cos(90 - (\theta_T + \gamma)). \tag{2.30}$$

Equating (2.27) and (2.30) and substituting in (2.28) and (2.29) gives the distance R_{AB} in terms of the point target location in the ground plane $(\rho, \gamma, 0)$ and the radar location (R_T, θ_T, ψ_T),

$$R_{AB} = R_T\left(1 + \frac{\rho^2}{R_T^2} - \frac{2\rho\cos\psi_T\sin(\theta_T + \gamma)}{R_T}\right)^{\frac{1}{2}}. \tag{2.31}$$

Substituting (2.31) into (2.25) and using (2.26) gives an expression for the distance R from the radar to the point target,

$$R = R_T\left(1 + \frac{\rho^2}{R_T^2} + \frac{z^2}{R_T^2} - \frac{2zh}{R_T^2} - \frac{2\rho\cos\psi_T\sin(\theta_T + \gamma)}{R_T}\right)^{\frac{1}{2}}. \tag{2.32}$$

Provided the scatterer height z is not too large compared to distance R_T then the dependence of the range R in (2.32) on z may be simplified by considering only the linear term in a Taylor series expansion about $z = 0$. This gives the following simple expression for the range R in terms of the range R_{AB},

$$R \approx R_{AB} - \frac{zh}{R_{AB}}. \tag{2.33}$$

A further approximation to the range R may be made for the case when the point target distance from the scene centre, namely ρ, is small compared to the radar standoff range R_T. In this case the expressions for R_{AB} and R_{AB}^{-1} in (2.33) may be expanded in a Taylor series about $\rho = 0$ and considering only the linear terms in ρ yields the approximations,

$$R_{AB} \approx R_T - \rho \cos\psi_T \sin(\theta_T + \gamma), \tag{2.34}$$

$$R_{AB}^{-1} \approx \frac{1}{R_T} + \frac{\rho}{R_T} \cos\psi_T \sin(\theta_T + \gamma). \tag{2.35}$$

The differential range $(R - R_T)$ may thus be written as,

$$R - R_T \approx -\rho \cos\psi_T \sin(\theta_T + \gamma) - z \sin\psi_T \left(1 + \frac{\rho \cos\psi_T \sin(\theta_T + \gamma)}{R_T}\right), \tag{2.36}$$

where, from Figure 2.5, $\sin\psi_T = h/R_T$. Defining the point target location in cartesian coordinates $(x = \rho\cos\gamma,\ y = \rho\sin\gamma,\ z)$ then,

$$\begin{aligned} R - R_T \approx\ & -x \sin\theta_T \cos\psi_T - y \cos\theta_T \cos\psi_T \\ & -z \sin\psi_T - \frac{xz \sin\psi_T \cos\psi_T \sin\theta_T}{R_T} - \frac{yz \sin\psi_T \cos\psi_T \cos\theta_T}{R_T}. \end{aligned} \tag{2.37}$$

In a typical spotlight SAR imaging scenario the size of the image patch is significantly less than the standoff range thus $\rho \ll R_T$ and also assuming $z \ll R_T$, the R_T^{-1} dependent terms in (2.37) may be ignored and the following expression of the differential range is obtained,

$$\begin{aligned} R - R_T &\approx -\begin{bmatrix} \cos\psi_T \sin\theta_T & \cos\psi_T \cos\theta_T & \sin\psi_T \end{bmatrix} \cdot \begin{bmatrix} x \\ y \\ z \end{bmatrix}, \\ &\approx -\underline{v}_T^T \cdot \underline{\rho}, \end{aligned} \tag{2.38}$$

where $\underline{v}_T^T = [\cos\psi_T \sin\theta_T, \cos\psi_T \cos\theta_T, \sin\psi_T]$ is the three dimensional pointing vector from the scene focus point to the antenna location and $\underline{\rho} = [x, y, z]$ is the vector from the scene focus point to the point scatterer location.

Returning to Figure 2.5 it can be seen that the expression (2.38) for the differential distance $(R - R_T)$ is simply the projection of the vector $\overline{OC}$, from the scene focus point to the point scatterer location, onto the vector $\overline{OA}$, from the scene focus point to the radar location. The differential range approximation in (2.38) may thus be considered to be a plane wave propagation approximation where the differential range is measured in terms of the distance traveled by a plane wave propagating along the line of sight from the radar to the scene centre. This forms the basis of the Polar Format algorithm and an analysis of the Taylor series approximations allows the conditions under which the projection-slice theorem and the subsequent tomographic interpretation of spotlight SAR imaging [MOJ83], [JWE+96] are valid, to be quantified.

Applying the differential range plane wave approximation in (2.38) to the phase of the deramp signal in (2.24) gives,

$$\begin{aligned} \phi &= k(R - R_T), \\ &\approx -k(\underline{v}_T^T \cdot \underline{\rho}), \\ &\approx -\underline{k}_T^T \cdot \underline{\rho}, \end{aligned} \tag{2.39}$$

where,

$$\underline{k}_T = \begin{bmatrix} k_x \\ k_y \\ k_z \end{bmatrix} = \begin{bmatrix} k\cos\psi_T \sin\theta_T \\ k\cos\psi_T \cos\theta_T \\ k\sin\psi_T \end{bmatrix}. \tag{2.40}$$

Using (2.39) and (2.40) the deramp signal in (2.24) may be written in the form,

$$G_p(k_x,k_y,k_z) = q_s exp(j\phi_s) rect\left(\frac{\sqrt{k_x^2+{k_y}^2+k_z^2}-k_0}{k_{bw}}\right) exp(-j(xk_x+yk_y+zk_z)). \tag{2.41}$$

It can be seen from (2.41) that the deramp demodulated echo samples $G_p(k_x,k_y,k_z)$ are in fact samples of the spatial Fourier transform of the point scatterer. The samples lie along a radial in the three dimensional Fourier space (k_x,k_y,k_z), defined by the pointing vector $\underline{k}_T$ on the interval $(k_0 - k_{bw}/2 < |\underline{k}_T| < k_0 + k_{bw}/2)$. Over the entire collection aperture the vector $\underline{k}_T$ sweeps out an acquisition aperture of support $A_{acq}(k_x,k_y,k_z)$ in the three dimensional Fourier space that is offset from the origin by an amount k_0. In general the form of A_{acq} is determined by the imaging geometry and may be expressed as a surface function,

$$A_{acq}(k_x,k_y,k_z) = A_{ac}(k_x,k_y)\delta(k_z - f(k_x,k_y)), \tag{2.42}$$

where the function $f(k_x,k_y)$ describes the acquisition surface in the three dimensional Fourier space and $A_{ac}(k_x,k_y) = 1$ inside the aperture of support and is 0 everywhere else. For the case of straight and level flight without squint over a flat surface, the angles (θ_T,ψ_T) vary such that the radial vector $\underline{k}_T$ sweeps out a sector of the plane $k_z = k_y\beta_0$ where $\beta_0 = \tan\psi_0$ and ψ_0 is the value of ψ_T when $\theta_T = 0$ in Figure 2.5. The associated collection of deramp demodulated echo samples are thus samples of the spatial Fourier transform of the point target in an annular portion of this sector, offset from the origin by k_0 and with width k_{bw} as shown in Figure 2.6. The acquisition aperture of support may thus be written as,

$$A_{acq}(k_x,k_y,k_z) = A_{ac}(k_x,k_y)\delta(k_z - \beta_0 k_y). \tag{2.43}$$

The deramp demodulated data acquired over the entire collection aperture is commonly referred to as the signal history.

This description of the acquired deramp echoes of a scene consisting of a single point target may be applied to arbitrary scenes with complex reflectivity $r(x,y,z)$ provided the acquisition process is linear. In this case the deramp signal samples, denoted by $G_{p_s}(k_x,k_y,k_z)$, are samples of the spatial Fourier transform of the scene reflectivity function $R(k_x,k_y,k_z) = FT\{r(x,y,z)\}$ along the radials $\underline{k}_T$ in the Fourier space, where FT denotes the Fourier transform with respect to x, y and z i.e.,

$$\begin{aligned} G_{p_s}(k_x,k_y,k_z) &= A_{acq}(k_x,k_y,k_z)\iiint r(x,y,z)exp(-j(xk_x+yk_y+zk_z))dxdydz, \\ &= A_{acq}(k_x,k_y,k_z)R(k_x,k_y,k_z). \end{aligned} \tag{2.44}$$

Given that the aperture of support for the collected data in the spatial frequency domain is offset from the (k_x,k_y,k_z) origin, as illustrated in Figure 2.6, it is convenient to define the following baseband form of equation (2.44) describing the collected data,

$$\begin{aligned} G(k_x,k_y,k_z) &= G_{p_s}(k_x,k_y+k_{0_g},k_z), \\ &= A_{ac}(k_x,k_y+k_{0_g})\delta(k_z - \beta_0(k_y+k_{0_g}))R(k_x,k_y+k_{0_g},k_z), \end{aligned} \tag{2.45}$$

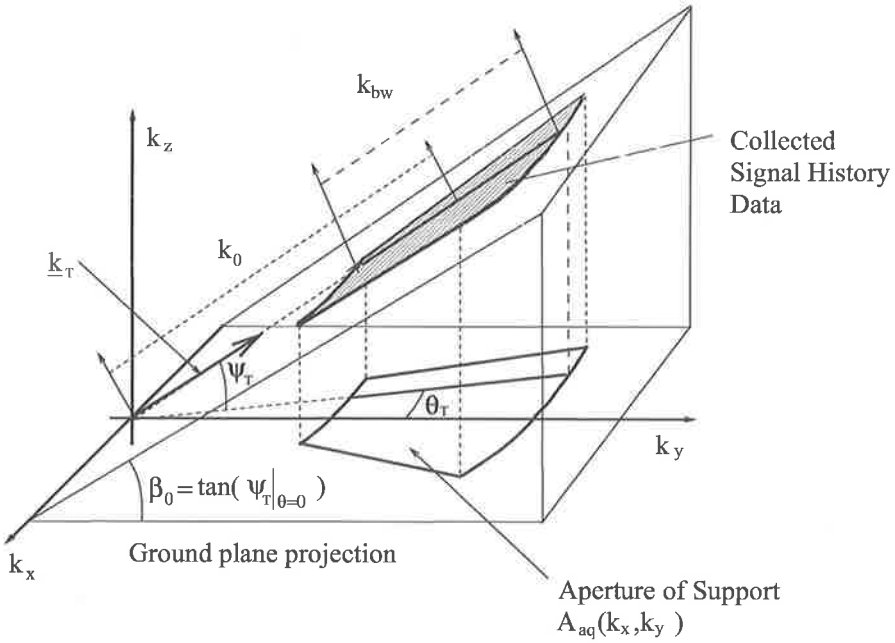


Figure 2.6: Deramp demodulated echo data acquired when the radar is at location (R_T, θ_T, ψ_T) evaluates the scene reflectivity in the spatial frequency domain along the radial defined by the same azimuth and depression angles. As the radar moves past the scene the deramp echo data sweep out a sector of the plane $k_z = k_y\beta_0$.

where $k_{0_g} = k_0 \cos(\psi_0)$, is the range spatial frequency offset at aperture centre. An image $g(x, y, z)$, of the scene reflectivity $r(x, y, z)$, may be recovered from $G(k_x, k_y, k_z)$ by applying a three dimensional inverse Fourier transform of the form,

$$g(x,y,z) = \frac{1}{8\pi^3}\iiint A_{ifp}(k_x,k_y)G(k_x,k_y,k_z)exp(j(xk_x+yk_y+zk_z))dk_xdk_ydk_z, \tag{2.46}$$

where $A_{ifp}(k_x, k_y)$ is a windowing function selected to restrict the processed spatial frequency domain extent used to recover the image. Typically A_{ifp} is chosen to be some region lying wholly within the acquired annular aperture A_{acq} such that,

$$A_{acq}(k_x,k_y+k_{0_g},k_z)A_{ifp}(k_x,k_y) = A_{ifp}(k_x,k_y)\delta(k_z-\beta_0(k_y+k_{0_g})). \tag{2.47}$$

Substituting (2.45) into (2.46) and using (2.47) gives,

$$\begin{aligned} g(x,y,z) &= \frac{1}{8\pi^3}\iiint A_{ifp}(k_x,k_y)A_{acq}(k_x,k_y+k_{0_g},k_z)R(k_x,k_y+k_{0_g},k_z) \\ &\qquad exp(j(xk_x+yk_y+zk_z))dk_xdk_ydk_z, \\ &= \frac{1}{8\pi^3}\iiint A_{ifp}(k_x,k_y)\delta(k_z-\beta_0(k_y+k_{0_g}))R(k_x,k_y+k_{0_g},k_z) \\ &\qquad exp(j(xk_x+yk_y+zk_z))dk_xdk_ydk_z, \end{aligned} \tag{2.48}$$

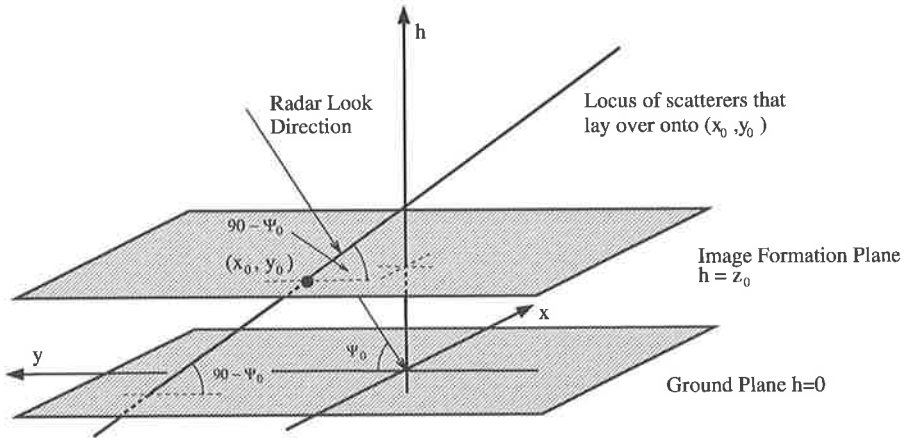


Figure 2.7: In the plane wave approximation the transduced reflectivity at location (x_0, y_0) in the image formation plane $z = z_0$ is determined by the superposition of scatterers lying along the line through (x_0, y_0, z_0) and perpendicular to the radar look direction i.e. $h = \beta_0(y_0 - y) + z_0$.

Substituting the form for $R(k_x, k_y, k_z)$ given in (2.44) into (2.48) gives,

$$\begin{aligned} g(x,y,z) &= \frac{1}{4\pi^2}\iint A_{ifp}(k_x,k_y)\iiint r(\bar{x},\bar{y},\bar{z})exp(-j(\bar{y}-z\beta_0+\bar{z}\beta_0)k_{0_g}) \\ &\qquad exp(j((x-\bar{x})k_x+(y+z\beta_0-\bar{y}-\bar{z}\beta_0)k_y))d\bar{x}d\bar{y}d\bar{z}dk_xdk_y, \\ &= \iiint r(\bar{x},\bar{y},\bar{z})exp(-j(\bar{y}+\bar{z}\beta_0-z\beta_0)k_{0_g})a(x-\bar{x},y+z\beta_0-\bar{y}-\bar{z}\beta_0)d\bar{x}d\bar{y}d\bar{z}, \end{aligned} \tag{2.49}$$

where $a(x, y)$ is the two dimensional inverse Fourier transform of the windowing function A_{ifp}. An examination of (2.49) shows that the recovered image $g(x, y, z)$ is a convolution of the windowing function point spread function $a(x, y)$ with a projected form of the reflectivity function given by $r_p(x, y, z)$ i.e.,

$$g(x,y,z) = r_p(x,y,z) \otimes a(x,y), \tag{2.50}$$

where,

$$r_p(x,y,z) = exp(-jyk_{0_g})\int r(x, y-h\beta_0+z\beta_0, h)dh. \tag{2.51}$$

An understanding of the nature of the projected reflectivity function r_p may be obtained by considering the formation of an image in the plane $z = z_0$ i.e., $g(x, y, z_0)$. From equation (2.51) the value of r_p at a given location (x_0, y_0) in the image plane $z = z_0$, is the superposition of scatterers in the scene lying along the line $h = \beta_0^{-1}(y_0 - y) + z_0$, as illustrated in Figure 2.7. Indeed the scatterer superposition described in (2.51) is simply the layover phenomenon in which a target at location (x_a, y_a, z_a) in the scene appears in the transduced image formation plane $z = z_0$, laid over towards the radar at a range $y = y_a + \beta_0(z_a - z_0)$.

Clearly it is not possible to distinguish between multiple scatterers that layover onto a common image location based on the single collection $G_{p_s}(k_x, k_y, k_z)$ given in (2.44). Inversion of the integral with respect to z in (2.51) requires two or more collections over a range of depression angles ψ, [JW00], [RM00] and [She00]. Since scatterers at different heights may not be resolved, the choice of

elevation for the image formation plane is somewhat arbitrary. However, in the case in which there is significant out-of-plane motion during the aperture formation, it is only those targets that lie in the image formation plane that will be properly focused [JWE+96], [Pay04]. A common approach therefore is to select the ground plane $z = 0$ as the image formation plane (as this is usually taken to be the mean height of the scene of interest) and all scatterers in the ground plane will appear in their true locations in the transduced image. Setting $z = 0$ in (2.49) gives the following simplified form for the recovered image,

$$g(x,y) = r_p(x,y) \otimes a(x,y), \tag{2.52}$$

where,

$$r_p(x,y) = exp(-jyk_{0_g}) \int r(x, y - h\beta_0, h)dh. \tag{2.53}$$

In the case where the reflectivity function may be described by a scattering surface,

$$r(x,y,z) = r_s(x,y)\delta(z - h(x,y)), \tag{2.54}$$

where the surface height $z = h(x,y)$ varies as a function of spatial location (x,y) then the recovered image given by (2.49) becomes,

$$g(x,y) = \iint r_s(\bar{x},\bar{y})exp(-j(\bar{y} + h(x,y)\beta_0)k_{0_g})a(x - \bar{x}, y - \bar{y} - h(x,y)\beta_0)d\bar{x}d\bar{y}. \tag{2.55}$$

Provided the terrain height function $h(x,y)$ varies sufficiently slowly so that it may be considered constant over the mainlobe width of the point spread function $a(x,y)$ then (2.55) may be written as a convolution [JWE+96],

$$g(x,y) = r_{p_s}(x,y) \otimes a(x,y), \tag{2.56}$$

where $r_{p_s}(x,y)$ is given by,

$$r_{p_s}(x,y) = exp(-jyk_{0_g})r_s(x, y - h(x,y)\beta_0). \tag{2.57}$$

In a practical implementation of the PFA the windowing function $A_{ifp}(k_x,k_y)$ is chosen to be a rectangular region lying wholely within the acquired annular aperture A_{acq} such that,

$$A_{ifp}(k_x,k_y) = rect\left(\frac{k_x}{k_{bw_x}}\right) rect\left(\frac{k_y}{k_{bw_y}}\right), \tag{2.58}$$

where k_{bw_x} and k_{bw_y} define the size of the rectangular region. In this case the point spread function $a(x,y)$ takes the form of a two dimensional sinc function,

$$\begin{aligned} a(x,y) &= \frac{1}{4\pi^2}\iint A_{ifp}(k_x,k_y)exp(j(xk_x + yk_y))dk_xdk_y, \\ &= \frac{k_{bw_x}k_{bw_y}}{4\pi^2} sinc\left(\frac{xk_{bw_x}}{2\pi}\right) sinc\left(\frac{yk_{bw_y}}{2\pi}\right), \end{aligned} \tag{2.59}$$

and the resolution of the recovered PFA image, defined by the distance from the mainlobe peak to the first null of the point spread function a, is thus,

$$\rho_x = \frac{2\pi}{k_{bw_x}}, \tag{2.60}$$

$$\rho_y = \frac{2\pi}{k_{bw_y}}. \tag{2.61}$$

A further aspect of the practical implementation of the PFA is that in order to use fast Fourier transform techniques to form the final image it is necessary to resample the polar sample grid onto a rectangular grid. Typically this is done in a two step process using one dimensional interpolators [JWE+96] and [CGM95] and represents a considerable portion of the overall computational burden of the PFA.

2.3.2 Limitations of the PFA

The PFA applies the filtering necessary to compensate for the phase modulation associated with a first order approximation to the differential range $(R - R_T)$ in the spotlight SAR deramp demodulated echo phase which is given by,

$$\begin{aligned} \phi &= k(R - R_T), \\ &\approx -[k_x, k_y, k_z] \cdot \begin{bmatrix} x \\ y \\ z \end{bmatrix}, \\ &\approx \phi_{pfa}(k_x, k_y, k_z). \end{aligned} \tag{2.62}$$

While (2.62) represents a first order approximation to the deramp signal phase, the complete phase variation may be represented in the Fourier space by an infinite Taylor series of the form,

$$\phi = \sum_{l=0}^{\infty} \sum_{m=0}^{\infty} \sum_{n=0}^{\infty} C_{lmn} k_x^l k_y^m k_z^n, \tag{2.63}$$

where the Taylor coefficients C_{lmn} are in general, terms dependent on the flight track geometry and vary spatially over the image. Indeed the PFA phase ϕ_{pfa} may be simply interpreted as providing the estimates, $C_{100} \approx x$, $C_{010} \approx y$ and $C_{001} \approx z$ for the first order coefficients in (2.63). The error in the PFA approximation to the deramp echo phase may thus be written as,

$$\begin{aligned} \phi_{res} &= \phi - \phi_{pfa}, \\ &= \phi + xk_x + yk_y + zk_z, \\ &= \sum_{l=0}^{\infty} \sum_{m=0}^{\infty} \sum_{n=0}^{\infty} C_{lmn}(x, y, z) k_x^l k_y^m k_z^n + xk_x + yk_y + zk_z. \end{aligned} \tag{2.64}$$

The impact of the uncompensated residual phase ϕ_{res} on the point spread function of the PFA processor may be found by considering a scene consisting of a single point scatterer with complex reflectivity given by,

$$r(x, y, z) = q_s exp(j\phi_s)\delta(x - x_s, y - y_s, z - z_s). \tag{2.65}$$

The acquired signal history data obtained over the entire collection aperture for the point scatterer scene may be written as,

$$\begin{aligned} G_p^c(k_x, k_y, k_z) &= q_s exp(j\phi_s) A_{acq}(k_x, k_y, k_z) exp(j\phi_{pfa}(k_x, k_y, k_z)) \\ &\qquad exp(j\phi_{res}(k_x, k_y, k_z, x_s, y_s, z_s)) \end{aligned} \tag{2.66}$$

where $\phi_{fpa}(k_x, k_y, k_z) = -(x_s k_x + y_s k_y + z_s k_z)$ and A_{acq} is the acquisition aperture of support, which for straight and level flight without squint takes the form,

$$A_{acq}(k_x, k_y, k_z) = A_{ac}(k_x, k_y)\delta(k_z - \beta_0 k_y). \tag{2.67}$$

The baseband form of the acquired signal history data is subsequently given by,

$$\begin{aligned} G^c(k_x,k_y,k_z) &= G_p^c(k_x,k_y+k_{0_g},k_z), \\ &= q_s exp(j\phi_s)A_{acq}(k_x,k_y+k_{0_g},k_z)exp(j\phi_{pfa}(k_x,k_y+k_{0_g},k_z)) \\ &\qquad exp(j\phi_{res}(k_x,k_y+k_{0_g},k_z,x_s,y_s,z_s)). \end{aligned} \tag{2.68}$$

The point scatterer response of the PFA is obtained by applying the windowing function A_{ifp}, defined in (2.47) in the previous section, followed by an inverse Fourier transform with respect to the spatial frequency variables k_x, k_y and k_z i.e.,

$$g^c(x,y,z) = \frac{1}{8\pi^3}\iiint A_{ifp}(k_x,k_y)G^c(k_x,k_y,k_z)exp(j(xk_x+yk_y+zk_z))dk_xdk_ydk_z. \tag{2.69}$$

A ground plane projection of the scene is formed by setting $z=0$ in (2.69),

$$\begin{aligned} g^c(x,y,z=0) &= \frac{1}{8\pi^3}\iiint A_{ifp}(k_x,k_y)G^c(k_x,k_y,k_z)exp(j(xk_x+yk_y))dk_xdk_ydk_z, \\ &= g^c(x,y). \end{aligned} \tag{2.70}$$

Assuming straight and level flight without squint with A_{ifp} chosen to be a region lying wholely within the acquired aperture as defined in (2.47) then the integral with respect to k_z in (2.70) may be evaluated and $g^c(x,y)$ is given by,

$$\begin{aligned} g^c(x,y) &= \frac{q_s exp(j\phi_s)}{4\pi^2}\iint A_{ifp}(k_x,k_y)exp(j\phi_{pfa}(k_x,k_y+k_{0_g},\beta_0(k_y+k_{0_g}))) \\ &\qquad exp(j\phi_{res}(k_x,k_y+k_{0_g},\beta_0(k_y+k_{0_g}),x_s,y_s,z_s))exp(j(xk_x+yk_y))dk_xdk_y, \\ &= \frac{q_s exp(j\phi_s)}{4\pi^2}\iint A_{ifp}(k_x,k_y)exp(j\phi_{res}(k_x,k_y+k_{0_g},\beta_0(k_y+k_{0_g}),x_s,y_s,z_s))) \\ &\qquad exp(-j(y_s+\beta_0 z_s)k_{0_g})exp(j((x-x_s)k_x+(y-y_s+\beta_0 z_s)k_y))dk_xdk_y, \\ &= q_s exp(j\phi_s)exp(-j(y_s+\beta_0 z_s)k_{0_g})\delta(x-x_s,y-y_s-z_s\beta_0)\otimes a_{res}(x,y,x_s,y_s,z_s), \\ &= r_p(x,y)\otimes a_{res}(x,y,x_s,y_s,z_s), \end{aligned} \tag{2.71}$$

where,

$$\begin{aligned} a_{res}(x,y,x_s,y_s,z_s) &= \frac{1}{4\pi^2}\iint A_{ifp}(k_x,k_y)exp(j(\phi_{res}(k_x,k_y+k_{0_g},\beta_0(k_y+k_{0_g}),x_s,y_s,z_s))) \\ &\qquad exp(j(xk_x+yk_y))dk_xdk_y, \end{aligned} \tag{2.72}$$

and,

$$r_p(x,y) = q_s exp(j\phi_s)exp(-j(y_s+\beta_0 z_s)k_{0_g})\delta(x-x_s,y-y_s-z_s\beta_0). \tag{2.73}$$

The reflectivity function r_p is simply the ground plane projection of the point scatter reflectivity defined in (2.65) modulated by a phase term dependent on the radar centre frequency k_{0_g}. The point spread function a_{res} is the two dimensional inverse Fourier transform of the product of the PFA windowing function A_{ifp} and the residual phase $exp(j\phi_{res})$ and may be written in the spatial image domain as,

$$a_{res}(x,y,x_s,y_s,z_s) = a(x,y)\otimes b(x,y,x_s,y_s,z_s), \tag{2.74}$$

where $a(x,y)$ is the inverse Fourier transform of $A_{ifp}(k_x,k_y)$ and $b(x,y,x_s,y_s,z_s)$ is the inverse Fourier transform of $exp(j\phi_{res})$. The recovered PFA image of the point scatterer given in (2.65) may thus be written as,

$$\begin{aligned} g^c(x,y) &= r_p(x,y) \otimes a(x,y) \otimes b(x,y,x_s,y_s,z_s), \\ &= g(x,y) \otimes b(x,y,x_s,y_s,z_s), \end{aligned} \tag{2.75}$$

where $g(x,y)$ is the PFA image defined in (2.50) that is recovered using the plane wave propagation assumption to describe the deramp signal history.

From equation (2.75) it can be seen that the uncompensated phase, ϕ_{res} manifests in the recovered PFA image of the point scatterer as a convolution kernel $b(x,y,x_s,y_s,z_s)$ that varies spatially over the scene. The nature of the convolution kernel and the resulting distortion and defocus of the PFA image depends on the size and nature of the most dominant terms in ϕ_{res} given in (2.64). In general the coefficients C_{lmn} decrease in significance with increasing polynominal order, thus the lower order terms are the most dominant and their image domain effects may be readily identified. In particular, uncompensated terms that are linearly dependent on k_x and k_y in ϕ_{res} cause, in the image domain, a translation of the point scatterer response from its true location where the magnitude of the translation is dependent on the scattering location. Uncompensated quadratic terms, on the other hand, manifest as a broadening of the main lobe width of the point spread function of the PFA resulting in image defocus. Finally uncompensated cubic and higher order terms lead to asymmetric sidelobes as well as a general increase in the integrated sidelobe energy of the point spread function which manifests as a loss in image contrast.

Expressions for the coefficients C_{lmn} defined in (2.64) may be found by considering additional terms in the Taylor series expansion of the differential range $(R - R_T)$ in the phase expression in (2.62). For modestly flat terrain the biggest contribution to ϕ_{res} arises from the Taylor expansion of R_{AB} about $\rho = 0$. Considering a second order approximation to R_{AB} gives,

$$R_{AB} \approx R_T - \rho\cos\psi_T\sin(\theta_T+\gamma) + \rho^2\frac{(1-\cos^2\psi_T\sin^2(\theta_T+\gamma))}{2R_T}, \tag{2.76}$$

while retaining the zeroth order approximation to R_{AB}^{-1} (since it is assumed that $z \ll \rho$) and substituting into (2.33) gives the following approximation to the uncompensated phase function,

$$\phi_{res} \approx \rho^2 k\left(\frac{1-\cos^2\psi_T\sin^2(\theta_T+\gamma)}{2R_{bs_g}}\right)\cos(\theta_T)\cos(\psi_T), \tag{2.77}$$

where R_{bs_g} is the ground range standoff distance at the aperture centre given by,

$$R_{bs_g} = R_T\cos\theta_T\cos\psi_T. \tag{2.78}$$

Writing the radial distance ρ in (2.77) in terms of the cartesian scatterer coordinates (x,y) and using the definition of the cartesian spatial frequency variables in (2.40) gives,

$$\phi_{res}(k_x,k_y,k_z,x,y,z) \approx \frac{(x^2+y^2)k_y}{2R_{bs_g}} - \frac{k_y}{2R_{bs_g}}\left(\frac{x^2k_x^2+2xyk_xk_y+y^2k_y^2}{k^2}\right). \tag{2.79}$$

Observe that in this approximation ϕ_{res} is independent of z_s (since it has been assumed that the terrain contains very little height variation) therefore in the subsequent derivations the z dependence of

ϕ_{res} will be ignored, i.e., $\phi_{res}(k_x, k_y, k_z, x, y, z)$ shall be written as $\phi_{res}(k_x, k_y, k_z, x, y)$. Assuming straight and level flight without squint, the baseband form of ϕ_{res} may be written as,

$$\phi_{res}(k_x, k_y + k_{0_g}, \beta_0(k_y + k_{0_g}), x, y) \approx \frac{(x^2+y^2)(k_y+k_{0_g})}{2R_{bs_g}} - \frac{(k_y+k_{0_g})}{2R_{bs_g}}\left(\frac{x^2k_x^2 + 2xyk_x(k_y+k_{0_g}) + y^2(k_y+k_{0_g})^2}{k^2}\right). \tag{2.80}$$

Applying the following Taylor expansion approximation for k^{-2} about $k_x = 0$ in (2.80) and using $k_z = \beta_0(k_y + k_{0_g})$,

$$\begin{aligned} k^{-2} &= \left(k_x^2 + (k_y+k_{0_g})^2 + k_z^2\right)^{-1}, \\ &= \left(k_x^2 + (1+\beta_0^2)(k_y+k_{0_g})^2\right)^{-1}, \\ &\approx \frac{\cos^2(\psi_0)}{(k_y+k_{0_g})^2} - \frac{\cos^4(\psi_0)k_x^2}{(k_y+k_{0_g})^4}, \end{aligned} \tag{2.81}$$

gives,

$$\begin{aligned} \phi_{res}(k_x, k_y + k_{0_g}, \beta_0(k_y + k_{0_g}), x, y) \approx & \frac{(x^2 + y^2\sin^2(\psi_0))}{2R_{bs_g}}(k_y+k_{0_g}) - \frac{xy\cos^2(\psi_0)}{R_{bs_g}}k_x - \frac{(x^2 - y^2\cos^2(\psi_0))\cos^2(\psi_0)}{2R_{bs_g}(k_y+k_{0_g})}k_x^2 \\ & + \frac{xy\cos^4(\psi_0)}{R_{bs_g}(k_y+k_{0_g})^2}k_x^3 + \frac{x^2\cos^4(\psi_0)}{2R_{bs_g}(k_y+k_{0_g})^3}k_x^4. \end{aligned} \tag{2.82}$$

The dominant terms in (2.82) are the linear and quadratic terms in k_x and $(k_y + k_{0_g})$ and applying the further narrow bandwidth approximation $(k_y + k_{0_g})^{-1} \approx k_{0_g}^{-1}$, a suitable second order approximation to the uncompensated phase ϕ_{res} is,

$$\begin{aligned} \phi_{pf2} \approx & \underbrace{\frac{(x^2 + y^2\sin^2(\psi_0))}{2R_{bs_g}}(k_y+k_{0_g}) - \frac{xy\cos^2(\psi_0)}{R_{bs_g}}k_x}_{\text{Image geometric distortion}} \\ & \underbrace{- \frac{(x^2 - y^2\cos^2(\psi_0))\cos^2(\psi_0)}{2R_{bs_g}k_{0_g}}k_x^2}_{\text{Spatially variant azimuthal defocus}}. \end{aligned} \tag{2.83}$$

In [JWTD97] Jakowatz derives a similar equation for the uncompensated phase terms in a PFA image arising due to wavefront curvature effects. Equation (2.83) however has some important differences compared to Jakowatz's result. In particular, the linear phase term in k_y in (2.83) has a dependency on the range coordinate y and the depression angle ψ_0 while the quadratic term in k_x has a dependency on ψ_0. The reason for these dependencies may be attributed to the formulation of the scatterer signal history in terms of the ground plane coordinates $(x, y, z = 0)$. The result given in [JWTD97] corresponds to the phase correction associated with a PFA image generated in the slant plane obtained by "projection of the scene reflectivity along circular arcs centred on and normal to the flight path". For interferometric applications the ground plane formulation of (2.83) is particularly useful as this allows multiple images to be formed in a common image plane to facilitate subsequent image registration and cross correlation estimation between image pairs. Slant plane imagery is not particularly suited

to interferometric processing as repeat pass image pairs collected with different depression angles will have different image pixel sizes and layover geometries complicating image registration. It is also difficult to correct for baseline decorrelation which reduces the cross correlation between image pairs.

Substituting the approximate form for ϕ_{res} given in (2.83) into the PFA point spread function a_{res} given in (2.72),

$$\begin{aligned} & a_{res}(x, y, x_s, y_s) \\ & = \frac{1}{4\pi^2} \iint A_{ifp}(k_x, k_y) exp(j\phi_{pf2}) exp(j(xk_x + yk_y)) dk_x dk_y, \\ & = \frac{exp(j\phi_2(x_s, y_s)k_{0_g})}{4\pi^2} \iint A_{ifp}(k_x, k_y) exp(j(\phi_1(x_s, y_s)k_x + \phi_2(x_s, y_s)k_y + \phi_3(x_s, y_s)k_x^2)) \\ & \qquad exp(j(xk_x + yk_y)) dk_x dk_y, \end{aligned} \tag{2.84}$$

where,

$$\phi_1(x_s, y_s) = -\frac{x_s y_s \cos^2(\psi_0)}{R_{bs_g}}, \tag{2.85}$$

$$\phi_2(x_s, y_s) = \frac{(x_s^2 + y_s^2 \sin^2(\psi_0))}{2R_{bs_g}}, \tag{2.86}$$

$$\phi_3(x_s, y_s) = -\frac{(x_s^2 - y_s^2 \cos^2(\psi_0)) \cos^2(\psi_0)}{2R_{bs_g} k_{0_g}}. \tag{2.87}$$

The inverse Fourier transform relation in (2.84) may be expressed in terms of the convolution,

$$a_{res}(x, y, x_s, y_s) = \int a(x + \phi_1(x_s, y_s) - \alpha, y + \phi_2(x_s, y_s)) b(\alpha, x_s, y_s) d\alpha, \tag{2.88}$$

where $a(x, y)$ and $b(x, x_s, y_s)$ are the inverse Fourier transforms of window function $A_{ifp}(k_x, k_y)$ and residual quadratic phase $exp(j\phi_3(x_s, y_s)k_x^2)$ respectively.

From (2.88) it can be seen that the linear terms k_x and k_y in (2.84) will cause a translation of the scatterer location in the image from its true location where the magnitude of the translation is dependent on the scattering location. In particular the point scatterer at (x_s, y_s, z_s) appears in the ground plane image at,

$$x = x_s + \phi_1(x_s, y_s), \tag{2.89}$$

$$y = y_s + z_s\beta_0 + \phi_2(x_s, y_s). \tag{2.90}$$

The phase term in (2.83) that is quadratic in k_x on the other hand, causes an azimuthal defocus given by $b(x, x_s, y_s)$ that varies as a function of the scattering location. The azimuthal width of the defocusing kernel b can be approximated by considering the frequency content, defined by $\frac{d\phi}{dk_x}$, of the quadratic phase $\phi = \phi_3(x_s, y_s)k_x^2$. Each frequency component in the quadratic phase may be thought of as broadening the mainlobe width of the PFA processor point spread function $a(x, y)$ by an amount proportional to that frequency. The highest instantaneous frequency of the quadratic phase occurs at the edge of the aperture of support $k_x = \pm k_{bw_x}/2$ and is given by,

$$\frac{d}{dk_x} \phi_3(x_s, y_s) k_x^2 \Big|_{\pm(k_{bw_x}/2)} = \pm \frac{(x^2 - y^2 \cos^2(\psi_0)) \cos^2(\psi_0) k_{bw_x}}{2R_{bs_g} k_{0_g}}. \tag{2.91}$$

Thus the nominal blur width is,

$$\begin{aligned} \text{azimuthal width}\,(x,y) &= 2\,\frac{d}{dk_x}\phi_3(x_s,y_s)k_x^2\Big|_{\pm(k_{bw_x}/2)}, \\ &= \frac{(x^2-y^2\cos^2(\psi_0))\cos^2(\psi_0)k_{bw_x}}{R_{bs_g}k_{0_g}}, \\ &= \frac{4\rho_x\phi_{peak}}{\pi}, \end{aligned} \tag{2.92}$$

where ϕ_{peak} is the peak quadratic phase value at the band edge given by,

$$\phi_{peak} = \frac{(x^2-y^2\cos^2(\psi_0))\cos^2(\psi_0)k_{bw_x}^2}{8R_{bs_g}k_{0_g}}, \tag{2.93}$$

and ρ_x is the azimuthal resolution determined by the azimuthal spatial frequency width of the image formation processor window A_{ifp} defined in (2.59).

A suitable criterion for minimal blurring is to maintain a quadratic phase error of less than $\pi/4$ across the aperture of support. This gives the following constraints on the image size and resolution that may be recovered by the PFA image processor,

$$x < \rho_x\sqrt{\frac{R_{bs_g}k_{0_g}}{2\pi\cos^2\psi_0}}, \tag{2.94}$$

$$y < \frac{\rho_x}{\cos\psi_0}\sqrt{\frac{R_{bs_g}k_{0_g}}{2\pi\cos^2\psi_0}}. \tag{2.95}$$

These results are different to those given in [JWE+96] and [JWTD97] as they define the limitations on a ground plane image as opposed to the slant plane formulation given in [JWE+96]. Equations (2.94) and (2.95) indicate that, for a given image resolution, the PFA image patch size is constrained by the imaging geometry parameters, namely the standoff range R_{bs_g} and the grazing angle ψ_0, and also the radar centre frequency parameter k_{0_g}. Increasing these parameters allows a larger image patch to be generated via the PFA while maintaining wavefront curvature defocus of the image to within acceptable limits.

Table 2.1 shows the system and imaging geometry parameters for the primary collection in a series of repeat pass interferometry experiments conducted using the DSTO's Ingara airborne X-band SAR, see Chapter 7. Table 2.2 shows the corresponding limitations on the image patch size for a variety of azimuth resolutions that may be generated from the acquired Ingara data. Note that in these imaging runs relatively small standoff ranges are employed and as a consequence the image patch sizes that may be generated via the PFA are commensurately small. Clearly, to recover well focused fine resolution imagery using the PFA requires restricting the image patch size to an unacceptably small area and so algorithms for the correction of wavefront curvature effects must be considered to process this data set.

2.4 PFA With Post Filtering - The PF2

In quantifying the limitations of the PFA in Section 2.3.2 a more accurate representation of the deramp demodulated echo phase was derived by considering a second order expansion of the differential range in the deramp signal phase. Given knowledge of the imaging geometry and in particular R_{bs_g} and ψ_0, the phase term ϕ_{pf2} in (2.83) may be computed and this may be used as the basis for a modified form

SAR Params	Imaging Scenario1	Imaging Scenario2	Imaging Scenario3
R_{bs_g}	7593.2 m	13149.2 m	15927.2 m
ψ_0	45 deg	30 deg	15 deg
k_{0_g}	276.94 rad/m	339.18 rad/m	378.31 rad/m

Table 2.1: Radar system parameters and imaging geometry used in repeat pass interferometry experiments conducted using the DSTO's Ingara airborne X-band SAR.

Azimuth Resolution ρ_x (m)	Imaging Scenario 1 Patch size limit (x,y) m	Imaging Scenario 2 Patch size limit (x,y) m	Imaging Scenario 3 Patch size limit (x,y) m
0.5	(409.1, 578.5)	(486.4, 561.6)	(506.9, 523.8)
0.2	(163.6, 231.4)	(194.6, 224.7)	(202.8, 209.9)
0.1	(81.8, 115.7)	(97.3, 112.4)	(101.4, 105.0)

Table 2.2: PFA image patch size limitations for a variety of azimuth resolutions. The patch size limitation arises from the plane wave propagation model used in the PFA. Processing larger patch sizes than those given produces imagery with a predominantly azimuthal defocus.

of the PFA which compensates for the dominant wavefront curvature effects. In [JWTD97] Jakowatz proposed a post PFA image domain filtering technique, called PF2, to efficiently compensate for ϕ_{pf2} and obtain suitably focused imagery free of the distortion and defocus effects associated with the PFA plane wave approximation. While the form for ϕ_{pf2} derived in [JWTD97] was specific to a *slant* plane formulation of the imaging equations, application of ϕ_{PF2} given in (2.83) using the same image domain filtering methodology may be used to recover a suitably focused *ground* plane image.

The key steps in the PF2 algorithm may be understood by considering the acquired deramp demodulated signal history data for the point scatterer $r(x,y,z) = q_s exp(j\phi_s)\delta(x-x_s, y-y_s, z-z_s)$ considered in the previous section. The baseband form of the acquired signal history data may be approximated by,

$$\begin{aligned} G^c(k_x,k_y,k_z) &= q_s exp(j\phi_s) A_{acq}(k_x, k_y+k_{0_g}, k_z) exp(-j(x_s k_x + y_s(k_y+k_{0_g}) + z_s k_z)) \\ &\quad exp(j\phi_{pf2}(k_x, k_y+k_{0_g}, x_s, y_s)). \end{aligned} \tag{2.96}$$

This description of the acquired deramp echo for a scene consisting of a single point target may be applied to scenes with complex reflectivity $r(x,y,z)$ provided the acquisition process is linear. In this case $G^c(k_x,k_y)$ takes the form,

$$\begin{aligned} G^c(k_x,k_y,k_z) &= A_{acq}(k_x, k_y+k_{0_g}, k_z) \iiint r(x,y,z) exp(-j(xk_x + y(k_y+k_{0_g}) + zk_z)) \\ &\quad exp(j\phi_{pf2}(k_x, k_y+k_{0_g}, x, y)) dx dy dz. \end{aligned} \tag{2.97}$$

As the residual phase term ϕ_{pf2} is dependent on both the spatial frequency variables k_x and k_y as well as the spatial location x and y it is not possible to write the signal history G^c simply in terms of the spatial Fourier transform of the scene reflectivity $R(k_x,k_y,k_z) = FT\{r(x,y,z)\}$. From the analysis in the previous section however, the phase ϕ_{pf2} was shown to vary only slowly with spatial location across the scene and so may be considered to be a constant phase term over sufficiently small localised regions of the scene. This forms the basis of the PF2 algorithm originally proposed by Jakowatz. In this technique the phase component of ϕ_{pf2} quadratically dependent on k_x is compensated for by

applying a filter to the PFA image that varies as a function of spatial location in the image. The linear phase components of ϕ_{pf2} that cause translational distortion of the PFA image are compensated for by performing a two dimensional resampling of the focused image obtained after the matched filtering operation.

In the PF2 algorithm the scene is partitioned into small local areas of size Δx in azimuth and Δy in range so that the $(i,j)^{th}$ scene region is given by,

$$r_{ij}(x,y,z) = A_{ij}(x,y)r(x,y,z), \tag{2.98}$$

where,

$$A_{ij}(k_x,k_y) = rect\left(\frac{x-i\Delta x}{\Delta x}\right) rect\left(\frac{y-j\Delta y}{\Delta y}\right), \tag{2.99}$$

and (i,j) vary such that $A_{i,j}(k_x,k_y)$ "sweeps" over the entire illuminated scene. Provided the local area size is sufficiently small, the residual phase component $\phi_{pf2_{ij}}$ of ϕ_{pf2} corresponding to the $(i,j)^{th}$ scene area, may be considered to be constant and equal to $\phi_{pf2}(x,y)$ evaluated at the centre of the local neighbourhood $(x = i\Delta x, y = j\Delta y)$. The acquired phase history for the $(i,j)^{th}$ scene area is thus given by,

$$\begin{aligned} G^c_{ij}(k_x,k_y,k_z) &= A_{acq}(k_x,k_y+k_{0_g},k_z)exp\left(j\phi_{pf2_{ij}}(k_x,k_y+k_{0_g})\right) \\ &\qquad \iiint r_{ij}(x,y,z)exp(-j(xk_x+y(k_y+k_{0_g})+zk_z))dxdydz, \\ &= A_{acq}(k_x,k_y+k_{0_g},k_z)exp\left(j\phi_{pf2_{ij}}(k_x,k_y+k_{0_g})\right) R_{ij}(k_x,k_y+k_{0_g},k_z). \end{aligned} \tag{2.100}$$

Given knowledge of the imaging acquisition flight track, in particular the depression angle and stand-off range at aperture centre the component of $\phi_{pf2_{ij}}$ quadratically dependent on k_x may be computed, i.e.,

$$\phi_{3_{ij}} = \phi_3(x,y)|_{(x=i\Delta x, y=j\Delta y)}. \tag{2.101}$$

Applying the complex conjugate of this phase function to the signal history $G^c_{ij}(k_x,k_y,k_z)$ allows a focused ground plane image of the scene reflectivity to be subsequently recovered via the PFA. In particular,

$$\begin{aligned} g^c_{ij}(x,y) = \frac{1}{8\pi^3}\iiint A_{ifp}(k_x,k_y)exp\left(-j\phi_{fil_{ij}}k_x^2\right) G^c_{ij}(k_x,k_y,k_z) \\ exp(j(xk_x+yk_y))dk_xdk_ydk_z, \end{aligned} \tag{2.102}$$

where $\phi_{fil_{ij}} = \phi_{3_{ij}}$. Selecting only that portion of g^c_{ij} corresponding to the area $A_{ij}(x,y)$ gives a focused ground plane projection image of $r_{ij}(x,y,z)$ that is essentially free of the azimuthal blurring. Applying the algorithm to all subchips in the illuminated scene a "patchwork" of focused image subchips may be recovered which together give a focused image of the entire scene. It should be noted that the filter $\phi_{fil_{ij}}$ is specifically matched to the quadratic phase function associated with the centre of the local region $A_{ij}(x,y)$. The filter therefore, only partially compensates for the defocus associated with other scattering locations in the local region $A_{ij}(x,y)$. The size of the region partitions is thus determined by the maximum tolerable residual phase that remains after application of the filter $\phi_{fil_{ij}}$. In the case of a quadratic phase error the residual phase that remains after phase compensation is limited less than $\pi/4$ across the PFA window $A_{ifp}(k_x,k_y)$. It should be noted that the magnitude

of the quadratic phase error, given by $|\phi_3(x,y)|$, generally increases with increasing distance from the scene centre (except for values of x and y satisfying $(x^2 - y^2\cos^2(\psi_0)) = 0$ in which case $\phi_3(x,y) = 0$). As a consequence, in order to maintain a residual phase error of not more than $\pi/4$ across azimuth spatial frequency extent of the PFA window $A_{ifp}(k_x,k_y)$ the size of the local areas, A_{ij}, must be made progressively smaller with increasing distance from the scene centre.

2.4.1 Limitations of the PF2 Algorithm

The PF2 algorithm, implemented using the filter kernel and resampling functions defined in Section 2.4, allows the formation of a larger, finer resolution ground plane image than can be achieved with the PFA. However, the PF2 algorithm, like the PFA, is based on a Taylor series approximation to the deramp signal history phase (albeit a more accurate approximation than that used in the PFA), thus the image quality is ultimately limited by residual uncompensated phase terms. In principle the PF2 filtering methodology can be extended to accommodate more accurate, higher order, estimates of the deramp signal phase, however the derivations of the required phase terms rapidly becomes mathematically intractable. For imaging applications that require the compensation of phase terms beyond the filter kernel specified in (2.83) alternative image formation techniques such as the RMA which provides a more accurate imaging solution should be considered. Despite this limitation the PF2 provides an efficient means of improving the resolution and patch size constraints of the PFA.

The range of image patch sizes and resolutions that may be focused using the PF2 may be found by quantifying the defocus that remains in the image point spread function after compensation for the phase function ϕ_{pf2} given in (2.83). The deramp signal history phase for a point scatterer with reflectivity $r(x,y,z) = \delta(x - x_s, y - y_s, z - z_s)$, may be expressed as,

$$\phi = \phi_{pfa} + \phi_{pf2} + \phi_{res}. \tag{2.103}$$

where $\phi_{pfa} = (-(x_s k_x + y_s k_y + z_s k_z)$, ϕ_{pf2} is given by (2.83) and ϕ_{res} now represents the residual phase that remains uncompensated by the PF2 algorithm. The baseband deramp signal history associated with a ground plane image, assuming straight and level flight without squint, may subsequently be written as,

$$G^c(k_x,k_y,k_z) = A_{acq}(k_x,k_y,k_z)exp(j\phi_{pfa})exp(j\phi_{pf2})exp(j\phi_{res}). \tag{2.104}$$

From the previous section, assuming the PF2 algorithm completely compensates for the phase function ϕ_{pf2}, the ground plane image point spread function recovered by applying an inverse Fourier transform to the windowed baseband signal history, $A_{ifp}(k_x,k_y)G^c(k_x,k_y,k_z)$ takes the form,

$$g^c(x,y) = \delta(x - x_s, y - y_s - z_s\beta_0)exp(-j(y_s + \beta_0 z_s)k_{0_g})exp(j\phi_2(x_s,y_s)k_{0_g}) \otimes b(x,y,x_s,y_s), \tag{2.105}$$

where $b(x,y,x_s,y_s)$ is the two dimensional inverse Fourier transform of the windowed residual phase function $B(k_x,k_y) = A_{ifp}(k_x,k_y)exp(j\phi_{res})$. By considering each of the higher order Taylor series terms contributing to the phase error function ϕ_{res} individually, as "modes" of defocus, the form of the image domain defocus $b(x,y,x_s,y_s)$ for each mode may be derived. Using suitable limits on the allowable defocus arising from each mode the image size and resolutions at which the defocus becomes significant may be quantified. While this analysis will not give the exact, complete form of the defocused point spread function (this requires consideration of all uncompensated phase contributions simultaneously), it does provide an indication of the form of the point spread function and the patch size limitations at which the defocus arising from a particular mode becomes prominent.

Range Defocus

In arriving at the quadratic phase term in k_x in (2.83) the approximation $(k_y + k_{0_g})^{-1} \approx 1/k_{0_g}$ was applied to equation (2.82). The image domain limitations imposed by this approximation may be quantified by considering the more accurate first order expansion,

$$\frac{1}{k_y + k_{0_g}} \approx \frac{1}{k_{0_g}} - \frac{k_y}{k_{0_g}^2}. \tag{2.106}$$

Applying this to the term in (2.82) that is dependent on k_x^2, yields an additional phase term of the form,

$$\phi_{res} = \frac{(x^2 - y^2\cos^2(\psi_0))\cos^2(\psi_0)}{2R_{bs_g}k_{0_g}^2} k_y k_x^2. \tag{2.107}$$

As this phase term is dependent on both k_x and k_y the resulting image domain blurring kernel is two dimensional. The significance of ϕ_{res} in (2.107) on the image point spread function may be assessed by applying an inverse Fourier transform with respect to k_y. Assuming a rectangular windowing function in (2.104) of the form,

$$A_{ifp}(k_x, k_y) = rect\left(\frac{k_x}{k_{bw_x}}\right) rect\left(\frac{k_y}{k_{bw_y}}\right), \tag{2.108}$$

the windowed residual phase function is given by,

$$B(k_x, k_y) = A_{ifp}(k_x, k_y) exp(j\phi_{res}). \tag{2.109}$$

Applying an inverse Fourier transform with respect to k_y gives,

$$\begin{aligned} b(k_x, y, x_s, y_s) \;=\; & rect\left(\frac{k_x}{k_{bw_x}}\right) \frac{k_{bw_y}}{2\pi} sinc\left(y\frac{k_{bw}}{2\pi}\right) \\ & \otimes\; \delta\left(y - \frac{(x_s^2 - y_s^2\cos^2(\psi_0))\cos^2\psi_0}{2R_{bs_g}k_{0_g}^2} k_x^2\right). \end{aligned} \tag{2.110}$$

The kernel $b(k_x, y, x_s, y_s)$ is of the form of a range cell migration in which the point scatterer is subject to a quadratic migration through range cells over the k_x aperture of support. That is, the scatterer range location at a given value of k_x is offset from its true location by an amount,

$$\Delta y = \frac{(x_s^2 - y_s^2\cos^2(\psi_0))\cos^2\psi_0}{2R_{bs_g}k_{0_g}^2} k_x^2. \tag{2.111}$$

Limiting the range migration to a maximum of a quarter of a range resolution cell over the k_x bandwidth, k_{bw_x} to maintain good image quality gives a patch size limitation of,

$$x_s^2 - y_s^2\cos^2(\psi_0) \leq \frac{\rho_x k_{0_g}}{\pi\cos(\psi_0)} \sqrt{\frac{R_{bs_g}\rho_y}{2}}, \tag{2.112}$$

which is most restrictive along the x axis ($y = 0$). For imaging scenario 1 in Table 2.1 and using a range resolution of 0.5 m and azimuth resolution of 0.1 m the patch size is limited to 543 m. For image patch sizes less than this ϕ_{res} in (2.107) may be ignored.

Azimuth Resolution ρ_x (m)	Imaging Scenario 1 Patch size limit (m)	Imaging Scenario 2 Patch size limit (m)	Imaging Scenario 3 Patch size limit (m)
0.5	2715	2918	2879
0.2	334	738	728
0.1	243	261	257

Table 2.3: PF2 image patch size and resolution constraints arising from the dominant uncompensated cubic phase error.

Cubic Azimuthal defocus

The uncompensated cubic phase term arising in the second order expansion (2.82) of the differential range takes the form,

$$\phi_{res} = \frac{xy\cos^4\psi_0}{R_{bs_g}k_{0_g}^2}k_x^3, \tag{2.113}$$

where the dependence on k_y has been neglected as a higher order effect. A cubic phase produces an asymmetry in the sidelobes of the point spread function $b(x, y, x_s, y_s)$ defined in (2.105) that varies spatially over the image. Limiting ϕ_{res} to less than $\pi/4$ across the k_x window yields a modest 1.5 dB increase in the first sidelobe of the point spread function. Applying the $\pi/4$ phase constraint to ϕ_{res} in (2.113) gives the following limit to the image patch size and azimuth resolution,

$$xy < \frac{\rho_x^3 k_{0_g}^2 R_{bs_g}}{4\pi^2\cos^4\psi_0}. \tag{2.114}$$

This constraint is most restrictive along the diagonal direction $x = y$ for which,

$$x < \frac{\rho_x k_{0_g}}{2\pi\cos^2\psi_0}\sqrt{\rho_x R_{bs_g}}. \tag{2.115}$$

Table 2.3 shows the patch size limitations arising from the constraint on the cubic phase phase error for each of the imaging scenarios detailed in Table 2.1.

Quadratic Azimuthal Defocus

A further source of uncompensated phase errors in the PF2 algorithm arise from the third order term in the expansion for the differential range $(R - R_T)$ about $\rho = 0$ given by,

$$\rho^3\frac{\cos\psi_T\sin(\theta_T+\gamma) - \cos^3\psi_T\sin^3(\theta_T+\gamma)}{2R_T^2}. \tag{2.116}$$

The phase associated with this correction to the differential range consists of linear, quadratic, cubic and higher order terms in k_x and k_y with the most significant being the quadratic component given by,

$$\phi_{res} = \left(-\frac{x^2y\cos^4(\psi_0)}{R_{bs_g}^2} - \frac{y(x^2 - y^2\cos^2(\psi_0))\cos^4(\psi_0)}{2R_{bg_s}^2} - \frac{y(x^2 + y^2\sin^2(\psi_0))\cos^4(\psi_0)}{2R_{bs_g}^2}\right)\frac{k_x^2}{(k_y + k_{0_g})},$$

Image Radial	Patch size constraint
$y = 0$, x axis	No quadratic phase error
$x = 0$, y axis	$y \leq \left(\frac{\rho_x^2 R_{bs_g}^2 k_{0_g}}{2\pi \cos(2\psi_0) \cos^4(\psi_0)} \right)^{\frac{1}{3}}$
$x = y$,	$y \leq \left(\frac{\rho_x^2 R_{bs_g}^2 k_{0_g}}{2\pi \cos^4(\psi_0)(4 - \cos(2\psi_0))} \right)^{\frac{1}{3}}$

Table 2.4: Analytical expressions for the PF2 image patch size limitations arising from the dominant uncompensated quadratic phase.

Azimuth Resolution ρ_x (m)	Imaging Scenario 1 Patch Size limit (m)	Imaging Scenario 2 Patch Size limit (m)	Imaging Scenario 3 Patch Size limit (m)
0.5	859	1058	1119
0.2	467	575	607
0.1	294	362	383

Table 2.5: Patch size limitations corresponding to the imaging scenarios of Table 2.1 arising from the uncompensated dominant quadratic phase in PF2 imagery.

$$
\begin{aligned}
&= \left(-4x^2 y \cos^4(\psi_0) + y^3 \cos^4(\psi_0) \cos(2\psi_0) \right) \frac{k_x^2}{2R_{bs_g}^2 (k_y + k_{0_g})}, \\
&\approx \left(-4x^2 y \cos^4(\psi_0) + y^3 \cos^4(\psi_0) \cos(2\psi_0) \right) \frac{k_x^2}{2R_{bs_g}^2 k_{0_g}}.
\end{aligned} \tag{2.117}
$$

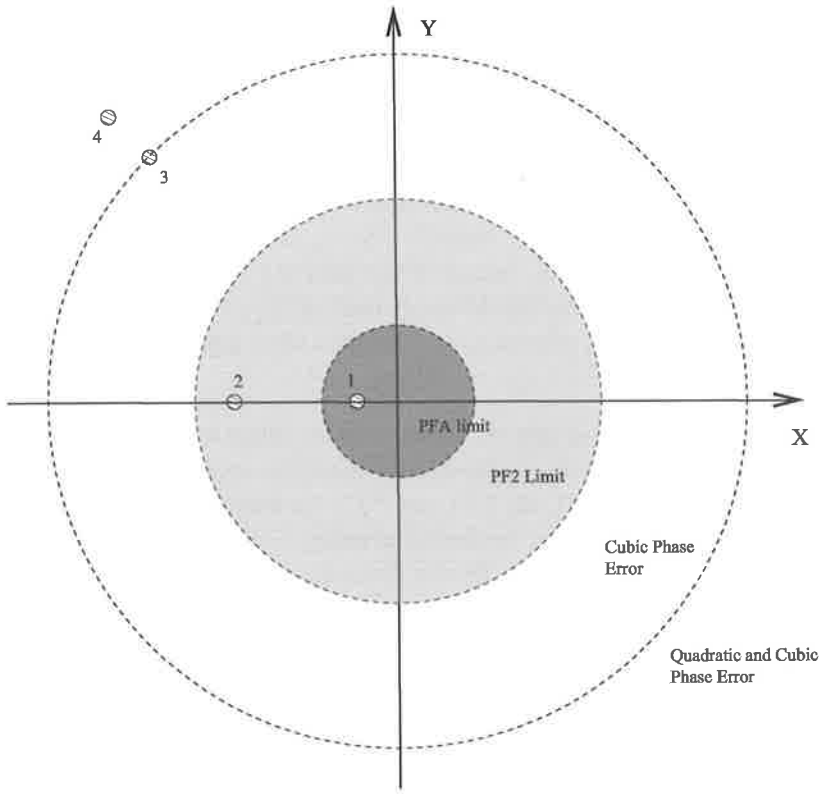
Observe that compared to the quadratic term in (2.82) ϕ_{res} above is inversely dependent on the square of the ground range standoff distance R_{bs_g} and thus is a significantly smaller phase error than the PF2 quadratic phase term. Using the $\pi/4$ peak quadratic phase error criteria over the k_x aperture of support the following patch size limitation is obtained,

$$
\left(-4x^2 y + y^3 \cos(2\psi_0) \right) \leq \frac{\rho_x^2 R_{bs_g}^2 k_{0_g}}{2\pi \cos^4(\psi_0)}, \tag{2.118}
$$

over which sufficiently well focused image may be obtained. Table 2.4 gives analytical expressions for the patch size limitations along various image domain axes. For the imaging scenarios described in Table 2.1 the patch size limitation along the $x = y$ radial is the most restrictive and is evaluated in Table 2.5 for each imaging scenario detailed in Table 2.1 for a variety of azimuth resolutions.

2.5 Simulation Results

In order to demonstrate the residual defocus of an image recovered using the PFA and PF2 algorithms the full signal history of a scene consisting of a number of point scatterers has been simulated for sub-



Scatterer	Location	Imaging Regime
1	(50, 0)	PFA
2	(200, 0)	PF2
3	(300, 300)	PF2 + Cubic Phase Error
4	(350, 350)	PF2 + Cubic and Quadratic Phase Error

Figure 2.8: Simulation scene consisting of four point scatterers in the ground plane. The scatterer locations have been selected to illustrate the variation in the point spread function obtained using the PFA and PF2 algorithms.

sequent image formation processing. The scene consists of four point scatterers at various locations, as shown in Figure 2.8, and the signal history data has been obtained using the parameters indicated in Table 2.1 under imaging scenario 1. A transmit bandwidth 400 MHz has been used to give a nominal ground plane range resolution of 0.53 m and an extended collection aperture has been simulated corresponding to a nominal ground plane azimuth resolution of 0.10 m. An unweighted rectangular aperture of support has been used thus the nominal fully focused point spread function has the form of a two dimensional sinc function as given in (2.59).

Figures 2.9 through 2.12 show the PFA images recovered from the simulated signal history of the four point scatterers while Figures 2.13 through 2.16 show the corresponding images recovered via the PF2 algorithm. On the left hand side of the recovered PFA and PF2 images is the transduced image of the point scatterer while on the right hand side is a plot of the azimuthal point spread function obtained as an azimuthal slice of the point scatterer image.

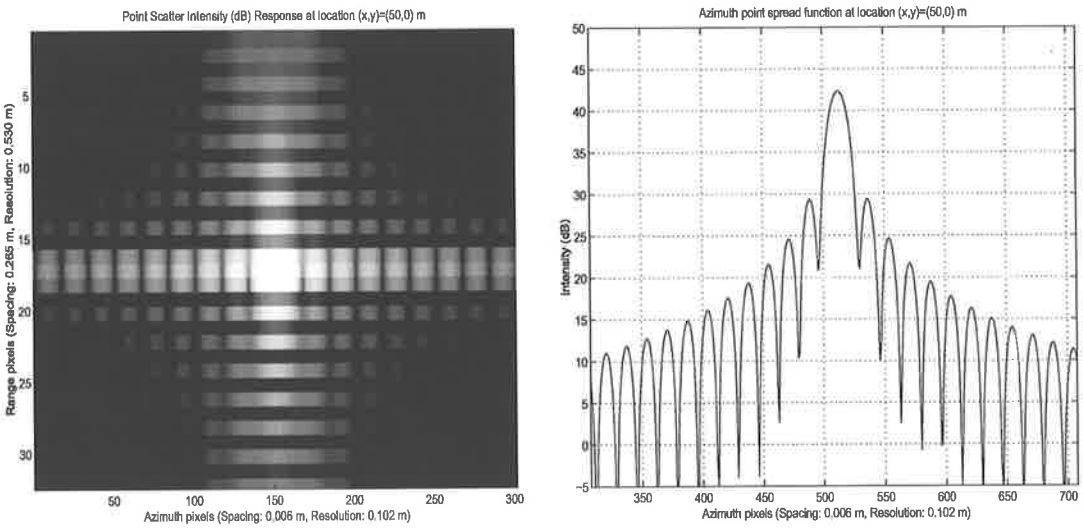
Scatterer (1) in the simulation scene lies sufficiently close to the scene centre ($x < 81.8$ m), see Table 2.2, so that the plane wave approximation is valid and the PFA generates an adequately focused

image of the scatterer, as shown in Figure 2.9. For scatterers in the plane wave scattering regime, defined by the patch size constraints in equations (2.94) and (2.95), the residual quadratic phase error that remains after PFA processing is less than $\pi/4$. (For scatterer (1) the peak value of the quadratic component of ϕ_{pf2} given in (2.83) evaluated at the azimuth spatial frequency band edge is -0.293 rad.) The PF2 algorithm thus does not need to apply any post filtering to the PFA image in this area to satisfy the $\pi/4$ peak quadratic phase error constraint. The implementation of the PF2 considered in this thesis however, applies appropriate spatially varying azimuthal filters across the entire scene. As a consequence, in generating the PF2 image of scatterer (1) shown in Figure 2.13, a filter which partially compensates for the quadratic phase component of ϕ_{pf2} has been applied. The peak value of the residual quadratic component of of ϕ_{pf2} that remains after application of the PF2 filter is 0.094 rad.

The remaining scatterers (2), (3), and (4) are outside the plane wave scattering regime and lie at progressively greater distances from the scene centre. As a consequence the recovered PFA images of these scatterers, as shown in Figures 2.10, 2.11 and 2.12, are subject to progressively larger uncompensated phase terms resulting in severe azimuthal blurring. The PF2 algorithm provides improved focusing for these scatterers by correcting for the dominant residual quadratic phase error, namely the quadratic component of ϕ_{pf2} in (2.83), that remains after PFA image formation. In particular, scatterer (2) is located such that the peak value of the quadratic component of ϕ_{pf2} is -4.688 rad. The PF2 algorithm provides partial compensation for this quadratic phase error with the peak value of the residual quadratic component of ϕ_{pf2} remaining after application of the PF2 filter being -0.032 rad. This is reflected in the significantly improved azimuthal point spread function for scatterer (2) in the PF2 image of Figure 2.14. Scatterers (3) and (4) lie sufficiently far away from the scene centre such that they are subject to higher order quadratic and cubic phase errors that remain uncompensated by the PF2 filtering kernel. In particular scatterer (3), located at (300 m, 300 m) from the scene centre, lies outside the cubic phase constraint given in equation (2.114) and thus the image recovered by the PF2 algorithm has a significant sidelobe asymmetry, see Figure 2.15. Finally scatterer (4), at location (350 m, 350 m) is subject to both a residual quadratic and cubic phase that manifests as a azimuthal blurring and raised point spread sidelobes as shown in Figure 2.16.

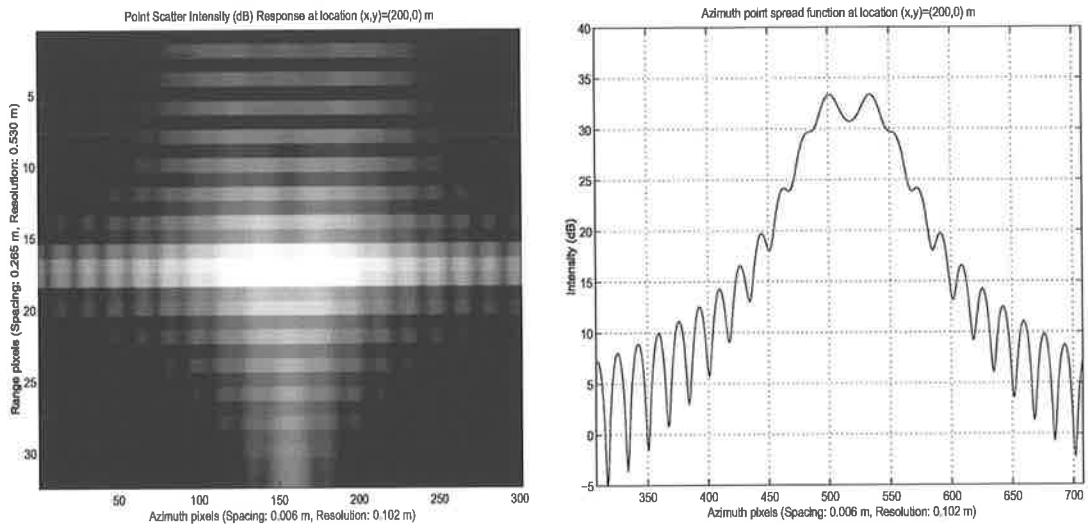
2.6 Application to Ingara SAR Data

The PF2 technique has been used to process real spotlight SAR data collected in a repeat pass interferometry experiment using the DSTO Ingara airborne X-band (9.35 GHz) SAR. The collection parameters for the data processed here are those listed as imaging scenario 2 in Table 2.1 while the maximum image patch size that can be formed using the Ingara spot mode is 1.5 km in range and 500 m in azimuth. An extended collection aperture of 8 degrees was considered for generating 0.15 m azimuth resolution imagery. For this imaging scenario the azimuthal limitation on the patch size for adequately focused imagery using the PFA is 146 m while, for the PF2 technique, the limits given in Table 2.4 are 907.2 m along the range direction ($x = 0$) and 474.2 m along the diagonal ($x = y$). Figure 2.17 shows an overview image of the imaged scene as well as enlarged views of an small image chip that has been processing using the PFA and the PF2 algorithms. This image chip is approximately 600 m down range from the scene center and thus the PFA image suffers from significant azimuth defocus which has largely been corrected by the PF2 algorithm.



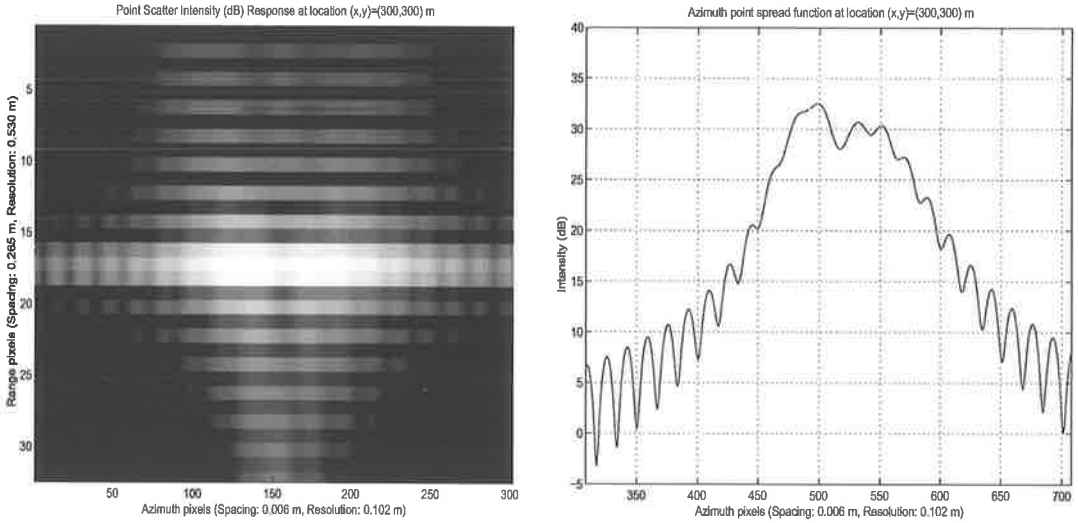
Scatterer Point Spread Function Azimuthal Point Spread Function

Figure 2.9: Point Spread function for scatterer (1) of Figure 2.8 recovered via the PFA. On the left hand side is the transduced PFA image while on the right hand side is a plot showing the associated azimuth point spread function.



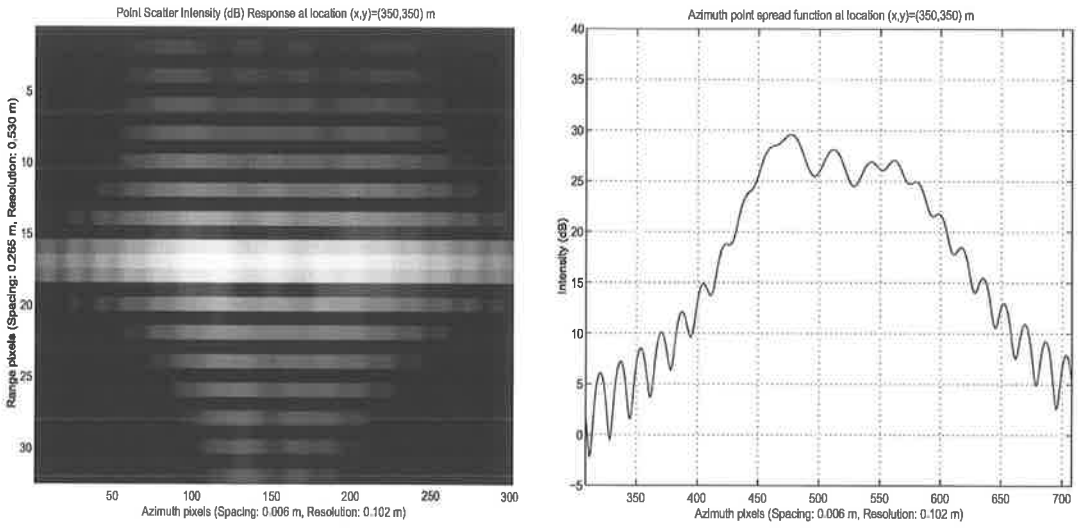
Scatterer Point Spread Function Azimuthal Point Spread Function

Figure 2.10: Point Spread function for scatterer (2) of Figure 2.8 recovered via the PFA. On the left hand side is the transduced PFA image while on the right hand side is a plot showing the associated azimuth point spread function.



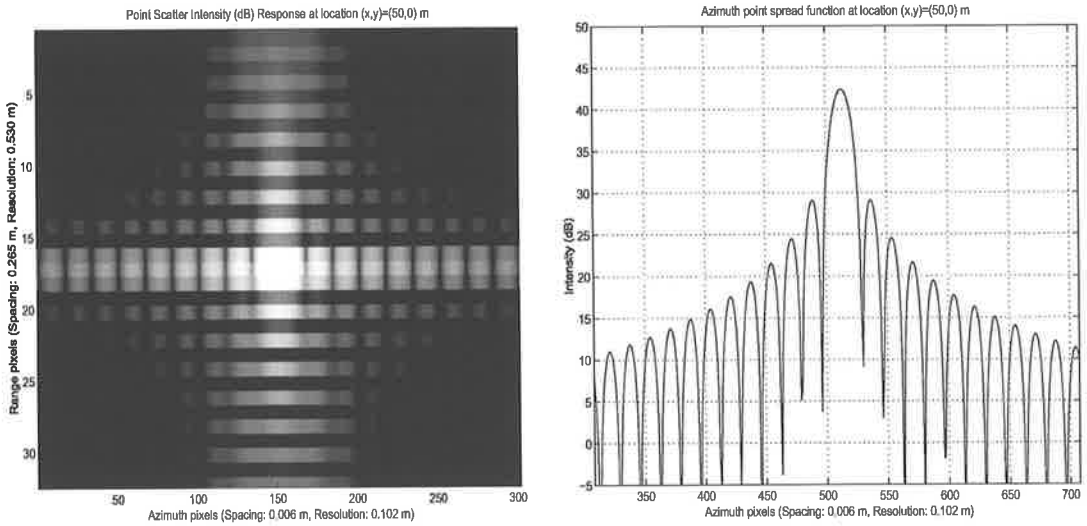
Scatterer Point Spread Function Azimuthal Point Spread Function

Figure 2.11: Point Spread function for scatterer (3) of Figure 2.8 recovered via the PFA. On the left hand side is the transduced PFA image while on the right hand side is a plot showing the associated azimuth point spread function.



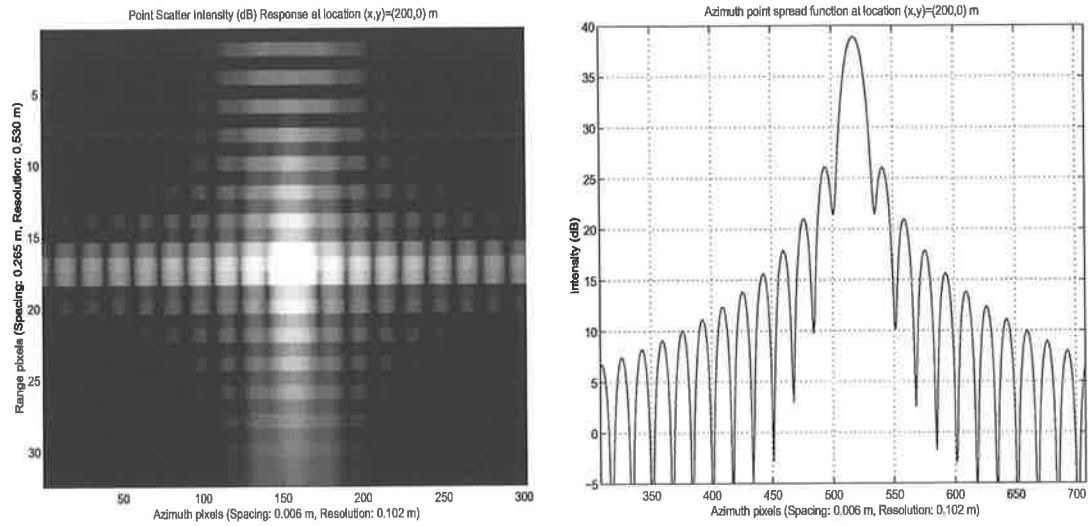
Scatterer Point Spread Function Azimuthal Point Spread Function

Figure 2.12: Point Spread function for scatterer (4) of Figure 2.8 recovered via the PFA. On the left hand side is the transduced PFA image while on the right hand side is a plot showing the associated azimuth point spread function.



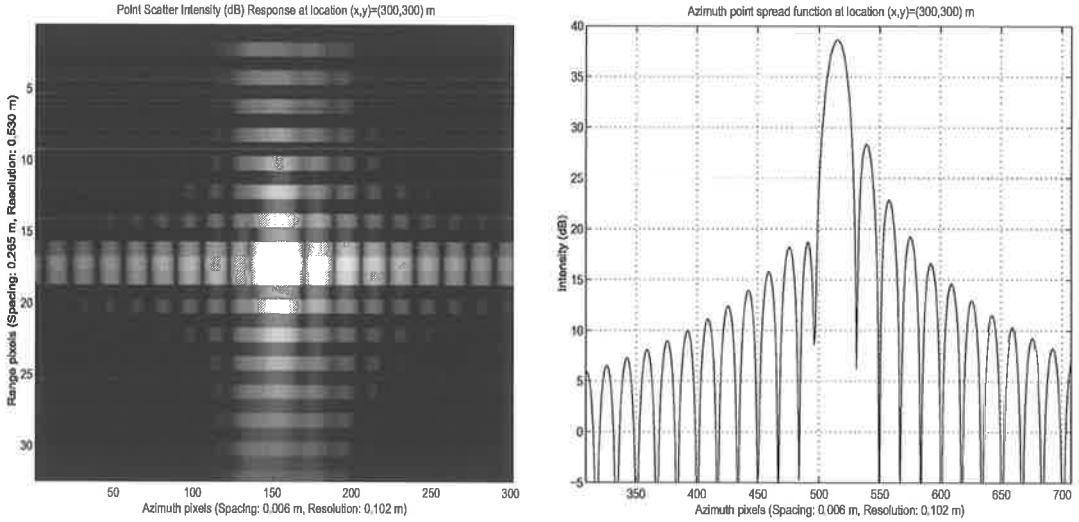
Scatterer Point Spread Function Azimuthal Point Spread Function

Figure 2.13: Point Spread function for scatterer (1) of Figure 2.8 recovered via the PF2 algorithm. On the left hand side is the transduced PFA image while on the right hand side is a plot showing the associated azimuth point spread function.



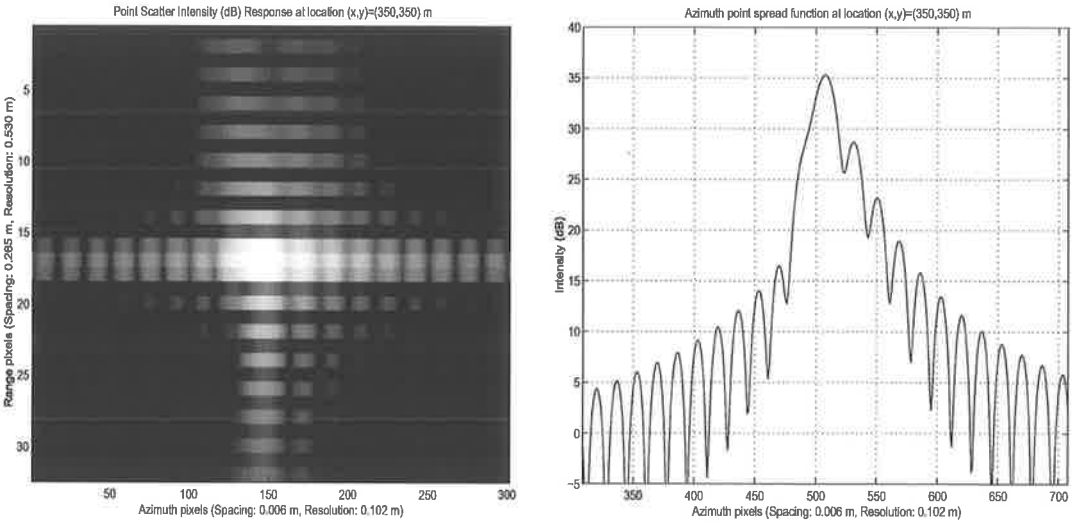
Scatterer Point Spread Function Azimuthal Point Spread Function

Figure 2.14: Point Spread function for scatterer (2) of Figure 2.8 recovered via the PF2 algorithm. On the left hand side is the transduced PFA image while on the right hand side is a plot showing the associated azimuth point spread function.



Scatterer Point Spread Function Azimuthal Point Spread Function

Figure 2.15: Point Spread function for scatterer (3) of Figure 2.8 recovered via the PF2 algorithm. On the left hand side is the transduced PFA image while on the right hand side is a plot showing the associated azimuth point spread function.



Scatterer Point Spread Function Azimuthal Point Spread Function

Figure 2.16: Point Spread function for scatterer (4) of Figure 2.8 recovered via the PF2 algorithm. On the left hand side is the transduced PFA image while on the right hand side is a plot showing the associated azimuth point spread function.

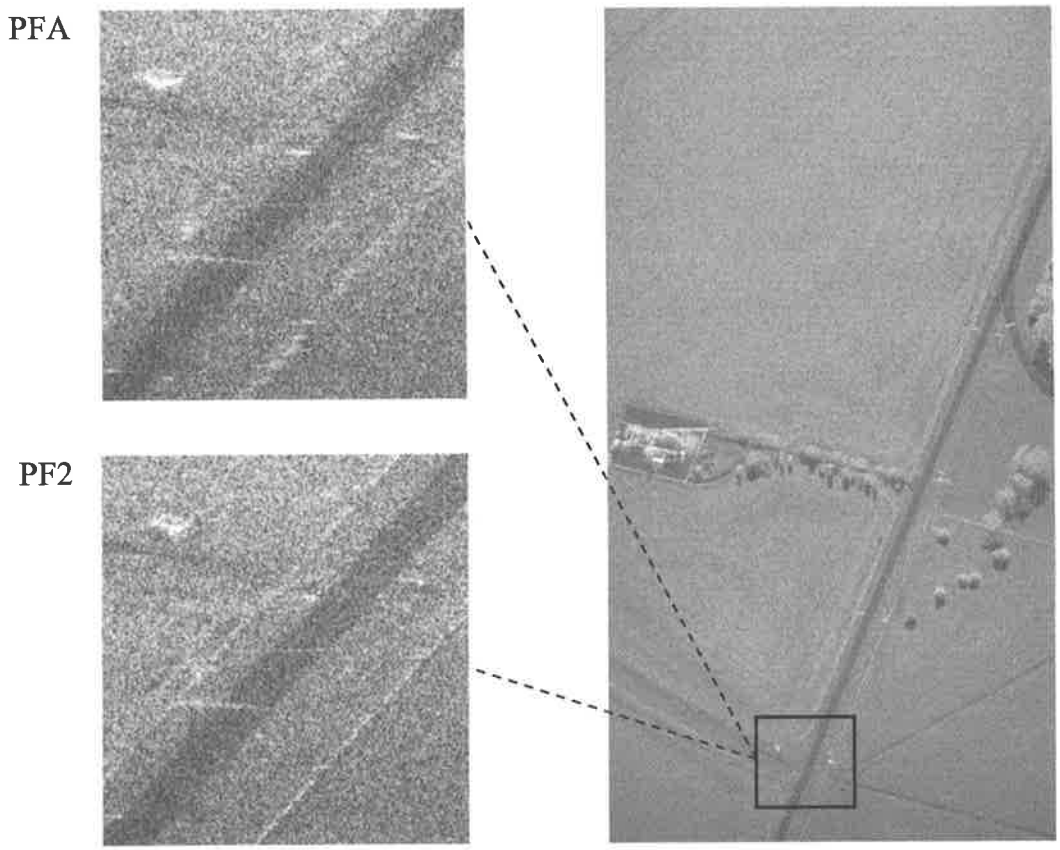


Figure 2.17: Ingara spotlight SAR image processed to 0.15 m azimuth and 0.5 m range resolution using the PF2 technique. The image on the right shows an overview of a portion of the total imaged scene while the images on the left show the full resolution imagery of a small image subchip recovered using the PFA and PF2.

2.7 Conclusions

In this chapter the problem of wide-angle spotlight SAR image formation for generating fine resolution imagery suitable for subsequent interferometric processing has been addressed. The PFA is a commonly used, efficient algorithm for focusing deramp demodulated spotlight data. It also facilitates the simple incorporation of autofocus algorithms for focusing fine resolution airborne spotlight SAR data. The PFA however, is based on a plane wave propagation assumption and thus may only be applied in imaging scenarios where the acquired collection aperture and the transmit waveform fractional bandwidth are not too large. In such scenarios the point spread function of the PFA processor is subject to defocus and translational image distortion that varies spatially over the image due to uncompensated wavefront curvature effects.

The main contribution in this chapter is an analysis of the residual uncompensated phase errors that arise in ground plane imagery formed using the PFA due to wavefront curvature effects. The analysis is based on a signal history representation of the spotlight data acquired over the collection aperture using a full three dimensional imaging geometry. The residual phase terms have been used to define a matched filter to be applied to the ground plane PFA image to improve the image focus in wide-angle spotlight collections. While the post filtering approach has been proposed previously

[JWTD97], the filter kernels in [JWTD97] were derived for the case of improving the focusing of slant plane PFA imagery. The present formulation allows the direct formation of a ground plane PFA image which may be subsequently used in repeat pass interferometric processing applications such as coherent change detection. Through further analysis of the residual phase terms that remain after application of the post PFA filtering kernel image patch size and resolution constraints have been derived for the PF2 ground plane imagery. Simulation results are provided, indicating the nature of the PFA and PF2 point spread functions and demonstrate the improved focusing capabilities of the technique. Finally the technique has been used to generate very fine azimuth resolution ground plane imagery (0.5 m range by 0.15 m azimuth) using spotlight data collected with the DSTO Ingara airborne SAR.

Chapter 3

Autofocus Algorithms for Spotlight SAR

3.1 Introduction

A crucial aspect of Synthetic Aperture Radar (SAR) image formation is the accurate measurement of the radar location over the coherent processing interval. As SAR is a coherent processing technique, utilising the phase relationship between received echo data to synthesize a large aperture, the required tolerance on the radar location measurements is of the order of a small fraction of the radar wavelength. A common approach to providing suitable position estimates is to use Inertial Navigation Units (INU) as well as differential GPS units on board the collection platform. While such systems generally provide adequate accuracy for modest resolution systems, the accurate measurement of the radar position over an extended collection aperture to produce fine resolution imagery is problematic and the measurements are typically subject to significant drifts. In the processing of the collected range echo spectra these measurement errors manifest as residual uncompensated phase errors and lead to significant defocus in the recovered image. Autofocus algorithms seek to estimate and correct for the uncompensated phase errors based on the recovered defocused image in an automated fashion. Thus they potentially allow the restoration of an image with near diffraction limited resolution. Autofocus algorithms however, are based on some limiting assumptions regarding the form of the phase function. The fidelity of the phase error model will determine the quality of the phase error estimate and the presence of residual image defocus that remains after phase error correction. In this chapter a detailed analysis of the phase errors that arise across the synthetic aperture due to errors in the measurement of the radar platform location is presented. The performance of the Phase Gradient Autofocus (PGA) algorithm is examined using the phase error model and the impact on the SAR point spread function and post processing applications such as interferometry are examined.

In Section 3.2 the commonly used model for demodulation phase errors that arise in the acquisition of deramp spotlight SAR is presented. This leads into a review of autofocus techniques proposed in the literature and a discussion of the shortcomings of the phase error model for the processing of extended aperture spotlight SAR collections. In Section 3.3 a description of the residual uncompensated motion phase error arising from errors in the range as well as the azimuth and elevation angle measurements of the radar location with respect to the scene focus point is derived for the case of wide-angle collections. A functional form of the phase error in terms of the azimuth and range spatial frequency variables k_x and k_y is found in Section 3.4 indicating that for wide-angle collections the phase error function has a range and azimuth dependence. The range dependence however is only modest and arises through subtle higher order terms in the imaging equations. To illustrate the nature of the two dimensional phase error function the case of an error in the measurement of the along track velocity is considered. Finally in Section 3.5 the impact of the two dimensional nature of the phase error function on the PGA algorithmic steps is considered. A simple range cell migration correction

step is proposed for compensating for the range dependence of the phase error function in the case when the phase error function has a dominant quadratic polynomial form. The point spread function of a Polar Format Algorithm (PFA), PGA image with and without the correction is examined and the impact on repeat pass interferometry is considered using experimental data collected with the DSTO Ingara X-band SAR.

3.2 Background

Synthetic aperture radar image formation is a two step process of data acquisition followed by image focusing. During data acquisition range echo data is acquired of the scene in which the aggregate scene backscatter response is transduced as a function of demodulation range delay and aperture position. The variation in the demodulation range delay associated with a given scattering location in the scene, over the collection aperture, is determined by the difference between the slant range from the radar to the scattering point and the reference range used to compute the demodulation reference functions at each transmit/receive point, see Section 2.2.1. The transduced point scatterer response in the acquisition data subsequently has a two dimensional form where the location of the range compressed echo varies through demodulation range resolution cells as a function of aperture position. It is also subject to a varying phase modulation determined by the demodulation range delay measured in terms of the radar wavelength.

Image formation algorithms seek to recover a focused image of the scene from the acquired data by applying two dimensional filters that are matched to the amplitude and phase variation for each scene scattering location. The performance of the matched filtering operation is thus crucially dependent on computing the demodulation range delay as a function of aperture position to within a small fraction of the radar wavelength. This requires accurate knowledge of the radar sensor location at all points along the synthetic aperture. To achieve the required positional accuracy inertial navigation units as well as differential GPS units are typically placed on board the radar platform. These systems however are prone to inaccuracies and measurement drifts over the collection aperture. For fine resolution SAR imaging, requiring the coherent processing of extended collection apertures, these measurement errors and drifts can lead to substantial mismatch in the computation of the phase response of the matched filters. As a result residual phase terms remain after image formation which manifest as an image domain blurring as well as a loss in image contrast.

Autofocus algorithms are phase error mitigation techniques that attempt to estimate the residual phase errors and compensate for them to allow the recovery of a well focused fine resolution image. These algorithms potentially allow for the recovery of near diffraction limited resolution imagery, however they are necessarily data driven methods that invariably rely on some form of model to describe the phase error functions as well as the imaged scene. In the following sections the dominant source of residual phase error arising from errors in the measurement of the effective radar location is derived. This leads into a review of various autofocus algorithms proposed in the literature for the estimation and compensation of this source of image defocus.

3.2.1 Demodulation Phase Error Model

A crucial aspect of the recovery of a well focused SAR image of a scene is the accurate measurement of the reference propagation delay τ_0 used to compute the reference functions in the quadrature demodulation of the received radar echoes. In deramp demodulation (see Section 2.2.1), which may be used when the transmit waveform is a chirp waveform, the received echo data is demodulated using a delayed copy of the transmit chirp waveform. In this case the reference propagation delay is the two way propagation delay, $\tau_0 = \frac{2R_T}{c}$, to and from the radar to the scene centre, where R_T

is the reference range measured from the radar to the scene centre. Over the synthetic aperture R_T varies from pulse to pulse and must be computed at each transmit/receive point using measurements of the radar location. In practice an estimate of τ_0 is computed based on measurements of the range from the radar position to the scene centre provided by INU/GPS systems placed onboard the radar platform and a model describing the two way propagation of the electromagnetic waves to the scene. Uncertainties in the measurement of the platform location as well as unmodelled turbulence in the propagating medium however, can lead to errors in the computation of τ_0. These errors manifest as an unknown slant range error R_e such that the measured propagation range R_m may be written as $R_m = R_T - R_e$ where R_T is the actual propagation range. Both R_T and R_e will vary from pulse to pulse over the acquisition aperture: R_T will vary as a function of the imaging geometry at each transmit/receive point while R_e will vary as a function of the errors in the INU/GPS measurements and will be sensitive to any propagation anomalies.

The recovered deramp demodulated range echo associated with a point scatterer with reflectivity $q_s exp(j\phi_s)$, obtained using the measured reference range R_m may be written as,

$$G_{m_2}(k_r) = q_s exp(j\phi_s) rect\left(\frac{k_r}{k_{bw}}\right) exp(-j(k_0 + k_r)(R - R_m)). \tag{3.1}$$

where $G_{m_2}(k_r)$ has the form of equation (2.24) in Chapter 2 with R_T replaced by R_m. As described in Chapter 2, the variables in k may be interpreted as spatial frequency variables and are related to the transmit chirp waveform parameters. The variable k_0 is related to the radar centre frequency f_0 and is given by $k_0 = 4\pi f_0/c$ while k_r is the demodulation range spatial frequency and is limited to the values $|k_r| \leq k_{bw}/2$ where $k_{bw} = 4\alpha T_c/c$ and α and T_c are the chirp rate and duration respectively. The range R is the distance from the radar to the point scatterer location (x_s, y_s, z_s), see Figure 3.1.

Substituting $R_m = R_T - R_e$ into (3.1) and applying an inverse Fourier transform with respect to the range spatial frequency variable k_r gives,

$$\begin{aligned} g_{m_2}(r) &= \frac{1}{2\pi} q_s exp(j\phi_s) \int rect\left(\frac{k_r}{k_{bw}}\right) exp(-j(k_0 + k_r)(R - (R_T - R_e)))exp(jk_r r)dk_r, \\ &= \frac{k_{bw}}{2\pi} q_s exp(j\phi_s) exp(jk_0(R - R_T))exp(-jk_0 R_e) sinc\left((r - (R - R_T + R_e))\frac{k_{bw}}{2\pi}\right), \\ &= g_2(r) \otimes exp(-jk_0 R_e)\delta(r - R_e), \end{aligned} \tag{3.2}$$

where $g_2(r)$ is the point response that would be obtained using the correct position information, i.e. with $R_e = 0$. The effect of the location measurement error is to produce a range migration of the response by an amount R_e and introduce a phase modulation $exp(-jk_0 R_e)$ across the range echo. In general R_e will vary in some non-linear way from pulse to pulse and thus over the collection aperture the image formation filters will not be matched to the actual transduced two dimensional scatterer response. The resulting residual uncompensated range migration and phase modulation that remains after image formation manifests in the image as defocus as well as a loss in contrast. The significance of the image domain effects depends on the size of R_e and the manner in which it varies from pulse to pulse. The contribution of the range migration becomes significant in the recovered image when R_e is of the order of a range resolution cell size while the phase modulation is significant when R_e is of the order of the radar wavelength. For most SAR systems the demodulation error is generally less than the resolution cell size and thus the phase modulation is the most significant source of image defocus.

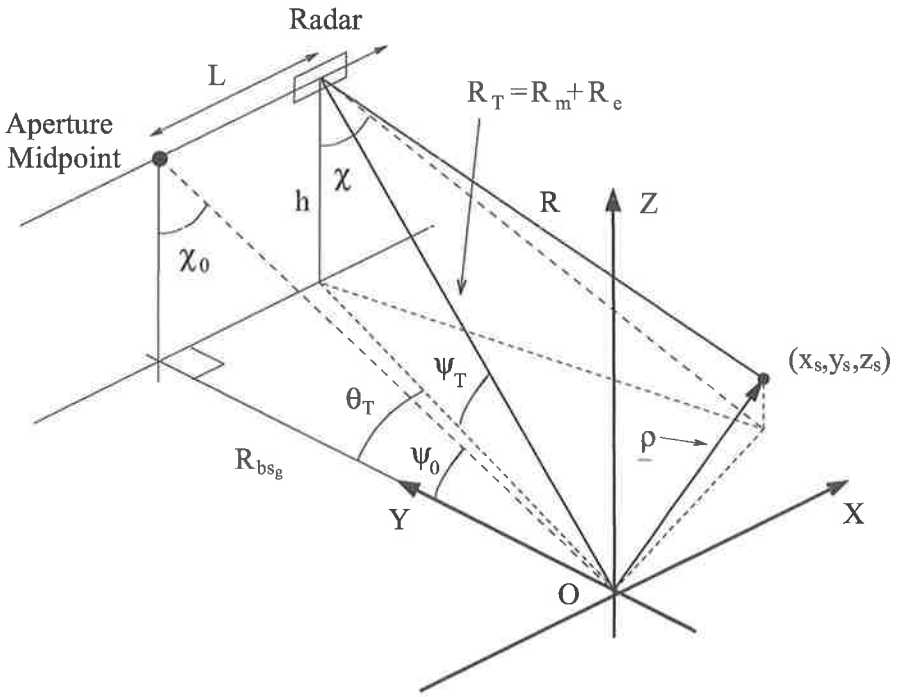


Figure 3.1: Spotlight SAR imaging geometry. The radar is a distance $R_T = R_m + R_e$ from the scene centre at altitude h, where R_m is the measured distance and R_e the error in the measured distance. Angles θ_T and ψ_T are the azimuth and depression angles defined by the vector from the scene centre to the radar. A point scatterer at location (x_s, y_s, z_s) lies a distance R from the radar.

3.2.2 Demodulation Errors and the PFA

In the PFA the range migration and phase relationship between successive demodulated range echoes for a given scattering location in the scene is derived using an approximate plane wave propagation model for the transmitted and backscattered signal associated with that location. Using the plane wave approximation the differential range $R - R_T$ is given by the length of the projection of the vector $\underline{\rho} = [x_s, y_s, z_s]^T$ from the scene centre to the scattering location, onto the unit pointing vector $\underline{v}_T$ given by,

$$\underline{v}_T = \begin{bmatrix} \cos\psi_T \sin\theta_T \\ \cos\psi_T \cos\theta_T \\ \sin\psi_T \end{bmatrix}, \tag{3.3}$$

where ψ_T and θ_T are the actual azimuth and elevation angles of the radar sensor measured from the scene centre as shown in Figure 3.1. (Note that in practice the angles (θ_T, ψ_T) must be estimated using the INU/GPS positional information and thus will be subject to measurement errors. The impact of these measurement errors will be considered in Section 3.3. In the current development however, they will be neglected.) The deramped echo phase in the presence of an unknown demodulation error thus may be written in the following approximate form,

$$\begin{aligned} \phi &= (k_0 + k_r)(R - R_T + R_e), \\ &\approx -(k_0 + k_r)\left(\underline{v}_T^T \cdot \underline{\rho}\right) + (k_0 + k_r)R_e. \end{aligned} \tag{3.4}$$

Defining the vector,

$$\underline{k}_T = \begin{bmatrix} (k_r + k_0)\cos\psi_T \sin\theta_T \\ (k_r + k_0)\cos\psi_T \cos\theta_T \\ (k_r + k_0)\sin\psi_T \end{bmatrix} = \begin{bmatrix} k_x \\ k_y \\ k_z \end{bmatrix}, \tag{3.5}$$

the demodulation phase may written as,

$$\phi = -\underline{k}_T^T \cdot \underline{\rho} + \phi_e, \tag{3.6}$$

where $\phi_e = (k_0 + k_r)R_e$. Substituting (3.5) and (3.6) into (3.1) gives the following approximate form for $G_{m_2}(k_r)$ under the plane wave propagation assumption,

$$\begin{aligned} G_{m_2}(\underline{k}_T) &\approx q_s exp(j\phi_s) rect\left(\frac{\sqrt{k_x^2 + k_y^2 + k_z^2} - k_0}{k_{bw}}\right) \\ &\qquad exp(-j(x_s k_x + y_s k_y + z_s k_z)) exp(j\phi_e), \\ &= G_p(\underline{k}_T) exp(j\phi_e). \end{aligned} \tag{3.7}$$

where $G_p(\underline{k}_T)$ is the acquired demodulated data in the absence of any demodulation range error given by,

$$G_p(\underline{k}_T) = q_s exp(j\phi_s) rect\left(\frac{\sqrt{k_x^2 + k_y^2 + k_z^2} - k_0}{k_{bw}}\right) exp(-j(x_s k_x + y_s k_y + z_s k_z)), \tag{3.8}$$

(c.f., equation (2.41) in Chapter 2). It can be seen from (3.7) that the deramped echo samples $G_{m_2}(\underline{k}_T)$ are samples of the spatial Fourier transform of the point scatterer modulated by an unknown phase term ϕ_e. The samples lie along a radial defined by the vector $\underline{k}_T$ in the three dimensional Fourier space (k_x, k_y, k_z) on the interval $(k_0 - k_{bw}/2 < |\underline{k}_T| < k_0 + k_{bw}/2)$ and the modulating phase, ϕ_e, introduces an unknown linear phase ramp over the samples along this radial. As the radar platform moves past the scene the azimuth and elevation angles (θ_T, ψ_T) vary and the vector $\underline{k}_T$ sweeps out an acquisition aperture of support $A_{acq}(k_x, k_y, k_z)$ in the three dimensional Fourier space of the scene's reflectivity. In general the acquisition aperture of support may be described as a surface function,

$$A_{acq}(k_x, k_y, k_z) = A_{ac}(k_x, k_y)\delta(k_z - f(k_x, k_y)), \tag{3.9}$$

where $A_{ac}(k_x, k_y)$ equals one for (k_x, k_y) inside the aperture and zero everywhere else. The function $f(k_x, k_y)$ describes the surface in the three dimensional Fourier space (k_x, k_y, k_z). In the case of straight and level flight without squint $f(k_x, k_y) = \beta_0 k_y$ where $\beta_0 = \tan(\psi_0)$ with ψ_0 being the depression angle at aperture centre. The acquisition aperture of support in this case is given by,

$$A_{acq}(k_x, k_y, k_z) = A_{ac}(k_x, k_y)\delta(k_z - \beta_0 k_y). \tag{3.10}$$

This will be the imaging scenario considered in the subsequent analysis. The acquired deramp demodulated data collected over the entire synthetic aperture, commonly referred to as the signal history data, may be written as,

$$G_{m_3}(\underline{k}_T) = A_{acq}(k_x, k_y, k_z) G_{m_2}(\underline{k}_T). \tag{3.11}$$

The demodulation range error R_e varies from pulse to pulse along the collection aperture and may be expressed as a function of the transmit/receive location, $L = R_{bs_g} \tan\theta_T$ where L and R_{bs_g} are specified in Figure 3.1, i.e.,

$$\phi_e = (k_0 + k_r) R_e(L). \tag{3.12}$$

Using the definition of $\underline{k}_T$ in (3.5) the phase error function may subsequently be written as a function of the azimuth, range and elevation spatial frequency variables as follows,

$$\begin{aligned}\phi_e(k_x,k_y,k_z) &= (k_0+k_r)R_e(R_{bs_g}\tan(\theta_T)),\\ &= \sqrt{(k_x^2+k_y^2+k_z^2)}R_e\left(\frac{R_{bs_g}k_x}{k_y}\right).\end{aligned} \tag{3.13}$$

As discussed in Section 2.3.1 Chapter 2, $A_{acq}(k_x,k_y)$ is offset from the k_y origin by an amount $k_{0_g} = k_0\cos(\psi_0)$ and so it is convenient to define the following baseband representation of the collected data,

$$\begin{aligned}G_m(k_x,k_y,k_z) &= G_{m_3}(k_x,k_y+k_{0_g},k_z),\\ &= A_{acq}(k_x,k_y+k_{0_g},k_z)G_p(k_x,k_y+k_{0_g},k_z)exp(j\phi_e(k_x,k_y+k_{0_g},k_z)).\end{aligned} \tag{3.14}$$

A ground plane PFA image of the point scatterer may be recovered from the collected data described in (3.14) by applying a three dimensional inverse Fourier transform (evaluated at $z=0$) to a windowed form of the acquired baseband data. Following the derivation of the PFA algorithm given in Chapter 2 the recovered PFA ground plane image may be written as,

$$g_m(x,y) = \frac{1}{8\pi^3}\iiint A_{ifp}(k_x,k_y)G_m(k_x,k_y,k_z)exp(j(xk_x+yk_y))dk_xdk_ydk_z, \tag{3.15}$$

where $A_{ifp}(k_x,k_y)$ is the windowing function typically chosen to be some region lying wholely within the acquired aperture of support A_{acq}, i.e.,

$$A_{acq}(k_x,k_y+k_{0_g},k_z)A_{ifp}(k_x,k_y) = A_{ifp}(k_x,k_y)\delta(k_z-\beta_0(k_y+k_{0_g})), \tag{3.16}$$

for the case of straight and level flight without squint. Assuming a rectangular windowing function of the form,

$$A_{ifp}(k_x,k_y) = rect\left(\frac{k_y}{k_{bw_y}}\right)rect\left(\frac{k_y}{k_{bw_x}}\right), \tag{3.17}$$

and substituting (3.14) into (3.15) and using the result (3.16) the recovered PFA ground plane image may be written as,

$$\begin{aligned}g_m(x,y) &= \frac{1}{8\pi^3}\iiint A_{ifp}(k_x,k_y)\delta(k_z-\beta_0(k_y+k_{0_g}))G_p(k_x,k_y+k_{0_g},k_z)\\ &\qquad exp(j\phi_e(k_x,k_y+k_{0_g},k_z))exp(j(xk_x+yk_y))dk_xdk_ydk_z,\\ &= \frac{1}{4\pi^2}\iint A_{ifp}(k_x,k_y)G_p(k_x,k_y+k_{0_g},\beta_0(k_y+k_{0_g}))\\ &\qquad exp(j\phi_e(k_x,k_y+k_{0_g},\beta_0(k_y+k_{0_g})))dk_xdk_y.\end{aligned} \tag{3.18}$$

The ground plane image given in (3.18) may be expressed as the convolution of the PFA image recovered in the absence of any demodulation errors (i.e., $\phi_e=0$) and a blurring filter kernel,

$$g_m(x,y) = g_p(x,y)\otimes b(x,y), \tag{3.19}$$

where (see Section 2.3.1, Chapter 2),

$$\begin{aligned}g_p(x,y) &= \frac{1}{4\pi^2}\iint A_{ifp}(k_x,k_y)G_p(k_x,k_y+k_{0_g},\beta_0(k_y+k_{0_g}))exp(j(xk_x+yk_y))dk_xdk_y,\\ &= \frac{k_{bw_x}k_{bw_y}}{4\pi^2}q_sexp(j\phi_s)exp(-jk_{0_g}(y_s+z_s\beta_0))\\ &\qquad sinc\left((x-x_s)\frac{k_{bw_x}}{2\pi}\right)sinc\left((y-y_s-z_s\beta_0)\frac{k_{bw_y}}{2\pi}\right),\end{aligned} \tag{3.20}$$

and

$$b(x,y) = \frac{1}{4\pi^2}\iint exp(j\phi_e(k_x,k_y,\beta_0(k_y+k_{0_g})))exp(j(xk_x+yk_y))dk_xdk_y, \tag{3.21}$$

with $\phi_e(k_x,k_y,k_z)$ given by (3.13). Equation (3.20) describes the PFA ground plane image that would be recovered with exact knowledge of the deramp demodulation delay while $b(x,y)$ is a convolution kernel that describes the image domain effects of the demodulation error ϕ_e. While the exact form of the convolution kernel depends on the functional dependence of ϕ_e on k_x and k_y, under the small fractional bandwidth and small angle approximation, the expression for ϕ_e given in (3.13) is usually approximated by,

$$\phi_e(k_x) \approx \left(\sqrt{1+\beta_0^2}\right)k_{0_g}R_e\left(R_{bs_g}\frac{k_x}{k_{0_g}}\right). \tag{3.22}$$

In this case the convolution kernel $b(x,y)$ reduces to,

$$b_s(x) = \frac{1}{2\pi}\int exp\left(j\left(\left(\sqrt{1+\beta_0^2}\right)k_{0_g}R_e'(k_x)+xk_x\right)\right)dk_x, \tag{3.23}$$

where,

$$R_e'(k_x) = R_e\left(R_{bs_g}\frac{k_x}{k_{0_g}}\right). \tag{3.24}$$

The form of the blurring function b_s is independent of the scatterer location (x_s,y_s,z_s) and produces an azimuthal blurring in the recovered PFA image. The functional form of the blurring kernel b_s is determined by the variation of R_e with k_x. In general platform position uncertainties manifest as demodulation errors with a low order polynomial dependence on aperture position. For example a constant bias in the measurement of the along track velocity of the sensor platform manifests as a quadratic phase error over the collection aperture producing a broadening of the mainlobe azimuthal width of the PFA point spread function [JWE+96]. Higher frequency errors can arise from unmodelled antenna jitter as well as unmodelled random transmission delays arising due to turbulence in the propagation medium. This is most prevalent in spaceborne SARs where the electromagnetic waves propagate through the troposphere and ionosphere [BG88]. The resulting phase error function has been found to have a power spectral density which may be modelled as a power-law random process,

$$S_{\phi_e}(k_x) = dk_x^{-p}, \tag{3.25}$$

where d is a constant of proportionality and p is the spectral index. Such high bandwidth phase error functions manifest as convolution kernels having large integrated sidelobe energy and result in a loss in contrast across the image recovered by the image formation processor.

3.2.3 Autofocus Algorithms

Autofocus algorithms attempt to estimate and compensate for residual unmodelled phase errors that remain after image formation processing in an automated way, independent of the sources of the phase errors. They are typically applied as a post processing operation on the image generated by the image formation processor and potentially allow the recovery of an image with near diffraction limited focusing. While the residual uncompensated phase errors generally manifest as a two dimensional blur kernel (3.21) most autofocus algorithms are developed using the small fractional bandwidth and small angular approximations given in (3.22). This simplifies the estimation of the phase errors as the resulting blur kernel b_s given in (3.23) is now independent of scattering location and a one dimensional function of azimuth only. A number of different techniques have been proposed in the literature for estimating and compensating for the unknown demodulation phase errors.

Map Drift Algorithm

The map drift algorithm [MS81], [BG83] uses a parameteric model to describe the phase error functional dependence on the aperture position k_x. In this approach the phase error is expressed as a linear combination of L basis functions $\varphi_i(k_x), i = 1 \ldots L$,

$$\phi_{model}(k_x) \approx \sum_{i=1}^{L} p_i \varphi_i(k_x), \tag{3.26}$$

where the coefficients $p_i, i = 1 \ldots L$, are unknown and remain to be estimated from the phase corrupted image recovered by the image formation processor. In the map drift algorithm the coefficients of the parametric model are estimated by firstly applying a Fourier transform with respect to azimuth in the recovered image $g_m(x, y)$ to give the range compressed signal history representation of the acquired data,

$$\mathcal{G}_m(k_x, y) = \int g_m(x, y) exp(-jxk_x) dx. \tag{3.27}$$

Substituting equation (3.18) for g_m above gives,

$$\begin{aligned}
\mathcal{G}_m(k_x, y) &= \frac{1}{4\pi^2} \iiint A_{ifp}(k'_x, k_y) G_p(k'_x, k_y, \beta_0(k_y + k_{0_g})) exp(j\phi_e(k'_x)) \\
&= exp(j(yk_y + xk'_x - xk_x)) dx dk'_x dk_y, \\
&= exp(j\phi_e(k_x)) \frac{1}{2\pi} \int A_{ifp}(k_x, k_y) G_p(k_x, k_y, \beta_0(k_y + k_{0_g})) exp(jyk_y) dk_y, \\
&= exp(j\phi_e(k_x)) \mathcal{G}_p(k_x, y),
\end{aligned} \tag{3.28}$$

where $\mathcal{G}_p(k_x, y)$ given by,

$$\mathcal{G}_p(k_x, y) = \frac{1}{2\pi} \int A_{ifp}(k_x, k_y) G_p(k_x, k_y + k_{0_g}, \beta_0(k_y + k_{0_g})) exp(jyk_y) dk_y, \tag{3.29}$$

is the range compressed deramp demodulated echo data in the absence of demodulation phase errors. The phase corrupted range compressed signal history data $\mathcal{G}_m$ is then partitioned into $L + 1$ equal width non-overlapping subapertures,

$$\mathcal{G}_m^{(i)}(k_x, y) = rect\left(\frac{k_x(L+1)}{k_{bw_x}}\right) \mathcal{G}_m\left(k_x + \Delta_i + \frac{k_{bw}}{2(L+1)}, y\right), \tag{3.30}$$

where,

$$\Delta_i = \frac{k_{bw}}{2(L+1)}(2i - L - 1), \text{ for } i = 0 \ldots L - 1. \tag{3.31}$$

An image of the scene may be recovered from each subaperture $\mathcal{G}_m^{(i)}$, albeit with a reduced resolution compared to that achieved by processing the entire available aperture, by applying an inverse Fourier transform with respect to k_x,

$$g_m^{(i)}(x, y) = \frac{1}{2\pi} \int \mathcal{G}_m^{(i)}(k_x, y) exp(jxk_x) dk_x. \tag{3.32}$$

Each subaperture image shall depict an image of the same scene in which the low spatial frequency features of the scene are visible, however each subaperture image will have a different uncorrelated

high frequency "speckle" pattern [MS84]. Any linear trend in the actual phase error over the subaperture, given by,

$$\bar{\omega}_i = \frac{1}{\Delta_{i+1} - \Delta_i} \int_{\Delta_i}^{\Delta_{i+1}} \frac{d\phi_e(k_x)}{dk_x} dk_x, \tag{3.33}$$

will cause an azimuthal translation of the associated subaperture image. As the low spatial frequency scene content is preserved in each subaperture image the associated intensity images $\left|g_m^{(i)}(x,y)\right|^2$ may be cross correlated to estimate the relative translation (map-drift),

$$\Delta\omega_i \quad = \quad \bar{\omega}_{i+1} - \bar{\omega}_i, \tag{3.34}$$

between neighbouring subaperture image pairs Using the phase error model ϕ_{model} in (3.26) in place of ϕ_e in equation (3.33) the value of $\Delta\omega_i$ may be expressed as a linear combination of the coefficients p_i. Estimating $\Delta\omega_i$ over all neighbouring subaperture image pairs and equating with the corresponding model based forms of $\Delta\omega_i$ gives a system of L linear equations with L unknowns which may be solved for the parametric model coefficients. The technique may be readily extended to provide a more robust estimate of the parametric coefficients by cross correlating all possible $(L-1)L/2$ pairs of subaperture images to generate an over-determined system of linear equations which may be solved via a least squares solution. An examination of the equations describing the relative azimuthal translation $\Delta\omega_i$ indicates that the map-drift may be interpreted as a coarse estimate of the second derivative of the phase error function evaluated at a point on the k_x axis midway between the two corresponding subapertures. As a consequence the map drift algorithm models only the non-linear portion of the phase error function ϕ_e.

In its most simplest form the map drift algorithm uses a quadratic polynomial description for the phase error function and an estimate of the quadratic coefficient may be retrieved by cross correlating a single pair of non-overlapping subaperture images. Historically the quadratic phase error function has been major source of azimuthal blurring in fine resolution SAR systems [CGM95] and this simple formulation of the map drift provides a robust and efficient approach to estimating this type of error. Clearly though, the use of this model becomes problematic if the phase error function ϕ_e contains higher order terms. In this case more sophisticated formulations of the map drift technique have been proposed using higher order polynomial and Legendre polynomial expansions [BG88], [GB88] for the parametric basis functions. A more recent proposal, [CD94], [Cal92] looks at replacing the polynomial model with a set of sinusoidal basis functions and it is found that the sinusoidal parameterisation improves the estimation of high-order phase errors arising from a power-law spectral description of ϕ_e.

The performance of the map drift technique is fundamentally limited by the validity of the particular parameterisation used to model the phase error function. While drifts in the radar location measurements arising from the INU may be adequately modelled as low order functions, turbulence buffeting the aircraft or propagation anomalies generally manifest as higher order functions and the scope for estimating and correcting these wide bandwidth errors is limited using model based approaches. A further limitation of the technique, when applied to high order parameterisations, is the accuracy with which the parameter coefficients may be estimated. In order to accommodate higher order parameterisations the available k_x bandwidth must be partitioned into more subapertures. Each subaperture is thus proportionately smaller and the resolution of the associated image is coarser. As a consequence noisier estimates of the cross correlation lags are obtained leading to poor estimates of the parameter coefficients.

Point Based Algorithms

An examination of the equations describing the relationship between the fully focused PFA image given in (3.20) and the image recovered in the presence of the phase error function ϕ_e given by (3.19) indicates that, for an idealised scene consisting of a single point target, an estimate of the phase error may be obtained by simple inverse filtering. This is the basis of the prominent point focusing algorithms that are more commonly used in Inverse SAR (ISAR) imaging [Ste88], [KSS90] and [WGDF95]. Given a single scatterer at location (x_s, y_s, z_s) with reflectivity given by,

$$r(x,y,z) = q_s exp(j\phi_s)\delta(x - x_s, y - y_s, z - z_s), \tag{3.35}$$

the recovered ground plane image assuming straight and level flight without squint, in the presence of a demodulation phase error ϕ_e is given by,

$$\begin{aligned} g_m(x,y) &= \frac{k_{bw_x} k_{bw_y}}{4\pi^2} q_s exp(j\phi_s) exp(-jk_{0_g}(y_s + z_s\beta_0)) \\ &\quad sinc\left((y - y_s - z_s\beta_0)\frac{k_{bw_y}}{2\pi}\right)\left(sinc\left((x - x_s)\frac{k_{bw_x}}{2\pi}\right) \otimes b_s(x)\right), \end{aligned} \tag{3.36}$$

where $b_s(x)$ is the uncompensated azimuthal blur function given in (3.23). Applying a Fourier transform with respect to k_x to obtain the range compressed data gives

$$\begin{aligned} \mathcal{G}_m(k_x,y) &= \frac{k_{bw_y}}{2\pi} q_s exp(j\phi_s) exp(-jk_{0_g}(y_s + z_s\beta_0)) rect\left(\frac{k_x}{k_{bw_x}}\right) \\ &\quad exp(j(\phi_e(k_x) - x_s k_x)) sinc\left((y - y_s - z_s\beta_0)\frac{k_{bw_y}}{2\pi}\right), \end{aligned} \tag{3.37}$$

which has a phase given by,

$$\phi_{\mathcal{G}_m} = \phi_s - k_{0_g}(y_s + z_s\beta_0) - x_s k_x + \phi_e(k_x). \tag{3.38}$$

An examination of the phase $\phi_{\mathcal{G}_m}$ shows that, while the constant and linear phase components of the phase are determined by the phase error ϕ_e, the scatterer's reflectivity ϕ_s and its spatial location the non-linear components of $\phi_{\mathcal{G}_m}$ are uniquely determined by the phase error ϕ_e. Thus the nonlinear components of ϕ_e may be estimated uniquely via a numerical differentiation of the phase $\phi_{\mathcal{G}_m}$. Unlike the mapdrift approach, the prominent point algorithm does not rely on a parametric representation of the phase error function and is therefore potentially able to estimate both high and low frequency phase errors. The technique however does rely on being able to identify a single, sufficiently isolated, high signal to clutter power, prominent point in the recovered imagery. In practice selection of a suitable prominent point generally requires user intervention in the algorithm and the unavoidable presence of noise and clutter in the vicinity of the prominent point leads to degradation in the phase error estimate [CGM95].

Phase Gradient Algorithm

While the prominent point focusing algorithm has the advantage of being non parametric the sensitivity of the phase estimate to clutter and noise contributions makes it a poor estimator. The fact that the phase error convolution kernel is independent of the point scatterer location under the small fractional bandwidth and small angle approximations however means that all scatterers in the scene are subject to the same azimuthal defocus. This redundancy in the phase corrupted image is exploited by the PGA algorithm [EGJ89] to yield a statistically based, optimal estimate of the phase error function.

Data Domain	Continuous Data	Sampled Data
Signal History	$G_p(k_x, k_y)$ $\lvert k_x\rvert \leq \frac{k_{bw_x}}{2}, \lvert k_y\rvert \leq \frac{k_{bw_y}}{2}$	$G_p(u,v)$ $u = 0 \ldots L-1, v = 0 \ldots M-1$
Range Compressed Signal History	$\mathcal{G}_p(k_x, y) =$ $\frac{1}{2\pi}\int G(k_x,k_y)exp(jyk_y)dk_y$	$\mathcal{G}_p(u,m) =$ $\frac{1}{\sqrt{M}}\sum_{v=0}^{M-1} G(u,v)exp\left(j\frac{2\pi vm}{M}\right)$
Image Domain	$g_p(x,y) =$ $\frac{1}{2\pi}\int \mathcal{G}_p(k_x,y)exp(jxk_x)dk_x$	$g_p(l,m) =$ $\frac{1}{\sqrt{L}}\sum_{u=0}^{L-1} \mathcal{G}_p(u,m)exp\left(j\frac{2\pi ul}{L}\right)$

Table 3.1: Relationships between the collected signal history data, the range compressed signal history and the image domain data for both continuous and sample data domains.

The PGA algorithm has been shown to be a robust method that allows the recovery of near diffraction limited resolution imagery over a wide variety of scenes and phase error functions [WEGJ94].

The theoretical basis for the PGA algorithm is most readily explained by formulating the autofocus problem as an optimal estimation problem [EJ89], [JW93] in terms of the discrete sampled data equivalents of the continuous data representations previously developed. Table 3.1 shows the continuous and discrete representations of the data in the absence of any demodulation errors (i.e. $R_e = 0$). The continuous data functions may be retrieved from the discrete sampled equivalents provided the sampling rate used to generate the discrete data samples satisfies the Nyquist sampling conditions. The signal history data, for the purposes of analysis of the PGA algorithm, is the collected demodulated data obtained after all reformatting (eg: polar to rectangular) has been performed. The range compressed signal history data is obtained after applying a inverse Fourier (or discrete inverse Fourier) transform to the range spatial frequency in the signal history data. The recovered image is obtained from the range compressed signal history data by applying an inverse Fourier transform in the azimuth spatial frequency variable.

In the sampled data domain, at a given range bin m, the range compressed signal history data and image domain data may be efficiently represented in vector notation by,

$$\underline{\mathcal{G}}_p(m) = \begin{bmatrix} \mathcal{G}_p(0,m) \\ \mathcal{G}_p(1,m) \\ \vdots \\ \mathcal{G}_p(L-1,m) \end{bmatrix} \quad \text{and} \quad \underline{g}_p(m) = \begin{bmatrix} g_p(0,m) \\ g_p(1,m) \\ \vdots \\ g_p(L-1,m) \end{bmatrix},$$

respectively. The Fourier transform relationship between range compressed signal history $\underline{\mathcal{G}}_p(m)$ and image domain $\underline{g}_p(m)$ vectors can be efficiently described by means of a unitary transform matrix W. Defining the column vector,

$$\underline{w}(k) = \begin{bmatrix} exp\left(j\frac{2\pi k}{L}(0)\right) \\ exp\left(j\frac{2\pi k}{L}(1)\right) \\ \vdots \\ exp\left(j\frac{2\pi k}{L}(L-1)\right) \end{bmatrix}, \tag{3.39}$$

the discrete forward Fourier transform is given by the matrix,

$$W = \frac{1}{\sqrt{L}} \begin{bmatrix} \underline{w}^H(0) \\ \underline{w}^H(1) \\ \vdots \\ \underline{w}^H(L-1) \end{bmatrix}, \tag{3.40}$$

and the discrete inverse Fourier transform is given by the matrix,

$$\begin{aligned} W^{-1} &= \frac{1}{\sqrt{L}} \begin{bmatrix} \underline{w}(0) & \underline{w}(1) & \cdots \underline{w}(M-1) \end{bmatrix}, \\ &= W^H. \end{aligned} \tag{3.41}$$

Thus given a vector slice $\underline{g}_p(m)$ of the image g_p at range bin m the corresponding range compressed signal history slice is obtained by applying the transform matrix W, such that $\underline{\mathcal{G}}_p(m) = W\underline{g}_p(m)$. Applying the inverse matrix $W^{-1} = W^H$ recovers the original image domain vector $\underline{g}_p(m) = W^H\underline{\mathcal{G}}_p(m)$.

An unknown demodulation phase error may be represented by the vector,

$$\underline{\phi}_e = \begin{bmatrix} exp(j\phi_0) \\ exp(j\phi_1) \\ \vdots \\ exp(\phi_{L-1}) \end{bmatrix}, \tag{3.42}$$

where $\phi_i, i = 0 \cdots L-1$ are uniformly spaced samples of $\phi_e(k_x)$ given in (3.22). The phase error vector $\underline{\phi}_e$ manifests in the range compressed signal history domain as,

$$\begin{aligned} \underline{\mathcal{G}}_m(m) &= diag(\underline{\phi}_e)\underline{\mathcal{G}}_p(m), \\ &= diag(\underline{\phi}_e)W\underline{g}_p(m), \\ &= P\underline{g}_p(m), \end{aligned} \tag{3.43}$$

where $diag(\underline{\phi}_e)$ is the diagonal matrix formed from the phase error vector $\underline{\phi}_e$ i.e.,

$$diag(\underline{\phi}_e) = \begin{bmatrix} e^{j\phi_0} & 0 & \cdots & 0 \\ 0 & e^{j\phi_1} & & 0 \\ \vdots & & \ddots & \vdots \\ 0 & \cdots & & e^{j\phi_{L-1}} \end{bmatrix}, \tag{3.44}$$

and P is a unitary matrix given by $P = diag(\underline{\phi}_e)W$. Applying W^H to $\underline{\mathcal{G}}_m(m)$ recovers the phase corrupted image domain slice,

$$\begin{aligned} \underline{g}_m(m) &= W^H\underline{\mathcal{G}}_m(m), \\ &= W^H diag(\underline{\phi}_e)W\underline{g}_p(m). \end{aligned} \tag{3.45}$$

The task of the autofocus algorithm is to obtain an estimate of $\underline{\phi}_e$ from the transduced L element vectors $\underline{\mathcal{G}}_m(m)$ and subsequently recover the fully focused image vectors $\underline{g}_p(m)$. The problem however, is ill posed as there are L more unknowns than there are available measurements. Thus to arrive at a solution a model based description of either the phase error function (cf: map drift) or the

scene reflectivity is required to reduce the effective number of unknowns and obtain a reliable, robust estimate of $\underline{\phi}_e$. In the PGA algorithm a statistically based model is utilised that permits the coherent combination of information across multiple range bins to arrive at a single optimal estimate of $\underline{\phi}_e$.

For natural distributed target environments the transduced backscatter in a given resolution cell may be modelled as a zero mean, complex, circular Gaussian random variable with variance σ^2. Using this model and assuming sampling at the Nyquist rate the image slice vector $\underline{g}_p(m)$ may be considered to be a vector of L independent random complex Gaussian processes characterised by the covariance matrix,

$$C_g = E\{\underline{g}_p \underline{g}_p^H\} = \begin{bmatrix} \sigma_0^2 & 0 & \cdots & 0 \\ 0 & \sigma_1^2 & & 0 \\ \vdots & & & \\ & & \ddots & \vdots \\ 0 & \cdots & & \sigma_{L-1}^2 \end{bmatrix} = diag(\underline{\sigma}^2). \tag{3.46}$$

(Note that the dependence of g_p on m has been dropped in the expression for C_g.) As the matrix P is a unitary matrix the range compressed signal history vector given by, $\underline{\mathcal{G}}_m = P\underline{g}_p$ may also be described as a vector of L zero mean, complex circular Gaussian processes with covariance matrix given by,

$$\begin{aligned} C_{\mathcal{G}_m} &= E\{\underline{\mathcal{G}}_m \underline{\mathcal{G}}_m^H\}, \\ &= E\{P\underline{g}_p \underline{g}_p^H P^H\}, \\ &= PC_g P^H. \end{aligned} \tag{3.47}$$

Substituting (3.46) into (3.47) and rearranging gives,

$$P^H C_{\mathcal{G}_m} P = diag(\underline{\sigma}^2). \tag{3.48}$$

The matrix P thus unitarily diagonalises $C_{\mathcal{G}_m}$ and therefore the columns vectors of the matrix P constitute L linearly independent eigenvectors of the covariance matrix $C_{\mathcal{G}_m}$, [AR87]. The eigenvalue associated with the eigenvector $\underline{p}_i$ given in the i^{th} column of P is given by the i^{th} leading diagonal term in the matrix $diag(\underline{\sigma}^2)$. The particular eigenvector of interest is the one that appears in the first column of P as this is simply the unknown phase error vector,

$$col_0(P) = \underline{p}_0 = \begin{bmatrix} e^{j\phi_0} \\ e^{j\phi_1} \\ \vdots \\ e^{j\phi_{L-1}} \end{bmatrix} = \underline{\phi}_e. \tag{3.49}$$

For the case in which the L image pixels in the vector $\underline{g}$ are all independent and identically distributed then the L eigenvalues are all identical, $\sigma_i^2 = \sigma^2, i = 0 \cdots L-1$. In this case the eigenvectors are not unique and the demodulation phase error vector $\underline{\phi}_e$ may not be recovered. However if the L image pixels have the following signal plus clutter form,

$$\begin{aligned} \underline{g}_p &= \underline{s} + \underline{n}, \\ &= s \begin{bmatrix} 1 \\ 0 \\ \vdots \\ 0 \end{bmatrix} + \begin{bmatrix} n_0 \\ n_1 \\ \vdots \\ n_{L-1} \end{bmatrix}, \end{aligned} \tag{3.50}$$

where s is some random signal process while $n_0, \cdots n_{L-1}$ are random clutter processes, then

$$C_g = E\{\underline{g}_p \underline{g}_p^H\} = \begin{bmatrix} \sigma_s^2 + \sigma_{n_0}^2 & 0 & \cdots & 0 \\ 0 & \sigma_{n_2}^2 & & 0 \\ \vdots & & & \\ & & \ddots & \vdots \\ 0 & \cdots & & \sigma_{n_{L-1}}^2 \end{bmatrix}. \tag{3.51}$$

Provided $\sigma_s^2 + \sigma_{n_0}^2 > \sigma_{n_1}^2, \cdots \sigma_{n_{L-1}}^2$ then the eigenvector associated with the largest eigenvalue of $C_{\mathcal{G}_m}$ is the unknown demodulation phase error vector.

The accuracy of this approach for recovering the unknown demodulation phase error vector is crucially dependent on obtaining an accurate estimate of the covariance matrix $C_{\mathcal{G}_m}$ and also on the validity of the signal model (3.50) in representing the scene vectors $\underline{g}_p(m)$. In a practical implementation of the PGA algorithm a sample estimate of the covariance matrix $C_{\mathcal{G}_m}$ is formed from the range compressed signal history slices $\mathcal{G}_m(M)$

$$\hat{C}_{\mathcal{G}_m} = \frac{1}{M} \sum_{m=0}^{M-1} \mathcal{G}_m(m) \mathcal{G}_m^H(m). \tag{3.52}$$

The sample estimate $\hat{C}_{\mathcal{G}_m}$ is a maximum likelihood estimate of the true covariance and its dominant eigenvector may be recovered using numerical techniques [AR87]. It should be noted however that while the eigenvector associated with the largest eigenvalue of $C_{\mathcal{G}_m}$ will be the phase only vector equal to $\underline{\phi}_e$, the corresponding eigenvector obtained from the sample estimate $\hat{C}_{\mathcal{G}_m}$ will generally not be phase only. For sufficiently large values L though, the sample covariance matrix closely approximates the true covariance and so it is sufficient to use the phase components of the sample covariance eigenvector as the phase error vector estimate [JW93].

The PGA algorithm also incorporates the additional steps of circular shifting and windowing in which image vectors $\underline{g}_m(m)$ are manipulated into the form of (3.50) without corrupting the non-linear components of the phase error vector. In the circular shifting step of the PGA the strongest scatterer in each slice $\underline{g}_m(m)$ for $m = 0 \ldots M-1$ is circularly shifted, in azimuth, to the zeroth azimuth position. This ensures a strong dominant signal component consistent with the model (3.50) while maintaining the non-linear component of the uncompensated phase error, see Appendix B. The windowing PGA step seeks to further improve the signal to clutter and noise ratio of the samples used in the covariance estimation by de-weighting contributions that arise predominantly due to the clutter rather than the signal in the model (3.50), see Appendix B. Without these steps the PGA has been demonstrated to generate inferior phase error estimates [WEGJ94].

3.2.4 Research Motivation

In the previous chapter on image formation the processing of wide-band, wide-angle spotlight SAR range echo data for generating fine resolution imagery was addressed. The coherent processing of range echo data over extended collection apertures however requires accurate measurement of the radar location over the entire aperture. Any measurement bias or drifts present in the onboard navigation systems can accumulate into substantial errors over extended collection apertures. Autofocus algorithms are thus crucial to realising the potential image resolution of these collection scenarios.

Of the autofocus algorithms discussed in Section 3.2.3, the PGA algorithm has been demonstrated to be a robust technique for recovering imagery with near diffraction limited resolution over a wide variety of scenes and phase error functions. The PGA steps of circular shifting, windowing and the

simultaneous processing of multiple targets to provide an optimal estimate of the common blurring function make the PGA a particularly powerful technique. The PGA however, does assume that the form of the phase error function is independent of scatterer location and produces an azimuthal blurring of the recovered image only. This means that all scatterers are subject to the same azimuthal blurring and this redundancy is specifically exploited by the PGA to arrive at a robust phase error estimate. It has been shown in the previous section that this phase error model is only applicable in the case of small fractional bandwidths and small collection apertures. In general the phase error function has a dependence on the range spatial frequency and manifests in the image domain as a two dimensional blurring convolution kernel. The two dimensional form of the phase error function can lead to corruption of the PGA phase error estimate and the presence of residual range and azimuthal blurring in the image recovered after PGA processing. A further subtle point is that errors in the measurement of the radar location at each transmit/receive point manifest as both errors in the demodulation reference delay as well as errors in the computation of the azimuth and elevation angles from the scene centre to the radar sensor. Use of these erroneous angle measurements in the PFA means that the deramp demodulated echo data will be mapped onto a distorted grid. While these sources of image domain defocus are generally small they can become significant in the focusing of wide-angle imaging considered in this thesis.

In the following sections the range dependence of the demodulation phase error function will be analysed and its impact on the PGA algorithm assessed. A simple modification is proposed to mitigate the dominant deleterious effects that arise in the case of a phase error function that is quadratic in azimuth spatial frequency. The presence of measurement errors in the azimuth and elevation angles will also be considered and the impact on the image domain defocus will be analysed.

3.3 A Complete Phase Error Model

In order to process spotlight SAR data using deramp demodulation and the PFA, accurate knowledge of the pointing vectors $\underline{P}_T = [R_T, \theta_T, \psi_T]^T$ specifying the range, azimuth and elevation look angles of the radar with respect to the scene focus point are required. The slant range R_T is used to compute the reference delay required to formulate the reference functions in the deramp demodulation technique. The azimuth and elevation angles on the other hand, are used in the PFA to specify the location of the deramp demodulated range echo data in the spatial frequency domain representation of the scene's reflectivity. Uncertainty in the radar platform location may be modelled at each transmit/receive point by considering a location measurement error $\underline{P}_e = [R_e, \theta_e, \psi_e]^T$ such that the true location $\underline{P}_T = [R_T, \theta_T, \psi_T]^T$ is obtained by adding the measurement error to the measured location $\underline{P}_m = [R_m, \theta_m, \psi_m]^T$, i.e.,

$$\underline{P}_T = \begin{bmatrix} R_T \\ \theta_T \\ \psi_T \end{bmatrix} = \begin{bmatrix} R_m \\ \theta_m \\ \psi_m \end{bmatrix} + \begin{bmatrix} R_e \\ \theta_e \\ \psi_e \end{bmatrix}. \tag{3.53}$$

The range error, R_e, leads to errors in the formation of the demodulation chirp used in the deramp processing and its impact on imagery recovered via the PFA has been analysed in Section 3.2.2. The azimuth and elevation angle errors (θ_e, ψ_e) will lead to errors in the computation of the spatial frequency vector $\underline{k}_T$ and hence errors in the polar to rectangular resampling step of the PFA.

3.3.1 Azimuth and Elevation Angle Errors in the Polar Format Algorithm

The point scatterer response of the PFA in the presence of a measurement error $\underline{P}_e = [R_e, \theta_e, \psi_e]^T$ may be derived by considering a scene consisting of an arbitrary point scatterer with reflectivity given

by,

$$r(x,y,z) = q_s exp(j\phi_s)\delta(x - x_s, y - y_s, z - z_s). \tag{3.54}$$

From Section 3.2.2 the acquired deramp demodulated echo data supplied to the image formation algorithm at a given transmit/receive point may be described by,

$$G_{m_2}(\underline{k}_T) = q_s exp(j\phi_s) rect\left(\frac{|\underline{k}_T| - k_0}{k_{bw}}\right) exp(j(-\underline{k}_T^T \cdot \underline{\rho} + |\underline{k}_T|R_e)), \tag{3.55}$$

where $\underline{\rho} = [x_s, y_s, z_s]^T$ is the vector from the scene focus point to the point scatterer location and,

$$\underline{k}_T = \begin{bmatrix} (k_r + k_0)\cos\psi_T \sin\theta_T \\ (k_r + k_0)\cos\psi_T \cos\theta_T \\ (k_r + k_0)\sin\psi_T \end{bmatrix}. \tag{3.56}$$

Equation (3.55) indicates that the deramp signal samples G_{m_2} may be interpreted as being samples of the spatial Fourier transform of the point scatterer evaluated on an interval $(k_0 - k_{bw}/2 < |\underline{k}_T| < k_0 + k_{bw}/2)$ defined along a radial with orientation given by the unit pointing vector,

$$\underline{v}_T = \begin{bmatrix} \cos\psi_T \sin\theta_T \\ \cos\psi_T \cos\theta_T \\ \sin\psi_T \end{bmatrix}. \tag{3.57}$$

The samples are also subject to an unknown phase modulation that is linearly dependent on $|\underline{k}_T|$ that arises due to the demodulation range error R_e.

The error $\underline{P}_e$, in the measured location $\underline{P}_m$, of the radar however means that the PFA image formation algorithm erroneously interprets the deramp spectral samples G_{m_2} as samples of the scene's spatial frequency representation evaluated at points along the measured spatial frequency vector given by,

$$\underline{k}_m = (k_r + k_0)\begin{bmatrix} \cos\psi_m \sin\theta_m \\ \cos\psi_m \cos\theta_m \\ \sin\psi_m \end{bmatrix} = \begin{bmatrix} k_x \\ k_y \\ k_z \end{bmatrix}. \tag{3.58}$$

(Note that in (3.58) the spatial frequency variables k_x, k_y and k_z are defined in terms of the measured azimuth and elevation angles as opposed to the true quantities as used in the definition given in (3.5). This is because the PFA recovers an image of the scene by operating on the measured spatial frequency vectors $\underline{k}_m$ and hence the range, azimuth and elevation spatial frequency variables, k_x, k_y and k_z as defined in (3.58).)

Over the coherent processing interval the pointing vectors $\underline{v}_T$ at each transmit/receive point describe the mapping of the associated deramp demodulated echo data into the spatial frequency domain representation of the scene. The spatial frequency vectors $\underline{k}_T = (k_r + k_0)\underline{v}_T$ thus specify a surface function in the scene's three dimensional spatial frequency domain that defines an acquisition aperture of support A_{acq_T}. However, as each measurement of the radar location is subject to a unknown error that varies from pulse to pulse, the spatial frequency vectors computed by the PFA, namely $\underline{k}_m = (k_r + k_0)\underline{v}_m$, will specify an acquisition aperture of support A_{acq} that is distorted with respect to the actual aperture A_{acq_T}. For example, Figure 3.2 shows the true and measured sample locations of the deramp echo data projected down onto the (k_x, k_y) plane that arises in the case of straight and level flight without squint in which the measured transmit/receive locations are subject to a bias in the measurement of the platform's along track velocity. It can be seen that the measured sample grid

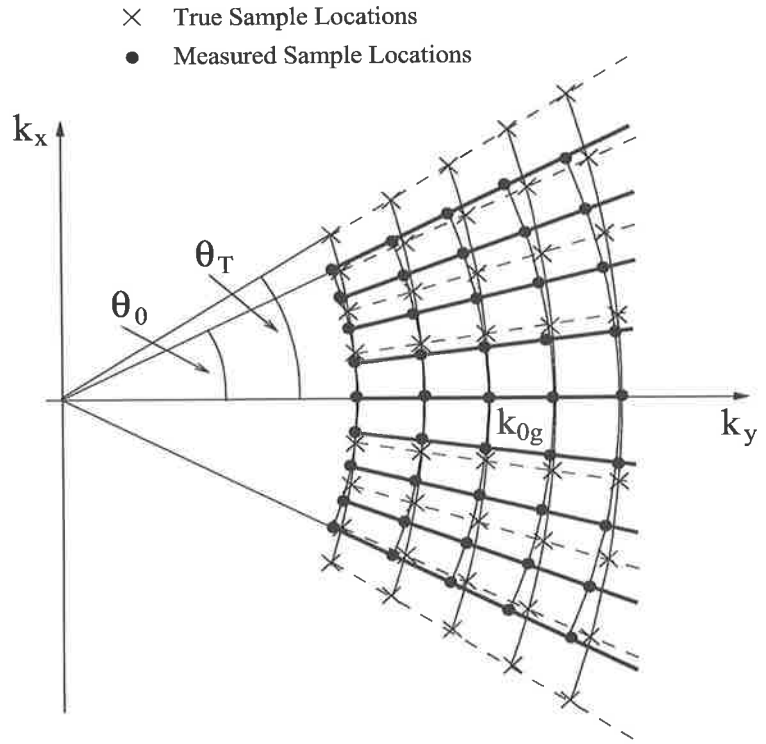


Figure 3.2: Ground plane projection of the polar raster grid of the collected signal history data obtained using the measured and true azimuth and depression look angles for the case of straight and level flight without squint subject to a bias in the measurement of the along track velocity.

locations are a "dilated" representation of the true sample grid locations. The impact of the distortion present in the measured sample grid locations on the recovered PFA image will now be considered.

Given that the measurement errors (θ_e, ψ_e) at a given transmit/receive point are typically small, a small angle approximation may be used to derive a relationship between the true spatial frequency vector $\underline{k}_T$ and the corresponding measured spatial frequency vector $\underline{k}_m$,

$$\begin{aligned} \underline{k}_T &= (k_r + k_0) \begin{bmatrix} \cos(\psi_m + \psi_e)\sin(\theta_m + \theta_e) \\ \cos(\psi_m + \psi_e)\cos(\theta_m + \theta_e) \\ \sin(\psi_m + \psi_e) \end{bmatrix}, \\ &\approx \underline{k}_m + \theta_e \underline{k}_1 + \psi_e \underline{k}_2, \end{aligned} \tag{3.59}$$

where $\underline{k}_m$ is given in (3.58) and,

$$\underline{k}_1 = (k_r + k_0) \begin{bmatrix} \cos(\psi_m)\cos(\theta_m) \\ -\cos(\psi_m)\sin(\theta_m) \\ 0 \end{bmatrix}, \tag{3.60}$$

$$\underline{k}_2 = (k_r + k_0) \begin{bmatrix} -\sin(\psi_m)\sin(\theta_m) \\ -\sin(\psi_m)\cos(\theta_m) \\ \cos(\psi_m) \end{bmatrix}. \tag{3.61}$$

Using the definitions of k_x, k_y and k_z in (3.58) the vectors $\underline{k}_1$ and $\underline{k}_2$ may be written as,

$$\underline{k}_1(k_x,k_y,k_z) = \begin{bmatrix} k_y \\ -k_x \\ 0 \end{bmatrix} \quad \text{and} \quad \underline{k}_2(k_x,k_y,k_z) = \begin{bmatrix} -\frac{k_z k_x}{\sqrt{k_x^2+k_y^2}} \\ -\frac{k_z k_y}{\sqrt{k_x^2+k_y^2}} \\ \frac{\sqrt{k_x^2+k_y^2}}{k_r+k_0} \end{bmatrix}. \tag{3.62}$$

Since $|\underline{k}_T| = |\underline{k}_m| = (k_r+k_0)$ (see the definitions of $\underline{k}_T$ and $\underline{k}_m$ in (3.56) and (3.58) respectively) and using the approximate relationship between $\underline{k}_T$ and $\underline{k}_m$ in (3.59) the acquired deramp demodulated echo data supplied to the image formation algorithm for the point target $r(x,y,z)$ in (3.54) may be written as

$$\begin{aligned} G_{m_2}(\underline{k}_T) &= q_s exp(j\phi_s) rect\left(\frac{|\underline{k}_T| - k_0}{k_{bw}}\right) exp(j(-\underline{k}_T^T \cdot \underline{\rho} + |\underline{k}_T| R_e)), \\ &\approx q_s exp(j\phi_s) rect\left(\frac{|\underline{k}_m| - k_0}{k_{bw}}\right) exp(j(-(\underline{k}_m + \theta_e \underline{k}_1 + \psi_e \underline{k}_2)^T \cdot \underline{\rho} + |\underline{k}_m| R_e)), \\ &\approx q_s exp(j\phi_s) rect\left(\frac{|\underline{k}_m| - k_0}{k_{bw}}\right) exp(-j\underline{k}_m^T \cdot \underline{\rho}) exp(j\phi_{uncomp}(k_x,k_y,k_z)), \end{aligned} \tag{3.63}$$

where the phase term $\phi_{uncomp}(k_x,k_y,k_z)$ is given by,

$$\phi_{uncomp}(k_x,k_y,k_z) = \phi_{(\theta_e,\psi_e)}(k_x,k_y,k_z) + \phi_{R_e}(k_x,k_y,k_z). \tag{3.64}$$

The phase contribution ϕ_{R_e} in ϕ_{uncomp} is the demodulation error arising from the slant range error R_e and takes the form,

$$\begin{aligned} \phi_{R_e}(k_x,k_y,k_z) &= |\underline{k}_m| R_e, \\ &= \sqrt{k_x^2+k_y^2+k_z^2} R_e, \end{aligned} \tag{3.65}$$

while the phase term $\phi_{(\theta_e,\psi_e)}$ is given by,

$$\phi_{(\theta_e,\psi_e)}(k_x,k_y,k_z) = -\theta_e \underline{k}_1^T(k_x,k_y,k_z) \cdot \underline{\rho} - \psi_e \underline{k}_2^T(k_x,k_y,k_z) \cdot \underline{\rho}, \tag{3.66}$$

and encapsulates the dominant residual uncompensated phase terms that arise due to the errors (θ_e,ψ_e) made in the measurement of the look direction from the scene centre to the radar platform at each transmit/receive point along the collection aperture.

Defining $G^a_{m_2}(\underline{k}_T)$ to be the approximate form for $G_{m_2}(\underline{k}_T)$ in (3.63) i.e.,

$$G^a_{m_2}(\underline{k}_T) = q_s exp(j\phi_s) rect\left(\frac{|\underline{k}_m| - k_0}{k_{bw}}\right) exp(-j\underline{k}_m^T \cdot \underline{\rho}) exp(j\phi_{uncomp}(k_x,k_y,k_z)), \tag{3.67}$$

then over the entire synthetic aperture the acquired deramp demodulated echo data takes the form,

$$G_{m_3}(k_x,k_y,k_z) = A_{acq_T}(k_x,k_y,k_z) G^a_{m_2}(\underline{k}_T), \tag{3.68}$$

where $A_{acq_T}(k_x,k_y,k_z)$ is the acquisition aperture of support defined by the variation in the spatial frequency vectors $\underline{k}_T$ over the coherent processing interval. As the acquisition aperture takes the form of a surface function defined in the scene's spatial frequency domain it may be written in the following form,

$$A_{acq_T}(k_x,k_y,k_z) = A_{ac}(k_x,k_y)\delta(k_z - f(k_x,k_y)), \tag{3.69}$$

where $f(k_x, k_y)$ defines the surface function in (k_x, k_y, k_z) space. Substituting the form for $G^a_{m_2}(\underline{k}_T)$ given in (3.67) into the expression for G_{m_3} gives,

$$\begin{aligned} G_{m_3}(k_x, k_y, k_z) &= A_{acq_T}(k_x, k_y, k_z) q_s exp(j\phi_s) rect\left(\frac{|\underline{k}_m| - k_0}{k_{bw}}\right) \\ &\qquad exp(-j\underline{k}_m^T \cdot \underline{\rho}) exp(j\phi_{uncomp}(k_x, k_y, k_z)), \\ &= A_{acq_T}(k_x, k_y, k_z) G_p(k_x, k_y, k_z) exp(j\phi_{uncomp}(k_x, k_y, k_z)), \end{aligned} \tag{3.70}$$

where,

$$G_p(k_x, k_y, k_z) = q_s exp(j\phi_s) rect\left(\frac{|\underline{k}_m| - k_0}{k_{bw}}\right) exp(-j\underline{k}_m^T \cdot \underline{\rho}). \tag{3.71}$$

Following the description of the PFA in Section 3.2.2 a ground plane PFA image is recovered from G_{m_3} by applying a three dimensional inverse Fourier transform to a windowed, baseband form of G_{m_3} given by,

$$\begin{aligned} G_m(k_x, k_y, k_z) &= G_{m_3}(k_x, k_y + k_{0_g}, k_z), \\ &= A_{acq_T}(k_x, k_y + k_{0_g}, k_z) G_p(k_x, k_y + k_{0_g}, k_z) exp(j\phi_{uncomp}(k_x, k_y + k_{0_g}, k_z)), \end{aligned} \tag{3.72}$$

where $k_{0_g} = k_0 \cos(\psi_0)$. The recovered PFA ground plane image is thus given by,

$$g_m(x, y) = \frac{1}{8\pi^3} \iiint A_{ifp}(k_x, k_y) G_m(k_x, k_y, k_z) exp(j(xk_x + yk_y)) dk_x dk_y dk_z, \tag{3.73}$$

where $A_{ifp}(k_x, k_y)$ is the windowing function typically chosen to be some region lying wholely within the acquired aperture of support such that

$$\begin{aligned} A_{ifp}(k_x, k_y) A_{acq_T}(k_x, k_y + k_{0_g}, k_z) &= A_{ifp}(k_x, k_y) A_{acq_T}(k_x, k_y + k_{0_g}) \delta(k_z - f(k_x, k_y + k_{0_g})), \\ &= A_{ifp}(k_x, k_y) \delta(k_z - f(k_x, k_y + k_{0_g})). \end{aligned} \tag{3.74}$$

Substituting (3.70) into (3.73) and using (3.74) gives,

$$\begin{aligned} g_m(x, y) &= \frac{1}{4\pi^2} \iint A_{ifp}(k_x, k_y) G_p(k_x, k_y + k_{0_g}, f(k_x, k_y + k_{0_g})) \\ &\qquad exp(j\phi_{uncomp}(k_x, k_y + k_{0_g}, f(k_x, k_y + k_{0_g}))) exp(j(xk_x + yk_y)) dk_x dk_y. \end{aligned} \tag{3.75}$$

Equation (3.75) may be written as the convolution of the PFA image $g_p(x, y)$ recovered in the absence of any demodulation errors (i.e. $\phi_{uncomp} = 0$) and a blurring filter kernel $b(x, y)$ to describe the image domain effects of the errors ϕ_{uncomp}, i.e.,

$$g_m(x, y) = g_p(x, y) \otimes b(x, y), \tag{3.76}$$

where,

$$g_p(x, y) = \frac{1}{4\pi^2} \iint A_{ifp}(k_x, k_y) G_p(k_x, k_y + k_{0_g}, f(k_x, k_y + k_{0_g})) exp(j(xk_x + yk_y)) dk_x dk_y, \tag{3.77}$$

and,

$$b(x,y) = \frac{1}{4\pi^2}\iint exp(j\phi_{uncomp}(k_x, k_y + k_{0_g}, f(k_x, k_y + k_{0_g})))exp(j(xk_x + yk_y))dk_x dk_y. \tag{3.78}$$

The form of the image domain blurring kernel $b(x,y)$ depends on the functional relationship between the components of the phase function $\phi_{uncomp}(k_x, k_y + k_{0_g}, k_z)$, namely $\phi_{R_e}(k_x, k_y + k_{0_g}, k_z)$ and $\phi_{(\theta_e,\psi_e)}(k_x, k_y + k_{0_g}, k_z)$, and the spatial frequency domain variables k_x, $k_y + k_{0_g}$ and $k_z = f(k_x, k_y + k_{0_g})$. In the previous section the form of $\phi_{R_e}(k_x, k_y + k_{0_g}, k_z)$ was analysed and its image domain effects quantified. The phase term $\phi_{(\theta_e,\psi_e)}(k_x, k_y + k_{0_g}, k_z)$ on the other hand is given by,

$$\phi_{(\theta_e,\psi_e)}(k_x, k_y + k_{0_g}, k_z) = -\theta_e \underline{k}_1^T(k_x, k_y + k_{0_g}, k_z) \cdot \underline{\rho} - \psi_e \underline{k}_2^T(k_x, k_y + k_{0_g}, k_z) \cdot \underline{\rho}, \tag{3.79}$$

where from (3.62),

$$\underline{k}_1(k_x, k_y + k_{0_g}, k_z) = \begin{bmatrix} k_y + k_{0_g} \\ -k_x \\ 0 \end{bmatrix}, \tag{3.80}$$

$$\underline{k}_2(k_x, k_y + k_{0_g}, k_z) = \begin{bmatrix} -\frac{k_z k_x}{\sqrt{k_x^2 + (k_y + k_{0_g})^2}} \\ -\frac{k_z(k_y + k_{0_g})}{\sqrt{k_x^2 + (k_y + k_{0_g})^2}} \\ \frac{\sqrt{k_x^2 + (k_y + k_{0_g})^2}}{k_r + k_0} \end{bmatrix}. \tag{3.81}$$

Provided k_{0_g} is sufficiently large compared to the azimuth spatial frequency bandwidth, $\underline{k}_2$ may be written in the following approximate form,

$$\underline{k}_2(k_x, k_y + k_{0_g}, k_z) \approx \begin{bmatrix} -\frac{k_z k_x}{(k_y + k_{0_g})} \\ -k_z \\ \left(1 + \frac{k_z^2}{(k_y + k_{0_g})^2}\right)^{-\frac{1}{2}} \end{bmatrix}, \tag{3.82}$$

where the relation $k_r + k_0 = \sqrt{k_x^2 + (k_y + k_{0_g})^2 + k_z^2}$ has been used. Substituting $\underline{k}_1$ and the approximate expression for $\underline{k}_2$ into the expression for $\phi_{(\theta_e,\psi_e)}(k_x, k_y + k_{0_g}, k_z)$ gives,

$$\begin{aligned}\phi_{(\theta_e,\psi_e)}(k_x, k_y + k_{0_g}, k_z) \approx\ & +\theta_e y_s k_x - \theta_e x_s(k_y + k_{0_g}) + \psi_e y_s k_z + \psi_e x_s \frac{k_z k_x}{(k_y + k_{0_g})} \\ & -\psi_e z_s \left(1 + \frac{k_z^2}{(k_y + k_{0_g})^2}\right)^{-\frac{1}{2}}.\end{aligned} \tag{3.83}$$

The form for $b(x,y)$ may now be evaluated given appropriate descriptions of the variation in the elements of the location error vector $\underline{P}_e = [R_e, \theta_e, \psi_e]^T$ over the coherent processing interval in terms of k_x and k_y. In the following section the form of $\underline{P}_e$ for the case of an along track measurement error will be considered and the image domain defocus computed.

3.4 Image Domain Defocus

In the case of measurement uncertainty arising due to inaccuracies in the radar platform navigation systems it is more convenient to specify the error vector $\underline{P}_e = [R_e, \theta_e, \psi_e]^T$ in terms of the displacement in cartesian coordinates, $\underline{P}_e^c = [\Delta x, \Delta y, \Delta z]^T$, as illustrated in Figure 3.3. In Figure 3.3 the

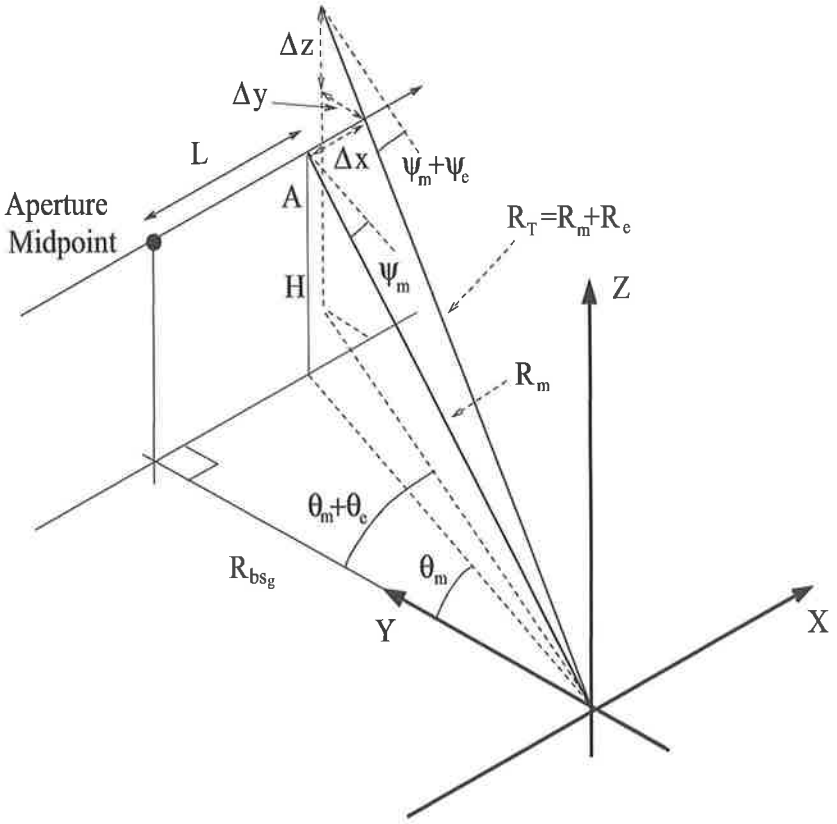


Figure 3.3: At each transmit/receive position along the synthetic aperture the measurement of the radar platform location is subject displacement errors Δx, Δy and Δz. The measured location of the radar in spherical coordinates with respect to the scene centre is given by (R_m, θ_m, ψ_m) while the true radar location is (R_T, θ_T, ψ_T).

measured radar location at a given transmit/receive point may be specified in cartesian coordinates by $\underline{P}_m^c = [L, R_{bs_g}, H]^T$, or equivalently in spherical coordinates by $\underline{P}_m = [R_m, \theta_m, \psi_m]^T$. The true radar location is given by $\underline{P}_T^c = \underline{P}_m^c + \underline{P}_e^c$. The displacements, $\underline{P}_e^c$, will vary over the synthetic aperture and may be expressed as a function of the along track location of the radar platform $L = R_{bs_g} \tan(\theta_m)$ over the coherent processing interval,

$$\Delta x(k_x, k_y) = f'(R_{bs_g} \tan(\theta_m)) = f\left(\frac{k_x}{k_y}\right), \tag{3.84}$$

$$\Delta y(k_x, k_y) = g'(R_{bs_g} \tan(\theta_m)) = g\left(\frac{k_x}{k_y}\right), \tag{3.85}$$

$$\Delta z(k_x, k_y) = h'(R_{bs_g} \tan(\theta_m)) = h\left(\frac{k_x}{k_y}\right), \tag{3.86}$$

where $\tan(\theta_m)$ has been expressed in terms of the azimuth and range spatial frequency variables defined in (3.58) and the R_{bs_g} scaling factor has been absorbed into the functions f, g and h. The form of these functional relationships are dependent on the sources of uncertainty in the platform location and will in general contain both high and low frequency terms.

The displacements $\underline{P}_e^c = [\Delta x, \Delta y, \Delta z]^T$ that arise at location $\underline{P}_m^c = [L, R_{bs_g}, H]^T$ may be expressed in spherical coordinates $\underline{P}_e = [R_e, \theta_e, \psi_e]^T$ using the simple geometrical relationships relating the location of a point in cartesian coordinates $[x, y, z]^T$ to its location expressed in spherical coordinates $[R, \theta, \psi]^T$,

$$\theta = \tan^{-1}\left(\frac{x}{y}\right), \tag{3.87}$$

$$\psi = \sin^{-1}\left(\frac{z}{\sqrt{(x^2+y^2+z^2)}}\right), \tag{3.88}$$

$$R = \sqrt{(x^2+y^2+z^2)}. \tag{3.89}$$

In particular, approximate expressions for $\underline{P}_e$ in terms of $\underline{P}_m$ may be derived by considering the first order terms of a Taylor series expansion for (3.87), (3.88) and (3.89), about $\underline{P}_m$. The azimuth angle error θ_e thus takes the form,

$$\begin{aligned}\theta_e &\approx \left.\frac{d\theta}{dx}\right|_{\underline{P}_m} \Delta x(k_x,k_y) + \left.\frac{d\theta}{dx}\right|_{\underline{P}_m} \Delta y(k_x,k_y), \\ &\approx \frac{\Delta x(k_x,k_y) - \tan(\theta_m)\Delta y(k_x,k_y)}{R_{bs_g}(1+\tan^2(\theta_m))}.\end{aligned} \tag{3.90}$$

The elevation angle error ψ_e takes the form,

$$\begin{aligned}\psi_e &\approx \left.\frac{d\psi}{dx}\right|_{\underline{P}_m} \Delta x(k_x,k_y) + \left.\frac{d\psi}{dy}\right|_{\underline{P}_m} \Delta y(k_x,k_y) + \left.\frac{d\psi}{dz}\right|_{\underline{P}_m} \Delta z(k_x,k_y), \\ &\approx -\sin(\psi_m)\sin(\theta_m)\cos(\psi_m)\cos(\theta_m)\frac{\Delta x(k_x,k_y)}{R_{bs_g}} \\ &\quad -\sin(\psi_m)\cos(\theta_m)\cos(\psi_m)\cos(\theta_m)\frac{\Delta y(k_x,k_y)}{R_{bs_g}} + \frac{\cos(\theta_m)\cos^2(\psi_m)}{R_{bs_g}}\Delta z(k_x,k_y).\end{aligned} \tag{3.91}$$

The range error R_e takes the form,

$$\begin{aligned}R_e &\approx \left.\frac{dR}{dx}\right|_{\underline{P}_m} \Delta x(k_x,k_y) + \left.\frac{dR}{dy}\right|_{\underline{P}_m} \Delta y(k_x,k_y) + \left.\frac{dR}{dz}\right|_{\underline{P}_m} \Delta z(k_x,k_y), \\ &\approx \sin(\theta_m)\cos(\psi_m)\Delta x(k_x,k_y) + \cos(\theta_m)\cos(\psi_m)\Delta y(k_x,k_y) + \sin(\psi_m)\Delta z(k_x,k_y).\end{aligned} \tag{3.92}$$

These equations, (3.90), (3.91) and (3.92), may be expressed in terms of the spatial frequency variables k_x, k_y and k_z using the definitions in (3.58) to give,

$$R_e(k_x,k_y,k_z) \approx \frac{k_x}{k_r+k_0}\Delta x(k_x,k_y) + \frac{k_y}{k_r+k_0}\Delta y(k_x,k_y) + \frac{k_z}{k_r+k_0}\Delta z(k_x,k_y), \tag{3.93}$$

$$\theta_e(k_x,k_y,k_z) \approx \frac{k_y^2}{R_{bs_g}(k_y^2+k_x^2)}\Delta x(k_x,k_y) - \frac{k_x k_y}{R_{bs_g}(k_y^2+k_x^2)}\Delta y(k_x,k_y), \tag{3.94}$$

$$\begin{aligned}\psi_e(k_x,k_y,k_z) \approx &-\frac{k_x k_z k_y}{(k_r+k_0)^2\sqrt{(k_x^2+k_y^2)}}\frac{\Delta x(k_x,k_y)}{R_{bs_g}} - \frac{-k_z k_y^2}{(k_r+k_0)^2\sqrt{(k_x^2+k_y^2)}}\frac{\Delta y(k_x,k_y)}{R_{bs_g}} + \\ &\frac{k_y\sqrt{(k_x^2+k_y^2)}}{(k_r+k_0)^2}\frac{\Delta z(k_x,k_y)}{R_{bs_g}},\end{aligned} \tag{3.95}$$

where $\Delta x(k_x, k_y)$, $\Delta y(k_x, k_y)$ and $\Delta z(k_x, k_y)$ are given by equations (3.84), (3.85) and (3.86) respectively. Substituting the above expressions for $\theta_e(k_x, k_y, k_z)$, $\psi_e(k_x, k_y, k_z)$ and $R_e(k_x, k_y, k_z)$ into the expressions for the uncompensated phase error functions $\phi_{(\theta_e,\psi_e)}(k_x, k_y, k_z)$ in (3.66) and $\phi_{R_e}(k_x, k_y, k_z)$ in (3.13) yields a form for $\phi_{uncomp}(k_x, k_y, k_z)$ from which the blurring filter kernel $b(x, y)$ in (3.78) may be computed The generality of the model for the phase errors however makes the derivation of the image domain description mathematically cumbersome. Instead the particular case of an along track velocity error, which is a common source of position uncertainty, will be considered in the following section.

3.4.1 An Example: An Along Track Velocity Error

In an airborne SAR system, where the predominant motion is in the along track direction, a common source of position uncertainty arises from errors in measuring the along track velocity. The impact of an error V_e in the measurement of the along track velocity V on the position uncertainty and the subsequent phase error function may be readily quantified using the relations derived in the previous section. For a straight and level, non squinted, imaging collection an along track velocity error produces an azimuth displacement error only, i.e., the error vector has the form $\underline{P}_e^c = [\Delta x, 0, 0]^T$. The measured radar location therefore at time t is given by $\underline{P}_m^c = [L, R_{bs_g}, H]^T$ while the true location of the radar at time t is $\underline{P}_m^c + \underline{P}_e^c = [L + \Delta x, R_{bs_g}, H]$ where $L = Vt$ and $\Delta x = V_e t$. The azimuth displacement, Δx, may be written in terms of k_x and k_y as follows,

$$\begin{aligned} \Delta x(k_x, k_y) &= V_e t, \\ &= \frac{V_e}{V} L, \\ &= \frac{V_e}{V} R_{bs_g} \tan(\theta_m), \\ &= R_{bs_g} \frac{V_e}{V} \frac{k_x}{k_y}. \end{aligned} \tag{3.96}$$

which may be substituted into equations (3.93), (3.94) and (3.95) to compute the phase error function.

Azimuth Angle Error θ_e

Substituting (3.96) into (3.94) gives,

$$\begin{aligned} \theta_e(k_x, k_y, k_z) &\approx \frac{k_y^2}{R_{bs_g}(k_y^2 + k_x^2)} \Delta x(k_x, k_y), \\ &\approx \frac{V_e k_y k_x}{V(k_y^2 + k_x^2)}. \end{aligned} \tag{3.97}$$

Depression Angle Error ψ_e

Substituting (3.96) into (3.95) gives,

$$\begin{aligned} \psi_e(k_x, k_y, k_z) &\approx -\frac{k_x k_z k_y}{(k_r + k_0)^2 \sqrt{(k_x^2 + k_y^2)}} \frac{\Delta x(k_x, k_y)}{R_{bs_g}}, \\ &\approx -\frac{\beta_0 k_x^2 k_y V_e}{V(k_r + k_0)^2 \sqrt{(k_x^2 + k_y^2)}}. \end{aligned} \tag{3.98}$$

where $\beta_0 = \tan(\psi_0)$, ψ_0 is the depression angle at the aperture centre and the relation $k_z = \beta_0 k_y$ for straight and level flight without squint has been used.

Range Error R_e

Substituting (3.96) in (3.93) gives an expression for the slant range error R_e,

$$\begin{aligned} R_e(k_x,k_y,k_z) &\approx \frac{k_x}{k_r+k_0}\Delta x(k_x,k_y), \\ &\approx R_{bs_g}\frac{V_e}{V}\frac{k_x^2}{(k_r+k_0)k_y}. \end{aligned} \tag{3.99}$$

Uncompensated Phase Error

Substituting the above expressions for R_e, θ_e and ψ_e into the expression for the uncompensated phase error functions $\phi_{R_e}(k_x,k_y,k_z)$ in (3.13) and $\phi_{(\theta_e,\psi_e)}(k_x,k_y,k_z)$ in (3.66) gives,

$$\phi_{R_e}(k_x,k_y,k_z) \approx R_{bs_g}\frac{V_e}{V}\frac{k_x^2}{k_y}, \tag{3.100}$$

$$\begin{aligned} \phi_{(\theta_e,\psi_e)}(k_x,k_y,k_z) \approx\ & y_s\left(\frac{V_e k_y^2 k_x}{V(k_y^2+k_x^2)} - \frac{\beta_0^2 k_x^2 k_y^2 V_e}{V(k_r+k_0)^2\sqrt{(k_x^2+k_y^2)}}\right) + \\ & x_s\left(-\frac{V_e k_y^2 k_x}{V(k_y^2+k_x^2)} - \frac{\beta_0^2 k_x^3 k_y V_e}{V(k_r+k_0)^2\sqrt{(k_x^2+k_y^2)}}\right) + \\ & z_s\left(\frac{\beta_0 k_x^2 k_y V_e}{V(k_r+k_0)^2\sqrt{(k_x^2+k_y^2)}\sqrt{(1+\beta_0^2)}}\right). \end{aligned} \tag{3.101}$$

The blurring convolution kernel associated with an image recovered via the PFA is defined as the inverse Fourier transform of the phase error function, (see equations (3.76), (3.77) and (3.78)),

$$\phi_{uncomp}(k_x,k_y+k_{0_g},k_z) = \phi_{R_e}(k_x,k_y+k_{0_g},k_z) + \phi_{(\theta_e,\psi_e)}(k_x,k_y+k_{0_g},k_z). \tag{3.102}$$

Substituting $k_y + k_{0_g}$ for k_y in $\phi_{R_e}(k_x,k_y,k_z)$ in (3.100) and $\phi_{(\theta_e,\psi_e)}(k_x,k_y,k_z)$ in (3.101) and assuming k_{0_g} is sufficiently larger than the range and azimuth spatial frequency bandwidths then,

$$\phi_{R_e}(k_x,k_y+k_{0_g},k_z) \approx R_{bs_g}\frac{V_e}{V}\frac{k_x^2}{k_{0_g}}, \tag{3.103}$$

$$\begin{aligned} \phi_{(\theta_e,\psi_e)}(k_x,k_y+k_{0_g},k_z) \approx\ & y_s\left(\frac{V_e k_x^2}{V k_{0_g}} - \frac{\beta_0^2 V_e k_x^2}{(1+\beta_0^2)V k_{0_g}}\right) + z_s\frac{\beta_0 V_e k_x^2}{V(1+\beta_0^2)^{\frac{3}{2}}k_{0_g}^2} + \\ & x_s\left(-\frac{V_e k_x}{V} - \frac{\beta_0^2 V_e k_x^3}{V(1+\beta_0^2)k_{0_g}^2}\right). \end{aligned} \tag{3.104}$$

Observe that in the above approximations, ϕ_{R_e} and $\phi_{(\theta_e,\psi_e)}$ are in fact independent of k_y and k_z and so the resulting image domain defocus convolution kernel may be recovered by applying an inverse Fourier transform with respect to k_x and so is an azimuthal function only. The phase terms ϕ_{R_e} and $\phi_{(\theta_e,\psi_e)}$ however are dependent on the scattering location (x_s,y_s,z_s), thus the form of the image domain defocus varies spatially over the scene. The linear term in k_x in $\phi_{(\theta_e,\psi_e)}$ azimuthally translates the scattering point from its true image location x_s to $x_s(1+V_e/V)$. The magnitude of the translation increases with increasing azimuthal distance from the scene centre. Although the scattering location

dependent translation introduces a geometric distortion to the recovered image it does not lead to any defocusing of the image. The quadratic terms in k_x, given by,

$$\phi_{quad}(k_x) = \left(R_{bs_g} + y_s - y_s \frac{\beta_0^2}{(1+\beta_0^2)} + z_s \frac{\beta_0}{(1+\beta_0^2)^{\frac{3}{2}} k_{0_g}} \right) \frac{V_e k_x^2}{V k_{0_g}}, \tag{3.105}$$

however introduce an azimuthal defocus to the scene image. Clearly the dominant term in (3.105) arises from the slant range demodulation phase error ϕ_{R_e}. This component of the quadratic phase is independent of the scattering location and is proportional to the ground range offset of the radar flight track from the scene centre R_{bs_g}. The remaining components of the quadratic error arising from the pointing vector phase error $\phi_{(\theta_e,\psi_e)}$ are dependent on the range y_s and elevation z_s. The contribution from the height dependent component however, is scaled by $1/k_{0_g}$ and thus may be ignored in comparison to the range dependent contributions. The image domain defocus arising from the range dependent quadratic phase contributions may be considered negligible if the peak quadratic phase of these components are less than $\pi/4$ at the azimuth spatial frequency band edges $k_x = \pm k_{bw_x}/2$. Applying this condition to the appropriate terms in ϕ_{quad} gives the following constraint on the image patch size,

$$y_s < \frac{(1+\beta_0^2) V k_{0_g} \rho_x^2}{4\pi V_e}, \tag{3.106}$$

where the $\rho_x = 2\pi/k_{bw_x}$ is the image azimuthal resolution. For images sizes smaller than this constraint the predominant phase error is the demodulation phase error ϕ_{R_e} which is independent of scattering location. It should be noted that the phase error $\phi_{(\theta_e,\psi_e)}$ also contains a cubic phase error that varies with azimuth location x_s. A constraint on the azimuth image patch size may be derived within which the image domain distortion is negligible however, the cubic phase error is inversely proportional to $k_{0_g}^2$ and so this constraint is not particularly restrictive.

3.5 Limitations of the PGA Phase Error Model

In spotlight SAR imaging the presence of uncompensated phase terms arising from inaccuracies in the measurement of the effective radar platform location across the collection aperture can lead to significant distortion and defocus in the SAR image. The recovery of well focused imagery in the presence of measurement errors requires the use of data driven autofocus algorithms to estimate and compensate for the unknown phase error functions. These algorithms generally rely on some simplifying assumptions on the form of the phase error and the fidelity of the particular model used in a given algorithm will determine the quality of the phase estimate and the residual phase errors that remain after phase error compensation.

The PGA has been proposed as an autofocus algorithm for the estimation and correction of uncompensated phase errors in the acquired SAR signal history data. It is based on a model for the phase error that is independent of spatial location in the scene and is also a one dimensional function of the azimuthal spatial frequency k_x only. These limiting assumptions are exploited by the PGA to generate a robust reliable estimate of the phase error function, however their accuracy in modelling the phase error function imposes some limitations on the range of imaging scenarios to which the algorithm may be applied.

In the previous section an analysis of the residual uncompensated phase error, ϕ_{uncomp}, arising from an error $\underline{P}_e = [R_e, \theta_e, \psi_e]^T$ in the measurement of the effective location of the radar with respect to the scene centre was presented. It was shown that the uncompensated phase error consists

of a demodulation phase error ϕ_{R_e} dependent on the slant range error R_e and an image formation component $\phi_{(\theta_e,\psi_e)}$ determined by the angular errors (θ_e, ψ_e) such that,

$$\phi_{uncomp}(k_x, k_y + k_{0_g}, k_z) = \phi_{(\theta_e,\psi_e)}(k_x, k_y + k_{0_g}, k_z) + \phi_{R_e}(k_x, k_y + k_{0_g}, k_z). \quad (3.107)$$

The image formation phase error $\phi_{(\theta_e,\psi_e)}$ was shown to vary spatially over the scene and thus manifests in the formulation of the PGA algorithm as a range compressed signal history covariance matrix $C_{\mathcal{G}_e}(x, y)$ that varies as a function of scattering location. In order to track this spatial variation the PGA algorithm must subsequently be applied in a patchwork fashion across the scene image to localised regions over which phase error function may be considered to be locally constant, [CGM95]. The analysis in Section 3.4 however showed that the angular errors θ_e and ψ_e are inversely proportional to the ground range offset R_{bs_g} of the radar from the scene centre, see equations (3.94) and (3.95). The image domain defocusing arising from $\phi_{(\theta_e,\psi_e)}$ is thus minimal except in the extreme scenario of near field imaging of large scenes.

The remaining contribution to the uncompensated phase error ϕ_{uncomp} is the demodulation phase error ϕ_{R_e} which is independent of scattering location. This phase term has a dependence on both range and azimuth spatial frequencies. Using the formulation for the slant range error R_e in terms of the along, across and above track displacements given in (3.93) the demodulation error takes the form,

$$\begin{aligned} \phi_{R_e}(k_x, k_y + k_{0_g}, k_z) &= (k_r + k_0)R_e(k_x, k_y + k_{0_g}, k_z), \\ &\approx k_x\Delta x(k_x, k_y + k_{0_g}) + (k_y + k_{0_g})\Delta y(k_x, k_y + k_{0_g}) + \\ &\qquad \beta_0(k_y + k_{0_g})\Delta z(k_x, k_y + k_{0_g}), \end{aligned} \quad (3.108)$$

where straight and level flight without squint has been assumed thus $k_z = \beta_0(k_y + k_{0_g})$. Substituting the functional forms given in equations (3.84), (3.85) and (3.86) for $\Delta x(k_x, k_y + k_{0_g})$, $\Delta y(k_x, k_y + k_{0_g})$ and $\Delta z(k_x, k_y + k_{0_g})$ gives the dependence of ϕ_{R_e} on the range and azimuth spatial frequencies,

$$\begin{aligned} \phi_{R_e}(k_x, k_y + k_{0_g}, k_z) &\approx k_x f\left(\frac{k_x}{k_y + k_{0_g}}\right) + (k_y + k_{0_g})g\left(\frac{k_x}{k_y + k_{0_g}}\right) + \\ &\qquad \beta_0(k_y + k_{0_g})h\left(\frac{k_x}{k_y + k_{0_g}}\right). \end{aligned} \quad (3.109)$$

The demodulation phase error is thus a two dimensional function in the spatial frequency domain and manifests as a two dimensional defocus and distortion in the recovered scene image. The PGA phase error model may be considered to be a small fractional bandwidth approximation to the demodulation phase error that may be applied provided $k_{0_g} \gg k_y$, in which case ϕ_{R_e} reduces to,

$$\phi_{R_e}(k_x) \approx k_x f\left(\frac{k_x}{k_{0_g}}\right) + k_{0_g} g\left(\frac{k_x}{k_{0_g}}\right) + \beta_0 k_{0_g} h\left(\frac{k_x}{k_{0_g}}\right). \quad (3.110)$$

While the dependence of ϕ_{R_e} on k_y is minimal in small fractional bandwidth systems, for the processing of extended collection apertures substantial measurement errors can accumulate over the coherent processing interval. As a consequence the functional dependence of the along, across and above track errors on k_y can become increasing significant. In the following sections the impact of the k_y dependence of the phase error function on the PGA algorithm and the subsequent focused image will be considered. The effect on post-processing applications, specifically the scene coherence in interferometric applications will also be addressed.

3.5.1 Range Dependence of the Demodulation Phase Error

Insight into the impact of the k_y dependence of the phase error, ϕ_{R_e}, on the PGA algorithm phase estimate and subsequent recovered image may be found by considering the following polynomial expansions for the azimuth, range and altitude displacements,

$$f\left(\frac{k_x}{k_y+k_{0_g}}\right) = \sum_{n=2}^{N} a_n \left(\frac{k_x}{k_y+k_{0_g}}\right)^n, \tag{3.111}$$

$$g\left(\frac{k_x}{k_y+k_{0_g}}\right) = \sum_{n=2}^{N} b_n \left(\frac{k_x}{k_y+k_{0_g}}\right)^n, \tag{3.112}$$

$$h\left(\frac{k_x}{k_y+k_{0_g}}\right) = \sum_{n=2}^{N} c_n \left(\frac{k_x}{k_y+k_{0_g}}\right)^n. \tag{3.113}$$

(Note that only the nonlinear components of the azimuth, range and altitude displacements have been modelled as it is only these components that manifest as image domain defocus.) Substituting these into the expression for ϕ_{R_e} given in (3.109) and considering the first two terms in a Taylor series expansion about $k_y = 0$ gives the following expression of the modulating phase,

$$\phi_{R_e}(k_x, k_y + k_{0_g}, k_z) = \phi_{nb}(k_x) + \phi_{rm}(k_x)k_y. \tag{3.114}$$

The phase term $\phi_{nb}(k_x)$ is the zeroth order term in the Taylor expansion and is a narrow band approximation to ϕ_{R_e} given by,

$$\phi_{nb}(k_x) = A(k_x) + B(k_x) + C(k_x), \tag{3.115}$$

where,

$$A(k_x) = \sum_{n=2}^{N} a_n \frac{k_x^{n+1}}{k_{0_g}^n}, \tag{3.116}$$

$$B(k_x) = \sum_{n=2}^{N} b_n \left(\frac{k_x^n}{k_{0_g}^{n-1}}\right), \tag{3.117}$$

$$C(k_x) = \beta_0 \sum_{n=2}^{N} c_n \left(\frac{k_x^n}{k_{0_g}^{n-1}}\right). \tag{3.118}$$

The phase term $\phi_{rm}(k_x)$ is the first order term in the Taylor expansion for ϕ_{R_e} and quantifies the linear dependence of the demodulation phase error on k_y,

$$\phi_{rm}(k_x) = A'(k_x) + B'(k_x) + C'(k_x), \tag{3.119}$$

where,

$$A'(k_x) = -\sum_{n=2}^{N} n a_n \frac{k_x^{n+1}}{k_{0_g}^{n+1}}, \tag{3.120}$$

$$B'(k_x) = \sum_{n=2}^{N} (1-n) b_n \left(\frac{k_x}{k_{0_g}}\right)^n, \tag{3.121}$$

$$C'(k_x) = \beta_0 \sum_{n=2}^{N} (1-n) c_n \left(\frac{k_x}{k_{0_g}}\right)^n. \tag{3.122}$$

The phase error model employed by the PGA ignores the range dependent term, $\phi_{rm}(k_x)k_y$ and the output of the PGA algorithm may be considered to be an estimate of the narrowband component of the modulating phase function. The range dependent terms however degrade the quality of the estimate and remain as residual uncompensated phase errors in the recovered scene image.

The impact of the range dependent terms in ϕ_{R_e} on the PGA phase estimate may be found by considering the point target response in the ground plane range compressed signal history domain. The ground plane range compressed signal history for a point target is obtained by applying an inverse Fourier transform with respect to k_y and also with respect k_z evaluated at $z = 0$, to the acquired signal history data $G_m(k_x, k_y, k_z)$ given in (3.72), with the window $A_{ifp}(k_x, k_y)$ given in (3.74) applied,

$$\begin{aligned}\mathcal{G}_m(k_x, y) &= \frac{1}{2\pi}\int A_{ifp}(k_x, k_y)G_p(k_x, k_y, f(k_x, (k_y + k_{0_g})))\\ &\quad exp(j\phi_{uncomp}(k_x, k_y + k_{0_g}, f(k_x, k_y + k_{0_g})))exp(jyk_y)dk_y, \quad (3.123)\end{aligned}$$

It shall be assumed that the image patch size satisfies the constraint (3.106) so that phase component $\phi_{(\theta_e,\psi_e)}$ of ϕ_{uncomp} may be ignored. Also assuming straight and level flight without squint such that $f(k_x, k_y + k_{0_g}) = \beta_0(k_y + k_{0_g})$ the following form of the range compressed signal history is obtained,

$$\begin{aligned}\mathcal{G}_m(k_x, y) &= \frac{1}{2\pi}\int A_{ifp}(k_x, k_y)G_p(k_x, k_y, \beta_0(k_y + k_{0_g}))\\ &\quad exp(j\phi_{R_e}(k_x, k_y + k_{0_g}, \beta_0(k_y + k_{0_g})))exp(jyk_y)dk_y,\\ &= \mathcal{G}_p(k_x, y) \otimes_y \mathcal{B}(k_x, y), \quad (3.124)\end{aligned}$$

where $\otimes_y$ represents convolution with respect to the range variable y. The term $\mathcal{G}_p(k_x, y)$ is the range compressed signal history of the point scatterer in the absence of measurement errors while $\mathcal{B}(k_x, y)$, given by,

$$\begin{aligned}\mathcal{B}(k_x, y) &= \frac{1}{2\pi}\int exp\left(j\phi_{R_e}(k_x, k_y + k_{0_g}, \beta_0(k_y + k_{0_g}))\right) exp(jyk_y)dk_y,\\ &= exp(j(A(k_x) + B(k_x) + C(k_x)))\delta(y + A'(k_x) + B'(k_x) + C'(k_x)),\\ &= exp(j\phi_{nb}(k_x))\delta(y + A'(k_x) + B'(k_x) + C'(k_x)), \quad (3.125)\end{aligned}$$

encapsulates the contribution of the phase error ϕ_{R_e} to the range compressed signal history data. The presence of the demodulation phase error manifests in the range compressed signal history domain as a modulating phase function $\phi_{nb}(k_x)$ that varies with k_x and also produces a k_x dependent range migration of the scatterer response by an amount $y = -A'(k_x) - B'(k_x) - C'(k_x)$. This can be seen most clearly by considering the simple along track velocity error scenario developed in Section 3.4.1. In this case the displacement at each transmit/receive point along the collection aperture is limited to an azimuthal displacement only of the form,

$$\begin{aligned}\Delta x(k_x, k_y + k_{0_g}) &= R_{bs_g}\frac{V_e}{V}\tan(\theta_m),\\ &= R_{bs_g}\frac{V_e}{V}\frac{k_x}{k_y + k_{0_g}}. \quad (3.126)\end{aligned}$$

The associated modulating phase error function is thus given by,

$$\begin{aligned}\phi_{R_e}(k_x, k_y + k_{0_g}, k_z) &= f\left(\frac{k_x}{k_y + k_{0_g}}\right)k_x,\\ &= R_{bs_g}\frac{V_e}{V}\frac{k_x^2}{k_y + k_{0_g}}. \quad (3.127)\end{aligned}$$

Applying a Taylor series expansion about k_y and retaining the first two terms gives,

$$\phi_{R_e}(k_x, k_y + k_{0_g}, k_z) \approx R_{bs_g}\frac{V_e}{V}\frac{k_x^2}{k_{0_g}} - R_{bs_g}\frac{V_e}{V}\frac{k_x^2}{k_{0_g}^2}k_y, \tag{3.128}$$

where the narrowband phase component is given by,

$$\phi_{nb}(k_x) = R_{bs_g}\frac{V_e}{V}\frac{k_x^2}{k_{0_g}}, \tag{3.129}$$

while the range migration phase component is given by,

$$\begin{aligned}\phi_{rm}(k_x) &= -R_{bs_g}\frac{V_e}{V}\frac{k_x^2}{k_{0_g}^2}, \\ &= -\frac{\phi_{nb}(k_x)}{k_{0_g}}.\end{aligned} \tag{3.130}$$

Assuming that the window $A_{ifp}(k_x, k_y)$ is unweighted and has the form,

$$A_{ifp}(k_x, k_y) = rect\left(\frac{k_x}{k_{bw_x}}\right) rect\left(\frac{k_y}{k_{bw_y}}\right), \tag{3.131}$$

the range compressed signal history for a single point scatterer at location (x_s, y_s, z_s) subject to the modulating phase error function (3.128) is thus,

$$\begin{aligned}\mathcal{G}_m(k_x, y) &= \mathcal{G}_p(k_x, y) \otimes_y \mathcal{B}(k_x, y), \\ &= \frac{k_{bw_y}}{2\pi} q_s exp(j\phi_s) exp(-j(y_s + \beta_0 z_s)k_{0_g}) rect\left(\frac{k_x}{k_{bw_x}}\right) exp(-jx_s k_x) \\ &\quad exp\left(j\phi_{nb}(k_x)\right) sinc\left(\left(y - y_s - \beta_0 z_s - \frac{\phi_{nb}(k_x)}{k_{0_g}}\right)\frac{k_{bw_y}}{2\pi}\right).\end{aligned} \tag{3.132}$$

Substituting the form for $\phi_{nb}(k_x)$ given in (3.129) yields,

$$\begin{aligned}\mathcal{G}_m(k_x, y) &= \frac{k_{bw_y}}{2\pi} q_s exp(j\phi_s) exp(-j(y_s + \beta_0 z_s)k_{0_g}) rect\left(\frac{k_x}{k_{bw_x}}\right) exp(-jx_s k_x) \\ &\quad exp\left(jR_{bs_g}\frac{V_e}{V}\frac{k_x^2}{k_{0_g}}\right) sinc\left(\left(y - y_s - \beta_0 z_s - R_{bs_g}\frac{V_e}{V}\frac{k_x^2}{k_{0_g}^2}\right)\frac{k_{bw_y}}{2\pi}\right).\end{aligned} \tag{3.133}$$

Equation (3.133) indicates that the scatterer's phase response in the range compressed signal history domain consists of a linear phase term in k_x that is dependent on the scatterer's azimuthal location x_s as well as a phase modulation, due to ϕ_{R_e}, that varies quadratically with k_x. The k_y dependence of the phase error function ϕ_{R_e} manifests in the point scatterer response as a range cell migration that varies quadratically with k_x. Since the phase error function ϕ_{R_e} is independent of scattering location all scatterers in the scene are subject to the same phase modulation and range migration given in (3.133). Figures 3.4 and 3.5 show the magnitude of the range compressed signal history, $|\mathcal{G}_m(k_x, y)|$, and the recovered image obtained using the PFA (without application of the PGA) respectively for a simulated scene with a single point scatterer at the scene centre and an along track velocity error

Parameter	Value (Units)
Radar centre frequency f_0	9.6 GHz
Depression angle at aperture centre ψ_0	30 deg
Ground plane range R_{bs_g}	13149.2 m
Along track velocity V	140.0 m/s
Along track velocity error V_e	0.5 m/s
Azimuth spatial freq. bandwidth k_{bw_x}	43.532 rad/m
Azimuth resolution ρ_x	0.14 m
Azimuth pixel spacing Δx	0.095 m
Ground range resolution ρ_y	0.29 m
Ground range pixel spacing Δy	0.11 m

Table 3.2: Simulation parameters corresponding to an imaging scenario in which the SAR motion sensor is subject to an error in the measurement of the along track component of the platform velocity.

V_e of 0.36 percent of the actual velocity V. The imaging parameters for the simulation scenario are described in Table 3.2. The peak quadratic phase error that occurs at the azimuth spatial frequency band edges is 63.9 radians and this manifests in the recovered image as a broadening of the mainlobe width of the azimuthal point spread function. Using the approach described in Section 2.3.2 the azimuthal mainlobe width may be estimated by computing the instantaneous "frequency" of the narrowband quadratic phase given by $d\phi_{nb}(k_x)/dk_x$ at the k_x spatial frequency limits. This approach gives an estimated width of approximately 11.4 m (or 120 azimuth pixels) which is consistent with the simulated point spread function illustrated in Figure 3.5. In Figure 3.4 the quadratic range cell migration of the scatterer response across the k_x bandwidth is clearly observed. The peak range cell migration that occurs at the band edges may be computed from (3.133) and is 0.18 m or 1.63 pixels in Figure 3.4.

3.5.2 PGA Algorithm in the Presence of Range Dependent Phase Errors

The PGA algorithm operates by firstly identifying a suitable number of dominant point scatterers in the recovered defocused PFA image. These are considered to be the signal components from which the unknown phase error is to be estimated. The remaining scene scattering contributions are considered to be noise sources in the estimation algorithm. As the phase error function, ϕ_{R_e} is independent of scattering location each scatterer has a response in the range compressed signal history of the form given in (3.132). By estimating the azimuthal location x_s of each signal scatterer in the defocused PFA image the linear phase term $exp(-jx_sk_x)$ can be compensated for in the associated range compressed signal history data. Having compensated for the linear phase term due to the azimuthal offset the PGA models the single point scatterer response in the range compressed signal history as,

$$\mathcal{G}_{pga}(k_x,y) = \frac{k_{bw_y}}{2\pi}q_s exp(j\phi_0)exp(j\phi_{nb}(k_x))rect\left(\frac{k_x}{k_{bw_x}}\right)sinc\left(\frac{(y-y_s-\beta_0 z_s)k_{bw_y}}{2\pi}\right)+ n(k_x,y), \quad (3.134)$$

where $n(k_x,y)$ is a noise term consisting of the remaining scene scattering contributions, $\phi_0 = \phi_s - (y_s+\beta_0 z_s)k_{0_g}$ and $\phi_{nb}(k_x)$ is given by 3.129. (Note that in general the PGA makes no assumptions regarding the form of $\phi_{nb}(k_x)$ other than it is some nonlinear function of k_x. In the following analysis

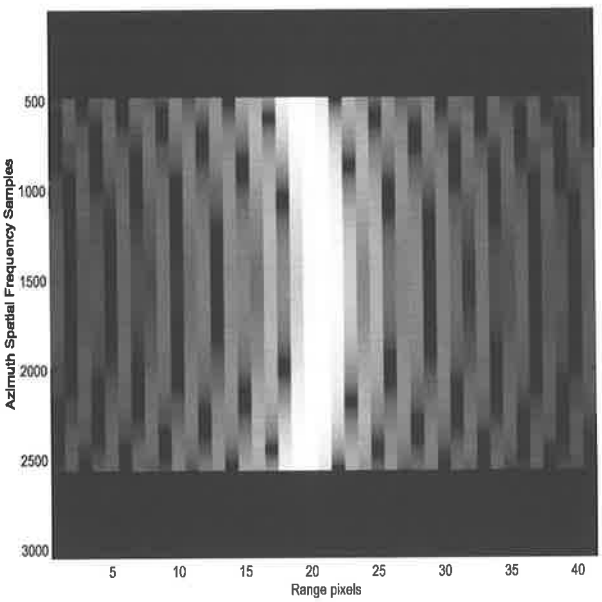


Figure 3.4: Range compressed history data obtained for a point scatterer located at the scene centre collected with an along track velocity error in the radar platform of 0.36 percent of the true platform along track velocity. The range point spread function is a sinc function with a resolution, given by the location of the first null, of 0.29 m. The range pixel spacing is 0.11 m.

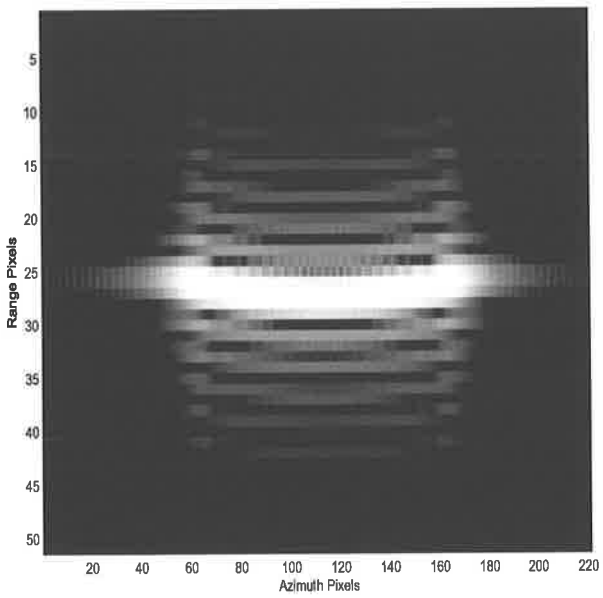


Figure 3.5: Image of a point scatterer located at the scene centre obtained using the PFA where at 0.36 percent error in the along track velocity of the radar platform. The image point spread function in the absence of phase phase errors is a sinc function with a nominal resolution of 0.14 m in azimuth and 0.29 m in range. The pixel spacing is 0.095 m in azimuth and 0.11 m in range.

however, the performance of the PGA will be considered for the along track velocity error scenario developed in the previous section.) The phase of $\mathcal{G}_{pga}(k_x, y)$ over the azimuth spatial frequency slice obtained at range $y = y_s + \beta_0 z_s$ equals the unknown narrowband phase modulation (to within an unknown constant given by ϕ_0), while the magnitude of the slice across k_x varies according to the k_x aperture weighting function, in this case $rect(k_x/k_{bw_x})$ for an unweighted windowing function. In estimating the phase error function $\phi_{nb}(k_x)$ the PGA considers a slice of $\underline{\mathcal{G}}_{pga}(k_x, y)$ over k_x at range $y = y_s + \beta_0 z_s$. This may be expressed in the sampled data matrix representation developed in Section 3.2.3 as follows,

$$\underline{\mathcal{G}}_{pga}(m = m_s) = q_s exp(j\phi_s) diag(\underline{\phi}_{nb}) W \begin{bmatrix} 1 \\ 0 \\ \vdots \\ 0 \end{bmatrix} + \begin{bmatrix} n_0 \\ n_1 \\ \vdots \\ n_{L-1} \end{bmatrix}, \tag{3.135}$$

where $\underline{\mathcal{G}}_{pga}(m = m_s)$ is the vector of k_x samples of $\mathcal{G}_{pga}(k_x, y)$ evaluated at the range sample bin m_s associated with the range $y = y_s + \beta_0 z_s$. The matrix W is formed from the Fourier transform coefficients (see (3.40)), $diag(\underline{\phi}_{nb})$ is the diagonal matrix where the terms down the leading diagonal are the samples of $exp(j\phi_{nb}(k_x))$ across the k_x bandwidth (see (3.42) and (3.44)).

The presence of the quadratic range migration in the true point scatterer response given in (3.133) however means that the actual range compressed signal history slice transduced at $y = y_s + \beta_0 z_s$ has a sinc like variation with k_x given by,

$$|\mathcal{G}_m(k_x, y = y_s + \beta_0 z_s)| = \frac{k_{bw_y}}{2\pi} q_s sinc\left(R_{bs_g} \frac{V_e}{V} \frac{k_x^2}{k_0^2} \frac{k_{bw_y}}{2\pi} \right). \tag{3.136}$$

Figures 3.6 and 3.7 show the amplitude and phase respectively of an azimuthal slice of the simulated range compressed history in Figure 3.4 obtained at range bin 21 corresponding to the range location of the simulated point target. The phase component of the slice is the unknown narrow band phase modulation given in (3.129). The magnitude of the slice however has been subject to a modulation due to the range cell migration with a 7 dB reduction in the amplitude observed at the band edges $k_x = \pm k_{bw_x}/2$ where the range migration is most significant.

The range migration manifests as a reduction in the contribution of the scatterer at (x_s, y_s, z_s) to the amplitude of the slice $\mathcal{G}_m(k_x, y)$ over azimuth spatial frequency at $y = y_s + \beta_0 z_s$ resulting in a progressive decrease in the signal to noise ratio across the k_x bandwidth. A more accurate description of the range compressed signal history slice in the formulation of the PGA algorithm is to apply a weighting vector $\underline{Y}$ which contains the samples of $|\mathcal{G}_m(k_x, y = y_s + \beta_0 z_s)|$ in (3.136). In this case the PGA signal model takes the form,

$$\underline{\mathcal{G}}_{pga}(m = m_s) = q_s exp(j\phi_0) diag(\underline{Y}) diag(\underline{\phi}_{nb}) W \begin{bmatrix} 1 \\ 0 \\ \vdots \\ 0 \end{bmatrix} + \begin{bmatrix} n_0 \\ n_1 \\ \vdots \\ n_{L-1} \end{bmatrix}. \tag{3.137}$$

where $diag(\underline{Y})$ is the diagonal matrix formed from the elements of the vector $\underline{Y}$. In the PGA algorithm, as described in Section 3.2.3, the reduced signal to clutter levels will manifest as a poorer estimate of the covariance matrix and hence a poorer estimate of the dominant eigenvector and subsequently the unknown phase modulation.

In the final, phase compensation step, of the PGA algorithm the negative of the estimated phase error, $exp(j\hat{\phi}_{nb}(k_x))$ is applied to the range compressed signal history $\mathcal{G}_m(k_x, y)$,

$$\mathcal{G}_{corr}(k_x, y) = exp(-j\hat{\phi}_{nb}(k_x) \mathcal{G}_m(k_x, y). \tag{3.138}$$

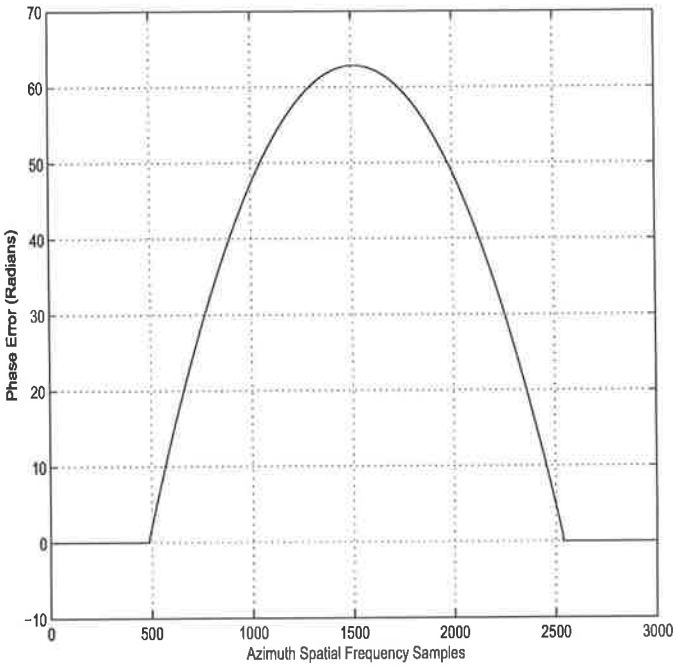


Figure 3.6: Narrow band phase error estimate obtained from a slice of the range compressed history generated using the simulation parameters described in Table 3.2.

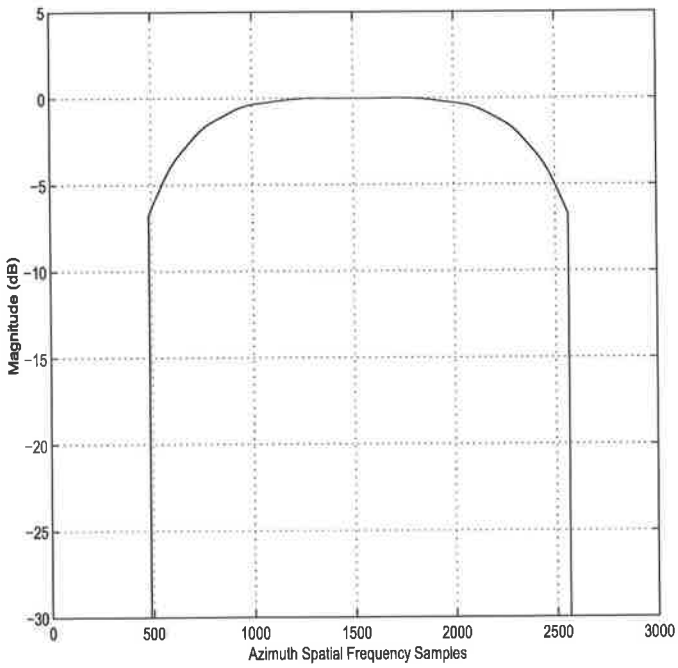


Figure 3.7: Magnitude envelope of the slice of the range compressed history data used to obtain the narrow band phase error estimate for the simulation parameters described in Table 3.2. The 7 dB roll off at the band edges arises due to the uncompensated range cell migration.

This compensates, to within the accuracy of the estimate, for the narrowband phase modulation present in the range compressed signal history data. However the range migration remains uncompensated in the recovered image. In the along track velocity error scenario the range compressed signal history data (3.133) after phase correction takes the form,

$$\begin{aligned} \mathcal{G}_{corr}(k_x, y) &= q_s exp(j\phi_s) rect\left(\frac{k_x}{k_{bw_x}}\right) \mathcal{G}_p(k_x, y) exp(j(\phi_{nb}(k_x) - \hat{\phi}_{nb}(k_x))) \frac{k_{bw_y}}{2\pi} \\ & sinc\left(\frac{(y - y_s - \beta_0 z_s) k_{bw_y}}{2\pi}\right) \otimes_y \delta\left(y - R_{bs_g} \frac{V_e}{V} \frac{k_x^2}{k_{0_g}^2}\right), \end{aligned} \tag{3.139}$$

and application of an inverse Fourier transform with respect to k_x recovers an image of the point scatterer subject to a residual range blur with a width nominally given by the range extent of the range migration across the k_x bandwidth. Figure 3.8 shows the point spread function of the scatterer that is recovered after applying the PGA algorithm to the simulated range compressed signal history data illustrated in Figure 3.4. In this case the PGA phase estimate $\hat{\phi}_{nb}(k_x)$ equals $\phi_{nb}(k_x)$. The image has been oversampled in range and azimuth so that the range and azimuth pixel spacing are 0.055 m and 0.024 m respectively. The distortion and range blur of the point spread function due to the residual uncompensated linear phase terms is clearly seen.

Assuming that the PGA is able to retrieve a sufficiently accurate estimate of the narrowband phase modulation $\phi_{nb}(k_x)$ the range migration term (3.139) can be readily estimated,

$$\hat{\phi}_{rm}(k_x) = \frac{-\hat{\phi}_{nb}(k_x)}{k_{0_g}}. \tag{3.140}$$

A simple method for compensating for the range migration term $\phi_{rm}(k_x)$ is to Fourier transform the range compressed signal history $\mathcal{G}_{corr}(k_x, y)$ with respect to k_y back into the signal history domain and apply the phase correction specified in (3.140), i.e.,

$$G_{corr_2}(k_x, k_y) = G_{corr}(k_x, k_y) exp\left(j\hat{\phi}_{rm}(k_x) \frac{k_y}{k_{0_g}}\right). \tag{3.141}$$

It should be noted that this proposed correction step is based on a first order Taylor expansion of the range spatial frequency dependence of the demodulation phase error for the along track velocity error given in (3.128). It therefore does not apply complete compensation of the k_y dependence of ϕ_{R_e}. A more accurate form of compensation can be achieved if the phase correction is applied to the signal history data as it is acquired in its "native" polar format form $G_{m_2}(\underline{k}_T)$ given in (3.55). In particular $\hat{\phi}_{nb}(k_x)$ is the narrowband form of ϕ_{R_e} given in (3.109) and may be considered to evaluate ϕ_{R_e} at $k_y = 0$ thus,

$$\begin{aligned} \phi_{nb}(k_x) &= \phi_{R_e}|_{k_y=0}, \\ &= (k_r - k_0) R_e|_{k_y=0}, \\ &= \sqrt{k_x^2 + (1+\beta_0)^2 k_{0_g}^2}\, R_e. \end{aligned} \tag{3.142}$$

Given the PGA estimate of $\phi_{nb}(k_x)$ an estimate $\hat{R}_e$ of the slant range error R_e may be obtained and the following correction applied to the signal history data in the acquired "native" polar format,

$$G_{corr}(\underline{k}_T) = G_{m_2}(\underline{k}_T) exp(-j(|\underline{k}_T| \hat{R}_e). \tag{3.143}$$

A focused image is subsequently recovered by re-applying the PFA algorithm to the phase corrected signal history. In practice this approach is considerable more computationally expensive as the recovery of the focused image requires recomputing the polar to rectangular resampling step of the PFA.

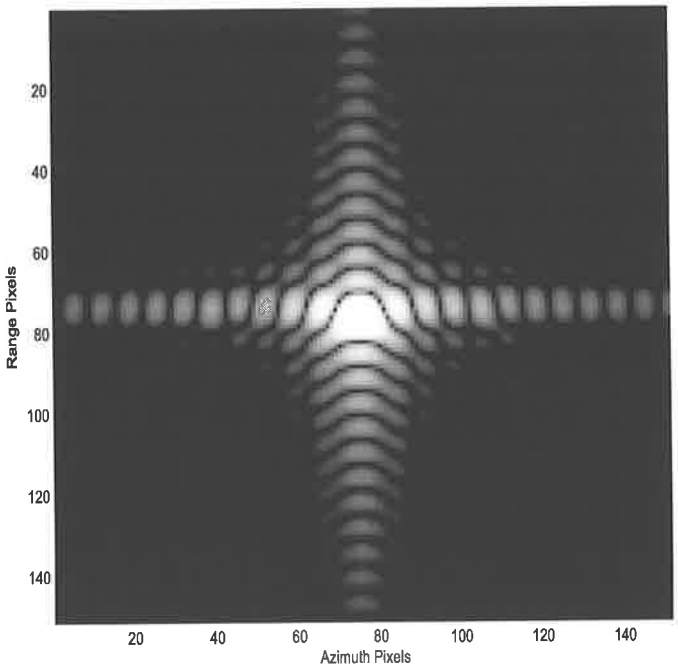


Figure 3.8: Point spread function for a PFA plus PGA SAR processor obtained using the imaging parameters described in Table 3.2.

The proposed correction method in (3.141) on the other hand, allows an approximate correction of the range spatial frequency dependent terms to be carried out in the signal history data after polar to rectangular resampling.

A comparison of Figures 3.8 and 3.9 indicates the improvement in the point target response that may be achieved with the range cell migration correction step of (3.141) applied. Figure 3.8 shows the point spread function obtained using the imaging parameters in Table 3.2 and the PFA and PGA algorithms without range cell migration correction. Figure 3.9 on the other hand shows the PFA and PGA algorithm point spread function with the addition of the range migration correction step. It is clear that the distortion evident in Figure 3.8 has largely been corrected in Figure 3.9.

Although the distortion of the point spread function is not large and may not have a significant impact on the interpretability of the restored image, for post processing applications, such as super-resolution and interferometry, the presence of residual uncompensated phase errors can potentially have a significant detrimental effect.

3.5.3 Impact on Interferogram Estimation

Repeat pass SAR interferometry, see Chapter 4, uses the image pixel amplitude and phase from a pair of SAR images, collected in separate imaging passes, to derive additional information about the geophysical properties of the scene [BH98], [RHJ+00]. The additional information is encapsulated in the complex cross correlation of the interferometric image pair,

$$\gamma exp(j\Phi) = \frac{E\{fg^*\}}{\sqrt{E\{|f|^2\}E\{|g|^2\}}}, \tag{3.144}$$

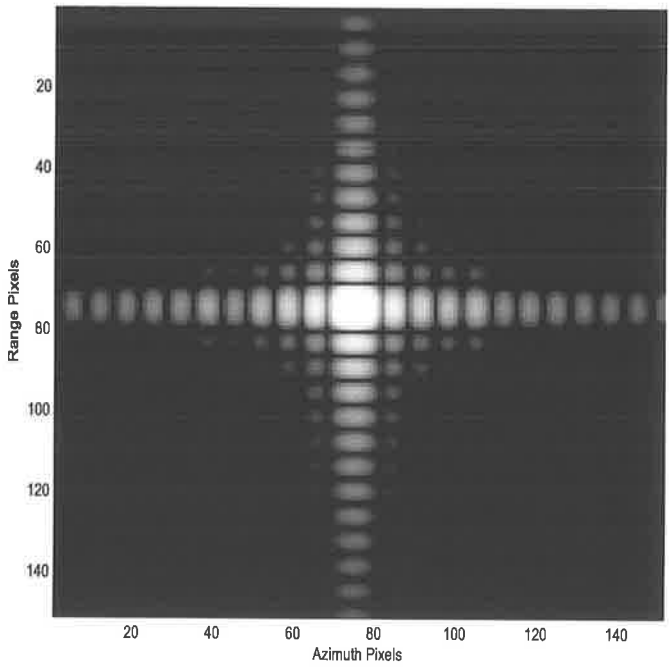


Figure 3.9: Point spread function for a PFA plus PGA SAR processor with correction of the residual range cell migration obtained using the imaging parameters described in Table 3.2.

where f is the primary image obtained from the first imaging collection and g is the repeat pass image from the second imaging collection. The interferometric magnitude γ, or coherence, is a value between 0 and 1 where a value of 1 indicates the images are identical, to within a scale factor and a value of 0 indicates the images are completely uncorrelated. The scene coherence can thus be used as sensitive change statistic for detecting subtle scene disturbances [JWE+96] as well as a test statistic for target classification [Yoc98]. The interferometric phase Φ on the other hand can be used to estimate the terrain topography.

The complex cross correlation coefficient is typically estimated via spatial averaging over a local estimation window in the repeat pass image pair. The accuracy of this estimate in measuring the underlying scene coherence and interferometric phase however is sensitive to the presence of any relative uncompensated phase differences between the signal histories of the image pair. In [JB94] Just has examined the impact of various low order residual phase differences and has shown that they contribute to an overall loss in coherence and an associated increase in the interferometric phase noise. In certain cases the residual phase differences may also introduce a bias into the interferometric phase estimate. For a repeat pass SAR pair formed using the PFA and PGA the residual uncompensated range dependent phase errors that remain after application of the PGA will be a source of relative phase errors leading to a reduction in the interferogram quality. For the case of a relative quadratic range migration phase error and unweighted aperture windows Just has shown that the true underlying scene coherence is scaled by a factor,

$$\gamma_{rm} = \frac{1}{\sqrt{\eta}} \int_0^{\sqrt{\eta}} sinc\left(u^2\right) du, \tag{3.145}$$

where η is the peak range migration across the k_x bandwidth normalised to the range resolution cell size. Figure 3.10 shows the loss in coherence as a function of η. Failure to provide adequate

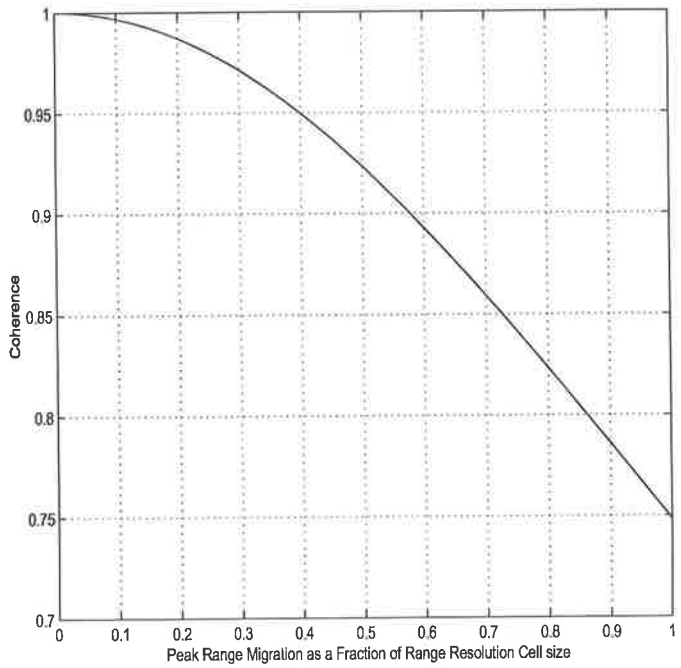


Figure 3.10: Loss in interferometric coherence obtained with a uncompensated quadratic range cell migration measured as a fraction of the range resolution cell size.

compensation for the relative range spatial frequency dependent phase errors thus leads to a reduction in the transduced scene coherence and hence a loss in contrast between changed and unchanged regions in change detection applications.

To demonstrate the impact of residual uncompensated range dependent phase errors on scene coherency, experimental data collected with the DSTO Ingara X-band airborne SAR have been processed using the PFA with post filtering and PGA algorithms. Figure 3.11 shows the primary image obtained using the PFA with post filtering and the PGA algorithm. The scene consists of an open lightly vegetated field with a line of trees on the right hand side of the scene and also running along the top of the scene. A building is present in the lower middle of the scene. The image resolution is 0.58 m in range by 0.12 m in azimuth. Figures 3.12 shows the PGA phase error estimate obtained for this particular imaging run. The phase error has a dominant quadratic component consistent with an along track velocity error of 0.23 percent of the true along track velocity and the associated range cell migration is 0.20 m or 0.35 of the range resolution cell size. The enlarged view of the PGA phase error estimate shown in Figure 3.13 indicates the presence of some high frequency components in the estimated phase error function. The PGA phase error estimate has been applied in the conventional sense as an azimuth spatial frequency dependent phase correction to the range compressed signal history data to form the focused image in Figure 3.11.

For the purposes of demonstrating the effects of uncompensated range dependent phase errors on scene coherency a repeat pass image has been formed using the same signal history data as the primary image. However, in forming the repeat pass image the PGA phase error estimate given in Figure 3.12 has been removed from into the acquired raw signal history data in the "native" polar format as described in equations (3.142) and (3.143). By applying the PGA phase error correction to the raw signal history data prior to polar to rectangular resampling the dependence of the demodulation phase error on range spatial frequency is completely compensated (to within the accuracy of the PGA phase

estimate). In terms of the coherence estimate, by using the same raw signal history data to form the primary and repeat pass interferometric image pair other sources of decorrelation such as misaligned collection apertures as well as geometric misregistration of the interferometric image pair have been eliminated. The transduced scene decorrelation can thus be attributed to the range spatial frequency dependence of the phase error function.

Figure 3.14 shows the interferogram formed between this repeat pass image and the primary image discussed above. The average sample coherence obtained over the open field region in the coherence map is 0.939. From Figure 3.10 this corresponds to a range cell migration of approximately 0.4 of the range resolution cell size, which is consistent with the calculated range cell migration of 0.35 obtained using the quadratic polynomial fit to the estimated phase error function. Figure 3.15 shows the interferogram formed between the repeat pass image reconstructed from the corrected signal history (3.143) and applying the range cell migration correction step given in (3.141) to the primary image discussed above. The additional range migration correction step clearly improves the scene coherence giving correlation coefficient values close to unity. The average coherence obtained over the field region in the coherence map is 0.987, an increase of approximately 5 percent compared to the coherence estimate obtained without the range migration correction step. Ideally the coherence value obtained should be unity as the same raw signal history data has been used in generating both the primary and repeat pass imagery. The slight reduction in coherence is most likely due to uncompensated higher order range dependent residual phase errors.

3.6 Conclusions

In this chapter the impact of errors in the measurement of the pointing vectors, describing the radar platform location with respect to the scene focus point, on spotlight SAR image formation has been examined. The contribution of errors in the measurement of the range, as well as errors in the azimuth and elevation angles, to the uncompensated residual phase error function have been derived. It has been shown that the error function manifests as a two dimensional blur function that varies spatially over the scene. For all but very wide-angle, large fractional bandwidth systems the defocusing blur function simplifies to the commonly used azimuthal blur function that is independent of scattering location. However, for wide-angle collections subtle higher order range dependent effects become increasingly significant and the full spatially varying, two dimensional nature of the image defocus begins to manifest. For wide-angle collections the range dependence of the image defocus interferes with the phase estimation steps of autofocus algorithms. It also remains as an uncompensated range dependent blur in the restored image degrading post processed products such as interferometric based measurements.

A formulation of the PGA algorithm in terms of a signal and noise subspace within a concise matrix based framework has been obtained and the impact of a two dimensional uncompensated phase error defocus on the PGA algorithm steps has been considered. The range dependent components of the phase error function are unmodelled by the PGA and therefore corrupt the PGA phase error estimate and will remain as residual uncompensated defocus in the restored image. For simple low order polynomial type phase error functions a simple range cell migration step has been proposed to correct for the dominant deleterious effects of the range dependent phase error function. The improvement of the correction in terms of the PFA and PGA processor point spread function and interferometric based image products has been demonstrated using data collected with the DSTO Ingara X-band airborne SAR. In particular a coherence improvement of 5% has been demonstrated illustrating the subtle higher order nature of this correction.



Figure 3.11: SAR image recovered from data collected using the DSTO Ingara X-band airborne SAR and processed using PFA with post filtering and application of the PGA algorithm. The resolution of the recovered image is 0.58 m in range and 0.12 m in azimuth and has been subsequently spatially averaged for display.

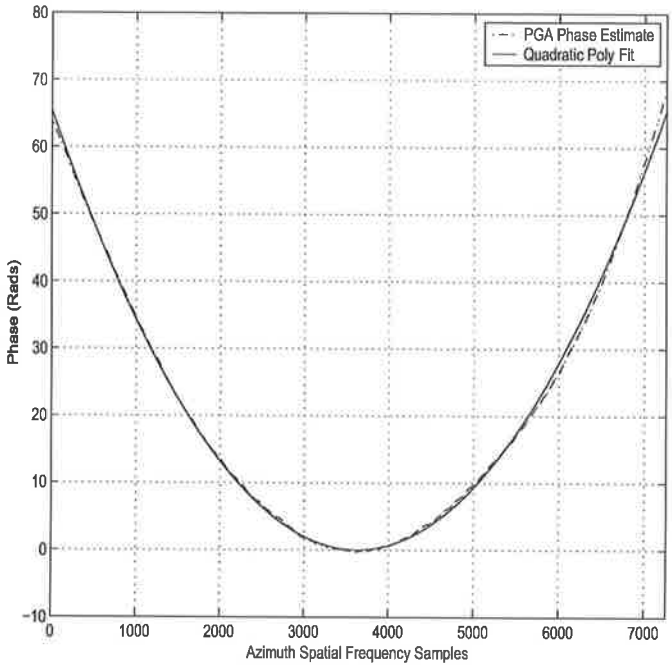


Figure 3.12: The PGA phase error estimate obtained from the experimental Ingara X-band data as a function of the azimuth spatial frequency. The phase error shows a dominant quadratic component consistent with a 0.23 percent error in the along track velocity measurement.

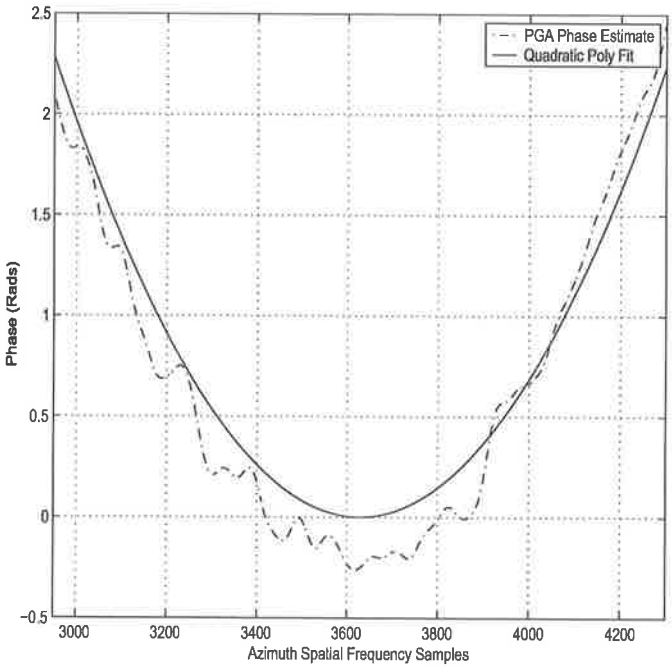
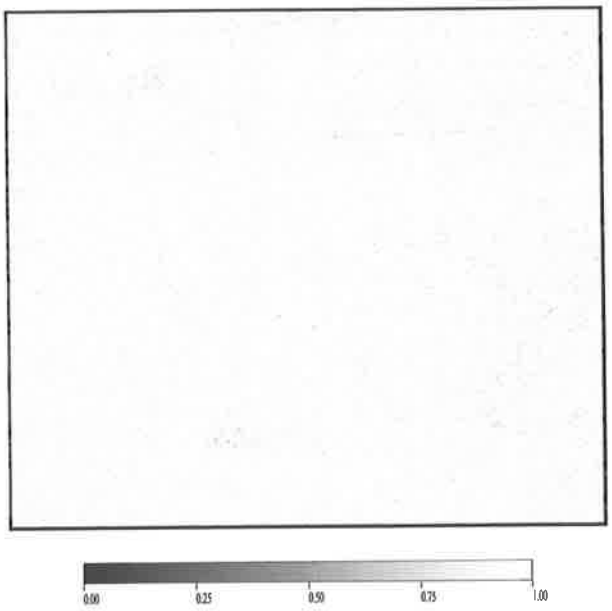
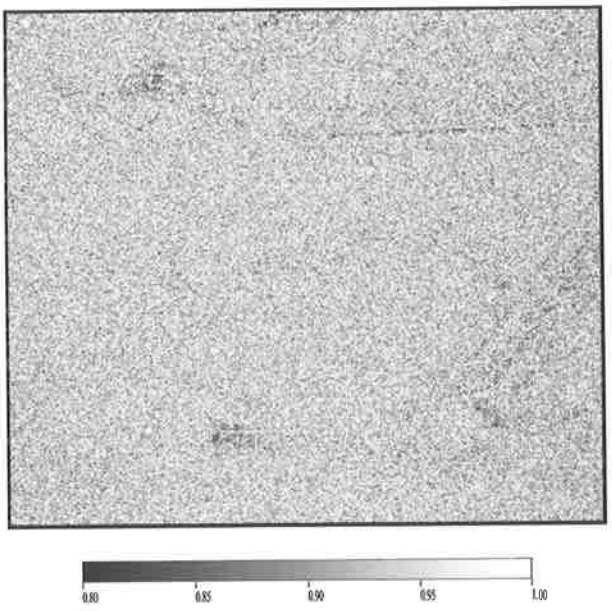


Figure 3.13: Enlarged view of the PGA phase error estimate for a region around the aperture centre. High frequency components in the phase error estimate are evident.

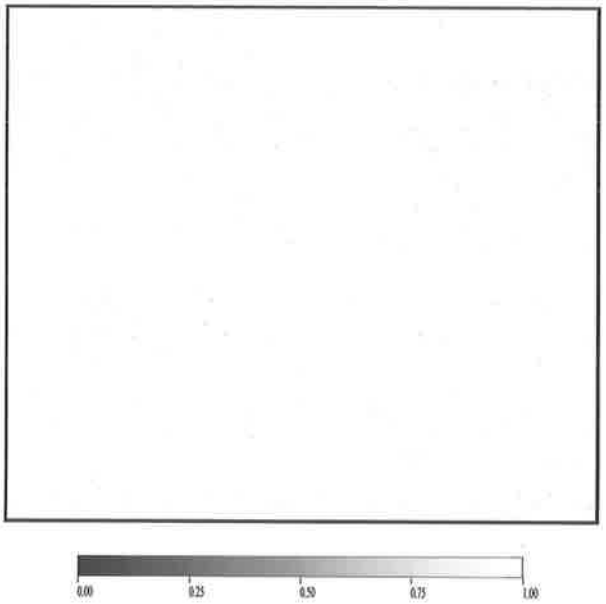


(a) Coherence map displayed with scale 0 to 1.

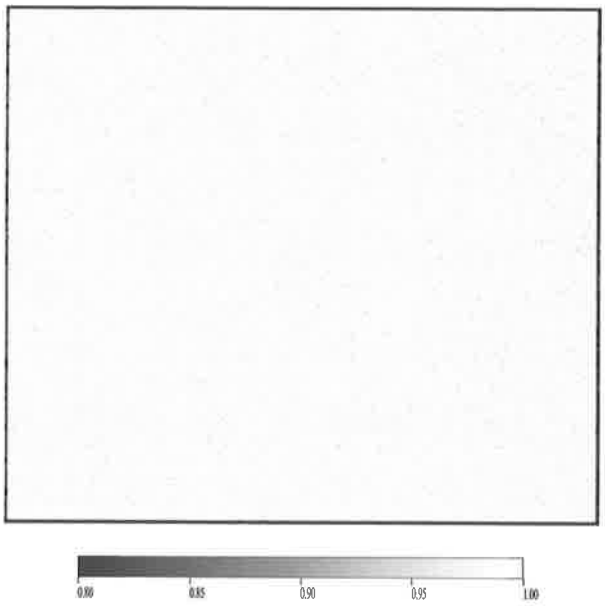


(b) Coherence map displayed with scale 0.8 to 1.

Figure 3.14: Coherence map estimate obtained from the primary and repeat pass image where the primary image is subject to uncompensated range dependent defocus which has been compensated for in the repeat pass image. Figures (a) and (b) show the same coherence map with different scales as indicated. Ideally the coherence should be unity however the residual relative range dependent defocus has reduced the coherence to 0.939 in the open field region of the scene which is consistent with a relative range cell migration of 0.4 of a range resolution cell size.



(a) Coherence map displayed with scale 0 to 1.



(b) Coherence map displayed with scale 0.8 to 1.

Figure 3.15: Coherence map estimate obtained from the primary and repeat pass image where a range cell migration correction step has been carried out on the primary image. Figures (a) and (b) show the same coherence map with different scales as indicated. The dominant deleterious effects of the relative range dependent defocus have largely been corrected with the coherence over the open field increased to 0.987.

Chapter 4

SAR Interferometry

4.1 Introduction

Synthetic Aperture Radar Interferometry (InSAR) employs two complex valued SAR images to derive additional information about a scene by exploiting differences in the amplitude and phase of the image pair. The information made available by the joint processing of an interferometric image pair is determined by the difference between the imaging geometries used for each collection and any scene changes arising in the temporal delay between the collections. In the terrain mapping application of interferometric SAR the image pair are acquired using imaging collections having a small baseline offset in a direction orthogonal to the radar flight track. The mismatch in the synthetic apertures used to form the image pair produces a height dependent phase difference between the images from which the terrain topography may be extracted with excellent accuracy [GZW88]. On the other hand for SAR image pairs obtained with a temporal separation and an identical imaging geometry, differences between the interferometric image pair may be attributed to changes in the scene complex backscatter. Temporal delays of the order of milliseconds may be obtained by using two radars mounted along the flight track axis of the radar platform. Such Along Track Interferometers (ATI) may be used as an extremely sensitive moving target indicator for detecting slow moving vehicles [Gie01a]. With a single antenna platform and matching flight tracks repeat pass interferometry may be used as a sensitive measure of scene disturbance that occurs over time scales ranging from hours to days [JWE+96], [CR98], [Cor97] and even years [Rei00]. Interferometric change detection is potentially a very sensitive measure of scene disturbance as only small scatterer displacements, of the order of a fraction of a wavelength can cause significant changes in the amplitude and phase between the image pair. Indeed the technique has been applied to spaceborne SARs to detect vehicle tracks in a scene [CR98].

In this chapter the principles of SAR interferometry will be introduced. In particular the interferometric processing of wide-angle fine resolution spotlight mode SAR for change detection will be addressed. This forms the theoretical basis for subsequent chapters that examine the theoretical as well as experimental performance of various interferometric change statistics. This chapter also describes an interferometric SAR processor developed for the generation of interferograms from experimental repeat pass SAR data collected with the DSTO Ingara X-band airborne SAR. In Sections 4.3 and 4.4 a statistical description of a joint interferometric image pair is discussed. It is shown that for natural homogeneous distributed targets the additional information provided by interferometric processing is encapsulated in the cross channel correlation coefficient and in Section 4.5 appropriate estimators for this quantity are discussed. The quality of the cross correlation coefficient estimate is crucially dependent on the identification, modelling, estimation and compensation of relative mismatch between the acquisition and image focusing functions used to generate the interferometric pair.

Section 4.6 discusses sources of relative mismatch between an interferometric image pair formed using the Polar Format Algorithm (PFA) and Polar Format Algorithm with Post Filtering (PF2) image formation algorithms as well as common techniques to mitigate the dominant first order effects. Finally an experimental system developed to process repeat pass interferometric data collected with the DSTO Ingara SAR is described and coherent change detection results are presented in Section 4.7.

4.2 Background

During SAR data acquisition complex range echo data are acquired over a synthetic aperture formed as the radar moves past the scene. Under an assumption of linearity the range echo acquired at a given transmit/receive point, after range compression, is the superposition of all scattering responses lying equidistant from the radar within the antenna illumination footprint. Thus over the coherent processing interval an aggregate complex scene response is transduced as a function of position along the collection aperture and propagation range delay. By accurately measuring the radar platform location at each transmit/receive point the variation in the amplitude and phase response for each scene scattering location in the integrated response over the synthetic aperture can be predicted. SAR image focusing algorithms invert the integrated scene response into a two dimensional image of the complex scene reflectivity by applying the necessary two dimensional filters matched to the amplitude and phase response for each scattering location in the scene. This allows the recovery of an image where the scene backscatter is resolved into a two dimensional map of range versus cross range. The elevation of scatterers in the scene however may not be resolved in a single pass SAR collection and are "projected" into the image plane appearing at a location in the image that is offset from their true location by an amount determined by the imaging geometry and the scatterer height.

In the case of spotlight SAR imaging collections, the PFA may be applied to recover a focused image of the scene when the standoff range of the radar from the scene is much greater than the image size. The PFA ground plane image point scatterer response for a target at location (x_s, y_s, z_s) has been derived in Chapter 2, Section 2.3 and for straight and level flight without squint is given by,

$$g(x,y) = exp(-j(y_s + z_s \tan\psi_0)k_{0_g})a(x - x_s, y - y_s - z_s \tan\psi_0). \tag{4.1}$$

The angle ψ_0 is the elevation angle measured between the local horizontal and the vector from the scene centre to the radar location at the aperture centre, a is the point spread function defined by the weighted aperture window applied to the acquired range echo data (see equation (2.59) in Chapter 2) and $k_{0_g} = 4\pi/\lambda \cos\psi_0$ where λ is the radar wavelength. A scatterer at location (x_s, y_s, z_s) thus appears in the recovered two dimensional ground plane image at location $(x_s, y_s + z_s \tan\psi_0)$ and is subject to a phase modulation given by $\phi = (y_s + z_s \tan\psi_0)k_{0_g}$. For a general scene consisting of an arbitrarily large number of scatterers, assuming the SAR acquisition process is linear, the transduced reflectivity recovered by the PFA at a location (x_0, y_0) will be the superposition of all scatterers at azimuthal location x_0 and lying along a line $z = (y_0 - y)/\tan\psi_0$. Thus despite the scatterers along the line $z = (y_0 - y)/\tan\psi_0$ having different elevation locations the PFA recovers only the integrated response along the line and the individual scatterer responses may not be resolved.

The scattering returns at different elevations in the scene however may be separated, in a limited sense, via the joint processing of a pair of SAR images. In particular if two scene images are acquired simultaneously using two receive antennas on the same sensor platform but with some across and/or above track baseline offset, the transduced image pair will be subject to amplitude and phase differences which are a function of the scatterer elevation. In this imaging modality each SAR image is acquired with a slightly different elevation angle ψ_1 and ψ_2, as defined by the baseline offset between the receive antennas, thus a scatterer at (x_s, y_s, z_s) will appear in the image pair at slightly different

range locations, with the difference given by,

$$\begin{aligned} \Delta y &= z_s(\tan\psi_1 - \tan\psi_2), \\ &= z_s\Delta\beta, \end{aligned} \tag{4.2}$$

and with a different modulating phase, giving a phase difference of,

$$\begin{aligned} \Delta\phi &= arg\{g(x_s, y_s + z_s\tan\psi_1)\} - arg\{g(x_s, y_s + z_s\tan\psi_2)\}, \\ &= z_s k_{0_g}(\tan\psi_1 - \tan\psi_2), \\ &= z_s k_{0_g}\Delta\beta, \end{aligned} \tag{4.3}$$

where $\Delta\beta = (\tan\psi_1 - \tan\psi_2)$. Given accurate measurements of ψ_1 and ψ_2 an estimate of z_s may be retrieved by estimating either Δy or $\Delta\phi$. Estimation of z_s via the differential layover Δy is a well known technique commonly referred to as stereoscopic terrain mapping [Leb90]. The accuracy of this approach however is limited by the accuracy of the estimate of Δy which will be of the order of the resolution cell size. An estimate of z_s obtained via the differential phase $\Delta\phi$ however will have an accuracy of the order of the radar wavelength and thus can potentially provide highly accurate estimates of the scatterer elevation. This forms the basis of the terrain height mapping application of SAR interferometry: By estimating and removing any misregistration between the image pair an estimate of the phase difference, modulo 2π, between the image pair may be recovered. The terrain elevation may subsequently be recovered via application of a phase unwrapping algorithm to remove the 2π phase ambiguity.

Interferometric terrain height mapping relies on a baseline offset $\Delta\beta$ to generate a height dependent phase difference between an image pair. An alternative application of the joint processing of a SAR image pair arises when the image pair are acquired at different times but using the same imaging geometry. In this imaging modality differences in the amplitude and phase between the image pair may be attributed to changes in the scene that arise in the time interval between collections. For example, by placing two antennas, displaced in the along track direction, on the same sensor platform image pairs may be acquired with a temporal delay of the order to a few milliseconds. Such Along Track Interferometers (ATI) allow the suppression of static, stable clutter scattering contributions to identify the presence of slow moving targets in a scene [Gie01a], [Gie01b] and may also be used for mapping ocean currents [GBZ89]. Alternatively using repeat pass collections, changes in the scene that occur over hours, days and even years may be transduced and used to quantify scene disturbances such as those arising from man-made scene changes, environmental effects as well as geophysical processes [RvZ93], [GGZ89] and [FPR01].

The application of SAR interferometry that has received the most attention in the literature has been the topographic mapping application as this allows digital elevation maps of a scene to be generated with unprecedented accuracy, resolution and coverage. The first demonstration of interferometric SAR applied to topographic mapping was obtained using radar observations of the Moon in 1972 [SZR+72], [Zis72a], [Zis72b]. In [Zis72a], [Zis72b] a radar interferometer was obtained using the Haystack radar system and a nearby communications antenna with subsequent interferometric height measurements yielding an accuracy of better than 500 m. In 1974 Graham [Gra74] applied the technique to radar data of the Earth acquired using an airborne platform. In Graham's system an additional receive antenna was placed in an existing airborne SAR to produce an across track interferometer. Analogue mixing of the signals received by the two antennas produced a beat pattern that tracked the interferometric phase fringe variation with the scene topography. While the soundness of the underlying principle was clearly demonstrated, the full potential of interferometric SAR for topographic mapping of the Earth was not realised until the late 1980s and early 1990s. In 1986 Zebker and Goldstein reported a practical demonstration of topographic mapping using an airborne

single pass system. Interferometric processing was also applied by Goldstein [GZW88] to repeat pass data acquired by the SeaSAT L band SAR instrument over the Cottonball basin of Death Valley and shown to generate topographic maps that were in close agreement with published U.S. Geological Survey maps. This demonstration of topographic mapping of the Earth using a spaceborne system hinted at the possibility of obtaining a world wide digital elevation map with unprecedented accuracy and provided the impetus to develop more advanced sensors. In particular the launch of the ERS-1 C-band SAR satellite in 1991 by the European Space Agency has provided researchers with a wealth of high quality, modest resolution imagery, suitable for repeat pass interferometric processing. The high stability of the satellite and accurate knowledge of its orbital parameters allowed the generation of high quality interferograms to assist in the development of phase unwrapping algorithms for the retrieval of terrain topography. Also the SIR-C/X-SAR sensors flown onboard the Space Shuttle Endeavour in 1994 provided a multifrequency, multipolarisation data set suitable for interferometric processing with revisit periods of 1, 2, 3 days and 6 months [SJW96], [SES+95].

These advances in technology were matched by a considerable amount of research into the development of a statistical description of dual, as well as, multiple channel SAR imaging modes. Statistical models describing single channel SAR data have been extensively studied over many decades in the literature [JP76]. For the case of natural homogeneous distributed clutter scenes such as open fields the generally accepted model used to describe the transduced scene reflectivity is the Gaussian speckle model [OQ98]. In this model the distributed target scene is represented as a layer of many independent, identically distributed discrete point scatterers randomly distributed throughout the scene. The transduced reflectivity in a resolution cell is thus a coherent sum of these point scattering contributions, each weighted by the point spread function and each subject to a different phase modulation, which measures the scatterer location in terms of the radar wavelength. Provided the resolution cell size is many wavelengths across the phase modulation is essentially a random phase factor and the coherent return may be described as a random walk in the complex plane [Goo76]. Provided there are a sufficiently large number of scatterers in the scene the central limit theorem may be applied to the random walk description and the resolution cell response may be modelled by a zero mean, complex, circular Gaussian random process.

In describing a multi-channel SAR system the same limiting assumptions and arguments have been applied to derive a joint statistical description of the image ensemble. In the multi-channel description each channel in the ensemble is modelled as a random walk in the complex plane. It is assumed that each channel "sees" the same scatterers so that the random walk in each channel has the same number of steps. Provided the modulating phase associated with each scattering contribution is random and there are many scattering contributions within a resolution cell the joint channel distribution may be modelled as a jointly Gaussian random process characterised by the covariance matrix formed between the channels [OQ98], [YKJ+89]. In the case of an interferometric image pair the covariance matrix is a two by two matrix and the information provided by the joint processing of the interferometric image pair is encapsulated in the complex cross channel correlation coefficient given by,

$$\gamma exp(j\Phi) = \frac{E\{fg^*\}}{\sqrt{E\{|f|^2\}E\{|g|^2\}}}, \tag{4.4}$$

where f and g are the two interferometric images. The phase of the correlation coefficient Φ is simply the interferometric phase difference between the image pair used for terrain height mapping while the magnitude of the correlation coefficient γ, commonly called the coherence, is a value between 0 and 1 and indicates the extent of decorrelation in the transduced scene. Scene decorrelation may arise through a change in the relative spatial distribution of the scattering contributions in the scene. This leads to a change in the random walk describing the transduced reflectivity that is quantified in a

statistical sense via the coherence.

In [Goo63] Goodman showed that the maximum likelihood estimator of the covariance matrix describing a jointly Gaussian process is the sample covariance matrix. In practice in InSAR sample averaging is achieved either by spatial averaging or multilook averaging [PGS02a]. Goodman was also able to show that the density function of the sample estimate is given by the complex Wishart distribution. This result allowed the derivation of the density functions and statistical properties for the sample interferometric phase and coherence estimates to be found [LHM94], [TBQ95], [TL96]. A linkage between the variance of the interferometric phase estimate and the cross correlation coefficient magnitude was established indicating that poorer estimates of the phase are obtained in scenes that suffer from decorrelation. In such scenes more extensive sample averaging is required to obtain robust, reliable interferometric phase estimates for use in phase unwrapping algorithms. This was of particular interest in the analysis of ERS-1 data as interferometric processing was restricted to the analysis of repeat pass pairs acquired with a minimum revisit period of 35 days.

The potential for significant scene decorrelation to occur in the relatively long revisit periods of ERS-1 prompted research into understanding the mechanisms by which scene decorrelation occurs and the sensitivity of the interferometric properties to the radar parameters. In [GZW88], [LG90] and [RM92] the across track baseline between imaging passes was identified as a major performance driver in an interferometric system. While a baseline offset is required to generate an interferometric phase difference between the image pair the relative path lengths between the scene scatterers and the radar will be slightly different. The transduced return in each resolution cell will thus exhibit a slightly different random walk leading to decorrelation in the transduced image pair. The relationship between the interferometric baseline and the resulting scene decorrelation was derived and a critical baseline was found beyond which the interferometric image pair exhibit total scene decorrelation.

In [ZV92] Zebker identified a number of other mechanisms by which decorrelation can arise in an interferometric repeat pass image pair. In particular Zebker showed that decorrelation can arise if the scene is imaged from two slightly different aspect angles. This may arise due to relative inaccuracies in the knowledge of the radar platform location in repeat pass collections or where operational constraints preclude the formation of images from the same look direction. Zebker arrived at a linear relationship between the decorrelation factor and misalignment in the look direction where the constant of proportionality is dependent on the azimuthal resolution and inversely proportional to the radar wavelength. In the case of ERS-1 imagery Zebker showed that complete decorrelation may arise for a relative rotation of 0.7 degrees. Zebker also proposed a model for temporal scene decorrelation due to environmental effects such as wind and rain. In Zebker's model the scene is assumed to consist of a large number of randomly distributed point scatterers that are subject to a random displacement in the interval between imaging collections. By considering the scatterer range, azimuth and elevation displacements to be described by independent Gaussian random variables Zebker showed that the scene decorrelation is principally determined by the component of the scatterer's displacement along the radar's line of sight direction, measured in terms of the radar wavelength. Thus perturbations in the scatterer's location in the range direction are most dominant in low elevation angle acquisitions while for high elevation angle collections perturbations in the height direction are most dominant. Zebker's result also indicates that shorter wavelength radars are more sensitive to scatterer perturbations.

Zebker's analysis of interferometric scene decorrelation and subsequent processing of SeaSAT data presented in [ZV92] prompted Zebker to speculate on the use of scene decorrelation itself as a remote sensing observable that may be used to infer some of the geophysical properties of the scene. Using ERS-1 data Askne [AH93] examined the mean backscatter and coherence over a range of land cover types and concluded that environmental conditions effect the observed mean backscatter power and coherence of different land cover types in different ways and suggested using the coherence as

a land cover classification statistic. In [HUA95] Hagberg proposed a simple extension to Zebker's scatterer perturbation model to facilitate a simple description of scene coherence across different scene types. In this model the scattering contribution in a resolution cell is decomposed into a stable scattering component that is unchanged over the collection interval and an unstable component that may potentially be modified by scene disturbances. For example over forested terrain a resolution cell may contain contributions from branches, leaves and trunks as well as returns from the ground associated with gaps in the canopy. Of these backscatter contributions, the leaves and branches are subject to perturbations due to wind and therefore will contribute to the unstable scatterer ensemble. The relative contributions of stable and unstable scatterers to the correlation will depend on the mean backscatter power associated with the scattering types as well as the nature and extent of the perturbation. As different land cover types such as fields, forests, urban areas as well as rivers etc will exhibit different stable and unstable scattering behaviour it follows that the scene correlation may be used as a land classification tool. In Hagberg's analysis of ERS-1 data, scene coherence was used to discriminate between open fields and forested terrain. In more recent work [Yoc98] a classifier based on both image intensity and correlation measured with a dual-antenna system was shown to give a classification accuracy of up to 13.5 percent higher than using image intensity alone over a scene consisting of three classes namely water, trees and open fields.

In Zebker's model for scene decorrelation arising from scatterer perturbations it is found that an RMS scatterer displacement of approximately 20 percent of the radar wavelength can lead to total scene decorrelation. For small wavelength systems such as C and X band SARs, man-made disturbances such as vehicle tracks across a field can potentially cause significant scatterer displacement without causing an appreciable change in the mean backscatter of the scene. Such scene disturbances thus may not be detected using commonly used intensity based change detection techniques yet may be detected as areas of low coherence. Since temporal decorrelation arising due to wind and rain can also lead to significant decorrelation across the scene this change detection technique generally requires relatively short revisit periods to ensure there is adequate discrimination between the various sources of scene disturbance.

While the potential of interferometric change detection for detecting very subtle scene changes has been known for some time [JWE+96] only a few applications of the technique have been reported in the literature. The relatively long, 35 day, revisit periods and modest resolution of ERS-1 generally limits the suitability of this sensor for interferometric change detection of fine scale scene disturbances. Instead ERS-1 has been used for detecting larger scale changes such as changes in urban development and also flood monitoring. The launch of ERS-2 in 1995, designed to operate in tandem with ERS-1, however permitted interferometric image pairs to be processed with a one day revisit period. Corr [CR98] was subsequently able to use ERS-1,2 imagery to detect scene changes caused by the movement of large vehicles over a grassed area in Salisbury Plain, United Kingdom. The modest resolution of the ERS imagery (20 m in range by 6 m in azimuth) however ultimately limited the detection performance achieved by Corr. In order to realise the full potential of the interferometric change detection technique fine resolution image commensurate with the size of the changes to be detected is required. In [JWE+96] results from a coherent change detection experiment carried out using a 1 m resolution X-band airborne SAR developed by Sandia National Laboratories were presented. In these results, changes arising due to earthworks in a land fill site are readily identified including tracks made by a self-loading earthmover as well as the grading of an unpaved road. The finer resolution measurements facilitate the formation of a more robust coherence estimate through increased spatial averaging as well as improving the detection of finer scale scene disturbances.

The past decade has seen the maturing of the technology and algorithms developed for the collection and processing of interferometric SAR imagery. Interferometric SAR is now routinely used in a diverse range of disciplines such as the study of seismic events such as earthquakes, volcanology,

subsidence monitoring and ocean currents. In these fields SAR interferometry can provide a highly accurate, sustained, board area measurement capability that can be used to assist in the understanding of the underlying geophysical processes. Indeed airborne SAR systems have now been demonstrated with resolutions down to 10 cm [BE03], [TPS+99] thus interferometric measurements may now be made with unprecedented fine resolution. The extensive experience gained in use of both airborne and spaceborne SAR in interferometric modes has given the SAR community a deeper understanding of the system design issues and processing methodologies. In this chapter the underlying principles and theory of SAR interferometry will be presented leading to the design of an interferometric SAR processor used to process very fine resolution X-band interferometric image pairs collected using the DSTO Ingara X-band SAR. This interferometric processor will be used in subsequent chapters to study the coherent change detection application of SAR interferometry using spotlight mode SAR data acquired over extended collection apertures.

4.3 Interferometric Spotlight SAR System Model

In Chapter 2 spotlight mode SAR imaging was described as a two step process of coherent data acquisition followed by image formation. The acquisition process describes the collection of the scene signal history data over the SAR coherent processing interval and represents the aggregate backscatter response of the scene as a function of position along the collection aperture and propagation delay. The image formation processor is an inversion operator in which the aggregate scene response is resolved into a two dimensional map of scene complex radar backscatter. In the following sections the equations describing the acquisition and image formation process in the absence of platform location measurement errors will be reviewed briefly and then extended to encompass an interferometric image pair.

4.3.1 Single Channel Spotlight SAR

For a scene described by the complex reflectivity function,

$$r(x,y,z) = r_{f_s}(x,y)\delta(z - h(x,y)), \tag{4.5}$$

where $r_{f_s}(x,y)$ is a two dimensional surface reflectivity and $h(x,y)$ is a slowly varying terrain height function, the collected deramp demodulated signal history data in the spatial frequency domain was shown, in Chapter 2, to take the form,

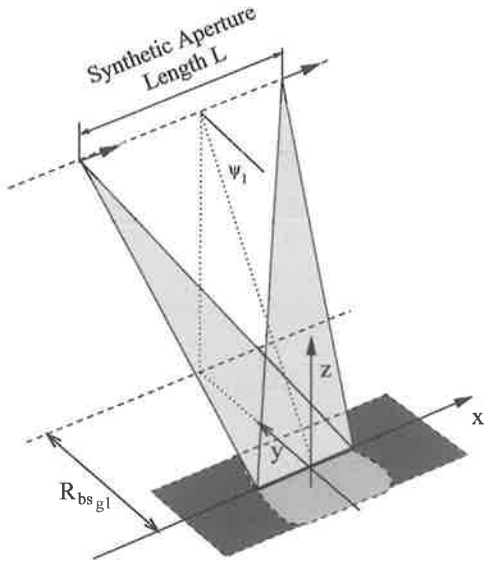
$$G_p(k_x,k_y,k_z) = A_{acq}(k_x,k_y,k_z)\iiint r(x,y,z)exp(j\phi_{acq}(k_x,k_y,k_z,R-R_T))dxdydz, \tag{4.6}$$

where ϕ_{acq} is the deramp demodulated signal history phase given by,

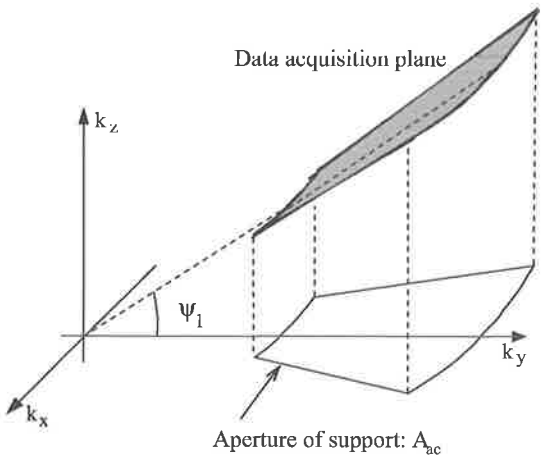
$$\phi_{acq}(k_x,k_y,k_z,R-R_T) = (R-R_T)\sqrt{k_x^2+k_y^2+k_z^2}. \tag{4.7}$$

The distance R is measured from the radar to a given point (x,y,z) in the scene, while R_T is the distance of the radar from the scene centre. The variables k_x, k_y and k_z are the spatial frequency variables associated with the spatial variables x, y and z. The region of support for the spatial frequency variables is defined by the acquisition aperture window $A_{acq}(k_x,k_y,k_z)$ which is determined by the transmit waveform parameters and the spatial extent of the acquisition aperture. For the case of straight and level flight without squint $A_{acq}(k_x,k_y,k_z)$ takes the form,

$$A_{acq}(k_x,k_y,k_z) = A_{ac}(k_x,k_y)\delta(k_z - \beta_1 k_y), \tag{4.8}$$



Spotlight SAR imaging geometry



Acquired signal history data in
the scene's spatial frequency domain

Figure 4.1: Spotlight SAR imaging geometry corresponding to straight and level flight without squint. The depression angle and standoff range at aperture centre are ψ_1 and $R_{bs_{g1}}$ respectively. The acquired range echo data are samples of the scene's complex reflectivity evaluated over an acquisition plane in the scene's spatial frequency domain given by $k_z = \tan\psi_1 k_y$.

where $\beta_1 = \tan\psi_1$ and ψ_1 is the elevation angle measured from the scene centre to the radar at the midaperture point. The aperture of support projected onto the (k_x, k_y) plane, $A_{ac}(k_x, k_y)$, is given by,

$$A_{ac}(k_x, k_y) = rect\left(\frac{\sqrt{k_x^2 + ((1+\beta_1)k_y)^2} - k_0}{k_{bw}}\right) rect\left(\frac{k_x}{k_y}\frac{R_{bs_{g1}}}{L}\right), \tag{4.9}$$

where $k_{bw} = 4\pi f_{bw}/c$ and f_{bw} is the transmit waveform bandwidth, $k_0 = 4\pi f_0/c$ and f_0 is the radar centre frequency, L is the length of the synthetic aperture, $R_{bs_{g1}}$ is the standoff distance of the radar from the scene centre at the mid-aperture point and the ratio $L/R_{bs_{g1}}$ indicates the angular width of the collection aperture. It can be seen from equations (4.8) and (4.9) that the acquisition aperture defines an angular sector in a plane in the three dimensional Fourier space (k_x, k_y, k_z) given by $k_z = \beta_1 k_y$. The sector is offset from the origin by an amount k_0 and has a radial width determined by the transmit waveform bandwidth and an angular width determined by the angular extent of the synthetic aperture. This is illustrated in Figure 4.1.

Using a Taylor series expansion for $(R - R_T)$ in terms of the scattering location (x, y, z) about the scene centre the following form for the phase function was derived in Section 2.3,

$$\phi_{acq} = -xk_x - yk_y - zk_z + \phi_{res}(k_x, k_y, x, y). \tag{4.10}$$

The linear terms in k_x, k_y and k_z in (4.10) correspond to a plane wave propagation model describing the propagation of the electromagnetic radiation to and from the scene. The additional phase term ϕ_{res}

accounts for the effects of wavefront curvature in the acquired deramp demodulated signal history phase. In deriving (4.10) it is assumed that the terrain height variation over the scene is small and thus the phase response in the acquired signal history for an elevated target at height z is adequately modelled by the linear phase term zk_z in (4.10) and so ϕ_{res} is independent of k_z and z. Substituting (4.10) into (4.6) gives the following form for the acquired signal history,

$$\begin{aligned} G_p(k_x,k_y,k_z) &= A_{acq}(k_x,k_y,k_z)\iiint r(x,y,z)exp\left(j\phi_{res}(k_x,k_y,x,y)\right) \\ &\qquad exp\left(-j(xk_x+yk_y+zk_z)\right)dxdydz. \end{aligned} \tag{4.11}$$

In general, when the standoff range of the radar from the scene is much greater than the scene size the linear terms in (4.10) dominate the acquisition phase ϕ_{acq} and the residual phase terms ϕ_{res} represent small higher order corrections. In Chapter 2 the form of the residual phase terms was extensively studied. It was shown that ϕ_{res} is a phase function that varies spatially over the image and becomes increasingly significant for wide-band, wide-angle, near-field imaging. While the phase ϕ_{res} varies spatially over the image, the phase varies only slowly with range and azimuth and may be considered to be a constant phase term over sufficiently small, localised regions of the scene. This formed the basis for the PF2 algorithm discussed in Chapter 2. Consistent with the PF2 formulation in Chapter 2 it shall be assumed in the following development, that the imaged scene, described by the reflectivity function $r(x,y,z)$, is sufficiently small, (or the acquired signal history has been filtered such that G_p corresponds to a sufficiently small sub-region of a larger scene) such that ϕ_{res} in (4.11) may be considered to be independent of the scattering location and equal to the value of ϕ_{res} computed at the centre of the region under consideration. Under this assumption the phase function $exp(j\phi_{res})$ may be taken out of the integral in (4.11).

The image formation processor is an inversion operator in which the aggregate scene response described by (4.11) is resolved into a two dimensional map of the scene's complex radar backscatter. Given that the aperture of support of the acquired deramp demodulated signal history data is offset from the (k_x,k_y,k_z) origin as shown in Figure 4.1 it is convenient to define the following baseband form for (4.11),

$$\begin{aligned} G(k_x,k_y,k_z) &= G_p(k_x,k_y+k_{0_g},k_z), \\ &= A_{acq}(k_x,k_y+k_{0_g},k_z)exp\left(j\phi_{res}(k_x,k_y+k_{0_g})\right)\iiint r(x,y,z) \\ &\qquad exp\left(-j(xk_x+y(k_y+k_{0_g})+zk_z)\right)dxdydz, \\ &= A_{acq}(k_x,k_y+k_{0_g},k_z)exp\left(j\phi_{res}(k_x,k_y+k_{0_g})\right)R(k_x,k_y+k_{0_g},k_z), \end{aligned} \tag{4.12}$$

where $R(k_x,k_y,k_z)$ is the Fourier transform of $r(x,y,z)$ and ϕ_{res} in (4.12) is the value of ϕ_{res} computed at the centre of the region of the scene under consideration. From (4.12) it can be seen that $G(k_x,k_y,k_z)$ is a baseband, Fourier domain description of the scene reflectivity. The Polar Format Algorithm (PFA) recovers a ground plane image from the baseband signal history $G(k_x,k_y,k_z)$ by applying a windowed, three dimensional inverse Fourier transform to $G(k_x,k_y,k_z)$ evaluated at $z=0$, i.e.,

$$g(x,y) = \frac{1}{8\pi^3}\iiint A_{ifp}(k_x,k_y)G(k_x,k_y,k_z)exp(j(xk_x+yk_y))dk_xdk_ydk_z, \tag{4.13}$$

where $A_{ifp}(k_x,k_y)$ is the windowing function. Substituting (4.12) into (4.13) gives the PFA image,

$$g(x,y) = \frac{1}{8\pi^3}\iiint A_{ifp}(k_x,k_y)A_{acq}(k_x,k_y+k_{0_g},k_z)exp(j\phi_{res}(k_x,k_y+k_{0_g}))$$

$$\iiint r(\bar{x},\bar{y},\bar{z})exp(-j\bar{y}k_{0_g})exp(j((x-\bar{x})k_x+(y-\bar{y})k_y)-\bar{z}k_z))$$
$$d\bar{x}d\bar{y}d\bar{z}dk_xdk_ydk_z. \quad (4.14)$$

The window function A_{ifp} is taken to be a rectangular region lying wholely within the acquisition aperture of support such that,

$$A_{ifp}(k_x,k_y)A_{acq}(k_x,k_y+k_{0_g},k_z)=A_{ifp}(k_x,k_y)\delta(k_z-\beta_1(k_y+k_{0_g})), \quad (4.15)$$

where $A_{ifp}(k_x,k_y)$ is given by,

$$A_{ifp}(k_x,k_y)=rect\left(\frac{k_x}{k_{bw_{x1}}}\right)rect\left(\frac{k_y}{k_{bw_{y1}}}\right). \quad (4.16)$$

Substituting (4.5) and (4.15) into (4.14) gives the following form for the recovered PFA ground plane image,

$$g(x,y)=\iint r_{f_s}(\bar{x},\bar{y})exp(-j(\bar{y}+h(\bar{x},\bar{y})\beta_1)k_{0_g})a(x-\bar{x},y-\bar{y}-h(\bar{x},\bar{y}))d\bar{x}d\bar{y}. \quad (4.17)$$

The convolution kernel $a(x,y)$ describes the point spread function of the combined acquisition and image formation process and is given by the three dimensional inverse Fourier transform of the product $A_{ifp}A_{acq}exp(j\phi_{res})$ evaluated on the $z=0$ ground plane i.e.,

$$a(x,y) = \frac{1}{8\pi^3}\iiint A_{ifp}(k_x,k_y)A_{acq}(k_x,k_y+k_{0_g},k_z)exp(j\phi_{res}(k_x,k_y+k_{0_g}))$$
$$exp(j(xk_x+yk_y))dk_xdk_ydk_z. \quad (4.18)$$

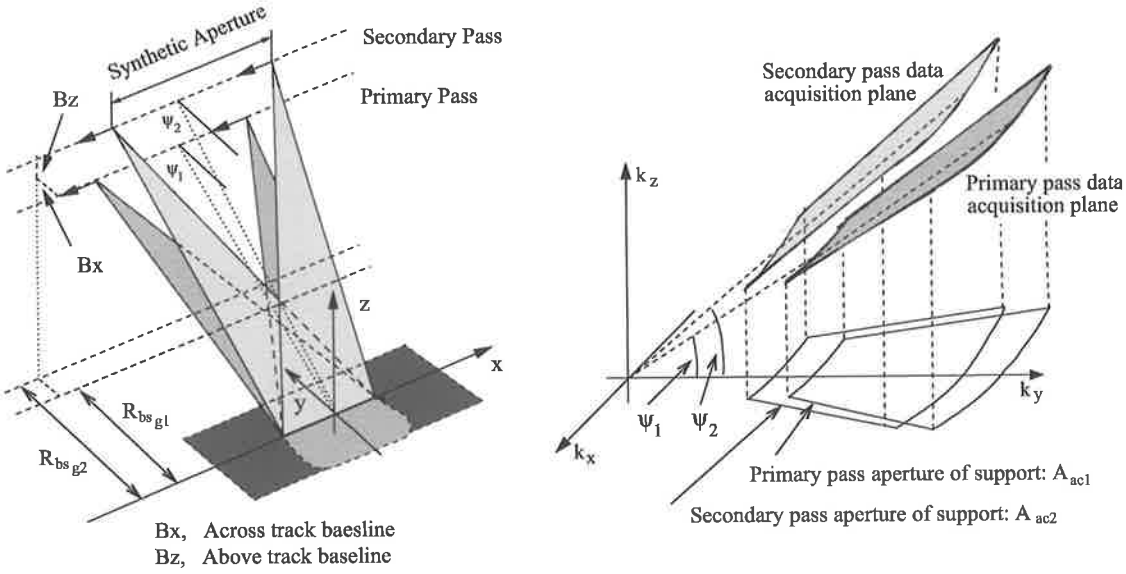
Substituting (4.16) into the expression for $a(x,y)$ above gives,

$$\begin{aligned} a(x,y) &= \frac{1}{4\pi^2}\iint rect\left(\frac{k_x}{k_{bw_{x1}}}\right)rect\left(\frac{k_y}{k_{bw_{y1}}}\right)exp(j\phi_{res}(k_x,k_y+k_{0_g})) \\ &\qquad exp(j(xk_x+yk_y))dk_xdk_y, \\ &= \frac{k_{bw_{x1}}k_{bw_{y1}}}{4\pi^2}sinc\left(\frac{xk_{bw_{x1}}}{2\pi}\right)sinc\left(\frac{yk_{bw_{y1}}}{2\pi}\right)\otimes b(x,y), \end{aligned} \quad (4.19)$$

where $b(x,y)$ is the inverse Fourier transform of the phase function $exp(j\phi_{res}(k_x,k_y+k_{0_g}))$. For the case when the imaged scene is sufficiently small and centred at the spatial origin, ϕ_{res} is negligible and $a(x,y)$ reduces to a two dimensional sinc function. For larger scenes the phase ϕ_{res} manifests as a convolution kernel $b(x,y)$ that varies spatially over the image leading to defocus and distortion of the recovered PFA image.

4.3.2 Interferometric Dual Channel Spotlight SAR

Figure 4.2 illustrates an interferometric spotlight SAR collection in which the primary and secondary collection apertures have an across and above track baseline offset of B_x and B_z respectively. In the case of single pass interferometry these offsets are defined by the relative locations of the two receive antennas on the radar platform. In a repeat pass interferometric acquisition on the other hand, the offsets would represent the differences between the primary and repeat pass flight tracks of the radar platform. Due to these baseline offsets the scene is viewed with a slightly different imaging geometry in each acquisition. In particular the primary and secondary acquisitions have slightly different mid-aperture elevation angles of ψ_1 and ψ_2 respectively as well as slightly different standoff ranges: $R_{bs_{g1}}$



Repeat pass interferometric spotlight SAR imaging geometry

Acquired signal history data in the scene's spatial frequency domain

Figure 4.2: Repeat pass spotlight SAR imaging geometry acquired with an across track baseline B_x and an above track baseline of B_z. The depression angles for the primary and repeat pass acquisitions at aperture centre are ψ_1 and ψ_2 respectively while the standoff ranges are $R_{bs_{g1}}$ and $R_{bs_{g2}}$ respectively. The acquired range echo data in the primary and repeat pass are samples of the scene's complex reflectivity evaluated over two offset acquisition planes in the scene's spatial frequency domain given by $k_z = \tan\psi_1 k_y$ in the case of the primary pass and $k_z = \tan\psi_2 k_y$ in the repeat pass.

in the primary collection and $R_{bs_{g2}}$ in the secondary collection. As a consequence the acquired signal history data in the primary and secondary acquisitions are samples of the scene's spatial frequency domain representation on two slightly different planes defined by $k_z = \tan\psi_1 k_y$ and $k_z = \tan\psi_2 k_y$ respectively as illustrated in Figure 4.2.

Defining the scene complex reflectivity in the primary acquisition as,

$$r_f(x,y,z) = r_{f_s}(x,y)\delta(z - h(x,y)), \tag{4.20}$$

and in the secondary acquisition as,

$$r_g(x,y,z) = r_{g_s}(x,y)\delta(z - h(x,y)), \tag{4.21}$$

(Note that in the case of single pass interferometry the scene reflectivity is the same in each channel in which case $r_f(x,y,z) = r_g(x,y,z)$.) the acquired signal history data for the two acquisitions may be written as,

$$\begin{aligned} G_{p_1}(k_x,k_y,k_z) &= A_{acq_1}(k_x,k_y,k_z)exp(j\phi_{res_1}(k_x,k_y)) \\ &\iiint r_f(x,y,z)exp\left(-j(xk_x+yk_y+zk_z)\right)dxdydz, \end{aligned} \tag{4.22}$$

and,

$$\begin{aligned} G_{p_2}(k_x,k_y,k_z) &= A_{acq_2}(k_x,k_y,k_z)exp(j\phi_{res_2}(k_x,k_y)) \\ &\iiint r_g(x,y,z)exp\left(-j(xk_x+yk_y+zk_z)\right)dxdydz. \end{aligned} \tag{4.23}$$

Due to the different acquisition geometries, the offsets as well as the dimensions of the apertures of support, in the (k_x, k_y) plane for the acquired deramp demodulated signal history differ, as illustrated in Figure 4.2. In defining the baseband signal history G_1 and G_2 for the primary and secondary acquisitions however, a common baseband spatial frequency k_{0_g} is employed and is chosen to be the centre of the overlapping portion of the acquisition apertures such that,

$$\begin{aligned} G_1(k_x, k_y, k_z) &= A_{acq_1}(k_x, k_y + k_{0_g}, k_z) exp(j\phi_{res_1}(k_x, k_y + k_{0_g})) \\ &\iiint r_f(x, y, z) exp\left(-j(xk_x + y(k_y + k_{0_g}) + zk_z)\right) dxdydz, \end{aligned} \tag{4.24}$$

and,

$$\begin{aligned} G_2(k_x, k_y, k_z) &= A_{acq_2}(k_x, k_y + k_{0_g}, k_z) exp(j\phi_{res_2}(k_x, k_y + k_{0_g})) \\ &\iiint r_g(x, y, z) exp\left(-j(xk_x + y(k_y + k_{0_g}) + zk_z)\right) dxdydz. \end{aligned} \tag{4.25}$$

As a consequence the acquisition apertures of support for G_1 and G_2 are misaligned in the baseband spatial frequency domain as illustrated in Figure 4.3. The primary and secondary image formation window functions may be defined as,

$$A_{ifp_1}(k_x, k_y) A_{acq_1}(k_x, k_y + k_{0_g}, k_z) = A_{ifp_1}(k_x, k_y)\delta(k_z - \beta_1(k_y + k_{0_g})), \tag{4.26}$$

$$A_{ifp_2}(k_x, k_y) A_{acq_2}(k_x, k_y + k_{0_g}, k_z) = A_{ifp_2}(k_x, k_y)\delta(k_z - \beta_2(k_y + k_{0_g})), \tag{4.27}$$

where, using an unweighted rectangular window function, $A_{ifp_1}(k_x, k_y)$ and $A_{ifp_2}(k_x, k_y)$ have the form,

$$A_{ifp_1}(k_x, k_y) = rect\left(\frac{k_x}{k_{bw_{x1}}}\right) rect\left(\frac{k_y - \Delta_1}{k_{bw_{y1}}}\right), \tag{4.28}$$

$$A_{ifp_2}(k_x, k_y) = rect\left(\frac{k_x}{k_{bw_{x2}}}\right) rect\left(\frac{k_y + \Delta_2}{k_{bw_{y2}}}\right). \tag{4.29}$$

The window dimensions $(k_{bw_{x1}}, k_{bw_{y1}})$ and $(k_{bw_{x2}}, k_{bw_{y2}})$ are chosen such that window functions $A_{ifp_1}(k_x, k_y)$ and $A_{ifp_2}(k_x, k_y)$ lie wholely within the acquisition apertures of support as illustrated in Figure 4.3. The terms Δ_1 and Δ_2 describe the offset of the window functions from the baseband k_y origin that arises due to the use of the common baseband spatial frequency k_{0_g}, see Figure 4.3. Note that due to the offsets Δ_1 and Δ_2 the window functions $A_{ifp_1}(k_x, k_y)$ and $A_{ifp_2}(k_x, k_y)$ define a common overlapping area, illustrated in Figure 4.3, which takes the form,

$$\begin{aligned} A_c(k_x, k_y) &= A_{ifp_1}(k_x, k_y) A_{ifp_2}(k_x, k_y), \\ &= rect\left(\frac{k_x}{k_{bw_c}}\right) rect\left(\frac{k_y}{k_{bw_c}}\right). \end{aligned} \tag{4.30}$$

Applying the image formation windows to the primary and secondary acquisition signal history data given in (4.24) and (4.25) followed by an inverse Fourier transform gives the following ground plane interferometric image pair,

$$g_1(x, y) = \iint r_{f_s}(\bar{x}, \bar{y}) exp(-j(\bar{y} + h(\bar{x}, \bar{y})\beta_1)k_{0_{g1}}) a_1(x - \bar{x}, y - \bar{y} - h(\bar{x}, \bar{y})\beta_1) d\bar{x}d\bar{y}, \tag{4.31}$$

$$g_2(x, y) = \iint r_{g_s}(\bar{x}, \bar{y}) exp(-j(\bar{y} + h(\bar{x}, \bar{y})\beta_2)k_{0_{g2}}) a_2(x - \bar{x}, y - \bar{y} - h(\bar{x}, \bar{y})\beta_2) d\bar{x}d\bar{y}. \tag{4.32}$$

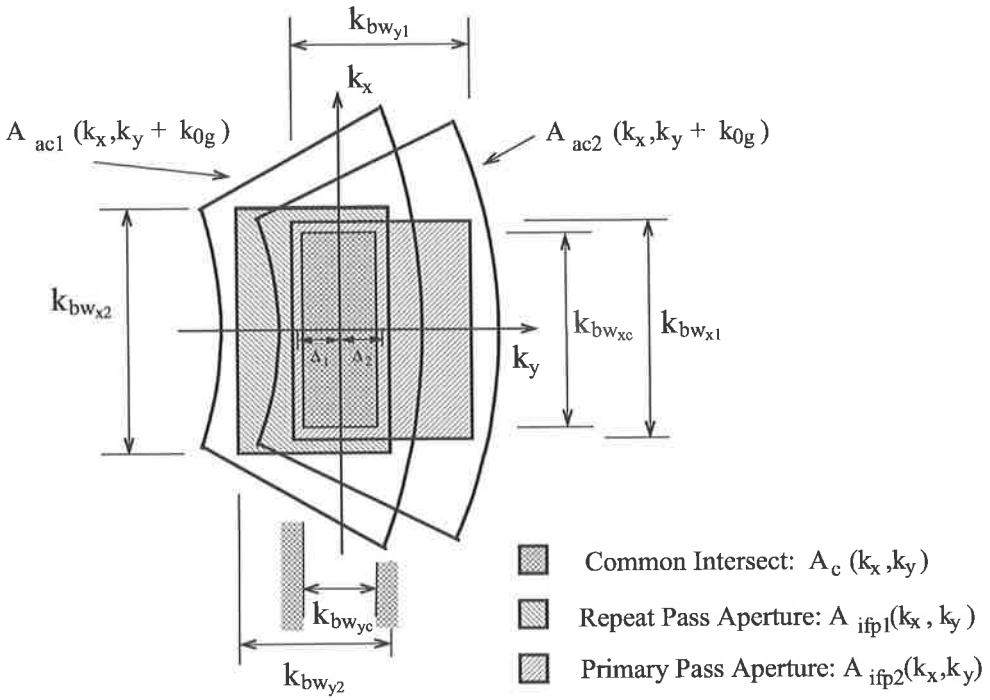


Figure 4.3: Apertures of support in the (k_x, k_y) plane for the acquisition and image formation transfer functions for a repeat pass image pair after baseband translation. Also shown is the common overlapping aperture of support. The size and k_y offsets of the apertures of support are determined by the baseline offsets between the primary and repeat pass collections.

The convolution kernels $a_1(x,y)$ and $a_2(x,y)$ are the point spread functions of the primary and secondary acquisitions respectively and are given by,

$$\begin{aligned} a_1(x,y) &= \frac{1}{8\pi^3}\iiint A_{ifp_1}(k_x,k_y)A_{acq_1}(k_x,k_y+k_{0_g},k_z)exp(j\phi_{res_1}(k_x,k_y+k_{0_g})) \\ &\qquad exp(j(xk_x+yk_y))dk_xdk_ydk_z, \\ &= \frac{k_{bw_{x1}}k_{bw_{y1}}}{4\pi^2}sinc\left(\frac{xk_{bw_{x1}}}{2\pi}\right)sinc\left(\frac{yk_{bw_{y1}}}{2\pi}\right)exp(jy\Delta_1)\otimes b_1(x,y), \end{aligned} \tag{4.33}$$

and,

$$\begin{aligned} a_2(x,y) &= \frac{1}{8\pi^3}\iiint A_{ifp_2}(k_x,k_y)A_{acq_2}(k_x,k_y+k_{0_g},k_z)exp(j\phi_{res_2}(k_x,k_y+k_{0_g})) \\ &\qquad exp(j(xk_x+yk_y))dk_xdk_ydk_z, \\ &= \frac{k_{bw_{x2}}k_{bw_{y2}}}{4\pi^2}sinc\left(\frac{xk_{bw_{x2}}}{2\pi}\right)sinc\left(\frac{yk_{bw_{y2}}}{2\pi}\right)exp(-jy\Delta_2)\otimes b_2(x,y), \end{aligned} \tag{4.34}$$

where $b_1(x,y)$ and $b_2(x,y)$ are the two dimensional inverse Fourier transforms of the phase functions $exp(j\phi_{res_1}(k_x,k_y+k_{0_g}))$ and $exp(j\phi_{res_2}(k_x,k_y+k_{0_g}))$ respectively.

4.4 Interferometric Scene Model

In order to determine the key information bearing parameters describing the transduced backscatter in an interferometric SAR image pair and define appropriate estimators of these parameters a model

of the backscattered field is required. In the following section the development of the statistically based speckle model for natural homogeneous distributed target types will be discussed. This shall then be extended to a joint statistical description for a interferometric image pair. It shall be shown that the additional information made available by the joint processing of an interferometric image pair is the cross channel correlation coefficient. It is found that the cross channel correlation coefficient consists of a scene dependent term determined by temporal changes in the scene between the image collections, a term dependent on the SAR imaging transfer functions used to form each image and also a term dependent on the additive radar receiver noise.

4.4.1 Single Channel Homogeneous Distributed Target Model

In Chapter 2 a deterministic description of a scene in terms of point scatterers each with a prescribed amplitude and phase response was used to develop the SAR image processor. The SAR image was subsequently shown to be a two dimensional, bandpass filtered version of the scene. In this description the transduced backscatter in a given resolution cell is the coherent sum over all scene scatterers illuminated by the antenna footprint where each scatterer contribution in the coherent sum is weighted by the point spread function of the SAR imaging system.

For natural distributed scenes such as forests, agricultural fields, soil and rock surfaces this deterministic description in terms of point scattering amplitudes and phases becomes inappropriate. Such scenes may be decomposed into an arbitrarily large number of scattering centres with many scatterers contributing to the transduced reflectivity in a given resolution cell. As the scattering centres may not be resolved they are not directly observable and a unique description for each scatterer is unattainable. Furthermore an arbitrary number of scattering centre realisations will yield the same backscatter transduced in a given resolution cell. The observed scattering behaviour in a resolution cell thus may only be described in a statistical sense in terms of its average characteristics which may be estimated from the transduced image.

Using the surface scattering model defined in (4.5) and modelling the surface reflectivity function $r_{f_s}(x,y)$ as N random independent identically distributed scatterers then,

$$r_{f_s}(x,y) = \sum_{k=1}^{N} \frac{q_k}{\sqrt{N}} exp(j\zeta_k)\delta(x-x_k, y-y_k), \tag{4.35}$$

where $q_k exp(j\zeta_k)/\sqrt{N}$ and (x_k, y_k) are the complex reflectivity and location respectively of the k^{th} scatterer. The backscattering power of the individual scatterers has been scaled by $1/\sqrt{N}$ so that the total scene backscatter power $\sigma^2_{q_T}$ of the scattering ensemble, which is given by,

$$\begin{aligned} E\{r_{f_s} r^*_{f_s}\} &= \frac{1}{N} E\left\{ \sum_{k=1}^{N} q_k exp(j\zeta_k)\delta(x-x_k, y-y_k) \sum_{l=1}^{N} q_l exp(-j\zeta_l)\delta(x-x_l, y-y_l) \right\}, \\ &= \frac{1}{N} \sum_{k=1}^{N} E\left\{q_k^2\right\}, \\ &= E\left\{q^2\right\}, \\ &= \sigma^2_{q_T}, \end{aligned} \tag{4.36}$$

is independent of the number of scatterers. Assuming the SAR acquisition process is linear the transduced complex reflectivity f at location (x,y) in the PFA image is given by (4.17) in Section 4.3.1. Substituting the scatterer model in (4.35) into (4.17) gives the following for the recovered PFA image,

$$f(x,y) = \iint r_{f_s}(\bar{x},\bar{y}) exp(-jk_{0_g}(\bar{y} + h(\bar{x},\bar{y})\beta_1)) a(x-\bar{x}, y-\bar{y}-h(\bar{x},\bar{y})\beta_1) d\bar{x} d\bar{y},$$

$$= \sum_{k=1}^{N} \frac{q_k}{\sqrt{N}} exp(j\zeta_k) exp(-jk_{0_g}(y_k + h(x_k, y_k)\beta_1)) a(x - x_k, y - y_k - h(x_k, y_k)\beta_1), \tag{4.37}$$

where $a(x, y)$ is the point spread function defined in (4.19).

Assuming that the scatterers are randomly distributed throughout the scene and given that a resolution cell is typically many wavelengths across the phase contributions of the scatterers may be considered to be uniformly distributed. Assuming also, that the scattering amplitude and phase are statistically independent then, for large N, it may be shown [Goo00a], [BS87] that the real and imaginary components of the transduced scene reflectivity $f_r = \Re\{f\}$ and $f_i = \Im\{f\}$, are asymptotically, jointly circular zero mean Gaussian random variables with probability density function given by,

$$p(f) = \frac{1}{\pi\sigma_f^2} exp\left(-\left(\frac{f_r^2 + f_i^2}{\sigma_f^2}\right)\right), \tag{4.38}$$

where the σ_f^2 is given by,

$$\begin{aligned} \sigma_f^2 &= E\{f(x, y)f^*(x, y)\}, \\ &= \frac{1}{N}\sum_{k=1}^{N} E\left\{q_k^2 |a(x - x_k, y - y_k - h(x_k, y_k)\beta_1)|^2\right\}, \end{aligned} \tag{4.39}$$

and the expectation is evaluated over the random variables q_k (scatterer amplitude) and (x_k, y_k) (scatterer position). Since q_k and (x_k, y_k) are independent random variables and the scatterers are uniformly distributed over the scene of area A then,

$$\begin{aligned} \sigma_f^2 &= \frac{1}{N}\sum_{k=1}^{N} E\left\{q_k^2\right\} E\left\{|a(x - x_k, y - y_k - h(x_k, y_k)\beta_1)|^2\right\}, \\ &= \frac{1}{A} E\left\{q^2\right\} \iint |a(x - x_k, y - y_k - h(x_k, y_k)\beta_1)|^2 dx_k dy_k. \end{aligned} \tag{4.40}$$

Assuming $h(x, y)$ is slowly varying and since $a(x, y)$ is the image point spread function (nominally a two dimensional sinc function) with most of its "mass" concentrated in neighbourhood where its argument is zero, $h(x, y)$ may be considered to be locally constant over the mainlobe width of $a(x, y)$ and thus,

$$\begin{aligned} \sigma_f^2 &= \frac{1}{A}\sigma_{q_T}^2 \iint |a(x, y)|^2 dxdy, \\ &= \sigma_q^2 \iint |a(x, y)|^2 dxdy. \end{aligned} \tag{4.41}$$

The term $\sigma_q^2 = \frac{\sigma_{q_T}^2}{A}$ is the backscatter power per unit area while the integral in (4.41) describes the area footprint of a resolution cell. The distributed scene is thus completely described by a single parameter, namely σ_f^2, which is the mean power in a resolution cell of the transduced image. With this result in mind the transduced scene backscatter may be re-written as,

$$f = \sigma_f(n_r + jn_i), \tag{4.42}$$

where n_r and n_i are jointly circular, zero mean Gaussian random variables with variances of $\frac{1}{2}$. In this form the transduced reflectivity may be interpreted as a mean backscatter value σ_f that is modulated

by a random noise like term $(n_r + jn_i)$ that manifests in the transduced imagery as speckle noise. The noise term does not contribute any useful information to the analysis and interpretation of the imagery, other than indicating that the resolution cells are made up of many individual scattering centres.

Under the given assumptions the number of contributing scatterers in a given resolution cell need not be particularly large, with a value of $N \approx 12$ giving strongly Gaussian behaviour [BS87]. Furthermore the assumptions may be relaxed, with the exception of independent amplitude and phases for each scatterer, and asymptotic Gaussian behaviour is still retained [BS87].

4.4.2 Dual Channel Homogeneous Distributed Target Model

In repeat pass interferometric SAR imaging of a natural distributed scene two images of the scene are acquired at different times using possibly different imaging geometries. In general, in the interval between collections, the scene will be subject to some form of temporal disturbance possibly due to environmental effects such as wind or rain or possibly due to man-made disturbances or even geophysical processes such as earthquakes or volcanic activity. The effects of these temporal processes on the scene reflectivity may be modelled by decomposing the scattering contributions in a resolution cell into a stable scattering contribution that is unchanged over the collection interval and an unstable component that is modified in the time interval between collections [HUA95]. The surface reflectivity function for the scene at the two collection times may thus be described by some ensemble of M point scatterers with reflectivity given by,

$$r(x,y) = \sum_{m=1}^{M} \frac{q_m}{\sqrt{M}} exp(j\zeta_m)\delta(x - x_m, y - y_m), \tag{4.43}$$

that is common between collections and an ensemble of L scatterers that contributes a reflectivity component given by,

$$r_1(x,y) = \sum_{l=1}^{L} \frac{p_l}{\sqrt{L}} exp(j\phi_l)\delta(x - x_{1_l}, y - y_{1_l}), \tag{4.44}$$

to the scene reflectivity in the primary acquisition that is subsequently transformed, via the temporal change processes, to an ensemble of K scatterers contributing a reflectivity,

$$r_2(x,y) = \sum_{k=1}^{K} \frac{s_k}{\sqrt{K}} exp(j\theta_k)\delta(x - x_{2_k}, y - y_{2_k}), \tag{4.45}$$

to the repeat pass image. The scene surface reflectivity in the primary and repeat pass collections are thus given by,

$$r_{f_s}(x,y) = r(x,y) + r_1(x,y), \tag{4.46}$$

$$r_{g_s}(x,y) = r(x,y) + r_2(x,y), \tag{4.47}$$

respectively and the primary and repeat pass images transduced by the SAR imaging process may be written as,

$$f(x,y) = \iint r_{f_s}(\bar{x},\bar{y}) exp(-jk_{0_g}(\bar{y} + h(\bar{x},\bar{y})\beta_1)) a_1(x - \bar{x}, y - \bar{y} - h(\bar{x},\bar{y})\beta_1) d\bar{x}d\bar{y}, \tag{4.48}$$

$$g(x,y) = \iint r_{g_s}(\bar{x},\bar{y}) exp(-jk_{0_g}(\bar{y} + h(\bar{x},\bar{y})\beta_2)) a_2(x - \bar{x}, y - \bar{y} - h(\bar{x},\bar{y})\beta_2) d\bar{x}d\bar{y}, \tag{4.49}$$

where $a_1(x,y)$ and $a_2(x,y)$ are the point spread functions defined in (4.33) and (4.34) respectively.

In [ZV92] Zebker develops a model for the temporal processes that relates the unstable scattering contributions r_1 and r_2. In this model the point scatterers contributing to the reflectivities r_1 and r_2 are identical, i.e., $K = L$, $p_l = s_k$ and $\phi_l = \theta_k$, however the scatterers in r_2 are subject to a random displacement in range and azimuth compared to their locations in r_1. Zebker shows that an RMS displacement of the scatterer ensemble of only a fraction of a wavelength can result in complete decorrelation between r_1 and r_2. In the subsequent analysis it will therefore be assumed that the scattering ensemble contributing to $r(x,y)$, $r_1(x,y)$ and $r_2(x,y)$ are all mutually independent identically distributed random variables.

As discussed in the single channel distributed target model considered in Section 4.4.1 the statistical behaviour of the images f and g taken individually is asymptotically Gaussian, however their joint distribution is required for a complete description of the interferometric pair. In general the joint distribution of two marginal Gaussian random variables is not necessarily Gaussian, [Pap91]. However, assuming that both the primary and repeat pass collections observe the same number of scatterers, N, such that $K = L = N - M$ then the joint distribution of the complex interferometric image pair $X = [f,g]^T$ may be shown to be a jointly circular, zero mean, Gaussian random vector, (see Appendix C), with density function given by,

$$p(\underline{X}) = \frac{1}{\pi^2|Q|} exp\left(-\underline{X}^H Q^{-1} \underline{X}\right), \tag{4.50}$$

where Q is the covariance matrix of the transduced pixel pair given by,

$$Q = E\{\underline{X}\underline{X}^H\} = \begin{bmatrix} \sigma_f^2 & \sigma_f\sigma_g\gamma exp(j\Phi) \\ \sigma_f\sigma_g\gamma exp(-j\Phi) & \sigma_g^2 \end{bmatrix}. \tag{4.51}$$

The terms down the leading diagonal of Q, namely σ_f^2 and σ_g^2, are the mean backscatter power transduced by the SAR in a pixel for the primary and repeat pass image respectively and have the form,

$$\begin{aligned} \sigma_f^2 &= E\{ff^*\}, \\ &= \frac{1}{A}\left(E\{q^2\} + E\{p^2\}\right) \iint |a_1(x,y)|^2 dxdy, \\ &= (\sigma_q^2 + \sigma_p^2) \iint |a_1(x,y)|^2 dxdy, \end{aligned} \tag{4.52}$$

and

$$\begin{aligned} \sigma_g^2 &= E\{gg^*\}, \\ &= \frac{1}{A}\left(E\{q^2\} + E\{s^2\}\right) \iint |a_2(x,y)|^2 dxdy, \\ &= (\sigma_q^2 + \sigma_s^2) \iint |a_2(x,y)|^2 dxdy, \end{aligned} \tag{4.53}$$

where σ_p^2 and σ_s^2 are the mean backscatter power per unit area from the unstable scatterers in the primary and repeat pass collection respectively and σ_q^2 is the mean backscatter power per unit area from the common stable scatterers in the scene. Using Parserval's theorem the integrals over the point spread functions may be expressed in terms of the corresponding Fourier transforms $A_1(k_x,k_y) = FT\{a_1(x,y)\}$ and $A_2(k_x,k_y) = FT\{a_2(x,y)\}$ as,

$$\sigma_f^2 = (\sigma_q^2 + \sigma_p^2)\frac{1}{4\pi^2} \iint |A_1(k_x,k_y)|^2 dk_x dk_y, \tag{4.54}$$

$$\sigma_g^2 = (\sigma_q^2 + \sigma_s^2)\frac{1}{4\pi^2} \iint |A_2(k_x,k_y)|^2 dk_x dk_y, \tag{4.55}$$

where from equations (4.33) and (4.34),

$$|A_1(k_x,k_y)| = rect\left(\frac{k_x}{k_{bw_{x1}}}\right) rect\left(\frac{k_y-\Delta_1}{k_{bw_{y1}}}\right), \quad (4.56)$$

$$|A_2(k_x,k_y)| = rect\left(\frac{k_x}{k_{bw_{x2}}}\right) rect\left(\frac{k_y+\Delta_2}{k_{bw_{y2}}}\right). \quad (4.57)$$

The additional information made available by considering the interferometric image pair is encapsulated in the complex cross channel correlated coefficient, $\gamma exp(j\Phi)$, given by,

$$\gamma exp(j\Phi) = \frac{E\{fg^*\}}{\sqrt{E\{|f|^2\}E\{|g|^2\}}}, \quad (4.58)$$

where γ takes values in the range 0 to 1. An expression for the cross correlation $E\{fg^*\}$ may found by substituting the expressions for f and g given in (4.48) and (4.49) respectively, i.e.,

$$\begin{aligned} E\{f(x,y)g^*(x,y)\} = & \\ & \iiint E\left\{r_{f_s}(\alpha,\beta)r^*_{g_s}(\alpha',\beta')\right\} exp(-jk_{0_g}(\alpha-\alpha'+h_{\alpha\beta}\beta_1-h_{\alpha'\beta'}\beta_2)) \\ & a_1(x-\alpha,y-\beta-h_{\alpha\beta}\beta_1)a_2^*(x-\alpha',y-\beta'-h_{\alpha'\beta'}\beta_2)d\alpha d\beta d\alpha' d\beta' \end{aligned} \quad (4.59)$$

where $h_{xy} = h(x,y)$. An expression for the cross correlation between the scene reflectivity functions r_{f_s} and r_{g_s} in (4.59) may be found by using the point scatterer models encapsulated in equations (4.46) and (4.47). Thus,

$$E\left\{r_{f_s}(x,y)r^*_{g_s}(x',y')\right\} = E\left\{(r(x,y)+r_1(x,y))(r^*(x',y')+r_2^*(x',y'))\right\}, \quad (4.60)$$

and since the scatterers contributing to r, r_1 and r_2 are all mutually independent, substituting (4.43), (4.44) and (4.45) into (4.60) reduces it to,

$$\begin{aligned} E\left\{r_{f_s}(x,y)r_{g_s}(x',y')\right\} &= E\left\{r(x,y)r^*(x',y')\right\}, \\ &= \frac{1}{M}E\left\{\sum_{m=1}^{M} q_m exp(j\zeta_m)\delta(x-x_m,y-y_m)\right. \\ &\qquad \left.\sum_{l=1}^{M} q_l exp(-j\zeta_l)\delta(x'-x_l,y'-y_l)\right\}. \end{aligned} \quad (4.61)$$

As the scatterers q_m and q_l are identical, independently randomly distributed, (4.61) becomes,

$$E\left\{r_{f_s}(x,y)r_{g_s}(x',y')\right\} = \sigma_q^2\delta(x-x',y-y'), \quad (4.62)$$

which may be substituted into (4.59) to give the following simplified form for the cross correlation between the transduced images,

$$\begin{aligned} E\{f(x,y)g^*(x,y)\} = \sigma_q^2 \iint & exp(-jk_{0_g}h_{\alpha\beta}\Delta\beta)a_1(x-\alpha,y-\beta-h_{\alpha\beta}\beta_1) \\ & a_2^*(x-\alpha,y-\beta-h_{\alpha\beta}\beta_2)d\alpha d\beta, \end{aligned} \quad (4.63)$$

where $\Delta\beta = \beta_1 - \beta_2$. The functions a_1 and a_2 are the primary and secondary image point spread functions (nominally two dimensional sinc functions) with most of their "mass" concentrated in the

neighbourhood where their arguments are zero. Also, in practice the baseline offsets between the primary and secondary acquisitions are small so that $\Delta\beta$ is also small. Therefore, under the assumption that the terrain height function is slowly varying, the term $h_{\alpha\beta}$ in the arguments of a_1 and a_2 may be considered constant and equal to the scene terrain height at the centre of the mainlobe of a_1. This value of the terrain height shall be labelled h'_{xy} where the subscripts (x, y) are the image domain spatial locations as opposed to the scene reflectivity function spatial locations. Furthermore the phase function $exp(-jk_{0_g}h_{\alpha\beta}\Delta\beta)$ may be taken out of the integral with $h_{\alpha\beta}$ replaced by h'_{xy}. The cross correlation may thus be written as,

$$E\{f(x,y)g^*(x,y)\} = \sigma_q^2 exp(-jk_{0_g}h'_{xy}\Delta\beta)\iint a_1(x-\alpha, y-\beta-h'_{xy}\beta_1) a_2^*(x-\alpha, y-\beta-h'_{xy}\beta_2)d\alpha d\beta. \quad (4.64)$$

Substituting the frequency domain descriptions for a_1 and a_2 given in (4.33) and (4.34) respectively into (4.64) gives the following frequency domain expression for the cross correlation,

$$\begin{aligned} E\{f(x,y)g^*(x,y)\} &= \sigma_q^2 exp(-jk_{0_g}h'_{xy}\Delta\beta)\iint A_{ifp_1}(k_x,k_y)exp(j\phi_{res_1})exp(-jk_y\beta_1 h'_{xy}) \\ &\quad A_{ifp_2}(k_x,k_y)exp(-j\phi_{res_2})exp(jk_y\beta_2 h'_{xy})dk_x dk_y, \\ &= \sigma_q^2 exp(-jk_{0_g}h'_{xy}\Delta\beta)\iint A_{ifp_1}(k_x,k_y)A_{ifp_2}(k_x,k_y) \\ &\quad exp(j\Delta\phi_{res})exp(-jk_y\Delta\beta h'_{xy})dk_x dk_y, \end{aligned} \quad (4.65)$$

where $\Delta\phi_{res} = \phi_{res_1} - \phi_{res_2}$ and $\Delta\beta = \beta_1 - \beta_2$. The above approximation to the interferometric image pair cross correlation is valid provided the terrain height is sufficiently slowly varying relative to the mainlobe width of the image point spread functions. A more accurate approximation for the cross correlation may be obtained by expanding the terrain height function at a localised region of the scene as a Taylor series. In [Mar95] Marechal considers the first two terms of a localised Taylor series expansion for the terrain height and shows that in this case the image pair cross correlation varies as a function of the local terrain gradient.

The cross correlation coefficient $\gamma exp(j\Phi)$ may now be written in terms of the mean backscatter power per unit area for the stable and unstable scattering contributions and the point spread functions for the primary and repeat pass imaging processes by substituting (4.65), (4.54) and (4.55) into (4.58) yielding,

$$\gamma exp(j\Phi) = \frac{\sigma_q^2}{\sqrt{(\sigma_q^2+\sigma_s^2)(\sigma_q^2+\sigma_p^2)}} \cdot \frac{exp(-jk_{0_g}h'_{xy}\Delta\beta)\iint A_{ifp_2}(k_x,k_y)A_{ifp_1}(k_x,k_y)exp(-jk_y\Delta\beta h'_{xy})exp(j\Delta\phi_{res})dk_x dk_y}{\sqrt{\iint |A_{ifp_1}(k_x,k_y)|^2 dk_x dk_y \iint |A_{ifp_2}(k_x,k_y)|^2 dk_x dk_y}}. \quad (4.66)$$

The cross channel correlation coefficient may thus be considered to consist of two components: A temporal correlation component determined by the ratio of stable scattering contributions to the total backscatter power,

$$\gamma_{temp} = \frac{\sigma_q^2}{\sqrt{(\sigma_q^2+\sigma_s^2)(\sigma_q^2+\sigma_p^2)}}, \quad (4.67)$$

and another describing the decorrelation due to the fact that the two transduced images have passed through different acquisition and image formation filters,

$$\gamma_{proc} = \frac{exp(-jk_{0_g}h'_{xy}\Delta\beta)\iint A_{ifp_2}(k_x,k_y)A_{ifp_1}(k_x,k_y)exp(-jk_y\Delta\beta h'_{xy})exp(j\Delta\phi_{res})dk_xdk_y}{\sqrt{\iint |A_{ifp_1}(k_x,k_y)|^2dk_xdk_y \iint |A_{ifp_2}(k_x,k_y)|^2dk_xdk_y}}. \tag{4.68}$$

Scattering Correlation - Change Detection

For the case when there is no baseline offset between the primary and secondary acquisitions the SAR point spread functions are identical with $A_{ifp_1} = A_{ifp_2}$, $\Delta\beta = 0$ and $\Delta\phi_{res} = 0$. Therefore, $\gamma_{proc} = 1$ and the cross correlation coefficient of the transduced image pair depends only on the underlying correlation between the scattering centres in the scene,

$$\begin{aligned} \gamma exp(j\Phi) &= \frac{\sigma_q^2}{\sqrt{(\sigma_q^2+\sigma_s^2)(\sigma_q^2+\sigma_p^2)}}, \\ &= \gamma_{temp}. \end{aligned} \tag{4.69}$$

The temporal correlation coefficient is a value between 0 and 1 with total decorrelation arising when $\sigma_q^2 = 0$ i.e., there are no stable scattering contributions in the interferometric pair, and complete correlation occurring when $\sigma_s^2 = \sigma_p^2 = 0$ i.e., there are no unstable scattering contributions in the image pair.

In deriving this expression for the temporal scene decorrelation it is assumed that the temporal processes affecting the unstable scene scatterers, given by r_1 in (4.44) and r_2 in (4.45), are sufficient to cause complete decorrelation of the unstable scattering contributions in the transduced interferometric image pair, i.e., $E\{r_1(x,y)r_2^*(x,y)\} = 0$. In this case the cross correlation of the scene reflectivity has been shown to be simply dependent on the mean backscatter power of the stable scattering contributions, see equation (4.62). The validity of this assumption may be assessed using Zebker's random displacement model [ZV92]. In this model the temporal change processes are assumed to give rise to a random displacement of the location of the unstable scattering contributions in the interval being imaging collections. Zebker subsequently found that an RMS displacement of around 20 percent of the radar wavelength caused total decorrelation between the unstable scattering contributions. Thus temporal disturbances causing displacements of only a fraction of a wavelength are required to cause complete decorrelation of the unstable scatterers.

For high frequency systems such as X-band radars, with wavelengths around 3 cm, man-made scene disturbances, such as the passage of vehicles over an open field, can potentially cause significant scatterer displacements over localised regions in the scene. The vehicle tracks will thus manifest as areas of low coherence and γ may be used as an extremely sensitive change statistic. The sensitivity of γ however is dependent on the relative mean backscatter power contributions of the stable and unstable scene scatterers within the affected resolution cells and also the loss in correlation that may arise due to other temporal processes, particularly wind. In practice a further source of decorrelation in the transduced image pair is mismatch between the acquisition and image formation processor used to generate the primary and repeat pass images, which yields a value of γ_{proc} less than 1. In order to achieve $\gamma_{proc} = 1$ requires flying the same flight track to reproduce the same synthetic aperture in each pass and using identical image formation processors. This is generally impractical, particularly in airborne systems where the effects of wind and turbulence can cause deviations in the actual flight track from the planned flight track.

Processing Correlation - Terrain Mapping

For the case when the primary and repeat pass scenes are unchanged, $\gamma_{temp} = 1$ and the cross correlation coefficient is determined by the mismatch in the SAR imaging transfer functions,

$$\begin{aligned}\gamma exp(j\Phi) &= \\ &\frac{exp(-jk_{0_g}h'_{xy}\Delta\beta)\iint A_{ifp_2}(k_x,k_y)A_{ifp_1}(k_x,k_y)exp(-jk_y\Delta\beta h'_{xy})exp(j\Delta\phi_{res})dk_xdk_y}{\sqrt{\iint |A_{ifp_1}(k_x,k_y)|^2dk_xdk_y \iint |A_{ifp_2}(k_x,k_y)|^2dk_xdk_y}}, \\ &= \gamma_{proc}.\end{aligned} \tag{4.70}$$

In general the processing correlation γ_{proc} is a complex quantity that varies spatially across the scene and is determined by any mismatch between the acquisition of the synthetic apertures from the primary and repeat pass flight tracks as well as any mismatch in the image formation processors. When the acquisition and image formation processors are identical $A_{ifp_1} = A_{ifp_2}$, $\Delta\beta = 0$, $\Delta\phi_{res} = 0$ and the transduced scene images are identical so $\gamma_{proc} = 1$. The processing correlation however, goes to zero when the repeat pass pair are acquired such that processing apertures of support A_{ifp_1} and A_{ifp_2} in (4.28) and (4.29) have no common intersect in the (k_x, k_y) plane i.e., $A_c = A_{ifp_1}A_{ifp_2} = 0$. This condition is called the critical baseline and will be discussed in further detail in Section 4.6.1.

Substituting the unweighted apertures for A_{ifp_1} and A_{ifp_2} defined in (4.28) and (4.29) and replacing the product $A_{ifp_1}A_{ifp_2}$ with the common intersect defined in (4.30), γ_{proc} reduces to,

$$\begin{aligned}\gamma_{proc} &= \frac{exp(-jk_{0_g}h'_{xy}\Delta\beta)\iint rect\left(\frac{k_x}{k_{bw_{x_c}}}\right)rect\left(\frac{k_y}{k_{bw_{y_c}}}\right)exp(-j(h'_{xy}\Delta\beta k_y - \Delta\phi_{res}))dk_ydk_y}{\sqrt{\iint rect\left(\frac{k_x}{k_{bw_{x_1}}}\right)rect\left(\frac{k_y}{k_{bw_{y_1}}}\right)dk_xdk_y \iint rect\left(\frac{k_x}{k_{bw_{x_2}}}\right)rect\left(\frac{k_y}{k_{bw_{y_2}}}\right)dk_xdk_y}}, \\ &= \frac{exp(-jk_{0_g}h'_{xy}\Delta\beta)\iint rect\left(\frac{k_x}{k_{bw_{x_c}}}\right)rect\left(\frac{k_y}{k_{bw_{y_c}}}\right)exp(-j(h'_{xy}\Delta\beta k_y - \Delta\phi_{res}))dk_ydk_y}{\sqrt{k_{bw_{x_1}}k_{bw_{y_1}}k_{bw_{x_2}}k_{bw_{y_2}}}}.\end{aligned} \tag{4.71}$$

Assuming the residual phase $\Delta\phi_{res}$ is small (the conditions under which this is not a valid assumption and the resulting form for γ_{proc} will be discussed in Section 4.6.2) then the integral in (4.71) may be computed and is given by,

$$\gamma_{proc} = \frac{k_{bw_{x_c}}k_{bw_{y_c}}}{\sqrt{\left(k_{bw_{x_1}}k_{bw_{y_1}}k_{bw_{x_2}}k_{bw_{y_2}}\right)}} \cdot sinc\left(\frac{h'_{xy}\Delta\beta k_{bw_{y_c}}}{2\pi}\right) \cdot exp(-j\Delta\beta h'_{xy}k_{0_g}). \tag{4.72}$$

From (4.72) it can be seen that the cross correlation coefficient phase, $arg\{\gamma_{proc}\}$, is proportional to the terrain height function h'_{xy} with the constant of proportionality dependent on the centre frequency associated with the common k_y aperture of support and the baseline offset measured in terms of the difference in the depression angles of the primary and repeat pass collections. This forms the basis of the terrain topographic mapping application of across track SAR interferometry. This technique is potentially highly accurate as the height is measured in terms of a phase i.e., as a fraction of a wavelength. The high accuracy of the terrain height measurement coupled with the dense spatial sampling afforded by fine resolution SAR makes interferometric terrain mapping an extremely powerful technique.

A key problem however, in extracting a terrain height map from the interferometric phase is that the phase is measured modulo 2π and consequently a two dimensional phase unwrapping (over range

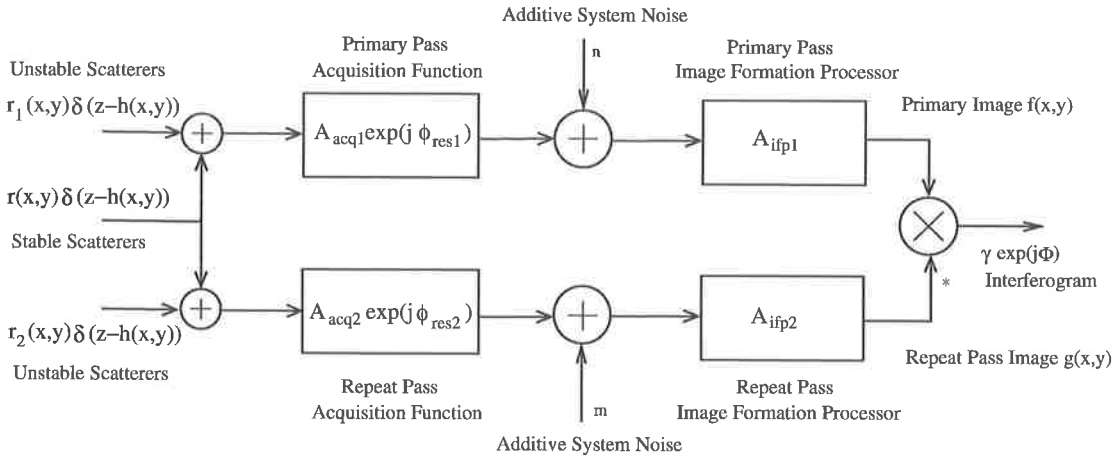


Figure 4.4: A repeat pass interferometric system model. The scene is modelled as an ensemble of stable and unstable scatterers, where the unstable contributions undergo a perturbation in the interval between collections. Noise sources m and n are additive receiver noise. The interferometric information is available in the cross correlation coefficient of the interferometric image pair.

and azimuth) step is required to retrieve an unambiguous phase estimate. The unwrapping, or integration, of the ambiguous phase $arg\{\gamma_{proc}\}$ is problematic due to noisy estimates obtained in areas of the scene with low coherence, as well as under sampling of the phase gradient in areas of rapid height variation. As a consequence different absolute phase values may be obtained depending on the particular integration path. A variety of approaches have been proposed to obtain correct and consistent unwrapped phase estimates such as the branch cut method [GZW88] and a least squares based approach [GR94]. Phase unwrapping remains an active area of research with recently proposed techniques including region growing [XC99], formulating the problem in a Bayesian inference framework [AW01] as well as the collection of multiple baselines [GW94] to assist in unwrapping.

4.4.3 Additive Receiver Noise

Equation (4.50) gives a complete first order statistical description of the repeat pass interferometric image pair in the absence of receiver system noise. Receiver noise may be modelled as an additive noise process that corrupts the received range echo data prior to application of the image formation processor. A complete interferometric system model incorporating additive receiver noise processes m and n to the primary and repeat pass imaging collections respectively is shown in Figure 4.4. The noise processes m and n are assumed to be mutually uncorrelated, stationary, white, circular Gaussian processes with variances σ_m^2 and σ_n^2 respectively. As the imaging process is a linear system the transduced image pair may be written as,

$$\underline{X}_T = \begin{bmatrix} f_m \\ g_n \end{bmatrix} = \begin{bmatrix} f + m' \\ g + n' \end{bmatrix}, \tag{4.73}$$

where m' and n' are the additive noise processes, m and n, filtered by the image formation processors A_{ifp_1} and A_{ifp_2} respectively. The filtered noise processes m' and n' remain mutually uncorrelated Gaussian processes [Pap91] however they are no longer white noise processes instead having power spectral densities given by,

$$\mathcal{S}_{n'n'} = \sigma_n^2 |A_{ifp_1}(k_x, k_y)|^2, \tag{4.74}$$

$$\mathcal{S}_{m'n'} = \sigma_m^2 |A_{ifp_2}(k_x, k_y)|^2, \tag{4.75}$$

and variances given by,

$$\sigma_{n'}^2 = \sigma_n^2 \frac{1}{4\pi^2} \iint |A_{ifp_1}(k_x, k_y)|^2 dk_x dk_y, \tag{4.76}$$

$$\sigma_{m'}^2 = \sigma_m^2 \frac{1}{4\pi^2} \iint |A_{ifp_2}(k_x, k_y)|^2 dk_x dk_y. \tag{4.77}$$

Since the transduced scene backscatter terms f and g are uncorrelated with the filtered additive noise processes m' and n' the noise corrupted image pair vector S must be jointly Gaussian with covariance matrix given by,

$$\begin{aligned} Q_T &= \begin{bmatrix} \sigma_{f_m}^2 & \sigma_{f_m}\sigma_{g_n}\gamma_T exp(j\Phi_T) \\ \sigma_{f_m}\sigma_{g_n}\gamma_T exp(-j\Phi_T) & \sigma_{g_n}^2 \end{bmatrix}, \\ &= \begin{bmatrix} \sigma_f^2 & \sigma_f\sigma_g\gamma exp(j\Phi) \\ \sigma_f\sigma_g\gamma exp(-j\Phi) & \sigma_g^2 \end{bmatrix} + \begin{bmatrix} \sigma_{m'}^2 & 0 \\ 0 & \sigma_{n'}^2 \end{bmatrix}. \end{aligned} \tag{4.78}$$

The cross channel correlation coefficient of the noise corrupted repeat pass interferometric pair is thus given by,

$$\gamma_T exp(j\Phi_T) = \frac{E\{(f+m')(g^*+n'^*)\}}{E\{|f+m'|^2\}E\{|g+n'|^2\}}, \tag{4.79}$$

$$= \gamma exp(j\Phi)\left(\frac{1}{\sqrt{1+SNR_1^{-1}}\sqrt{1+SNR_2^{-1}}}\right), \tag{4.80}$$

where $\gamma exp(j\Phi)$ is given by (4.66) and,

$$SNR_1 = \frac{\sigma_f^2}{\sigma_{m'}^2} = \frac{(\sigma_q^2+\sigma_p^2)\iint |A_{ac_1}(k_x,k_y)A_{ifp_1}(k_x,k_y)|^2 dk_x dk_y}{\sigma_m^2 \iint |A_{ifp_1}(k_x,k_y)|^2 dk_x dk_y}, \tag{4.81}$$

$$SNR_2 = \frac{\sigma_g^2}{\sigma_{n'}^2} = \frac{(\sigma_q^2+\sigma_s^2)\iint |A_{ac_2}(k_x,k_y)A_{ifp_2}(k_x,k_y)|^2 dk_x dk_y}{\sigma_n^2 \iint |A_{ifp_2}(k_x,k_y)|^2 dk_x dk_y}. \tag{4.82}$$

Defining,

$$\gamma_{snr} = \frac{1}{\sqrt{1+SNR_1^{-1}}\sqrt{1+SNR_2^{-1}}}, \tag{4.83}$$

and since $\gamma = \gamma_{temp}\gamma_{proc}$ the complete cross channel correlation coefficient γ_T may be written as the product of three correlation terms,

$$\gamma_T = \gamma_{temp}\gamma_{proc}\gamma_{snr}. \tag{4.84}$$

4.5 Estimating the Joint Channel Statistics

The information available in a repeat pass SAR interferometric image pair $X = [f_m, g_n]^T$ is completely defined by the backscatter coefficients of the primary and repeat pass images $\sigma_{g_n}^2$, $\sigma_{f_m}^2$ and the

complex cross correlation coefficient $\gamma_T exp(j\Phi_T)$. These variables are encapsulated in the covariance matrix of the jointly random process $\underline{X}_T$,

$$Q = E\{\underline{X}_T \underline{X}_T^H\} = \begin{bmatrix} \sigma_{f_m}^2 & \sigma_{g_n}\sigma_{f_m}\gamma_T exp(j\phi_T) \\ \sigma_{g_n}\sigma_{f_m}\gamma_T exp(-j\psi_T) & o_{g_n}^2 \end{bmatrix}. \tag{4.85}$$

It remains to determine suitable estimators of these parameters from the transduced image pair.

Given N independent realisations, $\underline{X}_{T_k} = [f_{m_k}, g_{n_k}]^T$ for $k = 1 \ldots N$, of the jointly random process X the maximum likelihood estimate of the covariance matrix is given by the sample covariance [Goo63],

$$\hat{Q} = \frac{1}{N}\sum_{k=1}^{N} \underline{X}_{T_k}\underline{X}_{T_k}^H = \frac{1}{N}\begin{bmatrix} \sum_{k=1}^N |f_{m_k}|^2 & \sum_{k=1}^N f_{m_k} g_{n_k}^* \\ \sum_{k=1}^N f_{m_k}^* g_{n_k} & \sum_{k=1}^N |g_{n_k}|^2 \end{bmatrix}. \tag{4.86}$$

Sample estimates of the primary and repeat pass backscatter coefficients are thus given by,

$$\hat{\sigma}_{f_m}^2 = \sum_{k=1}^{N} |f_{m_k}|^2, \tag{4.87}$$

and,

$$\hat{\sigma}_{g_n}^2 = \sum_{k=1}^{N} |g_{n_k}|^2, \tag{4.88}$$

while the sample cross correlation coefficient is given by,

$$\hat{\gamma}_T exp(j\hat{\Phi}_T) = \frac{\sum_{k=1}^N f_{m_k} g_{n_k}^*}{\sqrt{\sum_{k=1}^N |f_{m_k}|^2 \sum_{k=1}^N |g_{n_k}|^2}}. \tag{4.89}$$

Provided $\underline{X}_T = [f_m, g_n]^T$ is a jointly stationary vector and ergodic in mean the N independent realisations required to form the sample estimates may be obtained by simply taking N pixel pairs from the interferometric pair. In practice however, the random variables f_m and g_n are not stationary and the covariance Q varies across the scene depending on the scattering properties of the scene and any mismatch between the acquisition and processing functions. Provided the underlying statistics may be considered constant over a sufficiently small spatial neighbourhood of pixels then the image pair may be considered stationary in increments [TLBV99]. Local sample estimates of the backscatter and complex cross correlation may thus be obtained using a sliding estimation window. A map of the spatial variation of the sample complex cross correlation coefficient across the scene is called the complex interferogram with $\hat{\gamma}_T$ called the interferometric magnitude or coherence and $\hat{\Phi}_T$ is the interferometric phase.

The density function of the sample covariance matrix $\hat{Q}$ was derived by Goodman [Goo63] and has the form of a complex Wishart distribution given by,

$$p(\hat{Q}) = \frac{N^{2N}|\hat{Q}|^{N-2}}{\pi\Gamma(N)\Gamma(N-1)|Q|^N} exp\left(-tr(Q^{-1}\hat{Q})N\right). \tag{4.90}$$

where $tr(Q^{-1}\hat{Q})$ is the trace of matrix $Q^{-1}\hat{Q}$. The marginal density functions of $\hat{\sigma}_{f_m}^2$ and $\hat{\sigma}_{g_n}^2$ have the well known Gamma distribution with order parameter N,

$$p(\hat{\sigma}_{f_m}^2) = \frac{1}{\Gamma(N)}\left(\frac{N}{\sigma_{f_m}^2}\right)^N \left(\hat{\sigma}_{f_m}^2\right)^{N-1} exp\left(\frac{-N\hat{\sigma}_{f_m}^2}{\sigma_{f_m}^2}\right), \tag{4.91}$$

and similarly for $p(\hat{\sigma}^2_{g_n})$. An expression for the M^{th} order moments of these sample estimates have been derived in the literature [OQ98] and the mean and variance are given by,

$$E\left\{\hat{\sigma}^2_{f_m}\right\} = \sigma^2_{f_m}, \tag{4.92}$$

$$Var\left\{\hat{\sigma}^2_{f_m}\right\} = \frac{\left(\sigma^2_{f_m}\right)^2}{N}. \tag{4.93}$$

Thus the sample estimate of the mean backscatter values is asymptotically unbiased and the variance of the estimate is proportional to the square of the mean backscatter and inversely proportional to the number of samples in the sample average. The equivalent number of looks, defined by,

$$ENL = \frac{\left(E\left\{\hat{\sigma}^2_{f_m}\right\}\right)^2}{Var\left\{\hat{\sigma}^2_{f_m}\right\}}, \tag{4.94}$$

for the sample estimates of the mean backscatter is thus the number of samples in the sample average.

The statistics of the interferogram and the associated marginal density functions have been extensively studied in the context of interferometry as well as radar polarimetry [TL96], [TLBV99], [TBQ95], [QR95], [JWP94] and [LMH94]. The density function of the sample coherence is given by,

$$p(\hat{\gamma}_T) = 2(N-1)(1-\gamma_T^2)^N\hat{\gamma_T}(1-\hat{\gamma_T}^2)^{(N-2)}{}_2F_1(N,N;1;\gamma_T^2\hat{\gamma_T}^2), \tag{4.95}$$

while the density function of the sample interferometric phase is given by,

$$p(\hat{\Phi}_T) = \frac{\Gamma\left(N+\frac{1}{2}\right)(1-\gamma_T^2)^N\gamma_T\cos\left(\hat{\Phi}_T-\Phi_T\right)}{2\sqrt{\pi}\Gamma(N)\left(1-\left(\gamma_T\cos\left(\hat{\Phi}_T-\Phi_T\right)\right)^2\right)^{N+\frac{1}{2}}} + \frac{(1-\gamma_T^2)^N}{2\pi}{}_2F_1\left(N,1;\frac{1}{2};\left(\gamma_T\cos\left(\hat{\Phi}_T-\Phi_T\right)\right)^2\right), \tag{4.96}$$

where ${}_2F_1$ is the Gauss hypergeometric function [AS72]. It has been shown that while both $\hat{\gamma}_T$ and $\hat{\Phi}_T$ are asymptotically unbiased estimators, the sample coherence, $\hat{\gamma}_T$, is found to suffer from significant bias under low coherence conditions unless substantial averaging is carried out. The high bias in the estimator reduces the contrast between regions of differing low coherence limiting its performance as a classification and change statistic. The interferometric phase estimate on the other hand is unbiased, however its variance is dependent on the number of independent averages as well as the underlying coherence γ_T. In particular under low coherence conditions averaging over large regions is required to achieve a high quality estimate of the interferometric phase.

4.5.1 Heterogeneous Distributed Target Model

The jointly Gaussian model for an interferometric image pair is generally accepted as an accurate description for natural, homogeneous distributed target types such as open fields [OQ98]. Deviations from this model however, have been observed in describing the strong backscatter characteristics of buildings in urban scenes [LLN90], [FMYS97] as well as in very fine resolution imagery where the number of contributing scatterers in each resolution cell is not large. The model also breaks down in describing the statistics of imagery where radar shadowing is prominent such as in woodland where

forest canopy shadows modulate the observed backscatter. Indeed at low grazing angles such textural modulation due to radar shadowing becomes pronounced across a wide range of target types.

To model such non-homogeneous clutter texture target types a modified form of the Gaussian speckle model called the product model [War81] has been proposed. In the product model the scene texture is modelled by a randomly fluctuating mean backscatter that varies on spatial scales larger than the image resolution. The complex scene reflectivity is thus given by,

$$f = \sigma_f(n_r + jn_i), \tag{4.97}$$

where $n = n_r + jn_i$ is a zero mean, unit variance complex Gaussian random process describing the speckle phenomenon and σ_f is a random process that models the mean backscatter modulation across the scene. One possible form for the random process describing the backscatter fluctuations, originally proposed by Ward [War81] to describe sea clutter, is a gamma distribution,

$$p(\sigma_f) = \left(\frac{\nu}{\sigma}\right)^{\nu} \frac{\sigma_f^{\nu-1}}{\Gamma(\nu)} exp\left(\frac{-\nu\sigma_f}{\sigma}\right), \tag{4.98}$$

where σ is the mean backscatter power and ν is an order parameter describing the extent of the backscatter power fluctuations. Combining this model with the speckle density function yields the K distribution to describe the observed pixel amplitude,

$$p(|f|) = \frac{4}{\Gamma(\nu)}\sqrt{\frac{\nu}{\sigma^2}}\left(\sqrt{\frac{\nu|f|^2}{\sigma^2}}\right)^{\nu} K_{\nu-1}\left(2\sqrt{\frac{\nu|f|^2}{\sigma^2}}\right), \tag{4.99}$$

where $K_{\nu-1}$ is the modified Bessel function of order $(\nu - 1)$, [AS72]. The order parameter ν may be defined by,

$$\frac{E\{|f|^4\}}{(E\{|f|^2\})^2} = 2\left(1 + \frac{1}{\nu}\right). \tag{4.100}$$

and for large values of ν the K distribution approaches a Gaussian distribution with the same mean backscatter power. Generally speaking for values of ν above 10 the distribution may be regarded as Gaussian and values around 1 or below indicate markedly non-Gaussian behaviour [QR95].

The K distribution has been extensively used to represent both sea clutter [JP76], [War81] as well as land clutter [Oli84], [Jao84] with considerable success. Further justification for the K distribution has been provided by the theoretical derivation of the K distribution by Jakeman and Pusey [JP76] using a modified form of the random walk model describing coherent scattering from a large number of point targets. In [JP76] Jakeman and Pusey allowed the number of contributing scatterers in a resolution cell to vary. Using a random process of birth, death and migration to describe the number of scatterers leads to a negative binomial distribution for N and subsequently to a K distribution to describe the pixel amplitude.

A multi-channel form of the K distribution has been developed by Yueh [YKJ+89] to describe polarimetric SAR imagery and the model may also be used to describe interferometric image pairs [OQ98]. In this model the transduced complex reflectivity for a joint interferometric channel pair, is given by,

$$\underline{S} = T\underline{X}, \tag{4.101}$$

where T is a positive scalar texture random variable with the property that $E\{T^2\} = 1$ and $\underline{X}$ is a multivariate Gaussian. Observe that since the second moment of the texture parameter T is unity $\underline{X}$ and $\underline{S}$ will have the same covariance structure. Also observe that this model specifies the same texture parameter for both the primary and repeat pass images. Therefore the cross channel correlation coefficient and the associated sample estimate are independent of T and depend only on the correlation coefficient of the Gaussian component $\underline{X}$.

4.6 Processing Correlation - Acquisition and Processing Errors

In the previous sections it has been shown that the cross correlation coefficient γ_T of an interferometric image pair may be decomposed into three components,

$$\gamma_T = \gamma_{snr}\gamma_{temp}\gamma_{proc}. \tag{4.102}$$

In the coherent change detection application of interferometry the temporal correlation γ_{temp} is the correlation term of interest as it provides information about scene disturbances. In the transduced image pair however γ_{temp} is modulated by the noise and processing correlations. These terms reduce the overall correlation of the transduced image pair and so limit the contrast between regions of differing stable and unstable scattering. As a consequence the performance of γ_T as a change and classification statistic is degraded by these terms. The noise correlation γ_{snr} is a real valued quantity that is determined by the radar hardware and thus is fixed for a given sensor and imaging geometry. The processing correlation γ_{proc} on the other hand is a complex quantity determined by the mismatch between the transfer functions of the primary and repeat pass processors. This mismatch is a source of decorrelation and phase bias in the interferogram estimate that shall vary spatially over the image. The mismatch must therefore be adequately compensated for if the full potential of interferometric processing is to be realised. In the following sections the form of γ_{proc} will be discussed.

4.6.1 First Order Effects

In Section 4.4.2 it was shown that, in the case of unweighted image formation apertures, the processing correlation coefficient takes the form,

$$\gamma_{proc} = \frac{exp(-jk_{0_g}h'_{xy}\Delta\beta)\iint rect\left(\frac{k_x}{k_{bw_{x_c}}}\right)rect\left(\frac{k_y}{k_{bw_{y_c}}}\right)exp(-j(h'_{xy}\Delta\beta k_y - \Delta\phi_{res}))dk_y dk_y}{\sqrt{k_{bw_{x_1}}k_{bw_{y_1}}k_{bw_{x_2}}k_{bw_{y_2}}}}. \tag{4.103}$$

The phase term $\Delta\phi_{res}$ is the difference between the phase mismatch of the acquisition and image formation transfer functions for the primary and secondary SAR image pair and is given by,

$$\Delta\phi_{res} = \phi_{res_1} - \phi_{res_2}. \tag{4.104}$$

Phase mismatch between the acquisition and image formation transfer functions for a given SAR image arises due to calibration errors in the measurement of the synthetic aperture as well as approximations in modelling the point scatterer response in the signal history data acquired over the synthetic aperture. Provided sufficiently accurate point scatterer response models are used and autofocus algorithms are employed to estimate and remove calibration errors then $\Delta\phi_{res} \approx 0$. In this case the processing correlation coefficient reduces to,

$$\gamma_{proc} = \frac{k_{bw_{x_c}}k_{bw_{y_c}}}{\sqrt{\left(k_{bw_{x_1}}k_{bw_{y_1}}k_{bw_{x_2}}k_{bw_{y_2}}\right)}} \cdot sinc\left(\frac{h'_{xy}\Delta\beta k_{bw_{y_c}}}{2\pi}\right) \cdot exp(-j\Delta\beta h'_{xy}k_{0_g}). \tag{4.105}$$

From (4.105) it can be seen that the processing correlation coefficient consists of a phase term arising due to the terrain topography as discussed in Section 4.4.2 and two decorrelation terms associated with the difference in the depression angles between the imaging collections.

Baseline Decorrelation

For the case in which $h(x,y) = 0$, the scene reflectivity is simply a two dimensional surface function defined on the $z = 0$ ground plane and the processing correlation coefficient reduces to,

$$\begin{aligned} \gamma_{proc} &= \frac{k_{bw_{x_c}} k_{bw_{y_c}}}{\sqrt{\left(k_{bw_{x_1}} k_{bw_{y_1}} k_{bw_{x_2}} k_{bw_{y_2}}\right)}}, \\ &= \gamma_{baseline}, \end{aligned} \tag{4.106}$$

which is commonly referred to as baseline decorrelation [GGP94] and [ZV92]. The extent of the baseline decorrelation is determined by the mismatch between image formation processor windows A_{ifp_1} and A_{ifp_2} used to form the the primary and repeat pass images. With reference to Figure 4.3 it can be seen that $\gamma_{baseline}$ is the ratio of the overlapping area defined by A_c to the geometric mean of the areas of defined by A_{ifp_1} and A_{ifp_2}. From Figures 4.2 and 4.3 it can also be seen that increasing the depression angle difference between the image acquisitions reduces the overlapping aperture size reducing $\gamma_{baseline}$ until the critical baseline is reached at which point the aperture of support for the image pair are no longer overlapping and the processing correlation falls to zero.

In the design of the image formation processor there is some flexibility in choosing the location and size of the image formation windows A_{ifp_1} and A_{ifp_2} in the (k_x, k_y) plane. Given measurements of the depression angles ψ_1 and ψ_2 the common overlapping aperture of support $A_c(k_x, k_y)$ may be pre-computed prior to defining the primary and repeat pass image formation processors. A simple approach to mitigating the baseline decorrelation then is to restrict the image formation processors to only process the common overlapping portion of the acquired data aperture defined by A_c, such that,

$$A_{ipf_1}(k_x, k_y) = A_{ifp_2}(k_x, k_y) = A_c(k_x, k_y), \tag{4.107}$$

in which case $\gamma_{baseline} = 1$. This method is commonly referred to as aperture trimming. While this approach reduces the processed range and azimuth spatial frequency bandwidth, leading to a reduction in the range and azimuth resolution of the interferogram, the improvement in the processing correlation improves the quality of the subsequent interferometric products.

Another approach to minimising baseline decorrelation proposed in [GGP94] is to consider a Tunable Interferometric SAR system in which the radar transmit frequency is shifted by an amount corresponding to the collection aperture mismatch. In this case the full system bandwidth may be processed giving full resolution interferogram at the expense of increase radar hardware complexity. The approach also facilitates the processing of interferometric pairs with larger baselines than is allowed in a fixed frequency radar collection.

Image Pair Misregistration

With appropriate aperture trimming the magnitude of the processing correlation coefficient (4.105) reduces to the following form,

$$|\gamma_{proc}| = sinc\left(\frac{h'_{xy} \Delta\beta k_{bw_{y_c}}}{2\pi}\right). \tag{4.108}$$

This form for γ_{proc} indicates that the scene terrain height coupled with a depression angle difference between the interferometric imaging geometries produces a loss in correlation. This may be explained in terms of the differential projection of an elevated scatter into the image plane when using flight tracks with different depression angles. For a target at location (x_s, y_s, h_s) imaged with a mid-aperture depression angle of ψ_1, the target is appears at location $(x_s, y_s + h_s \tan\psi_1)$ in the resulting

ground plane image. The differential layover for the same target imaged at a different mid-aperture depression angle ψ_2 is $\Delta y = h_s(\tan\psi_1 - \tan\psi_2) = h_s\Delta\beta$. The resulting decorrelation arising from this range misregistration Δy is governed by the point spread function of the acquisition and image formation processor. For the case of an unweighted aperture the decorrelation takes the form of a sinc function as indicated in (4.108). Observe that for a misregistration of one resolution cell $\rho_y = \frac{2\pi}{k_{bw_{y_c}}}$ the correlation falls to zero rendering the interferogram completely useless. An important aspect of the design and implementation of a practical interferometric processor is the estimation and compensation of image misregistration. For fine resolution SAR systems small, sub-resolution cell image misregistrations can have a significant deleterious effect on the performance of interferometric processing. In the change detection application of interferometry, the loss in correlation between a misregistered interferometric pair reduces the contrast between changed and changed regions in the scene. Similarly for terrain mapping the loss in correlation contributes to a noisier estimate of the interferometric phase. Aside from layover, other sources contributing to a image misregistration in range and azimuth include deviations from the ideal desired flight path as well as navigation measurement errors.

4.6.2 Higher Order Effects

In arriving at the expression for γ_{proc} given in (4.105) it was assumed that $\Delta\phi_{res} \approx 0$. From Chapter 2 this approximation arises if a plane wave model is used to describe the propagation of the transmitted and received the electromagnetic radiation to and from the scene. The plane wave propagation model is valid provided the standoff range of the SAR is sufficiently large compared to the imaged scene size and that the image resolution is not too fine (see Section 2.3.2 in Chapter 2). In the case of wide-band, wide-angle, near-field imaging the plane wave propagation assumption begins to break down and unmodelled wavefront curvature effects appear in the acquisition transfer function which will remain uncompensated by the PFA processor. In Chapter 2 it was shown that in the case of range echo data acquired via deramp demodulation with respect to a scene focus point the dominant wavefront curvature phase terms in the acquisition transfer function are given by,

$$\phi_{res} \approx \frac{(x^2 + y^2\sin^2(\psi_0))}{2R_{bs_g}}(k_y + k_{0_g}) - \frac{xy\cos^2(\psi_0)}{R_{bs_g}}k_x - \frac{(x^2 - y^2\cos^2(\psi_0))\cos^2(\psi_0)}{2R_{bs_g}k_{0_g}}k_x^2, \tag{4.109}$$

where ψ_0 and R_{bs_g} are the depression angle and standoff range respectively at the mid-aperture point. This phase term remains uncompensated by the image formation processor and manifests in the recovered image as both distortion and defocus that varies spatially over the image. In the case of repeat pass interferometry the image pair are acquired with a baseline offset such that the primary acquisition has a standoff range $R_{bs_{g1}}$ and depression angle ψ_1 while the repeat pass acquisition is specified by $R_{bs_{g2}}$ and ψ_2. The residual phase present in the primary image is given by $\phi_{res_1} = \phi_{res}(R_{bs_g} = R_{bs_{g1}}, \psi_0 = \psi_1)$ and for the repeat pass image $\phi_{res_2} = \phi_{res}(R_{bs_g} = R_{bs_{g2}}, \psi_0 = \psi_2)$. For interferometric processing it is the relative residual phase $\Delta\phi_{res} = \phi_{res_1} - \phi_{res_2}$ that produces decorrelation in the image pair. The processing correlation in the case of an aperture trimmed interferometric image pair can be written as,

$$\begin{aligned}
\gamma_{proc} &= \frac{exp(jAk_{0_g})}{a_{cx}(0)a_{cy}(0)}\iint A_c^2(k_x,k_y)exp\left(j\left(Ak_y + Bk_x + Ck_x^2\right)\right)dk_xdk_y, \\
&= exp(jAk_{0_g})\frac{1}{a_{cy}(0)}\int A_{cy}^2(k_y)exp\left(jAk_y\right)dk_y \\
&\qquad \frac{1}{a_{cx}(0)}\int A_{cx}^2(k_x)exp\left(j\left(Bk_x + Ck_x^2\right)\right)dk_x,
\end{aligned} \tag{4.110}$$

where,

$$A = \frac{(x^2 + y^2\sin^2(\psi_1))}{2R_{bs_{g1}}} - \frac{(x^2 + y^2\sin^2(\psi_2))}{2R_{bs_{g2}}} - h_{xy}\Delta\beta, \tag{4.111}$$

$$B = -\frac{xy\cos^2(\psi_1)}{R_{bs_{g1}}} + \frac{xy\cos^2(\psi_2)}{R_{bs_{g2}}}, \tag{4.112}$$

$$C = -\frac{(x^2 - y^2\cos^2(\psi_1))\cos^2(\psi_1)}{2R_{bs_{g1}}k_{0_g}} + \frac{(x^2 - y^2\cos^2(\psi_2))\cos^2(\psi_2)}{2R_{bs_{g2}}k_{0_g}}. \tag{4.113}$$

In the above expression for γ_{proc} note that the form of the aperture weighting $A_c(k_x, k_y)$ has been not been specified, however it has been assumed that it is a separable function such that,

$$A_c^2(k_x, k_y) = A_{cx}^2(k_x)A_{cy}^2(k_y), \tag{4.114}$$

and,

$$a_{cx}(x) = \int A_{cx}^2(k_x)\, exp(jxk_x)dk_x, \tag{4.115}$$

$$a_{cy}(y) = \int A_{cy}^2(k_y)\, exp(jyk_y)dk_y. \tag{4.116}$$

The linear phase terms Ak_y and Bk_x in (4.110) represent decorrelation arising from a misregistration between the image pair along the range and azimuth axes respectively while the quadratic phase Ck_x^2 describes decorrelation arising from the residual relative quadratic defocus between the image pair.

The integral with respect to k_y may be readily evaluated using standard Fourier transform theory and corresponds to a loss in coherence due to the misregistration term A,

$$\begin{aligned}\gamma_{proc_y} &= \frac{1}{a_{cy}(0)}\int A_{cy}^2(k_y)exp\left(jAk_y\right)dk_y, \\ &= \frac{a_{cy}(A)}{a_{cy}(0)}.\end{aligned} \tag{4.117}$$

In the idealised case when there is no azimuth misregistration, $B = 0$, Just [JB94] analysed the decorrelation arising from a residual quadratic phase error and showed that, for an unweighted aperture, $A_{cx}^2(k_x) = rect(k_x/k_{bw_{cx}})$, the integral with respect to k_x in (4.110) may be expressed in terms of the Fresnel integrals as follows,

$$\begin{aligned}\gamma_{proc_x} &= \frac{1}{a_{cy}(0)}\int A_{cx}^2(k_x)exp\left(j\left(Ck_x^2\right)\right)dk_x, \\ &= \frac{2}{k_{bw_{cx}}}\int_0^{\frac{k_{bw_{cx}}}{2}} exp\left(j\left(Ck_x^2\right)\right)dk_x, \\ &= \frac{2}{k_{bw_{cx}}}\left(\int_0^{\frac{k_{bw_{cx}}}{2}}\cos\left(Ck_x^2\right)dk_x + j\int_0^{\frac{k_{bw_{cx}}}{2}}\sin\left(Ck_x^2\right)dk_x\right), \\ &= \frac{\sqrt{2\pi}}{\sqrt{C}k_{bw_{cx}}}\left(\mathcal{C}\left(\frac{\sqrt{C}k_{bw_{cx}}}{\sqrt{2\pi}}\right) + j\mathcal{S}\left(\frac{\sqrt{C}k_{bw_{cx}}}{\sqrt{2\pi}}\right)\right),\end{aligned} \tag{4.118}$$

where,

$$\mathcal{C}(z) = \int_0^z cos\left(\frac{\pi}{2}t^2\right)dt, \tag{4.119}$$

$$\mathcal{S}(z) = \int_0^z sin\left(\frac{\pi}{2}t^2\right)dt, \tag{4.120}$$

Parameter	Value (Units)
Transmit waveform	LFM Chirp waveform
Transmit bandwidth f_{bw}	400 MHz
Transmitter power	8 kW
Polarization	HH
Radar centre frequency f_0	9.35 GHz
Depression angle	45 to 11 Degrees
Navigation	Combined INU and DGPS

Table 4.1: The Ingara X-Band airborne SAR system configuration parameters for the repeat pass interferometric change detection experiments conducted in 1999 and 2000.

are the Fresnel integrals [GR80]. For B non zero, the integral with respect to k_x may be found in an approximate form for particular values of C by employing the Principle of Stationary Phase [Won89].

While the above analysis pertains to the interferometric processing of imagery formed using the PFA, other image formation algorithms provide improved compensation for wavefront curvature effects. In particular the PF2 algorithm discussed in Chapter 2 incorporates an additional filtering step to the PFA that largely corrects for the uncompensated phase terms ϕ_{res_1} and ϕ_{res_2}. The relative residual phase mismatch between the acquisition and image formation transfer functions is thus minimal and the resulting image decorrelation is negligible. Azimuthal misregistration and phase errors that vary quadratically with k_x however are common errors that arise due to miscalibration in the synthetic aperture array, see Chapter 3. The above analysis thus provides a means of quantifying the impact of these residual errors on interferometric processing.

4.7 Results From a Repeat Pass Interferometric SAR Experiment

In this section an interferometric processor developed for processing repeat pass interferometric data collected with the DSTO Ingara X-band airborne SAR is described. Using the Ingara system parameters and the imaging geometries of the repeat pass experimental collections, the nature and extent of the acquisition and image formation processor mismatch discussed in the previous sections may be numerically quantified.

4.7.1 The Ingara X-band SAR Interferometry Experiments

The DSTO Ingara X-band airborne SAR [SBMS96], [SB94] is a multimode imaging radar that, for the repeat pass interferometry experiments discussed here (conducted in 1999 and 2000), was installed on a Beech 350 Super KingAir aircraft. The operating parameters for the radar as configured for the repeat pass interferometry experiments are detailed in Table 4.1. In the Ingara spotlight SAR mode deramp demodulation is employed to generate fine resolution image over a modest swath width of 1.5 km in range and 500 m in azimuth.

The repeat pass interferometry experiments, conducted with the Ingara SAR, were specifically designed to study the coherent change detection application of interferometry. In these experiments repeat pass spotlight SAR imagery was collected over a number of open fields consisting mostly of crop stubble with a number of ground truthed scene modifications carried out in the interval between the primary and repeat pass collections. The exact nature of the scene changes and the temporal baselines are discussed in detail in Chapter 7. The repeat pass imaging collections were conducted at

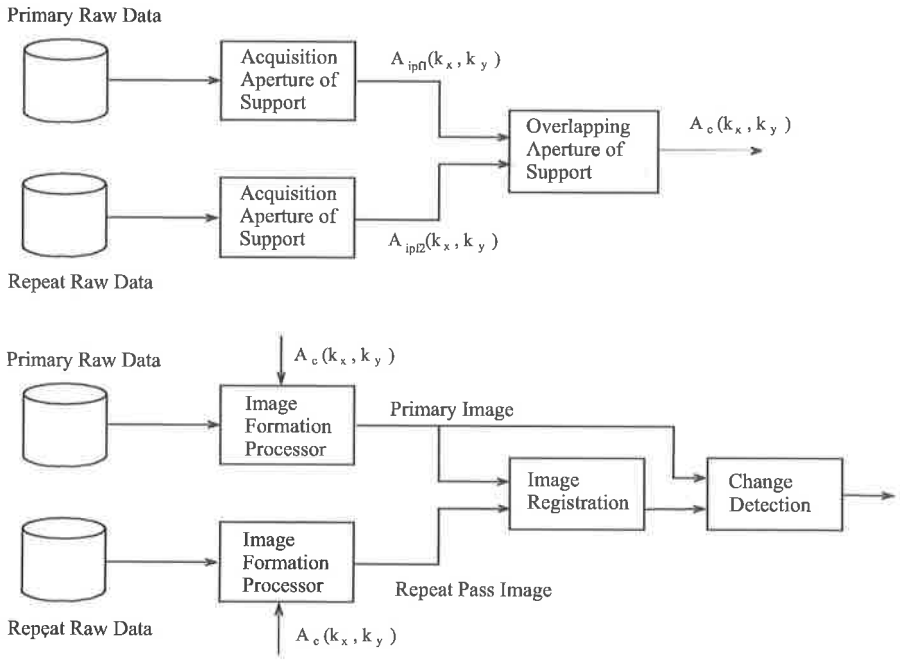


Figure 4.5: Flow chart of the processing steps required to generate an image pair repeat pass SAR data suitable for applying interferometric change detection algorithms.

three different depression angles and standoff ranges namely 45 deg., 7.5 km and 30 deg., 13.1 km and 15 deg., 16.0 km. Since the collections were specifically acquired to assess the change detection application of interferometry the same nominal flight tracks were used for the primary and repeat pass collections. Any baseline offset between the flight tracks pairs is thus a function of the accuracy of the aircraft Flight Management System (FMS) and the effects of wind and turbulence during the imaging collections.

4.7.2 The Interferometric Processor

Figure 4.5 is a flow chart of the interferometric processing chain developed to process the data from the measurement campaign. The details of the components in the processing chain shall now be discussed.

Compute Acquisition Apertures of Support

Given the radar deramp demodulated echo data and associated navigation data the first step in the interferometric processing chain is the computation of the pointing vectors $[R, \theta, \psi]^T$ describing the location of the radar with respect to the scene focus point at each transmit/receive point along the radar flight track. The radar flight track is measured with high precision using the combined INU and GPS information recorded during the data collection and a common scene focus point is used for the imaging collections. Over a coherent processing interval the pointing vectors associated with each imaging collection define the acquisition apertures of support $A_{acq_1}(k_x, k_y, k_z)$ and $A_{acq_2}(k_x, k_y, k_z)$ for the primary and repeat pass collections respectively.

Primary Depression Angle (Deg.)	Repeat pass Max Depression angle (Deg.)	Repeat pass Min Depression angle (Deg.)
15	22.37	NA
30	34.21	24.93
45	47.83	41.89

Table 4.2: Maximum and minimum repeat pass collection depression angles at which the primary and repeat pass acquisition apertures of support have no common overlapping intersection for primary collection depression angles of 15, 30 and 45 degrees.

Determine the Common Overlapping Aperture of Support

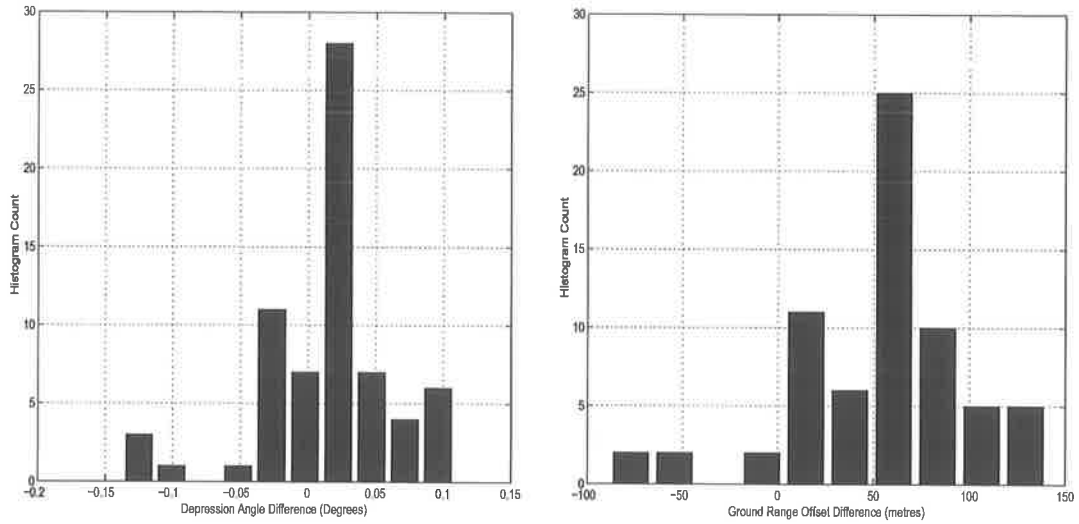
Given the acquisition apertures of support $A_{acq_1}(k_x, k_y, k_z)$ and $A_{acq_2}(k_x, k_y, k_z)$ for the primary and repeat pass collections the next step is to compute the centre frequency k_{0_g} and bandwidths $k_{bw_{xc}}$ and $k_{bw_{yc}}$ of the region given by the common overlapping intersection of A_{acq_1} and A_{acq_2} in the (k_x, k_y) plane. The depression angles at mid aperture will determine the acquisition aperture mismatch along the k_y axis and hence the location and size of the common overlapping region. For fine resolution, large transmit bandwidth systems, a relatively large difference in depression angle can be tolerated while still retaining some degree of aperture overlap. For the Ingara imaging scenarios Table 4.2 shows the minimum and maximum depression angle differences leading to complete mismatch (i.e., no common overlap) of the collection apertures. Figures 4.6 and 4.7 show histograms of the depression angle difference and ground range offset at the mid collection point obtained during the Ingara repeat pass interferometry collections. It can be seen that the repeat pass accuracy is well within the baseline decorrelation constraints. At a depression angle of 15 deg. the maximum angle difference is 0.12 deg. leading to a baseline decorrelation of $\gamma_{proc} = 0.977$, while for the collection at depression angle 30 deg. the maximum angle difference is 0.22 deg. giving $\gamma_{proc} = 0.947$. Of course this decorrelation is largely mitigated by restricting the processed aperture of support to the common overlapping portion of the collection aperture.

Image Formation

The choice of image formation processor is governed by the processors ability to adequately focus the scatterer signal history over the coherent processing interval. Generally, efficient frequency domain processors, such as the PFA, RMA and CSA (see Chapter 2), make approximations to the scatterer signal history which break down in wideband, wide-angle, near-field imaging. Under these scenarios the imagery suffers from distortion, defocus and a loss in contrast, while interferometric products suffer from a loss in coherence and increased noise and bias on the interferometric phase estimates.

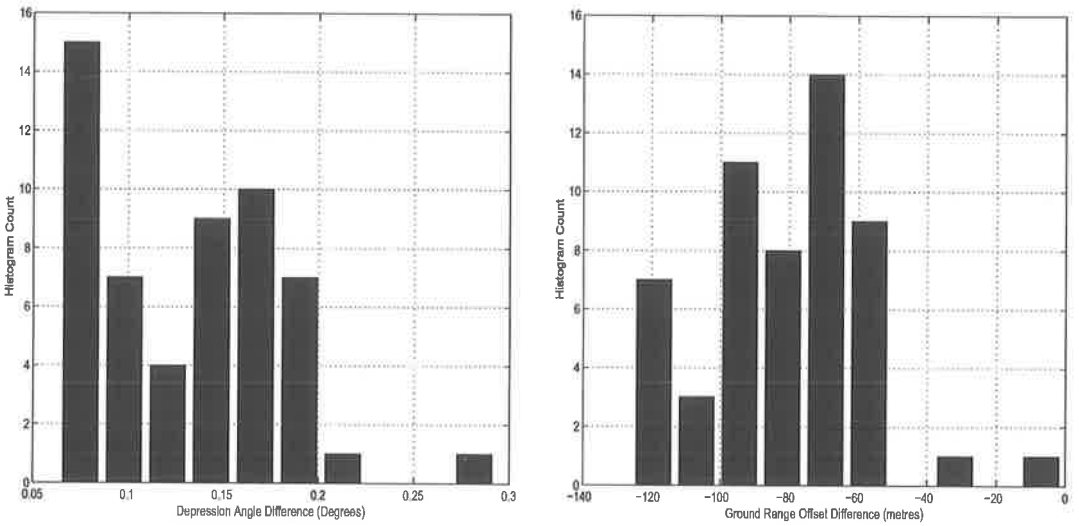
For the Ingara system configuration used in the repeat pass interferometry experiments the transmit bandwidth is limited to 400 MHz giving a nominal slant range resolution of 0.375 m (unweighted) while an azimuth angular collection of around 3 deg. gives similar azimuth resolution. Given the experimental standoff ranges and image size limits, the PFA provides adequately focused imagery suitable for interferometric processing at these range and azimuth resolutions, see Table 2.2 in Chapter 2.

The Ingara system however facilitates significantly wider angle collections thus potentially allowing the generation of much finer azimuth resolution imagery. This is advantageous for interferometry applications, such as coherent change detection, as this allows finer resolution, higher quality coherency estimates to be obtained. In practice the collection aperture will ultimately be limited by



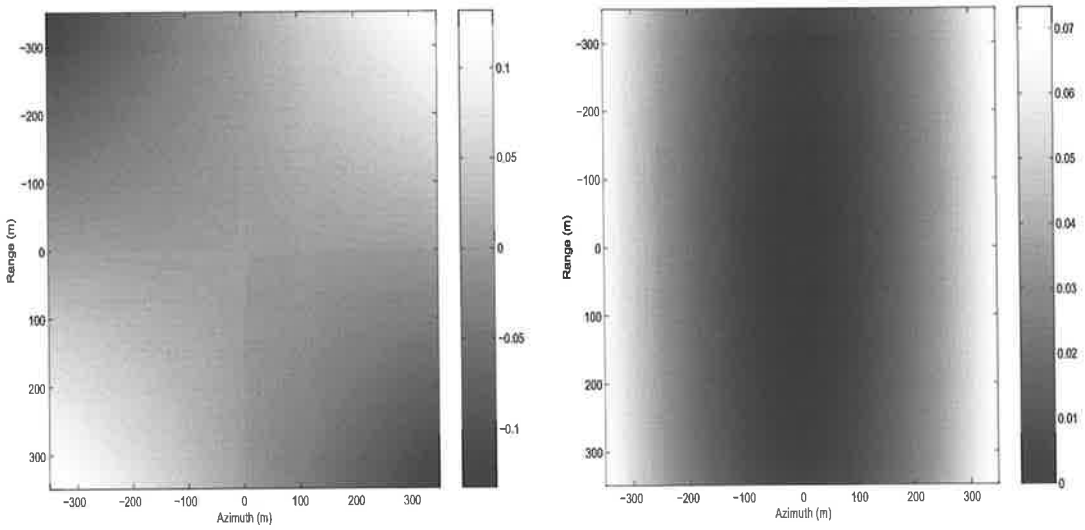
Depression angle offset Ground Range offset

Figure 4.6: Histograms of the depression angle difference and ground range offset difference between the primary and repeat pass collections obtained at a nominal depression angle of 15 degrees.



Depression angle offset Ground range offset

Figure 4.7: Histograms of the depression angle difference and ground range offset difference between the primary and repeat pass collections obtained at a nominal depression angle of 30 degrees.



Azimuth Misregistration: A in (4.112) Range Misregistration: B in (4.113)

Figure 4.8: Azimuth and range misregistration in metres, given by equations (4.112) and (4.113) respectively, of a PFA interferometric image pair collected with a nominal depression angle of 30 degrees and standoff range 13.1 km with baseline offsets of $\Delta\psi = 0.2$ degrees and $\Delta R_{bs_g} = 200$ m.

the phase stability of the radar, the precision of the flight track measurements of the extended aperture and the image formation processor's ability to focus the signal history data over the wide-angle collections.

For the Ingara repeat pass imaging scenarios to achieve 0.1 m (unweighted) azimuth resolution in the ground plane image an angular collection of the order of 10 degrees is required. For this collection aperture the patch size over which the PFA generates an adequately focused image is limited to around 100 m in radius, see Table 2.2 in Chapter 2. Scatterers at distances greater than this suffer from uncompensated residual frequency domain phase errors that manifest as an azimuth defocus that varies spatially over the image. Interferograms formed from such PFA imagery will also suffer from a loss in coherence and increased noise and bias in the interferometric phase given by (4.110).

Figure 4.8 shows the range and azimuth misregistration terms A and B given in equations (4.112) and (4.113) respectively over an image patch 700 m by 700 m for an image pair acquired with a nominal 30 degrees depression angle and 13.1 km standoff range and baseline offsets of $\Delta\psi_0 = 0.2$ degrees and $\Delta R_{bs_g} = 200$ m. The azimuth registration varies from -0.12 m to 0.12 m across the transduced image while the range misregistration varies from 0 at the scene center to 0.07 m at the image edges. Given the nominal range resolution of 0.45 m (unweighted) and azimuth resolution of 0.1 m (unweighted) the azimuth misregistration will dominate the image pair correlation. Figure 4.9 shows the peak value of the quadratic phase difference $C\left(k_{bw_{cx}}/2\right)^2$, (i.e., the quadratic phase Ck_x^2 evaluated at the band edge $k_x = k_{bw_{cx}}/2$.), for an azimuthal resolution of 0.1 m (unweighted), evaluated across the image patch. It can be seen the relative quadratic phase difference between the image pair that arises due to wavefront curvature effects is negligible (less than 0.15 radians across the recovered image) and so its contribution to the decorrelation of the PFA image pair is also negligibly small. Figure 4.10 shows the decorrelation γ_{proc} in (4.110) evaluated across the scene that arises due to the azimuthal and range misregistrations as well as the residual relative quadratic defocus. At the corners of the recovered images the cross correlation magnitude falls to 0.4. Note that in practice the decorrelation arising due to the azimuthal and range misregistration is largely corrected for by the

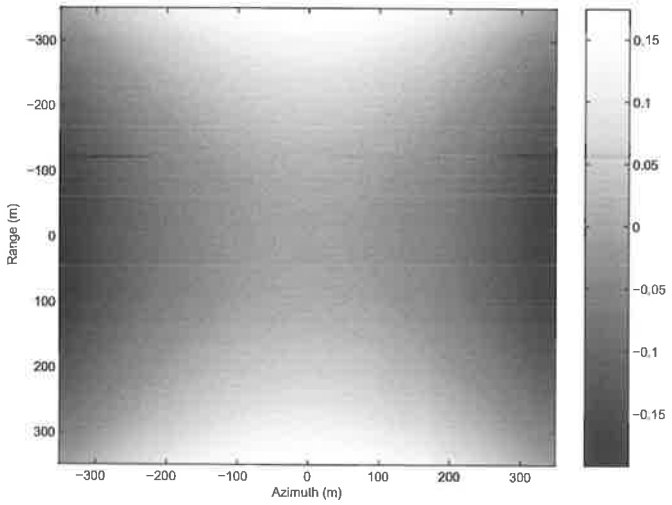


Figure 4.9: Peak value of the quadratic phase difference in radians associated with a PFA interferometric image pair processed to 0.1 m unweighted azimuth resolution and collected with a nominal depression angle of 30 degrees, a standoff range of 13.1 km and a baseline offset of $\Delta\psi = 0.2$ degrees and $\Delta R_{bs_g} = 200$ m.

image registration resampling and warping functions.

In Chapter 2 the PF2 algorithm was considered for focusing wide angle, fine azimuth resolution imagery. In the PF2 algorithm a filter is applied across a ground plane PFA image to remove the dominant quadratic defocus present in the PFA image. For the repeat pass experimental scenarios and an azimuth resolution of 0.1 m the PF2 image patch size radius is constrained to approximately 500 m. Thus the Ingara imagery formed using the PF2 algorithm will show only minor defocus at the edges of the illuminated patch.

An interferogram may be formed from a PF2 image pair with the interferogram quality determined by the residual relative phase differences that remain uncompensated by the PF2 as well as any approximations made in the implementation and application of the PF2 filter. Given the small depression angle differences and range offsets obtained in the Ingara repeat pass interferometric collections the residual uncompensated phase terms will not significant and the PF2 may be used to process the wide-angle fine azimuth resolution interferometric image pairs.

Image Pair Registration

A crucial step in interferometric processing is a precise co-registration of the interferometric image pair to subresolution cell accuracy (An accuracy of 0.1 of a resolution cell is generally considered necessary to achieve high quality interferograms [SM00], [JB94].). In repeat pass interferometry scene misregistration which varies spatially over the scene may arisc through a number of mechanisms. As discussed in Section 4.6.1 the differential projection of elevated targets into the transduced image plane will contribute to image misregistration. In particular, for the Ingara repeat pass imaging scenarios at a depression angle of 30 degrees and a depression angle difference of 0.2 degrees a misregistration of 10 percent of the nominal 0.5 m range resolution is obtained for scattering elements at heights of 10.7 m. Another source of misregistration are residual linear phase terms in the signal history data that remain uncompensated by the image formation processor. Finally platform navigation errors can lead to misregistrations which may be of the order of the point spread function of the SAR

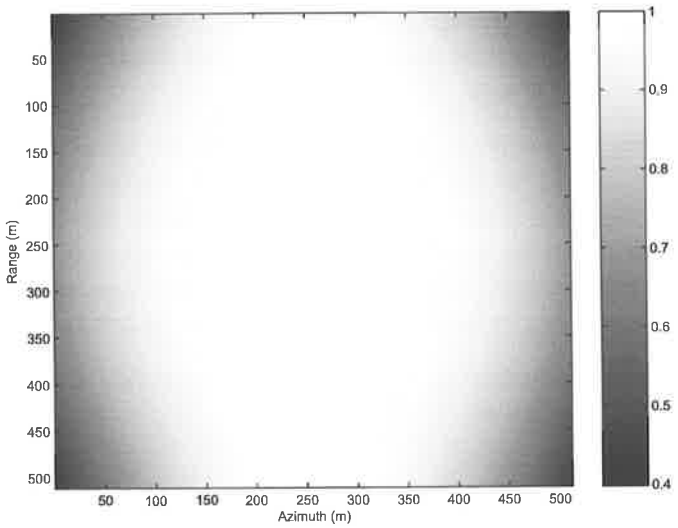


Figure 4.10: Cross correlation coefficient magnitude obtained for a PFA image pair processed to 0.1 m unweighted azimuth resolution and collected with a nominal depression angle of 30 degrees, a standoff range of 13.1 km and a baseline offset of $\Delta\psi = 0.2$ degrees and $\Delta R_{bs_g} = 200$ m.

processor [JWE+96].

A plethora of registration techniques exist in the literature for estimating the pixel by pixel misregistration and the subsequent resampling step. In [JWE+96] the misregistration over a local neighbourhood of pixels is found by maximizing the complex cross correlation between the image pair over the local area. By obtaining a number of such local spot estimates of the misregistration distributed over the scene a model of the misregistration at all points in the transduced image pair may be obtained by fitting a two dimensional surface function to the sample estimates. An alternative approach proposed by [SM00] makes use of the phase information available in interferograms obtained from different spectral subapertures. The phase differences may be used to obtain local estimates of the misregistration.

The registration processor used to process the Ingara repeat interferometric pairs uses a multistage approach based similar to that described in [JWE+96]:

1. Estimate a coarse global misregistration of the image pair by finding the range and azimuth shift that maximizes the cross correlation of the intensity images.

2. Based on the global misregistration partition the image pair into multiple corresponding image subchips. Compute the intensity cross correlation of the image subchips as a function of misregistration in range and azimuth. Interpolation of the cross correlation map to find the sub-resolution cell location of the correlation map maximum gives a fine registration estimate.

3. Using the multiple local misregistration estimates obtained over the entire scene model the misregistration using a pair of thin plate splines [Boo89], [Gos88]. These splines will describe, for each pixel (x, y) in the primary image, the location $(x + \Delta x, y + \Delta y)$ of the corresponding scene resolution cell in the repeat pass image.

4. Using the spline warping function resample the complex repeat pass image onto the sample grid of the primary image using a two dimensional truncated sinc interpolator.

5. Using the complex registered image pair estimate any dominant relative linear phase term between the primary image and the resampled repeat pass image and remove this linear phase term from the repeat pass image.

6. Having removed the dominant relative linear phase from the repeat pass image, recompute the fine registration estimates for the image subchips used in step 2 based on cross correlation of the complex image pair. Cross correlation of the complex transduced imagery produces a sharper correlation peak than cross correlating the image intensities as the cross correlation estimate is now computed using coherent, or vector addition, as opposed to scalar addition. As a consequence a more accurate estimate of the correlation peak lag can be obtained.

7. Recompute the warping surface to describe the misregistration and resample the images to obtained a registered image pair.

Interferogram Estimation

An interferogram is formed from an aperture trimmed, registered interferometric image pair by computing the sample cross correlation coefficient given by,

$$\hat{\gamma} exp(j\hat{\phi}) = \frac{\sum_{k=1}^{N} f_k g_k^*}{\sqrt{\sum_{k=1}^{N} |f_k|^2 \sum_{k=1}^{N} |g_k|^2}}, \tag{4.121}$$

over a sliding estimation window. The size of the estimation window is a compromise between obtaining a sufficiently fine resolution cross correlation map, capable of tracking the spatial variation in the underlying complex correlation coefficient and the required accuracy of the estimated quantities. For example, in the change detection application of SAR interferometry wherein man-made scene disturbances such as vehicle tracks are to be detected, the scene correlation can be highly spatially non-stationary with spatially small isolated, abrupt changes. Thus a small window commensurate with the spatial size of the scene disturbances is required. However, if the number of independent pixel samples in the window is too small the estimate will be excessively noisy making it difficult to distinguish between the changed and unchanged regions of the scene.

Another consideration in the formation of an interferogram is the image pixel sampling requirements to ensure alias free interferometric measurements. Given the bandlimited image pair f and g, with range and azimuth bandwidths of $k_{bw_{cx}}$ and $k_{bw_{cy}}$ respectively, the coherence is estimated by firstly forming the three product images $|f|^2 = f \cdot f^*$, $|g|^2 = g \cdot g^*$ and fg^*. These product images are noisy single point estimates of the mean backscatter and cross correlation of the primary and repeat pass images. As multiplication in the image domain corresponds to convolution in the spatial frequency domain the range and azimuth bandwidth of the product images are $2k_{bw_{cy}}$ and $2k_{bw_{cx}}$ respectively. Thus in order to avoid aliasing in the product images the image pair f and g must first be oversampled by a factor of two.

While the range and azimuth bandwidths of the product images are $2k_{bw_{cy}}$ and $2k_{bw_{cx}}$ respectively the underlying scene statistics are assumed to vary only slowly over the spatial estimation window and are modeled as being stationary in increments [TLBV99]. High spatial frequency energy in the product images may thus be attributed to noise, while low spatial frequency energy corresponds to the slow variations in the scene statistics permitted by the stationary in increments model. The product images $|f|^2 = f \cdot f^*$, $|g|^2 = g \cdot g^*$ and fg^* may thus each be spatially averaged using a N pixel sliding estimation window which simply functions as a low pass filter that attenuates the high spatial frequency "noise" content of the product image and gives an improved local estimate of the slowly varying scene statistics. As the product images have been low pass filtered they may be used directly in (4.121) to compute the interferogram without significant aliasing.

4.7.3 Experimental Results

Experimental repeat pass interferometric SAR data collected with the DSTO Ingara SAR has been processed using the techniques discussed in the previous section. Figures 4.11 and 4.12 shows the intensity images of a registered, aperture trimmed primary and repeat pass interferometric image pair collected at a nominal depression angle of 30 degrees. The images have been processed using the PF2 algorithm and have a 3 dB resolution of 0.58 m in range and 0.15 m in azimuth with a Hamming spectral window applied and a pixel spacing of 0.41 m by 0.1 m. The image is of an open field with a building visible in the lower middle of the image. A drainage trench runs along the left side of the image and a dirt track lies in the upper portion of the image. Both of these scene features appear in the images as areas of low backscatterer return. In the case of the drainage trench the area of low backscatter corresponds to radar shadow while in the case of the dirt track the low backscatterer is possibly due to the passage of vehicles compacting and smoothing the soil and the absence of vegetation in these areas. The baseline offset for this image pair is very small with a depression angle difference of 0.012 degrees and a ground range offset difference of 4.59 m. The temporal baseline for this collection is only 12 minutes corresponding to the time required to maneuver the aircraft back to the start of the imaging track for the repeat pass collection. For this experiment no controlled scene changes were carried out and no ground truth observations were made during the collection interval.

Figures 4.13 and 4.14 show the sample coherence and interferometric phase obtained from the repeat pass pair using a 2 (range) by 6 (azimuth) pixel spatial estimation window. The coherence in the field is very high at 0.94 (see Section 7.4 in Chapter 7) consistent with the small temporal delay and baseline offset between the repeat pass collections. Figure 4.15 is an enlarged view of the coherence map over the dirt track in the upper portion of the scene. As the track has a low backscatter power the transduced image has a low signal to noise level in these regions and hence there is significant decorrelation. On the other hand the areas between the tracks show high coherence due to the stronger vegetation and ground returns in these areas.

A feature of particular interest in Figure 4.13 are the random track like areas of low coherence in the middle of the field. Figure 4.16 shows an enlarged view of these track like disturbances. The tracks appear to have a low but non zero coherence possibly because the tracks are on a much finer scale that the resolution of the sample coherence map so the estimation window includes pixels containing both changed and unchanged scattering contributions. In addition a number of the tracks appear to be terminated by a somewhat larger area of very low coherence. It is believed that these low coherence tracks may be due to the movement of sheep while grazing during the 12 minute temporal baseline with the "ends" of the tracks being the sheep themselves. Figure 4.17 shows an enlarged view of the primary and repeat pass intensity images obtained over one of the tracks. It can be seen that the speckle pattern of the pair of intensity images is nearly identical and there is a significantly stronger return (approximately 3.9 dB stronger) appearing in the centre of the repeat pass image subchip shown in Figure 4.17 that is absent in the primary intensity image. Unfortunately no ground truth observation were made on the day of the repeat pass collections however grazing sheep were present in the field on the following day.

4.8 Conclusions

This chapter has provided an overview of interferometric SAR processing techniques and described the theoretical basis for interferometric change detection. A statistically based description for an interferometric SAR image pair was given in which the extra information provided by the joint processing of the image pair is encapsulated in the complex cross correlation coefficient. In this formulation the scene is modelled as a homogeneous random ensemble of mutually independent stable and unstable



Figure 4.11: Primary collection intensity image. The image has been processed to a resolution of 0.58 m (range) x 0.150 m (azimuth) with a Hamming window applied.



Figure 4.12: Repeat pass collection intensity image. The image has been processed to a resolution of 0.58 m (range) x 0.150 m (azimuth) with a Hamming window applied. The temporal baseline for the repeat pass interferometric pair is approximately 12 minutes

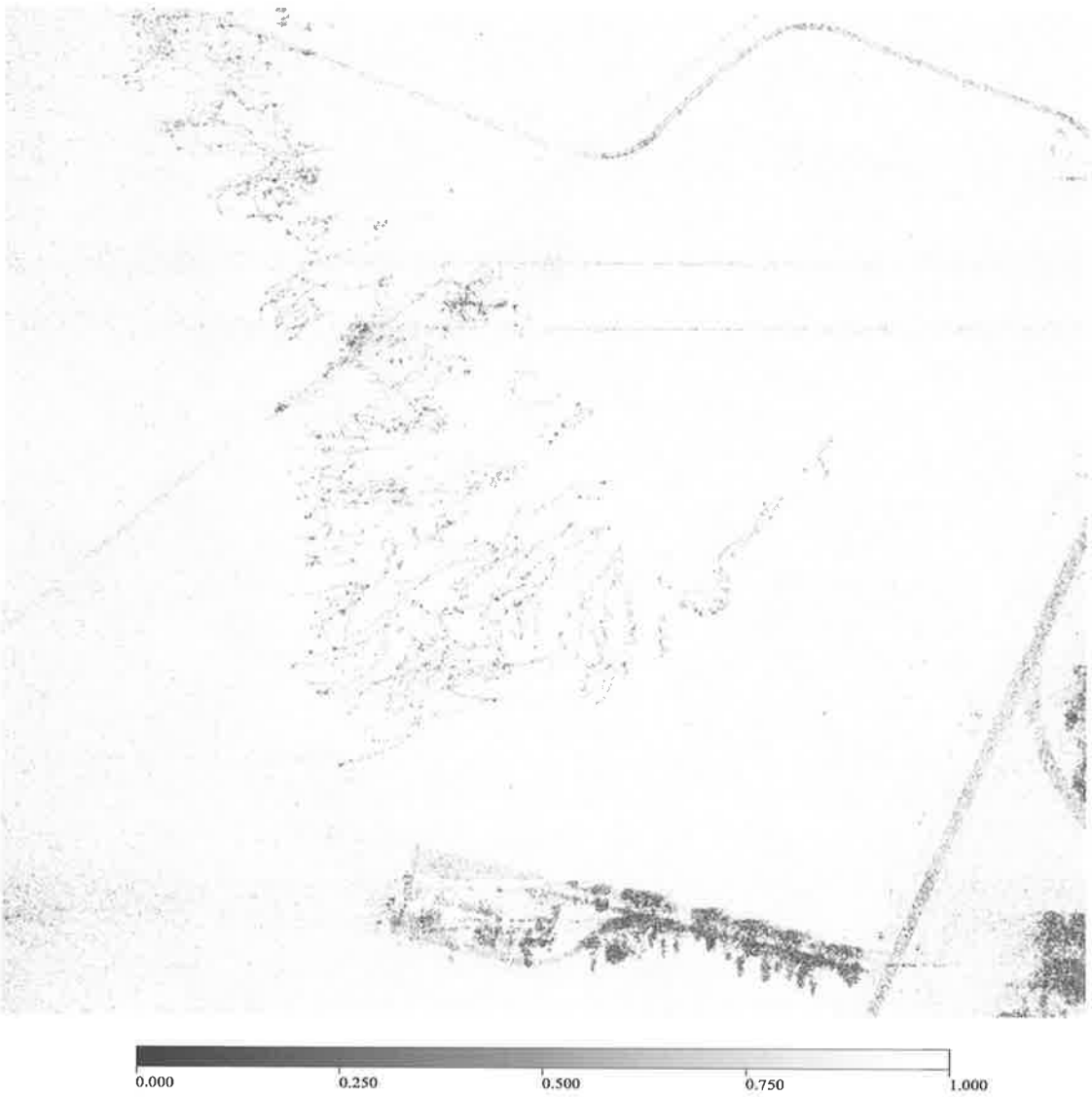


Figure 4.13: Magnitude image of the sample complex cross correlation coefficient obtained by spatially averaging over a sliding estimation window (2 by 6 pixels in range and azimuth respectively).

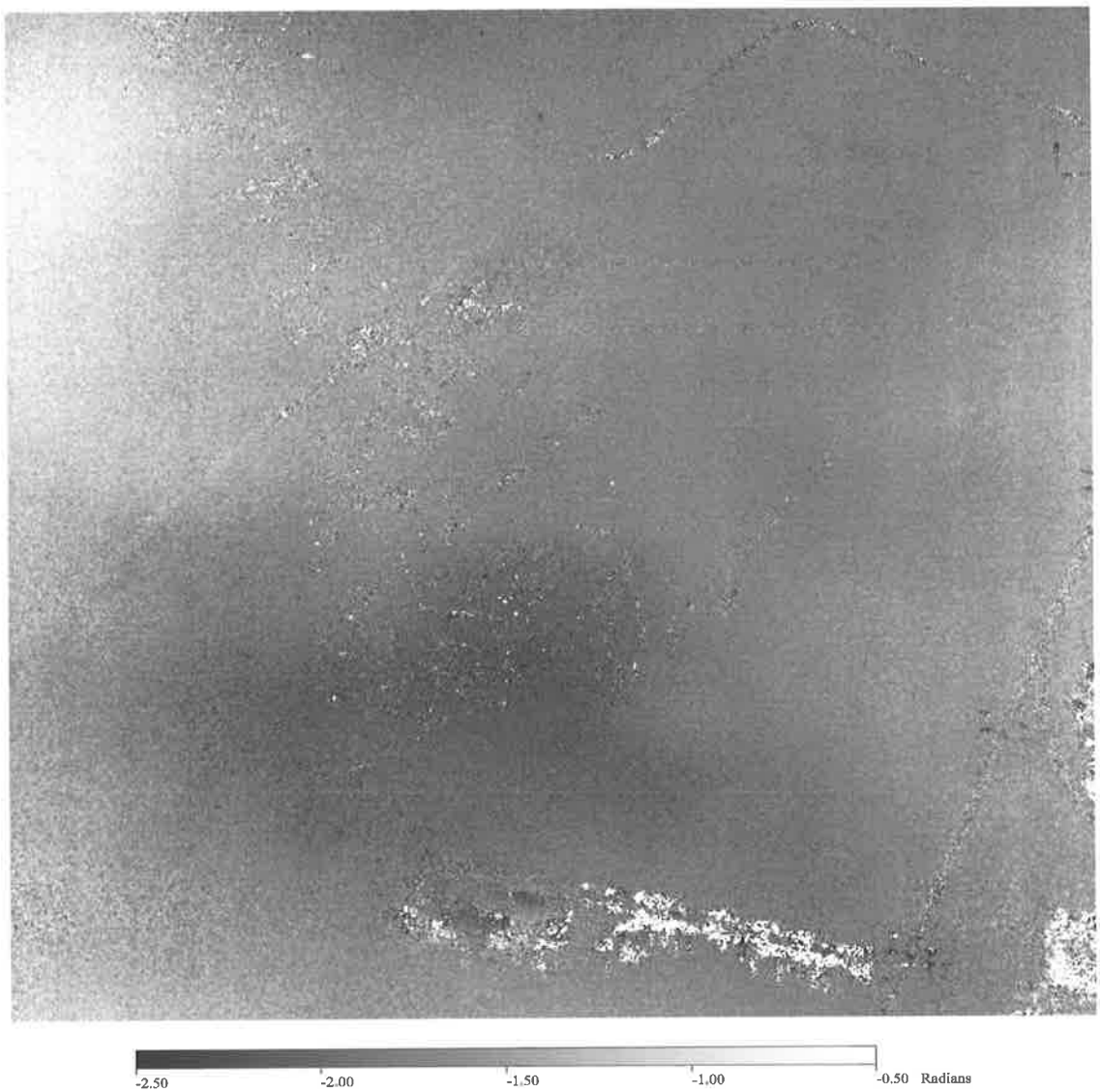


Figure 4.14: Phase image of the sample complex cross correlation coefficient obtained by spatially averaging over a sliding estimation window (2 by 6 pixels in range and azimuth respectively).

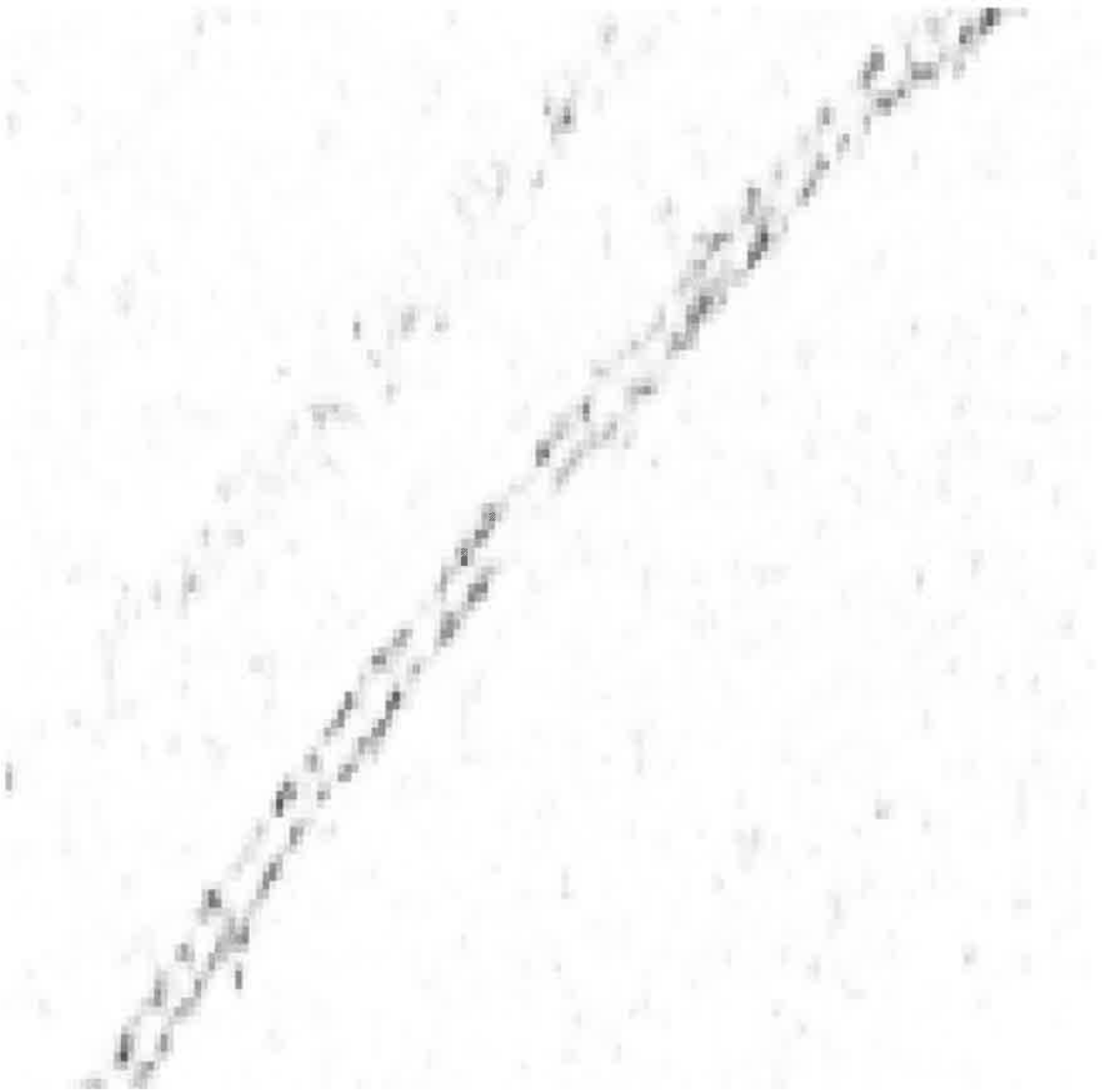


Figure 4.15: Enlarged view of the coherence map over the dirt track that appears along the top of the scene image.

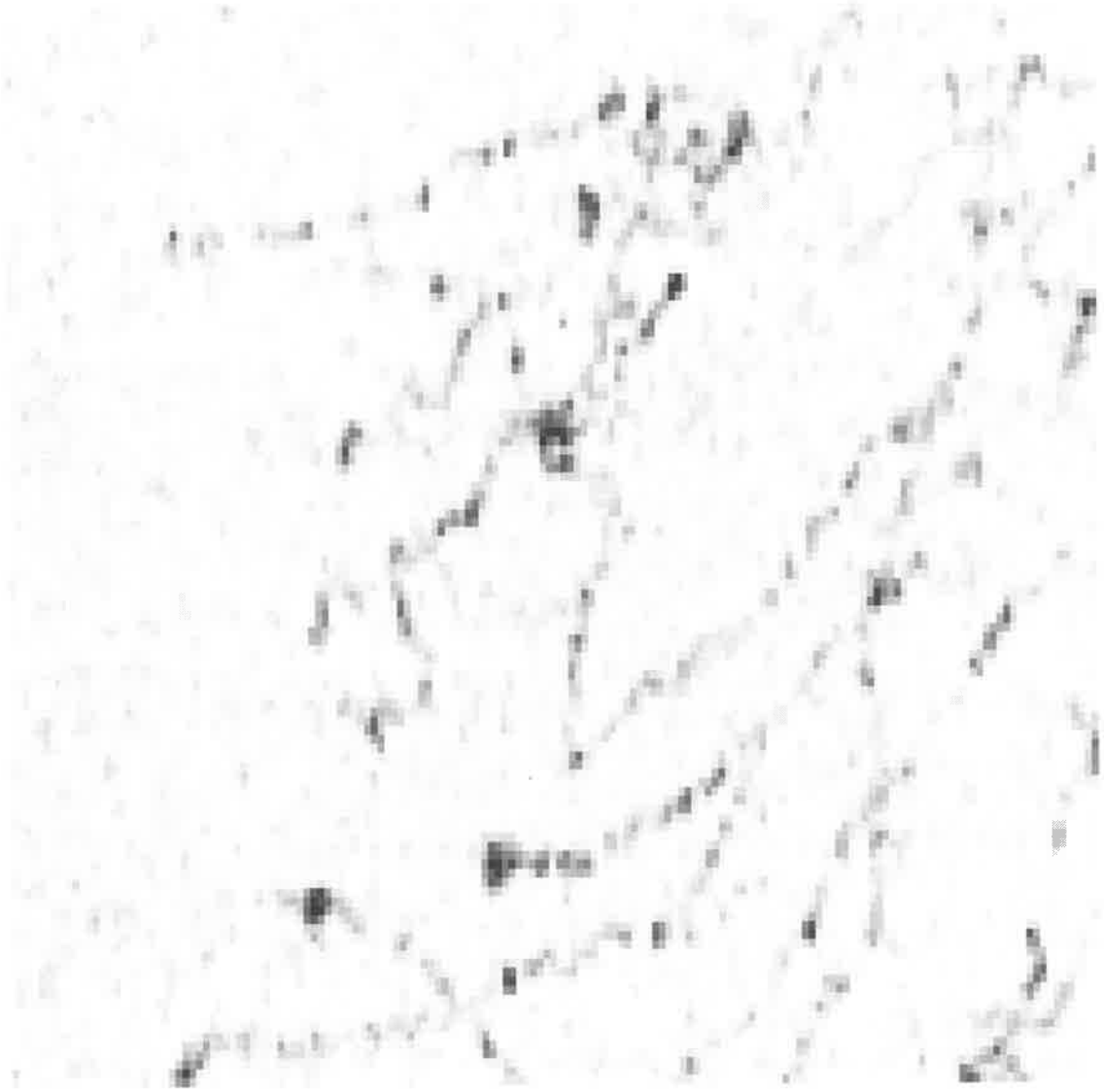


Figure 4.16: Enlarged view of the coherence map over the low coherence random tracks appearing in middle portion of the scene.

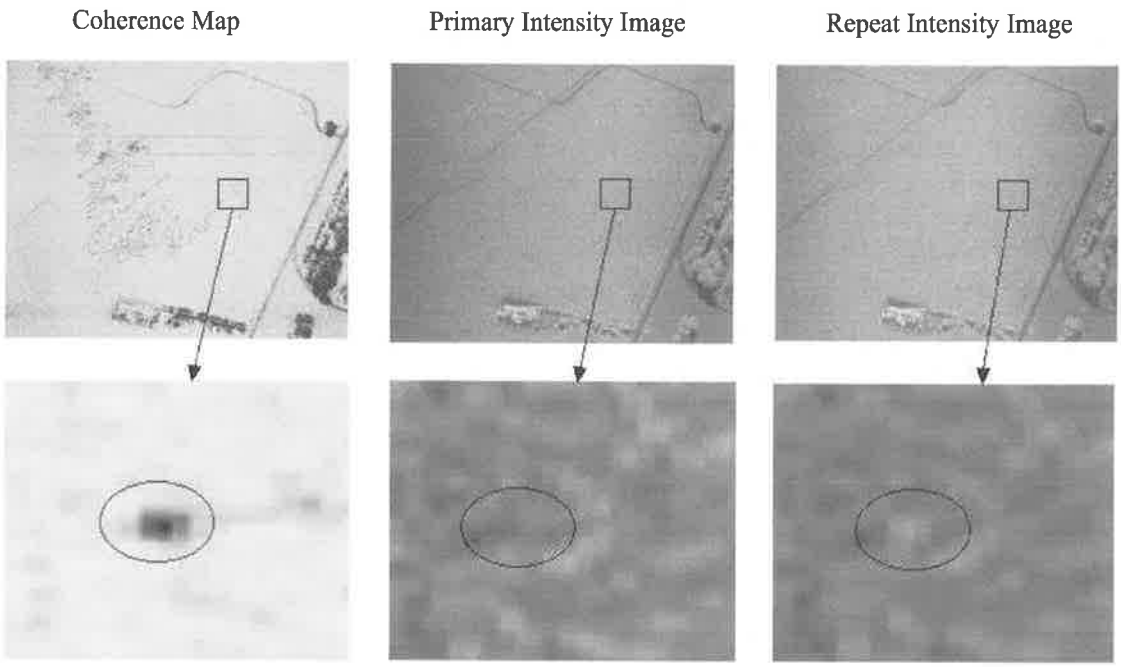


Figure 4.17: Enlarged view of the coherence map as well as the primary and repeat pass intensity images over one of the track like disturbances.

scatterers while the SAR acquisition and image formation processors are modelled as linear operators. The cross correlation coefficient is subsequently shown to consist of the cross correlation coefficient of the scattering ensemble modulated by a SAR image processor correlation. The processor correlation is determined by the mismatch between the acquisition and image formation transfer functions of the primary and repeat pass images. In the case of the PFA the processor correlation was shown to be a function of the uncompensated wavefront curvature effects present in the image as well as any miscalibration of the primary and repeat pass synthetic apertures. Finally the design of an interferometric SAR processor developed for the processing repeat pass data acquired with the DSTO Ingara X-band SAR was discussed and a repeat pass interferogram generated.

Chapter 5

Interferometric Change Detection

5.1 Introduction

For natural homogeneous distributed scenes it was shown in Chapter 4 that the joint first order density function for a repeat pass interferometric image pair $\underline{X} = [f, g]^T$ is a zero mean, complex, circular Gaussian random process. An interferometric image pair is thus completely described by the four parameters defined in the associated covariance matrix $E\{\underline{X}\underline{X}^H\}$, namely the mean backscatter power of the two images, defined by $E\{ff^*\} = \sigma_f^2$ and $E\{gg^*\} = \sigma_g^2$ and the amplitude γ and phase Φ of the complex cross correlation, defined by $E\{fg^*\} = \sigma_f \sigma_g \gamma exp(j\Phi)$. These parameters measure different aspects of the underlying scattering behaviour of the scene. The mean backscatter power of a scene is a function of the structural and dielectric properties of the scattering medium while the cross correlation is sensitive to perturbations in the sub-resolution scattering structure of the scene. Scene disturbances arising from man-made changes that occur in the interval between repeat collections may potentially cause changes over a broad range of scattering properties and mechanisms in a scene and thus manifest as changes in both the mean backscatter power of the scene as well as a reduction in the correlation between the image pairs. These parameters thus provide complementary characterisations of scene change and together provide a complete description of scene changes in a SAR image pair.

In this chapter a review of change detection techniques based on the mean backscatter power and the magnitude of the cross correlation coefficient for identifying man-made scene disturbances are discussed. In particular the performance of these change statistics are quantified and compared by evaluating the associated Receiver Operator Characteristic (ROC) curves describing the probability of detection and false alarm as a function of the detection threshold. Section 5.2 considers a form of the mean backscatter ratio of the primary and repeat pass images, originally proposed by Touzi [TLB88] for SAR image edge detection, as a possible change statistic. From the density function of the ratio change statistic expressions for the probability of detection and false alarm of a threshold detector are found and ROC curves computed. Section 5.3 considers the magnitude of the sample complex cross correlation coefficient, or coherence, as a change statistic. In this statistic scene changes are identified as regions of total decorrelation against undisturbed regions described by some degree of partial correlation. Expressions for the probability of detection and false alarm are found and compared to the backscatter ratio statistic. Alternative estimators of the sample coherence are considered in Section 5.4. These estimators allow coherency based change detection to be performed without the need for the complete complex interferometric image data however they suffer from a degraded detection performance. Finally in Section 5.5 the change statistics discussed in Sections 5.2, 5.3 and 5.4 are evaluated using experimental data collected with the DSTO Ingara airborne SAR.

5.2 Change Detection Using the SAR Image Intensity

Change detection based on the mean SAR image pixel intensity seeks to identify changes in the underlying mean backscatter power of a scene. The mean backscatter power of a scene is a geophysical quantity describing the local interaction of the propagating incident electromagnetic wave with the scene's scattering volume. The mean power in the backscattered field is thus determined by the structural and electromagnetic properties of the scattering elements in the volume, such as their size, shape, density, orientation and dielectric constant, as well as the properties of the incident wave such as the wavelength, polarisation and the incidence angle. The nature of the interaction between the scattering volume and incident wave is governed by the electromagnetic wave equations and is difficult to solve unless the scene is described in terms of simple models of the dominant scattering mechanisms [KF83], [KF88]. For example, the radar backscatter from forest and crop canopies may be modelled as scattering from randomly oriented dielectric geometric structures with shape and dielectric constants based on the physical vegetation components [KFA88]. Such modelling can provide predictions of the mean backscatter power and its sensitivity to the scene parameters.

The estimation of the mean backscatter power from a SAR image is corrupted by multiplicative speckle noise, which is an inherent aspect of coherent imaging systems [Goo00b], as well as additive receiver noise, antenna pointing errors and imaging artifacts arising from propagation and processing effects. As a consequence estimation of the mean backscatter power from the transduced speckle SAR intensity image requires some form of averaging. The design of appropriate filters for speckle noise suppression and mean backscatter reconstruction has been a highly active area of research [Zel76], [PMIM76], [Lee83], [FSSH82] and [Whi95] for many years.

Estimating the mean backscatter

For a homogeneous natural distributed scene the transduced complex SAR image f is modelled by a zero mean, complex circular Gaussian random process,

$$f = f_r + jf_i, \tag{5.1}$$

where,

$$p(f) = \frac{1}{\pi\sigma_f^2} exp\left(-\left(\frac{f_r^2 + f_i^2}{\sigma_f^2}\right)\right). \tag{5.2}$$

The complex image may be re-written as the mean backscatter power modulated by a zero mean, circular, unit variance complex Gaussian random process, i.e.,

$$f = \sigma_f \left(n_r + jn_i\right). \tag{5.3}$$

The random process $(n_r + jn_i)$ is commonly called multiplicative speckle noise as it modulates the information bearing parameter, σ_f, describing the imaged scene. Speckle noise however, is a manifestation of the sub-resolution scattering structure of the scene. In particular, it is a result of the coherent interfering contributions of a large number of scatterers and thus is a deterministic quantity that may be reproduced provided the same imaging geometry is used for each measurement.

Given a single pixel f_k from the transduced image of a scene the maximum likelihood estimate of the mean backscatter power σ_f^2 is the pixel intensity $I_k = |f_k|^2$ [OQ98] and its density function is given by the negative exponential,

$$P(I_k|\sigma_f^2) = \frac{1}{\sigma_f^2} exp\left(-\frac{I_k}{\sigma_f^2}\right). \tag{5.4}$$

The pixel intensity is an unbiased estimator of the scene backscatter power however, its variance is equal to the mean backscatter power and therefore the estimate is noisier in regions of high backscatter. This problem is obviated by considering the log intensity $log(I_k)$ for which the variance is independent of the mean value [QR95]. In practice SAR images of the pixel intensities are often displayed using a log scale as such images have a uniform variance.

In a homogeneous region, wherein the underlying scattering properties and mechanisms are uniform over the region, the mean backscatter power describing the scene in the transduced image will be constant in that region. The multiplicative speckle noise that manifests in each image pixel however, will vary from pixel to pixel due to the particular coherent interfering sub-resolution scattering contributions associated with each resolution cell. Each image pixel may thus be interpreted as a particular realisation of the same underlying random scattering phenomenon and may be averaged to yield an improved estimate of the mean backscatter. An estimate of the mean backscatter power obtained by spatially averaging over N resolution cells is given by,

$$I = \frac{1}{N}\sum_{k=1}^{N} I_k. \tag{5.5}$$

Provided the N pixel realisations, I_k, are independent then I has a gamma distribution with order parameter N given by,

$$P(I|\sigma_f^2) = \frac{1}{\Gamma(N)}\left(\frac{N}{\sigma_f^2}\right)^N I^{N-1} exp\left(-\frac{NI}{\sigma_f^2}\right). \tag{5.6}$$

The N look intensity average is a consistent estimator of the mean backscatter σ_f^2 as the expected value $E\{I\} = \sigma_f^2$ and the variance, $VAR\{I\} = \sigma_f^4/N$, tends to zero as N increases. The Equivalent Number of Looks (ENL), defined as,

$$ENL = \frac{E^2\{I\}}{VAR\{I\}}, \tag{5.7}$$

indicates the number of independent observations used in a sample estimate of the backscatter. If all N samples used in (5.5) are independent then $ENL = N$. However, when the N samples are correlated via the point spread function of the SAR then the ENL will, in general, be some non-integer value less than N.

A Backscatter Change Statistic

For a repeat pass SAR image pair the N look sample estimates of the mean backscatter of the primary and repeat pass image pair have density functions given by,

$$P(I_f|\sigma_f^2) = \frac{1}{\Gamma(N)}\left(\frac{N}{\sigma_f^2}\right)^N I_f^{N-1} exp\left(-\frac{NI_f}{\sigma_f^2}\right), \tag{5.8}$$

$$P(I_g|\sigma_g^2) = \frac{1}{\Gamma(N)}\left(\frac{N}{\sigma_g^2}\right)^N I_g^{N-1} exp\left(-\frac{NI_g}{\sigma_g^2}\right), \tag{5.9}$$

where I_f and I_g are the spatially averaged pixel intensities of the primary and repeat pass images respectively and σ_f^2 and σ_g^2 are the associated scene mean backscatter powers. In the absence of calibration errors such as radiometric miscalibration and antenna pointing errors, regions in the scene

that remain undisturbed in the interval between collections have the same mean backscatter power i.e., $\sigma_f^2 = \sigma_g^2$. Areas in which $\sigma_f^2 \neq \sigma_g^2$, are indicative of areas of scene change.

A common approach to detecting changes in the image intensity of non-coherent data sets (eg: passively sensed data) [Sin89] is to consider the difference statistic,

$$D = I_f - I_g = \sum_{k=1}^{N} |f_k|^2 - \sum_{k=1}^{N} |g_k|^2. \tag{5.10}$$

This statistic however is found to be ill suited to change detection in SAR imagery [RvZ93], [TLBV99] and [QR95]. Under the premise that the two measurements of the scene's radar reflectivity are independent [RvZ93], the variance of the difference statistic is simply the sum of the variances of the two intensity estimates,

$$var\{D\} = \frac{\sigma_f^2 + \sigma_g^2}{N}. \tag{5.11}$$

Therefore application of a simple threshold detector to the difference statistic to distinguish between areas of differing mean backscatter will have an error performance dependent on the mean backscatter. For example, in areas of no change in backscatter, $\sigma_f^2 = \sigma_g^2$, the probability of false alarm for the threshold detector (i.e., labelling a pixel pair in an unchanged scene as having changed backscatter values) will be lower in areas of lower mean backscatter power.

An alternative approach to forming a change statistic is to consider the log intensity estimate as it has a variance independent of the absolute value of the mean backscatter. The difference of the log intensity estimates,

$$D_L = log(I_f) - log(I_g), \tag{5.12}$$

$$= log\left(\frac{I_f}{I_g}\right), \tag{5.13}$$

or alternatively the ratio change statistic,

$$\hat{R} = exp(D_L) = \frac{I_f}{I_g}, \tag{5.14}$$

are commonly used in SAR image change statistics. The ratio change statistics has a density function given by [TLB88],

$$p(\hat{R}|R) = \frac{(2N-1)!}{((N-1)!)^2} \frac{R^N \hat{R}^{N-1}}{(R+\hat{R})^{2N}}, \tag{5.15}$$

where $R = \frac{\sigma_f^2}{\sigma_g^2}$. The mean and variance of $\hat{R}$ are given,

$$E\{\hat{R}\} = \frac{N}{N-1} R, \tag{5.16}$$

$$Var\{\hat{R}\} = \left(\frac{N(2N-1)R}{(N-1)^2(N-2)}\right)^2, \tag{5.17}$$

and are dependent only on the relative backscatter ratio $R = \sigma_f^2/\sigma_g^2$ and the number of independent samples N. The ratio statistic $\hat{R}$ takes values in the range $(0, \infty)$ and in practice requires two thresholds to identify scene changes causing either a reduction or an increase in the mean backscatter power. A more convenient detector proposed by Touzi [TLB88] based on the ratio statistic is,

$$\hat{r} = \begin{cases} \hat{R}, & \text{if } \hat{R} \leq 1, \\ \hat{R}^{-1}, & \text{if } \hat{R} > 1. \end{cases} \tag{5.18}$$

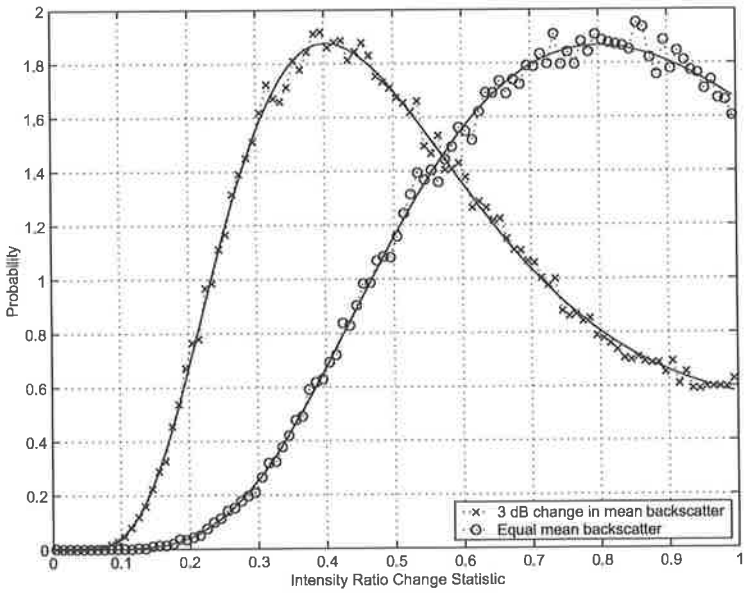


Figure 5.1: Simulated and theoretically obtained density functions for the mean backscatter ratio change statistic corresponding to an unchanged scene and a scene with a 3 dB change in the backscatter. The number of independent averages used in the intensity estimates is $N = 9$.

This statistic takes values between 0 and 1 and a single threshold may be applied to generate change detections. The probability density function is given by [TLB88],

$$p(\hat{r}|R) = \frac{\Gamma(2N)}{\Gamma(N)^2}\left(\frac{R^N}{(\hat{r}+R)^{2N}} + \frac{R^{-N}}{(\hat{r}+R^{-1})^{2N}}\right)\hat{r}^{N-1}. \tag{5.19}$$

Figure 5.1 shows simulated and theoretical density functions for the ratio statistic for an unchanged scene in the absence of calibration errors (equal mean backscatter power) and a scene with a 3 dB change in the mean backscatter power between image collections obtained using $N = 9$ independent samples. The performance of the ratio statistic $\hat{r}$ may be gauged by the degree of overlap of the two density functions shown in Figure 5.1. Using a simple threshold detector, pixel pairs with ratio values greater than some threshold T, $(\hat{r} > T)$, are labelled as being unchanged and pixel pairs with ratio values less than T, $(\hat{r} < T)$, are labelled as being changed. The probability of correctly making a change detection corresponds to the area under the changed density function in Figure 5.1 to the left of the ratio threshold T, while the probability of a false alarm corresponds to the area under the unchanged density function to the left of the ratio threshold T. Analytical expressions for the probability of detection and the probability of false alarm may be computed by evaluating the following integrals. The probability of false alarm is given by,

$$\begin{aligned} P_{fa} &= \int_0^T p(\hat{r}|R = R_0)d\hat{r}, \\ &= \frac{\Gamma(2N)}{\Gamma^2(N)}\int_0^T \left(\frac{R_0^N}{(\hat{r}+R_0)^{2N}} + \frac{R_0^{-N}}{(\hat{r}+R_0^{-1})^{2N}}\right)\hat{r}^{N-1}d\hat{r}, \\ &= \frac{\Gamma(2N)T^N}{\Gamma(N-1)}\left(\frac{1}{R_0^N}{}_1F_2\left(2N, N, N-1, \frac{T}{R_0}\right) + R_0^N{}_1F_2\left(2N, N, N-1, TR_0\right)\right), \end{aligned} \tag{5.20}$$

where $R_0 = \sigma_f^2/\sigma_g^2$ with σ_f^2 and σ_g^2 taken to be the mean backscattered power in the unchanged regions of the scene. In the absence of miscalibration errors $R_0 = 1$ however, in practice radiometric miscalibration and antenna pointing errors may yield $R_0 \neq 1$. The probability of detection is,

$$\begin{aligned} P_d &= \int_0^T p(\hat{r}|R = R_1)d\hat{r}, \\ &= \frac{\Gamma(2N)}{\Gamma^2(N)} \int_0^T \left(\frac{R_1^N}{(\hat{r} + R_1)^{2N}} + \frac{R_1^{-N}}{(\hat{r} + R_1^{-1})^{2N}} \right) \hat{r}^{N-1} d\hat{r}, \\ &= \frac{\Gamma(2N)T^N}{\Gamma(N-1)} \left(\frac{1}{R_1^N} {}_1F_2\left(2N, N, N-1, \frac{T}{R_1}\right) + R_1^N {}_1F_2\left(2N, N, N-1, TR_1\right) \right), \quad (5.21) \end{aligned}$$

where $R_1 = \sigma_f^2/\sigma_g^2$ with σ_f^2 and σ_g^2 taken to be the mean backscattered power in the changed regions of the scene in the primary and repeat pass images respectively. In equations (5.20) and (5.21) ${}_1F_2$ is the hypergeometric function given in equation 15.3.1 in [AS72].

Figure 5.2 shows simulated and theoretical ROC curves (plots of the probability of detection versus the probability of false alarm) for the ratio detector obtained with $R_0 = 0$ dB and $R_1 = 1, 3, 5$ and 10 dB and $N = 9$. It is clear that for small changes in the mean backscatter power the detector suffers from a significant false alarm rate. To achieve a probability of detection of 0.7 for a mean backscatter power change of 3 dB the associated probability of false alarm is unacceptably high at 0.35. The false alarm rate may be reduced by increasing the estimation window size and hence the value of N. Figure 5.3 shows the ROC performance associated with a mean backscatter power change of 3 dB as the ENL is increased. Increasing the ENL from 9 to 36 provides approximately an order of magnitude improvement in the false alarm rate. This performance improvement however, is only realised if the scene's mean backscatter power over the estimation window is locally stationary. In the change detection application the estimation window must be commensurate with the size of the scene disturbances to be detected otherwise the change statistic local estimate contains contributions from changed and unchanged image pixels and the improvements suggested in Figure 5.3 are not realised.

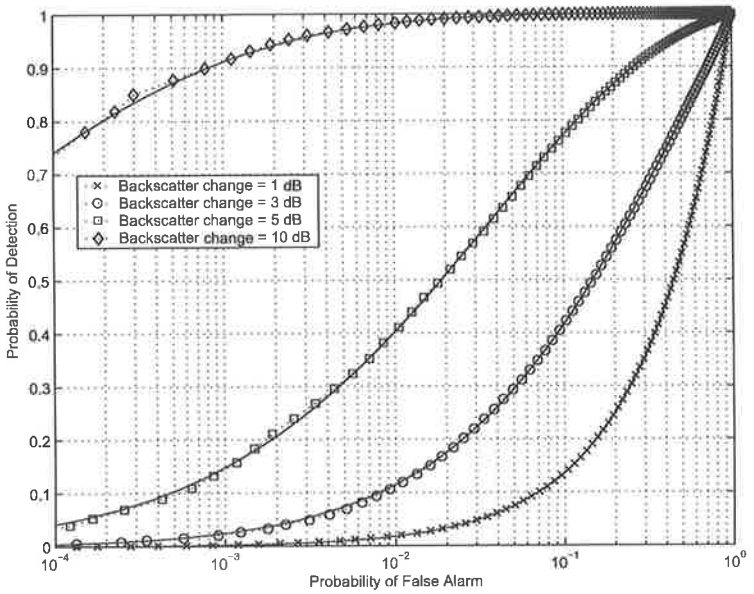


Figure 5.2: Simulated and theoretical ROC curves for the intensity ratio change statistic obtained using an $N = 9$ and mean backscatter power changes of 1, 3, 5 and 10 dB.

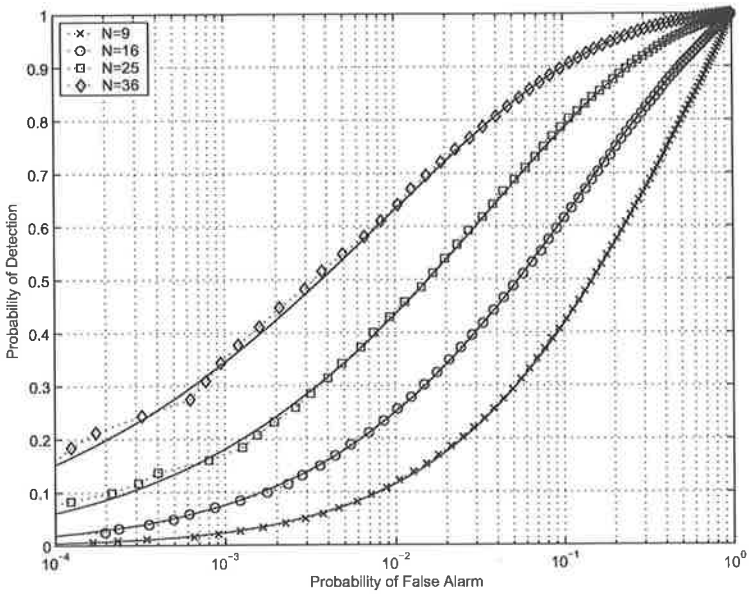


Figure 5.3: Simulated and theoretical ROC curves for the intensity ratio change statistic for a mean backscatter power change of 3 dB and values of N of 9, 16, 25 and 36.

5.3 Change Detection Based on the Cross Correlation Coefficient

The complex cross correlation coefficient of two complex SAR images f and g given by,

$$\gamma exp(j\Phi) = \frac{E\{fg^*\}}{\sqrt{E\{|f|^2\}E\{|g|^2\}}}, \tag{5.22}$$

quantifies the extent to which the scene reflectivities and associated SAR image processors are common between the two transduced images. Provided the image pair are appropriately aperture trimmed and registered the impact of image processor mismatch may be minimised and the cross correlation is a measure of the scene disturbance between the imaging collections.

The interferometric phase Φ, in the absence of any processing aberrations and scene disturbances, is determined by the baseline offset between the primary and repeat pass collections and the terrain topography plus any bulk displacement of the scattering scene between the two data collections. Change detection based on measurement of the phase shift associated with the bulk displacement is called differential interferometry and may be used to monitor small scale surface deformations that typically arise in glaciers or tectonic plate activity such as earthquakes [Zeb00]. For the case of random, zero mean scatterer displacement there is no bulk displacement and change detection is performed on the associated loss in the magnitude of the cross correlation coefficient, γ commonly referred to as the coherence. The coherence takes values in the range 0 to 1 and is sensitive to relatively small changes in the distribution of scatterers within a resolution cell.

For the case when the two channels are jointly Gaussian the image pair f and g may be expressed as a mean backscatter power coefficient modulated by a unit variance complex Gaussian speckle noise,

$$f = \sigma_f(m_r + jm_i), \tag{5.23}$$
$$g = \sigma_g(n_r + jn_i), \tag{5.24}$$

where $m_r + jm_i$ and $n_r + jn_i$ are the unit variance speckle noise components of the two channels and σ_f^2 and σ_g^2 are the mean backscatter powers. In analyzing a single SAR image the information bearing quantity is the mean backscatter, while the speckle noise simply indicates that the resolution cell consists of interfering contributions from a large number of scattering centres. In interferometric analysis however, the speckle noise is the source of the additional information that is provided by the joint processing of an image pair. Substituting (5.23) and (5.24) into (5.22) gives,

$$\begin{aligned} \gamma &= \frac{\sigma_f\sigma_g|E\{(m_r + jm_i)(n_r - jn_i)\}|}{\sigma_f\sigma_g}, \\ &= E\{(m_r + jm_i)(n_r - jn_i)\}. \end{aligned} \tag{5.25}$$

The correlation coefficient is thus statistically independent of the mean backscatter power σ_f^2 and σ_g^2 of the scene and is solely determined by the speckle noise in the two channels. The sensitivity of the coherence as a change statistic arises because the speckle component of the transduced complex reflectivity is dependent on the coherent interference of a large number of complex scattering contributions. Perturbations, of the order of a fraction of a wavelength, in the locations of the scattering contributions leads to significant changes in the phase of each component and hence significantly different coherent summations. Man-made disturbances such as vehicle tracks over a field, can potentially cause significant scatterer displacement causing a total loss in scene coherence. The performance of the coherence has a change statistic however, is degraded by other sources of scene disturbance such wind and rain.

5.3.1 A Temporal Decorrelation Model

The sensitivity of the correlation coefficient to perturbations to the scatterers and their relative arrangement within a resolution cell may be quantified by applying the displacement model proposed in [ZV92] to the distributed clutter scene reflectivity model developed in Chapter 4. Modelling the scene as a surface scattering layer the scene reflectivity may be written as,

$$r_f(x,y,z) = r_1(x,y)\delta(z - h(x,y)), \tag{5.26}$$

for the primary imaging collection and,

$$r_g(x,y,z) = r_2(x,y)\delta(z - h(x,y)), \tag{5.27}$$

for the repeat pass imaging collection. The reflectivity functions r_1 and r_2 consist of an ensemble of N mutually independent, identically distributed complex scatterers given by,

$$r_1(x,y) = \sum_{k=1}^{N} \frac{p_k}{\sqrt{N}} exp(j\phi_k)\delta(x - x_{1_k}, y - y_{1_k}), \tag{5.28}$$

$$r_2(x,y) = \sum_{k=1}^{N} \frac{s_k}{\sqrt{N}} exp(j\theta_k)\delta(x - x_{2_k}, y - y_{2_k}), \tag{5.29}$$

where $p_k exp(j\phi_k)/\sqrt{N}$ and $s_k exp(j\theta_k)/\sqrt{N}$ are the complex reflectivities of the k^{th} scattering contribution in the primary and repeat pass scene's respectively. The scattering locations (x_{1_k}, y_{1_k}) and (x_{2_k}, y_{2_k}) are the locations of the k^{th} scatterer in the primary and repeat pass acquisitions respectively and the scatterers are assumed to be mutually independent and uniformly distributed throughout the scene. Using the PFA imaging equations for straight and level flight developed in Chapter 2, specifically equations (2.49) and (2.59), the primary and repeat pass ground plane images may be written as,

$$f(x,y) = \frac{k_{bw_x} k_{bw_y}}{4\pi^2} \iiint sinc\left(\frac{(x-x')k_{bw_x}}{2\pi}\right) sinc\left(\frac{(y-y'-z'\beta_1)k_{bw_y}}{2\pi}\right) r_f(x',y',z') exp(-j(y'+z'\beta_1)k_{0_g}) dx'dy'dz', \tag{5.30}$$

and,

$$g(x,y) = \frac{k_{bw_x} k_{bw_y}}{4\pi^2} \iiint sinc\left(\frac{(x-x')k_{bw_x}}{2\pi}\right) sinc\left(\frac{(y-y'-z'\beta_2)k_{bw_y}}{2\pi}\right) r_g(x',y',z') exp(-j(y'+z'\beta_2)k_{0_g}) dx'dy'dz', \tag{5.31}$$

respectively. In the above equations $\beta_1 = tan(\psi_1)$ and $\beta_2 = \tan(\psi_2)$ where ψ_1 and ψ_2 are the depression angles at the mid-aperture point in the primary and repeat pass acquisitions. It has been assumed that aperture trimming as been performed so k_{0_g} is the k_y offset of the common aperture of support in the (k_x, k_y) domain and k_{bw_x} and k_{bw_y} are the azimuthal and range spatial frequency dimensions of the common aperture of support. Observe that in the primary and repeat pass image equations a given scatterer at height z in the primary and repeat pass scenes is subject to layover and appears at slightly different locations in the image pair. This misregistration is removed by an appropriate image registration step and the image pair after image registration may be written as,

$$f_r(x,y) = \frac{k_{bw_x} k_{bw_y}}{4\pi^2} \iiint sinc\left(\frac{(x-x')k_{bw_x}}{2\pi}\right) sinc\left(\frac{(y-y')k_{bw_y}}{2\pi}\right) r_f(x',y',z') exp(-j(y'+z'\beta_1)k_{0_g}) dx'dy'dz', \tag{5.32}$$

and,

$$g_r(x,y) = \frac{k_{bw_x}k_{bw_y}}{4\pi^2}\iiint sinc\left(\frac{(x-x')k_{bw_x}}{2\pi}\right) sinc\left(\frac{(y-y')k_{bw_y}}{2\pi}\right) r_g(x',y',z')exp(-j(y'+z'\beta_2)k_{0_g})dx'dy'dz'. \quad (5.33)$$

In the model proposed by Zebker [ZV92] the scattering functions r_f and r_g consist of the same scattering centres i.e., $p_k exp(j\phi_k) = s_k exp(j\theta_k)$ in equations (5.28) and (5.29) however, each scatterer in the repeat pass scene is subject to a random displacement $(\Delta x_k, \Delta y_k, \Delta z_k)$ such that,

$$x_{2_k} = x_{1_k} + \Delta x_k, \quad (5.34)$$
$$y_{2_k} = y_{1_k} + \Delta y_k, \quad (5.35)$$
$$h_k = h_k + \Delta z_k, \quad (5.36)$$

where $h_k = h(x_k, y_k)$. Using this model for the scene reflectivity in a repeat pass acquisition the cross correlation between the registered repeat pass image pair may be written as,

$$\begin{aligned} C &= E\{f_r(x,y)g_r^*(x,y)\}, \\ &= \frac{k_{bw_x}^2 k_{bw_y}^2}{16\pi^2 N} E\left\{\sum_{k=1}^{N}\sum_{l=1}^{N} p_k s_k exp(j(\phi_k - \theta_l))\right. \\ &\quad sinc\left(\frac{k_{bw_x}(x-x_{1_k})}{2\pi}\right) sinc\left(\frac{k_{bw_x}(x-x_{1_l}-\Delta x_l)}{2\pi}\right) \\ &\quad sinc\left(\frac{k_{bw_y}(y-y_{1_k})}{2\pi}\right) sinc\left(\frac{k_{bw_y}(y-y_{1_l}-\Delta y_l-\Delta z_l\beta_2)}{2\pi}\right) \\ &\quad \left. exp(-jk_{0_g}(y_{1_k}+h_k\beta_1-(y_{1_l}+\Delta y_l+\beta_2 h_l+\beta_2\Delta z_l)))\right\}, \end{aligned} \quad (5.37)$$

where the expectation is over the random complex scattering values $r_k exp(j\phi_k), r_l exp(j\theta_l)$, the random scatterer locations (x_{1_k}, y_{1_k}) and also the random displacements $(\Delta x_l, \Delta y_l, \Delta h_l)$. Given that the scattering values and scattering centre locations are all mutually independent the cross correlation may be written as,

$$\begin{aligned} C &= \frac{k_{bw_x}^2 k_{bw_y}^2}{16\pi^2 N}\sum_{k=1}^{N}\left[E\left\{p_k^2\right\} E\left\{sinc\left(\frac{k_{bw_x}(x-x_{1_k})}{2\pi}\right) sinc\left(\frac{k_{bw_x}(x-x_{1_k}-\Delta x_k)}{2\pi}\right)\right.\right. \\ &\quad sinc\left(\frac{k_{bw_y}(y-y_{1_k})}{2\pi}\right) sinc\left(\frac{k_{bw_y}(y-y_{1_k}-\Delta y_k-\Delta z_k\beta_2)}{2\pi}\right) \\ &\quad \left.\left. exp(-jk_{0_g}(\Delta\beta h_k-(\Delta y_k+\beta_2\Delta z_k)))\right\}\right], \end{aligned} \quad (5.38)$$

where $\Delta\beta = \beta_1 - \beta_2$. Furthermore, given that the scatterers are identically and uniformly distributed over the illuminated scene the cross correlation may be simplified to,

$$\begin{aligned} C &= \frac{k_{bw_x}^2 k_{bw_y}^2}{16\pi^2}\left[E\left\{p^2\right\} E\left\{sinc\left(\frac{k_{bw_x}(x-x_1)}{2\pi}\right) sinc\left(\frac{k_{bw_x}(x-x_1-\Delta x)}{2\pi}\right)\right.\right. \\ &\quad sinc\left(\frac{k_{bw_y}(y-y_1)}{2\pi}\right) sinc\left(\frac{k_{bw_y}(y-y_1-\Delta y-\Delta z_k\beta_2)}{2\pi}\right) \\ &\quad \left.\left. exp(-jk_{0_g}(\Delta\beta h-(\Delta y+\beta_2\Delta z)))\right\}\right]. \end{aligned} \quad (5.39)$$

Since the scattering centres are uniformly distributed over the illuminated scene of area A and their locations (x_1, y_1) are independent of the random displacements $(\Delta x, \Delta y, \Delta z)$ the expectation with respect to x_1 and y_1 in (5.39) may be explicitly evaluated as follows,

$$\begin{aligned} & E\left\{ sinc\left(\frac{k_{bw_x}(x-x_1)}{2\pi}\right) sinc\left(\frac{k_{bw_x}(x-x_1-\Delta x)}{2\pi}\right) \right. \\ & \qquad \left. sinc\left(\frac{k_{bw_y}(y-y_1)}{2\pi}\right) sinc\left(\frac{k_{bw_y}(y-y_1-\Delta y_k-\Delta z\beta_2)}{2\pi}\right)\right\} \\ & = \frac{1}{A}\int sinc\left(\frac{k_{bw_x}(x-x_1)}{2\pi}\right) sinc\left(\frac{k_{bw_x}(x-x_1-\Delta x)}{2\pi}\right) dx_1 \\ & \qquad \int sinc\left(\frac{k_{bw_y}(y-y_1)}{2\pi}\right) sinc\left(\frac{k_{bw_y}(y-y_1-\Delta y-\Delta z\beta_2)}{2\pi}\right) dy_1 \\ & = \frac{1}{A} sinc\left(\frac{k_{bw_x}(\Delta x)}{2\pi}\right) sinc\left(\frac{k_{bw_y}(\Delta y+\Delta z\beta_2)}{2\pi}\right), \end{aligned} \tag{5.40}$$

where the effects due to finite scene illumination footprint have been ignored and the integrals with respect to x_1 and y_1 above have been evaluated using standard Fourier transform relations. Defining the mean backscatter power per unit area as $\sigma_p^2 = \frac{1}{A}E\{p^2\}$, the cross correlation C may finally be written as,

$$\begin{aligned} C &= \frac{k_{bw_x}^2 k_{bw_y}^2}{16\pi^2}\sigma_p^2 exp(-jk_{0_g}\Delta\beta h) \\ & \quad E\left\{ sinc\left(\frac{k_{bw_x}(\Delta x)}{2\pi}\right) sinc\left(\frac{k_{bw_y}(\Delta y+\Delta z\beta_2)}{2\pi}\right) exp(jk_{0_g}(\Delta y+\beta_2\Delta z))\right\}, \end{aligned} \tag{5.41}$$

where the expectation in (5.41) is over the random displacements $(\Delta x, \Delta y, \Delta z)$. To proceed and compute the expectation in (5.41) the probability density function of the random displacements $p(\Delta x, \Delta y, \Delta z)$ is required. A physical model for these displacements would require a detailed description of the scattering scene and the interaction of the scene change disturbance with the scene scatterers. Instead Zebker proposes a simple Gaussian probability density function to describe the displacements,

$$p(\Delta x, \Delta y, \Delta z) = \frac{1}{(2\pi)^{\frac{3}{2}}\sigma_x\sigma_y\sigma_z} exp\left(-\frac{\Delta x}{2\sigma_x^2} - \frac{\Delta y}{2\sigma_y^2} - \frac{\Delta z}{2\sigma_z^2}\right). \tag{5.42}$$

Using this PDF to compute the expectation in (5.39) and applying the appropriate normalisation the following expression for the cross correlation coefficient is obtained,

$$\begin{aligned} \gamma &= \frac{|E\{f_r g_r^*\}|}{\sqrt{E\{|f_r|^2\}E\{|g_r|^2\}}}, \\ &= \frac{1}{\sqrt{2\pi}\sigma_x}\int sinc\left(\frac{k_{bw_x}(\Delta x)}{2\pi}\right) exp\left(-\frac{(\Delta x)^2}{2\sigma_x^2}\right) d(\Delta x) \iint sinc\left(\frac{k_{bw_y}(\Delta y+\beta_2\Delta z)}{2\pi}\right) \\ & \qquad \frac{1}{2\pi\sigma_y\sigma_z} exp(-jk_{0_g}(\Delta y+\beta_2\Delta z)) exp\left(-\frac{(\Delta y)^2}{2\sigma_y^2} - \frac{(\Delta z)^2}{2\sigma_z^2}\right) d(\Delta y)d(\Delta z), \end{aligned} \tag{5.43}$$

Equation (5.43) indicates that there are two distinct modes of decorrelation; One associated with the misregistration that arises from the random perturbation and the other associated with the phase

change due to the component of the scatter displacement along the radar's line of sight. The misregistration decorrelation mode is dependent on the size of the random displacements $(\Delta x, \Delta y, \Delta z)$ measured with respect to the resolution cell size given by $\rho_x = \frac{2\pi}{k_{bw_x}}$ in azimuth and $\rho_y = \frac{2\pi}{k_{bw_y}}$ in range and may be written as,

$$\gamma_{rego} = \frac{1}{(2\pi)^{\frac{3}{2}}\sigma_y\sigma_z\sigma_x} \int sinc\left(\frac{k_{bw_x}(\Delta x)}{2\pi}\right) exp\left(-\frac{(\Delta x)^2}{2\sigma_x^2}\right) d(\Delta x) \iint sinc\left(\frac{k_{bw_y}(\Delta y + \beta_2 \Delta z)}{2\pi}\right) exp\left(-\frac{(\Delta y)^2}{2\sigma_y^2} - \frac{(\Delta z)^2}{2\sigma_z^2}\right) d(\Delta y) d(\Delta z). \tag{5.44}$$

The phase dependent decorrelation mode in equation (5.43) depends on the size of the random displacements measured with respect to the radar wavelength $\lambda = \frac{4\pi}{k_{0_g}}$ and may be written as,

$$\gamma_{phase} = \frac{1}{2\pi\sigma_y\sigma_z} \iint exp(-jk_{0_g}(\Delta y + \beta_2 \Delta z)) exp\left(-\frac{(\Delta y)^2}{2\sigma_y^2} - \frac{(\Delta z)^2}{2\sigma_z^2}\right) d(\Delta y) d(\Delta z). \tag{5.45}$$

Considering each of these modes in isolation provides insight into the impact of each on the overall scene coherence under the perturbation model.

Misregistration Decorrelation

The decorrelation arising from the misregistration of the scattering centres takes the form,

$$\gamma_{rego} = \gamma_x \gamma_y, \tag{5.46}$$

where,

$$\gamma_x = \frac{1}{\sqrt{2\pi}\sigma_x} \int sinc\left(\frac{k_{bw_x}\Delta x}{2\pi}\right) exp\left(-\frac{(\Delta x)^2}{2\sigma_x^2}\right) d(\Delta x), \tag{5.47}$$

is the azimuthal misregistration decorrelation and,

$$\gamma_y = \frac{1}{2\pi\sigma_y\sigma_z} \iint sinc\left(\frac{k_{bw_y}(\Delta y + \beta \Delta z)}{2\pi}\right) exp\left(-\frac{(\Delta y)^2}{2\sigma_y^2} - \frac{(\Delta z)^2}{2\sigma_z^2}\right) d(\Delta y) d(\Delta z), \tag{5.48}$$

is the range misregistration decorrelation. The azimuth misregistration decorrelation, γ_x, may be expressed in terms of the error function, $erf(x)$, as follows. Writing the integral expression for γ_x in (5.47) as an integral in the spatial frequency domain gives,

$$\begin{aligned} \gamma_x &= \frac{1}{k_{bw_x}} \int rect\left(\frac{k_x}{k_{bw_x}}\right) exp\left(-\frac{k_x^2\sigma_x^2}{2}\right) dk_x, \\ &= \frac{2}{k_{bw_x}} \int_0^{\frac{k_{bw_x}}{2}} exp\left(-\frac{k_x^2\sigma_x^2}{2}\right) dk_x, \\ &= \frac{\sqrt{2\pi}}{k_{bw_x}\sigma_x} erf\left(\frac{\sigma_x k_{bw_x}}{2\sqrt{2}}\right), \end{aligned} \tag{5.49}$$

where $erf(x)$ is the error function defined by the integral,

$$erf(x) = \frac{2}{\sqrt{\pi}} \int_0^x exp(-w^2) dw. \tag{5.50}$$

The resolution cell size corresponding to the bandwidth k_{bw_x} is $\rho_x = 2\pi/k_{bw_x}$, thus the azimuth decorrelation may be written as,

$$\gamma_x = \frac{\rho_x}{\sqrt{2\pi}\sigma_x} erf\left(\frac{\sigma_x \pi}{\sqrt{2}\rho_x}\right). \tag{5.51}$$

The range misregistration decorrelation, γ_y, may be evaluated similarly. Observe from (5.48) that $\gamma_y = E\{sinc(k_{bw_y}(\Delta y + \beta \Delta z)/(2\pi))\}$ where the expectation is over the random variables Δy and Δz. Since Δy and Δz are mutually independent, zero mean Gaussian random variables with variances σ_y^2 and σ_z^2, the random variable s, defined by $s = \Delta y + \beta_2 \Delta z$, is also a zero mean Gaussian random variable with variance $\sigma_s^2 = \sigma_y^2 + \beta_2^2 \sigma_z^2$. The range misregistration decorrelation may therefore be written as, $\gamma_y = E\{sinc(k_{bw_y} s/(2\pi))\}$, where the expectation is now over s, i.e.,

$$\begin{aligned} \gamma_y &= \frac{1}{\sqrt{2\pi}\sigma_s} \int sinc\left(\frac{k_{bw_y} s}{2\pi}\right) exp\left(-\frac{s^2}{2\sigma_s^2}\right) ds, \\ &= \frac{\sqrt{2\pi}}{k_{bw_y}\sigma_s} erf\left(\frac{\sigma_s k_{bw_y}}{2\sqrt{2}}\right), \\ &= \frac{\rho_y}{\sqrt{2\pi}\sigma_s} erf\left(\frac{\sigma_s \pi}{\sqrt{2}\rho_y}\right), \end{aligned} \tag{5.52}$$

and $\rho_y = 2\pi/k_{bw_y}$ is the range resolution. Figure 5.4 shows the misregistration component along a single spatial dimension of the cross correlation coefficient where the standard deviation, or equivalently the RMS value, of the Gaussian displacement has been normalised to the image resolution cell size. Observe that for a RMS displacement of 0.6 of a resolution cell size the image pair are practically uncorrelated with the correlation coefficient approximately equal to 0.1. For RMS displacements of up to 0.04 of a resolution cell size (0.6 cm for a 0.15 m azimuth resolution wide-angle spotlight collection) the cross correlation coefficient is greater than 0.9.

Phase Component of Decorrelation

The decorrelation arising from the phase shift associated with each scatterer under the perturbation model takes the form,

$$\gamma_{phase} = \frac{1}{2\pi\sigma_y\sigma_z} \iint exp(-jk_{0_g}(\Delta y + \beta_2 \Delta z)) exp\left(-\frac{(\Delta y)^2}{2\sigma_y^2} - \frac{(\Delta z)^2}{2\sigma_z^2}\right) d(\Delta y) d(\Delta z). \tag{5.53}$$

This integral has the form of a Fourier transform and an analytic solution may be obtained and is given by [ZV92],

$$\gamma_{phase} = exp\left(-\frac{1}{2}k_{0_g}^2 \sigma_y^2\right) exp\left(-\frac{1}{2}k_{0_g}^2 \beta_2^2 \sigma_z^2\right). \tag{5.54}$$

The spatial frequency k_{0_g}, which is the offset of the common aperture of support of the image pair in the (k_x, k_y) domain along the k_y axis, may be written in terms of an effective radar wavelength λ_{eff} and the depression angle of the repeat pass collection ψ_2,

$$k_{0_g} = \frac{4\pi}{\lambda_{eff}} \cos(\psi_2). \tag{5.55}$$

Substituting (5.55) into (5.54) gives,

$$\gamma_{phase} = exp\left(-\frac{1}{2}\left(\frac{4\pi}{\lambda_{eff}}\right)^2\left(\sigma_y^2\cos^2(\psi_2) + \sigma_z^2\sin^2(\psi_2)\right)\right). \tag{5.56}$$

Figure 5.5 shows the cross correlation coefficient in (5.56) as a function of the RMS displacement, normalised by the radar wavelength, for a Gaussian random displacement in range only (i.e., $\sigma_z^2 = 0$). The cross correlation coefficient has been computed for depression angles of 15 and 45 degrees which span the range of depression angles commonly used in airborne SAR imaging scenarios. It can be seen that total correlation of the image pair occurs for an RMS displacement of approximately 20 percent of the radar wavelength. For an X-band radar with a wavelength of the order of 3.2 cm this corresponds to a standard deviation of 0.64 cm. Thus for an X-band radar used in a wide-angle spotlight collection, with azimuth resolution of 0.15 m the dominant decorrelation will be that associated with the phase component of the perturbation model.

Scene disturbances that cause a change in the arrangement of scatterers over a localised area in a scene may therefore be detectable as a loss in the cross correlation over that local area. In particular at X-band, where λ_{eff} is of the order of 3 cm man-made disturbances such as vehicle tracks across a grass field can potentially cause significant scatterer displacement and hence a complete loss in coherence without any appreciable change in the mean backscatter power of the scene. The detectability of such man-made disturbances however may be compromised by other sources of temporal disturbance such as wind and rain. Such disturbances can cause a change in the complex reflectivity of the scattering contributions within resolution cells as well as random perturbations in the scatterer spatial locations leading to an overall loss in the scene coherence. Change detection using the scene coherence thus relies on adequate contrast between the man-made disturbance and other sources of temporal decorrelation.

The loss in coherence predicted by the perturbation model in [ZV92] is somewhat pessimistic as it assumes that all scattering contributions are subject to a random displacement. In [HUA95] a more realistic model is considered in which the scattering contributions are divided into stable and unstable components. In this case only the unstable contributions are subject to a random perturbation causing scene decorrelation. The overall scene coherence is therefore determined by the decorrelation of the unstable scatterers and the relative mean backscatter power associated with the two scattering types. A further point is that the physical structure of the vegetation in a scene will generally restrict the free and independent movement of the scattering centres in the three orthogonal directions (x, y, z) thereby limiting the validity of the perturbation model.

Equation (5.56) indicates that the decorrelation is determined by the component of the scatter displacement along the radar's line of sight direction. Thus for small depression angles, less than 45 degrees, typically used in airborne SAR imaging scenarios the cross correlation is more sensitive to displacements in the range direction than changes in the vertical height direction. For a typical change detection scene consisting of an open field of grass vegetation with some mean height this suggests that the scene coherence will be more sensitive to wind decorrelation which will generally cause perturbations in a horizontal direction aligned with the wind velocity vector. The sensitivity of the cross correlation to wind effects may reduced if larger depression angles are used.

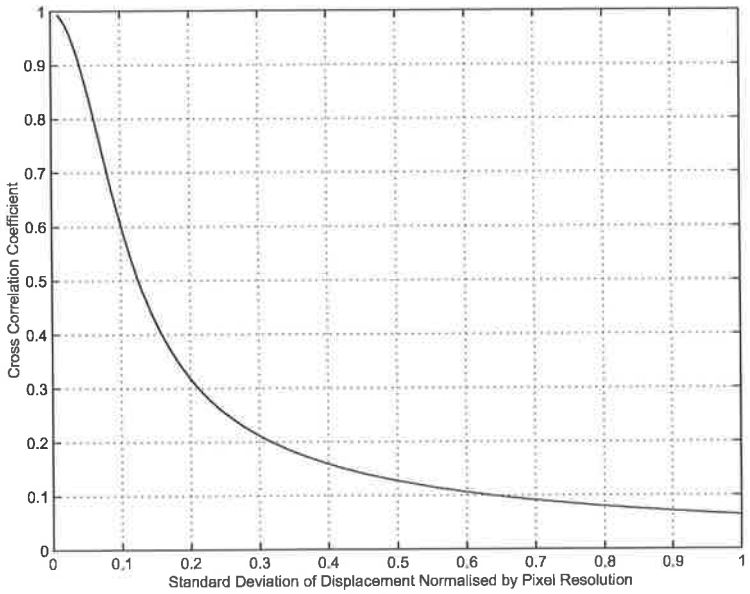


Figure 5.4: Misregistration component of the cross correlation coefficient for an interferometric image pair where the scatterers in the scene have been subject to a random Gaussian displacement in the interval between imaging collections. The standard deviation, or equivalently the RMS value, of the random displacement has been normalised to the image resolution cell size.

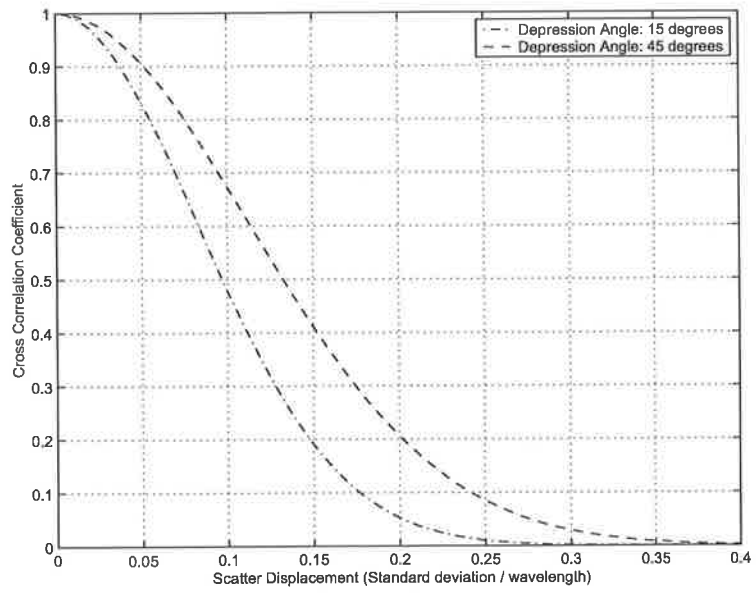


Figure 5.5: Phase component of the cross correlation coefficient of an interferometric image pair where the scatterers in the scene have been subject to a random Gaussian displacement in range and imaged with depression angles of 15 and 45 degrees. The RMS displacement has been normalised to the effective radar wavelength.

5.3.2 Sample Cross Correlation Coefficient Change Statistic

In the previous section it was shown that regions of man-made scene disturbance may be detected as areas of very low coherence against undisturbed areas that may be characterised by some degree of partial coherence. A simple threshold change detector based on the sample coherence evaluated over an N pixel window,

$$\hat{\gamma} = \frac{|\sum_{k=1}^{N} f_{r_k} g_{r_k}^*|}{\sqrt{\sum_{k=1}^{N} |f_{r_k}|^2 \sum_{k=1}^{N} |g_{r_k}|^2}}, \tag{5.57}$$

may be used to detect the regions of low coherence. The performance of this detector however, is dependent on the statistical properties of the sample coherence and the contrast in coherence between the disturbed low coherence areas and the unchanged partial coherence areas.

Sample Coherence Statistics

The density function of the sample coherence is given by [TL96],

$$\begin{aligned} p(\hat{\gamma}|\gamma, N) &= 2(N-1)(1-\gamma^2)^N \hat{\gamma}(1-\hat{\gamma}^2)^{(N-2)} {}_2F_1(N, N; 1; \gamma^2\hat{\gamma}^2), \\ &= \frac{2(1-\gamma^2)^N \hat{\gamma}(1-\hat{\gamma}^2)^{(N-2)}}{\Gamma(N)\Gamma(N-1)} \sum_{l=0}^{\infty} \left[\frac{\Gamma(N+l)}{\Gamma(l+1)}\right]^2 (\gamma\hat{\gamma})^{2l}, \end{aligned} \tag{5.58}$$

where ${}_2F_1$ is the Gauss hypergeometric function. The density function is dependent on the underlying scene coherence γ and the number of independent pixels N used in the estimation window. Insight into the nature of this dependence may be obtained by computing the mean of the sample coherence. The m^{th} order moments of the sample coherence have been derived from (5.58) [OQ98] and are given by,

$$\begin{aligned} E\{\hat{\gamma}^m\} &= \int_0^1 \hat{\gamma}^m p(\hat{\gamma}|\gamma) d\hat{\gamma}, \\ &= (1-\gamma^2)^N \Gamma(N) \frac{\Gamma\left(\frac{m}{2}+1\right)}{\Gamma\left(\frac{m}{2}+N\right)} {}_3F_2\left(\frac{m}{2}+1, N, N; 1, \frac{m}{2}+N; \gamma^2\right). \end{aligned} \tag{5.59}$$

The mean of the sample coherence is subsequently given by,

$$E\{\hat{\gamma}\} = (1-\gamma^2)^N \Gamma(N) \frac{\Gamma\left(\frac{1}{2}+1\right)}{\Gamma\left(\frac{1}{2}+N\right)} {}_3F_2\left(\frac{1}{2}+1, N, N; 1, \frac{1}{2}+N; \gamma^2\right), \tag{5.60}$$

where ${}_aF_b$ is the generalised hypergeometric function [AS72]. Figure 5.6 shows the mean of the sample coherence $\hat{\gamma}$ as a function of the true coherence γ for various values for N. From Figure 5.6 it is clear that for low values of underlying coherence the sample coherence is significantly biased towards higher values. This reduces the contrast of the sample coherence map especially in regions of differing low coherence.

In [TLBV99] Touzi investigates techniques for the unbiased estimation of coherence. In particular he shows that any arbitrary function of the sample coherence leads to a biased estimate of the coherence and improvements in the bias may only be obtained by appropriate averaging over a larger sample size. An alternative approach, originally proposed in [FG67], is to use the known density

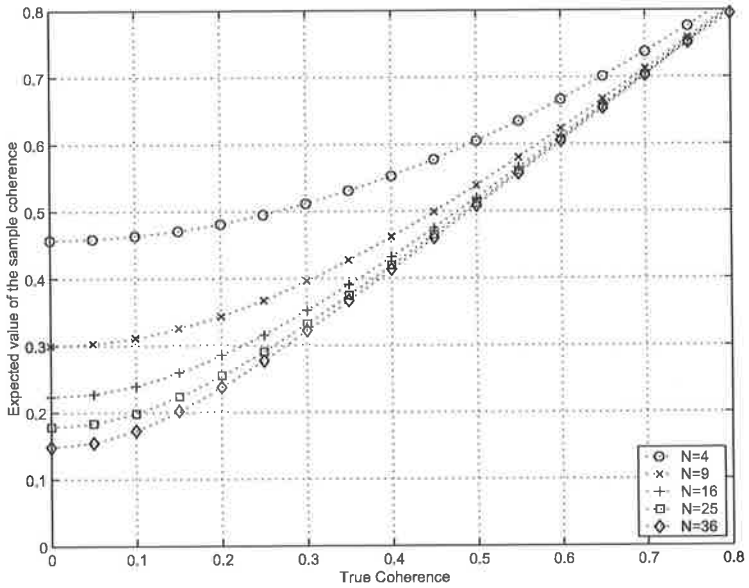


Figure 5.6: Expected value of the coherence estimate plotted against the underlying true coherence for a range of sample estimate sizes.

function of the sample coherence and find the value of coherence that maximises the a-posteriori conditional probability of observing $\hat{\gamma}$. Given the density function of the underlying coherence $p(\gamma)$ the a-posteriori density is given by,

$$p(\gamma|\hat{\gamma}, N) = \frac{p(\hat{\gamma}|\gamma, N)p(\gamma)}{\int_0^1 p(\hat{\gamma}|\gamma, N)p(\gamma)d\gamma}. \tag{5.61}$$

Assuming γ is uniformly distributed then (5.61) may be simplified to,

$$p(\gamma|\hat{\gamma}, N) = \frac{p(\hat{\gamma}|\gamma, N)}{\int_0^1 p(\hat{\gamma}|\gamma, N)d\gamma}, \tag{5.62}$$

and the value of γ that maximises this function gives the maximum likelihood estimate of the true coherence. In order to obtain a well defined maximum and hence a good quality estimate the sample size N generally must be large.

A similar approach recently proposed [Gie01b] uses the statistics of the sample interferometric phase to derive a novel maximum likelihood estimator of the true coherence for the specific case of Along-Track Interferometry (ATI). Given N independent measurements of the interferometric phase within a locally stationary region then the maximum likelihood estimator of the coherence γ is,

$$\hat{\gamma} = \max_{\gamma < 1} \sum_{k=1}^{N} log\left(p(\hat{\Phi}|\gamma)\right), \tag{5.63}$$

where $p(\hat{\Phi}|\gamma)$ is the first order density function of a N sample interferometric phase estimate derived under the assumption of jointly Gaussian statistics for the interferometric image pair [LMH94],

$$p(\hat{\Phi}|\gamma) = \frac{\Gamma\left(N+\frac{1}{2}\right)(1-\gamma^2)^N\gamma\cos(\hat{\Phi})}{2\sqrt{\pi}\Gamma(N)(1-\gamma^2)^{N+\frac{1}{2}}} + \frac{(1-(\gamma\cos(\hat{\Phi}))^2)^N}{2\pi}{}_2F_1\left(N, 1; \frac{1}{2}; (\gamma\cos(\hat{\Phi}))^2\right). \tag{5.64}$$

In (5.64) it has been assumed that for properly calibrated ATI data the true interferometric phase is zero. In [Gie01b] Gierull shows that the MLE in (5.63) is unbiased even for small values of coherence and small sample sizes. Furthermore the technique may be applied to a broad range of scenes as the phase density function has been shown to apply even in highly heterogeneous, textured clutter. The technique may not be applied directly to repeat pass interferometric data however, as such data is invariably collected with a spatial baseline offset between the collections resulting in a non-zero interferometric phase. A further disadvantage of the technique is that the phase function is highly non linear and the calculation and maximisation of (5.63) is numerically difficult and computationally intensive.

Undisturbed Scene Partial Coherence

The degree of partial coherence characterising the undisturbed regions will depend on the nature of the distributed target, the duration between imaging passes and the severity of the temporal sources of decorrelation as well as the sensor and processing parameters. The temporal decorrelation of a variety of different target types, sensor bands and repeat pass delays have been studied in the literature [HUA95], [AH93], [TLBV99], [CKW95] and [RS02].

The European Remote Sensing (ERS) spaceborne SAR instrument has provided a wealth of high quality repeat pass data sets to facilitate the measurement of coherence over a range of target types and temporal baselines. The ERS SAR operates at C-band 15.3 MHz (λ=5.6 cm) with VV polarisation at a mid-swath incidence angle of 23 degrees. The nominal resolution of the system is 20 m in range by 6 m in azimuth. The precise orbit control of the ERS satellites allows repeat pass observations with spatial baseline separations of a few hundred metres to be obtained with a temporal baseline of 35 days. In the ERS-1,2 tandem mission an additional satellite ERS-2 was flow in conjunction with ERS-1 allowing interferometric pairs with 1 day separation to be collected.

In [CKW95] Corr examined the coherence of tandem ERS SAR images of forested and cultivated scenes in south east England. Temporal baselines of 3, 6, 12, 21 and 69 days were obtained over the scenes during summer and a 35 day separation was recorded during winter. For temporal baselines of 35 days or more the coherence of the woodland was found to be around 0.2 irrespective of the season while the 3 day coherence was reported to be approximately 0.4. Over the cultivated fields a high scene coherence of approximately 0.9 was obtained in the 3 day coherence map and this decreased slowly to around 0.4 in the case of the 69 day temporal separation. In summer it was found the 35 day coherence was only 0.2 owing to the rapid growth of the field crops. These observations are in broad agreement with numerous other analyses reported in the literature [HUA95], [AH93] over similar target types.

Results from a limited number of airborne repeat pass experiments have been published in the literature. Generally the use of airborne systems is restricted to limited measurement campaigns thus, unlike spaceborne systems, extensive historical data sets are not available. The DLR E-SAR system [Hor96] however has collected multi-polarimetric repeat pass data at L-band over a test site with temporal baselines ranging from 1 hour, to several months and almost 1 year [RS02]. It is found that the L-band response is less affected by disturbances in the vegetation such as tree leaves and grass. Instead stable dominant scattering contributions from bare soil and ground-stem interaction in woodland provide appreciable coherence over temporal baselines of 1 year.

Detector Performance

The detection performance of the sample coherence change statistic may be quantified by comparing the probability density functions of the change statistic for changed and unchanged scenarios.

Figure 5.7 shows the density functions associated a scene characterised by an underlying coherence of $\gamma_{unchanged} = 0.6$ (this being the aggregate decorrelation attributed to environmental effects, processing mismatch and system noise) and a man-made disturbance characterised by a total loss in coherence $\gamma_{changed} = 0$.

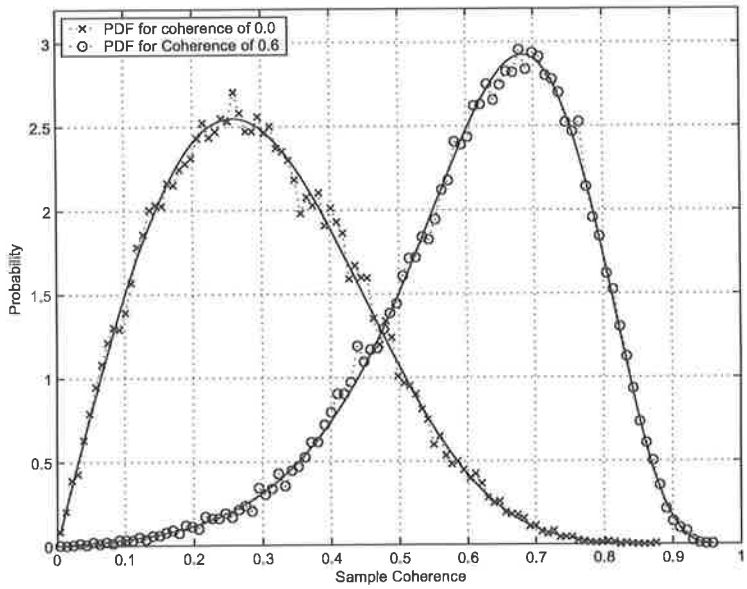


Figure 5.7: Simulated and theoretical probability density functions of the sample coherence corresponding to a true underlying coherence of 0 and 0.6. The sample estimate has been obtained by averaging over $N = 9$ independent pixel pairs.

A simple threshold detector applied to the sample coherence may be used distinguish between the changed and unchanged regions in the scene. The performance of the detector may be evaluated by computing the associated ROC curve which indicates, for a given detection threshold T, the probability of detecting a changed pixel P_d and the corresponding probability of a false alarm P_{fa},

$$P_d = \int_0^T p(\hat{\gamma}|\gamma = \gamma_{changed}) d\hat{\gamma}, \tag{5.65}$$

$$P_{fa} = \int_0^T p(\hat{\gamma}|\gamma = \gamma_{unchanged}) d\hat{\gamma}. \tag{5.66}$$

Substituting the density function given in (5.58) into (5.65) and (5.66) gives the following series solution for the probability of detection and false alarm as a function of the number of samples N, $\gamma_{unchanged}$ and $\gamma_{changed}$,

$$P = \frac{2(N-1)(1-\gamma^2)^N}{\Gamma(N)\Gamma(N-1)} \sum_{k=0}^{N-2} \binom{N-2}{k} (-1)^{N-2-k} \sum_{l=0}^{\infty} \left[\frac{\Gamma(N+l)}{\Gamma(l+1)}\right]^2 \gamma^{2l} \frac{T^{2N+2l-2-2k}}{2N+2l-2-2k}, \tag{5.67}$$

where,

$$P = \begin{cases} P_d, & \text{for } \gamma = \gamma_{changed}, \\ P_{fa}, & \text{for } \gamma = \gamma_{unchanged}. \end{cases} \tag{5.68}$$

In the case when $\gamma_{changed} = 0$ then $P = P_d$ reduces to the following form,

$$P = 2(N-1)^2 \sum_{k=0}^{N-2} \left(\begin{array}{c} N-2 \\ k \end{array} \right) (-1)^{N-2-k} \frac{T^{2N-2-2k}}{2N-2-2k}. \tag{5.69}$$

Figure 5.8 shows the ROC curves for $N = 9$, $\gamma_{changed} = 0$ and $\gamma_{unchanged}$ = 0.45, 0.6, 0.75 and 0.9. A comparison of Figure 5.8 with the ROC curve for the backscatter ratio change statistic in Figure 5.2 shows that for an estimation window size of $N = 9$ pixels and a $P_d = 0.7$ a change in the mean backscatter power of 5 dB and $\gamma_{unchanged} = 0.6$ give a similar false alarm rate of 0.07.

The detection performance of the sample coherence change statistic may be improved by increasing the estimation window size. Figure 5.9 shows the ROC curves for $\gamma_{unchanged} = 0.6$ and $\gamma_{changed} = 0.0$ and increasing values of N. It can be seen that increasing the estimation window size from 9 to 16 pixels reduces the false alarm rate by an order of magnitude. The window size however must be commensurate with the size of the scene disturbances to be detected otherwise the sample coherence contains contributions from changed and unchanged pixels.

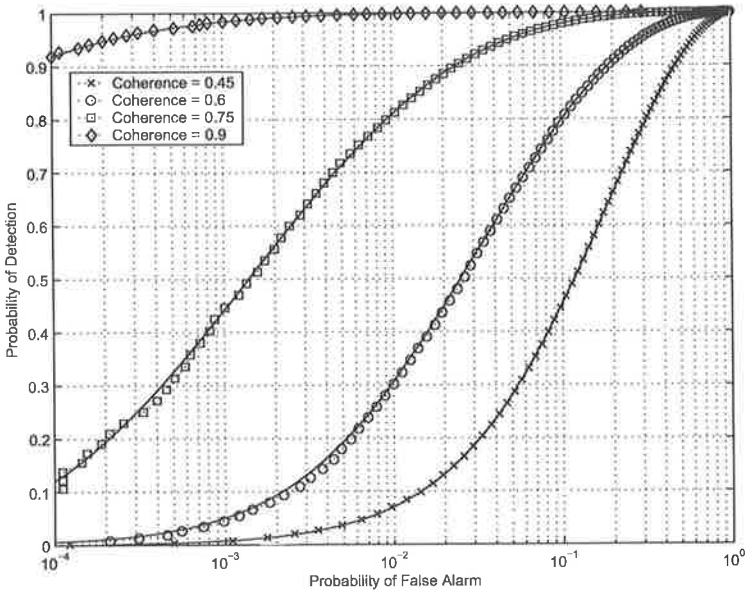


Figure 5.8: Simulated and theoretical ROC curves for sample coherence change statistic obtained with an unchanged scene partial coherence $\gamma_{unchanged}$ = 0.45, 0.6, 0.75 and 0.9, a changed scene coherence of $\gamma_{changed}$ = 0 and an estimation window size of $N = 9$ independent pixels

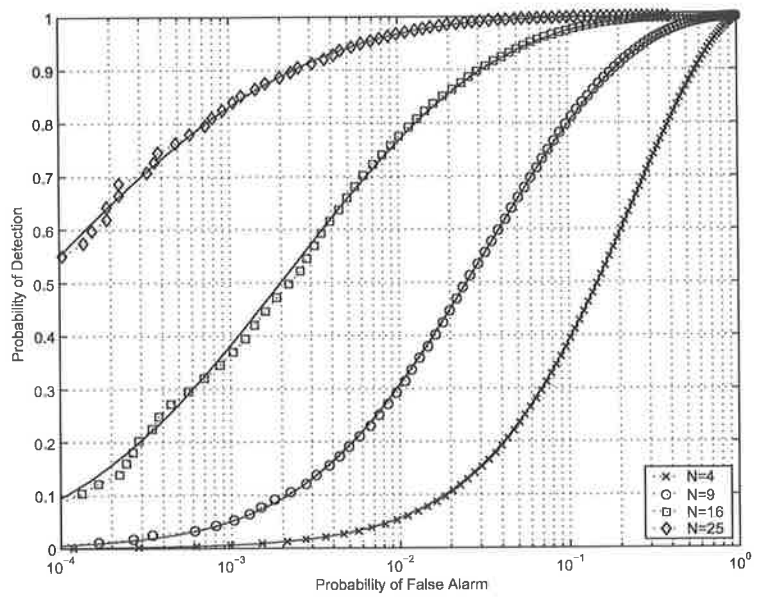


Figure 5.9: Simulated and theoretical ROC curves for sample coherence change statistic obtained with an unchanged scene partial coherence of $\gamma_{unchanged}$ = 0.6, a changed scene coherence of $\gamma_{changed}$ = 0 and estimation window sizes of N =4, 9, 16 and 25 independent pixels

5.4 Other Coherence Estimators

The sample coherence of a pair of complex jointly Gaussian random variables $\underline{X} = [f_r + jf_i, g_r + jg_i]^T$ is a maximum likelihood estimator of the true coherence [Goo63]. From Section 4.4.2 however, it was shown that for a homogeneous distributed scene not only are a SAR interferometric image pair jointly Gaussian but they are also circular and satisfy the relations, (See Appendix C),

$$E\{\underline{X}_r\underline{X}_r^T\} = E\{\underline{X}_i\underline{X}_i^T\}, \tag{5.70}$$
$$E\{\underline{X}_r\underline{X}_i^T\} = -E\{\underline{X}_i\underline{X}_r^T\}, \tag{5.71}$$

where $\underline{X}_R = [f_r, g_r]^T$ and $\underline{X}_i = [f_i, g_i]^T$. Under these more restrictive conditions some alternative, though suboptimal, estimators of coherence may be derived which are based on a reduced set of the four variables describing the transduced complex reflectivity of an image pixel pair. This allows coherency based change detection to be performed with reduced data storage requirements without the need for full complex imagery, albeit with a degraded detection performance.

5.4.1 Intensity Correlation

Writing the transduced scene reflectivity of the interferometric image pair as,

$$f = \sigma_f(m_r + jm_i), \tag{5.72}$$
$$g = \sigma_g(n_r + jn_i), \tag{5.73}$$

where the mean backscatter coefficient of the distributed target is σ_f^2 and σ_g^2 for the primary and repeat pass images respectively and $m_r + jm_i$ and $n_r + jn_i$ are zero mean, circular, complex Gaussian processes with unit variance describing the image speckle. The correlation of the two intensity channels $I_f = |f|^2$ and $I_g = |g|^2$ is given by,

$$\begin{aligned} R_{intensity} &= E\{(I_f - E\{I_f\})(I_g - E\{I_g\})\}, \\ &= E\{I_fI_g\} - E\{I_f\}E\{I_g\}, \\ &= \sigma_f^2\sigma_g^2(E\{|m|^2|n|^2\} - E\{|m|^2\}E\{|n|^2\}), \end{aligned} \tag{5.74}$$

where $m = m_r + jm_i$ and $n = n_r + jn_i$. Normalising the intensity correlation (5.74) by the variance of each intensity channel gives the intensity correlation coefficient,

$$\begin{aligned} \gamma_{intensity} &= \frac{R_{intensity}}{\sqrt{Var\{I_f\}Var\{I_g\}}}, \\ &= \frac{E\{I_fI_g\} - E\{I_f\}E\{I_g\}}{\sqrt{(E\{I_f^2\} - E\{I_f\}^2)(E\{I_g^2\} - E\{I_g\}^2)}}, \\ &= \frac{\sigma_f^2\sigma_g^2(E\{|m|^2|n|^2\} - E\{|m|^2\}E\{|n|^2\}}{\sqrt{(E\{I_f^2\} - E\{I_f\}^2)(E\{I_g^2\} - E\{I_g\}^2)}}, \end{aligned} \tag{5.75}$$

$$= E\{|m|^2|n|^2\} - E\{|m|^2\}E\{|n|^2\}, \tag{5.76}$$

which is solely determined by the correlation of the speckle components m and n of the two channels. Since m and n are zero mean Gaussian random variables the fourth order cross correlation $E\{|m|^2|n|^2\}$ may be expressed in terms of the second order moments of m and n [Ree62],

$$E\{|m|^2|n|^2\} = E\{mm^*\}E\{nn^*\} + E\{mn^*\}E\{m^*n\} + E\{mn\}E\{m^*n^*\}, \tag{5.77}$$

and using the circular Gaussian property that $E\{mn\} = 0$ and $E\{m^*n^*\} = 0$ then

$$E\{|m|^2|n|^2\} = E\{|m|^2\}E\{|n|^2\} + |E\{mn^*\}|^2. \tag{5.78}$$

Substituting (5.78) into the expression for the intensity correlation coefficient (5.76) gives,

$$\gamma_{intensity} = |E\{mn^*\}|^2. \tag{5.79}$$

which is simply the magnitude square of the complex cross correlation coefficient (see equation (5.25)) thus,

$$\gamma_{intensity} = |\gamma|^2. \tag{5.80}$$

The intensity correlation coefficient may be used as an alternative measure of the complex correlation coefficient provided the two interferometric channels have circular Gaussian statistics.

Assuming the random processes f and g are locally stationary and also ergodic in mean then the ensemble averaging in (5.75) may be replaced with spatial averaging to provide a sample estimate of the intensity correlation coefficient. Given a local neighbourhood of N samples $|f_k|^2$ and $|g_k|^2$ where $k = 1 \ldots N$ the sample intensity correlation coefficient is given by,

$$\hat{\gamma}_{intensity} = \frac{\sum_{k=1}^{N} I_{f_k} I_{g_k} - \sum_{k=1}^{N} I_{f_k} \sum_{k=1}^{N} I_{g_k}}{\sqrt{(\sum_{k=1}^{N} I_{f_k}^2 - (\sum_{k=1}^{N} I_{f_k})^2)}\sqrt{(\sum_{k=1}^{N} I_{g_k}^2 - (\sum_{k=1}^{N} I_{g_k})^2)}}. \tag{5.81}$$

It should be noted that the intensity correlation coefficient is a value on the range $[-1, 1]$ as it evaluates the correlation between two real quantities.

Figure 5.10 shows the probability density function, obtained via simulation, of the intensity correlation coefficient for true underlying coherence values of 0 and 0.6 and $N = 9$. Observe that the two density functions shown in Figure 5.10 exhibit a significantly greater degree of overlap compared to the corresponding complex sample correlation coefficient density functions shown in Figure 5.7. The probability of detection and false alarm for a simple threshold detector applied to the sample intensity correlation coefficient are defined as,

$$P_d = \int_{-1}^{T} p(\hat{\gamma}|\gamma = \gamma_{changed}) d\hat{\gamma}, \tag{5.82}$$

$$P_{fa} = \int_{-1}^{T} p(\hat{\gamma}|\gamma = \gamma_{unchanged}) d\hat{\gamma}. \tag{5.83}$$

Figure 5.11 shows simulated ROC curves indicating the probability of detection and false alarm for $\gamma_{changed} = 0$ and $\gamma_{unchanged} = 0.45$, 0.6, 0.75 and 0.9 using $N = 9$ independent pixel pairs. The performance of the intensity correlation coefficient change statistic is significantly worse than the complex correlation coefficient. For $\gamma_{unchanged} = 0.6$ at a probability of detection of 0.7 the false alarm rate is 0.4 compared to 0.06 for the complex correlation coefficient.

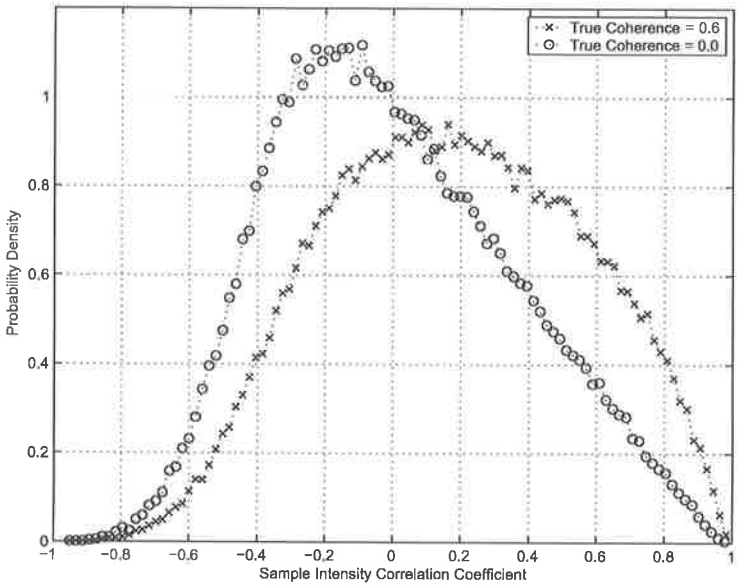


Figure 5.10: Simulated probability density functions for the sample intensity correlation coefficient for underlying true coherence values of 0.6 and 0.0 obtained using an estimation window size of $N = 9$ independent pixels.

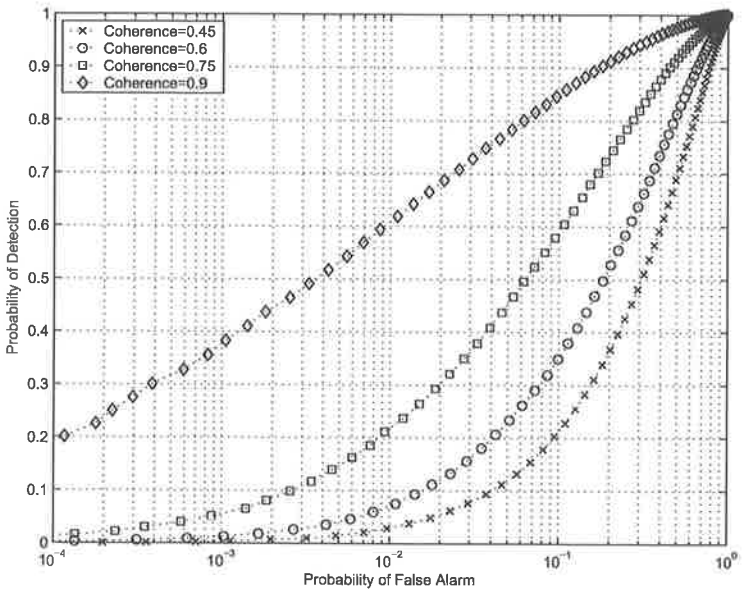


Figure 5.11: Simulated ROC curves for the sample intensity correlation coefficient change statistic obtained using $N = 9$ and $\gamma_{changed} = 0.0$ and $\gamma_{unchanged} = 0.45$, 0.6, 0.75 and 0.9.

5.4.2 The Multiple Correlation Coefficient

The intensity correlation coefficient provides an estimate of the scene coherence only and the interferometric phase is lost. By considering three of the available four channels an estimate of the complex correlation coefficient can be derived. The complex correlation coefficient may be written in the form,

$$\begin{aligned}\gamma exp(j\Phi) &= \frac{E\{fg^*\}}{\sqrt{E\{|f|^2\}E\{|g|^2\}}}, \\ &= \frac{\sigma_f\sigma_g E\{(m_r+jm_i)(n_r-jn_i)\}}{\sigma_f\sigma_g}, \\ &= E\{m_rn_r\}+E\{m_in_i\}+j\left(E\{m_in_r\}-E\{m_rn_i\}\right). \end{aligned} \tag{5.84}$$

For f and g having circular Gaussian statistics $E\{m_rn_r\} = E\{m_in_i\}$ and $E\{m_in_r\} = -E\{m_rn_i\}$ and so,

$$\begin{aligned}\gamma exp(j\Phi) &= 2E\{m_rn_r\}+j2E\{m_rn_i\}, \\ &= \gamma_{rr}+j\gamma_{ri}, \end{aligned} \tag{5.85}$$

where $\gamma_{rr} = 2E\{m_rn_r\}$ and $\gamma_{ri} = 2E\{m_rn_i\}$. The complex correlation coefficient may thus be written in terms of three of the four available channels. In particular the in-phase component of the cross correlation coefficient is given by the correlation between the in-phase components of the primary and repeat pass images. Whilst the quadrature component is given by the correlation between the in-phase and quadrature phase of the primary and repeat pass images respectively. The corresponding sample estimate obtained by averaging over a local neighbourhood of N pixels is given by,

$$\begin{aligned}\hat{\gamma}_{multi}exp(j\hat{\Phi}_{multi}) &= \hat{\gamma}_{rr}+j\hat{\gamma}_{ri}, \\ &= \frac{\sum_{k=1}^{N} f_{r_k}g_{r_k}}{\sqrt{\sum_{k=1}^{N} f_{r_k}^2 \sum_{k=1}^{N} g_{r_k}^2}}+j\frac{\sum_{k=1}^{N} f_{r_k}g_{i_k}}{\sqrt{\sum_{k=1}^{N} f_{r_k}^2 \sum_{k=1}^{N} g_{i_k}^2}}. \end{aligned} \tag{5.86}$$

The statistic,

$$|\gamma_{multi}|^2 = \hat{\gamma}_{rr}^2+\hat{\gamma}_{ri}^2, \tag{5.87}$$

is a value in the range $[0,2]$ and may be used as a change statistic to distinguish between areas of differing coherence. Figure 5.12 shows simulation results indicating the ROC performance of this change statistic where $\gamma_{changed} = 0$ and $\gamma_{unchanged} = 0.45$, 0.6, 0.75 and 0.9. Comparing Figures 5.12 and 5.11 it is observed that the performance of the sample multiple correlation coefficient is marginally better than that of the sample intensity correlation coefficient. For $\gamma_{unchanged} = 0.6$ at a probability of detection of 0.7 the probability of false alarm for the sample coherence, multi-correlation coefficient and the intensity correlation coefficient are 0.06, 0.1 and 0.18 respectively.

Unlike the intensity correlation change statistic the multiple correlation estimate is statistically independent of any texture modulating variable and thus is suitable for a broad range of scenes. Furthermore in [OP58] an unbiased estimator of the cross correlation between two real Gaussian processes based on the sample correlation coefficient has been found,

$$G(\hat{\gamma}) = \hat{\gamma}_2F_1\left(\frac{1}{2},\frac{1}{2};\frac{N-2}{2};1-\hat{\gamma}^2\right), \tag{5.88}$$

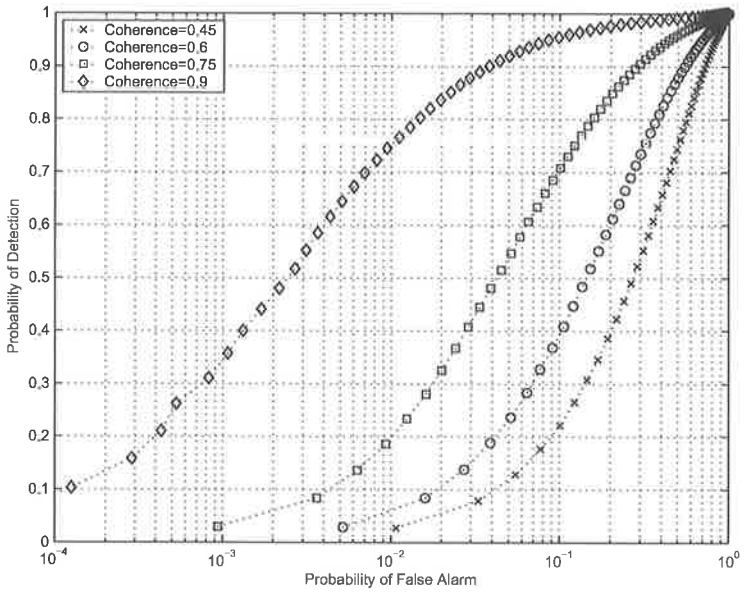


Figure 5.12: Simulated ROC curves for multiple correlation coefficient change statistic obtained by averaging over $N = 9$ independent pixels and $\gamma_{changed}$=0.0 and $\gamma_{unchanged}$ = 0.45, 0.6, 0.75 and 0.9 assuming the interferometric phase is zero.

where ${}_2F_1$ is the hypergeometric function. In [TLBV99] Touzi proposes applying (5.88) to $\hat{\gamma}_{rr}$ and $\hat{\gamma}_{ri}$ to obtain an unbiased estimate of the scene coherence. The multiple correlation coefficient change statistic (5.87) however suffers from a modulation arising from the underlying interferometric phase. This is shown in Figure 5.13 where simulated jointly complex Gaussian image pairs have been generated with true coherence values of 1.0, 0.9 and 0.8 and a spatially varying interferometric phase has been applied to the repeat pass image. The effect of the interferometric phase on the multiple correlation coefficient change statistic is clearly observed in the case when the true coherence is 1. In regions of the simulated scene where the interferometric phase is equal to 0, 90, 180 or 270 degrees the variance of the multiple correlation coefficient change statistic is at a minimum. While for other values of interferometric phase the variance is significantly greater. As the true scene coherence is reduced the variance in the sample multiple correlation coefficient change statistic is dominated by the scene partial coherence rather than the phase modulation.

5.5 Experimental Results

The four change statistics described in this chapter namely,

- Ratio change statistic, (Equation (5.18)),
- Complex cross correlation coefficient, (Equation (5.57)),
- Intensity cross correlation coefficient, (Equation (5.81)),
- Multiple cross correlation coefficient, (Equation (5.87)),

have been computed using the experimental interferometric image pair described in Section 4.7.3.

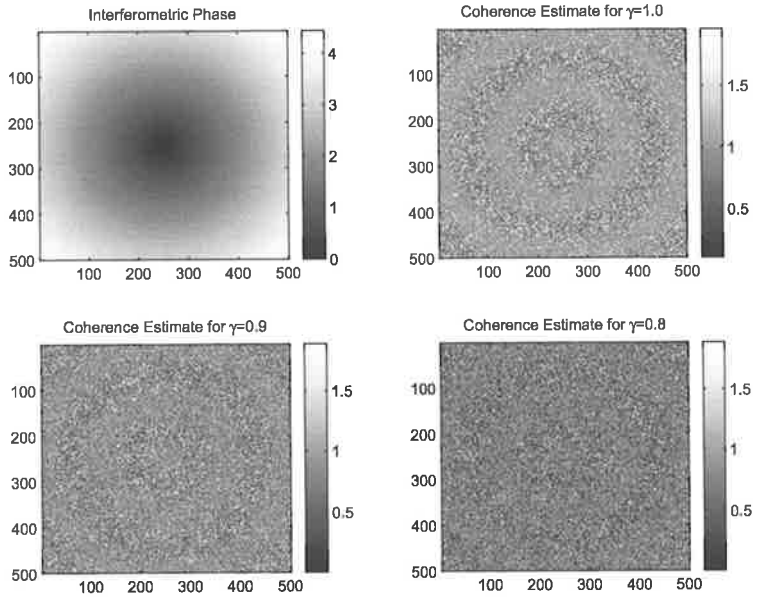


Figure 5.13: Scene coherence maps obtained using the multi-correlation coefficient. The top left figure shows the interferometric phase modulation applied to the repeat pass image. The remaining figures show the estimated coherency maps obtained with the phase modulation applied and underlying true coherence values of 1.0, 0.9 and 0.8.

Figure 5.14 shows the intensity ratio change statistic map obtained by using a 2 x 6 (range x azimuth) resolution cell spatial window to estimate the mean scene backscatter in the primary and repeat pass images. The tracks identified in Section 4.7.3 are evident in the intensity ratio statistic, however they are not as readily discernible as in the complex cross correlation coefficient map, given in Figure 4.13 of Chapter 4. Figure 5.15 shows the square root of the intensity cross correlation (where negative values in the intensity cross correlation have been set to zero prior to taking the square root). The tracks are readily identified however, the estimate of the change statistic is subject to an increased level of noise compared to the magnitude of the sample complex cross correlation coefficient shown in Figure 4.13 in Chapter 4. Figure 5.16 shows the square root of the multiple cross correlation coefficient map while Figure 5.17 shows the sample interferometric phase estimate across the scene. It can be seen that the variance in the estimate of the multiple correlation coefficient varies according to the variation in the interferometric phase as discussed in Section 5.4.2. An examination of Figure 5.16 shows that the variation in the variance of the coherence estimate obtained from the multiple correlation coefficient leads to some obscuration of the low coherence track-like scene disturbances making this change statistic somewhat less effective than the intensity correlation for this particular change detection scenario.

5.6 Conclusions

The original work presented in this chapter is a detailed review and analysis of change detection techniques used to detect man-made changes in repeat pass interferometric SAR. In particular four change detection statistics have been analysed and a detailed quantitative comparison made based on their respective ROC (Probability of Detection (P_d) versus Probability of False Alarm (P_{fa}))

performance.

Based on the jointly Gaussian speckle model for a repeat pass interferometric image pair change detection may be performed based on both changes in the mean pixel intensity of the image or a loss in the cross correlation coefficient of the image. It has been explicitly shown that the mean intensity and cross correlation coefficient are independent parameters with the intensity determined by the mean backscatter power and the the cross correlation coefficient determined by the speckle component of the imagery. Change statistics based on the mean backscatter will therefore detect changes in the dielectric and structural properties of the scene such as changes in the moisture content or the surface roughness. The cross correlation coefficient however can potentially detect subtle changes in the subresolution scattering structure of the scene.

A modified form of the intensity ratio change statistic, originally proposed for SAR edge detection, has been applied to the problem of change detection in SAR imagery. Expressions for the P_d and P_{fa} have been derived to quantify the performance of this change detector. The sample coherence has also been considered as a change statistic wherein man-made changes are assumed to cause complete scene decorrelation. Expressions for the P_d and P_{fa} have also been derived. In addition, two alternative estimators for scene coherence based on a reduced set of the complete available complex data have also been considered as change detectors. These allow coherency based change detection to be carried out without the need for full complex imagery, albeit with a degradation in the change detection performance. Finally the four change statistics have been applied to experimental data obtained with the DSTO Ingara SAR to illustrate the potential of the techniques and facilitate their comparison in a real detection scenario.

The theoretical analysis of the coherence based change statistics and their application to real experiment data shows that the sample complex cross correlation coefficient provides the best overall detection performance. However, in order to compute the sample complex cross correlation coefficient the full single look complex imagery from the primary and repeat pass imaging collections is required. As a consequence large volumes of data must be manipulated which can be computationally burdensome. Furthermore, single look complex imagery may not be readily available, especially in historical image sequences in which only image intensity data may have been generated by the SAR processor. The intensity correlation coefficient may be applied in such cases to provide an estimate of the underlying scene coherence and may be used as a change statistic. The ROC analysis presented in this chapter however shows that, in comparison to the sample complex cross correlation coefficient, the intensity correlation suffers an increase in the false alarm rate by approximately an order of magnitude. Also an estimate of the interferometric phase may not be recovered from the intensity data. The multiple correlation coefficient considered in this chapter operates on the full complex data of either the primary or repeat pass image and the real component only of the other image in the repeat pass image pair. As a consequence an estimate of the interferometric phase and scene coherence may be recovered. It has been shown however, that the variance of the coherence estimate obtained from the multiple correlation coefficient is modulated by the underlying scene interferometric phase. This can lead to localised increases in the variance of the coherence estimate which can obscure low coherence scene changes limiting the effectiveness of this change statistic. Finally, it has been shown that both the intensity ratio and sample coherence change statistics suffer from high false alarm rates, especially in the detection of spatially small, subtle scene changes which preclude the use of extensive multi-look averaging. The high false alarm rates of these change statistics can present difficulties when they are used in automated change detection algorithms for the processing of large image data sets.

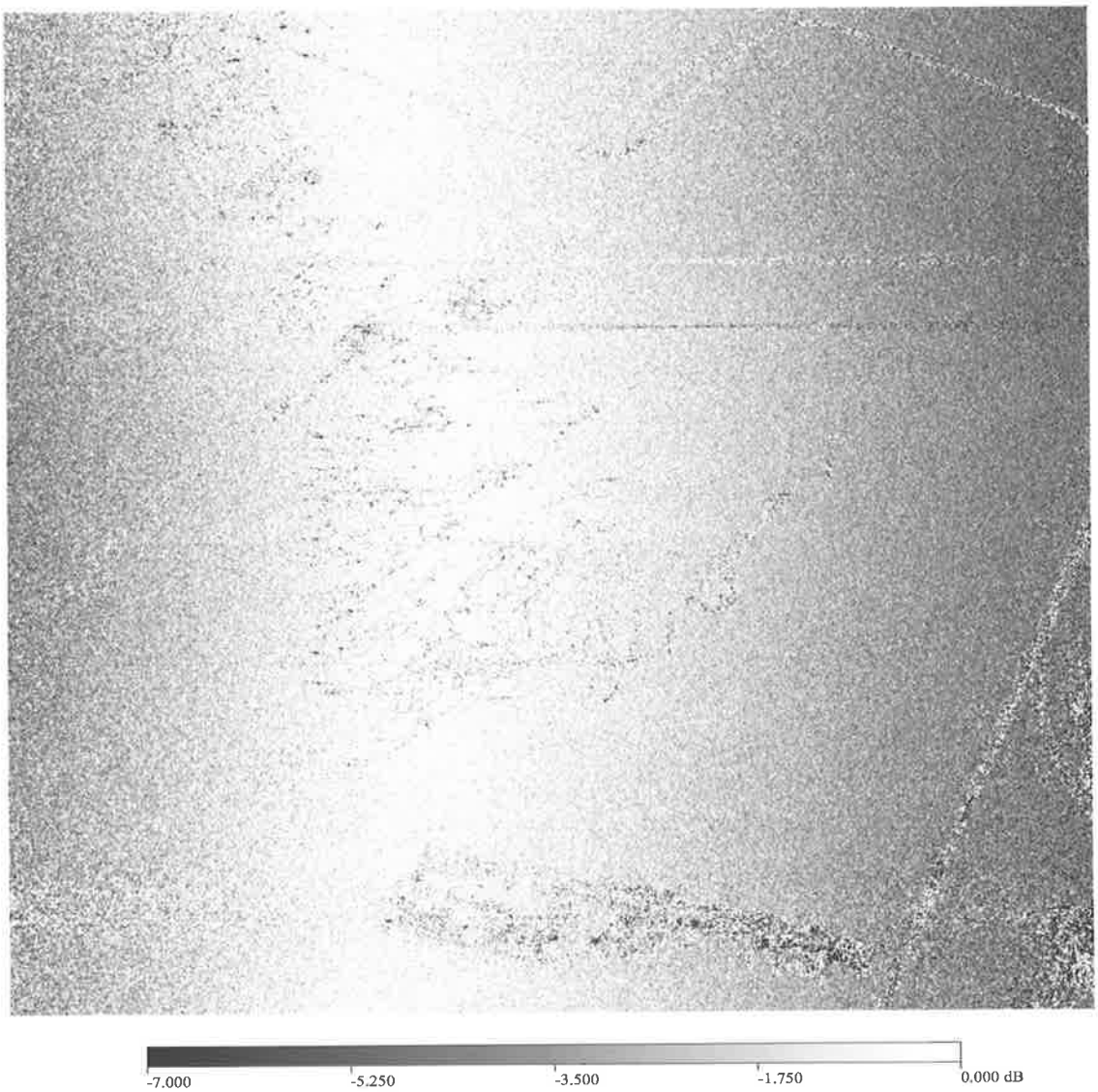


Figure 5.14: Intensity ratio change statistic map obtained by spatially averaging over a sliding estimation window (2x6 pixels in range and azimuth respectively).

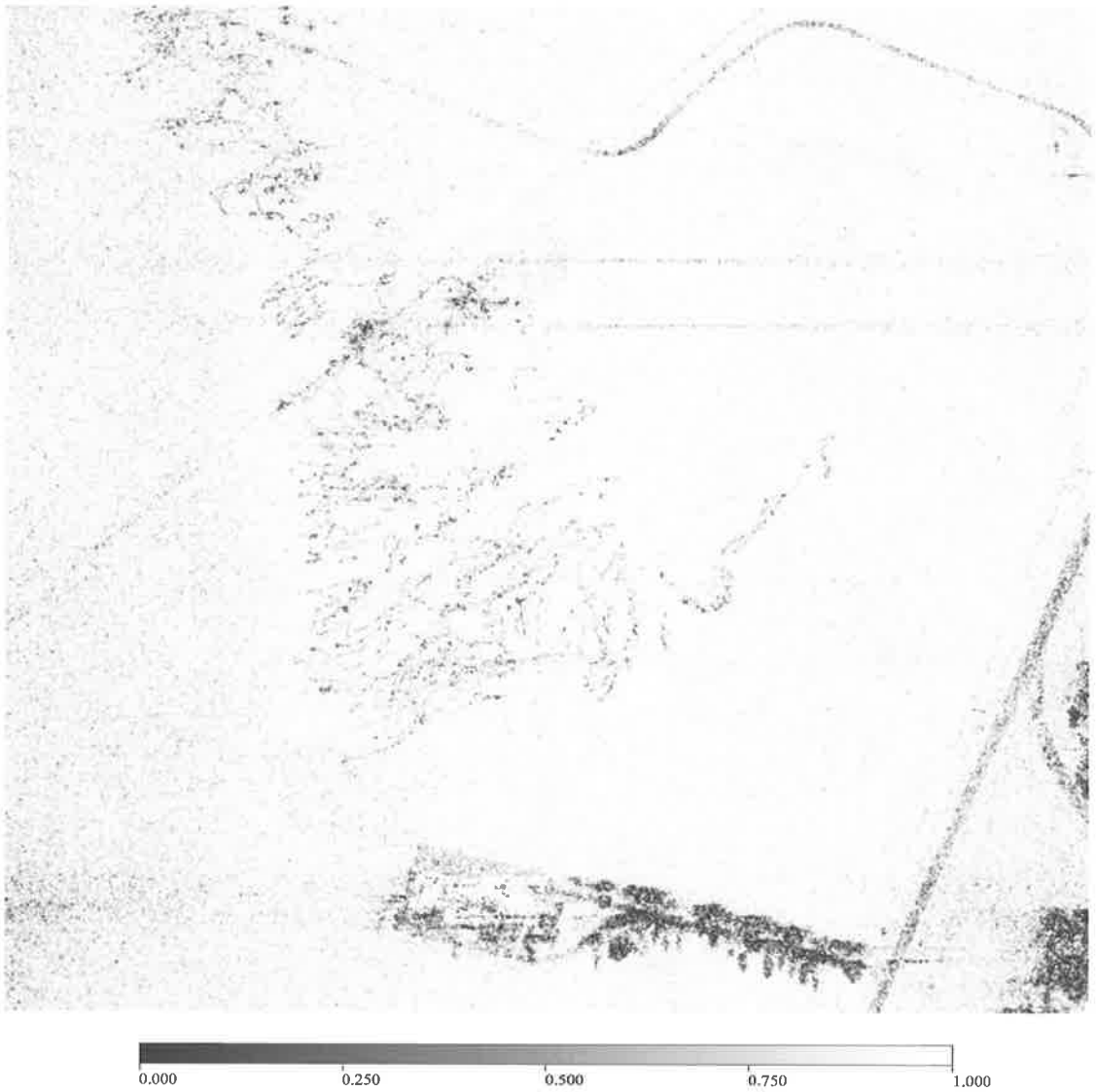


Figure 5.15: Square root of the intensity cross correlation change statistic map obtained by spatially averaging over a sliding estimation window (2x6 pixels in range and azimuth respectively).

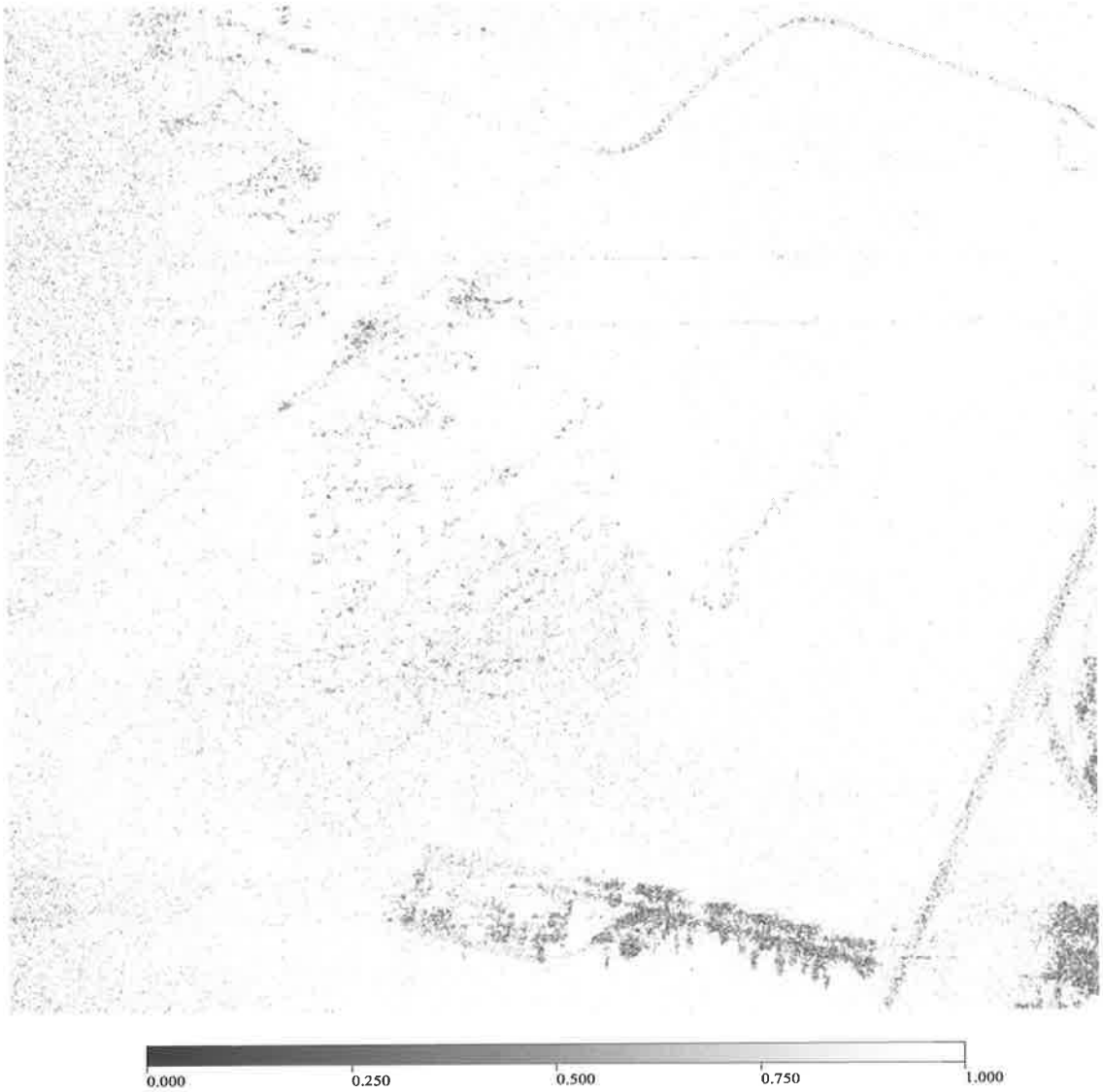


Figure 5.16: Square root of the multiple cross correlation change statistic map obtained by spatially averaging over a sliding estimation window (2x6 pixels in range and azimuth respectively).

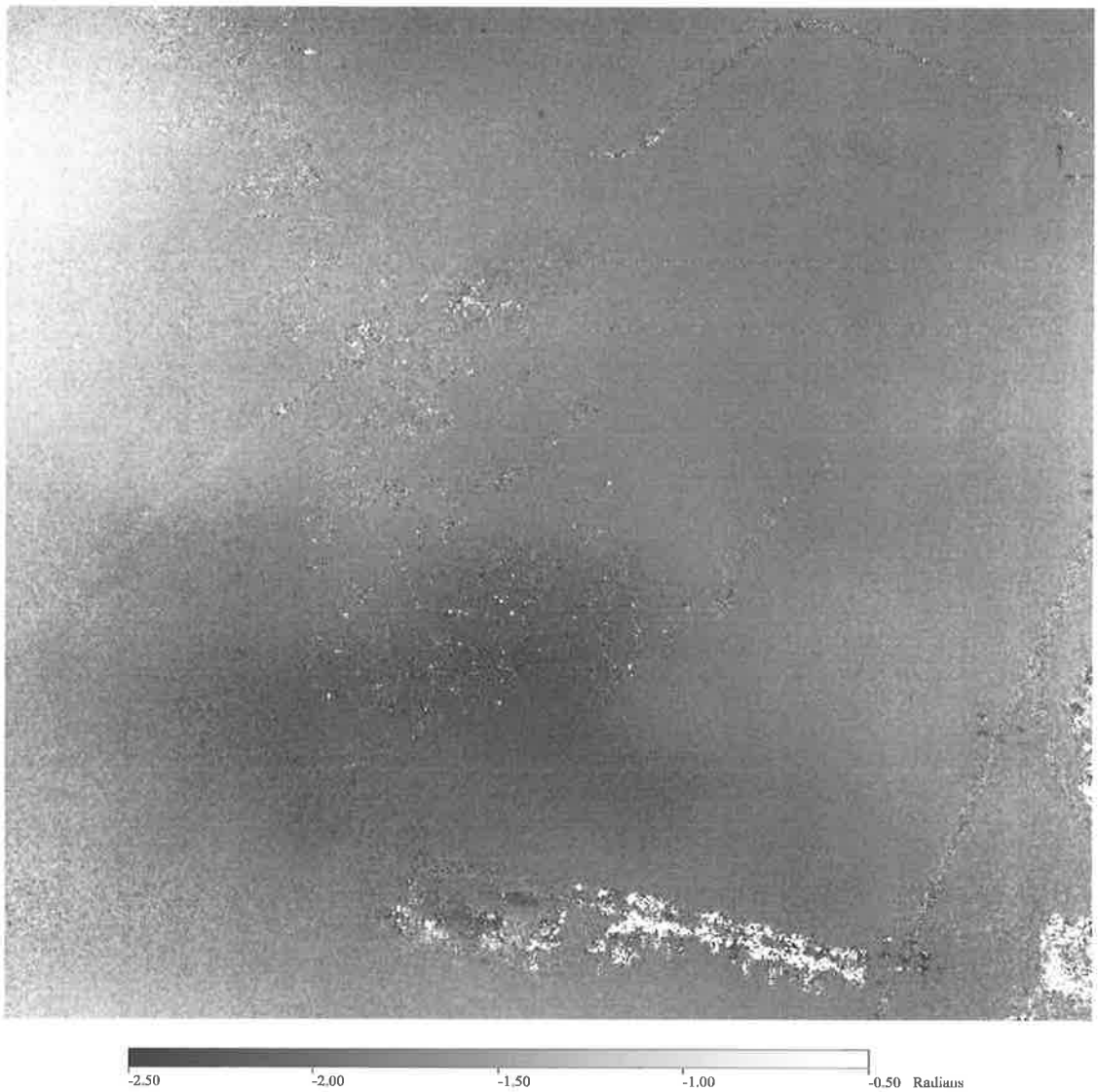


Figure 5.17: Sample interferometric phase obtained by spatially averaging over a sliding estimation window (2x6 pixels in range and azimuth respectively).

Chapter 6

A Log-Likelihood Interferometric Change Statistic

6.1 Introduction

In the repeat pass SAR scene change detection problem man-made scene disturbances may be identified as areas of low coherence or possibly as areas of changed mean backscatter power. The performance of sample coherence as a change statistic depends on its ability to distinguish between the decorrelation due to the man-made scene disturbances as opposed to other possible sources of temporal decorrelation. While man-made changes typically cause total decorrelation in localised areas of the scene, environmental effects such as wind and rain can also lead to significant decorrelation across the scene, especially for image pairs collected with long revisit periods. As a consequence the sample coherence change detector is susceptible to high false alarm rates. The mean backscatter power of a scene on the other hand is less susceptible to environmental effects such as wind and processing aberrations. However, in order to produce a measurable change in the scene backscatter any man-made disturbances must cause a significant modification to the physical properties of the scattering layer of the scene.

The analysis of the previous chapter indicated that, where there has been significant temporal decorrelation, or only modest changes in the mean backscatter power, the poor false alarm rate of the sample coherence and mean backscatter power ratio change statistics may be mitigated if extensive averaging is carried out. Increased averaging via either spatial windows or over multiple subapertures however degrades the resolution of the change maps. Furthermore in regions of scene change local estimates of the change statistics may contain contributions from both changed and unchanged pixels leading to a degradation in the detection performance.

In this chapter, models describing the changed and unchanged regions of a scene are postulated and the detection problem is expressed in a Bayesian hypothesis testing framework. Section 6.2 formulates the changed and unchanged hypotheses that may be used to describe a local neighbourhood of pixels in the primary and repeat pass image pair. This leads to the formulation of a new log likelihood change statistic, described in Section 6.3, that encodes both coherence and mean backscatter power changes for discriminating between changed and unchanged regions in a SAR image pair. The change statistic however contains a number of unknown parameters that must be quantified before a practical detector based on the change statistic can be implemented. The theoretical probability density function of a clairvoyant detector, obtained assuming perfect knowledge of the unknown parameters, is derived in Section 6.4 and the special case of no backscatter change is addressed in Section 6.5. The detection performance of the clairvoyant change statistic is quantified in Section 6.7 and a signifi-

cant improvement over the mean backscatter power ratio and sample coherence change statistics is demonstrated through theoretical analysis and verified by simulation. For a given probability of detection this allows finer resolution change maps to be generated or a significant reduction in the false alarm rate compared to the sample coherence or the mean backscatter ratio change statistics. Finally in Section 6.8 a practical implementation of the change statistic namely a generalised likelihood ratio detector is discussed in which the unknown parameters are replaced with their maximum likelihood estimates. Provided sufficient samples are available to generate the ML estimates the degradation in performance of the change statistic from the optimal is small.

6.2 Complex Reflectivity Change Model and Hypothesis Statement

Consider the k^{th} pixel in a repeat pass SAR image pair $\underline{X}_k = [f_k, g_k]^T$, where f and g denote the primary and repeat pass images respectively. Assuming that autofocusing, aperture trimming and image registration have been done to sufficient accuracy as described in Chapter 4 then the change detection problem is to determine whether $\underline{X}_k$ is a realisation of an unchanged (null) hypothesis or a changed (alternative) hypothesis as described in Table 6.1.

Hypothesis	Description
Null Hypothesis: H_0	No Scene Change $f_k = r_k + n_{1_k}$ $g_k = r_k exp(-j\Phi_k) + n_{2_k}$
Alternative Hypothesis: H_1	Scene Change $f_k = r_k + n_{1_k}$ $g_k = s_k + n_{2_k}$

Table 6.1: Hypothesis statements for the unchanged scene (null) hypothesis and the changed scene (alternative) hypothesis.

In Table 6.1 r_k is the stable scattering component of the transduced complex reflectivity in the k^{th} ground patch resolution cell that is common to both images f and g under the no change, null hypothesis. The interferometric phase term Φ_k arises in the null hypothesis as the repeat pass images are correlated and is dependent on baseline separation of the imaging geometries of the primary and repeat pass collections as well as the terrain topography. In the alternative hypothesis the stable scattering contribution r_k is assumed to be subject to a man-made scene disturbance that gives rise to a complex reflectivity component s_k that is completely uncorrelated with r_k. The additive terms n_{1_k} and n_{2_k} are mutually independent of both each other and the reflectivities r_k and s_k and represent unstable scene scattering contributions, as well as system noise and aberrations in the acquisition and subsequent processing of the collected range echo data.

For homogeneous natural distributed target environments, such as open fields, the transduced complex backscatter in the joint repeat pass image pair $\underline{X}_k = [f_k, g_k]^T$ may be modelled as zero mean, circular, jointly Gaussian random variables under each hypothesis H_0 and H_1,

$$p(\underline{X}_k; H_0) = \frac{1}{\pi^2 |Q_0|} exp(-\underline{X}_k^H Q_0^{-1} \underline{X}_k), \tag{6.1}$$

$$p(\underline{X}_k; H_1) = \frac{1}{\pi^2 |Q_1|} exp(-\underline{X}_k^H Q_1^{-1} \underline{X}_k), \tag{6.2}$$

where $Q_0 = E\{\underline{X}\underline{X}^H | H_0\}$ and $Q_1 = E\{\underline{X}\underline{X}^H | H_1\}$ are the covariance matrices under the null and alternative hypotheses respectively. In the case of the unchanged scene hypothesis the covariance

matrix is given by,

$$Q_0 = \begin{bmatrix} \sigma_f^2 & \sigma_f\sigma_{g_0}\gamma exp(j\Phi) \\ \sigma_f\sigma_{g_0}\gamma exp(-j\Phi) & \sigma_{g_0}^2 \end{bmatrix}, \tag{6.3}$$

where $\gamma exp(j\Phi)$ is the complex cross correlation coefficient given by,

$$\begin{aligned} \gamma exp(j\Phi) &= \frac{E\{fg^*\}}{\sqrt{E\{|f|^2\}E\{|g|^2\}}}, \\ &= \frac{\sigma_r^2 exp(j\Phi)}{\sqrt{\sigma_f^2\sigma_{g_0}^2}}, \\ &= \frac{\sigma_r^2 exp(j\Phi)}{\sqrt{(\sigma_r^2+\sigma_{n_1}^2)(\sigma_r^2+\sigma_{n_2}^2)}}, \end{aligned} \tag{6.4}$$

and $\sigma_f^2 = \sigma_r^2 + \sigma_{n_1}^2$ and $\sigma_{g_0}^2 = \sigma_r^2 + \sigma_{n_2}^2$. Under the changed scene hypothesis the covariance matrix is given by,

$$Q_1 = \begin{bmatrix} \sigma_f^2 & 0 \\ 0 & \sigma_{g_1}^2 \end{bmatrix}, \tag{6.5}$$

where $\sigma_{g_1}^2 = \sigma_s^2 + \sigma_{n_2}^2$.

The scene models under each hypothesis are completely described by the covariance matrices Q_0 and Q_1. These matrices however consist of a number of unknown parameters. In the case of the null hypothesis the unknown parameters are $\underline{v}_{H_0} = [\gamma, \Phi, \sigma_f^2, \sigma_{g_0}^2]^T$ while for the alternative hypothesis the unknown parameters are $\underline{v}_{H_1} = [\sigma_f^2, \sigma_{g_1}^2]^T$. The hypotheses, H_0 and H_1, are thus composite [Pap91], [Kay98] and the unknown parameters must be estimated before a given image pixel pair $\underline{X}_k$ may be determined as being a realisation of the changed or unchanged hypothesis.

In general, a practical decision statistic may be designed using either a Bayesian approach, or a Generalised Likelihood Ratio Test (GLRT) to distinguish between the two hypotheses. In the Bayesian approach the unknown parameters are assumed to be realisations of random variables which may be quantified by assigning prior density functions to the unknown parameters, $p(\underline{v}_{H_0})$ and $p(\underline{v}_{H_1})$. In the context of repeat pass SAR imagery knowledge of the physical properties of the scene such as the geometric and dielectric properties of the vegetation cover and underlying soil as well as their respective temporal decorrelation properties may facilitate the formulation of appropriate prior density functions. In practice the choice of prior density functions can prove difficult and in the absence of a detailed scene description a non-informative prior must be used wherein all parameter values are taken to be equally likely. Solutions obtained using the Bayesian approach generally require multidimensional integration and closed form solutions quantifying the detection performance of the decision statistic are generally not attainable.

The GLRT is an alternative approach in which the unknown parameters are replaced with their maximum likelihood estimates obtained from the observed data. Provided sufficiently large data sets are available for estimating the unknown parameters and through judicious use of prior knowledge regarding the nature of the scene and man-made disturbances, detection performance approaching the performance of an optimal detector based on known parameters is attainable.

6.3 Likelihood Ratio Change Statistic

Under the assumption that the covariance matrices Q_0 and Q_1 are known, the density functions describing the observations under each hypothesis are completely specified. In this case the Neyman-

Pearson theorem defines a simple decision statistic and associated decision region that maximises the probability of detection for a specified probability of false alarm. Defining the likelihood ratio decision statistic,

$$L = \frac{p(\underline{X}_k; H_0)}{p(\underline{X}_k; H_1)}, \tag{6.6}$$

the Neyman-Pearson theorem states the maximum probability of detection for a given probability of false alarm is obtained if the observation $\underline{X}_k$ is declared a realisation of the H_1 hypothesis when $L < T$, where the threshold T is specified by,

$$P_{fa} = \int_{\{\underline{X}_k : L<T\}} p(\underline{X}_k; H_0) d\underline{X}_k. \tag{6.7}$$

The region of integration $\{\underline{X}_k : L < T\}$ is the subspace of $\underline{X}_k$ for which the statistic L is less than T. For the case in which the parameters are unknown the Neyman-Pearson detector is, in general, unrealisable and is referred to as a clairvoyant detector [Kay98]. The clairvoyant detector indicates the optimal detection performance achievable given perfect knowledge of the unknown parameters. In practice suboptimal tests are implemented in which the unknown parameters are specified by either, a probability density function as in the Bayesian approach, or by their maximum likelihood estimates in the GRLT. In either approach the specification of the unknown parameters is subject to some degree of uncertainty and the detection performance of these practical realisable detectors is subject to some degradation compared to that of the clairvoyant detector. The clairvoyant detector thus provides an upper bound on the performance of any practical implementation of the decision statistic and is analogous to the Cramer-Rao lower bound used to quantify estimator performance.

6.3.1 An Optimal Clairvoyant Detector

At any given location in the registered image pair consider a local neighbourhood of N pixels $X_k, k = 1 \cdots N$. Assuming that the terrain topography is slowly varying so that Φ_k may be considered constant over the local area. Also, assuming that the observations $\underline{X}_k$ are mutually independent observations of random processes that may be considered to be stationary over the N pixel neighbourhood, the likelihood ratio is given by,

$$\begin{aligned} L &= \frac{P(\underline{X}_1, \underline{X}_2, \cdots \underline{X}_N | H_0)}{P(\underline{X}_1, \underline{X}_2, \cdots \underline{X}_N | H_1)}, \\ &= \prod_{k=1}^{N} \frac{P(\underline{X}_k | H_0)}{P(\underline{X}_k | H_1)}. \end{aligned} \tag{6.8}$$

Substituting (6.1) and (6.2) for the density functions $p(\underline{X}_k|H_0)$ and $p(\underline{X}_k|H_1)$ into (6.8) gives,

$$\begin{aligned} L &= \left(\frac{|Q_1|}{|Q_0|}\right)^N exp\left(-\sum_{k=1}^{N} \underline{X}_k^H \left(Q_0^{-1} - Q_1^{-1}\right) \underline{X}_k\right), \\ &- \left(\frac{|Q_1|}{|Q_0|}\right)^N exp\left(-Tr\left\{\left(Q_0^{-1} - Q_1^{-1}\right) \sum_{k=1}^{N} \underline{X}_k \underline{X}_k^H\right\}\right), \end{aligned} \tag{6.9}$$

where $Tr\{A\}$ denotes the trace of matrix A. Forming the log likelihood ratio and ignoring the constant term yields the following decision statistic for discriminating between the two hypotheses,

$$\begin{aligned} z &= Tr\left\{\left(Q_0^{-1} - Q_1^{-1}\right) \sum_{k=1}^{N} \underline{X}_k \underline{X}_k^H\right\}, \\ &= Tr\left\{Q_d G\right\}, \end{aligned} \tag{6.10}$$

where $G = \sum_{k=1}^{N} \underline{X}_k \underline{X}_k^H$ is the "sample covariance matrix" formed from the N observations and $Q_d = Q_0^{-1} - Q_1^{-1}$.

In [Goo63] it is shown that G, normalised by the number of samples N, is the maximum likelihood estimate of the covariance matrix of the random vector $\underline{X}$ given N independent observations $\underline{X}_k, k = 1 \cdots N$. Furthermore, G is also an unbiased estimator thus,

$$E\{G\} = \begin{cases} NQ_0, & \text{under } H_0, \\ NQ_1, & \text{under } H_1. \end{cases} \tag{6.11}$$

Evaluating the expected value of the decision statistic, under each hypothesis provides some insight into the behaviour of the change statistic and its dependence on the coherence γ and the mean backscatter power of the primary and repeat pass image pair. Under the unchanged H_0 hypothesis,

$$\begin{aligned} E\{z; H_0\} &= E\left\{Tr\left\{\left(Q_0^{-1} - Q_1^{-1}\right) G\right\}\right\}, \\ &= Tr\left\{\left(Q_0^{-1} - Q_1^{-1}\right) E\{G\}\right\}, \\ &= N(1-r), \end{aligned} \tag{6.12}$$

where $r = \frac{\sigma_{g0}^2}{\sigma_{g1}^2}$. Similarly under the changed H_1 hypothesis,

$$\begin{aligned} E\{z; H_1\} &= E\left\{Tr\left\{\left(Q_0^{-1} - Q_1^{-1}\right) G\right\}\right\}, \\ &= Tr\left\{\left(Q_0^{-1} - Q_1^{-1}\right) E\{G\}\right\}, \\ &= N\frac{2\gamma^2 + r^{-1} - 1}{1-\gamma^2}. \end{aligned} \tag{6.13}$$

Given that the ratio r lies in the range $(0, \infty)$ and the coherence γ in the range $[0, 1]$ a simple proof by contradiction can be used to demonstrate that $E\{z|H_0\} \leq E\{z|H_1\}$ with equality when $r = 1$ and $\gamma = 0$ i.e., when the two hypotheses are identical, $Q_0 = Q_1$.

Two particular cases are of interest namely: The case when the mean backscatter power is unchanged and discrimination is based solely on the degree of partial coherence between the image pair and the case in which the image pair is uncorrelated under H_0 and discrimination is possible based only on a change in the mean backscatter power.

For the case when the mean backscatter is unchanged, $\sigma_{g0}^2 = \sigma_{g1}^2$ in the H_1 hypothesis, thus $r = 1$ and the expected values of the decision statistic are determined solely by the degree of partial coherence between the image pair,

$$E\{z\} = \begin{cases} 0, & \text{under } H_0, \\ N\frac{2\gamma^2}{1-\gamma^2}, & \text{under } H_1. \end{cases} \tag{6.14}$$

Such a scenario may arise when subtle scene disturbances cause a rearrangement in the relative spatial distribution of the contributing scatterers resulting in a loss in coherence without an accompanying change in the physical properties of the scatterers and hence no change in the mean backscatter power. Figure 6.1 shows $E\{z; H_1\}$, normalised by the number of samples N, as a function of the coherence γ. As the coherence increases the expected value of the decision statistic under H_1 increases making it easier to discriminate between the changed and unchanged hypotheses.

For the case when the coherence γ is zero under H_0 the expected value of the decision statistic is determined solely by changes in the mean backscatter power,

$$E\{z\} = \begin{cases} (1-r), & \text{under } H_0, \\ \left(1 - \frac{1}{r}\right), & \text{under } H_1. \end{cases} \tag{6.15}$$

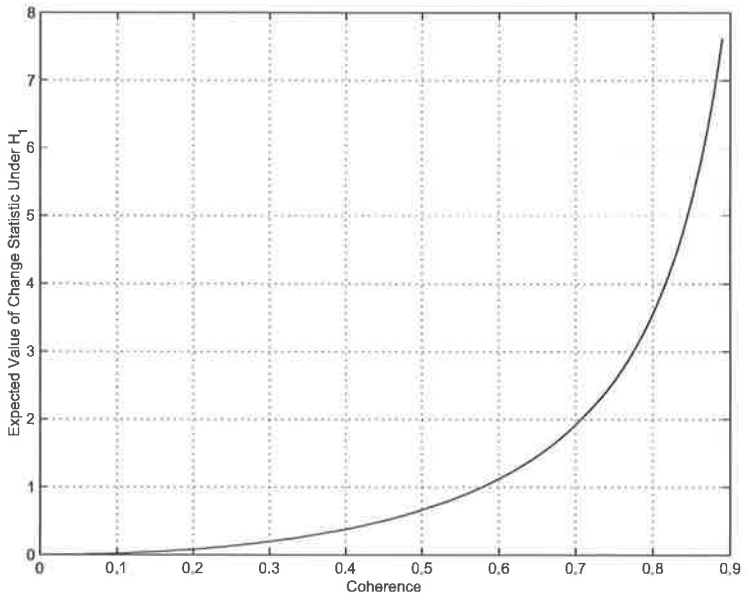


Figure 6.1: The expected value of the decision statistic z under H_1, normalised by the number of samples, as a function of the coherence γ.

This scenario may arise when temporal decorrelation due to environmental effects cause a complete loss in coherence across the regions of interest. Therefore changes may only be identified where they cause a change in the physical properties of the scatterers that manifests as a change in mean backscatter power. Figure 6.2 shows $E\{z; H_0\}$ and $E\{z; H_1\}$, normalised by the number of samples N, as a function of the mean backscatter power ratio r. When the ratio $r = 1$ the expected values of the decision statistic under H_0 and H_1 are equal and thus discrimination between the hypotheses is not possible. However, as the ratio increases or decreases the absolute value of the difference $(E\{z; H_1\} - E\{z; H_0\})$ increases making it easier to discriminate between the changed and unchanged hypotheses.

6.4 Density Functions of the Change Statistic

In order to quantify the detection performance of the clairvoyant decision statistic z and hence define an upper bound on the performance of any practical implementation of the decision statistic the density function of z is required under each hypothesis. From these density functions the probability of detection and false alarm may be computed for various thresholds on z and an ROC curve generated for comparison with the commonly used change statistics discussed in Chapter 5.

The log likelihood ratio decision statistic in (6.10) may be expanded into the following form,

$$\begin{aligned} z &= Tr\{Q_d G\}, \\ &= Tr\left\{ \begin{bmatrix} Q_{d_{11}} & Q_{d_{12}} \\ Q_{d_{21}} & Q_{d_{22}} \end{bmatrix} \begin{bmatrix} \sum_{k=1}^{N} |f_k|^2 & \sum_{k=1}^{N} f_k g_k^* \\ \sum_{k=1}^{N} f_k^* g_k & \sum_{k=1}^{N} |g_k|^2 \end{bmatrix} \right\}. \end{aligned} \tag{6.16}$$

Using (6.3) and (6.5) the elements of matrix Q_d may be evaluated and it may be shown that $Q_{d_{12}} = Q_{d_{21}}^*$ therefore the decision statistic can be shown to be a linear combination of three random variables

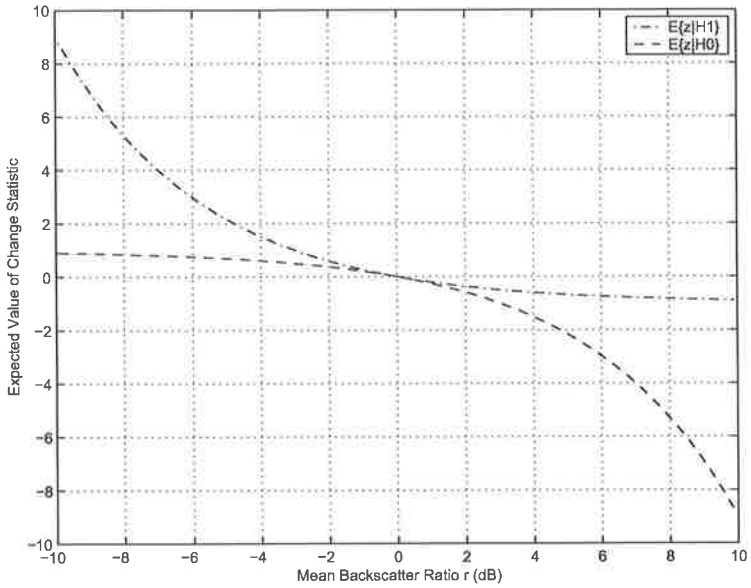


Figure 6.2: The expected value of the decision statistic under H_0 and H_1, normalised by the number of samples, as a function of the backscatter ratio r expressed in dB.

i.e.,

$$z = Q_{d_{11}} \sum_{k=1}^{N} |f_k|^2 + Q_{d_{22}} \sum_{k=1}^{N} |g_k|^2 + 2\Re \left\{ \sum_{k=1}^{N} Q_{d_{12}} f^* g_k \right\}. \tag{6.17}$$

The density function of the sample covariance and its associated marginal distributions have been extensively studied in the literature. The joint density function of the terms in the sample covariance G matrix is given by the Wishart distribution [Goo63],

$$p(G) = \frac{|G|^{N-2}}{\pi \Gamma(N)\Gamma(N-1)|C|^N} exp\left(-tr(C^{-1}G)\right), \tag{6.18}$$

where $C = E\{\underline{X}\underline{X}^H\}$ and $|G|$ and $|C|$ are the determinants of the matrices G and C respectively. Furthermore the marginal density functions of the individual elements of the sample covariance matrix have been studied in the context of SAR interferometry and polarimetry research [LMH94], [OQ98], [TBQ95], [JWP94] and [TL96]. The three component random variables in (6.17) however, are not mutually independent under either H_0 or H_1, therefore the marginal density functions are of no use in computing the density function of z. Instead computation of the density function of z may proceed by, firstly, marginalising the Wishart distribution to recover the joint density function of the three random variables and then integrating over appropriate ranges of the three variables [Pap91]. While the recovery of the density function of z may be possible via this approach, it appears mathematically intractable. An alternative more elegant solution is to consider applying a linear transform P to the image pixel pair vectors $\underline{X}_k = [f_k, g_k]^T$. Through an appropriate linear transform the decision statistic can be simplified into a linear combination of two random variables from which the density function of z may be more readily derived. The choice of linear transform is governed by the form of the matrix Q_d. Provided the Q_d matrix has rank two then a transform matrix P may be found such

that it diagonalises Q_d,

$$\begin{aligned} P^H Q_d P &= \begin{bmatrix} \lambda_1 & 0 \\ 0 & \lambda_2 \end{bmatrix}, \\ &= diag(\lambda_1, \lambda_2), \end{aligned} \tag{6.19}$$

where λ_1 and λ_2 are the eigenvalues of Q_d and the columns of P are the corresponding eigenvectors [AR87]. Furthermore it may be shown that, given the forms for Q_0 in (6.3) and Q_1 in (6.5), one of the eigenvectors is negative while the other is positive. In the following analysis it will be assumed that the first eigenvalue is negative and λ_1 will be taken to mean the absolute value the first eigenvalue (Similar forms for the density functions as those derived in the following analysis may be obtained for the case when the second eigenvalue is negative.). Defining the new transform variables u and v such that,

$$\underline{X} = \begin{bmatrix} f \\ g \end{bmatrix} = P \begin{bmatrix} u \\ v \end{bmatrix}, \tag{6.20}$$

the decision statistic may subsequently be written as,

$$\begin{aligned} z &= \sum_{k=1}^{N} \left(\begin{bmatrix} f_k^* & g_k^* \end{bmatrix} Q_d \begin{bmatrix} f_k \\ g_k \end{bmatrix} \right), \\ &= \sum_{k=1}^{N} \left(\begin{bmatrix} u_k^* & v_k^* \end{bmatrix} P^H Q P \begin{bmatrix} u_k \\ v_k \end{bmatrix} \right), \\ &= \sum_{k=1}^{N} \left(\begin{bmatrix} u_k^* & v_k^* \end{bmatrix} diag(-\lambda_1, \lambda_2) \begin{bmatrix} u_k \\ v_k \end{bmatrix} \right), \\ &= -\lambda_1 \sum_{k=1}^{N} |u_k|^2 + \lambda_2 \sum_{k=1}^{N} |v_k|^2. \end{aligned} \tag{6.21}$$

In general under the transform P the new transform variables u and v are dependent zero mean complex circular Gaussian random variables with a covariance matrix of the form,

$$C = \begin{bmatrix} C_{11} & \sqrt{C_{11}C_{22}}\rho e^{j\theta} \\ \sqrt{C_{11}C_{22}}\rho e^{-j\theta} & C_{22} \end{bmatrix}, \tag{6.22}$$

where,

$$C = \begin{cases} P^H Q_0 P, & \text{for } u \text{ and } v \text{ realisations of } H_0, \\ P^H Q_1 P, & \text{for } u \text{ and } v \text{ realisations of } H_1. \end{cases} \tag{6.23}$$

Therefore the variables $a = \lambda_1 \sum_{k=1}^{N} |u_k|^2$ and $b = \lambda_2 \sum_{k=1}^{N} |v_k|^2$ that form the decision statistic (6.21) are mutually dependent Chi square random variables with 2N degrees of freedom [Kay98]. The joint density function of two dependent Chi square random variables has been derived by Lee [LMH94]. Applying Lee's result the joint density of a and b may be written as,

$$p(a,b) = \frac{(1-\rho^2)^N (ab)^{N-1} exp\left\{ -\left(\frac{a}{\alpha} + \frac{b}{\beta} \right) \right\}}{(\alpha\beta)^N \Gamma^2(N)} {}_1F_2\left(1; 1, N; \frac{ab\rho^2}{\alpha\beta} \right), \tag{6.24}$$

where ${}_1F_2$ is a hypergeometric function given by,

$$ {}_1F_2\left(1;1,N;\frac{ab\rho^2}{\alpha\beta}\right) = \Gamma(N)\sum_{k=0}^{\infty}\frac{1}{\Gamma(N+k)k!}\left(\frac{ab\rho^2}{\alpha\beta}\right)^k, \tag{6.25} $$

and,

$$ \alpha = \lambda_1 C_{11}(1-\rho^2), \tag{6.26} $$

$$ \beta = \lambda_2 C_{22}(1-\rho^2). \tag{6.27} $$

The density function of the decision statistic $z = -a + b$ may subsequently be found from (6.24) by direct evaluation of the following integrals,

$$ p(z) = \begin{cases} \int_0^\infty p(b-z,b)db, & \text{for } z \le 0, \\ \int_0^\infty p(a,a+z)da, & \text{for } z > 0, \end{cases} \tag{6.28} $$

where the lower limit in each integral arises because, $\lambda_1 \ge 0$, $\lambda_2 \ge 0$ and so $a \ge 0$ and $b \ge 0$. Note that equation (6.28) is a general expression for the density function of z. To obtain $p(z;H_0)$ and $p(z;H_1)$ the appropriate values for C_{11}, C_{22} and ρ, defined in (6.23) are used. For $z \le 0$, setting $a = b - z$ in (6.24) gives,

$$ p(z) = \int_0^\infty \frac{(1-\rho^2)^N (b^2-zb)^{N-1} exp\left\{-\left(\frac{b-z}{\alpha}+\frac{b}{\beta}\right)\right\}}{(\alpha\beta)^N\Gamma^2(N)} {}_1F_2\left(1;1,N;\frac{(b^2-zb)\rho^2}{\alpha\beta}\right)db. \tag{6.29} $$

Substituting the series expansion for the hypergeometric function (6.25) into (6.29) gives,

$$ p(z) = \frac{(1-\rho^2)^N e^{\left(\frac{z}{\alpha}\right)}}{\Gamma(N)(\alpha\beta)^N}\sum_{k=0}^{\infty}\mu_k\int_0^\infty (b^2-zb)^{N+k-1}exp(-b\nu)db, \tag{6.30} $$

where,

$$ \mu_k = \frac{1}{\Gamma(N+k)k!}\left(\frac{\rho^2}{\alpha\beta}\right)^k, \tag{6.31} $$

$$ \nu = \frac{1}{\alpha}+\frac{1}{\beta}. \tag{6.32} $$

Using the binomial expansion,

$$ (b^2-zb)^{N+k-1} = \sum_{p=0}^{N+k-1}\binom{N+k-1}{p} b^{2N+2k-p-2}(-z)^p, \tag{6.33} $$

then,

$$ p(z) = \frac{(1-\rho^2)^N e^{\left(\frac{z}{\alpha}\right)}}{\Gamma(N)(\alpha\beta)^N}\sum_{k=0}^{\infty}\mu_k\sum_{p=0}^{N+k-1}\binom{N+k-1}{p}(-z)^p\int_0^\infty exp(-b\nu)b^{(2N+2k-p-2)}db. \tag{6.34} $$

The integral with respect to b in (6.34) is in the form of a Gamma function [AS72] and thus $p(z)$ may be written as

$$ p(z) = \frac{(1-\rho^2)^N e^{\left(\frac{z}{\alpha}\right)}}{\Gamma(N)(\alpha\beta)^N}\sum_{k=0}^{\infty}\left[\mu_k\sum_{p=0}^{N+k-1}\left[\binom{N+k-1}{p}\frac{\Gamma(2k+2N-p-1)}{\nu^{2k+2N-p-1}}(-z)^p\right]\right], \tag{6.35} $$

where,

$$\Gamma(x) = \int_0^\infty t^{x-1} exp(-t) dt, \tag{6.36}$$

which for integer values of x reduces to the factorial function $\Gamma(x) = (x-1)!$. Similarly, for $z > 0$, $p(z)$ may be written as,

$$p(z) = \frac{(1-\rho^2)^N e^{\left(\frac{-z}{\beta}\right)}}{\Gamma(N)(\alpha\beta)^N} \sum_{k=0}^{\infty} \left[\mu_k \sum_{p=0}^{N+k-1} \left[\binom{N+k-1}{p} \frac{\Gamma(2k+2N-p-1)}{\nu^{2k+2N-p-1}} (z)^p \right] \right], \tag{6.37}$$

Figure 6.3 shows simulated and theoretical density functions for the decision statistic z under each hypothesis obtained using (6.35) and (6.37) with $N = 9$ and the following covariance matrices to describe the changed and unchanged scene hypotheses,

Unchanged Hypothesis:

$$Q_0 = 1e8 \begin{bmatrix} 2.2686 & 0.45 \cdot 2.0121 \cdot exp(j\Phi) \\ 0.45 \cdot 2.0121 \cdot exp(-j\Phi) & 1.7847 \end{bmatrix}, \tag{6.38}$$

Changed Hypothesis:

$$Q_1 = 1e8 \begin{bmatrix} 2.2686 & 0 \\ 0 & 0.95070 \end{bmatrix}. \tag{6.39}$$

The values for the scene coherence in Q_0 and the mean backscatter powers in the primary and repeat pass images in Q_0 and Q_1 are in fact experimental values obtained from a scene change experiment conducted with the DSTO Ingara SAR, see Chapter 7. Observe that under H_0 there is a 1.04 dB reduction in the transduced mean backscatter power due to a radiometric miscalibration. Under H_1 however, there is a 3.77 dB reduction in the mean backscatter power between the primary and repeat pass images, indicating that scene changes have caused a 2.73 dB reduction in the mean backscatter power of the scene. The coherence under H_0 is 0.45 while the interferometric phase Φ for scene change scenario considered here has been set to zero. For comparison, Figures 6.4 and 6.5 show the density functions of the sample coherence and mean backscatter power ratio change statistic for the same change scenario. Change detections based on the log likelihood decision statistic, the sample coherence and mean backscatter ratio statistic may be obtained by evaluating the particular decision statistic over the scene, applying a threshold to the decision statistic map and assigning the values to either the changed or unchanged hypotheses. The ability of a change statistic to distinguish between the two hypotheses is thus determined by the degree of overlap of the density functions of the decision statistic under each hypothesis which, in turn, is predominantly dependent on the mean and variance of the density functions under each hypothesis. An examination of Figures 6.4 and 6.5 shows that while the mean values of the PDFs under the changed and unchanged hypotheses appear reasonably well separated, the variances of the PDFs are large hence there is considerable overlap of the density functions. These change statistics will therefore suffer from significant false alarms and missed detections. The PDFs for the log likelihood change statistic under the changed and unchanged hypotheses shown in Figure 6.3 however have a much "narrower" spread and exhibit less overlap. The log likelihood statistic thus provides better discrimination between the two hypotheses. The detection performance improvement in terms of the probability of detection as a function of the probability of false alarm for a given decision threshold will be quantified in Section 6.7.

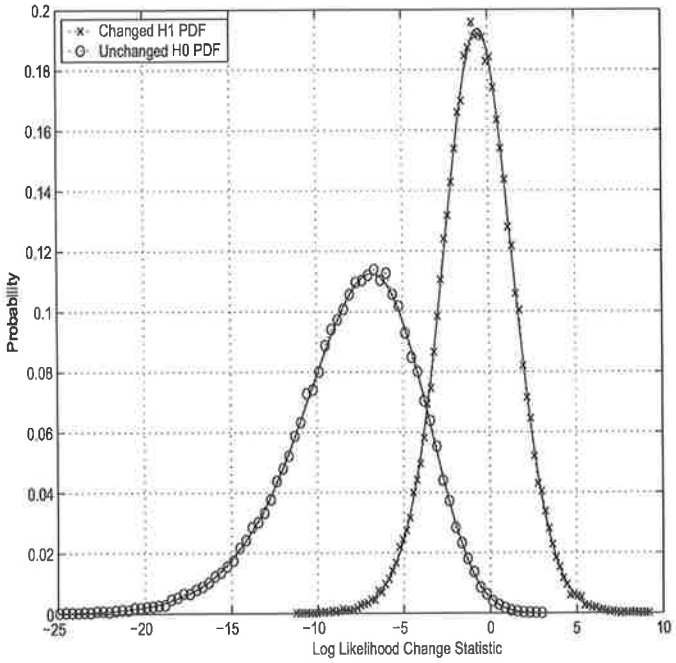


Figure 6.3: Simulated and theoretical density functions of the likelihood ratio change statistic for the unchanged H_0 hypothesis and the changed H_1 hypothesis. The mean backscatter ratio of the primary and repeat pass images is 1.04 dB under H_0 and 3.77 dB under H_1, $N = 9$ and $\gamma = 0.45$.

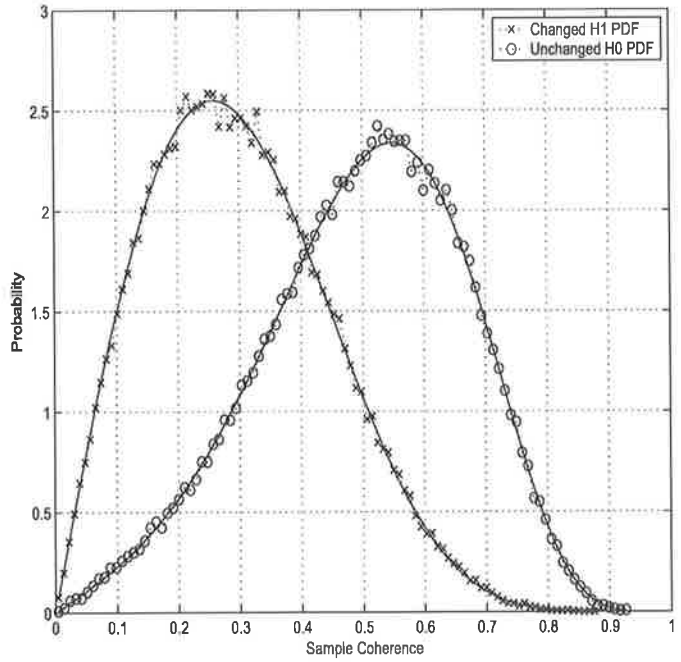


Figure 6.4: Simulated and theoretical density functions of the sample coherence for the unchanged H_0 hypothesis and the changed H_1 hypothesis. Under H_0 the true underlying coherence is $\gamma = 0.45$ while under H_1 $\gamma = 0$ and $N = 9$.

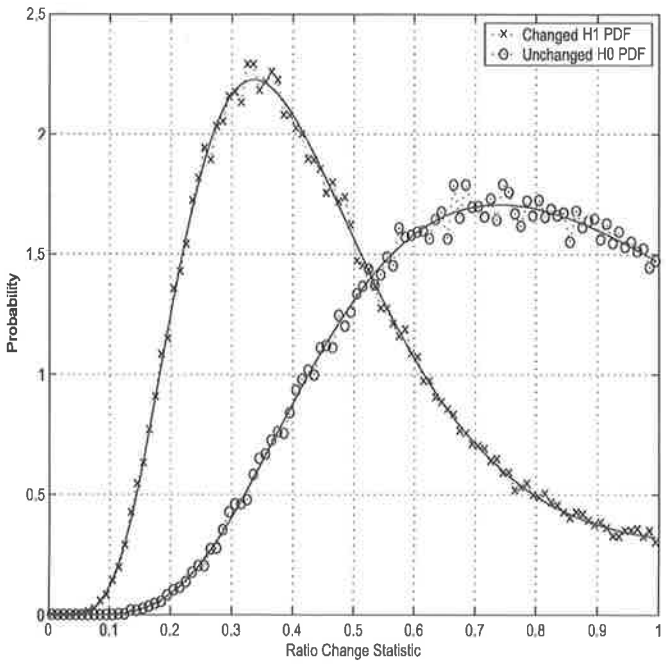


Figure 6.5: Simulated and theoretical density functions of the ratio statistic r for the unchanged H_0 hypothesis and the changed H_1 hypothesis. The mean backscatter ratio of the primary and repeat pass images is 1.04 dB under H_0 and 3.77 dB under H_1 and $N = 9$.

6.5 Change Statistic PDF Under Equal Channel Power

For the case when the scene disturbances do not result in a change in the mean backscatter power in the scene $\sigma_{g_0}^2 = \sigma_{g_1}^2 = \sigma_g^2$ and discrimination between the two hypotheses is possible based solely on the complex cross correlation coefficient $\gamma exp(j\Phi)$. In the ideal imaging scenario wherein there is no baseline offset between the primary and repeat pass flight tracks and assuming stable radar hardware and high antenna pointing accuracy then $\sigma_f^2 = \sigma_g^2$. In practice these conditions are not generally obtained and some radiometric calibration as well as compensation for relative differences in the antenna pointing location between the image pairs may be required to achieve $\sigma_f^2 = \sigma_g^2$. In this case, for calibrated image pairs, the transform variables u and v are independent and a simpler closed form solution for the density function of the clairvoyant decision statistic may be derived.

Substituting $\sigma_f^2 = \sigma_g^2$ into (6.3) and (6.5) the Q_d matrix may be written as,

$$\begin{aligned} Q_d &= Q_0^{-1} - Q_1^{-1}, \\ &= \frac{\gamma}{\sigma_f^2(1-\gamma^2)} \begin{bmatrix} \gamma & -exp(j\Phi) \\ -exp(-j\Phi) & \gamma \end{bmatrix}. \end{aligned} \tag{6.40}$$

The eigenvalues of Q_d are given by,

$$\lambda_1 = -\frac{\gamma}{\sigma_f^2(1+\gamma)} \text{ and } \lambda_2 = \frac{\gamma}{\sigma_f^2(1-\gamma)}, \tag{6.41}$$

and the corresponding eigenvectors form the columns of the transform matrix P that diagonalises Q_d,

$$P = \frac{1}{\sqrt{2}} \begin{bmatrix} exp(j\Phi) & -exp(j\Phi) \\ 1 & 1 \end{bmatrix}. \tag{6.42}$$

The transform variables u and v, obtained by applying P to the observations f and g, are now independent, zero mean complex Gaussian random variables with a covariance matrix given by

$$C = \begin{bmatrix} C_{11} & C_{12} \\ C_{21} & C_{22} \end{bmatrix} = \begin{cases} P^H Q_0 P = \sigma_f^2 \begin{bmatrix} 1+\gamma & 0 \\ 0 & 1-\gamma \end{bmatrix}, & \text{under } H_0, \\ P^H Q_1 P = \sigma_f^2 \begin{bmatrix} 1 & 0 \\ 0 & 1 \end{bmatrix}, & \text{under } H_1. \end{cases} \tag{6.43}$$

The decision statistic thus takes the form,

$$z = -\lambda_1 \sum_{k=1}^{N} |u_k|^2 + \lambda_2 \sum_{k=1}^{N} |v_k|^2, \tag{6.44}$$

where λ_1 is taken to mean the absolute value of the first eigenvalue of Q_d. The variables $a = \lambda_1 \sum |u_k|^2$ and $b = \lambda_1 \sum |v_k|^2$ in this case are mutually independent Chi square random variables with density functions,

$$p(a) = \frac{1}{\Gamma(N)\lambda_1 C_{11}} \left(\frac{a}{\lambda_1 C_{11}}\right)^{N-1} exp\left(-\frac{a}{\lambda_1 C_{11}}\right), \tag{6.45}$$

$$p(b) = \frac{1}{\Gamma(N)\lambda_2 C_{22}} \left(\frac{b}{\lambda_2 C_{22}}\right)^{N-1} exp\left(-\frac{b}{\lambda_2 C_{22}}\right). \tag{6.46}$$

The density function of the log likelihood decision statistic $z = -a + b$ may subsequently be found by direct evaluation of the integrals,

$$p(z) = \begin{cases} \int_0^\infty p(a)p(a+z)da, & z > 0, \\ \int_0^\infty p(b-z)p(b)db, & z \leq 0. \end{cases} \tag{6.47}$$

Note that (6.47) is a general expression of the density function of z. To obtain $p(z; H_0)$ and $p(z; H_1)$ the appropriate values for C_{11} and C_{22}, defined in (6.43) are used. For $z < 0$,

$$p(z) = \frac{1}{\Gamma^2(N)(\lambda_1 C_{11}\lambda_2 C_{22})^N} \int_0^\infty (b-z)^{N-1} b^{N-1} exp\left(-\frac{b-z}{\lambda_1 C_{11}} - \frac{b}{\lambda_2 C_{22}}\right) db. \tag{6.48}$$

Using the binomial expansion,

$$(b-z)^{N-1} = \sum_{p=0}^{N-1} \binom{N-1}{p} b^{N-p-1}(-z)^p, \tag{6.49}$$

gives,

$$p(z) = \frac{exp\left(\frac{z}{\lambda_1 C_{11}}\right)}{\Gamma^2(N)(\lambda_1 C_{11}\lambda_2 C_{22})^N} \sum_{p=0}^{N-1} \binom{N-1}{p} (-z)^p \int_0^\infty b^{2N-p-2} exp\left(-b\left(\frac{1}{\lambda_1 C_{11}} + \frac{1}{\lambda_2 C_{22}}\right)\right) db. \tag{6.50}$$

The integral in (6.50) is in the form of a Gamma function and so [AS72],

$$\int_0^\infty b^{2N-p-2} exp\left(-b\left(\frac{1}{\lambda_1 C_{11}} + \frac{1}{\lambda_2 C_{22}}\right)\right) db = \frac{\Gamma(2N-p-1)}{\nu^{2N-p-1}}, \tag{6.51}$$

where,

$$\nu = \frac{1}{\lambda_1 C_{11}} + \frac{1}{\lambda_2 C_{22}}. \tag{6.52}$$

Therefore $p(z)$ may be simplified to,

$$p(z) = \frac{exp\left(\frac{z}{\lambda_1 C_{11}}\right)}{\Gamma^2(N)(\lambda_1 C_{11}\lambda_2 C_{22})^N} \sum_{p=0}^{N-1} \left[\binom{N-1}{p} \frac{\Gamma(2N-p-1)}{\nu^{2N-p-1}} (-z)^p \right]. \tag{6.53}$$

Similarly for $z > 0$,

$$p(z) = \frac{exp\left(\frac{-z}{\lambda_2 C_{22}}\right)}{\Gamma^2(N)(\lambda_1 C_{11}\lambda_2 C_{22})^N} \sum_{p=0}^{N-1} \left[\binom{N-1}{p} z^p \frac{\Gamma(2N-p-1)}{\nu^{2N-p-1}} \right]. \tag{6.54}$$

Equations (6.53) and (6.54) are simple closed form polynominal solutions for the probability density functions of the decision statistic.

Density Function Under H_0

From (6.43), under H_0, the transform variables u and v are independent zero mean Gaussian random variables with variances given by,

$$\sigma_u^2 = \sigma_f^2(1+\gamma), \tag{6.55}$$
$$\sigma_v^2 = \sigma_f^2(1-\gamma). \tag{6.56}$$

Hence $\lambda_1 C_{11} = \lambda_2 C_{22} = \gamma$ and the density function for z, under H_0, is an even function and may be expressed as a single equation for all z directly in terms of the coherence γ,

$$p(z; H_0) = \frac{exp\left(\frac{-|z|}{\gamma}\right)}{\Gamma^2(N)(\gamma)^{2N}} \sum_{p=0}^{N-1} \left[\binom{N-1}{p} \left(\frac{\gamma}{2}\right)^{2N-p-1} \Gamma(2N-p-1)|z|^p \right]. \tag{6.57}$$

Density Function Under H_1

Similarly from (6.43), under H_1, the transform variables u and v are zero mean Gaussian random variables with equal variances given by $\sigma_u^2 = \sigma_v^2 = \sigma_f^2$. Hence,

$$\lambda_1 C_{11} = \frac{\gamma}{1+\gamma}, \tag{6.58}$$
$$\lambda_2 C_{22} = \frac{\gamma}{1-\gamma}, \tag{6.59}$$

thus the density function for z, under H_1, may be expressed directly in terms of the coherence γ. For $z \leq 0$,

$$p(z; H_1) = \frac{exp\left(\frac{z(1+\gamma)}{\gamma}\right)(1-\gamma^2)^N}{\Gamma^2(N)(\gamma)^{2N}} \sum_{p=0}^{N-1} \left[\binom{N-1}{p} \left(\frac{\gamma}{2}\right)^{2N-p-1} \Gamma(2N-p-1)(-z)^p \right], \tag{6.60}$$

and for $z > 0$,

$$p(z; H_1) = \frac{exp\left(\frac{-z(1-\gamma)}{\gamma}\right)(1-\gamma^2)^N}{\Gamma^2(N)(\gamma)^{2N}} \sum_{p=0}^{N-1} \left[\binom{N-1}{p} \left(\frac{\gamma}{2}\right)^{2N-p-1} \Gamma(2N-p-1)(z)^p \right]. \tag{6.61}$$

Figure 6.6 shows the density function of the decision statistic z for both H_0 and H_1 obtained by direct computation of (6.57), (6.60) and (6.61) and also obtained via simulation for a coherence under H_0 of $\gamma = 0.45$.

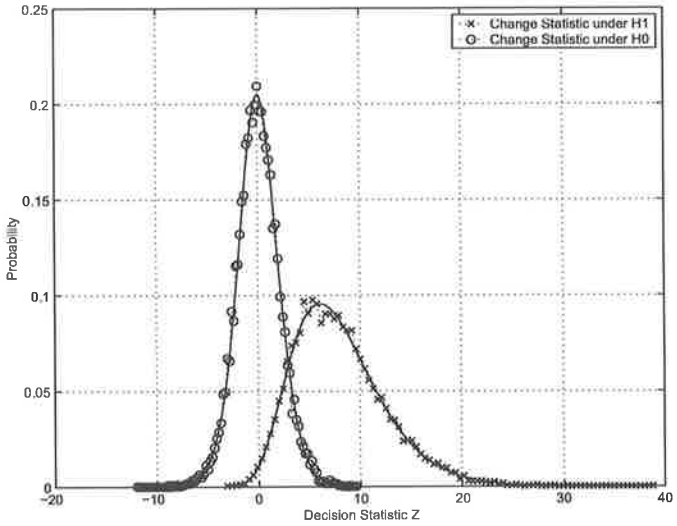


Figure 6.6: Density functions for the decision statistic under H_0 and H_1 for the case of equal backscatter powers $\sigma_f^2 = \sigma_g^2$ with a partial coherence under H_0 of $\gamma = 0.45$ and $N = 9$.

6.6 Change Statistic PDF Under Zero Coherence

For the case in which the coherence under H_0 is zero, discrimination between the two hypotheses is possible only where the scene disturbance has caused a change in the mean backscatter power in the repeat pass image. For $\gamma = 0$ in (6.3) the change statistic (6.10) reduces to the following simple form,

$$z = \frac{\sigma_{g_1}^2 - \sigma_{g_0}^2}{\sigma_{g_0}^2 \sigma_{g_1}^2} \sum_{k=1}^{N} |g_k|^2. \tag{6.62}$$

Observe that (6.62) is independent of the mean backscatter power, σ_f^2 of the primary image. This is consistent with the fact that the images are completely uncorrelated and so there is no additional information that may be exploited by their joint processing. Instead the change detection problem reduces to identifying regions of the repeat pass image that are consistent with the postulated mean backscatter power values $\sigma_{g_0}^2$ and $\sigma_{g_1}^2$ under the changed and unchanged hypotheses.

The complex repeat pass image pixel values g_k are realisations of a zero mean, complex Gaussian random variable with variance $\sigma_{g_0}^2$ under H_0 and $\sigma_{g_1}^2$ under H_1. The change statistic z therefore has a Chi square density function under each hypothesis given by,

$$p(z; H_0) = \frac{1}{\Gamma(N)\sigma_{H_0}^2} \left(\frac{z}{\sigma_{H_0}^2} \right)^{N-1} exp\left(\frac{-z}{\sigma_{H_0}^2} \right), \tag{6.63}$$

$$p(z; H_1) = \frac{1}{\Gamma(N)\sigma_{H_1}^2} \left(\frac{z}{\sigma_{H_1}^2} \right)^{N-1} exp\left(\frac{-z}{\sigma_{H_1}^2} \right), \tag{6.64}$$

where,

$$\sigma_{H_0}^2 = \frac{(\sigma_{g_1}^2 - \sigma_{g_0}^2)}{\sigma_{g_1}^2}, \tag{6.65}$$

$$\sigma_{H_1}^2 = \frac{(\sigma_{g_1}^2 - \sigma_{g_0}^2)}{\sigma_{g_0}^2}. \tag{6.66}$$

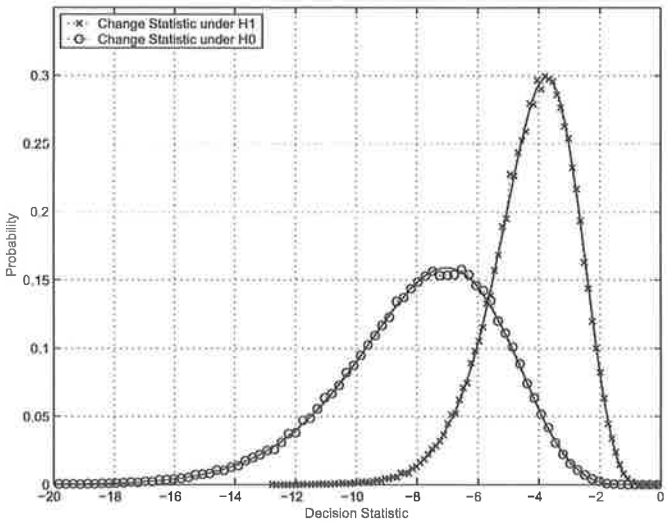


Figure 6.7: Density functions for the decision statistic under H_0 and H_1 for the case of zero coherence $\gamma = 0$ and mean backscatter powers of $\sigma^2_{g_0} = 1.7847e8$ and $\sigma^2_{g_1} = 0.95067e8$ (a 2.73 dB reduction in the mean backscatter power) and $N = 9$.

Figure 6.7 shows the density function of the decision statistic z for both H_0 and H_1 obtained by direct computation of (6.63) and (6.64) and via simulation for the experimental change scenario in which $\sigma^2_{g_0} = 1.7847e8$ and $\sigma^2_{g_1} = 0.95070e8$. These values correspond to the same scene change detection scenario considered in Section 7.3 in which the scene disturbances have caused a 2.73 dB reduction in the mean backscatter power in the repeat pass image.

6.7 Detection Performance of Clairvoyant Detector

The detection performance of the log likelihood change statistic is concisely described by means of an ROC curve indicating the probability of detection P_d and probability of false alarm P_{fa} corresponding to a particular decision threshold T,

$$P_{fa} = \int_T^\infty p(z; H_0)dz, \tag{6.67}$$

$$P_d = \int_T^\infty p(z; H_1)dz. \tag{6.68}$$

Expressions for P_d and P_{fa} as a function of the decision threshold for the change statistic may be derived using the density functions $p(z; H_0)$ and $p(z; H_1)$ given in (6.35) and (6.37). The probability of detection and the probability false alarm thus both take the following general form, for $T > 0$,

$$\begin{aligned} P &= \frac{(1-\rho^2)^N}{\Gamma(N)(\alpha\beta)^N} \sum_{k=0}^{\infty} \left[\mu_k \sum_{p=0}^{N+k-1} \left[\binom{N+k-1}{p} \frac{\Gamma(2N+2k-p-1)}{\nu^{2k+2N-p-1}} \int_T^\infty e^{\left(-\frac{z}{\beta}\right)} (z)^p dz \right] \right], \\ &= \frac{(1-\rho^2)^N}{\Gamma(N)(\alpha\beta)^N} \sum_{k=0}^{\infty} \left[\mu_k \sum_{p=0}^{N+k-1} \left[\binom{N+k-1}{p} \beta^{p+1} \frac{\Gamma(2N+2k-p-1)}{\nu^{2k+2N-p-1}} \right. \right. \\ &\qquad \left. \left. \Gamma_{inc}\left(p+1, \frac{T}{\beta}\right) \right] \right], \end{aligned} \tag{6.69}$$

where Γ_{inc} is the complementary incomplete gamma function given by,

$$\Gamma_{inc}(a,t) = \int_t^\infty exp(-x)x^{a-1}dx. \tag{6.70}$$

For $T \leq 0$ the integrals giving the probability of false alarm (6.67) and probability of detection (6.68) must be partitioned into integrals from T to 0 where $p(z)$ is given by (6.35) plus integrals from 0 to ∞ where $p(z)$ is given by (6.37). The probability of detection and probability of false alarm thus both take the following form for $T < 0$,

$$\begin{aligned}
P &= \frac{(1-\rho^2)^N}{\Gamma(N)(\alpha\beta)^N}\sum_{k=0}^{\infty}\left[\mu_k\sum_{p=0}^{N+k-1}\left[\binom{N+k-1}{p}\frac{\Gamma(2N+2k-p-1)}{\nu^{2k+2N-p-1}}\right.\right. \\
&\qquad \left.\left.\left[\int_0^\infty e^{(-\frac{z}{\beta})}(z)^p dz + \int_T^0 e^{(\frac{z}{\alpha})}(-z)^p dz\right]\right]\right], \\
&= \frac{(1-\rho^2)^N}{\Gamma(N)(\alpha\beta)^N}\sum_{k=0}^{\infty}\left[\mu_k\sum_{p=0}^{N+k-1}\left[\binom{N+k-1}{p}\frac{\Gamma(2N+2k-p-1)}{\nu^{2k+2N-p-1}}\right.\right. , \\
&\qquad \left.\left.\left[\beta^{p+1}\Gamma(p+1) + \int_0^{-T} e^{-(\frac{z}{\alpha})}(z)^p dz\right]\right]\right], \\
&= \frac{(1-\rho^2)}{\Gamma(N)(\alpha\beta)^N}\sum_{k=0}^{\infty}\left[\mu_k\sum_{p=0}^{N+k-1}\left[\binom{N+k-1}{p}\frac{\Gamma(2N+2k-p-1)}{\nu^{2k+2N-p-1}}\right.\right. \\
&\qquad \left.\left.\left[\beta^{p+1}\Gamma(p+1) + \alpha^{p+1}\left(\Gamma(p+1) - \Gamma_{inc}\left(p+1, \frac{-T}{\alpha}\right)\right)\right]\right]\right],
\end{aligned} \tag{6.71}$$

where the following relation has been used [AS72],

$$\int_0^t exp(-x)x^{(a-1)}dx = \Gamma(a) - \Gamma_{inc}(a,t). \tag{6.72}$$

The values for C_{11}, C_{22} and ρ used in the computation of μ_k, α and β in (6.69) and (6.71) are defined in (6.23) for each hypotheses.

Detection Performance Under Equal Backscatter Power

In the case where the primary and repeat pass images have equal mean backscatter parameters under both H_0 and H_1 the following simpler general forms for the probability of detection or probability of false alarm are obtained, for $T > 0$,

$$\begin{aligned}
P &= \frac{1}{\Gamma^2(N)(\lambda_1 C_{11}\lambda_2 C_{22})^N}\sum_{p=0}^{N-1}\left[\binom{N-1}{p}\frac{\Gamma(2N-p-1)}{\nu^{2N-p-1}}\int_T^\infty exp\left(\frac{-z}{\lambda_2 C_{22}}\right)z^p dz\right], \\
&= \frac{1}{\Gamma^2(N)(\lambda_1 C_{11}\lambda_2 C_{22})^N}\sum_{p=0}^{N-1}\left[\binom{N-1}{p}\frac{\Gamma(2N-p-1)}{\nu^{2N-p-1}}\right. \\
&\qquad \left.(\lambda_2 C_{22})^{p+1}\Gamma_{inc}\left(p+1, \frac{T}{\lambda_2 C_{22}}\right)\right],
\end{aligned} \tag{6.73}$$

and for $T \leq 0$,

$$\begin{aligned} P &= \frac{1}{\Gamma^2(N)(\lambda_1 C_{11}\lambda_2 C_{22})^N} \sum_{p=0}^{N-1} \left[\begin{pmatrix} N-1 \\ p \end{pmatrix} \frac{\Gamma(2N-p-1)}{\nu^{2N-p-1}} \right. \\ &\qquad \left. \left[\int_T^0 exp\left(\frac{-z}{\lambda_1 C_{11}}\right)(-z)^p dz + \int_0^\infty exp\left(\frac{-z}{\lambda_2 C_{22}}\right)(z)^p dz \right] \right], \\ &= \frac{1}{\Gamma^2(N)(\lambda_1 C_{11}\lambda_2 C_{22})^N} \sum_{p=0}^{N-1} \left[\begin{pmatrix} N-1 \\ p \end{pmatrix} \frac{\Gamma(2N-p-1)}{\nu^{2N-p-1}} \right. \\ &\qquad \left. \left[(\lambda_2 C_{22})^{p+1}\Gamma(p+1) + (\lambda_1 C_{11})^{p+1}\Gamma_{inc}\left(p+1, \frac{-T}{\lambda_1 C_{11}}\right) \right] \right]. \end{aligned} \tag{6.74}$$

Detection Performance Under Zero Coherence

For the case in which the coherence under H_0 is zero, substituting equation (6.63) into the probability of false alarm integral gives,

$$\begin{aligned} P_{fa} &= \frac{1}{\Gamma(N)\sigma_{H_0}^{2N}} \int_T^\infty z^{(N-1)} exp\left(-\frac{z}{\sigma_{H_0}^2}\right) dz, \\ &= \frac{1}{\Gamma(N)} \int_{\frac{T}{\sigma_{H_0}^2}}^\infty t^{(N-1)} exp(-t) dt, \end{aligned} \tag{6.75}$$

where the substitution $t = z/\sigma_{H_0}^2$ has been used. The integral in (6.75) may be rewritten using the relation,

$$\int_x^\infty t^{(N-1)} exp(-t) dt = \Gamma(N)\left(1 - \frac{1}{\Gamma(N)} \int_0^x t^{(N-1)} exp(-t) dt\right), \tag{6.76}$$

(equation 6.5.3 in [AS72]) to give,

$$P_{fa} = \left(1 - \frac{1}{\Gamma(N)} \int_0^{\frac{T}{\sigma_{H_0}^2}} t^{(N-1)} exp(-t) dt\right), \tag{6.77}$$

However from equation 6.5.13 in [AS72],

$$\frac{1}{\Gamma(N)} \int_0^x t^{(N-1)} exp(-t) dt = 1 - exp(-x) \sum_{k=0}^{N-1} \frac{x^k}{k!}, \tag{6.78}$$

thus the proability of false alarm is given by,

$$P_{fa} = exp\left(-\frac{T}{\sigma_{H_0}^2}\right) \sum_{k=0}^{N-1} \frac{1}{k!} \left(\frac{T}{\sigma_{H_0}^2}\right)^k. \tag{6.79}$$

Similarly, substituting equation (6.64) into the probability of detection integral it may be shown that

$$P_d = exp\left(-\frac{T}{\sigma_{H_1}^2}\right) \sum_{k=0}^{N-1} \frac{1}{k!} \left(\frac{T}{\sigma_{H_1}^2}\right)^k. \tag{6.80}$$

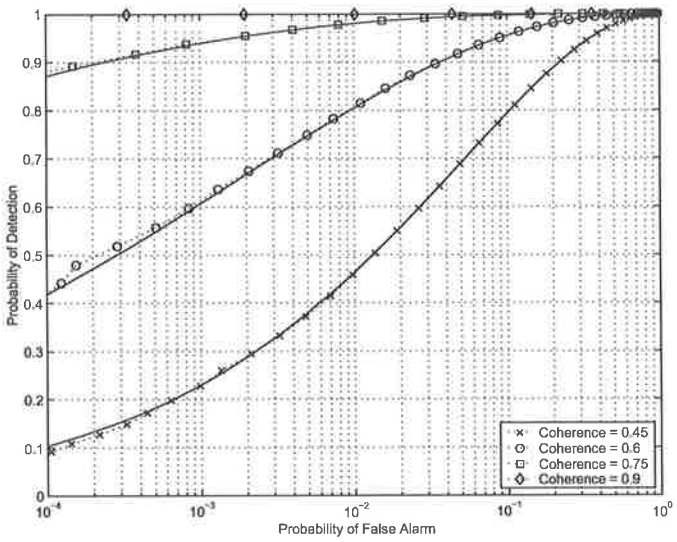


Figure 6.8: Theoretical and simulated ROC curves for equal channel powers and coherence values of 0.45, 0.6, 0.75 and 0.9 with $N = 9$.

Theoretical and Simulated ROC Curves

Figures 6.8 and 6.9 give the theoretical and simulated ROC curves of the clairvoyant decision statistic for the equal backscatter power case for various values of coherence γ and various values of N respectively. From Figure 6.8 the sensitivity of the clairvoyant decision statistic to the scene coherence can be assessed. For $N = 9$ and a probability of detection of 0.7 the probability of false alarm for $\gamma = 0.45$ is approximately 0.05 while at $\gamma = 0.6$ the probability of false alarm is reduced by over an order to magnitude to 0.002. Increasing the coherence to $\gamma = 0.75$ yields false alarm rates of well below 10^{-4}. From Figure 6.9 it can be seen that increasing the number of pixels N in the decision statistic calculation can provide significant improvements in the detection performance albeit at the expense of resolution in the change detection map. At a probability of detection of 0.7 and $N = 4$ the probability of false alarm is approximately 0.06 while for $N = 9$ this is reduced by over an order to magnitude to 0.002.

As Figures 6.8 and 6.9 describe the ROC performance of the log likelihood change statistic where discrimination between the hypotheses is based solely on the scene coherence under H_0, these ROC curves may be directly compared with those of the sample coherence change statistic examined in Chapter 5. A comparison of Figures 6.8 and 6.9 with the corresponding ROC curves of the sample coherence given in Figures 5.8 and 5.9 indicates that the log likelihood change statistic offers a significantly improved detection performance with false alarm rates typically an order of magnitude better than those of the sample coherence. For a probability of detection of 0.7 at a coherence of $\gamma = 0.45$ the probability of false alarm for the sample coherence is 0.25 while for the log likelihood statistic it is 0.05. For a coherence of 0.6 the improvement is more pronounced with the probability of false alarm for the sample coherence being 0.06 compared to 0.003 for the log likelihood statistic.

Figures 6.10 and 6.11 give the theoretical and simulated ROC curves for the clairvoyant decision statistic for the case when the image pair are uncompletely correlated ($\gamma = 0$) under both H_0 and H_1. In this case discrimination between the hypotheses is made solely on the basis of differing mean backscatter power. A comparison of the ROC curves in Figure 6.10 and those in Figure 6.8 indicates that the detection performance of the log likelihood decision statistic for a mean backscatter change

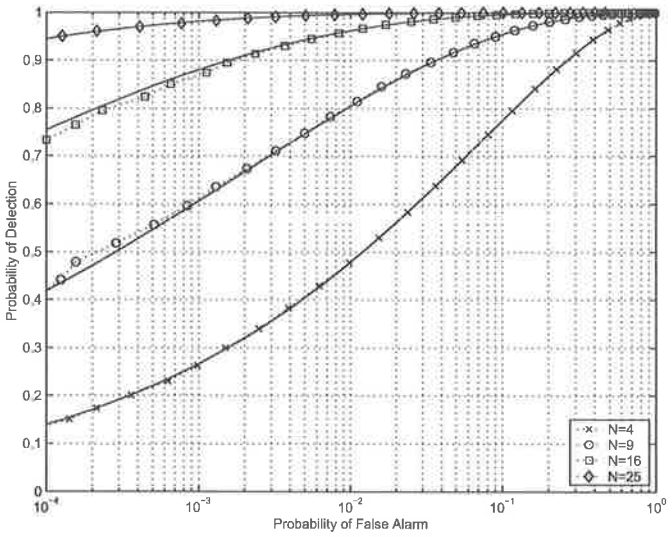


Figure 6.9: Theoretical and simulated ROC curves for equal channel powers and N = 4, 9, 16, 25 with a coherence of 0.6.

of 3 dB is similar to that achieved with a partial coherence under H_1 of $\gamma = 0.45$. Figure 6.11 shows the ROC curves for $\gamma = 0$ and various values of N used in the calculation of the decision statistic. Increasing the size of the calculation window improves the detection performance at the expense of resolution in the change detection map.

Figure 6.12 shows the ROC curves for the clairvoyant log likelihood decision statistic, the sample coherence and the mean backscatter ratio statistic for the experimental scene change scenario, i.e., a mean backscatter change of 1.04 dB under H_0 and 3.77 dB under H_1, a coherence $\gamma = 0.45$ for H_0 and $N = 9$. It can be seen from Figure 6.12 that the sample coherence and mean backscatter ratio statistics have similar detection performance. The clairvoyant log likelihood statistic however provides a significantly better detection performance. For a probability of detection of 0.7 the probability of false alarm in the log likelihood detector is 0.03 which is almost an order of magnitude better than that of either the sample coherence or the mean backscatter ratio which is approximately 0.25.

The ROC curves in Figures 6.8 to 6.12 inclusive describe the performance of a clairvoyant detector in which perfect knowledge of the unknown parameters has been assumed. The performance comparisons thus made between the log likelihood decision statistic, the sample coherence and mean backscatter ratio statistic represent an upper bound on the improvement that may be achieved in any practical implementation of the log likelihood decision statistic. Achieving this level of improvement in a practical implementation requires the unknown parameters to be quantified with high precision and this will be discussed in the following section.

6.8 A Generalised Likelihood Ratio Test

The detection performance of the log likelihood change statistic derived in the previous section pertains to a clairvoyant detector in which perfect knowledge of the unknown scene parameters given by,

$$\underline{v} = \begin{cases} \underline{v}_{H_0} = [\gamma, \Phi, \sigma_f^2, \sigma_{g_0}^2]^T, & \text{under } H_0, \\ \underline{v}_{H_1} = [\sigma_f^2, \sigma_{g_1}^2]^T, & \text{under } H_1, \end{cases} \tag{6.81}$$

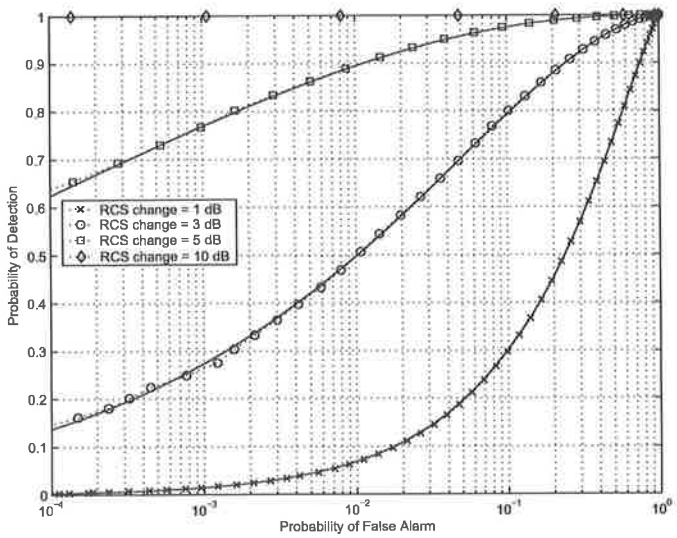


Figure 6.10: Theoretical and simulated ROC curves for zero coherence under H_0 and changes in the backscatter power of $\sigma_{g1}^2/\sigma_{g0}^2$ = 1 dB, 3 dB, 5 dB and 10 dB with $N = 9$.

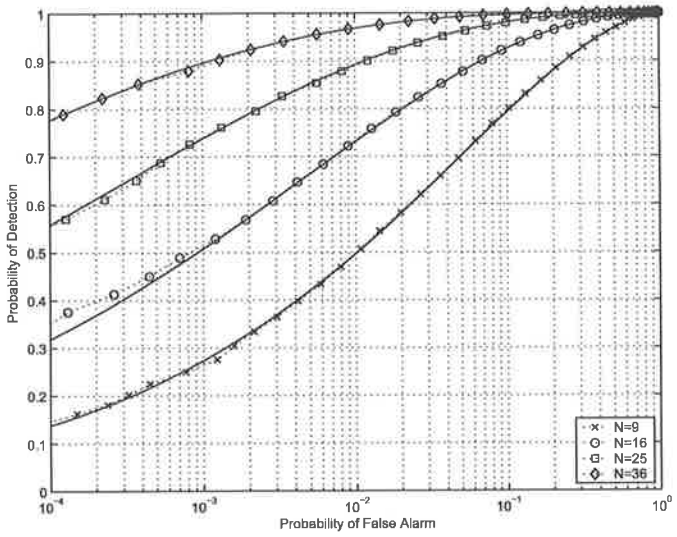


Figure 6.11: Theoretical and simulated ROC curves for zero coherence under H_0 and N = 9, 16, 25 and 36 with a change in the backscatter power value of $\sigma_{g1}^2/\sigma_{g0}^2$ = 3 dB.

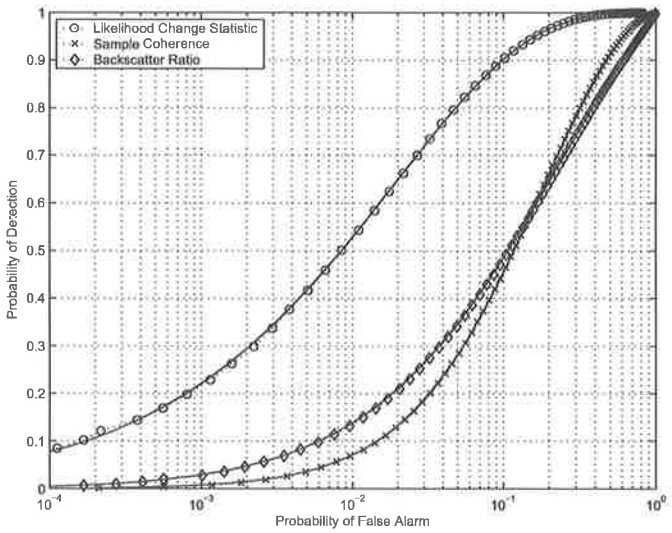


Figure 6.12: Theoretical and simulated ROC curves for a scene change scenario where the mean backscatter ratio of the primary and repeat pass images is 1.04 dB under H_0 and 3.77 under H_1, $N = 9$ and $\gamma = 0.45$.

has been assumed. While such a detector is unrealisable, it is an optimal Neyman-Pearson detector and gives an upper bound on the detection performance of any practical detector implementation. A Generalised Likelihood Ratio Test (GLRT) is an easy to implement practical detector in which the unknown scene parameters are replaced with their maximum likelihood estimates obtained from the observed data,

$$\underline{\hat{v}}_{H_0} = \max_{\underline{v}} p(\underline{x}_k; \underline{v}, H_0), \tag{6.82}$$

$$\underline{\hat{v}}_{H_1} = \max_{\underline{v}} p(\underline{x}_k; \underline{v}, H_1). \tag{6.83}$$

The resultant degradation in the performance of the GLRT from the optimal clairvoyant detector is dependent on the quality of the sample estimates $\underline{\hat{v}}_{H_0}$ and $\underline{\hat{v}}_{H_1}$. Using Bayes theorem the density function of the GLRT may be written in terms of the density function of the clairvoyant detector and the conditional density function of the parameter estimates,

$$p(z, \underline{v}) = p(\underline{v}) \int p(z|\underline{\hat{v}}) p(\underline{\hat{v}}|\underline{v}) d\underline{\hat{v}}. \tag{6.84}$$

The function $p(z|\underline{\hat{v}})$ is the probability density of the decision statistic given the parameter estimate $\underline{\hat{v}}$. It has the same form as the density function of the clairvoyant detector given by (6.35) and (6.37) or (6.57), (6.60) and (6.61) in the case of equal channel powers, or (6.79) and (6.79) in the case of zero coherence. The conditional joint density function $p(\underline{\hat{v}}|\underline{v})$ measures the quality of the parameter estimates that are retrieved from the observed data set. In equation (6.84) $p(\underline{\hat{v}}|\underline{v})$ scales the performance of the clairvoyant detector by the uncertainty inherent in the parameter estimates. In this Bayesian framework prior knowledge regarding the parameters may be incorporated via the density function $p(\underline{v})$. Given a sufficiently detailed description of the physical properties of the scene and the sources of temporal decorrelation a probabilistic description $p(\underline{v})$ of the scene parameters may be constructed. However in general a non-informative prior is used in which all parameter values are assumed to be equally likely thus $p(\underline{v})$ is effectively a normalisation constant.

6.8.1 Parameter Estimates

The log likelihood change statistic is computed over a local N pixel area under test. In order to compute the GLRT regions in the primary and repeat pass must be identified from which suitable estimates of the unknown scene parameters may be obtained. Furthermore the pixels in these estimation regions must be characteristic of the N pixel region under test. That is, they must be realisations of the H_0 and H_1 hypotheses used to construct the log likelihood change statistic in the local N pixel area under test. In general, provided a sufficiently large number of data samples M, characteristic of the local area under test are available, high quality parameter estimates may be recovered. Furthermore the existence of prior knowledge regarding the nature of the scene disturbances and the backscatter characteristics of the region under test may be used to help refine the parameter estimates and near optimal detection performance may be achieved using the GRLT.

In the change detection scenarios considered in this thesis, such as the detection of vehicle tracks across an open field, the scene disturbances are typically localised and isolated to specific regions in the scene. Furthermore the scene changes are also typically on a significantly smaller spatial scale than variations in the underlying statistical properties of the scene's complex radar backscatter. Under these conditions large homogeneous areas for estimating the unknown scene parameters may be readily identified. Indeed using a fine resolution sensor and processing a wide-angle collection aperture estimation windows consisting of a statistically significant number of samples, suitable for estimating the unknown parameters may be readily obtained. An example of the change detection problem has previously been considered in Chapter 4. Figures 4.11 and 4.12 show the primary and repeat pass image of an open field over which the transduced scene backscatter is relatively homogeneous. Figures 4.13 and 4.14 show the sample coherence estimate and interferometric phase estimate respectively obtained from the interferometric image pair. The track like areas of low coherence correspond to scene disturbances and are spatially quite small. The coherence and interferometric phase across the scene, aside from the changed areas, appears relatively constant. For this scene change scenario it is clear that a large estimation window may be selected containing pixels characteristic of the local area under test.

Estimating the Mean Backscatter

The maximum likelihood estimate of the mean backscatter power over a locally stationary neighbourhood of M pixels $p_k, k = 1 \cdots M$, is given by,

$$\hat{\sigma}_p^2 = \frac{1}{M} \sum_{k=1}^{M} |p_k|^2. \tag{6.85}$$

In general neighbouring pixels will exhibit some degree of correlation defined by the point spread function of the radar as well as correlation induced by the underlying mean backscatter power of the scene. This correlation may be mitigated to some extent by subsampling the image pixels. This improves the quality of the estimate at the expense of resolution in the estimate. Alternatively, given knowledge of the correlation matrix C_s of the M complex pixels the maximum likelihood estimate is given by

$$\hat{\sigma}_p^2 = \frac{1}{M} \underline{p}^H C_S^{-1} \underline{p} \tag{6.86}$$

where $\underline{p}$ is the vector of the M image pixels.

In order to provide a complete description of a repeat pass interferometric pair an estimate of the mean backscatter power in the primary image σ_f^2 is required, as well as an estimate of the mean

backscatter in the repeat pass image under the unchanged hypothesis, $\sigma^2_{g_0}$ and under the changed hypothesis, $\sigma^2_{g_1}$. An estimate of σ^2_f may be retrieved from the primary image by identifying an M pixel area which is characteristic of the local area under test and computing (6.85) or (6.86). For scenes consisting of open fields with homogeneous clutter characteristics good quality estimates of σ^2_f are readily obtained. In general, for more complicated scenes, some form of image segmentation for identifying homogeneous regions is desirable. Image segmentation based on the mean backscatter characteristics has been an active area of research over many years and as such a plethora of speckle reduction and segmentation techniques are available in the literature [FSSH82], [LMH94], [Whi95] for identifying and estimating the backscatter of homogeneous regions.

Estimation of the mean backscatter power terms $\sigma^2_{g_0}$ and $\sigma^2_{g_1}$ in the repeat pass image requires identifying neighbourhoods of pixels that are realisations of each hypotheses. This may only be achieved with some form of a-priori information describing the scene and the likely change detection scenario. For change scenarios in which small localised isolated man-made disturbances such as vehicle tracks are to be detected it may be sufficient to assume that the disturbance has not significantly altered the underlying backscattering properties in which case $\sigma^2_{g_0} = \sigma^2_{g_1}$. The repeat pass backscatter power may thus be estimated using (6.85) evaluated over an M pixel neighbourhood using the same methodology used to estimate σ^2_f as discussed above. Alternatively in the case of more significant disturbances such as earth works which may cause a measurable change to the underlying backscatter characteristics calculation of the mean backscatter ratio change statistic defined in Chapter 5 in equation (5.18) may allow an approximate segmentation of the repeat pass image into changed and unchanged regions to allow the estimation of $\sigma^2_{g_0}$ and $\sigma^2_{g_1}$.

Estimating the Scene Complex Coherence

In the unchanged scene hypothesis H_0 the scene coherence γ is related to the stable scattering component of the transduced scene radar reflectivity in the primary and repeat pass image pair. The interferometric phase Φ on the other hand is determined by the baseline offset between the imaging geometries used in the primary and repeat pass collections as well as the scene topography. The coherence and interferometric phase may be estimated over an M pixel window by,

$$\hat{\gamma} = \frac{|\sum_{k=1}^{M} f_k g_k^*|}{\sqrt{\sum_{k=1}^{M} |f_k|^2 \sum_{k=1}^{M} |g_k|^2}}, \tag{6.87}$$

$$\hat{\Phi} = arg\left\{\sum_{k=1}^{M} f_k g_k^*\right\}, \tag{6.88}$$

respectively, provided γ and Φ are constant over the spatial extent of the window. The variability of the underlying true coherence across the scene will depend on the homogeneity of the vegetation cover and the sources of temporal decorrelation. In the case of an open field in which the vegetation cover is expected to be homogeneous over relatively large areas and subject to the same degree of temporal decorrelation suitably large estimation windows may be defined. The resultant estimate of coherence may then be used in computing the log likelihood change statistic for testing local areas within the field. In general the estimation window should be located in an area without man-made scene disturbances otherwise the estimate will contain a mixture of changed and unchanged pixels. However, provided the scene disturbances are spatially small, as is the case for the image pair in Figures 4.11 and 4.12, and the estimation window sufficiently large, the estimation window may include change areas without any significant impact on the quality of the estimate.

The interferometric phase Φ is related to the terrain topography thus the estimation window must be restricted to locally flat regions. However, given the interferometric baseline between the primary

and repeat pass collections, as measured by the radar navigation instruments, plus a digital elevation map of the scene the spatial variation of the interferometric phase due to the terrain topography may be removed. This potentially allows larger windows to be used for the estimation of the complex coherence.

6.8.2 Application to Experimental Data

Given the joint density function of the parameter estimates the degradation in the detection performance of the log likelihood change statistic may be quantified by computing (6.84). This is mathematically difficult and a solution has not been found. However, given suitably large estimation windows high quality estimates of the parameters $\underline{v}_{H_0}$ and $\underline{v}_{H_1}$ are readily retrieved and the degradation in detection performance is minimal.

An indication of the average change detection performance that may be expected for a given sample size M used in the estimation of $\underline{v}_{H_0}$ and $\underline{v}_{H_1}$ can be obtained using Monte-Carlo simulation techniques. In this approach a large number of independent sample estimates of $\underline{v}_{H_0}$ and $\underline{v}_{H_1}$ are generated using the estimation window size M. (Note that the size of the sample window (M) used to estimate the parameters and that of the one (N) used to calculate the log likelihood statistic will not, in general, be the same.) Each such sample estimate of $\underline{v}_{H_0}$ and $\underline{v}_{H_1}$ may be used to specify estimates of Q_0 and Q_1 in the log likelihood change statistic defined in (6.10). An ROC curve for this "realisation" of the log likelihood change statistic may be generated by evaluating this instance of the change statistic over simulation scenes described by the changed and unchanged scene hypotheses. Subsequent averaging of the ROC performance of all log likelihood ratio change statistics obtained from the sample estimates of $\underline{v}_{H_0}$ and $\underline{v}_{H_1}$ yields an ROC curve indicating the average detection performance for the given scene change scenario and sample window sizes M and N.

Figure 6.13 shows the average ROC curves for the log likelihood change statistic obtained via Monte-Carlo simulation for sample window sizes of $M = 25, 64, 121$ and 400 and $N = 7$. The true changed and unchanged scene covariance matrices used in this simulation are based on the experimental repeat pass interferometric change detection scenario considered in Chapter 7 Section 7.5 where, $\gamma = 0.62$ and $\sigma_{g_0}^2 = \sigma_{g_1}^2$. Also shown in Figure 6.13 are the theoretical ROC curves for the clairvoyant log likelihood change statistic and the sample coherence change statistic. From Figure 6.13, for the given change detection scenario, it is clear that even with a modest window size of $M = 25$ the average detection performance of the log likelihood change statistic is better than that achieved with the sample coherence change statistic. However, to achieve an average detection performance comparable to the clairvoyant detector window sizes (M) of the order of several hundred pixels are required.

In Chapter 7 the log likelihood change statistic is applied to experimental repeat pass interferometric data collected with the DSTO Ingara airborne X-band SAR and the significant performance improvement of the change statistic over the sample coherence and mean backscatter power ratio is demonstrated.

6.9 Conclusions

In this chapter a new change statistic is proposed for detecting man-made scene disturbances in repeat pass SAR interferometry. The change statistic was derived by formulating the detection problem in a hypothesis testing framework and forming the log likelihood ratio. The change statistic is capable of identifying scene disturbances through changes in the scene coherence as well as changes in the scene backscatter coefficient via a single change statistic. Theoretical analysis of a clairvoyant

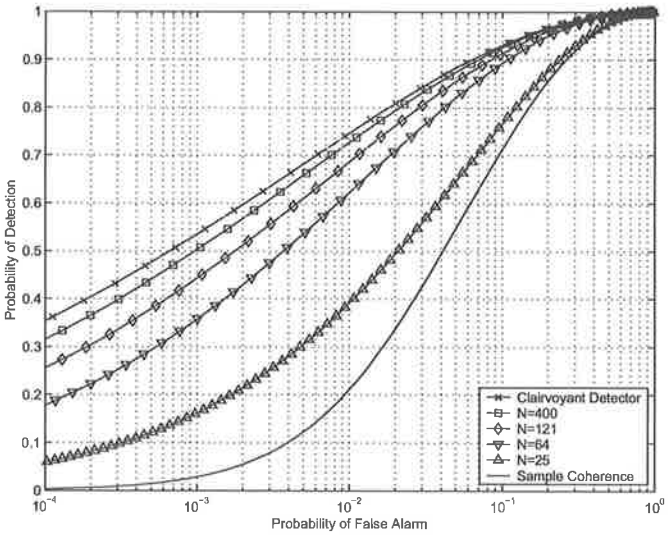


Figure 6.13: Average ROC curves for the log likelihood change statistic obtained using Monte-Carlo simulation techniques. Sample window sizes of $M = 25, 64, 121$ and 400 have been used to estimate $\underline{v}_{H_0}$ and $\underline{v}_{H_1}$ and a window size of $N = 7$ has been used to compute the log likelihood statistic. The unchanged scene coherence is $\gamma = 0.62$ and it has been assumed that $\sigma^2_{g_0} = \sigma^2_{g_1}$.

detector based on the change statistic, where perfect knowledge of the unknown hypothesis parameters is assumed, gives significantly better detection performance than that of the sample coherence and the backscatter coefficient ratio change statistics. Through the use of a-priori information good quality estimates of the unknown parameters may be obtained and a practical detector based on the log likelihood decision statistic may be implemented with only a modest reduction in detection performance. The significant improvements in the detection performance that can be achieved using the log likelihood change statistic represent an important step towards the design of an automated change detection algorithm suitable for the processing of large data sets.

Chapter 7

Experimental Results

7.1 Introduction

Man-made scene disturbances manifest in a repeat pass interferometric SAR image pair as a loss in coherence between the image pair as well as a possible change in the mean backscatter power. In Chapter 5 the mean backscatter power ratio and sample coherence were considered as possible change statistics and their detection performance analysed. In general the ability of these statistics to detect subtle, fine-scale changes is limited by high false alarm rates unless significant averaging is carried out resulting in a degradation in the resolution of the change statistics. In Chapter 6 an alternative log likelihood change statistic was proposed based on an hypothesis testing formulation of the change detection problem. Theoretical and simulation results indicated that the new log likelihood change statistic provides significantly improved detection performance over both the mean backscatter power ratio and the sample coherence, provided the underlying assumptions and models describing the changed and unchanged hypotheses are valid.

In this chapter the mean backscatter power ratio, sample coherence and log likelihood change statistics are applied to experimental repeat pass interferometric SAR data collected using the Defence Science and Technology Organisation's (DSTO) Ingara X-band airborne SAR. In these experiments a variety of ground truthed scene changes were carried out and repeat pass imagery was collected with a range of imaging geometries and revisit periods. In this chapter three different repeat pass experiments are selected for change detection analysis and the theoretical and experimental detection performance of the change statistics are compared.

Section 7.2 outlines the repeat pass interferometry experiments conducted using the Ingara airborne SAR. The interferometric processing methodology applied to the raw signal history data and the validation of the log likelihood models are also discussed. In Sections 7.3, 7.4 and 7.5 the change detection statistics are applied to three different experimental scene change scenarios. In Section 7.3 a change scenario consisting of a change in mean backscatter power and a loss of coherence is examined. In Section 7.4 a change scenario involving subtle, fine scale track like disturbances resulting in a loss of coherence is processed. Finally in Section 7.5 the detection of ground truthed scene changes is examined using high incidence angle collections in which the processed image pairs deviate from the complex Gaussian scattering model. For each of these experimental change scenarios the superior detection performance of the log likelihood change statistic is demonstrated.

7.2 Experimental Interferometric Data

In order to examine the practical performance of the mean backscatter power ratio, sample coherence and log likelihood change statistics experimental repeat pass interferometric image pairs with the following attributes are required.

1. Single look complex SAR imagery.
   - In formulating the log likelihood change statistic the interferometric phase is an important parameter both in the evaluation of the change statistic over the image pair and in the formulation of the unchanged scene hypothesis. Single look complex SAR imagery is required to provide the necessary interferometric phase estimates.
   - The scene coherence change statistic may be estimated by computing the sample complex cross correlation coefficient using the full complex primary and repeat pass imagery. For the case in which the image pair exhibit jointly Gaussian scattering behaviour the scene coherence may also be estimated using the correlation of the image intensities alone. In Chapter 5 however, this statistic was shown to be a poor estimator of the scene coherence compared to the sample complex cross correlation coefficient estimate. As a consequence the detection performance of the intensity correlation statistic is significantly worse than that of the sample complex cross correlation coefficient and will not be considered.
   - The mean backscatter power ratio change statistic is simply based on changes in the mean backscatter power which may be estimated, in a maximum likelihood sense, from the image intensity data alone.

2. Minimal baseline offset between primary and repeat pass collections.
   In the terrain mapping application of interferometry the cross track baseline offset between the primary and repeat pass image collections is crucial to defining the relationship between the transduced interferometric phase and the terrain height of the scene. For change detection however, the baseline offset is a source of decorrelation between the primary and repeat pass image pairs which can degrade the detection performance of coherence based change statistics. The baseline decorrelation may be compensated for via aperture trimming during image formation but only at the expense of resolution in the image pairs and ultimately in the change detection map. To minimise baseline decorrelation and maintain resolution in the change detection maps it is thus desirable to fly identical repeat pass flight tracks for change detection applications.

3. Image pair resolution.
   The repeat pass image pairs should be generated with a resolution commensurate with the size of the scene disturbance to be detected. Each of the change statistics considered here requires spatial averaging over a local neighbourhood of pixels to achieve good quality parameter estimates. Spatial averaging however, assumes that the underlying scene statistics in the local neighbourhood are stationary otherwise the parameter estimates will contain contributions from pixels described by differing random processes. In particular, man-made scene disturbances such as vehicle tracks may occur abruptly in the scene and may be spatially small. Therefore unless the image resolutions are sufficiently fine, the spatial estimates will contain contributions from both changed and unchanged image pixels leading to a degradation in the ability to distinguish between changed and unchanged regions in the scene.

4. Radar wavelength.
   In Chapter 5 Zebker's model [ZV92] describing the effects of temporal decorrelation on an imaged scene in a repeat pass SAR acquisition was considered. In this model the ensemble of

scene scatterers contributing to the transduced scene backscatter are subject to random displacements in the interval between image collections. Assuming that the scatterer displacements in range, azimuth and elevation are independent, identically Gaussian distributed random variables a simple relationship between the imaging incidence angle, RMS scatterer displacement, radar wavelength and the scene coherence may be derived. For the range of incidence angles encountered in typical airborne SAR imaging geometries the model indicates that a scatterer RMS displacement of around 20 percent of the radar wavelength leads to total scene decorrelation. The model thus indicates that smaller wavelength systems are more sensitive to temporal decorrelation. For example, for X-band radars with a wavelength of the order of 3 cm, complete scene decorrelation occurs with an RMS scatterer movement of 0.6 cm while for L-band radars the RMS movement is of the order of 5 cm.

5. Revisit period.
   The revisit period required to ensure reliable change detection performance is dependent on the evolution of the scene coherence over time in both the changed and unchanged regions of the scene and the ability of the change statistic to distinguish between the two. The change in the scene coherence over time is dependent on the sources and severity of environmental disturbances such as wind and rain. From Zebker's model describing the relationship between the scene decorrelation as a function of the radar wavelength, incidence angle and RMS scatterer displacement, it is clear that smaller wavelength SAR systems are more susceptible to temporal decorrelation than longer wavelength systems. Smaller wavelength systems thus require shorted revisit periods in order to reliably distinguish between scene disturbances of interest and other temporal decorrelation effects.

6. Detection of ground truthed scene disturbances.
   In order to verify the sensitivity of the change statistics and measure their respective performance controlled experiments are required in which repeat pass imagery is collected over ground truthed scene changes.

A large number of operational and experimental airborne and spaceborne SAR systems capable of generating repeat pass interferometric image pairs are currently in use around the world. The design of these systems, in particular their operating modes, system parameters and other capabilities however are generally not ideal for interferometric change detection applications. In particular there is a paucity of readily available fine resolution single look complex data with suitable revisit periods over well ground truthed data sets for demonstrating the full potential of coherent change detection and conducting research into the associated radar phenomenology.

Prior to the launch of the ERS-1 spaceborne SAR mission, research into repeat pass SAR interferometry was restricted to a few suitable data sets collected with the L-band Seasat SAR. In particular Goldstein [GZW88] was able to interferometrically process two, 50 m by 50 m resolution Seasat images, of the Cottonball Basin of Death Valley acquired 3 days apart to recover estimates of the terrain topography which were in close agreement with U.S. Geological Survey maps. The large wavelength and coarse resolution of the Seasat SAR however makes this system unsuitable for the detection of fine scale scene changes.

With the launch of the C-band ERS-1 SAR by the European Space Agency in July 1991, the ready availability of high quality modest resolution data sets with a revisit period of 35 days spurred the development of repeat pass SAR interferometry techniques, especially the terrain mapping application of interferometry. While there have been many other spaceborne SAR missions such as JERS-1 operated by the National Space Development Agency of Japan, RadarSAT-1 operated by the Canadian Space Agency and the Space Shuttle SIR-C system operated by NASA, the extensive his-

torical archive of high quality ERS SAR imagery spanning over a decade is unparalleled. Indeed the archive has facilitated the development of the Permanent Scatterer (PS) technique [FPR01] for fine scale mapping of surface deformations.

The potential for repeat pass interferometric change detection experiments using ERS-1 was greatly enhanced with the launch of ERS-2 in 1995. Careful selection of the orbital parameters of ERS-2 allowed ERS-1 and ERS-2 to be used in a tandem configuration giving minimum revisit periods of one day. Indeed the tandem mission data sets have been used with some success in demonstrating the potential of the sample coherence in detecting fine scale scene change. In [CR98] Corr was able to detect scene changes caused by the movement of large vehicles over a predominantly grassed area in Salisbury Plain, United Kingdom, using ERS imagery with 20 m resolution in range and 6 m resolution in azimuth. Over the changed areas Corr found an average coherence of 0.4 compared to 0.7 in the surrounding unmodified areas. Corr identified image resolution as an important parameter affecting the detection performance of the sample coherence change statistic. Unless a significant area is affected by the scene disturbance to be detected then a spatially averaged coherence estimate will contain contributions from both changed and unchanged pixels. This is reflected in the small separation in the estimated coherence of the changed and unchanged areas of the scene. The potential of the ERS data is thus limited in its ability to detect fine scale scene change. However, it has been used for detecting larger scale changes such as flood monitoring [GWV96] and changes in urban scenes such as detecting the construction or demolition of buildings [Cor97].

While spaceborne SAR systems offer systematic broad area global coverage, airborne systems provide considerable flexibility for the planning and conduct of specific ground truth experiments to study change detection techniques and the associated radar phenomenology. Repeat pass interferometry using airborne radars however is challenging due to the unstable radar platform and the difficulty in flying controlled repeat pass tracks within prescribed baseline tolerances. Despite these difficulties a number of advanced experimental airborne SAR systems operating over a range of bands including P, L, C and X-band are currently in use for conducting research into advanced interferometric techniques. The E-SAR [Hor96], [SRU+99] system flown in a Do-228 aircraft operated by the German Aerospace Centre (DLR) operates in X, C, S, L and P-band in either single pass or repeat pass interferometric modes. This system has been used in the conception and demonstration of new interferometric radar modes such as multipass three dimensional tomography [RM00] and polarimetric interferometry [CP98]. Another system used in repeat pass interferometry experiments is the Canadian Centre for Remote Sensing (CCRS) fully polarimetric C and X-band SAR flown on a Convair-580 aircraft [LGH+95]. The system has also been configured with a second C-band antenna to provide a single pass across track interferometer. An along track interferometric capability has also been developed via a pair of contiguously mounted sub-array antennas. The CCRS system has been used extensively for studies into coherence estimation [TLBV99], polarimetry [TL96] and along track interferometry [Gie01a]. Numerous other systems operate throughout the world providing high quality repeat pass fine resolution imagery. Despite the plethora of systems capable of generating suitable interferometric change detection data sets there is a paucity of published results in the open literature specifically addressing the detection of fine scale scene changes via coherent change detection techniques.

Given the lack of suitable data sets available for studying the practical performance of the change statistics considered in the previous chapters, a number of repeat pass interferometry experiments were conducted with the DSTO Ingara SAR [SBMS96], [SB94]. Use of the Ingara SAR system provided a number of distinct advantages in conducting research into interferometric change detection. The Ingara system is an X-band radar that offers a spotlight SAR mode capable of 0.5 m range resolution. Furthermore, access to the raw collected echo signal history permits the processing of wide angle, fine azimuth resolution imagery, with resolutions down to 0.15 m [PGS01]. For the detection

of spatially small, localised scene disturbances the fine resolution capability allows the formation of suitably small estimation windows commensurate with the size of the scene disturbances. Access to the raw signal history data also permits the optimal coherent aperture to be selected for the primary and repeat pass imagery so as to achieve maximal overlapping apertures of support for subsequent interferogram formation. Finally, as Ingara is an airborne system this allows considerable flexibility in defining imaging geometries, revisit periods and in obtaining ground truthed change detection data. This facilitates the compilation of a temporal history over a broad range of scene disturbances with acquisition intervals ranging from minutes to hours to days apart.

7.2.1 Ingara Repeat Pass SAR Experiments

At the time when the repeat pass interferometry experiments discussed below were conducted the Ingara airborne SAR was installed on a Beech 350 Super KingAir aircraft. Since that time the radar has been upgraded to provide a fully polarimetric X-band capability and has been rehosted onto a Beech 1900C [SBG+03]. The operating parameters for the radar, as configured for the repeat pass interferometry experiments, are detailed in Table 7.1.

Parameter	Value
Transmit waveform	LFM chirp, 400 MHz bandwidth
Transmitter power	8 kW
Polarization	HH
Radar centre frequency	9.35 GHz
Range resolution	0.5 m slant range resolution in spotlight mode
Incidence angle range	45 to 89 degrees

Table 7.1: System parameters for the Ingara airborne SAR as configured for the repeat pass interferometry experiments.

The first repeat pass change detection experiment with the Ingara SAR was performed in September 1999 and a later, more extensive, experiment was conducted in May 2000. The first change detection experiment was carried out in an open lightly grassed field. The field, shown in the SAR intensity image of Figure 7.1, has drainage trenches approximately 1.5 m wide and 0.8 m deep that are visible as lines of low backscatter running through the field. The field is bordered by a line of trees on the right hand side and by buildings and trees on the left hand side. Azimuthal smear evident in the imagery of the trees is due to the effects of wind moving the leaves and branches during the coherent processing interval of approximately 20 sec. Imaging sorties were flown at incidence angles of 75, 60 and 45 degrees both prior to, and at the completion of, a series of ground truthed scene changes. The scene changes, shown in Figure 7.1, consist of a series of strips of varying lengths and widths carried out using a rotary hoe and a lawn mower.

In the second repeat pass experiment conducted in May 2000 a more extensive measurement campaign was conducted providing a more detailed temporal history of a set of ground truthed scene disturbances. The scene, shown in Figure 7.2, consists of an open, lightly grassed field with a building located at the bottom of the image. A sealed road runs along the right hand side of the image and an unsealed road runs along the top of the scene. An open drainage trench is visible in the upper left hand corner of the image. In this change detection experiment a 20 m by 20 m scene change was performed using a rotary hoe and a long strip was modified using a lawn mower, as indicated in Figure 7.2. Imaging runs were conducted at a variety of incidence angles and revisit periods.

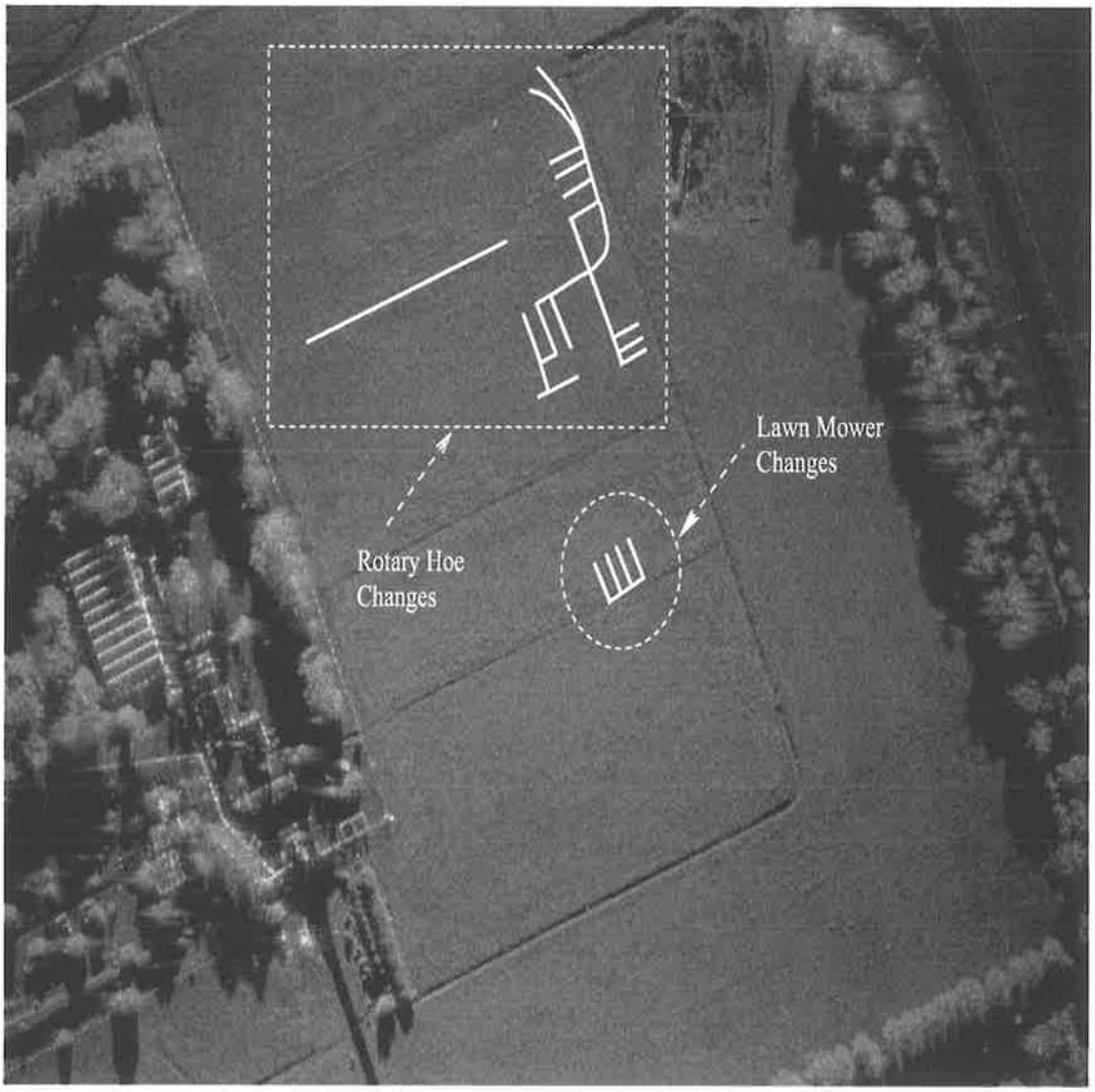


Figure 7.1: Intensity SAR image of the scene used for the September 1999 repeat pass interferometry experiments. Superimposed on the image is a schematic showing the scene changes carried out with the rotary hoe and lawn mower.

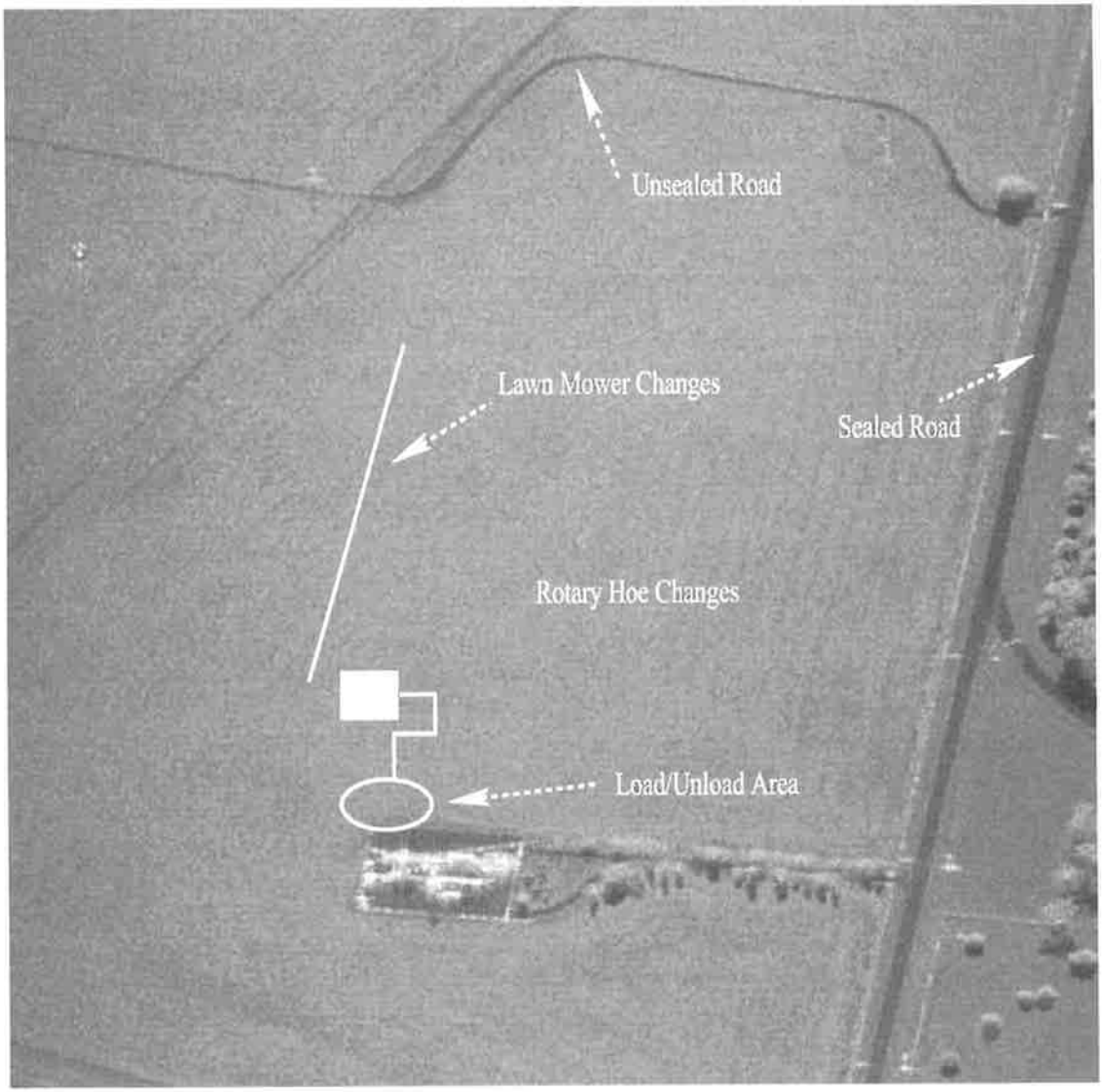


Figure 7.2: Intensity SAR image of the scene used for the May 2000 repeat pass interferometry experiments. Superimposed on the image is a schematic showing the scene changes carried out with the rotary hoe and lawn mower.

Of the large quantity of available repeat pass interferometric image pairs, the pairs shown in Table 7.2 have been selected for further processing and analysis in the remaining sections.

Pair	Collection	Revisit Period	Incidence Angle	Ground Changes
1	May 2000	24 hours	60 deg	20 m by 20 m area modified with rotary hoe.
2	May 2000	12 minutes	60 deg	No man-made changes during temporal baseline.
3	Sept. 1999	2 hours	75 deg	Strips of varying widths and lengths modified with a rotary hoe and a lawn mower.

Table 7.2: Experimental SAR interferometric image pairs selected for change detection analysis.

7.2.2 Processing and Analysis Methodology

Figure 7.3 shows the processing steps required to implement the sample coherence, mean backscatter power ratio and the log likelihood change statistics using experimental data collected with the Ingara airborne SAR. The first three processing blocks illustrate the interferometric processor described in detail in Section 4.7.2. The validation stage measures the statistics of the repeat pass interferometric image pair and compares them to the jointly Gaussian assumption used in the derivation and performance analysis of the change statistics. Given the focused, registered image pair the three change statistics may then be computed and thresholds applied to generate change detections.

Interferometric Processor

Given the raw echo data for a primary and repeat pass imaging collection the interferometric processor generates a registered image pair $|f|exp(j\phi_f)$ and $|g|exp(j\phi_g)$ suitable for subsequent interferometric processing. The matching pairs processing block selects portions of the collected signal history in the repeat pass raw data pair that may be processed coherently to form an interferometric image pair. Aperture trimming is performed to eliminate decorrelation due to baseline offsets between the imaging geometries of the two collections. The image formation processor applies the Polar Format Algorithm with Post Filtering (PF2) to produce a ground plane image that is essentially free of wavefront curvature effects, as described in Chapter 2. Autofocusing is carried out on the image pair using the Phase Gradient Autofocus (PGA) algorithm and the range cell migration step developed in Chapter 3 is used to minimise residual uncompensated relative phase errors between the interferometric image pair. Image pair registration is carried out using the correlation maximisation method described in Section 4.7.2.

Model Validation

An underlying assumption in the derivation of the three change statistics and their associated detection performance is that a complex interferometric image pixel pair is adequately modelled by a first order, jointly circular, complex Gaussian random vector $\underline{X} = [f, g]^T$,

$$p(\underline{X}) = \frac{1}{\pi^2 |Q|} exp\left(-\underline{X}^H Q^{-1} \underline{X}\right), \tag{7.1}$$

where Q is the covariance matrix given by,

$$Q = E\left\{\underline{X}\underline{X}^H\right\},$$

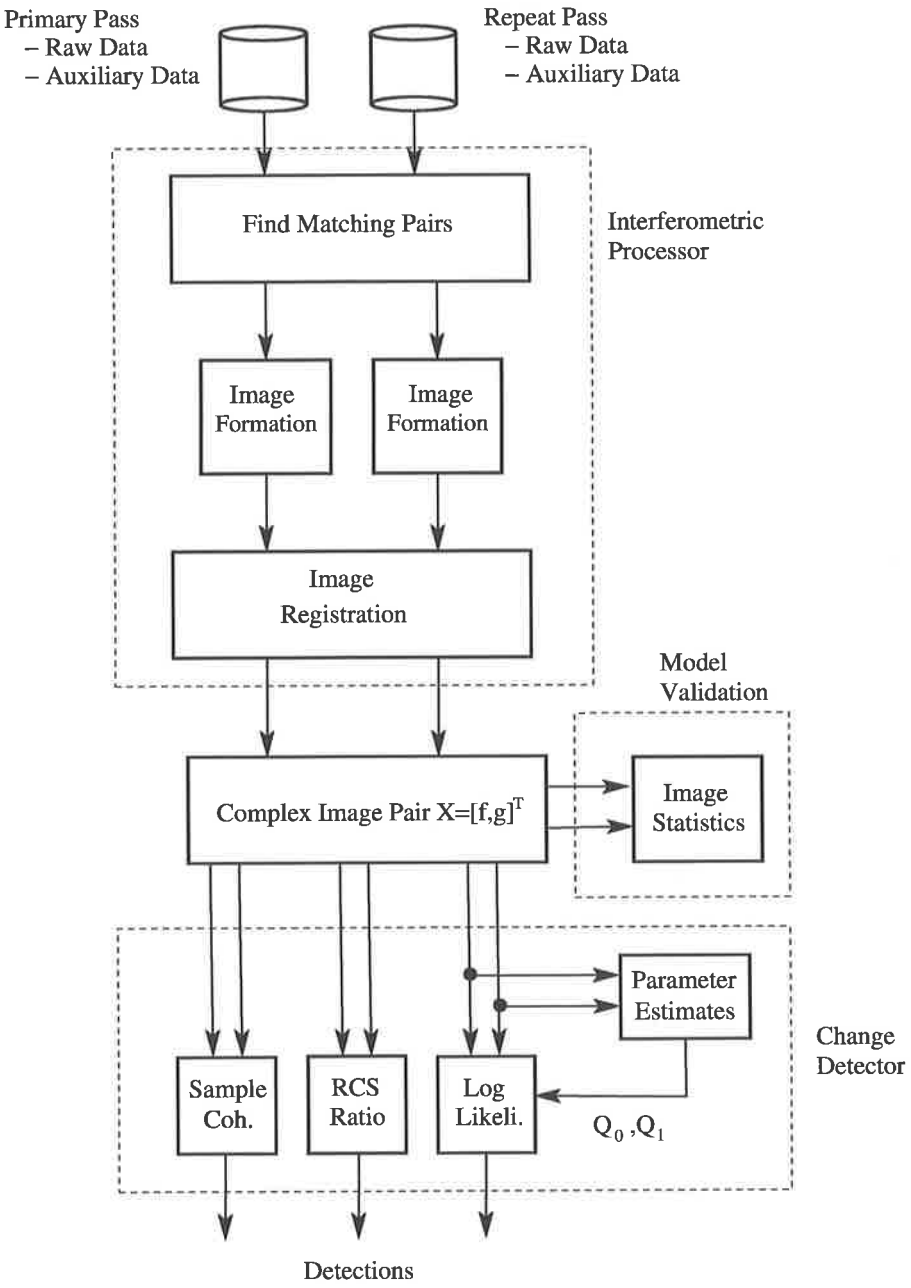


Figure 7.3: Diagram outlining the processing steps required to generate a repeat pass SAR image pair suitable for applying interferometric change detection algorithms.

$$= \begin{bmatrix} \sigma_f^2 & \sigma_f\sigma_g\gamma exp(j\Phi) \\ \sigma_f\sigma_g\gamma exp(-j\Phi) & \sigma_g^2 \end{bmatrix}. \tag{7.2}$$

In general Q will vary across the scene depending on the spatial variation in the backscatter characteristics of the scene, the scene topography and the nature of sources of decorrelation that arise between the interferometric image pair. Local estimates of the parameters in the covariance matrix may be obtained by spatially averaging over a local neighbourhood of N pixels,

$$\hat{\sigma}_f^2 = \frac{1}{N}\sum_{k=1}^{N}|f_k|^2, \tag{7.3}$$

$$\hat{\sigma}_g^2 = \frac{1}{N}\sum_{k=1}^{N}|g_k|^2, \tag{7.4}$$

$$\hat{\gamma} = \frac{|\sum_{k=1}^{N} f_k g_k^*|}{\sqrt{\sum_{k=1}^{N}|f_k|^2 \sum_{k=1}^{N}|g_k|^2}}, \tag{7.5}$$

$$\hat{\Phi} = arg\left(\sum_{k=1}^{N} f_k g_k^*\right). \tag{7.6}$$

Under the jointly Gaussian assumption the density functions of the parameter estimates (7.3) through (7.6) have been derived in the literature. The mean backscatter power estimates have a Gamma density function given by,

$$p(\hat{\sigma}_f^2) = \frac{1}{\Gamma(N)}\left(\frac{N}{\sigma_f^2}\right)^N (\hat{\sigma}_f^2)^{N-1} exp\left(-\frac{N\hat{\sigma}_f^2}{\sigma_f^2}\right), \tag{7.7}$$

$$p(\hat{\sigma}_g^2) = \frac{1}{\Gamma(N)}\left(\frac{N}{\sigma_g^2}\right)^N (\hat{\sigma}_g^2)^{N-1} exp\left(-\frac{N\hat{\sigma}_g^2}{\sigma_g^2}\right), \tag{7.8}$$

while the single look ($N = 1$) amplitude distribution reduces to the Rayleigh density function given by,

$$p(\hat{\sigma}_f) = 2\frac{\hat{\sigma}_f}{\sigma_f^2} exp\left(-\frac{\hat{\sigma}_f^2}{\sigma_f^2}\right), \tag{7.9}$$

and similarly for $\hat{\sigma}_g$. Note that since the images are modelled as circular Gaussian random processes the pixel phase is uniformly distributed.

The cross correlation amplitude and phase, termed the coherence and interferometric phase respectively have density functions given by [TL96],

$$p(\hat{\gamma}) = 2(N-1)(1-\gamma^2)^N\hat{\gamma}(1-\hat{\gamma}^2)^{(N-2)}{}_2F_1(N,N;1;\gamma^2\hat{\gamma}^2), \tag{7.10}$$

$$p(\hat{\Phi}) = \frac{\Gamma\left(N+\frac{1}{2}\right)(1-\gamma^2)^N\gamma\cos\left(\hat{\Phi}-\Phi\right)}{2\sqrt{\pi}\Gamma(N)\left(1-\left(\gamma\cos\left(\hat{\Phi}-\Phi\right)\right)^2\right)^{N+\frac{1}{2}}} + \frac{(1-\gamma^2)^N}{2\pi}{}_2F_1\left(N,1;\frac{1}{2};\left(\gamma\cos\left(\hat{\Phi}-\Phi\right)\right)^2\right), \tag{7.11}$$

where ${}_2F_1(a,b;c;d)$ is the Gauss hypergeometric function [AS72].

The jointly Gaussian model for an interferometric image pair is generally accepted as an accurate description for natural, homogeneous distributed target types such as open fields [OQ98]. However, its ability to accurately represent the observed Ingara experimental data must be validated. As discussed in Chapter 4 a variety of distributed target types and imaging scenarios exhibit a spatially fluctuating mean backscatter power which gives rise to textural modulation in the transduced imagery. In these cases the K distribution has been found to provide a good fit to experimental image amplitude data [Jao84], [Oli84], [Oli91] and [YKJ+89],

$$p(|f|) = \frac{4}{\Gamma(\nu)}\sqrt{\frac{\nu}{\sigma_f^2}}\left(\sqrt{\frac{\nu|f|^2}{\sigma_f^2}}\right)^{\nu} K_{\nu-1}\left(2\sqrt{\frac{\nu|f|^2}{\sigma_f^2}}\right), \tag{7.12}$$

$$p(arg(f)) = \frac{1}{2\pi}, \tag{7.13}$$

where $K_{\nu-1}$ is the modified Bessel function of order $\nu - 1$, σ_f^2 is the mean backscatter power and ν is given by,

$$\frac{E\{|f|^4\}}{(E\{|f|^2\})^2} = 2\left(1 + \frac{1}{\nu}\right). \tag{7.14}$$

The order parameter ν quantifies the extent of the fluctuations of the mean backscatter power. For large values of ν (> 10) the fluctuations are small and the K distribution approaches a Gaussian distribution with the same mean backscatter power. On the other hand, large fluctuations occur when $\nu < 1$ and the amplitude statistics are markedly non-Gaussian [QR95]. An estimate of the order parameter may be obtained by computing the second and fourth order moments in (7.14) using a spatial average over a local neighbourhood of pixels. It should be noted however, other more accurate methods have been proposed including a maximum likelihood method proposed by Joughin [JWP94] and a solution using the log intensity [QR95]. However, the evaluation of the second and fourth order moments in (7.14) provides a simple and effective method for assessing the scattering regime of the interferometric image pair under consideration.

The multi-channel form of the K distribution, see Chapter 4, is suitable for modelling the unchanged scene hypothesis where the main difference between the image pairs arises simply from temporal decorrelation due to environmental effects. In this model the complex cross correlation coefficient may still be estimated using the sample estimate with the sample coherence density function given by (7.10) and the interferometric phase density function given by (7.11). For the changed scene hypothesis however, this model is not necessarily appropriate. Scene changes may give rise to changes in the mean underlying backscatter as well as a complete loss in coherence. It is also conceivable that the scene disturbances may contribute to a change in the texture of the modified region. For example, ploughing a field may remove the vegetation cover changing the shadowing characteristics of imagery collected at low grazing angles. Thus a more appropriate model may consist of two independent random processes with possibly different texture parameters to describe the joint interferometric image pair. This model permits the possibility of detecting scene change via the detection of texture anomalies and texture boundaries. While this is beyond the scope of this thesis change detection using texture based statistics offers the potential for improved scene change detection that may be considered in future research.

Based on the preceding discussion a number of simple tests to determine whether the statistics of the repeat pass image pairs are consistent with the Gaussian scattering model may be proposed:

1. Comparison of the theoretical marginal distributions of the amplitude and phase of the primary and repeat pass images for the Gaussian scattering case with histograms obtained from the imagery.

2. Computation of the K distribution order parameter ν to assess the scattering regime of the primary and repeat pass images.

3. Comparison of the marginal distributions of the coherence and interferometric phase with histograms of sample estimates obtained from the interferometric image pair.

These tests shall be applied to the interferometric image pairs listed in Table 7.2 prior to application of the change detection algorithms.

Change Detections

Given the focused, aperture trimmed, registered interferometric image pair $\underline{X} = [f, g]^T$ the sample coherence and the mean backscatter power ratio change statistics may be readily computed over a sliding N pixel estimation window to obtain a change map and are given by,

$$\text{Sample Coherence: } \hat{\gamma} = \frac{|\sum_{k=1}^{N} f_k g_k^*|}{\sqrt{\sum_{k=1}^{N} |f_k|^2 \sum_{k=1}^{N} |g_k|^2}}, \tag{7.15}$$

$$\text{Mean Backscatter Pwr Statistic: } \hat{r} = \begin{cases} \hat{R}, & \text{if } \hat{R} \leq 1, \\ \hat{R}^{-1}, & \text{if } \hat{R} > 1, \end{cases} \quad \text{where } \hat{R} = \frac{\sum_{k=1}^{N} |f_k|^2}{\sum_{k=1}^{N} |g_k|^2}, \tag{7.16}$$

$$\text{Log Likelihood Statistic: } z = Tr\left\{ \left(\hat{Q}_0^{-1} - \hat{Q}_1^{-1} \right) \sum_{k=1} \underline{X}_k \underline{X}_k^H \right\}. \tag{7.17}$$

Observe that computation of the log likelihood change statistic requires the estimation of the unknown covariance matrices Q_0 and Q_1 describing the scene under the unchanged and changed scenarios respectively. This may be done using the methods outlined in Section 6.8. Change detections may then be obtained by applying a threshold to the change maps with values above the threshold being labelled changed pixels (or unchanged as appropriate of the particular change statistic). Typically it is convenient to select a threshold to achieve an acceptable false alarm rate and measure the detection performance at this particular false alarm rate.

7.3 Coherent Image Pair 1

7.3.1 Experimental Description and Parameters

Figures 7.4 and 7.5 show the primary and repeat pass intensity images of interferometric pair 1 listed in Table 7.2. The 3 dB resolution of the generated image pair is 0.61 m range by 0.15 m azimuth with a Hamming window applied and the pixel spacing is 0.3 m by 0.1 m. The primary and repeat pass images were collected 24 hours apart at an incidence angle of nominally 59.1 degrees. The slant range offset and depression angle differences at the aperture midpoint are 70.94 m and 0.182 degrees respectively. In the interval between collections a substantial 20 m by 20 m scene change was carried using the rotary hoe to provide a large area with modified scene backscatter characteristics. This area is clearly observed in Figure 7.5 as an area of lower mean backscatter power in the area to the upper left of the building and is readily seen in the mean backscatter power ratio change map in Figure 7.6.

The local estimates of the scene backscatter power, required to compute the mean backscatter power ratio change map of Figure 7.6, were obtained by averaging the image pixel intensity values over a 3 (range) by 7 (azimuth) pixel sliding spatial estimation window. Due to the Hamming aperture windowing function applied by the image processor and the pixel oversample rate neighbouring image



Figure 7.4: Intensity SAR image generated from the primary pass collection. The imagery has been processed to a resolution of 0.61 m (range) x 0.150 m (azimuth) with a Hamming window applied. Also shown is the image subchip selected for further processing and change detection analysis.



Figure 7.5: Intensity SAR image generated from the repeat pass collection. The imagery has been processed to a resolution of 0.61 m (range) x 0.150 m (azimuth) with a Hamming window applied. The temporal baseline between the primary and repeat pass collection is approximately 24 hours and in this period scene changes were carried out with a rotary hoe and lawn mower, see Figure 7.2. Also shown is the image subchip selected for further processing and change detection analysis.

pixels are not independent. The ENL of the backscatter power estimates is therefore significantly less than the number of pixels in the estimation window. Given the point spread function defined by the Hamming window and the pixel sample size, a numerically obtained theoretical estimate of ENL = 5.4 is found assuming the underlying backscatter process is a white complex Gaussian random process. The 3 dB resolution of the mean backscatter power ratio change map is 0.64 m by 0.22 m with a pixel spacing of 0.45 m by 0.34 m.

Figures 7.7 and 7.8 show the coherence and interferometric phase images given by the amplitude and phase of the complex sample cross correlation coefficient. The complex sample cross correlation coefficient has been estimated using the same 3 by 7 pixel window as that used in computing the backscatter power above. The coherence and interferometric phase images thus have the same 3 dB resolution, pixel spacing and nominal ENL. The modified ground truth area is clearly visible as an area of low coherence in Figure 7.7 and is also discernible in the interferometric phase map as an area of rapid, random phase fluctuations. Other areas of low coherence visible in the sample coherence map are evident in the region between the building and the area modified with the rotary hoe and also in the upper left corner below the unsealed road. From ground truth observations these regions correspond to areas of taller, denser, broad leaf grass cover, see Figure 7.9, that are more susceptible to temporal decorrelation over the 24 revisit period. The remaining "undisturbed" areas have also been subject temporal decorrelation during the revisit period however these areas are more sparsely covered, see Figure 7.9 and thus exhibit a modest degree of coherence of 0.45. It is interesting to note that while the denser vegetation regions are clearly observed in the sample coherence map the same areas are not readily discerned in the intensity imagery of Figure 7.4 indicating that the coherence may be used as an additional statistic for scene classification applications.

While environment effects such as wind are a significant source of temporal decorrelation in a repeat pass interferometric image pair, for this particular image pair another source of decorrelation to be considered is the effect of grazing sheep. When the scene changes were carried out, just prior to the repeat pass collection, a flock of sheep was discovered in the field, which were probably present in the field over the entire 24 hour repeat pass interval. The sheep had access to the entire field in the imaged scene except an area on the right hand side of the sealed road. It can be seen that with the absence of the sheep in this area, which has similar vegetation to that inside the field, a somewhat higher level of coherence is observed.

7.3.2 Interferometric Image Pair Statistics

In this section the statistical behaviour of the transduced complex backscatter of the primary and repeat pass images will be examined. In particular the image pixel amplitude and phase, as well as the sample coherence and interferometric phase distributions will be estimated and compared to the theoretical density functions derived for the case when the image pair are jointly Gaussian. The parameter estimates here will also be used in the formulation of the changed and unchanged scene hypotheses in the evaluation of the log likelihood ratio in the subsequent section.

For the purposes of examining the image statistics and applying the change detection algorithms a small image subchip, as indicated in Figure 7.4, has been extracted from both the primary and repeat pass images. This image subchip contains the area modified by the rotary hoe while the remaining unmodified areas are essentially homogeneous in terms of their vegetation cover. As the primary and repeat pass images are significantly oversampled the extracted image subchips have been subsampled by a factor of two in range and azimuth to reduce the correlation between neighbouring pixels. The subsampled image subchip is 230 by 100 pixels in size.

Averaging the image pixel intensities over the entire $N = 23,000$ pixel subsampled primary and

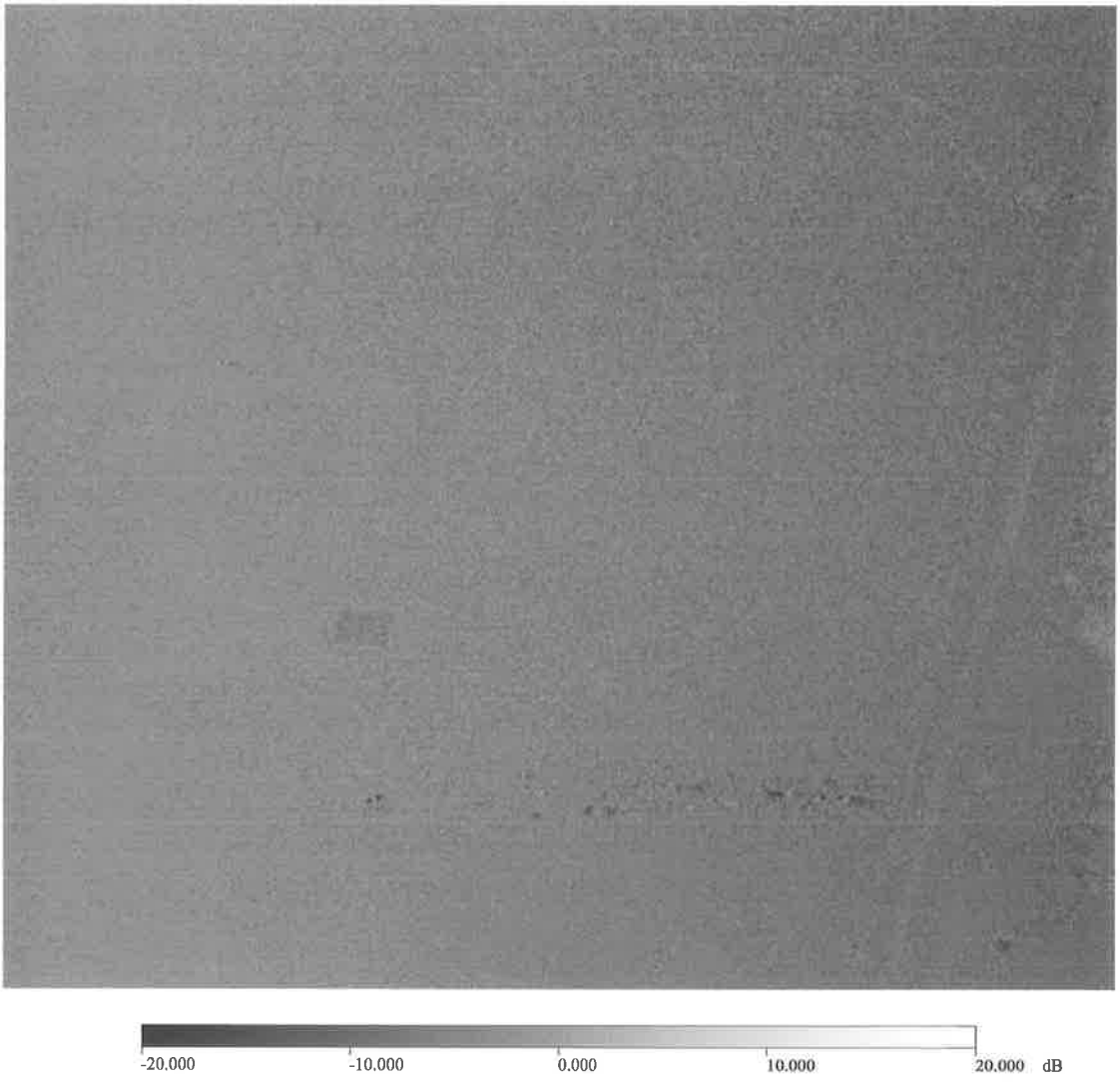


Figure 7.6: Mean backscatter power ratio change statistic evaluated over the primary and repeat pass image pair using a 3 by 7 pixel spatial estimation window. The resolution of the estimate is 0.64 m by 0.22 m with a pixel spacing of 0.45 m by 0.34 m. The 20 m x 20 m area with a modified backscatter coefficient is clearly visible as a darker region in the lower left of the image.

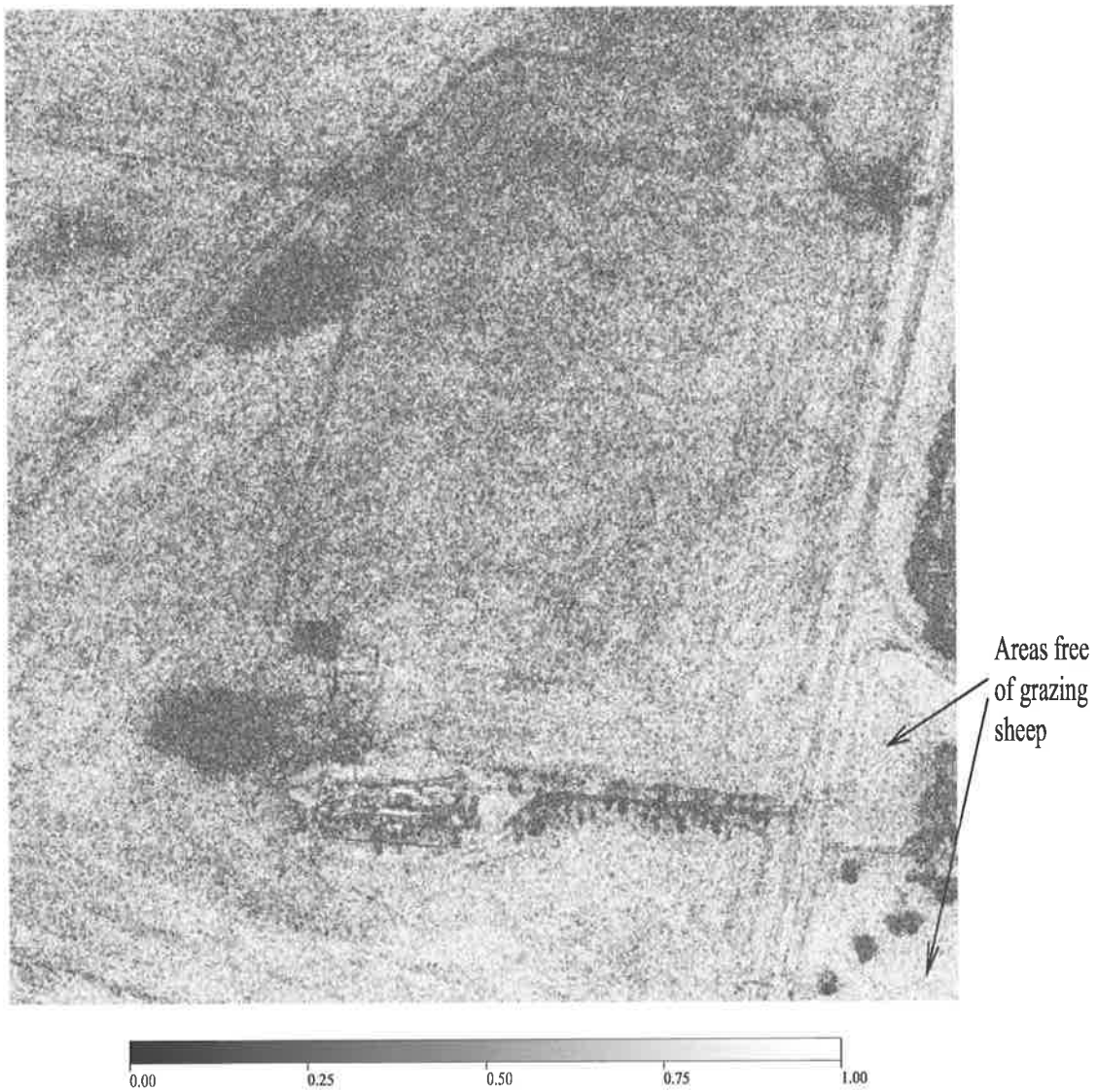


Figure 7.7: Sample coherence evaluated over the repeat pass image pair using a 3 by 7 pixel spatial estimation window. The resolution of the estimate is 0.64 m by 0.22 m with a pixel spacing of 0.45 m by 0.34 m. The modified 20 m x 20 m area is clearly visible as an area of low coherence. Other regions of low coherence are visible below and above the modified area and are associated with a different vegetation type that is more susceptible to temporal change over the 24 hour revisit period.

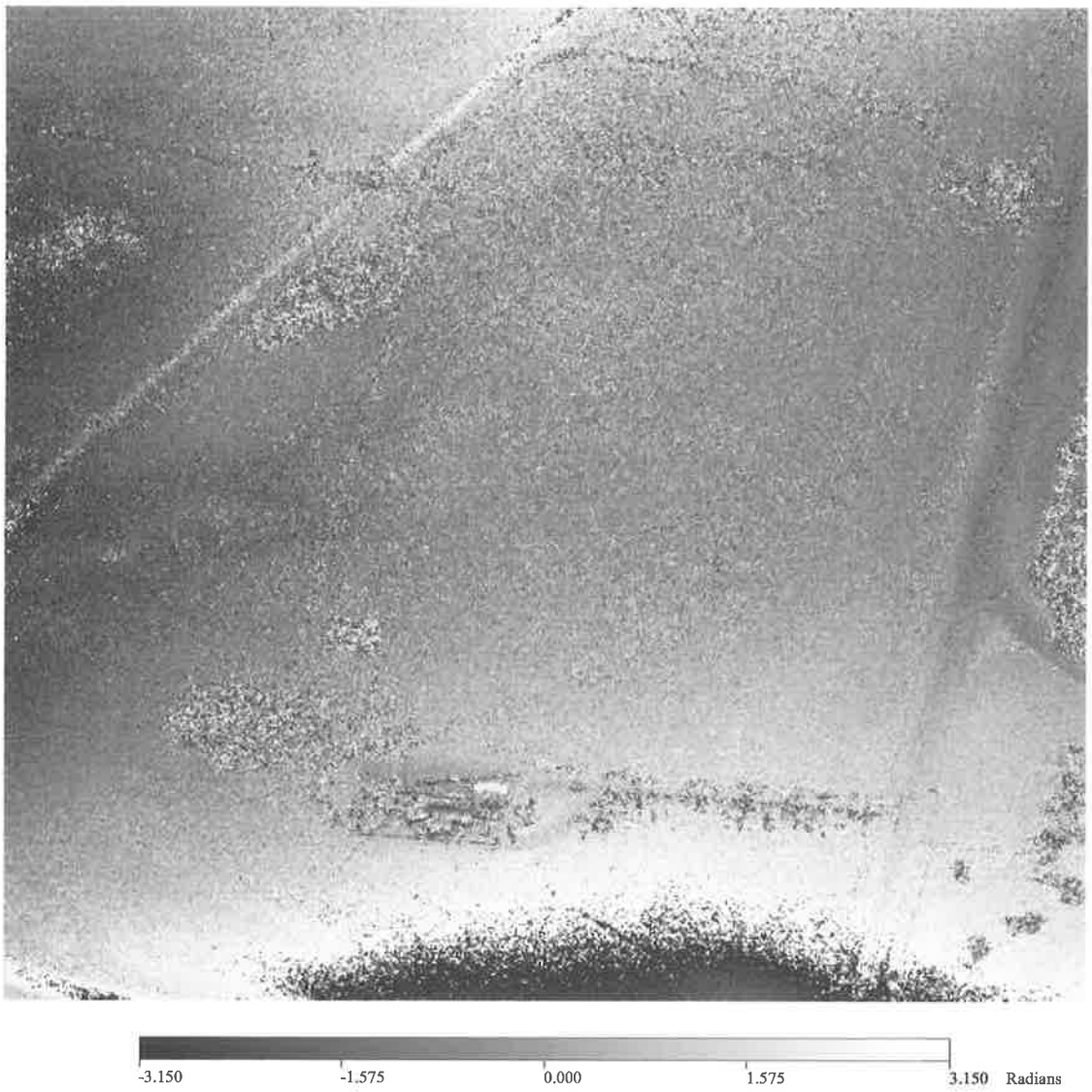


Figure 7.8: Sample interferometric phase evaluated over the repeat pass image pair using a 3 by 7 pixel spatial estimation window. The resolution of the estimate is 0.64 m by 0.22 m with a pixel spacing of 0.45 m by 0.34 m. The modified 20 m x 20 m area is clearly visible as an area of rapid phase fluctuations. Other regions of random phase variation are associated with regions of low coherence in the scene.

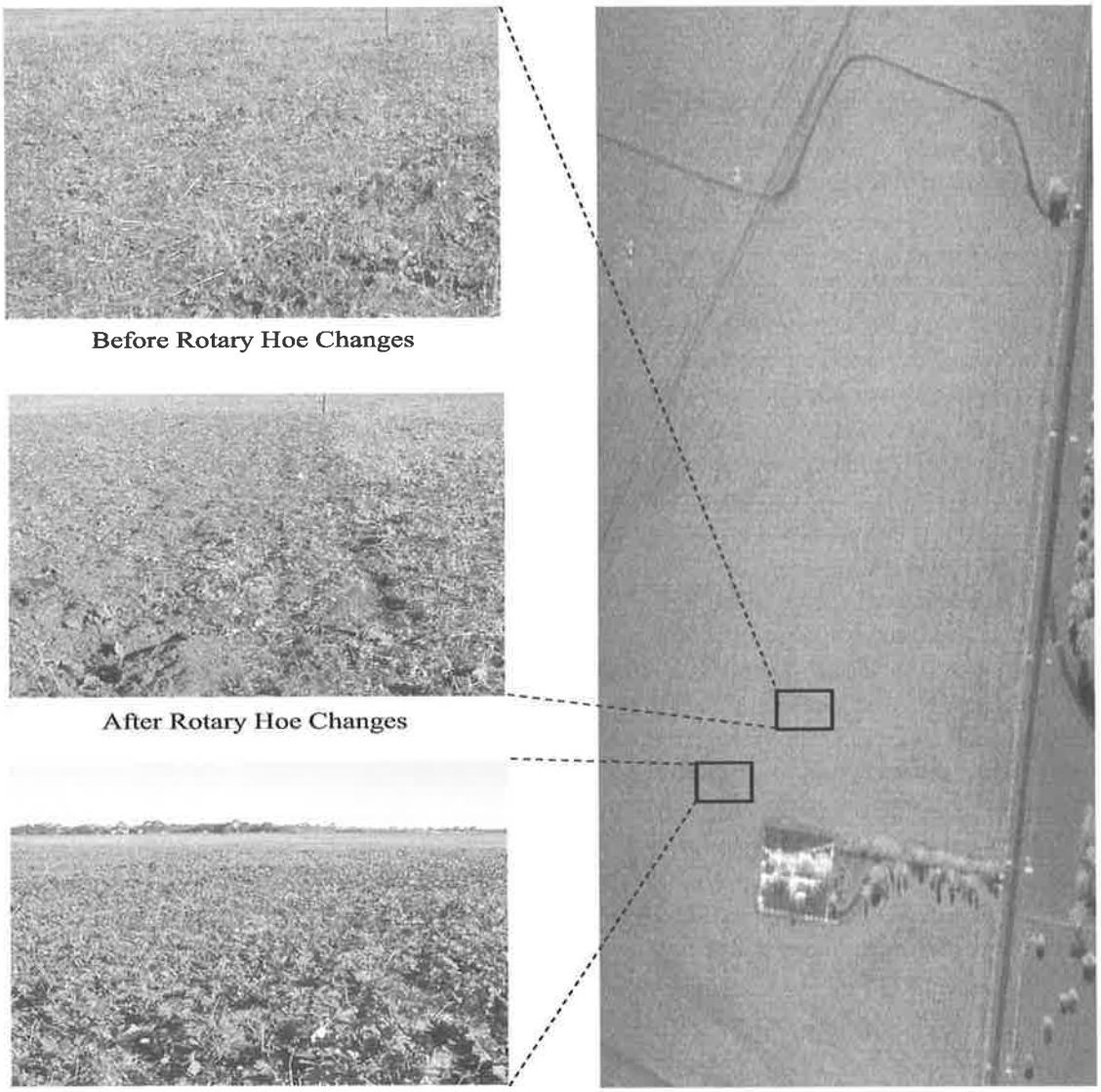


Figure 7.9: Ground truth observations of the scene disturbances. Different areas of the field have different types of vegetation cover which are distinguishable by their differing coherence properties over the 24 hour revisit period. The rotary hoe has been used to clear a 20 m by 20 m area of vegetation.

repeat pass image subchips gives the following estimates for the mean backscatter powers,

$$\hat{\sigma}_f^2 = \frac{1}{N}\sum_{k=1}^{N}|f_k|^2 = 2.2686e8, \tag{7.18}$$

$$\hat{\sigma}_g^2 = \frac{1}{N}\sum_{k=1}^{N}|g_k|^2 = 1.5380e8. \tag{7.19}$$

Substituting $\sigma_f^2 = \hat{\sigma}_f^2$ and $\sigma_g^2 = \hat{\sigma}_g^2$ into the Rayleigh density function, (7.9) gives the theoretical density functions for the pixel amplitude while the pixel phase is uniformly distributed for the case when the complex images are each described by a zero mean, circular Gaussian random process. Figure 7.10 shows the amplitude and phase histograms of each image subchip using all the pixels in each subchip as well as the theoretical Rayleigh amplitude and uniform phase density functions. Also shown in the plots of Figure 7.10 is the likely range in variation of the histogram estimates of the PDF that are to be expected assuming the Rayleigh amplitude and uniform phase PDFs are accurate models. The range of expected values shown are the $\pm$ three standard deviations about the mean expected at each histogram sample bin, see Appendix D. The good agreement between the amplitude and phase histograms and the theoretical density functions indicates the image subchips have a strongly Gaussian behaviour. Indeed computing the order parameter $\hat{\nu}$ given in (7.14) gives values of 37.0 and 16.8 for the primary and repeat pass image subchips respectively. These values are both clearly in the Gaussian scattering regime ($\nu > 10$). It should be noted that the repeat pass subchip mean backscatter power estimate as well as the order parameter estimate have been obtained by averaging over both the modified and unmodified regions in the repeat pass image subchip. The mean backscatter power estimated over the 20 m x 20 m modified area of the scene is $\hat{\sigma}_g^2 = 9.5070e7$ while the mean backscatter power for the area outside the modified region is $1.7847e8$. The scene modifications have thus caused an reduction in the mean backscatter power of 2.73 dB. This is reflected in the reduction in the order parameter of the repeat pass subchip compared to the primary subchip as the changed mean backscatter has effectively introduced a textural modulation across the image subchip.

The complex sample cross correlation coefficient has been computed across the subsampled subchip pair by averaging over a 3 by 3 pixel spatial estimation window. Figure 7.11 shows a histogram of the magnitude of the cross correlation coefficient, i.e., the coherence, obtained using sample estimates from the entire image subchip pair. The histogram consists of a mixture of modified, low coherence areas and unmodified, partial coherence areas. Superimposed on the histogram of Figure 7.11 is the theoretical density of the sample coherence obtained using equation (7.10) where a true coherence of $\gamma = 0.45$ and an ENL of 7 have been found to provide the best fit to the experimental histogram. Also shown in Figure 7.11 is the likely range in variation (three standard deviations) of the histogram estimate of the PDF that is to be expected assuming the jointly Gaussian model is correct. The histogram and theoretical density functions show reasonable agreement and deviations between the plots, outside the anticipated histogram deviation from the theoretical PDF, may be attributed to the mixture of sample estimates obtained over both modified and unmodified regions in the image subchips used to produce the histogram. It has been found that the best theoretical fit for the observed sample coherence is obtained with an ENL of 7. This is less than the number of pixels in the spatial estimation window indicating that some residual correlation exists between neighbouring pixels in the subsampled imagery. Further subsampling of the image subchips does yield ENL values closer to the spatial window size however only with an unacceptable loss in resolution of the coherence estimate.

The Maximum Likelihood (ML) estimate of the interferometric phase obtained over an N pixel local neighbourhood is given in (7.6) and has a PDF given by (7.11). In order to generate a meaningful

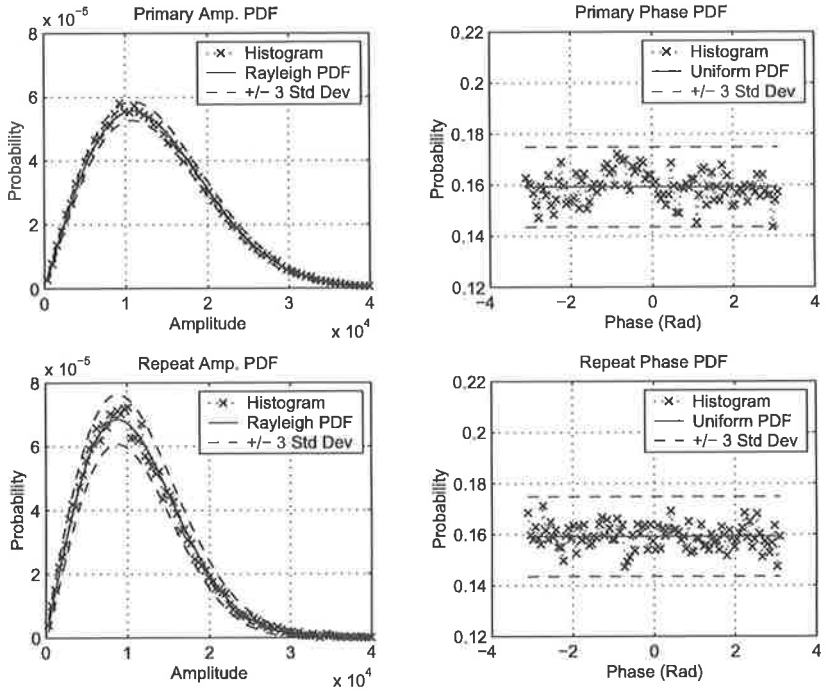


Figure 7.10: Amplitude and phase histograms for the primary and repeat pass image subchips. Superimposed on the histograms are the theoretical Rayleigh amplitude and uniform phase density functions that are associated with complex Gaussian scattering behaviour. Also shown is the likely range (three standard deviations) in variation of the histogram estimates of the PDF that are to be expected assuming the Rayleigh amplitude and uniform phase PDFs are accurate models

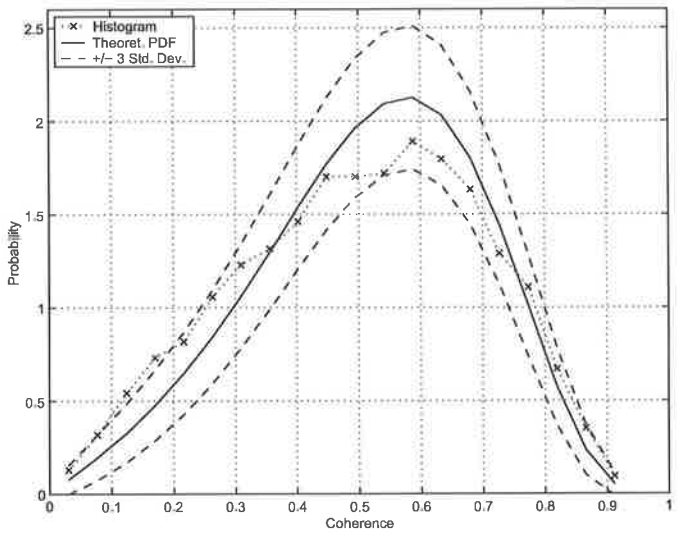


Figure 7.11: Histogram and theoretical density function of the sample coherence. The estimated true coherence and ENL used to calculate the theoretical fit are 0.45 and 7 respectively. Also shown is the likely range in variation (three standard deviations) of the histogram estimate of the PDF that is to be expected assuming the jointly Gaussian model is correct.

comparison between the theoretical PDF of an N pixel spatially averaged phase estimate and a histogram based estimate of the PDF requires computing the histogram samples over an area where the underlying interferometric phase and coherence is essentially constant. Variations in the underlying interferometric phase manifest as variations in the expected value of the N pixel ML phase estimate, while variations in the scene coherence lead to increases in the higher order moments (e.g. the variance). The spatial variability of the scene coherence is determined by the nature of the sources of temporal decorrelation and the backscattering medium while the interferometric phase is dependent on the terrain topography as well as any relative uncompensated phase components in the processed image pairs. While there is some variability in the scene coherence over the image subchip, primarily due to the scene changes, an examination of the sample interferometric phase evaluated over the scene shown in Figure 7.8 indicates that there is considerable variability in the underlying interferometric phase over the subchip pair. Since the scene is topographically flat the interferometric phase is most likely due to relative uncompensated phase components in the processed image pairs. As the underlying interferometric phase directly effects the mean of the ML estimate its variability over the image subchip pair must be considered in forming the histogram PDF estimates. As a consequence a single histogram formed from N pixel ML interferometric phase estimates taken over the image subchip will not yield a meaningful result. Instead the image subchip can be partitioned into sufficiently small regions, over which the interferometric phase may be considered to be constant, and individual histograms formed from the ML phase estimates obtained within these regions. An alternative more rigorous approach is to fit a two dimensional surface function model, such as a thin plate spline [Gos88], [Boo89], to local estimates of the interferometric phase obtained over the scene. This surface model is an estimate of the mean underlying interferometric phase and may be removed from the N pixel ML sample estimates so that a single histogram over the area may be obtained. This approach will be considered in Section 7.5 in which a spatially large image subchip is considered. For the current image pair under consideration however, partitioning the image subchips into regions is sufficient to obtain suitable histograms.

Figure 7.12 shows histograms of the interferometric phase recovered from the complex sample cross correlation coefficient. Each of the four histograms corresponds to sample estimates of the interferometric phase obtained, using a 3 by 3 sliding estimation window applied to four equally sized, non-overlapping quadrants of the image subchip pair. Superimposed onto the histograms are theoretical density functions calculated using a coherence of $\gamma = 0.45$, ENL$= 7$ and mean interferometric phase values of -0.25, 0.04, -0.02 and 0.25 radians for the four quadrants. Also shown in the plots of Figure 7.12 is the likely range in variation (three standard deviations) of the histogram estimate of the PDF that is to be expected assuming the jointly Gaussian model is correct. The histograms and theoretical density functions show reasonable agreement. Sources of deviation between the histograms and the theoretical density functions include variations in the underlying phase across the quadrants as well as variations in the underlying coherence across the quadrants which include both changed (low coherence) and unchanged (high coherence) regions.

7.3.3 Change Detections

From the previous section the statistics of the primary and repeat pass image subchips are consistent with the jointly Gaussian model with a covariance matrix $Q(x, y)$ that varies spatially over the image and is given by,

Unchanged Hypothesis:

$$Q_0(x,y) = 1e8 \begin{bmatrix} 2.2686 & 0.45 \cdot 2.0121 \cdot exp(j\Phi(x,y)) \\ 0.45 \cdot 2.0121 \cdot exp(-j\Phi(x,y)) & 1.7847 \end{bmatrix}, \quad (7.20)$$

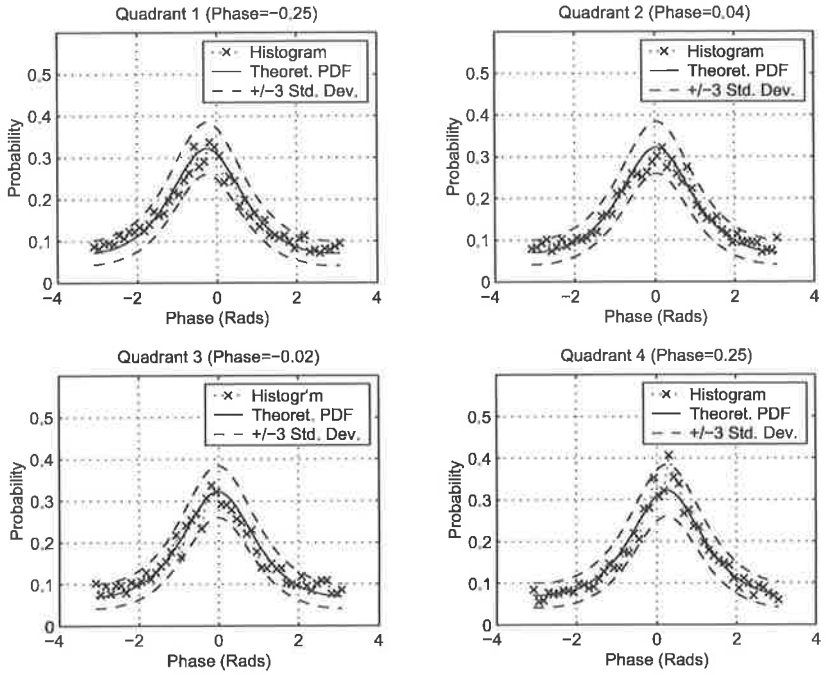


Figure 7.12: Histograms and theoretical density functions of the sample interferometric phase obtained by partitioning the image subchips into four equally sized, non-overlapping quadrants. The estimated mean underlying phase is indicated in each subplot and the coherence and ENL used to calculate the theoretical fits are 0.45 and 7 respectively. Also shown is the likely range in variation (three standard deviations) of the histogram estimate of the PDF that is to be expected assuming the jointly Gaussian model is correct.

Changed Hypothesis:

$$Q_1(x,y) = 1e8 \begin{bmatrix} 2.2686 & 0 \\ 0 & 0.95070 \end{bmatrix}, \tag{7.21}$$

where $\Phi(x,y)$ is the mean interferometric phase estimates identified in the previous section,

$$\Phi(x,y) = \begin{cases} -0.25 \text{ rad}, & (x,y) \text{ in Quadrant 1}, \\ +0.04 \text{ rad}, & (x,y) \text{ in Quadrant 2}, \\ -0.02 \text{ rad}, & (x,y) \text{ in Quadrant 3}, \\ +0.25 \text{ rad}, & (x,y) \text{ in Quadrant 4}. \end{cases} \tag{7.22}$$

For simplicity the interferometric phase will be modelled as being constant over each of the four quadrants considered in the previous section with a step change in phase across the quadrants.

Using the covariance matrix estimates Q_0 and Q_1 in (7.20) and an ENL of 7 the detection performance of the mean backscatter power ratio, the sample coherence and the log likelihood change statistic may be computed using theoretical expressions for the probability of detection P_d and false alarm P_{fa} derived in Chapters 5 and 6. Figure 7.13 shows the theoretical and simulated ROC curves for the three change statistics. It is evident that the log likelihood ratio statistic gives almost an order of magnitude improvement in the false alarm rate over both the sample coherence and mean backscatter power ratio statistics over a wide range of detection probabilities. The mean backscatter power

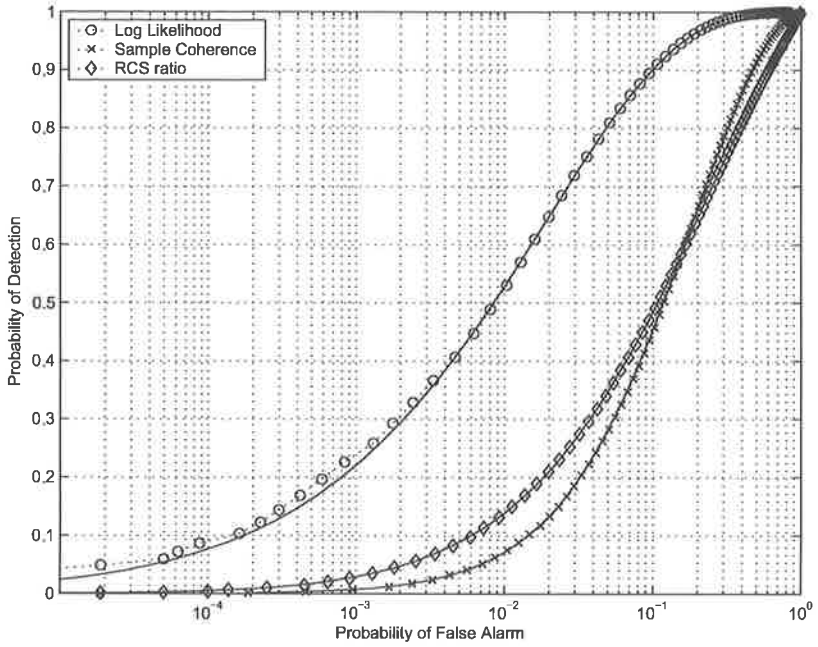


Figure 7.13: Theoretical and simulated ROC curves of the three change statistics obtained using the covariance matrix estimates given in (7.20) with an ENL=7.

ratio and sample coherence change statistics both give somewhat similar detection performance characteristics with the mean backscatter power ratio statistic showing a modest detection improvement over the sample coherence at values of P_d less than 0.6.

The images on the left hand side of Figure 7.14 shows the three change statistics evaluated over the primary and repeat pass image pair using a 3 by 3 sliding computation window. In the case of the mean backscatter power ratio and sample coherence change statistic, areas subject to some form of disturbance are associated with low values for the change statistics and thus are visible as dark pixels. On the other hand for the log likelihood change statistic scene disturbances are associated with large values of the change statistic. In Figure 7.14 however, the negative of the log likelihood change statistic is displayed so that changed areas are visible as dark pixels. The area of the scene modified by the rotary hoe is readily identified in the three change statistic maps however the sample coherence and mean backscatter power ratio maps appear somewhat noisier than the log likelihood change map.

On the right hand side of Figure 7.14 are the change detections obtained by applying a threshold to the corresponding change statistic maps. The threshold has been adjusted experimentally in each case, to achieve a fixed number of detections (false alarms) in the 2000 pixel area lying outside the modified region, thereby giving a fixed false alarm rate of 0.05. It can be readily seen that for the same total number of false detections in the region surrounding the modified area the log likelihood change statistic has generated far more detections within the modified area than either the mean backscatter power ratio map or the sample coherence, i.e., the log likelihood change statistic has generated a significant number of new detections that are not identified by either the sample coherence or the mean backscatter power ratio statistic. Furthermore the mean backscatter power ratio and sample coherence statistics do not necessarily generate false detections at the same spatial locations. Therefore a simple fusion of the mean backscatter power ratio and sample coherence detection results will not necessarily

Change Statistic	ROC threshold	Theoretical P_d	Expt. Threshold	Expt. Pd
Log Likelihood	-1.45	0.70	-0.45	0.71
Sample Corr.	0.19	0.21	0.18	0.23
Intensity Ratio	0.31	0.28	0.33	0.42

Table 7.3: Theoretical threshold levels and probability of detection values of the three change statistics corresponding to a false alarm probability of 0.05. Also shown is the experimentally set threshold required to achieve the same probability of false alarm and the measured probability of detection over the 20 m by 20 m modified area.

generate an improved detection performance.

The probability of detection for each change statistic may be estimated experimentally by assuming all pixels within the modified region are realisations of the H_1 hypothesis, i.e., changed, and counting the total number of detections in this area. The probability of detection for each change statistic may then be compared to the theoretical performance given in the ROC curve of Figure 7.13. Table 7.3 shows the theoretical and experimentally determined detection performance and associated threshold required to achieve a false alarm rate of 0.05. There appears to be reasonably good agreement between the theoretical and experimentally determined results. The trends identified in the ROC curve of Figure 7.13 are evident with the log likelihood giving significantly better detection performance than both the mean backscatter power ratio and sample coherence change statistics. A number of differences between the experimental and theoretical values do appear. The experimentally determined threshold for the log likelihood change statistic is somewhat larger than predicted theoretically. The theoretically derived ROC performance however is an upper bound as it fails to consider the impact of the estimates of Q_0 and Q_1 which would tend to broaden the density functions of the change statistic under H_0 and H_1 leading higher false alarms for a given probability of detection. A higher detection threshold might thus be anticipated in order to maintain a desired false alarm rate. The mean backscatter power ratio statistic gives a somewhat better detection performance than predicted theoretically possibly indicating a greater mean backscatter power change than the estimated 2.73 dB change.

Finally Figure 7.15 shows the histogram of the log likelihood change statistic as well as the theoretical density functions obtained under H_0 and H_1. Also shown in Figure 7.15 is the likely range in variation (three standard deviations) of the histogram estimate of the PDF that is to be expected under the changed and unchanged hypotheses. The histogram is a mixture of changed and unchanged pixels and appears consistent with the theoretical curves.

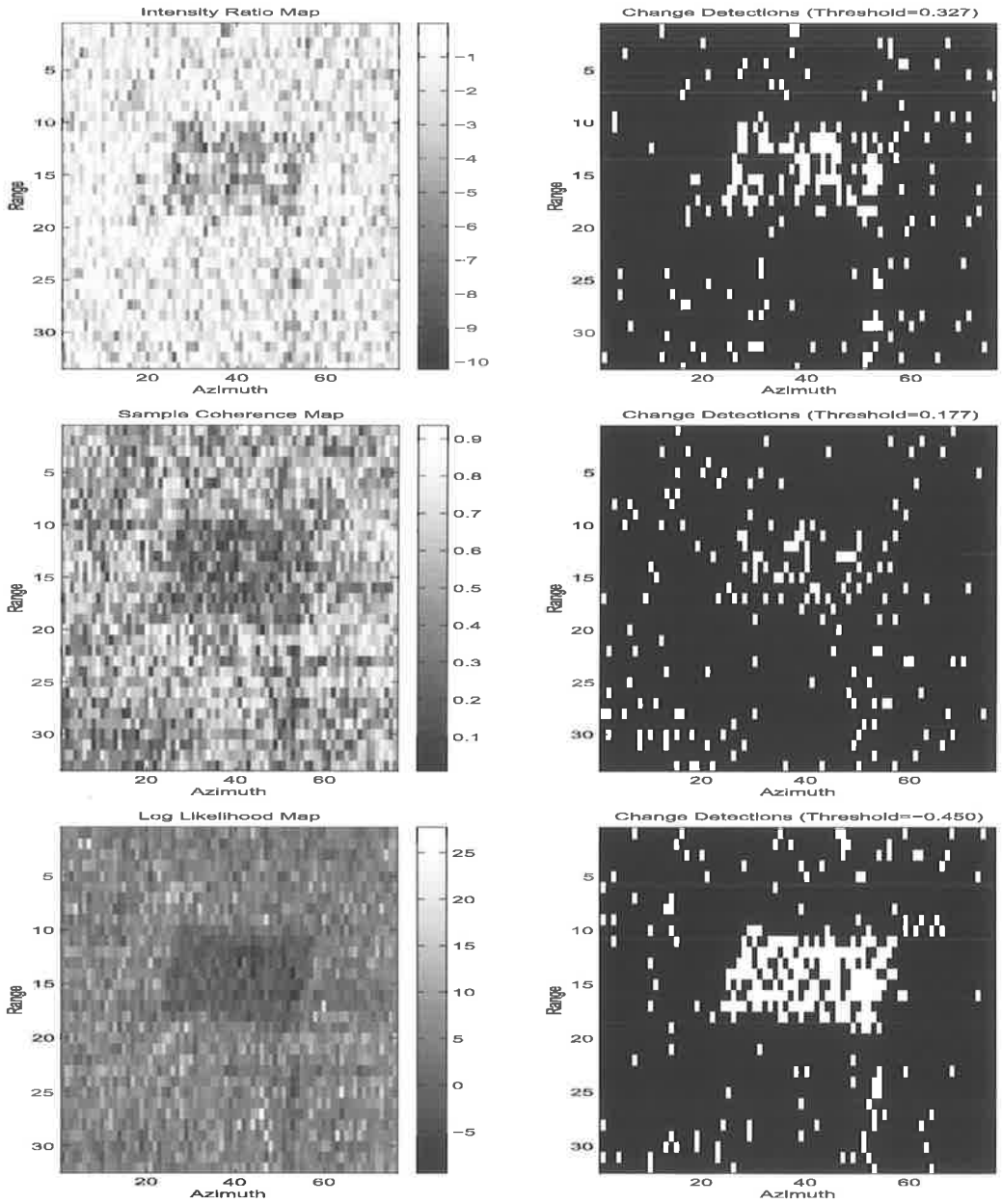


Figure 7.14: The images on the left hand side show, from top to bottom, the mean backscatter power ratio, sample coherence and log likelihood change statistic maps evaluated over the subsampled sub-chip image pair using a 3 by 3 pixel sliding estimation window. Scene changes are identified as dark pixels. The images on the right hand size show the detections obtained by applying a threshold to the corresponding change maps. The threshold has been experimentally selected to give a false alarm rate of 0.05.

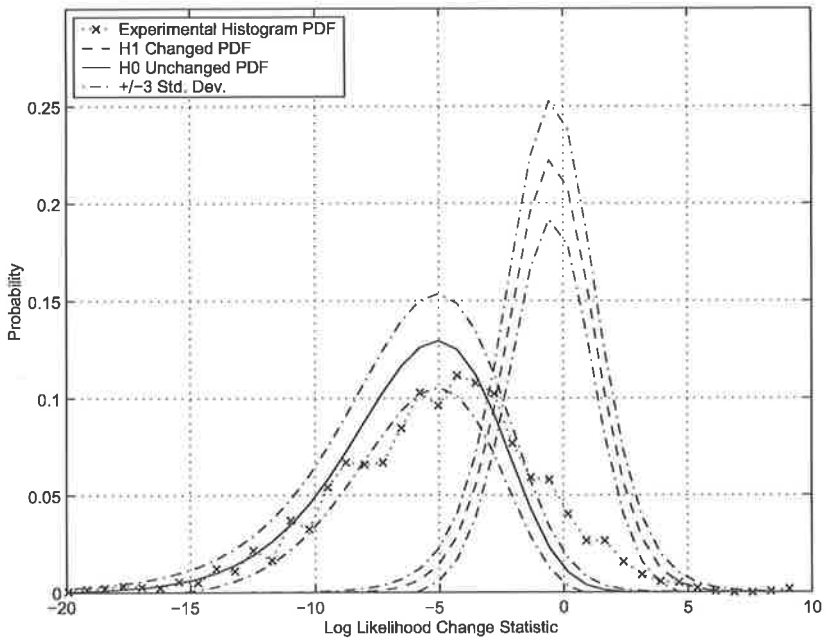


Figure 7.15: Experimentally obtained histogram of the log likelihood change statistic obtained using a 3 by 3 sliding estimation window over the entire image subchip pair. The histogram is thus a mixture of values obtained over both changed and unchanged areas. The theoretical density functions for the changed and unchanged hypotheses are shown along with the likely range in variation (three standard deviations) of the histogram estimate of the PDF that is to be expected under the changed and unchanged hypotheses.

7.4 Coherent Image Pair 2

7.4.1 Experimental Description and Parameters

In May 2000 repeat pass imagery of the scene shown in Figure 7.2 was collected with a revisit period of 12 minutes. These collections were made prior to performing the man-made scene changes considered in the previous section and no ground truth observations were made during the repeat interval. Given the short time delay between collections the temporal decorrelation effects are minimised and the correlation between the image pair is indicative of the maximum achievable for the particular environmental conditions, radar and processing system.

The primary and repeat pass intensity image pair generated from these collections are shown in Figures 7.16 and 7.17 respectively. The nominal incidence angle for the two imaging collections is 59.1 degrees and the slant range offset and incidence angle differences at the aperture midpoint are 4.59 m and 0.012 degrees respectively. The primary image used in this interferometric pair is in fact formed using the same look direction and coherent aperture as that of the primary image in Section 7.3. The aperture of support along the range spatial frequency in this case however, is slightly larger, owing to the smaller baseline offset between the primary and repeat pass acquisitions. The larger aperture of support yields an image pair with a marginally finer 3 dB Hamming window range resolution of 0.58 m while the azimuthal resolution is maintained at 0.15 m. The pixel spacing is 0.41 m by 0.10 m.

Figure 7.18 shows the mean backscatter power ratio change map obtained from the repeat pass image pair where the scene backscatter power for each image has been estimated using a 2 (range) by 7 (azimuth) pixel sliding spatial estimation window. The ENL of the backscatter power estimates is significantly less than the number of pixels in the estimation window size as the images are oversampled. Using the point spread function for a Hamming aperture weighting function and the pixel oversample rate a numerically obtained theoretical estimate for the ENL of 5.4 is found assuming the underlying backscatter process is a white complex Gaussian random process. The 3 dB resolution of the mean backscatter power ratio change map is 0.595 m by 0.225 m with a pixel spacing of 0.405 m by 0.358 m. From 7.18 there is no significant change in the mean backscatter power within the scene.

Figures 7.19 and 7.20 show the sample coherence and interferometric phase images obtained from the amplitude and phase of the complex sample cross correlation coefficient respectively. The same 2 by 7 pixel estimation window used to compute the mean backscatter power has been used to compute the sample complex cross correlation coefficient. The 3 dB resolution of the coherence and interferometric phase images is therefore 0.595 m by 0.225 m and the ENL = 5.4. The average coherence estimated over the field is very high at 0.94 and the scene decorrelation may be attributed to environmental effects that arise over the 12 minute revisit period as well as system noise and processing aberrations in generating the focused, registered image pair. Of particular interest in Figure 7.19 are the track like areas of low coherence. The tracks appear to have a low but non zero coherence possibly because the scene disturbances are on a much finer scale than the resolution of the sample coherence map so the estimation window encompasses pixels consisting of changed and unchanged contributions. In addition a number of the tracks end abruptly at a somewhat larger area of very low coherence. While there is no ground truth data available over this period of collection, it is believed that the tracks may be due to the movement of sheep while grazing during the temporal baseline. As discussed in Section 7.3 sheep were found in the field the following day and were most likely present during the collection of this interferometric image pair.



Figure 7.16: Intensity SAR image generated from the primary pass collects. The imagery has been processed to a resolution of 0.58 m (range) x 0.150 m (azimuth) with a Hamming window applied. Also shown is the image subchip selected for further processing and change detection analysis.



Figure 7.17: Intensity SAR image generated from the repeat pass collection. The imagery has been processed to a resolution of 0.58 m (range) x 0.150 m (azimuth) with a Hamming window applied. The temporal baseline between the primary and repeat pass images is approximately 12 minutes. Also shown is the image subchip selected for further processing and change detection analysis.

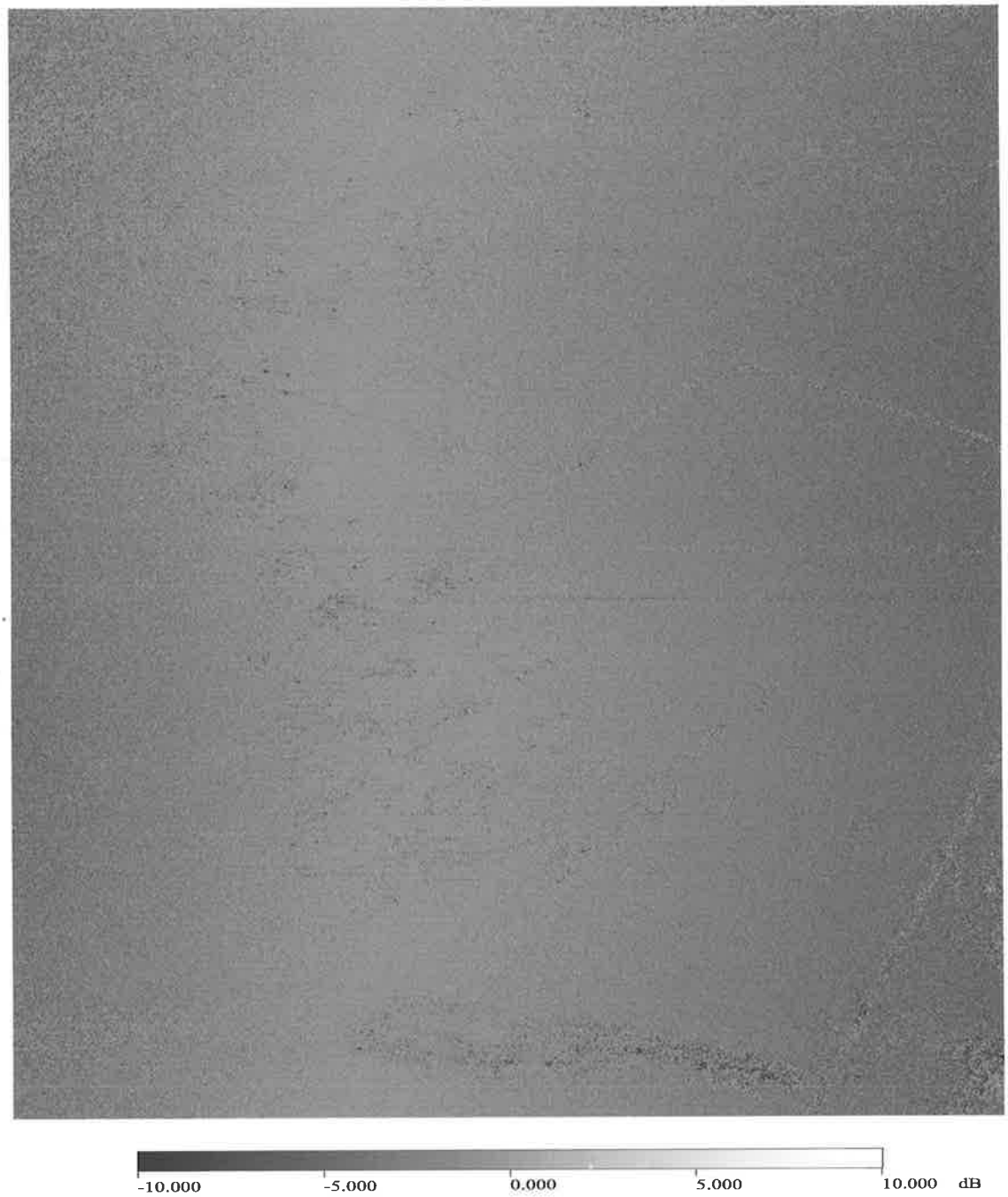


Figure 7.18: Mean backscatter power ratio change statistic in dB evaluated over the primary and repeat pass image pair using a 2 by 7 pixel spatial estimation window. The resolution of the estimate is 0.595 m by 0.225 m with a pixel spacing of 0.405 m by 0.358 m.



Figure 7.19: Sample coherence evaluated over the repeat pass image pair using a 2 by 7 pixel spatial estimation window. The resolution of the estimate is 0.595 m by 0.225 m with a pixel spacing of 0.405 m by 0.358 m. The track like areas of low coherence in the middle of the scene may possibly be due to the movements of grazing sheep during the 12 minute revisit period between imaging collections.



Figure 7.20: Sample interferometric phase evaluated over the repeat pass image pair using a 2 by 7 pixel spatial estimation window. The resolution of the estimate is 0.595 m by 0.225 m with a pixel spacing of 0.405 m by 0.358 m. Areas of low coherence manifest as regions of rapid, random phase fluctuations in the interferometric phase map.

7.4.2 Interferometric Image Pair Statistics

In this section the statistical behaviour of the transduced complex backscatter of the primary and repeat pass images will be examined. For validation of the statistical models used to describe the image pair and subsequent application of the change detection algorithms a small image subchip 480 by 400 pixels in size has been extracted from the primary and repeat pass images, as indicated in Figure 7.16. The image subchip has been selected to include a significant portion of the track like disturbances observed in the coherence map. For the purposes of parameter estimation, to reduce the correlation between neighbouring samples the image subchip pair has been subsampled by a factor of 2 in range and azimuth.

Averaging the image pixel intensities over the entire N = 48,000 pixel primary and repeat pass subsampled image subchips gives a mean backscatter power estimate of $\hat{\sigma}_f^2 = 1.4866e8$ for the primary image subchip and $\hat{\sigma}_g^2 = 1.7127e8$ for the repeat pass image subchip. Figure 7.21 shows the pixel amplitude and phase histograms of the primary and repeat pass image subchips as well as the theoretical Rayleigh amplitude and uniform phase density functions obtained using the estimates $\hat{\sigma}_f^2$ and $\hat{\sigma}_g^2$ for the mean backscatter power in the Rayleigh density function. Also shown in the plots of Figure 7.10 is the likely range in variation (three standard deviations) of the histogram estimates of the PDF that are to be expected assuming the Rayleigh amplitude and uniform phase PDFs are accurate models. The good agreement between the histograms and theoretical density functions indicate that the image subchips are consistent with the Gaussian scattering model. Furthermore the order parameter estimates $\hat{\nu}$ for the primary and repeat pass image subchips are 20.7 and 22.5 respectively which lie within the Gaussian scattering regime.

Figure 7.22 shows a histogram of the magnitude of the complex sample cross correlation coefficient of the image subchip pair obtained by using a 3 x 3 sliding estimation window. Superimposed on the histogram is the theoretical density function obtained assuming jointly Gaussian statistics with a true coherence of 0.94 and ENL = 7. Also shown in Figure 7.22 is the likely range in variation (three standard deviations) of the histogram estimate of the PDF that is to be expected assuming the jointly Gaussian model is correct. The histogram and theoretical density function are in very good agreement indicating the primary and repeat pass image pair statistics are consistent with the jointly Gaussian model.

To allow for a possible spatial variation in the interferometric phase the image subchips have been partitioned into four equally sized quadrants and interferometric phase estimates obtained in each quadrant using a 3 x 3 sliding estimation window. Figure 7.23 shows the interferometric phase histograms and theoretical density functions produced for each quadrant, where a true coherence of 0.94 and ENL = 7 have been used for each quadrant. Also shown in Figure 7.23 is the likely range in variation (three standard deviations) of the histogram estimate of the PDF that is to be expected assuming the jointly Gaussian model is correct. In this case there is very little spatial variation in the interferometric phase across the image subchip pair with the interferometric phase in each quadrant approximately equal to 1.95 radians.

7.4.3 Change Detections

The track like disturbances visible in the sample coherence map of Figure 7.19 are on a very fine spatial scale. Therefore in order to obtain change detections at the finest resolution available the following change detection algorithms have been applied to the primary and repeat pass image subchips without any subsampling. Given the significant oversampling of the image pixels, adjacent pixels are highly correlated and it is found experimentally that using a 3 by 3 pixel estimation window gives an ENL of 4.

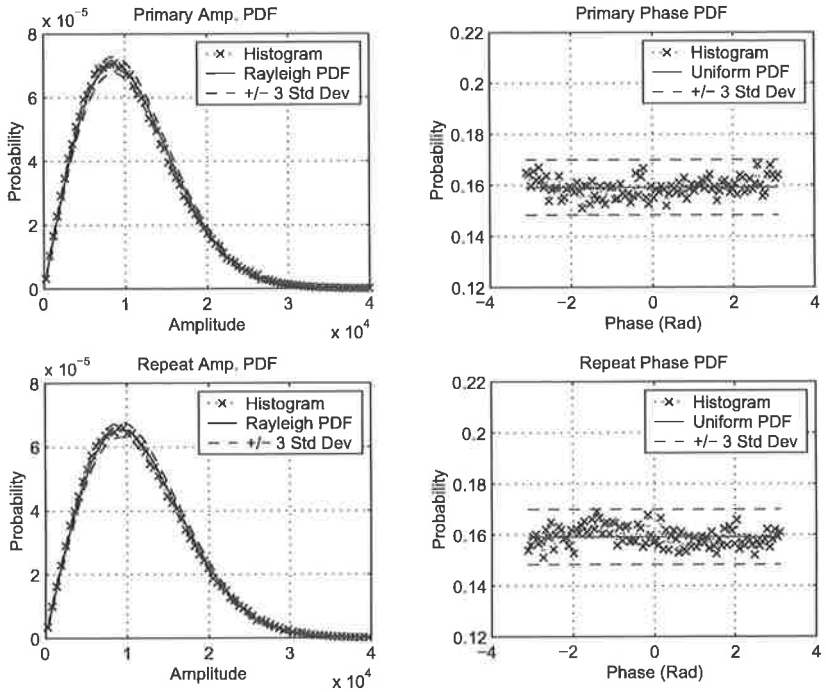


Figure 7.21: Amplitude and phase histograms for the primary and repeat pass image subchips. Superimposed on the histograms are the theoretical Rayleigh amplitude and uniform phase density functions associated with complex Gaussian scattering behaviour. Also shown in the plots are the likely range in variation (three standard deviations) of the histogram estimate of the PDF that is to be expected assuming the Rayleigh and uniform PDF are correct.

The statistics of the primary and repeat pass image pair subchips analysed in the previous section are consistent with a jointly Gaussian model with the covariance matrices for the changed and unchanged hypotheses given by,

Unchanged Hypothesis:

$$Q_0 = 1e8 \begin{bmatrix} 1.4866 & 0.94 \cdot 1.5957 \cdot exp(-j1.95) \\ 0.94 \cdot 1.5957 \cdot exp(j1.95) & 1.7127 \end{bmatrix}, \tag{7.23}$$

Changed Hypothesis:

$$Q_1 = 1e8 \begin{bmatrix} 1.4886 & 0 \\ 0 & 1.7127 \end{bmatrix}. \tag{7.24}$$

Using these covariance matrices and an ENL of 4 theoretical ROC curves for the sample coherence and log likelihood change statistics have been computed and are given in Figure 7.24. The mean backscatter power ratio statistic is not considered in this case as there has been no significant change in the mean backscatter power between the repeat pass image pair. It is clear that the log likelihood ratio change statistic significantly out performs the sample coherence change statistic.

Figure 7.25 shows the sample coherence and log likelihood change maps and also the change detections obtained by applying a threshold to the change maps. Note that the negative of the log likelihood change statistic is displayed in the change map of Figure 7.25 so that dark pixels are indicative of areas of scene change in both the log likelihood change map as well as the sample coher-

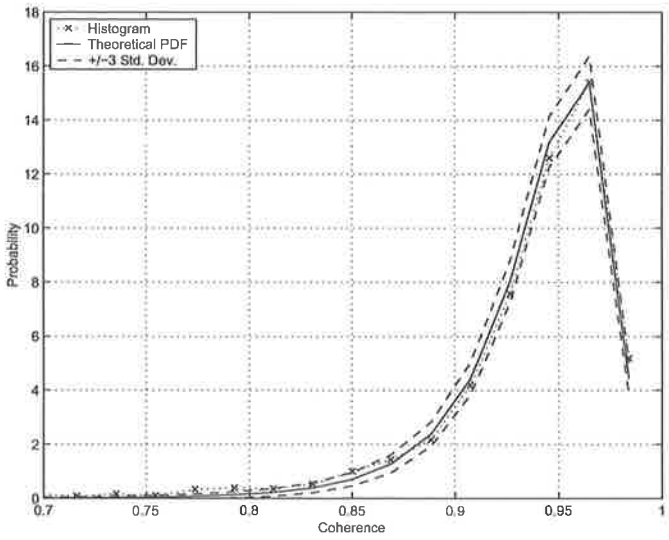


Figure 7.22: Histogram and theoretical density function for the sample coherence obtained from the primary and repeat pass subsampled image subchips. A true coherence of 0.94 and and ENL = 7 have been used to obtain the theoretical density function of the sample coherence. Also shown is the likely range in variation (three standard deviations) of the histogram estimate of the PDF that is to be expected assuming the jointly Gaussian model is correct.

ence. The track like scene disturbances are visible in both the sample coherence and log likelihood change map, however the disturbances are most prominent in the log likelihood map. The threshold applied to each change map to generate the change detections has been experimentally determined in each case to achieve a fixed number of detections (corresponding to a false alarm rate of 0.05) in the region to the right of the image where there are no obvious scene disturbances. (Unfortunately no ground truth observations are available to determine the extent of the scene changes in this image pair. However, there are no obvious scene disturbances in the right hand side of the change maps and thus it seems reasonable to assume that detections in the region are in fact false alarms.) Given the lack of ground truth observations and the fine scale structure of the track like disturbances it is difficult to compute quantitative comparisons of the two change statistics. However, it is clear from Figure 7.25 that for the same false alarm rate the scene disturbances are more clearly delineated by the log likelihood change statistic.

Finally Figures 7.26 and 7.27 show the histogram of the change statistic evaluated over the image pair subchip. In Figure 7.26 the theoretical density functions of the log likelihood change statistic corresponding to the changed and unchanged scenarios are also shown. While in Figure 7.27 an enlarged view of the change statistic histogram is shown along with the unchanged hypothesis theoretical density function. Given the three standard deviation allowance for variation in the histogram density function shown in Figures 7.26 and 7.27 the histogram is not inconsistent with the theoretical derived PDFs.

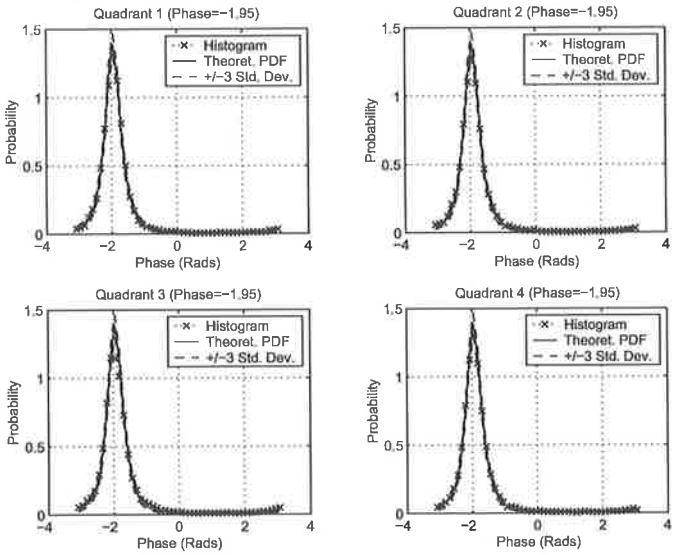


Figure 7.23: Histograms and theoretical density functions for the interferometric phase obtained by partitioning the subsampled image subchips into four equally size non-overlapping image quadrants. A true coherence of 0.94, an ENL = 7 and an underlying true interferometric phase of 1.95 radians have been used to obtain the theoretical density functions. Also shown is the likely range in variation (three standard deviations) of the histogram estimates of the PDF that are to be expected assuming the jointly Gaussian model is correct.

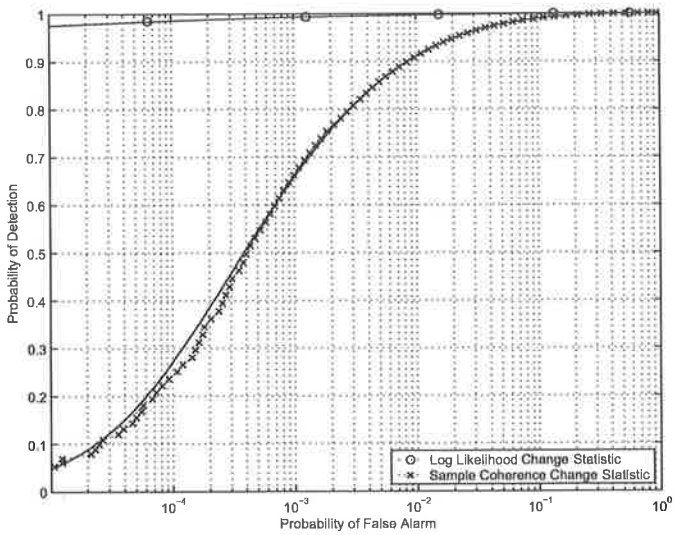


Figure 7.24: Theoretical and simulated ROC curves of the sample coherence and log likelihood ratio change statistics using change detection scenario described by the covariance matrices given in (7.23).

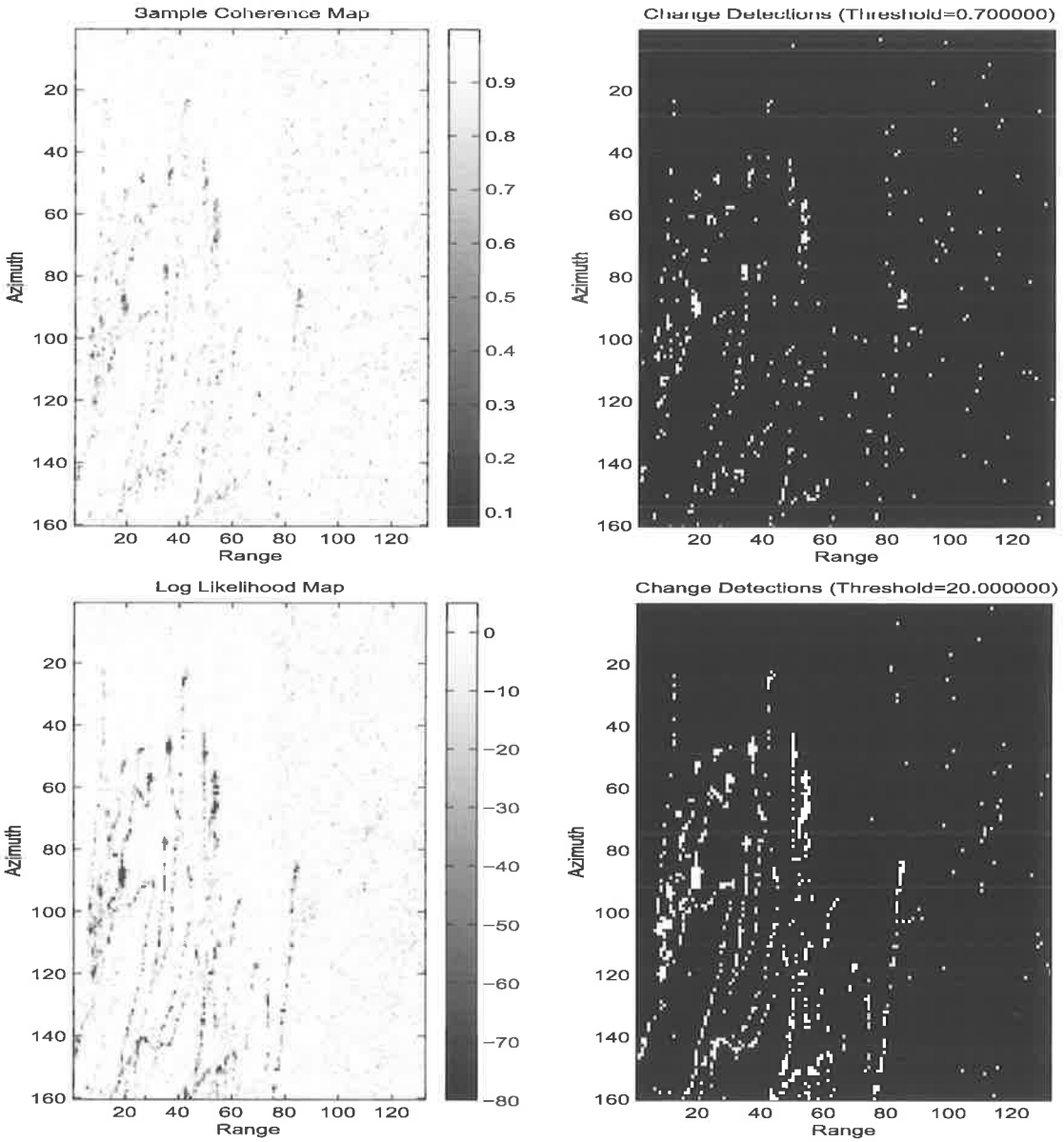


Figure 7.25: The images on the left hand side show, from top to bottom, the sample coherence and log likelihood change statistic maps, evaluated over the subsampled subchip image pair using a 3 by 3 pixel sliding estimation window. The images on the right hand size show the associated change detections obtained by applying a threshold to the change maps. The threshold has been experimentally selected to give a false alarm rate of 0.05.

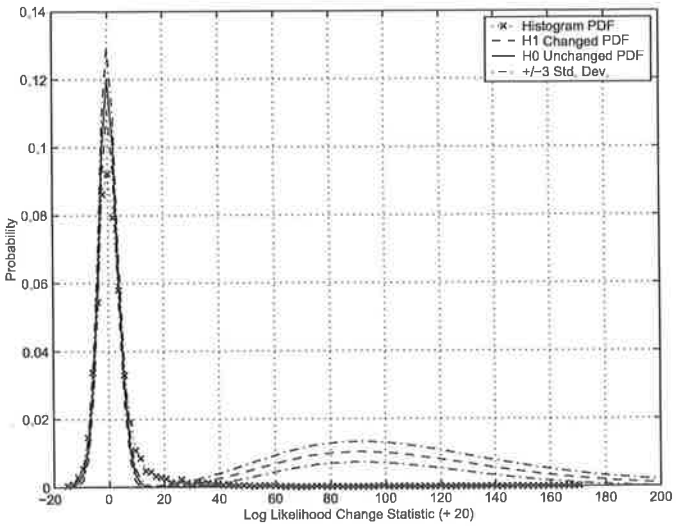


Figure 7.26: Experimentally obtained histogram of the log likelihood change statistic obtained using a 3 by 3 sliding estimation window over the entire image subchip pair. The histogram is thus a mixture of values obtained over both changed and unchanged areas. Also shown are the theoretical density functions as well as the anticipated range in variation (three standard deviation) of the histogram PDF estimate under the changed and unchanged hypotheses.

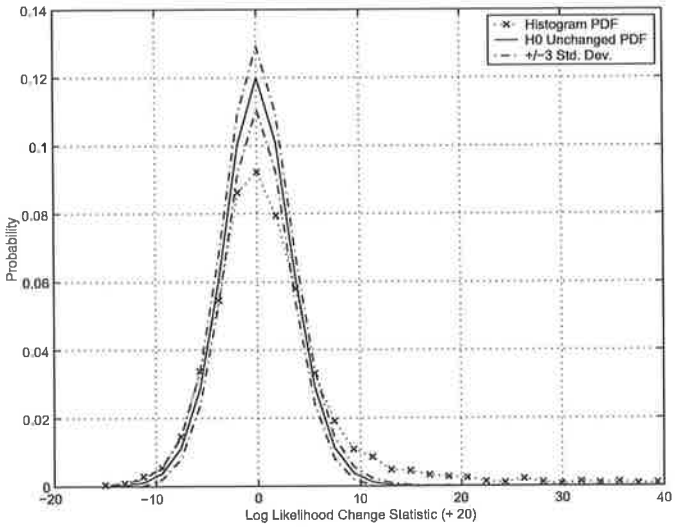


Figure 7.27: Enlarged view of the histogram of the log likelihood change statistic obtained using a 3 by 3 sliding estimation window over the entire image subchip pair. Also shown is the theoretical density function and the anticipated range in variation (three standard deviation) of the histogram PDF estimate for the unchanged scene hypothesis.

7.4.4 Detection Improvements Arising from the Modified PGA

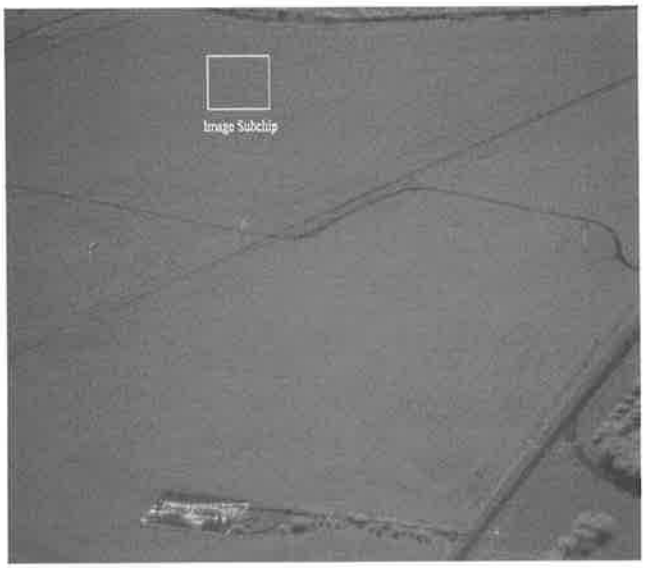
The detection performance achievable using the sample coherence or the log likelihood change statistic is dependent on the ability of the statistic to discriminate between the changed areas in the scene (characterised by low coherence) and the unchanged areas of the scene (characterised by some degree of partial coherence). The coherence in the unchanged areas of the scene is sensitive to the presence of any relative uncompensated phase differences between the signal histories of the image pair, see Chapter 4. One possible source of relative mismatch between collections arises through errors made in the measurement of the radar platform position during the aperture formation. In Chapter 3 it was shown that for wide-angle spotlight SAR collections that are subject to platform measurement errors, residual range dependent phase errors remain after image formation using the PFA and PGA. In a repeat pass pair such residual errors will be a source of relative mismatch between the focused image pair resulting in a reduction in the overall coherence. For the case of an error in the measurement of the along track velocity in the aperture formation a simple range cell migration correction step was proposed for compensation of the dominant range dependent components of the phase error function. This was shown to largely eliminate this source of decorrelation in an interferometric pair. In this section the effect of the range cell migration correction step on the detection performance of the sample coherence and log likelihood change statistic is demonstrated.

Figures 7.28 (a) and (b) show the primary and repeat pass images used to compute the sample coherence and log likelihood change statistics. The images have been generated from the May 2000 data set and incorporate the sheep track changes discussed in the previous subsection. The 3 dB resolution of the images are 0.45 m in range and 0.12 m in azimuth using an unweighted window. Figures 7.29 (a) and (b) show the PGA phase error obtained from the primary and repeat pass images respectively. Observe that there is a relative quadratic phase error between the interferometric pair of approximately 70 rad. The mid aperture k_y offset is $k_{0_g} = 335.96$ thus from Section 3.5 the relative quadratic phase error corresponds to a peak value of range cell migration of 0.208 m. From Figure 3.10 it can be seen that this level of quadratic range migration corresponds to a reduction in the coherence of the interferometric pair by a factor of approximately 0.94. By applying the range cell migration correction step proposed in Chapter 3 this source of interferometric correlation can be largely eliminated.

Figures 7.30 (a) and (b) show the sample coherence and the associated detection maps for the primary and repeat pass images focused with and without the range cell migration correction step. Note that the sample coherence change statistic is shown in full scale where white represents a coherence of 1 and black a coherence of 0. The sheep tracks are evident in the lower portion of the coherence map while the upper portion is free of the sheep disturbances. The coherence evaluated over the unchanged portion of the scene without the range cell migration correction step is 0.91. With the range cell migration step in place the unchanged scene coherence is 0.95, an increase of approximately 4%. Figures 7.31 (a) and (b) show the log likelihood change statistic evaluated using the primary and repeat pass images with and without the aid of the range cell migration correction step.

Given the lack of ground truth data for this image pair it is difficult to quantify the detection improvements obtained with the range cell migration correction focusing step. However, assuming the low coherence "tracks" are scene changes, it can be seen from Figures 7.30 and 7.31 that the small 4% improvement in the coherence of the image pair has produced a noticeable improvement in the detection performance of both the sample coherence and log likelihood change statistic. Comparing the detection performance of the sample coherence with and without the range cell migration correction step shown in Figure 7.30 it can be seen that there has been a noticeable decrease in the false detections in the unchanged upper portion of the image subchip. Comparing the detection performance of the log likelihood change statistic with and without the range cell migration correction step shown in

Figure 7.31 there appears to be greater discrimination between the track changes and the unchanged regions of the scene with the correction step in place. This is reflected in the increase in the number of track detections evident in Figure 7.31 (b).

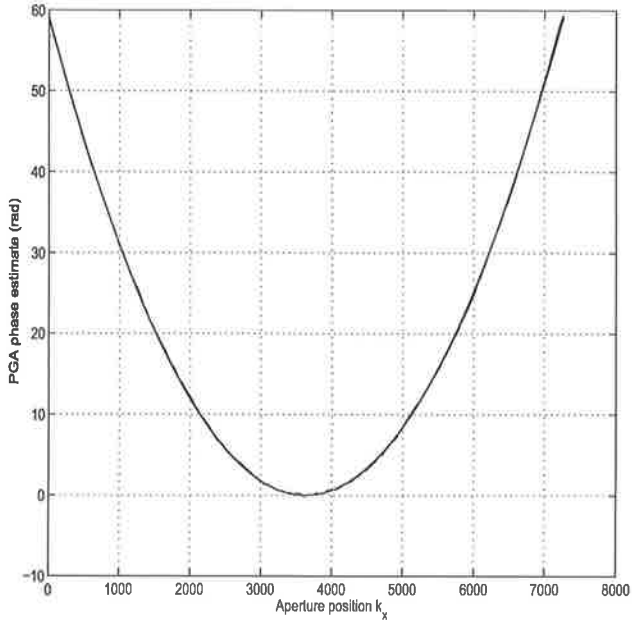


(a) Primary Intensity SAR Image.

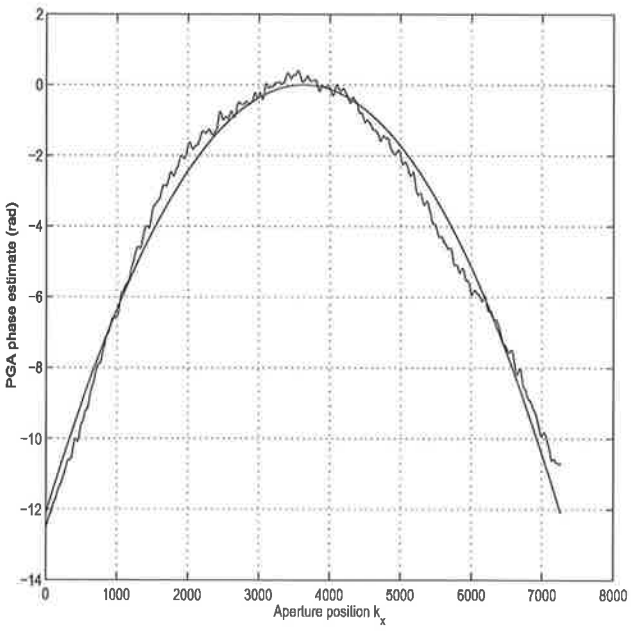


(b) Repeat Pass Intensity SAR Image.

Figure 7.28: Primary and repeat pass intensity SAR images. The imagery has been processed to a resolution of 0.45 m (range) and 0.12 m (azimuth) with an unweighted aperture. Also shown is the image subchip selected for further processing and change detection analysis.

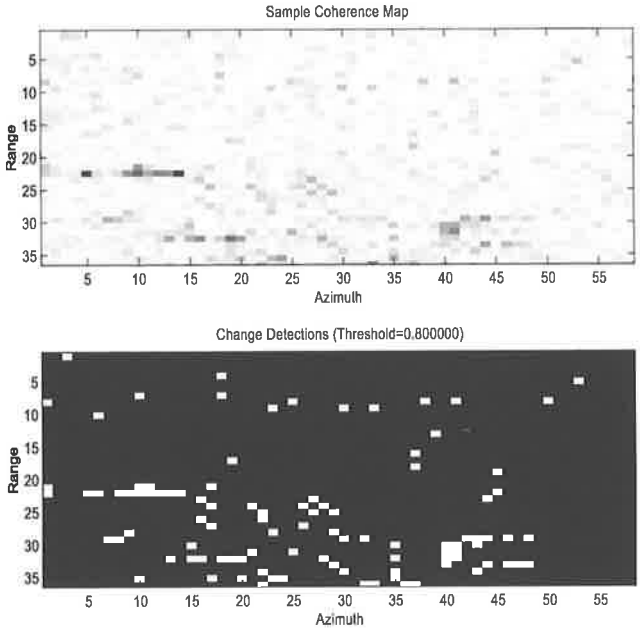


(a) Primary Image PGA Phase.

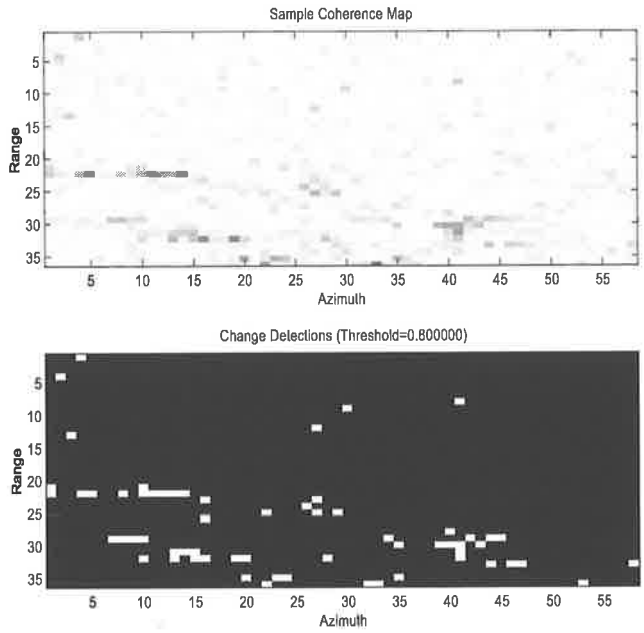


(b) Repeat Pass Image PGA Phase.

Figure 7.29: Primary and repeat pass PGA phase error estimates.

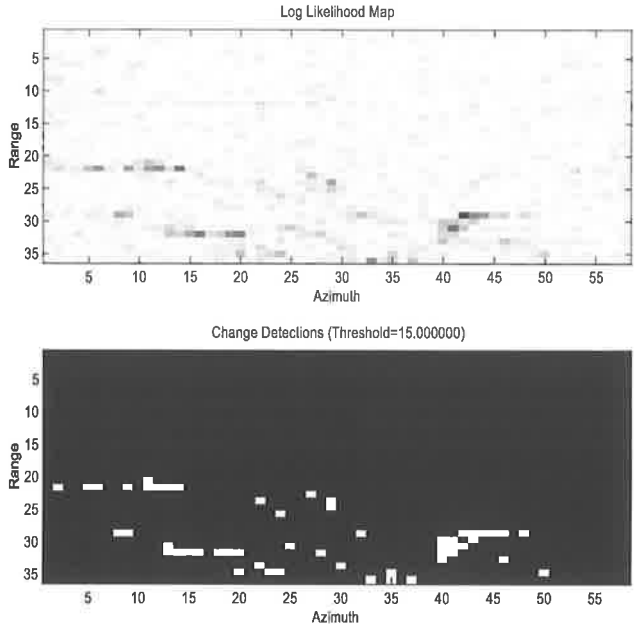


(a) Sample Coherence without range cell migration correction.

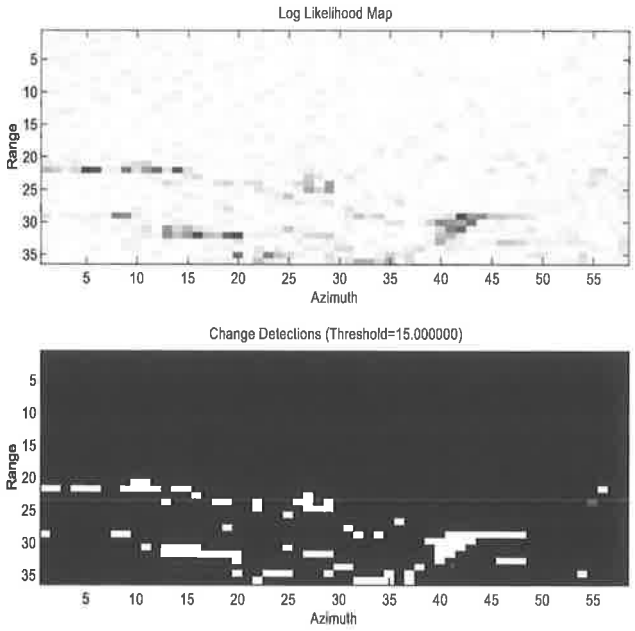


(b) Sample Coherence with range cell migration correction.

Figure 7.30: Sample coherence and change detections evaluated using a 3x3 pixel sliding estimation window with and without the range cell migration correction step. The sample coherence is shown on a full scale where black denotes zero coherence and white denotes unity coherence Also shown are the detections obtained by applying a threshold of 0.8.



(a) Log Likelihood Change Statistic without range cell migration correction.



(b) Log Likelihood Change Statistic with range cell migration correction.

Figure 7.31: Log likelihood change statistic and change detections evaluated using a 3x3 pixel sliding estimation window with and without the range cell migration correction step. Also shown are the detections obtained by applying a threshold of 15.0.

7.5 Coherent Image Pair 3

7.5.1 Experimental Description and Parameters

The image pair selected for analysis from the September 1999 interferometry experiments was collected with a revisit period of two hours and a nominal grazing angle of 15.9 degrees. Given the low grazing angle of the imaging geometry some degree of textural modulation of the imagery due to radar shadowing is anticipated for this image pair. The deviation from the Gaussian scattering model however is expected to be only modest and analysis of this pair provides some indication of the sensitivity of the performance of the change statistic in textured scenes.

Figures 7.32 and 7.33 show the primary and repeat pass image pair selected for change detection analysis. The 3 dB resolution of the image pair is 0.52 m range by 0.15 m azimuth with a Hamming window applied and a pixel spacing of 0.34 m by 0.11 m. The slant range and depression angle offsets at aperture midpoint are 69.65 m and 0.035 degrees respectively. Local estimates of the mean backscatter power and complex sample cross correlation coefficient of the primary and repeat pass image pair have been obtained by applying a 2 (range) by 6 (azimuth) pixel sliding estimation window. Given the oversampling rate and Hamming point spread function of the imagery a theoretically derived ENL of 5.7 for the sample estimates has been computed assuming the underlying backscatter is a white complex Gaussian process. The 3 dB resolution of the mean backscatter power ratio change map and the coherence and interferometric phase subsequently formed is 0.57 m in range and 0.22 m in azimuth with a pixel spacing of 0.343 m in range and 0.34 m in azimuth.

Figure 7.34 shows the mean backscatter power ratio change map for the image pair while Figures 7.35 and 7.36 show the coherence and interferometric phase respectively. The ground truthed scene changes carried out with the rotary hoe and lawn mower outlined in Figure 7.1 are difficult to discern in the mean backscatter power ratio change map, however appear quite clearly in the coherence map as areas of low coherence and as areas of rapid, random phase fluctuations in the interferometric phase map. Other areas of low coherence (or rapid phase fluctuations) include the shadowed areas as well as the road. In these areas there is little backscattered signal evident in the transduced imagery and hence the coherence estimated is dominated by the uncorrelated radar system noise. The tree returns in the image also appear as areas of low coherence due to the movement of the leaves and branches that occurs both during data collection and in the interval between collection.



Figure 7.32: Intensity SAR image generated from the primary pass imaging collection. The imagery has been processed to a resolution of 0.52 m (range) x 0.150 m (azimuth) with a Hamming window applied.

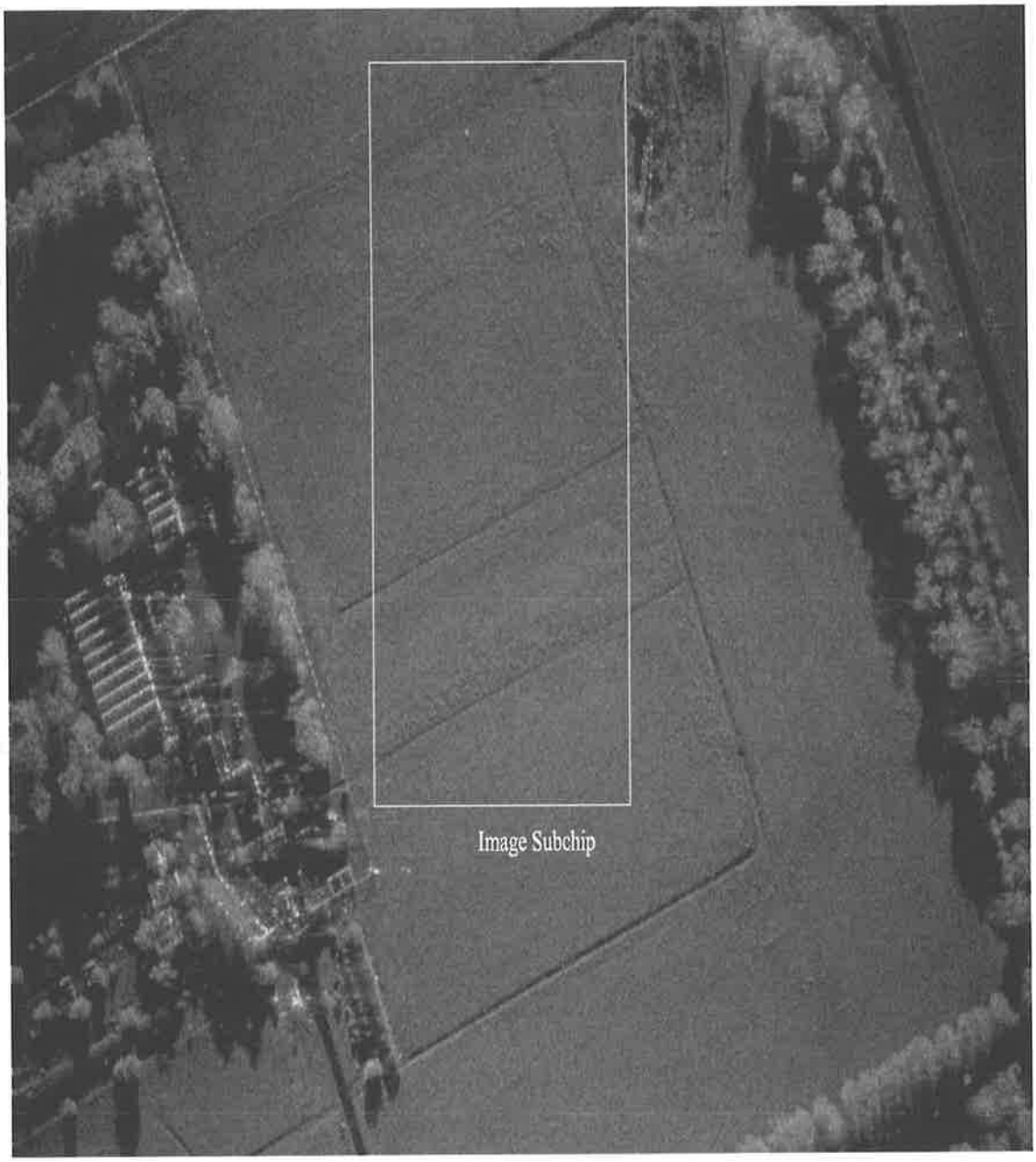


Figure 7.33: Intensity SAR image generated from the repeat pass imaging collection. The imagery has been processed to a resolution of 0.52 m (range) x 0.150 m (azimuth) with a Hamming window applied. The temporal baseline between the primary and repeat pass collections is approximately two hours and in this period scene changes were carried out with a rotary hoe and a lawn mower, see Figure 7.1.

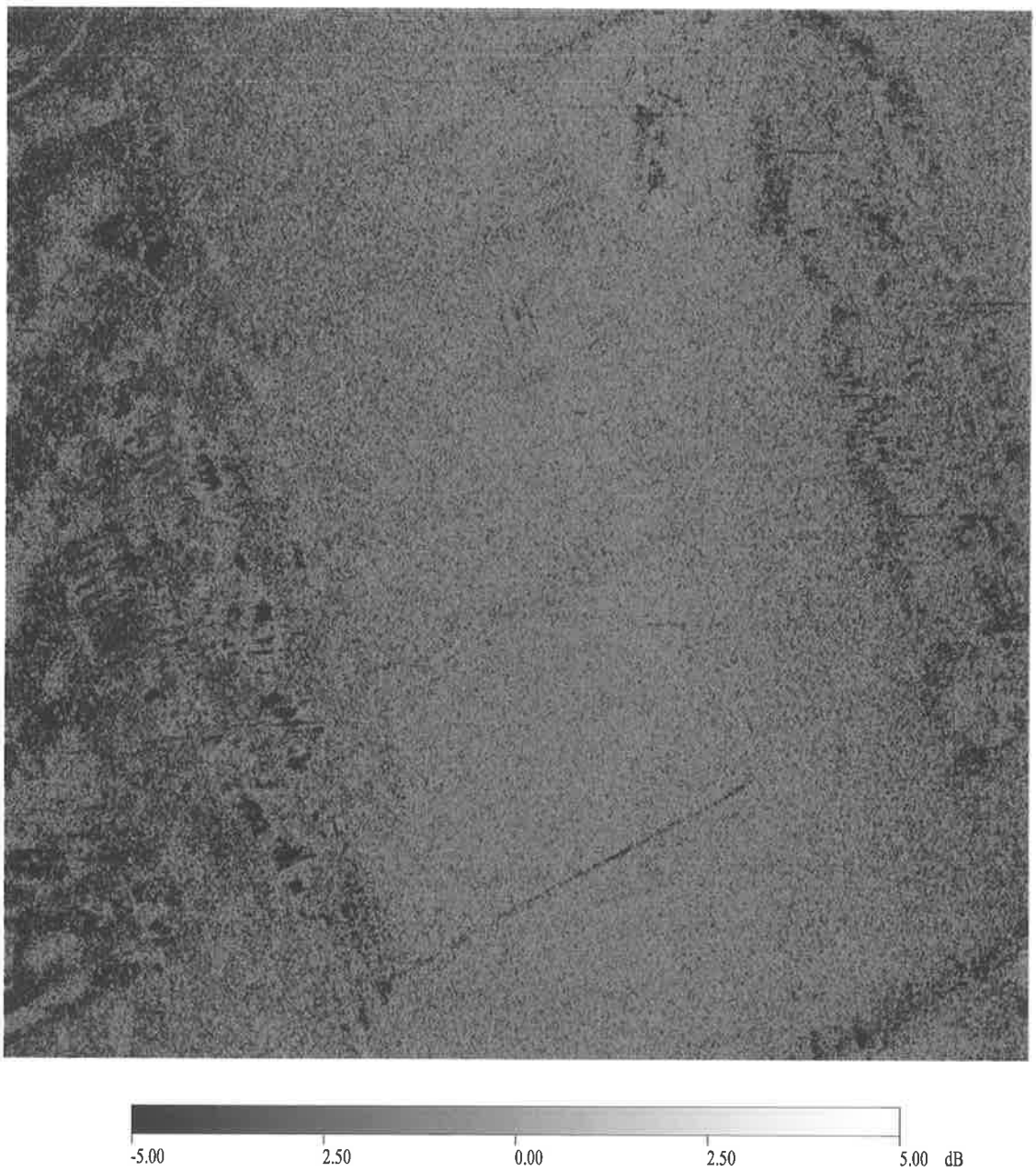


Figure 7.34: Mean backscatter power ratio change statistic evaluated over the primary and repeat pass image pair using a 2 (range) by 6 (azimuth) pixel spatial estimation window. The resolution of the estimate is 0.57 m by 0.22 m with a pixel spacing of 0.343 m by 0.34 m.

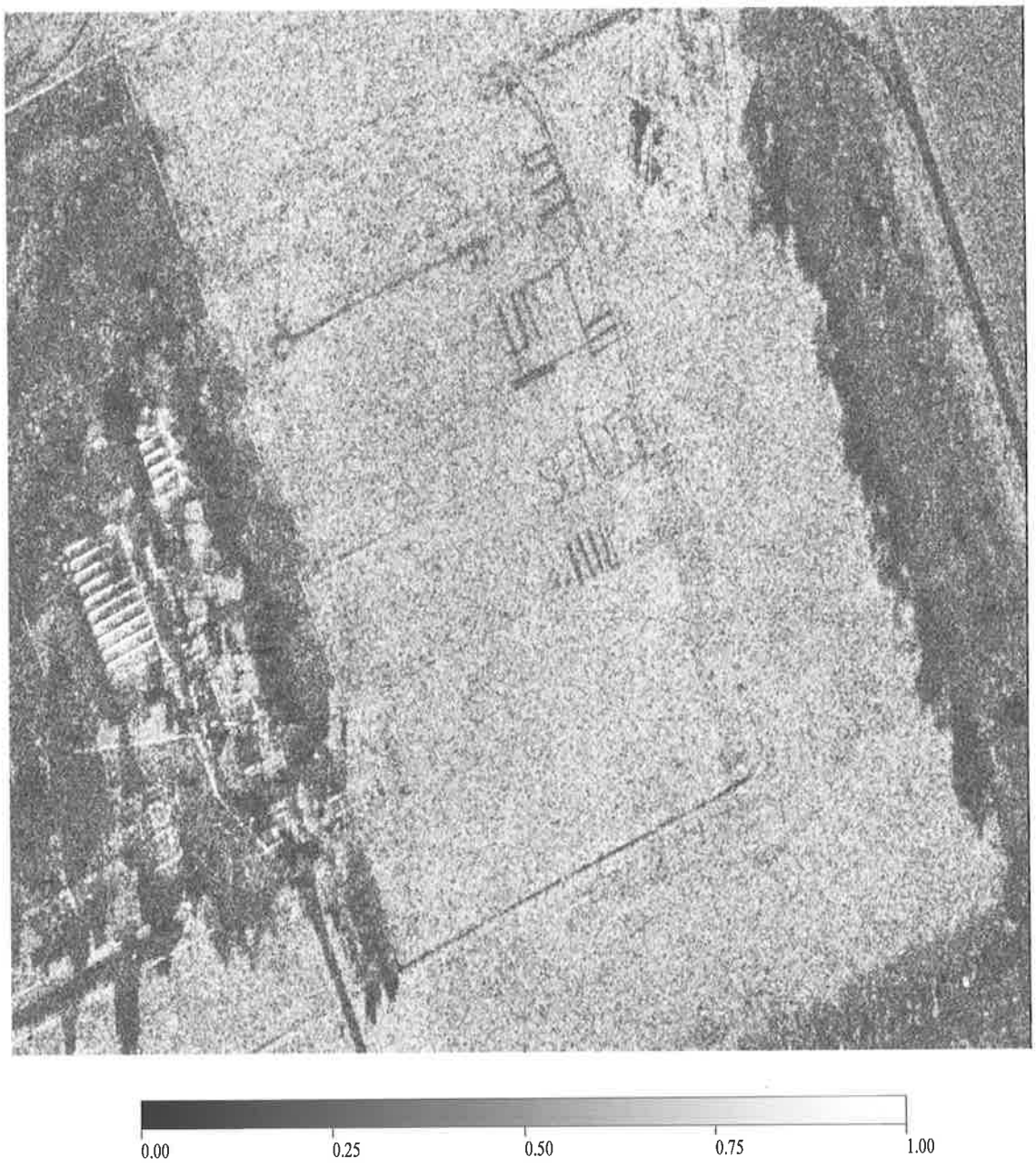


Figure 7.35: Sample coherence evaluated over the repeat pass image pair using a 2 by 7 pixel spatial estimation window. The resolution of the estimate is 0.57 m by 0.22 m with a pixel spacing of 0.343 m by 0.34 m. The areas modified using the rotary hoe and lawn mower are clearly visible as areas of low coherence.

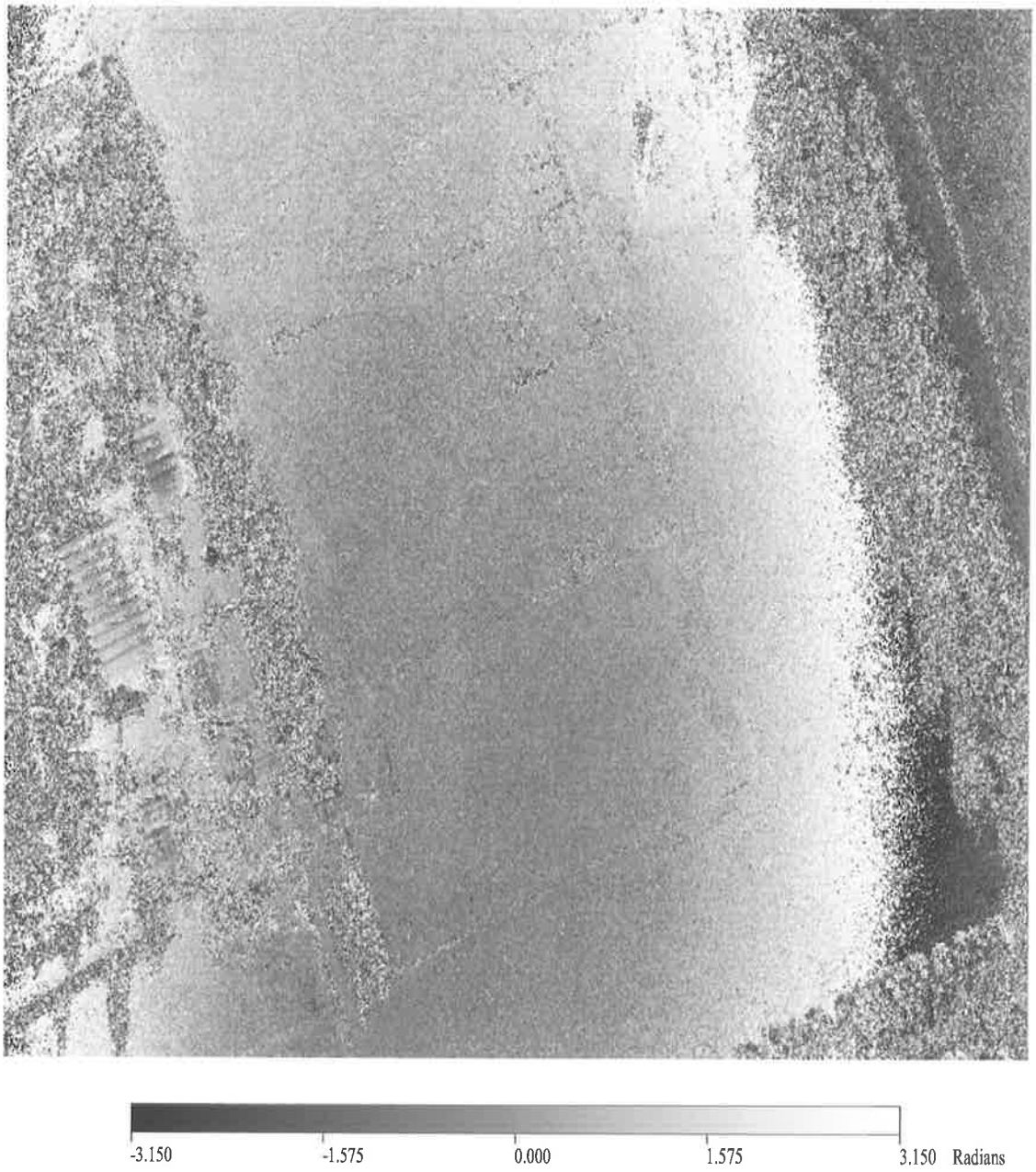
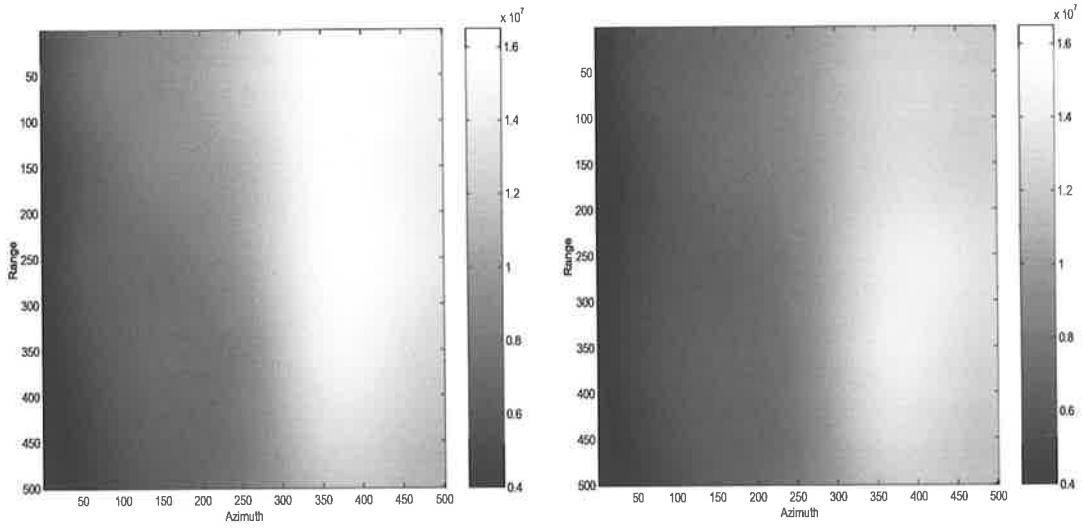


Figure 7.36: Sample interferometric phase evaluated over the repeat pass image pair using a 2 by 7 pixel spatial estimation window. The resolution of the estimate is 0.57 m by 0.22 m with a pixel spacing of 0.343 m by 0.34 m. The modified regions of the scene appear as areas of random phase fluctuations.



Primary Backscatter Power Model Repeat Pass Backscatter Power Model

Figure 7.37: Thin plate spline models describing the spatial variation of the mean backscatter power of the primary pass image subchip, indicated on the left and repeat pass image subchip indicated on the right.

7.5.2 Interferometric Image Pair Statistics

For the purposes of examining the image statistics and applying the change detection algorithms an image subchip, as indicated in Figure 7.32, has been extracted from the primary and repeat pass images. This image subchip pair encompasses a large portion of the open field including the ground truthed scene changes described in Section 7.2.1. As the primary and repeat pass images are significantly oversampled the extracted image subchips have been subsampled by a factor of two in range and azimuth giving a subsampled subchip size of 500 by 500 pixels for subsequent processing.

To allow for possible variation in the mean backscatter power across the subchip pair each subchip has been partitioned into 25 non-overlapping regions each 100 by 100 pixels in size over which sample estimates of the backscatter power have been computed. A thin plate spline has been fitted to both the primary and repeat pass sample estimates to model the spatial variation of the backscatter power across the scene. Figure 7.37 shows the thin plate spline models obtained for the mean backscatter power of the primary and repeat pass image subchips. The models indicate that the mean backscatter power across the image subchips varies by approximately 6 dB. This may possibly be due to an error in the antenna pointing accuracy resulting in an antenna beampattern variation across the scene.

The amplitude and phase statistics of one of the 100 by 100 pixel regions, having approximately uniform mean backscatter power, have been computed and compared to the Gaussian and K distribution models. Figure 7.38 shows the amplitude histograms of the primary and repeat pass 100 by 100 pixel image region. Superimposed on the histograms are the theoretical Rayleigh amplitude density functions that arise in the case when the scattering may be modelled by a complex Gaussian process, as well as the K distribution amplitude for modelling textured scenes. Figure 7.39 shows the phase histograms associated with the 100 by 100 pixel regions computed for the primary and repeat pass images as well as the theoretical uniform phase probability density function. Also shown in the plots of Figures 7.38 and 7.39 are the likely ranges in variation of the histogram estimates of the PDFs, that are to be expected assuming the Rayleigh amplitude, K distributed amplitude and uniform phase

PDFs are accurate models. The range of expected values shown are the ± three standard deviations about the mean expected at each histogram sample bin. The mean backscatter power coefficients required to specify the theoretical amplitude distributions have been estimated by averaging the image pixel intensities over the entire 100 by 100 pixel region,

$$\hat{\sigma}_f^2 = \frac{1}{N}\sum_{k=1}^{N}|f_k|^2 = 1.0728e7, \tag{7.25}$$

$$\hat{\sigma}_g^2 = \frac{1}{N}\sum_{k=1}^{N}|g_k|^2 = 9.6785e6, \tag{7.26}$$

where N = 10,000.

The phase histograms of the primary and repeat pass image subchips in Figure 7.39 show good agreement with the theoretical uniform distribution. The amplitude histograms shown in Figure 7.38 however, exhibit a statistically significant deviation from the Rayleigh density function that is usually expected under Gaussian scattering conditions. The K distribution on the other hand appears to provide a much better fit to the amplitude data. Computing the K distribution order parameter $\hat{\nu}$ using spatial estimates of the second and fourth order moments in equation (7.14) gives $\hat{\nu} = 7.9$ and $\hat{\nu} = 6.8$ for the primary and repeat pass images respectively. These values indicate that the statistics of the image subchips lie in the transition region between Gaussian and markedly non-Gaussian scattering behaviour. The modest non-Gaussian behaviour may possibly be attributed to textural modulation across the image subchips arising from the effects of radar shadowing that is most pronounced at low grazing angles. In this case the unchanged portions of the image subchips may be described by the multi-channel form of the K distribution described in Section 7.2.2. Assuming the textural modulation spatial variation over the scene is on a scale greater than the image resolution cell then it has been demonstrated [Gie01a], [JWP94] that the sample correlation coefficient may be used to estimate the underlying cross correlation of the image pair in the unchanged regions. Also the sample estimate will have the same probability density function as in the Gaussian scattering case.

Ground truth observations indicate that the field in the imaged scene is relatively homogeneous with respect to the type of vegetation, its coverage and size. Therefore the scene coherence of the image subchips is expected to be constant and a histogram of sample estimates computed over the entire image subchip pair may be obtained and compared to the theoretical density function given in equation (7.10). Figure 7.40 shows the sample coherence histogram obtained using a 3 by 3 sliding estimation window applied over the entire image subchip pair. Also shown is the theoretical density function of the sample coherence where a true coherence of 0.62 and and ENL of 7 have been found to provide the best fit to the experimental histogram. Also shown in Figure 7.40 is the likely range in variation (three standard deviations) of the histogram estimate of the PDF that is to be expected assuming the sample estimate has the same PDF as the Gaussian scattering case. The theoretical density function and experimental histogram are in excellent agreement with only a slight deviation at low coherence values due to the inclusion of the modified low coherence areas in the computation of the sample coherence.

The interferometric phase may vary across the scene depending on the terrain topography and any uncompensated relative phase terms that remain after image formation. To allow for this possible spatial variation, the sample estimates of the interferometric phase obtained from the 3 by 3 pixel sliding estimation window have been used to generate a thin plate spline model of the interferometric phase variation across the image subchip pair. Figure 7.41 shows the sample estimates of the scene and the corresponding thin plate spline model. From the model the phase varies by 134 degrees across the image subchip scene.

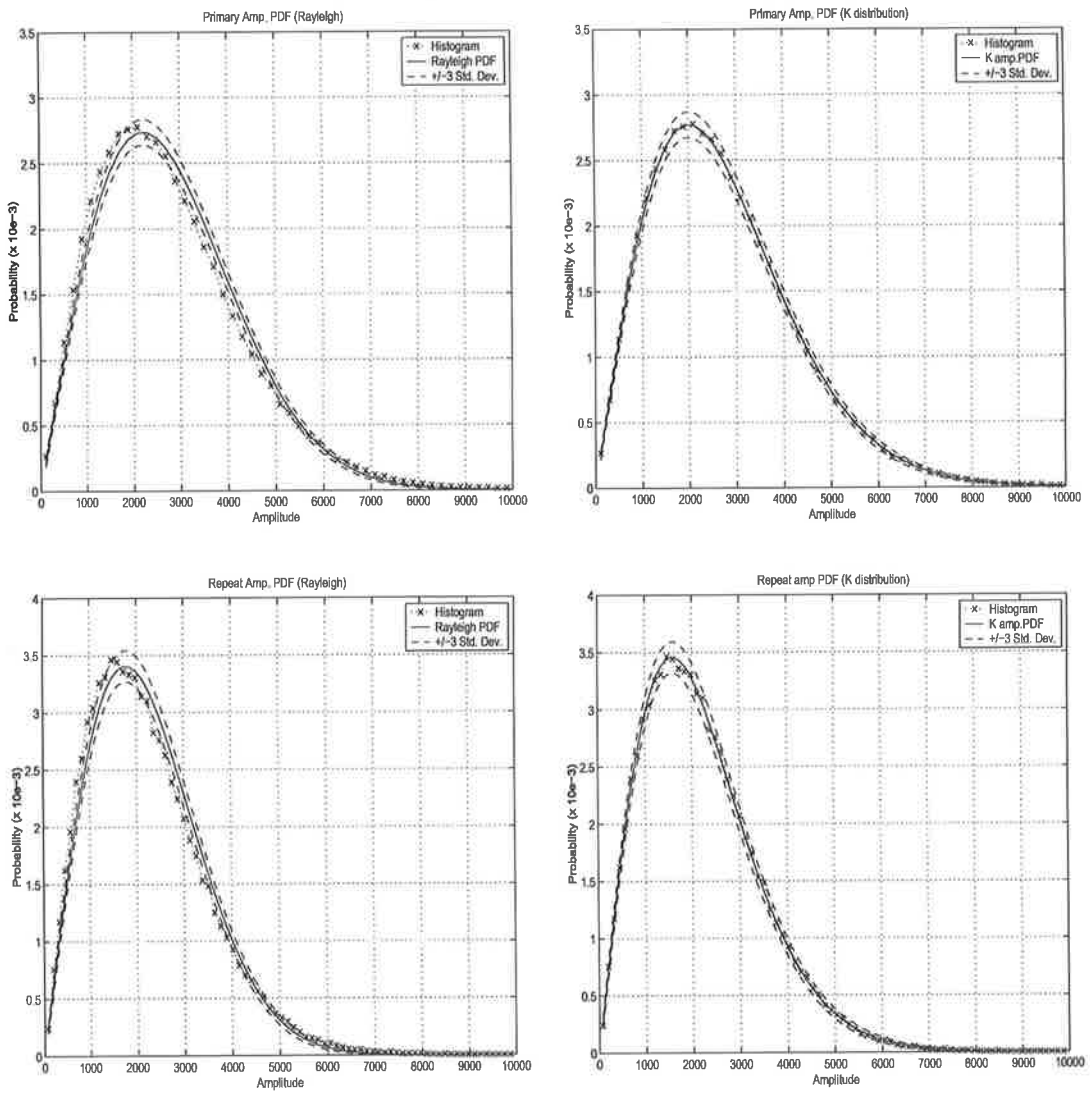
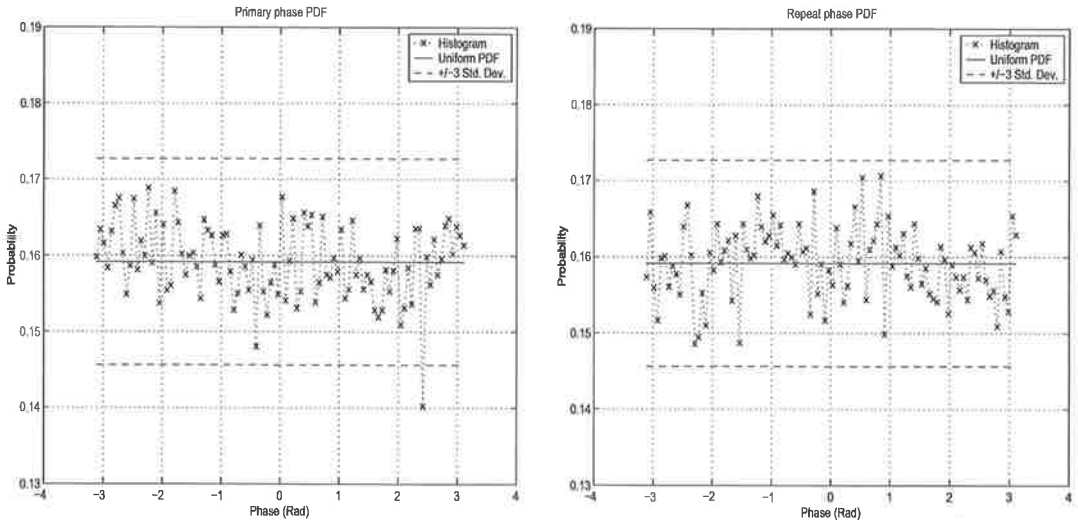


Figure 7.38: Amplitude histograms for the 100 by 100 pixel primary and repeat pass image region. Superposed on the histograms are the theoretical amplitude distributions corresponding the Gaussian and K distributions. Also shown in the plots are the the likely ranges in variation (three standard deviations) of the histogram estimates of the PDFs that are to be expected assuming the theoretical PDFs are correct.



Primary Backscatter Power Model Repeat Pass Backscatter Power Model

Figure 7.39: Phase histograms for the 100 by 100 pixel primary and repeat pass image region. Superposed on the histograms is the theoretical uniform phase probability density function. Also shown in the plots are the the likely ranges in variation (three standard deviations) of the histogram estimates of the PDF that are to be expected assuming the theoretical PDF is correct.

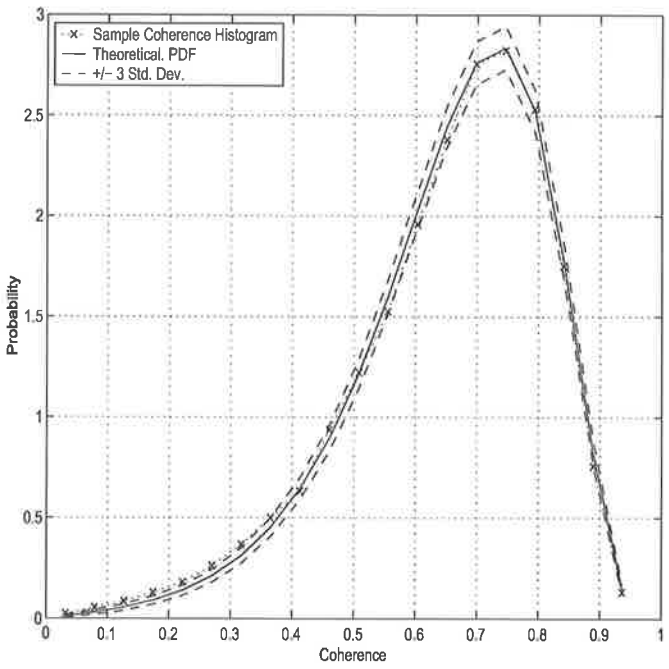
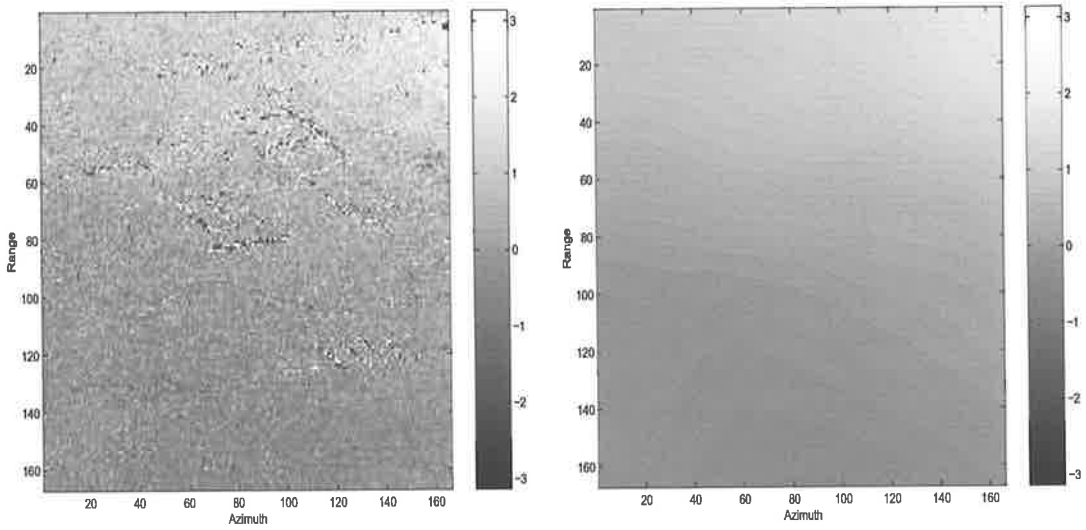


Figure 7.40: Histogram and theoretical density functions for the sample coherence evaluated of the primary and repeat pass image subchips. The histogram has been obtained using a 3 by 3 pixel sliding spatial estimation window. A true coherence of 0.62 and an ENL = 7 have been used to specify the theoretical sample coherence density function. Also shown is the likely range in variation (three standard deviations) of the histogram estimate of the PDF that is to be expected.



InSAR Phase Sample Estimates InSAR Phase Model

Figure 7.41: The image on the left hand side indicates sample estimates of the interferometric phase obtained using a 3 by 3 pixel sliding estimation window applied over the image subchip pair. On the right hand side is a thin plate spline fit to the sample estimates of the interferometric phase.

7.5.3 Change Detections

From the previous section the statistics of a pixel pair from the primary and repeat pass image subchips show a modest departure from Gaussian scattering behaviour possibly due to the radar shadowing that is most pronounced at the low grazing angles used for this collection. Nevertheless the speckle component of the image pair may still be described by the covariance matrices, $Q_0(x,y)$ under the unchanged hypothesis and $Q_1(x,y)$ under the changed hypothesis,

Unchanged Hypothesis:

$$Q_0(x,y) = \begin{bmatrix} \sigma_f^2 & 0.62\sigma_f\sigma_g exp(j\Phi) \\ 0.62\sigma_f\sigma_g exp(-j\Phi) & \sigma_g^2 \end{bmatrix}, \tag{7.27}$$

Changed Hypothesis:

$$Q_1(x,y) = \begin{bmatrix} \sigma_f^2 & 0 \\ 0 & \sigma_g^2 \end{bmatrix}, \tag{7.28}$$

where σ_f^2 and σ_g^2 are the mean backscatter power models of the primary and repeat pass image subchips shown in figure 7.37. The interferometric phase Φ is given by the model illustrated in Figure 7.41. While this covariance based description of the scene is incomplete as it neglects the texture component of the jointly K distribution model, the image pair are not markedly non-Gaussian and so the log likelihood change statistic may still be applied and potentially offer some performance improvement.

Using the estimated matrices Q_0 and Q_1 given above the detection performance of the sample coherence and the log likelihood change statistics may be computed using the theoretical Gaussian expressions for P_d and P_{fa} derived in Chapter 6. Figure 7.42 shows the theoretical as well as simulated ROC curves for the two change statistics. It is evident that, under the jointly Gaussian scattering

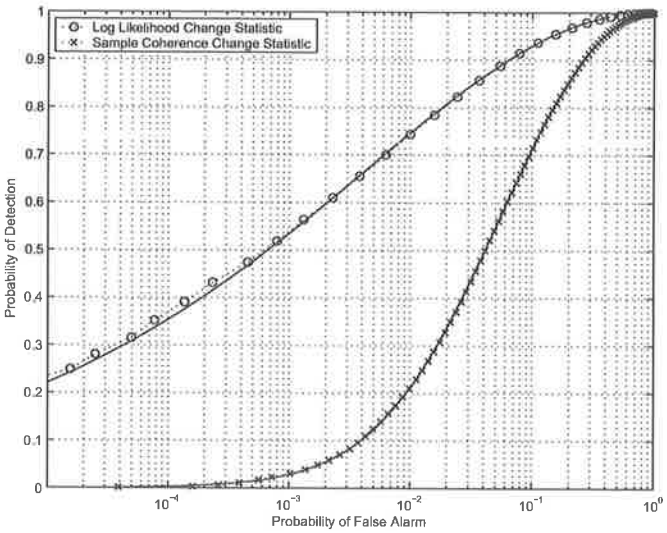


Figure 7.42: Theoretical and simulated ROC curves of the sample coherence and log likelihood change statistics applied to the pair of image subchips using the change scenario specified by the covariance matrices given in (7.27) and (7.28).

assumption, the log likelihood change statistic offers over an order of magnitude improvement in the detection performance over the sample coherence change statistic.

Figure 7.43 shows the sample coherence and log likelihood change maps evaluated over the scene using the covariance models Q_0 and Q_1 above. Also shown are the change detections obtained by applying appropriate thresholds to the coherence and log likelihood change maps. The thresholds applied in each case have been experimentally determined to achieve a fixed number of false alarms in an area known to have no ground changes thereby giving a $P_{fa} = 0.018$. It is clear that the log likelihood change statistic has a significantly better detection performance allowing the scene disturbances to be more readily discerned. While it is difficult to quantify the experimental P_d given the size and geometry of the disturbances, an estimate based on one of the modified strips yields a P_d of 0.68 for the log likelihood change statistic and 0.30 for the sample coherence. These compare favourably with the theoretical values obtained from Figure 7.42 of 0.795 for the log likelihood and 0.31 for the sample coherence. The experimental probability of detection for the log likelihood change statistic is slightly less than the theoretically predicted value. Possible reasons for this discrepancy include deviations from the theoretical density functions due to the presence of texture in the scene imagery, small errors in the estimation of the covariance matrices Q_0 and Q_1 and their spatial variation, as well as inaccuracies in the estimation of the experimental P_d due to the small sample size.

Finally Figure 7.44 shows the histogram of the log likelihood change statistic evaluated over the entire image subchip pair as well as the theoretical probability density functions obtained under changed and unchanged scene hypotheses. Also shown in Figure 7.44 is the likely range in variation (three standard deviations) of the histogram estimate of the PDF that is to be expected under the changed and unchanged hypotheses. The histogram is a mixture of changed and unchanged pixels and is not inconsistent of the theoretically derived functions.

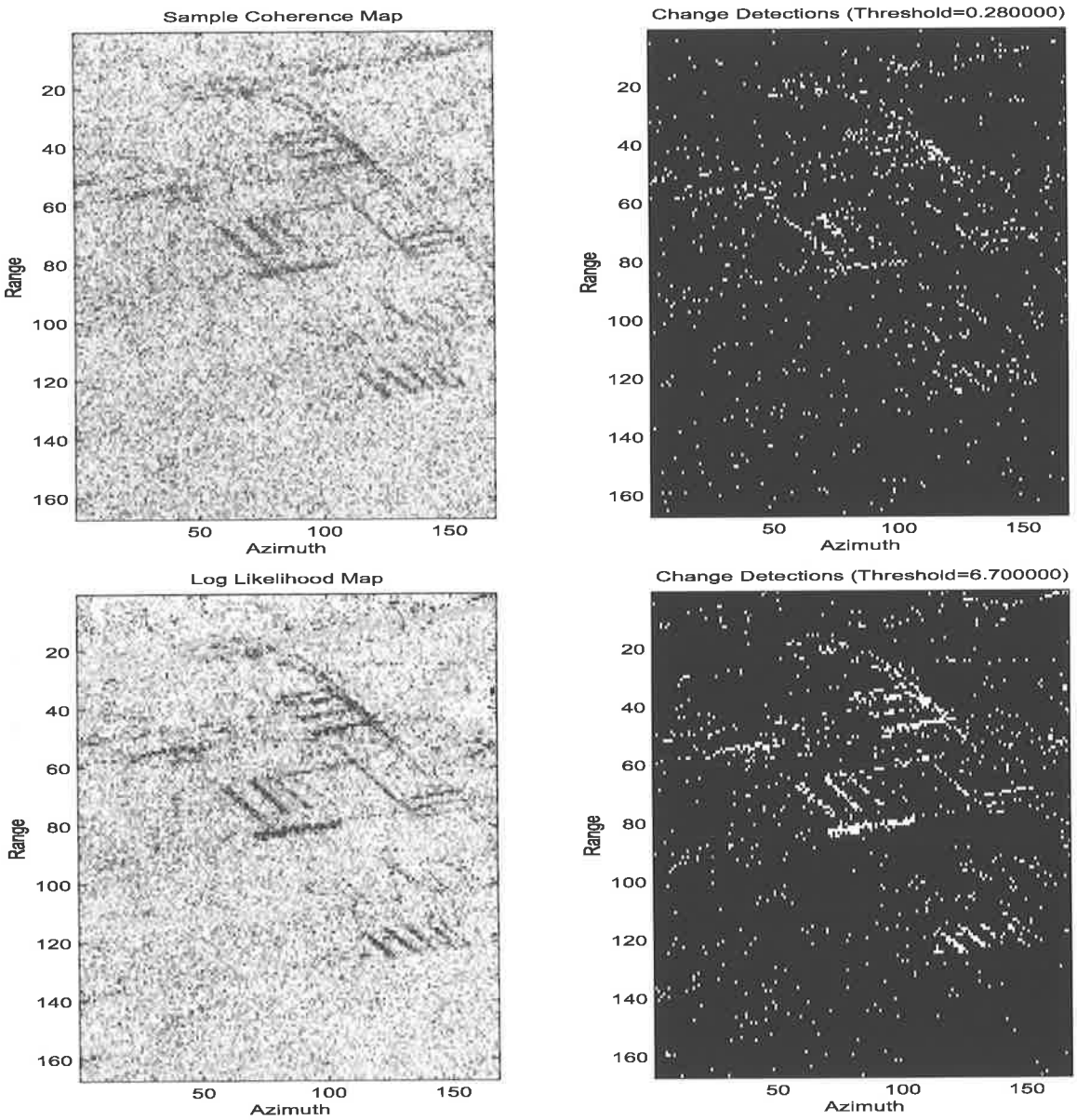


Figure 7.43: The images on the left hand side show, from top to bottom, the sample coherence and log likelihood change statistic maps evaluated over the subchip image pair using a 3 by 3 pixel spatial estimation window. The images on the right hand size show the detections obtained by applying a threshold to the corresponding change maps. The thresholds have been experimentally selected to give a false alarm rate of 0.018

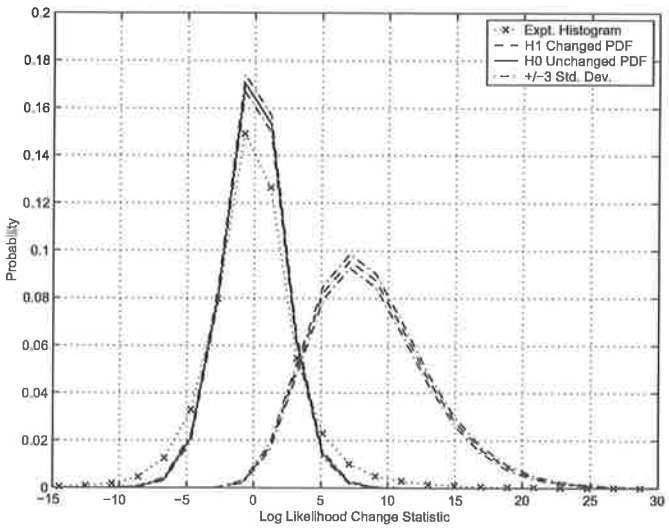


Figure 7.44: Experimentally obtained histogram of the log likelihood change statistic obtained using a 3 by 3 sliding estimation window over the entire image subchip pair. The histogram is thus a mixture of values obtained over both changed and unchanged areas. Superimposed on the histogram are the theoretical density functions as well as the likely range in variation (three standard deviations) of the histogram estimate of the PDF for the changed and unchanged hypotheses.

7.6 Conclusions

In this chapter the sample coherence, log likelihood and mean backscatter power ratio change statistics have been applied to experimental repeat pass interferometric SAR data collected with the DSTO Ingara airborne X-band SAR. In order to compare the change statistics over a range of scene change scenarios three different repeat pass experiments have been considered. These change scenarios include:

1. A range of revisit periods from a minimum of 12 minutes to a 24 hour revisit period.
2. Collections with incidence angles of 60 and 75 degrees to assess the impact of radar shadowing and associated textural modulation on the change detection performance.
3. A variety of ground truthed scene changes carried out with a lawn mower and rotary hoe to provide a range of scene disturbances with differing severity.

As a first step towards implementing the three change detection algorithms the statistics of the processed interferometric image pair were computed and compared to theoretical distributions that arise in the case of complex Gaussian scattering as well as the case of textural fluctuations. For the imagery collected at an incidence angle of 60 degrees the image statistics were found to be in good agreement with the Gaussian scattering model. The imagery collected at an incidence angle of 75 degrees however, was found to be more accurately described by the K distribution which is usually associated with textured imagery The presence of scene texture in this case may be attributed to the more pronounced radar shadows that arise in high incidence angle imagery.

For each of the three change detection experiments the superior detection performance of the log likelihood change statistic predicted theoretically in Chapter 6 was demonstrated. In particular for two of the change scenarios, it was possible to obtained experimentally derived values of the probability of detection at a specified false alarm rate. These values were found to be in good agreement with the theoretically determined values obtained using the equations derived in Chapters 5 and 6. The demonstration of the log likelihood change statistic and comparison with the sample coherence and mean backscatter power ratio change statistics using experimental data provides an important validation of the assumptions used to formulate the changed and unchanged hypotheses and the models describing the scattering behaviour of the interferometric image pair.

It has also been demonstrated that only modest increases in the coherence in the unchanged regions of an image pair can have a measurable impact on the detection performance of the sample coherence and log likelihood change statistics. In particular applying the range cell migration correction step proposed in Chapter 3 to an image pair having a large relative PGA quadratic phase error yielded a modest increase in the measured coherence of 4%. This small increase however, was demonstrated to produce fewer false alarms in the sample coherence change statistic while the contrast between the changed and unchanged regions of the scene was improved in the log likelihood change statistic map.

Chapter 8

Conclusion

In this thesis the problem of detecting fine scale scene changes using repeat pass SAR interferometry has been addressed. Change detection is an application to which SAR is particularly well suited since SARs can produce consistent high quality imagery with good radiometric calibration and geolocation accuracy. Indeed SARs can readily produce large volumes of multi-date, multi-baseline imagery and thus the design of a reliable automated detection algorithm for identifying areas of scene change is an important objective in managing such large data sets.

The unique characteristics of SAR imagery require careful consideration in formulating appropriate change statistics. In particular, as SAR is a coherent imaging system the transduced backscatter in a resolution cell has both an amplitude and a phase. Two forms of change detection may therefore be considered, namely incoherent and coherent change detection. Incoherent change detection identifies changes in the mean backscatter power of a scene by computing the average resolution cell intensity of the image pair. Coherent change detection using properly processed interferometric SAR image pairs, on the other hand, identifies changes in the scene that arise in the interval between collections by quantifying changes in the amplitude and phase of the image pairs. In the random walk model for the imaging of distributed target scenes the transduced complex backscatter in a resolution cell is the vector sum of many complex scattering contributions. A scene disturbance that causes a simple random rearrangement of the scatterers without altering their structural or dielectric properties will thus manifest as a change in the transduced amplitude and phase without a corresponding change in the mean backscatter power. Coherent change detection thus has the potential to detect very subtle scene changes.

In order to realise the full potential of coherent change detection interferometric SAR imagery must be acquired with very careful control of the repeat pass imaging geometries. Furthermore additional processing steps are generally required to model, estimate and compensate for any mismatch between the SAR acquisition functions and image formation processors employed to form the primary and repeat image pair. In this thesis a number potential sources of acquisition and image formation processor mismatch have been identified that arise in the case of wide-angle spotlight mode SAR imaging. In these imaging scenarios it has been found that narrow-band, small-angle approximations commonly made in the formulation of image formation processors and also in the modelling of platform location measurement errors can lead to residual image defocus that will vary from one imaging collection to another. The dominant components of the residual defocus have been analysed for the case of deramp demodulated spotlight SAR acquisitions and techniques proposed to compensate for the defocus and maintain coherency across repeat pass collections.

A further crucial aspect in the design of SAR image change statistics is the use of appropriate models to describe an interferometric image pair. Through these models any changes in the transduced amplitude and phase may be quantified in a statistically appropriate way. In the random walk model

for homogeneous distributed scenes a SAR image is described in a statistical sense in terms of a single parameter, namely the mean backscatter power. In the context of interferometry a multi-channel random walk model has been used to derive the joint statistical description of an image pair. In this model each image is described by a mean backscatter power and the relationship between an image pair is described by the complex cross correlation coefficient. In the literature change statistics have been proposed based on identifying regions of the scene where there has been a change in the mean backscatter power or a loss in the magnitude of the cross correlation coefficient. In this thesis an alternative approach has been considered in which models, based on the joint statistical description, have been postulated for the changed and unchanged regions of a scene. Discrimination between the models may thus be made using a simple statistical hypothesis test. A new change statistic has been proposed based on the statistical hypothesis formulation that has been shown to yield superior detection performance and thus represents a useful step forward in the design of a reliable automated change detection algorithm.

Finally estimation of the key statistical parameters describing an imaged scene requires some form of sample averaging, be it spatial or multilook averaging, to obtain reliable good quality estimates. This can be problematic in detecting man-made scene changes such as vehicle tracks across a field, which can be highly spatially non-stationary with abrupt changes and variations that may be smaller than the estimation window. In this case spatial averaging may include contributions from both changed and unchanged pixels making it difficult to distinguish between the changed and unchanged regions of the scene using the sample estimate. Image resolution is thus a key parameter limiting the performance of any statistically based change detection technique. In this thesis the formation of well focused fine azimuthal resolution imagery has been considered using wide-angle spotlight mode SAR acquisitions. The use of fine resolution imagery allows improved sample estimates of the interferometric parameters to be obtained and also offers the potential for the detection of very fine scale scene disturbances.

Much of the work in this thesis has been motivated by problems encountered in the practical application of interferometric change detection techniques to experimental repeat pass interferometric SAR data acquired with the DSTO Ingara SAR. The Ingara SAR is an airborne, single polarisation, X-band SAR with a spotlight SAR mode employing deramp on receive to achieve range resolutions of the order of 0.5 m. The resolution and operating wavelength of this sensor make it well suited to the detection of fine-scale scene changes using interferometry. As part of this thesis a number of repeat pass experiments where conducted in which various ground truthed scene changes were performed in the interval between collections. This experimental data set has been used extensively throughout the thesis to demonstrate the new techniques developed and validate the theoretical models and analysis.

8.1 Detailed Chapter Summaries and Contributions

The range and azimuth resolution of a SAR image is determined by the transmit waveform bandwidth and the extent of the synthetic aperture respectively. While the range resolution is limited by the radar hardware, in spotlight SAR mode, by continually steering the antenna onto a single focus point in the scene as the radar moves past, range echo data can be acquired over an extended collection aperture and processed to yield fine azimuth resolution imagery. In the case of the Ingara system, to achieve 0.15 m azimuth resolution an angular aperture of approximately 10 degrees is required. At a standoff range of 20 km this corresponds to a synthetic aperture of 3.5 km which is acquired using Ingara in approximately 30 sec. Aside from the physical antenna steering constraints, the size of the collection aperture that may acquired and processed to generate well focused imagery is limited by the phase stability of the radar over the acquisition period, the accuracy of the navigation

systems measuring the position of radar sensor along the synthetic aperture and the extent to which narrow-band, small angle approximations are used in the image formation processor. The required tolerance on the accuracy of the radar sensor location measurements is of the order of a fraction of a wavelength. In extended aperture collections this accuracy is difficult to maintain and measurement errors manifest in the image as defocus, geometric distortion as well as a loss in image contrast. Also in these imaging scenarios, narrow-band small-angle approximations commonly employed in efficient frequency domain image formation processors are no longer appropriate. The resulting mismatch between the SAR acquisition function and image formation processor acts as a further source of image domain defocus and distortion. Techniques to mitigate these effects were examined in Chapters 2 and 3.

In Chapter 2 the problem of the efficient processing of wide-angle spotlight SAR deramp demodulated range echo data was examined. While a number of techniques such as the RMA and CSA have been proposed for wide-band, wide-angle processing they do not operate on deramp demodulated range echo data and also have significantly greater synthetic aperture sampling requirements. An alternative approach, originally proposed by Jakowatz and Doren [JWTD97], [DJWT97], was considered in which an efficient image domain spatially varying filter is applied to imagery recovered by the PFA. The PFA is a simple efficient image formation algorithm that operates on deramp demodulated range echo data. It is however, based on a narrow-band, small angle approximation and so wide-angle SAR data processed with the PFA suffers from excessive defocus and distortion. The post PFA image domain filter proposed by Jakowatz and Doren compensates for the dominant components of this image domain defocus. Their approach however does not facilitate the formation of interferometric image pairs in a common image plane. In Chapter 2 a rigorous analysis of the SAR acquisition function using a full three dimensional imaging geometry was performed leading to the specification of a new filter for generating focused fine resolution ground plane imagery. Repeat pass imagery may thus be acquired and processed into fine resolution imagery in the same image ground plane for subsequent interferometric processing. The residual image domain defocus remaining after application of the post PFA filter was quantified and image resolution and patch size constraints were derived for which the technique may be applied to generate adequately focused imagery. The formation of a ground plane image using the filter was demonstrated using a synthetic scene consisting of various point scatterers. The residual image domain effects were also demonstrated by evaluating the point scatterer response for point targets located beyond the derived patch size constraint. The technique was also applied to Ingara X-band SAR imagery to yield a focused image with 3 dB resolution of 0.58 m in range and 0.15 m in azimuth with a Hamming window applied.

The detailed analysis of the SAR acquisition function presented in Chapter 2 was extended to include the presence of errors in the measurement of the radar platform location in Chapter 3. It was shown that in general for wide-angle collections array calibration errors manifest as a spatially varying, two dimensional phase error function in the acquired deramp demodulated range echo data. In the recovered image the phase error produces a range and azimuth defocus that varies spatially across the image. For narrow-band small-angle collections this defocus reduces to the conventional azimuthal only, defocus model that is independent of scattering location. For increasing collection apertures however, subtle higher order effects become increasingly significant and the full spatially varying, two dimensional nature of the phase error function begins to manifest. This can pose problems for autofocus algorithms such as the map drift and PGA algorithms which are primarily developed and implemented using a narrow band phase error model. In particular the spatially varying, two dimensional nature of the phase error function can cause corruption of the phase error estimate in the autofocus algorithm and residual phase errors remain after phase error compensation. Indeed this can be a source of relative mismatch between interferometric image pairs and can manifest as decorrelation in a transduced image pair. The specific case of an error in the measurement of the along track

velocity of the radar platform in a wide-angle spotlight SAR collection was considered and its impact on the PGA algorithm examined. A simple range cell migration correction step was proposed for compensating for the range dependence of the phase error function. The impact of this phase error function on the correlation of an interferometric image pair was considered using the PGA both, with and without, the range cell migration correction step using the Ingara experimental spotlight SAR data. In particular a coherence improvement of only 5% was demonstrated illustrating the subtle higher order nature of the correction. Such small improvements however, can assist in discriminating between the changed and unchanged regions of the scene yielding more reliable automated change detection systems. The improvement in detection performance afforded by a modest 4% increase in scene coherence was demonstrated in Chapter 7.

In Chapter 4 the multi-channel random walk model was used to describe a joint interferometric image pair. This model indicates that, where a scene consists of a large number mutually independent randomly distributed scatterers and the resolution cell size is much greater than the radar wavelength then, provided all channels see the same number of scatterers, the transduced images may be modelled as complex zero mean, circular, jointly Gaussian random processes. The information content of a joint interferometric image pair is thus completely encapsulated in the covariance matrix of the image pair and the complex cross correlation coefficient is the additional parameter made available by the joint interferometric processing of the image pair. Using Hagberg's model describing the relationship between scattering contributions between a primary and repeat pass collection, along with the wide-angle spotlight SAR acquisition and image formation processor transfer functions derived in Chapter 2, the form of the covariance matrix for an interferometric pair was derived. This model indicated that the complex cross channel correlation coefficient could be decomposed into a component dependent on the relative contributions of the stable and unstable scattering centres in the scene, as defined in Hagberg's model, and a component dependent on the mismatch between the SAR acquisition and image formation processor transfer functions. Common techniques proposed in the literature to estimate and remove the first order components of the transfer function mismatch were discussed leading to the design of an interferometric processor to process the Ingara experimental repeat pass interferometric SAR data. The processor was applied to one of the Ingara experimental repeat pass data sets acquired with a repeat pass interval of 12 minutes. In the sample cross correlation coefficient estimate a number of low correlation track like disturbances were observed. It is believed that these low correlation tracks may be due to the movement of sheep while grazing during the 12 minute revisit period.

Based on the joint statistical description of a repeat pass interferometric image pair a number of change statistics have been proposed in the literature. Changes in the mean backscatter power of the scene may be detected by examining the ratio of the sample average resolution cell intensity of the primary and repeat pass images. Alternatively areas of significant decorrelation (i.e., cross correlation coefficient magnitude close to zero), compared to other areas of partial scene correlation are indicative of scene disturbances and may be detecting using the sample cross correlation coefficient. In Chapter 5 the detection performance of a modified form of the average intensity ratio statistic, originally proposed by Touzi [TLB88] for edge detection, and the sample cross correlation coefficient change statistics were quantified. Using the probability density functions for these change statistics theoretical forms for the probability of detection and false alarm were derived as a function of various decision thresholds and sample sizes and ROC curves generated for comparison. As an indication of the relative sensitivity of the two change statistics it is found that a 5 dB change in the mean backscatter or a scene disturbance resulting in total decorrelation versus a scene partial correlation of 0.6 in the undisturbed regions of the scene yield approximately the same detection performance using a sample average of 9. Of course these change statistics are based on independent statistical parameters describing the joint interferometric image pair and both change statistics are required to

give a complete characterisation of the scene disturbances. Both statistics were shown to suffer from high false alarm rates unless there was a significant difference between the changed and unchanged regions of the scene. The high false alarm rate can be mitigated by multilook averaging however, the extent to which averaging can be performed is limited by the spatial size of the scene changes. For subtle, spatially small, scene changes the high false alarm rates of the intensity ratio and sample coherence change statistics limit their usefulness in automated change detection algorithms.

In Chapter 6 an alternative approach to detecting scene changes was developed based on an hypothesis testing formulation of the change detection problem. In this technique hypothesized models describing the changed and unchanged regions of a scene are postulated. Using the jointly Gaussian statistical description of an interferometric image pair and forming the log likelihood ratio yields a new change statistic for discriminating between the unchanged and changed scene models. This statistic encodes changes in both the mean backscatter power as well as a loss in correlation thus providing a single statistic for the complete characterisation of the scene disturbances. Expressions for the probability of detection and false alarm were derived for the case of a clairvoyant detector in which perfect knowledge of the changed and unchanged scene models is assumed. It was shown that the detection performance of the log likelihood based detector is significantly better than that of the intensity ratio and sample correlation coefficient statistics under a wide range of scene change scenarios. The theoretical analysis was verified via extensive simulation. In practice the parameters describing the hypothesized scene models need to be estimated from the observed imagery in a preprocessing step. The detection performance of a practical implementation of the detector thus suffers some degradation depending on the accuracy of the parameter estimates. The degradation in detection performance however, was shown to be only modest provided resonable parameters estimates are used. Given the significant improvements in change detection performance demonstrated, the log likelihood change statistic represents an important step towards the design of a reliable automated change detection algorithm for the cross cueing of analysts to areas of significant scene change.

In Chapter 7 the average intensity ratio, the sample cross correlation coefficient and the new log likelihood change statistics were applied to the repeat pass change detection experimental data acquired with Ingara. Three change scenarios were considered. One in which the image pair was acquired 24 hours apart and included scene changes identifiable via a change in the mean backscatter as well as a loss in scene correlation. Another change detection scenario in which the image pair was acquired two hours apart with the scene changes manifesting as a loss in correlation without any appreciable change in mean backscatter power. Finally, the image pair interferometrically processed in Chapter 4 with the track like disturbances was also considered. In each of the three change detection scenarios the superior detection performance of the log likelihood change statistic was demonstrated.

8.2 Future Work

This thesis has investigated techniques to improve the detection of fine-scale scene changes using repeat pass interferometric complex SAR imagery. One of the main contributions presented in this thesis has been the development of a new log likelihood change statistic for discriminating between changed and unchanged regions of a scene. Through theoretical analysis and extensive simulation and application to experimental data it has been shown that the the new statistic provides significant improvements in the detection performance over other commonly used change statistics. However, a number of issues regarding the robustness of the change statistic and the development of a practical implementation warrant further investigation.

The log likelihood change statistic is formulated by considering simple statistical descriptions of the scene under the changed and unchanged hypotheses. These statistical models are defined in

terms of key parameters which need to be estimated from the observed imagery. The sensitivity of the change statistic to the assumptions used in formulating the statistical models and also the accuracy of the model parameter estimates needs to be understood to determine the robustness of the approach. Some simple simulation based investigations have been carried out by the author [PGS03c] however a systematic theoretical analysis is required to properly quantify the robustness of the technique.

The practical implementation of a detector based on the log likelihood statistic poses a number of challenges. An implicit assumption in the formulation of the changed and unchanged scene models is that the scene is a homogeneously distributioned clutter environment. The unchanged regions may thus be described by a stationary statistical model. For example, in the experimental data sets considered, the scene changes were carried out in an open field so that the joint image pair could be described by a single covariance matrix. In a practical implementation, where the scene may include distributed targets with many different backscattering properties, some form of image segmentation would therefore be necessary to identify those regions of the scene to which the change detection algorithm could be applied. This would also assist in delineating regions which could be used to estimate the model parameters required to compute the log likelihood change statistic and would be another important step in the design of a robust, reliable automated change detection algorithm.

The change statistics considered in this thesis are based on single first order point statistics and so the detection of scene changes is performed on pixel by pixel basis. A simple visual inspection of the sample cross correlation coefficient for the experimental scene change scenarios however shows that a strong visual cue to detecting the scene changes is the spatial correlation of the disturbances. For example, the track-like disturbances identified in Chapter 4 and 7 exhibit only a modest drop in correlation and so can be difficult to discern on a pixel by pixel basis however the overall track-like nature of the disturbances is clearly observed. Improvements in the detection of scene changes may thus possibly be achieved by incorporating some form of correlated neighbourhood model in the changed scene hypothesis. Alternatively the change statistic detections may be supplied as input into a tracking algorithm, to exploit the spatial structure of the scene disturbances.

Extracting useful information from SAR imagery remains a challenging problem. The complex backscattered signal transduced by a SAR is determined by many physical and geometric properties of the imaged scene. The inversion of transduced imagery into useful information thus suffers from severe ambiguity. Repeat pass interferometry is a technique that uses multiple images of a scene acquired at different times to separate the stable and unstable scattering contributions of the scene. In this thesis this inversion process is exploited to detect scene disturbances. Improvements in resolving different scattering mechanisms present in a scene, which may assist in discriminating between different physical sources of scene change, may be achieved by making additional observations. In particular fully polarimetric SAR observations as well as observations at different wavelengths, incidence angles and over different time scales can potentially offer significant improvements in detecting and discriminating between different scene change mechanisms and warrant further investigation.

Appendix A

Deramp Demodulation

Demodulation of the received radar echo data is usually carried out by mixing the echoes with a reference carrier $G_{ref}(\tau) = G^I_{ref}(\tau) + jG^Q_{ref}(\tau)$ at the radar centre frequency, ω_0. The demodulated range echo is given by,

$$g(\tau) = LPF\{G^I_{ref}(\tau)g_{rx}(\tau)\} + jLPF\{G^Q_{ref}(\tau)g_{rx}(\tau)\}, \tag{A.1}$$

where,

$$G^I_{ref}(\tau) = 2\Re\{e^{j\omega_0\tau}\}, \tag{A.2}$$

$$G^Q_{ref}(\tau) = -2\Im\{e^{j\omega_0\tau}\}, \tag{A.3}$$

$g_{rx}(\tau)$ is the received radar echo data and LPF is a low pass filter operator. The resulting baseband signal $g(\tau)$ can then be digitised at a sample rate determined by the transmit signal bandwidth and the image formation steps can be carried out in the digital domain. In practice though, in order to achieve fine range resolution a large transmit bandwidth is required and so the sampling requirements for the demodulated baseband signal are commensurately large.

An alternative demodulation method called deramping or dechirping may be used where the imaging mode operates within a relatively small range swath size and when the transmit waveform is a chirp of the form,

$$s(t) = rect\left(\frac{t}{T}\right)\Re\left\{exp(j\alpha t^2)exp(j\omega_0 t)\right\}, \tag{A.4}$$

where α is the chirp rate, ω_0 is the radar centre frequency and T is the chirp duration. In the deramp demodulation method the received echo is mixed with a delayed copy of the transmit chirp and the resulting demodulated signal bandwidth is now determined by the spatial extent of the transduced scene rather than the bandwidth of the chirp. The deramp demodulated signal may thus be sampled at a rate significantly less than the transmit chirp waveform bandwidth with the sample rate limiting the range swath of the scene image.

For an illuminated scene of patch size R_p centred at a distance R_T from the radar at a given transmit/receive point, the delay τ_0 used in the demodulation reference function is the round trip propagation time of the electromagnetic radiation to the scene centre, i.e., $\tau_0 = 2R_T/c$. This delay needs to be evaluated at each transmit/receive point along the synthetic aperture using position information from the navigation system on board the sensor platform such as an INU/GPS system. The demodulation reference signal may be written as,

$$G^I_{ref}(\tau) = 2rect\left(\frac{\tau - \tau_0}{T_{ref}}\right)\cos\left(\omega_0(\tau - \tau_0) + \alpha(\tau - \tau_0)^2\right), \tag{A.5}$$

$$G^{Q}_{ref}(\tau) = -2rect\left(\frac{\tau-\tau_0}{T_{ref}}\right)\sin\left(\omega_0(\tau-\tau_0)+\alpha(\tau-\tau_0)^2\right), \quad \text{(A.6)}$$

where T_{ref} is the duration of the reference chirp. For the illuminated scene patch of size R_p note that the echo that arrives from the near edge of the illuminated patch will be centred about $\tau = \tau_0 - \frac{2}{c}\frac{R_p}{2}$ and the echo that arrives from the far edge of the patch will be centred about $\tau = \tau_0 + \frac{2}{c}\frac{R_p}{2}$, as shown in Figure A.1. In order to correctly demodulate the patch echoes the demodulation reference chirp

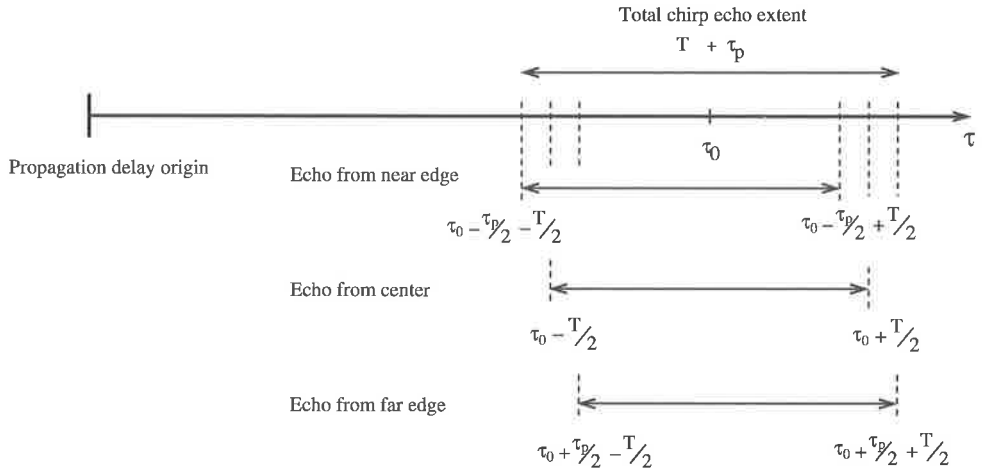


Figure A.1: Two way propagation delay extent of chirp echoes received from the near, centre and far edges of the illuminated scene. τ_0 is the two propagation delay to the scene centre, T is the chirp duration and $\tau_p = 2R_p/c$ is the two way propagation delay extent of the image swath.

should have a duration that encompasses the received echo chirps from all scattering locations in the illuminated scene, i.e., $T_{ref} = T + \tau_p$, where $\tau_p = 2R_p/c$. The appropriate form for the reference chirp is thus given by,

$$G^{ref}_{I}(\tau) = 2rect\left(\frac{\tau-\tau_0}{T+\tau_p}\right)\cos\left(\omega_o(\tau-\tau_0)+\alpha(\tau-\tau_0)^2\right), \quad \text{(A.7)}$$

$$G^{ref}_{Q}(\tau) = -2rect\left(\frac{\tau-\tau_0}{T+\tau_p}\right)\sin\left(\omega_o(\tau-\tau_0)+\alpha(\tau-\tau_0)^2\right). \quad \text{(A.8)}$$

An expression relating the received range echo to the scene reflectivity and the transmit signal was developed in Chapter 2 equation (2.5) and is given by,

$$g_{rx}(\tau) = \int_{\tau_0-\frac{\tau_p}{2}}^{\tau_0+\frac{\tau_p}{2}} f(t)s(\tau-t)dt, \quad \text{(A.9)}$$

where $f(\tau)$ is the integrated reflectivity function given in equation (2.2) Chapter 2, $s(\tau)$ is the chirp waveform given in (A.4) and τ takes values in the range $\tau_0 - \tau_p/2 - T/2 \leq \tau \leq \tau_0 + \tau_p/2 + T/2$. Defining a new variable of integration $t_r = t - \tau_0$ (A.9) becomes,

$$g_{rx}(\tau) = \int_{-\frac{\tau_p}{2}}^{\frac{\tau_p}{2}} f_{c_t}(t_r)s(\tau-\tau_0-t_r)dt_r, \quad \text{(A.10)}$$

where $f_{c_t}(t) = f(t+\tau_0)$. Substituting (A.10) along with the demodulation reference functions given in (A.7) and (A.8) into the demodulation operator in (A.1) gives,

$$G(\tau) = G^I_{demod}(\tau) + jG^Q_{demod}(\tau), \tag{A.11}$$

where,

$$\begin{aligned} G^I_{demod}(\tau) &= LPF\{G^I_{ref}(\tau)g_{rx}(\tau)\} && \text{(A.12)} \\ &= rect\left(\frac{\tau-\tau_0}{T+\tau_p}\right)\int_{-\frac{\tau_p}{2}}^{\frac{\tau_p}{2}} f_{c_t}(t_r)\cos\left(-t_r(\omega_0+2\alpha(\tau-\tau_0))+\alpha t_r^2\right)dt_r, && \text{(A.13)} \\ G^Q_{demod}(\tau) &= LPF\{G^I_{ref}(\tau)g_{rx}(\tau)\} && \text{(A.14)} \\ &= rect\left(\frac{\tau-\tau_0}{T+\tau_p}\right)\int_{-\frac{\tau_p}{2}}^{\frac{\tau_p}{2}} f_{c_t}(t_r)\sin\left(-t_r(\omega_0+2\alpha(\tau-\tau_0))+\alpha t_r^2\right)dt_r. && \text{(A.15)} \end{aligned}$$

This can be written more compactly as,

$$G_{demod}(\tau) = rect\left(\frac{\tau-\tau_0}{T+\tau_p}\right)\int_{-\frac{\tau_p}{2}}^{\frac{\tau_p}{2}} f_{c_t}(t_r)exp\left(j\left(-t_r\left(\omega_0+2\alpha(\tau-\tau_0)\right)\right)\right)exp\left(j\alpha t_r^2\right)dt_r. \tag{A.16}$$

The last exponential phase term αt_r^2 in (A.16) is termed the Residual Video Phase (RVP) term and is an undesirable artifact of the deramp demodulation technique. It manifests as a spatially varying defocus in the recovered SAR image that becomes progressively bigger with increasing distance from the scene focus point. Jakowatz [JWE+96] gives image size limits for which the RVP term is sufficiently small to give negligible image distortion. Alternatively in [CGM95] a technique to remove the RVP phase is given. Ignoring the RVP term and defining,

$$\begin{aligned} k_0 &= \frac{2\omega_0}{c}, && \text{(A.17)} \\ k_r &= \frac{4\alpha}{c}(\tau-\tau_0), && \text{(A.18)} \\ k_{bw} &= \frac{4\alpha(T+\tau_p)}{c}, && \text{(A.19)} \\ t_r &= \frac{2r}{c}, && \text{(A.20)} \end{aligned}$$

then the deramp demodulated echo in (A.16) reduces to,

$$G_{demod_r}(k_r) = rect\left(\frac{k_r}{k_{bw}}\right)\int_{-c\tau_p/4}^{c\tau_p/4} f_c(r)exp(-j(k_r+k_0)r)dr, \tag{A.21}$$

where,

$$\begin{aligned} f_c(r) &= f_{c_t}\left(\frac{2r}{c}\right), && \text{(A.22)} \\ G_{demod_r}(k_r) &= \frac{c}{2}G_{demod}\left(\frac{k_r c}{4\alpha}+\tau_0\right). && \text{(A.23)} \end{aligned}$$

Note that in practice typically $\tau_p \ll T$ and so $k_{bw} \approx 4\alpha T/c$. With this approximation equation (A.21) gives the form of the deramp demodulated range echo data used in Chapter 2 and given in equation (2.16). Observe also that since $t_r = t - \tau_0$, where t and τ_0 are the two propagation time delays to some point in the scene and the scene centre respectively, r may be interpreted as the difference in propagation range between the radar and a point in the scene and the radar and the scene centre.

Appendix B

The PGA Algorithmic Steps

In Chapter 3 a concise description of the Phase Gradient Autofocus (PGA) algorithm was developed using a matrix based mathematical framework to describe the image data and the demodulation phase error function. In this matrix based formulation the range compressed signal history data and image domain data at range bin m are represented by the vectors,

$$\underline{\mathcal{G}}(m) = \begin{bmatrix} \mathcal{G}(0,m) \\ \mathcal{G}(1,m) \\ \vdots \\ \mathcal{G}(L-1,m) \end{bmatrix} \quad \text{and} \quad \underline{g}(m) = \begin{bmatrix} g(0,m) \\ g(1,m) \\ \vdots \\ g(L-1,m) \end{bmatrix},$$

respectively, where $\mathcal{G}$ is the two dimensional range compressed signal history data and g is the recovered image as defined in Table 3.1 in Chapter 3. These vectors are related via the equations $\underline{\mathcal{G}}(m) = W\underline{g}(m)$ and $\underline{g}(m) = W^H\underline{\mathcal{G}}(m)$, where W is the Fourier transform operator defined in (3.40) and W^H is the inverse operator defined in (3.41). The demodulated phase error function is represented by the vector,

$$\underline{\phi}_e = \begin{bmatrix} exp(j\phi_0) \\ exp(j\phi_1) \\ \vdots \\ exp(\phi_{L-1}) \end{bmatrix}, \tag{B.1}$$

and is applied to the range compressed signal history vector yielding the phase corrupted range compressed signal history vector,

$$\underline{\mathcal{G}}_e(m) = diag(\underline{\phi}_e)\underline{\mathcal{G}}(m), \tag{B.2}$$

where $diag(\underline{\phi}_e)$ is the matrix whose diagonal elements are the elements of the vector $\underline{\phi}_e$. The recovered phase corrupted image domain vector is subsequently given by,

$$\begin{aligned} \underline{g}_e(m) &= W^H\underline{\mathcal{G}}_e(m), \\ &= W^H diag(\underline{\phi}_e)\underline{\mathcal{G}}(m), \end{aligned} \tag{B.3}$$

which may be expressed in terms of the error free image vector as,

$$\underline{g}_e(m) = W^H diag(\underline{\phi}_e)W\underline{g}(m). \tag{B.4}$$

It was subsequently shown in Chapter 3 that an estimate of the phase error function could be recovered via eigen-decomposition of the covariance matrix, $C_{\underline{\mathcal{G}}_e} = E\{\underline{\mathcal{G}}_e\underline{\mathcal{G}}_e^H\}$ of the phase corrupted range

compressed signal history vector. The eigen-decomposition however, was based on the assumption that the image vector $\underline{g}$ has the following signal plus clutter form,

$$\begin{aligned} \underline{g} &= \underline{s} + \underline{n}, \\ &= s \begin{bmatrix} 1 \\ 0 \\ \vdots \\ 0 \end{bmatrix} + \begin{bmatrix} n_0 \\ n_1 \\ \vdots \\ n_{L-1} \end{bmatrix}, \end{aligned} \tag{B.5}$$

where s is a random signal process modelled as a zero mean, complex, circular Gaussian random variable with variance σ_s^2, while $n_0, \ldots n_{L-1}$ are mutually independent random clutter processes modelled as zero mean, complex, circular Gaussian random variables with variances $\sigma_{n_0}^2, \cdots \sigma_{n_{L-1}}^2$. Furthermore, to carry out the eigen-decomposition and obtain an estimate of $\underline{\phi}_e$, it is necessary that $\sigma_s^2 + \sigma_{n_0}^2 > \sigma_{n_1}^2, \cdots \sigma_{n_{L-1}}^2$. In practice however, the image is unlikely to conform to the required signal plus clutter model and so a robust, reliable estimate of the phase error vector cannot be obtained without suitable preprocessing. In the following sections two techniques for transforming the image data into the required signal model form with a high signal to clutter power ratio are discussed. Without these steps the PGA has been demonstrated to give poor phase error estimates [WEGJ94].

B.1 The Signal Model - Circular Shifting

The signal model (B.5) assumes that the first element in the true image vector slice $\underline{g}$ consists of a dominant signal plus clutter term $g_0 = s + n_0$, while the remaining samples in the vector contain clutter only $g_i = n_i$ for $i \neq 0$. In practice, while a single strong dominant scatter may be found in a given image domain slice vector and interpreted as a realisation of the signal plus clutter model, the location of this scatter will not necessarily be in the first element of the image slice vector. Furthermore, across range bins the location of the dominant scattering pixel will vary randomly depending on the physical nature of the scene. Therefore a more appropriate model to describe the image vector $\underline{g}$ is,

$$\underline{g} = s \begin{bmatrix} I_0 \\ I_1 \\ \vdots \\ I_{L-1} \end{bmatrix} + \begin{bmatrix} n_0 \\ n_2 \\ \vdots \\ n_{L-1} \end{bmatrix}, \tag{B.6}$$

where,

$$I_i = \begin{cases} 0, & \text{for } i = 0 \ldots L-1, i \neq l, \\ 1, & \text{for } i = l, \end{cases} \tag{B.7}$$

and the location of the dominant signal component, namely pixel l, is itself a random variable taking values in the range $[0, L-1]$. Defining the linear phase ramp vector $\underline{Z} = [1, z^l, z^{2l}, \cdots z^{(L-1)l}]^T$, where l is the location of the signal pixel in (B.6) and $z = exp(j2\pi/L)$, a modified form of the phase corrupted range compressed signal history vector may be derived, $\underline{\mathcal{G}}_{shift} = diag(\underline{Z})\underline{\mathcal{G}}_e$. The covariance matrix of $\underline{\mathcal{G}}_{shift}$ is given by,

$$\begin{aligned} C_{\mathcal{G}_{shift}} &= E\{\underline{\mathcal{G}}_{shift}\underline{\mathcal{G}}_{shift}^H\}, \\ &= E\{diag(\underline{Z})\underline{\mathcal{G}}_e\underline{\mathcal{G}}_e^H diag(\underline{Z})^H\}. \end{aligned} \tag{B.8}$$

Substituting the expression in (B.4) for $\underline{\mathcal{G}}_e$ into (B.8) gives,

$$C_{\mathcal{G}_{shift}} = E\{diag(\underline{Z})diag(\underline{\phi}_e)W\underline{g}\underline{g}^H W^H diag(\underline{\phi}_e)^H diag(\underline{Z})^H\}. \quad \text{(B.9)}$$

The order of the matrix product $diag(\underline{Z})diag(\underline{\phi}_e)$ may be reversed as the component matrices are diagonal to give,

$$C_{\mathcal{G}_{shift}} = E\{diag(\underline{\phi}_e)diag(\underline{Z})W\underline{g}\underline{g}^H W^H diag(\underline{Z})^H diag(\underline{\phi}_e)^H\}. \quad \text{(B.10)}$$

The matrix pair $diag(\underline{Z})W$ can be shown to be equal to the matrix product WJ where J is a modified form of the identity matrix in which each row in the identity matrix has been circularly shifted by l columns to form J thus the covariance matrix becomes,

$$\begin{aligned} C_{\mathcal{G}_{shift}} &= E\{diag(\underline{\phi}_e)WJ\underline{g}\underline{g}^H J^H W^H diag(\underline{\phi}_e)^H\}, \\ &= PE\{J\underline{g}\underline{g}^H J^H\}P^H, \end{aligned} \quad \text{(B.11)}$$

where $P = diag(\underline{\phi}_e)W$. Applying J to the signal model for $\underline{g}$ in (B.6) circularly shifts $\underline{g}$ through azimuth pixels so that the dominant scatterer lies at the first element of the vector slice, i.e.,

$$J\underline{g} = s\begin{bmatrix} 1 \\ 0 \\ \vdots \\ 0 \end{bmatrix} + \begin{bmatrix} n_l \\ n_{l+1} \\ \vdots \\ n_{L-1} \\ n_0 \\ \vdots \\ n_{l-1} \end{bmatrix}. \quad \text{(B.12)}$$

The covariance matrix of the phase corrupted range compressed history slice vector with the linear phase ramp matrix $diag(\underline{Z})$ applied is thus given by,

$$C_{\mathcal{G}_{shift}} = P\begin{bmatrix} \sigma_s^2 + \sigma_{n_l}^2 & 0 & \cdots & 0 \\ 0 & \sigma_{n_{l+1}}^2 & & 0 \\ \vdots & & & \\ & & \ddots & \vdots \\ 0 & \cdots & & \sigma_{n_{l-1}}^2 \end{bmatrix} P^H. \quad \text{(B.13)}$$

The covariance matrix $C_{\mathcal{G}_{shift}}$ is diagonalised by the matrix P and the columns of the matrix P are the eigenvectors of $C_{\mathcal{G}_{shift}}$. In particular, the first column of matrix P is the demodulation phase error vector and its associated eigenvalue is $\sigma_s^2 + \sigma_{n_l}^2$. Since the dominant signal scatterer has been placed at the first element in the image vector $\sigma_s^2 > \sigma_{n_0}^2 \cdots \sigma_{n_{L-1}}^2$ and the demodulation phase error vector may be retrieved by computing the eigenvector of $C_{\mathcal{G}_{shift}}$ associated with the largest eigenvalue.

In practice given an image with M range bins, M realisations of $\underline{\mathcal{G}}_e(m)$ where $m = 0 \cdots M-1$, are available to form a sample covariance matrix estimate. For each realisation an estimate of the location of the dominant signal pixel l may be obtained by computing the location of the peak value of $\underline{g}_e = W^H\underline{\mathcal{G}}_e$. Circular shifting $\underline{g}_e$ so that l^{th} pixel lies at in the first vector element and applying the Fourier transform operator W to return to the range compressed signal history domain generates a suitable estimate of $\underline{\mathcal{G}}_{shift}$. This estimate may subsequently be used in the computation of the sample covariance matrix estimate.

B.2 Covariance Estimation - Filtering

A further preprocessing step applied prior to estimation of the demodulation phase error function is the filtering of the range compressed signal history data to improve the signal to clutter power and yield an improved estimate of the covariance matrix $C_{\mathcal{G}_{shift}}$.

The corrupted range compressed history data vector $\underline{\mathcal{G}}$ is related to the true image vector slice $\underline{g}$ by,

$$\underline{\mathcal{G}}_e = diag(\underline{\phi}_e)W\underline{g}. \tag{B.14}$$

Applying the signal model (B.5),

$$\begin{aligned} \underline{\mathcal{G}}_e &= diag(\underline{\phi}_e)W(\underline{s}+\underline{n}), \\ &= diag(\underline{\phi}_e)s\begin{bmatrix}1\\1\\\vdots\\1\end{bmatrix} + diag(\underline{\phi}_e)\begin{bmatrix}n'_0\\n'_1\\\vdots\\n'_{L-1}\end{bmatrix}, \end{aligned} \tag{B.15}$$

where $n'_l = \underline{w}^H(l)\cdot\underline{n}$. In the signal plus clutter model the clutter vector $\underline{n}$ is taken to consist of complex zero mean mutually independent, identically distributed Gaussian random variables with uniformly distributed phase. As the Fourier transform matrix W is a unitary linear transform the transformed clutter samples are also zero mean mutually independent, identically distributed Gaussian random variables [Pap91] and so the phase corrupted range compressed signal history vector may be written as,

$$\begin{aligned} \underline{\mathcal{G}}_e &= s\begin{bmatrix}exp(j\phi_0)\\exp(j\phi_1)\\\vdots\\exp(j\phi_{L-1})\end{bmatrix} + \begin{bmatrix}n'_0\\n'_1\\\vdots\\n'_{L-1}\end{bmatrix}, \\ &= s\underline{\phi}_e + \underline{n}', \end{aligned} \tag{B.16}$$

where the phase contribution from the phase error vector has been absorbed into the transformed noise variables n'_i. For the case in which the motion error vector $\underline{\phi}_e$ varies slowly across the range compressed history slice (i.e. $\underline{\phi}_e$ has a low frequency content) then a low pass filter, such as a sliding boxcar filter of B samples, may be applied to the azimuthal spatial frequency samples in $\underline{\mathcal{G}}_e$. Under the low pass filter the signal contributions in $\underline{\mathcal{G}}_e$, namely $s\ exp(j\phi_l)$ will sum quasi-coherently as the complex samples have approximately the same phase. This coherent summation increases the signal power by approximately a factor of B^2. The clutter contributions however sum incoherently as the clutter has a uniformly distributed phase. The clutter power is thus only increased by a factor of B. The filtering thus improves the signal to clutter power ratio of the particular realisation of the signal plus clutter model available in the given range compressed signal history slice vector $\underline{\mathcal{G}}_e$ and may subsequently be used to yield an improved sample covariance estimate of $C_{\mathcal{G}}$.

A crucial aspect of the filtering step is the choice of bandwidth of the low pass filter to be applied to $\underline{\mathcal{G}}_e$. This is governed by the frequency content of the demodulation phase error vector which may be found by applying a Fourier transform to $\underline{\mathcal{G}}_e$, i.e.,

$$W\underline{\mathcal{G}}_e = sW\underline{\phi}_e + W\underline{n}',$$

$$= s\begin{bmatrix} \underline{w}^H(0)\cdot\underline{\phi}_e \\ \underline{w}^H(1)\cdot\underline{\phi}_e \\ \vdots \\ \underline{w}^H(L-1)\cdot\underline{\phi}_e \end{bmatrix} + \begin{bmatrix} \underline{w}^H(0)\cdot\underline{n} \\ \underline{w}^H(1)\cdot\underline{n} \\ \vdots \\ \underline{w}^H(L-1)\cdot\underline{n} \end{bmatrix}. \tag{B.17}$$

The magnitude of the vector $sW\underline{\phi}_e$ at frequency bin l, i.e. $s\underline{w}^H(l)\cdot\underline{\phi}_e$, gives the energy in $\underline{\phi}_e$ at that particular frequency, scaled by the signal level s, while $\underline{w}^H(l)\cdot\underline{n}$ gives the energy in the clutter contribution at frequency l. Given M realisations of $\underline{\mathcal{G}}_e(m)$, $m = 0\cdots M-1$, an estimate of the bandwidth of $\underline{\phi}_e$ may be found by computing,

$$\underline{P}_{\phi_e} = \sum_{m=0}^{M-1} |W\underline{\mathcal{G}}_e(m)|^2, \tag{B.18}$$

and determining the frequency interval over which $\underline{P}_{\phi_e}$ is significant. Typically values of $\underline{P}_{\phi_e}$ within 10 dB of the peak value are considered to be significant in determining the spectral bandwidth of the phase error vector [WEGJ94].

Appendix C

Dual Channel Distributed Target Model

In this appendix the joint probability density function describing a complex interferometric image pair of a homogeneous distributed clutter scene is derived using a multi-channel random walk model. In the random walk model, the complex reflectivity of a homogeneous distributed clutter scene is modelled as the phasor sum of complex reflectivity contributions from some random ensemble of N mutually independent, identically distributed point scatterers. The scene complex reflectivity may thus be expressed as,

$$r_f(x,y) = \frac{1}{\sqrt{N}} \sum_{n=1}^{N} p_{1_n} exp(j\theta_{1_n}) exp(j\phi_n) \delta(x - x_{1_n}, y - y_{1_n}), \tag{C.1}$$

where $p_{1_n} exp(j\theta_{1_n})$ is the complex reflectivity of the point scatterer n which is located in the scene at (x_{1_n}, y_{1_n}) and ϕ_n is related to the propagation distance from the radar sensor to the point scatterer. Assuming that the scatterers are randomly distributed throughout the scene and that the resolution cell size is many wavelengths across ϕ_n may be modelled as a uniformly distributed random variable.

In a repeat pass acquisition, where the point scatterer ensemble has been subject to various temporal disturbances causing changes in the scatterer complex reflectivity as well as random displacements in the scattering positions during the revisit period, the scene reflectivity may be written as,

$$r_g(x,y) = \frac{1}{\sqrt{N}} \sum_{n=1}^{N} p_{2_n} exp(j\theta_{2_n}) exp(j\phi_n) \delta(x - x_{2_n}, y - y_{2_n}). \tag{C.2}$$

The complex reflectivity of the n^{th} point scatterer is now given by $p_{2_n} exp(j\theta_{2_n})$ and is located at (x_{2_n}, y_{2_n}). The geometrical phase component ϕ_n has been retained as a common modulating phase factor and it has been assumed that both channels observe that same number of scatterers N.

The primary and repeat pass images transduced by the SAR imaging process may subsequently be written as,

$$\begin{aligned} f(x,y) &= \iint r_f(\alpha,\beta) h_1(x-\alpha, y-\beta) d\alpha d\beta, \\ &= \frac{1}{\sqrt{N}} \sum_{n=1}^{N} p_{1_n} exp(j\theta_{1_n}) exp(j\phi_n) h_1(x - x_{1_n}, y - y_{1_n}), \end{aligned} \tag{C.3}$$

and

$$\begin{aligned} g(x,y) &= \iint r_g(\alpha,\beta) h_2(x-\alpha, y-\beta) d\alpha d\beta, \\ &= \frac{1}{\sqrt{N}} \sum_{n=1}^{N} p_{2_n} exp(j\theta_{2_n}) exp(j\phi_n) h_2(x - x_{2_n}, y - y_{2_n}), \end{aligned} \tag{C.4}$$

where h_1 and h_2 are the point spread functions of the primary and repeat pass acquisition and image formation processes respectively. The primary and repeat pass image pair may be expressed in terms of their real and imaginary components in vector format as,

$$\underline{X} = \begin{bmatrix} f_r \\ f_i \\ g_r \\ g_i \end{bmatrix} = \frac{1}{\sqrt{N}} \sum_{n=1}^{N} \underline{S}_n, \tag{C.5}$$

where,

$$\underline{S}_n = \begin{bmatrix} p_{1_n} \cos(\theta_{1_n} + \phi_n) \\ p_{1_n} \sin(\theta_{1_n} + \phi_n) \\ p_{2_n} \cos(\theta_{2_n} + \phi_n) \\ p_{2_n} \sin(\theta_{2_n} + \phi_n) \end{bmatrix}. \tag{C.6}$$

For conciseness of notation, the point spread function terms h_1 and h_2 have been absorbed into the point scattering amplitudes, p_{1_n} and p_{1_n} respectively. Using simple trigonometric identities the expression for $\underline{S}_n$ may be expanded as,

$$\begin{aligned} \underline{S}_n &= \begin{bmatrix} p_{1_n} \cos(\theta_{1_n}) \cos(\phi_n) \\ p_{1_n} \sin(\theta_{1_n}) \cos(\phi_n) \\ p_{2_n} \cos(\theta_{2_n}) \cos(\phi_n) \\ p_{2_n} \sin(\theta_{2_n}) \cos(\phi_n) \end{bmatrix} + \begin{bmatrix} -p_{1_n} \cos(\theta_{1_n}) \sin(\phi_n) \\ p_{1_n} \sin(\theta_{1_n}) \sin(\phi_n) \\ -p_{2_n} \cos(\theta_{2_n}) \sin(\phi_n) \\ p_{2_n} \sin(\theta_{2_n}) \sin(\phi_n) \end{bmatrix}, \\ &= \left(\cos(\phi_n) I + \sin(\phi_n) I'\right) \underline{S}'_n, \end{aligned} \tag{C.7}$$

where,

$$\underline{S}'_n = \begin{bmatrix} p_{1_n} \cos(\theta_{1_n}) \\ p_{1_n} \sin(\theta_{1_n}) \\ p_{2_n} \cos(\theta_{2_n}) \\ p_{2_n} \sin(\theta_{2_n}) \end{bmatrix}, \tag{C.8}$$

$$I' = \begin{bmatrix} 0 & -1 & 0 & 0 \\ 1 & 0 & 0 & 0 \\ 0 & 0 & 0 & -1 \\ 0 & 0 & 1 & 0 \end{bmatrix}, \tag{C.9}$$

and I is the 4x4 identity matrix.

The task is to find the joint probability density function $p(\underline{X})$ of the random vector $\underline{X}$. This may be achieved indirectly by firstly finding a form for the characteristic function of $\underline{X}$ given by,

$$\begin{aligned} M(\underline{\omega}) &= \int p(\underline{X}) exp\left(j\underline{\omega}^T \cdot \underline{X}\right) d\underline{X}, \\ &= E\left\{exp\left(j\underline{\omega}^T \cdot \underline{X}\right)\right\}, \end{aligned} \tag{C.10}$$

where,

$$\underline{\omega} = \begin{bmatrix} \omega_1 \cos(\alpha_1) \\ \omega_1 \sin(\alpha_2) \\ \omega_2 \cos(\alpha_2) \\ \omega_2 \sin(\alpha_2) \end{bmatrix}, \tag{C.11}$$

and the expectation is with respect to the random variables $(\phi, p_1, p_2, \theta_1, \theta_2, x_1, y_1, x_2, y_2)$. The probability density function $p(\underline{X})$ may subsequently be recovered by applying the inverse transform,

$$p(\underline{X}) = \frac{1}{(2\pi)^4} \int M(\underline{\omega}) exp\left(-j\underline{\omega}^T \cdot \underline{X}\right) d\underline{X}. \tag{C.12}$$

The phase term $\underline{\omega}^T \cdot \underline{X}$ in the characteristic function may be written as,

$$\begin{aligned} \underline{\omega}^T \cdot \underline{X} &= \underline{\omega}^T \cdot \frac{1}{\sqrt{N}} \sum_{n=1}^{N} \underline{S}_n, \\ &= \frac{1}{\sqrt{N}} \sum_{n=1}^{N} \underline{\omega}^T \cdot \underline{S}_n. \end{aligned} \tag{C.13}$$

Substituting equation (C.7) into (C.13) gives,

$$\begin{aligned} \underline{\omega}^T \cdot \underline{X} &= \frac{1}{\sqrt{N}} \sum_{i=1}^{N} \left(\cos(\phi_n) \underline{\omega}^T I \underline{S}'_n + \sin(\phi_n) \underline{\omega}^T I' \underline{S}'_n\right), \\ &= \frac{1}{\sqrt{N}} \sum_{n=1}^{N} \left[A_n \cos\phi_n + B_n \sin\phi_n\right], \end{aligned} \tag{C.14}$$

where $A_n = \underline{\omega}^T I \underline{S}'_n$ and $B_n = \underline{\omega}^T I' \underline{S}'_n$. The characteristic function phase may thus be written as,

$$\underline{\omega}^T \cdot \underline{X} = \frac{1}{\sqrt{N}} \sum_{n=1}^{N} R_n \cos(\phi_n + \gamma_n), \tag{C.15}$$

where $R_n = \sqrt{A_n^2 + B_n^2}$ and $\tan\gamma_n = B_n/A_n$. Substituting (C.15) into (C.10) gives,

$$M(\underline{\omega}) = E\left\{exp\left(j\frac{1}{\sqrt{N}} \sum_{n=1}^{N} R_n \cos(\phi_n + \gamma_n)\right)\right\}. \tag{C.16}$$

Since the scattering ensemble are all mutually independent $M(\underline{\omega})$ may be written as,

$$M(\underline{\omega}) = \prod_{n=1}^{N} E\left\{exp\left(j\frac{1}{\sqrt{N}} R_n \cos(\phi_n + \gamma_n)\right)\right\}. \tag{C.17}$$

The expectation with respect to the uniformly distributed random variable ϕ_n may now be evaluated,

$$\begin{aligned} E\left\{exp\left(j\frac{1}{\sqrt{N}} R_n \cos(\phi_n + \gamma_n)\right)\right\} = \\ E_\phi\left\{\frac{1}{2\pi} \int_0^{2\pi} exp\left(j\frac{1}{\sqrt{N}} R_n \cos(\phi_n + \gamma_n)\right) d\phi_n\right\}, \end{aligned} \tag{C.18}$$

where the expectation E_ϕ on the right hand side of equation (C.18) is now over the variables,

$$(p_1, p_2, \theta_1, \theta_2, x_1, y_1, x_2, y_2). \tag{C.19}$$

Using equation 9.1.21 in [AS72] (C.18) may be written in terms of the zero-order Bessel function, J_0 as,

$$E\left\{exp\left(j\frac{1}{\sqrt{N}} R_n \cos(\phi_n + \gamma_n)\right)\right\} = E_\phi\left\{J_0\left(\frac{R_n}{\sqrt{N}}\right)\right\}, \tag{C.20}$$

As the number of scatterers grows large the argument of the Bessel function grows small allowing the function to be approximated by the first two terms of its power series expansion about the origin,

$$J_0\left(\frac{R_n}{\sqrt{N}}\right) \approx \left(1 - \frac{1}{4}\frac{R_n^2}{N}\right). \tag{C.21}$$

Substituting (C.21) into (C.20) and given that the ensemble of scatterers are all identically distributed then the characteristic function becomes,

$$\begin{aligned} M(\underline{\omega}) &\approx E_\phi\left\{\left(1 - \frac{1}{4}\frac{R^2}{N}\right)^N\right\}, \\ &\approx \left(1 - \frac{1}{4}\frac{E_\phi\{R^2\}}{N}\right)^N, \end{aligned} \tag{C.22}$$

where the expectation E_ϕ is over the variables $(p_1, p_2, \theta_1, \theta_2, x_1, y_1, x_2, y_2)$ and the subscript on R has been dropped as R is independent of n. Using equation 4.2.21 in [AS72], in the limit for large N (C.22) reduces to,

$$\lim_{N\to\infty} M(\underline{\omega}) = exp\left(-\frac{1}{4}E_\phi\{R^2\}\right). \tag{C.23}$$

It now remains to find a form for $E_\phi\{R^2\}$. From equation (C.15) and using the definitions in (C.14) gives,

$$\begin{aligned} R^2 &= A^2 + B^2, \\ &= \left(\underline{\omega}^T I \underline{S}'\right)^2 + \left(\underline{\omega}^T I' \underline{S}'\right)^2, \\ &= \underline{\omega}^T\left(\underline{S}'\underline{S}'^T + I'\underline{S}'\underline{S}'^T I'^T\right)\underline{\omega}. \end{aligned} \tag{C.24}$$

The expectation $E_\phi\{R^2\}$ in (C.23) thus can be written as,

$$\begin{aligned} E_\phi\{R^2\} &= \underline{\omega}^T\left(E_\phi\{\underline{S}'\underline{S}'^T\} + I'E_\phi\{\underline{S}'\underline{S}'^T\}I'^T\right)\underline{\omega}, \\ &= \underline{\omega}^T\left(C' + I'C'I'^T\right)\underline{\omega}, \end{aligned} \tag{C.25}$$

where $C' = E_\phi\{\underline{S}'\underline{S}'^T\}$. Using the definitions (C.7) and (C.9) it can be readily shown that,

$$\begin{aligned} C &= E_\phi\{\underline{S}\underline{S}^T\}, \\ &= \frac{1}{2}\left(C' + I'C'I'^T\right). \end{aligned} \tag{C.26}$$

Thus the characteristic function becomes,

$$M(\underline{\omega}) = exp\left(-\frac{1}{2}\underline{\omega}^T C \underline{\omega}\right). \tag{C.27}$$

Applying the inverse transform (C.12) to (C.27) gives the zero mean, jointly Gaussian probability density function [Pap91],

$$p(\underline{X}) = \frac{1}{(2\pi)^2|C|}exp\left(-\frac{1}{2}\underline{X}^T C^{-1}\underline{X}\right) \tag{C.28}$$

Furthermore, by explicitly writing out the form of the covariance matrix C it may be shown that $\underline{X}$ are circular complex jointly Gaussian random variables. That is, forming the vectors $\underline{X}_R = [f_r, g_r]^T$ and $\underline{X}_I = [f_i, g_i]^T$ and defining the covariance matrices,

$$C_{RR} = E\{\underline{X}_R \underline{X}_R^T\}, \tag{C.29}$$
$$C_{II} = E\{\underline{X}_I \underline{X}_I^T\}, \tag{C.30}$$
$$C_{RI} = E\{\underline{X}_R \underline{X}_I^T\}, \tag{C.31}$$
$$C_{IR} = E\{\underline{X}_I \underline{X}_R^T\}, \tag{C.32}$$

it may be readily shown that,

$$C_{RR} = C_{II}, \tag{C.33}$$
$$C_{RI} = -C_{IR}. \tag{C.34}$$

and hence $\underline{X}$ may be described as a zero mean, circular complex Gaussian random vector [Goo00a].

Appendix D

Comparison of Theoretical PDFs and Histogram Estimates

A number of statistical hypothesis tests are available in the literature to determine whether a given sample data set is consistent with a particular known theoretical distribution. For the case of binned data sets e.g. histogram data, the the Chi-square test is the generally accepted hypothesis test [Kre93], while for continuous data sets the Kolmogorov-Smirnov test is appropriate [PTVF94].

The Chi-square test computes the following test statistic,

$$\chi^2 = \sum_{i=1}^{N} \frac{(n_i - m_i)^2}{m_i}, \tag{D.1}$$

where n_i is the number of events observed in the i^{th} bin, m_i is the expected number of events in the i^{th} bin based on the hypothesized known distribution and the sum is over all N histogram bins. A large value of χ^2 indicates that the hypothesized distribution is not a good fit to the sample data set. Indeed when the number of events n_i in each bin is large then the χ^2 statistic has a Chi-square probability distribution and the decision to either accept or reject the hypothesized distribution may be made with a specified confidence level.

A simpler and somewhat less rigorous approach to determine whether a histogram of a sample data set is consistent with a known distribution is to model the number of events observed in the i^{th} bin using a binomial distribution. Given the total sample data size, N_T the probability of obtaining n_i samples in bin i is given by,

$$P(n_i) = \left(\begin{array}{c} N_T \\ n_i \end{array} \right) p_i^{n_i} (1 - p_i)^{N_T - n_i}, \tag{D.2}$$

where p_i is the probability of a sample occurring in the i^{th} bin which may be computed using the hypothesized known distribution. The mean number of samples and the variance in the i^{th} bin in the binomial model are given by,

$$\mu_i = N_T p_i, \tag{D.3}$$

$$\sigma_i^2 = N_T p_i (1 - p_i), \tag{D.4}$$

respectively. These values indicate the number samples that are to be anticipated in each histogram bin as well as the likely range in the number of samples about the expected value assuming the sample data set is described by the hypothesized distribution. For the case when the number of samples in a

particular bin is large the central limit theorem may be applied and the binomial distribution may be approximated by a Gaussian with the same mean and variance. Therefore a histogram bin in which the number of samples n_i is greater than three standard deviations from the mean ($|n_i - m_i| > 3\sigma_i$) might be considered statistically unlikely, suggesting the hypothesized known distribution is not representative of the sample data set.

This binomial model based approach has been adopted in comparing the histogram plots, in Chapter 7, of the amplitude, phase, coherence, interferometric phase and log likelihood change statistic with the theoretical distributions obtained using the theoretically derived jointly Gaussian interferometric SAR image model. In the histogram plots of these random variables the expected value of the histogram is shown along with plots of the expected value plus and minus three standard deviations, under the assumption that the jointly Gaussian interferometric SAR image model is a valid model for the experimental image pairs.

Bibliography

[AH93] J. Askne and J. O. Hagberg. Potential of interferometric SAR for classification of land surfaces. In *Proceedings of the 1993 International Geoscience and Remote Sensing Symposium*, volume 3, pages 985–987, 1993.

[AR87] H. Anton and C. Rorres. *Elementary Linear Algebra With Applications*. John Wiley and sons, 1987.

[AS72] M. Abramowitz and I. A. Segun. *Handbook of Mathematical Functions with Formulas, Graphs and Mathematical Tables*. Dover Publications, 1972.

[AW01] A. Ashok and A. J. Wilkinson. Topographic mapping with multiple antenna SAR interferometry: A bayesian model-based approach. In *Proceedings of the 2001 International Geoscience and Remote Sensing Symposium*, volume 5, pages 2058–2060, 2001.

[BB02] L Brule and H. Baeggli. RADARSAT-2 program update. In *Proceedings of the 2002 IEEE International Geoscience and Remote Sensing Symposium*, volume 3, pages 1462–1464, 2002.

[BBM+03] S. Buckreuss, W. Balzer, P. Muhlbauer, R. Werninghaus, and W. Pitz. The TerraSAR-X satellite project. In *Proceedings of the 2003 IEEE International Geoscience and Remote Sensing Symposium*, volume 5, pages 3096–3098, 2003.

[BE02] A. R. Brenner and J. H. G. Ender. First experimental results achieved with the new very wideband SAR system PAMIR. In *Proceedings of the 4th European Conference on Synthetic Aperture Radar*, pages 81–86, 2002.

[BE03] A. R. Brenner and J. H. G. Ender. Very wideband radar imaging with the airborne SAR sensor PAMIR. In *Proceedings of the 2003 IEEE International Geoscience and Remote Sensing Symposium*, volume 1, pages 544–535, 2003.

[BG83] G. A. Bendor and T. W. Gedra. Single pass fine-resolution SAR autofocus. In *Proceedings of the IEEE National Aerospace and Electronics Conference*, pages 482–488, 1983.

[BG88] W. D. Brown and D. C. Ghiglia. Some methods for reducing propagation-induced phase errors in coherence imaging systems. I. Formalism. *Journal of the Optical Society of America, A*, 5(6):924–941, June 1988.

[BH98] R. Bamler and P. Hartl. Synthetic aperture radar interferometry. *Inverse Problems*, 14:1–54, 1998.

[Boo89] F. L. Bookstein. Principal warps: Thin-plate splines and the decomposition of deformations. *IEEE Transactions on Pattern Analysis and Machine Intelligence*, 11(6):567–585, June 1989.

[Bre02] A. R. Brenner. Distributed SAR processing in the time domain. In *Proceedings of the 4th European Conference on Synthetic Aperture Radar*, pages 573–576, 2002.

[BS87] P. Beckmann and A. Spizzichino. *The Scattering of Electromagnetic Waves from Rough Surfaces*. Artech House, Norwood, Massachusetts, 1987.

[Cal92] T. M. Calloway. *Automatic Focus and Registration of Synthetic Aperture Radar Images*. PhD thesis, Department of Electrical and Computer Engineering, University of New Mexico, 1992.

[CD94] T. M. Calloway and G. W. Donohoe. Subaperture autofocus for synthetic aperture radar. *IEEE Transactions on Aerospace and Electronic Systems*, 30(2):617–621, April 1994.

[CDF03] H. M. J. Cantalloube and P. Dubois-Fernandez. Airborne X-band SAR imaging with 10 cm resolution - Technical challenges and preliminary results. In *Proceedings of the 2003 International Geoscience and Remote Sensing Symposium*, volume 1, pages 185–187, 2003.

[CGM95] W. G. Carrara, R. S. Goodman, and R. M. Majewski. *Spotlight synthetic aperture radar signal processing algorithms*. Artech House, 1995.

[CKW95] D. G. Corr, G. E. Keyte, and S. Whitehouse. Studies of decorrelation in multi-temporal SAR imagery. In *Proceedings of the 1995 International Geoscience and Remote Sensing Symposium*, pages 1026–1028, 1995.

[Cor97] D. G. Corr. Coherence change detection for urban development monitoring. In *Proceedings of the 1997 IEE Colloquium on Radar Interferometry*, volume 6, pages 1–6, 1997.

[CP98] S. R. Cloude and K. P. Papathanassiou. Polarimetric SAR interferometry. *IEEE Transactions on Geoscience and Remote Sensing*, 36(5):1551–1565, September 1998.

[CPR91a] C. Cafforio, C. Prati, and F. Rocca. Full resolution focusing of SEASAT SAR images in the frequency wave number domain. *International Journal of Remote Sensing*, 12(3):491–510, March 1991.

[CPR91b] C. Cafforio, C. Prati, and F. Rocca. SAR data focusing using seismic migration techniques. *IEEE Transactions on Aerospace and Electronic Systems*, 27(2):194–206, March 1991.

[CR98] D. G. Corr and A. Rodrigues. Coherent change detection of vehicle movements. In *Proceedings of the 1998 International Geoscience and Remote Sensing Symposium*, volume 5, pages 2451–2453, 1998.

[CSVM98] F. Caltagirone, P. Spera, R. Vigliotti, and G. Manoni. SkyMed/COSMO mission overview. In *Proceedings of the 1998 IEEE International Geoscience and Remote Sensing Symposium*, volume 2, pages 683–685, 1998.

[DJ92] M. D. Desai and W. K. Jenkins. Convolution backprojection image reconstruction for spotlight mode synthetic aperture radar. *IEEE Transactions on Image Processing*, 1(4):505–516, 1992.

[DJWT97] N. E. Doren, C. V. Jakowatz Jr., D. E. Wahl, and P. A. Thompson. General formulation for wavefront curvature correction in polar-formatted spotlight-mode SAR images using space-variant post-filtering. In *Proceedings of the 1997 International Conference on Image Processing*, volume 1, pages 861–864, 1997.

[EGJ89] P. H. Eichel, D. C. Ghiglia, and C. V. Jakowatz Jr. Speckle processing method for synthetic aperture radar phase correction. *Optics Letters*, 14:1–3, 1989.

[EJ89] P. H. Eichel and C. V. Jakowatz Jr. Phase-gradient algorithm as an optimal estimator of the phase derivative. *Optics Letters*, 14:1101–1103, 1989.

[FG67] M. R. Foster and N. J. Guinzy. The coefficient of coherence: Its estimation and use in geophysical data processing. *Geophysics*, 32(4):602–616, 1967.

[FMYS97] A. C. Frery, H.-J. Muller, C. F. Yanasse, and S. J. S Sant'Anna. A model for extremely heterogeneous clutter. *IEEE Transactions on Geoscience and Remote Sensing*, 35(3):648–659, 1997.

[FPR01] A. Ferretti, C. Prati, and F. Rocca. Permanent scatterers in SAR interferometry. *IEEE Transactions on Geoscience and Remote Sensing*, 39(1):8–20, 2001.

[FRP89] C. Cafforio F. Rocca and C. Prati. Synthetic aperture radar: A new application for wave equation techniques. *Geophysical Prospecting*, 37:809–830, 1989.

[FSSH82] V. S. Frost, J. A. Stiles, K. S. Shanmugan, and J. C. Holtzman. A model for radar images and its application to adaptive filtering of multiplicative noise. *IEEE Transactions on Pattern Analysis and Machine Intelligence*, 4:157–166, 1982.

[GB88] D. C. Ghiglia and W. D. Brown. Some methods for reducing propagation-induced phase errors in coherence imaging systems. II. Numerical results. *Journal of the Optical Society of America, A*, 5(6):942–957, June 1988.

[GBZ89] R. M. Goldstein, T. P. Barnett, and H. A. Zebker. Remote sensing of ocean currents. *Science*, 246:1282–1285, 1989.

[GGP94] F. Gatelli, A. M. Guamieri, and F. Parizzi. The wavenumber shift in interferometry. *IEEE Transactions on Geoscience and Remote Sensing*, 32(4):855–865, July 1994.

[GGZ89] A. K. Gabriel, R. M. Goldstein, and H. A. Zebker. Mapping small elevation changes over large areas: Differential radar interferometry. *Journal of Geophysical Research*, 94(B7):9183–9191, July 1989.

[Gie01a] C. H. Gierull. *Statistics of SAR interferograms with application to moving target detection*. Defence Research Establishment Ottawa, Canada, July Tech. Rep. TR2001-045, 2001.

[Gie01b] C. H. Gierull. Unbiased coherence estimator for SAR interferometry with application to moving target detection. *Electronics Letters*, 37(14):913–915, 2001.

[Goo63] J. W. Goodman. Statistical analysis based on a certain multivariate complex Gaussian distribution (An introduction). *Annals of Statistical Analysis*, 34:152–177, 1963.

[Goo76] J. W. Goodman. Some fundamental properties of speckle. *Journal of the Optical Society of America*, 66:1145–1150, 1976.

[Goo00a] J. W. Goodman. *Statistical Optics*. Wiley, 2000.

[Goo00b] J. W. Goodman. *Statistical properties of laser speckle patterns*. Wiley, 2000.

[Gos88] A. Goshtasby. Registration of images with geometric distortions. *IEEE Transactions on Geoscience and Remote Sensing*, 26(1):60–64, 1988.

[GR80] I. S. Gradshteyn and I. M. Ryzhik. *Table of Integrals, Series and Products*. Academic Press, 1980.

[GR94] D. C. Ghiglia and L. A. Romero. Robust two-dimensional weighted and unweighted phase unwrapping that uses fast transforms and iterative methods. *Journal of the Optical Society of America A.*, 11(1):107–117, 1994.

[Gra74] L. C. Graham. Synthetic interferometric radar for topographic mapping. *Proceedings of the IEEE*, 62:763–768, 1974.

[GUMdP02] A. Gustavsson, L. M. H. Ulander, P. Martineau, and O. du Plessis. Some results on detection of targets deployed in hide under foliage. In *Proceedings of the Fourth European Conference on Synthetic Aperture Radar*, pages 57–60, 2002.

[GW94] D. C. Ghiglia and D. E. Wahl. Interferometric synthetic aperture radar terrain elevation mapping from multiple observations. In *Proceedings of the Sixth IEEE Digital Signal Processing Workshop*, pages 33–36, 1994.

[GWET94] A. Golden, S. C. Wei, K. K. Ellis, and S. Tummula. Migration processing of spotlight SAR data. In *Proceedings of the SPIE Symposium on Algorithms for SAR Imagery*, pages 25–35, 1994.

[GWV96] D. Geudtner, R. Winter, and P. W. Vachon. Flood monitoring using ERS-1 SAR interferometry coherence maps. In *Proceedings of the 1998 International Geoscience and Remote Sensing Symposium*, volume 2, pages 966–968, 1996.

[GZW88] R. M. Goldstein, H. A. Zebker, and C. L. Werner. Satellite radar interferometry: Two-dimensional phase unwrapping. *Radio Science*, 23(4):713–720, 1988.

[Hay90] J. Haystead. JSTARS - Real-Time warning and control for surface warfare. *Defense Electronics*, pages 31–39, July 1990.

[Hor96] R. Horn. The DLR airborne SAR project E-SAR. In *Proceedings of the 1996 International Geoscience and Remote Sensing Symposium*, volume 3, pages 1624–1628, 1996.

[HUA95] J. O. Hagberg, Lars M. H. Ulander, and Jan Askne. Repeat-pass SAR interferometry over forested terrain. *IEEE transactions on Geoscience and Remote Sensing*, 33(2):331–340, 1995.

[HUGL96] H. Hellsten, L. M. Ulander, A. Gustavsson, and B. Larsson. Development of VHF CARABAS II SAR. In *Proceedings of the SPIE Conference on Radar Sensor Technology*, volume 2747, pages 48–60, 1996.

[Jao84] J. K. Jao. Amplitude distribution of composite terrain radar clutter and the K-distribution. *IEEE transactions on Antennas and Propagation*, 32:1049–1062, 1984.

[JB94] D. Just and R. Bamler. Phase statistics of interferograms with applications to synthetic aperture radar. *Applied Optics*, 33(20):4361–4368, July 1994.

[JP76] E. Jakeman and P. N. Pusey. A model for non-rayleigh sea echo. *IEEE transactions on Antennas and Propagation*, 24:806–814, 1976.

[JW93] C. V. Jakowatz Jr. and D. E. Wahl. Eigenvector method for maximum likelihood estimation of phase errors in SAR imagery. *Journal of the Optical Society of America A*, 10(12):2539–2546, 1993.

[JW00] C. V. Jakowatz Jr. and D. E. Wahl. Three-dimensional tomographic imaging for foliage penetration using multiple-pass spotlight-mode SAR. In *Conference Record of the Thirty-Fifth Asilomar Conference on Signals, Systems and Computers*, volume 1, pages 121–125, 2000.

[JWE+96] C. V. Jakowatz Jr., D. E. Wahl, P. H Eichel, D. C. Ghiglia, and P. A. Thompson. *Spotlight-Mode Synthetic Aperture Radar: A Signal Processing Approach*. Kluwer Academic Publishers, 1996.

[JWP94] I. R. Joughin, D. P. Winebrenner, and D. B. Percival. Probability density functions for multilook polarimetric signatures. *IEEE transactions on Geoscience and Remote Sensing*, 32(3):562–574, 1994.

[JWTD97] C. V. Jakowatz Jr., D. E. Wahl, P. A. Thompson, and N. E. Doren. Space-variant filtering for correction of wavefront curvature effects in spotlight-mode SAR imagery formed via polar formatting. In *Proceedings of the SPIE 11th Annual International Symposium on Aerospace Defence Sensing and Controls*, 1997.

[Kay98] S. M. Kay. *Fundamentals of statistic signal processing. Vol 2. Detection theory*. Prentice Hall, 1998.

[KF83] M. A. Karam and A. K. Fung. Scattering from randomly oriented circular discs with application to vegetation. *Radio Science*, 18(4):557–565, 1983.

[KF88] M. A. Karam and A. K. Fung. Electromagnetic scattering from a finite-length, randomly oriented dielectric circular cylinder over a rough interface with application to vegetation. *Internation Journal of Remote Sensing*, 9(6):1109–1134, 1988.

[KFA88] M. A. Karam, A. K. Fung, and Y. M. M. Antar. Electromagnetic wave scattering from some vegetation samples. *IEEE transactions on Geoscience and Remote Sensing*, 26(6):799–808, 1988.

[KI00] H. Kimura and N. Ito. ALOS/PALSAR: The Japanese second-generation spaceborne SAR and its applications. In *Proceedings of the Internation Society for Optical Engineering (SPIE)*, volume 4152, pages 110–119, 2000.

[Kre93] E. Kreyszig. *Advanced engineering mathematics*. John Wiley and Sons, 1993.

[KSS90] B. Kang, H. Subbaram, and B. D. Steinberg. Improved adaptive-beamforming target for self-calibrating a distorted phased array. *IEEE Transactions on Antenna and Propagation*, 38(2):186–194, 1990.

[Leb90] F. W. Leberl. *Radargrammetric image processing*. Artech House, 1990.

[Lee83] J.S. Lee. A simple speckle smoothing algorithm for synthetic aperture radar images. *IEEE transactions on Systems, man and Cybernetics*, 13:85–89, 1983.

[LG90] F. K. Li and R. M. Goldstein. Studies of multibaseline spaceborne interferometric synthetic aperture radars. *IEEE transactions on Geoscience and Remote Sensing*, 128(1):88–97, 1990.

[LGH+95] C. E. Livingstone, A. L. Gray, R. K. Hawkins, P. Vachon, T. I. Lukowski, and M. Lalonde. The CCRS airborne SAR systems: Radar for remote sensing research. *Canadian Journal of Remote Sensing*, 21(4):468–491, 1995.

[LHM94] J.S. Lee, K. W. Hoppel, and A. R. Miller. Intensity and phase statistics of multilook polarimetric and interferometric SAR imagery. *IEEE transactions on Geoscience and Remote Sensing*, 32(5):1017–1027, 1994.

[LLN90] A. Lopes, H. Laur, and E. Nezry. Statistical distribution and texture in multilook and complex SAR images. In *Proceedings of the 1990 International Geoscience and Remote Sensing Symposium*, volume 3, pages 2427–2430, 1990.

[LMH94] J.S. Lee, A. R. Miller, and K. W. Hoppel. Statistics of phase difference and product magnitude of multi-look processed Gaussian signals. *Waves in Random Media*, 4:307–319, 1994.

[Mar95] N. Marechal. Tomographic formulation of interferometric SAR for terrain elevation mapping. *IEEE Transactions on Geoscience and Remote Sensing*, 33(3):726–739, 1995.

[MMS96] A. Moreira, J. Mittermayer, and R. Scheiber. Extended chirp scaling algorithm for air- and spaceborne SAR data processing in stripmap and scanSAR imaging modes. *IEEE Transactions on Geoscience and Remote Sensing*, 34(5), 1996.

[MOJ83] D. C. Munson, J. D. O'Brien, and W. K. Jenkins. A tomographic formulation of spotlight-mode synthetic aperture radar. *Proceedings of the IEEE*, 71(8):917–925, 1983.

[MS81] C. E. Mancill and J. M. Swiger. A map drift autofocus technique for correcting higher order SAR phase errors. In *Proceedings of the Tri-Service Radar Conference*, 1981.

[MS84] D. C. Munson and J. L. C. Sanz. Image reconstruction from frequency-offset fourier data. *Proceedings of the IEEE*, 72:661–669, 1984.

[NOW99] L. M. Novak, G. J. Owirka, and A. L. Weaver. Automatic target recognition using enhanced resolution SAR data. *IEEE Transactions on Aerospace and Electronic Systems*, 35:157–175, 1999.

[Off01] USAF System Program Office. RQ-4A Global Hawk high altitude endurance unmanned aerial reconnaissance system. Public Release Presentation 452-AS-3948, February 2001.

[Oli84] C. J. Oliver. A model for non-Rayleigh scattering statistics. *Opt Acta*, 31:701–722, 1984.

[Oli91] C. J. Oliver. Information from SAR images. *Journal of Physics D:Applied Physics*, 24:1493–1514, 1991.

[OP58] I. Olkin and J. W. Pratt. Unbiased estimation of certain correlation coefficients. *Annals of Mathematical Statistics*, 29:201–211, 1958.

[OQ98] C. Oliver and S. Quegan. *Understanding Synthetic Aperture Radar Images*. Artech House, 1998.

[Pap91] A. Papoulis. *Probability, Random Variables, and Stochastic Processes*. McGraw Hill, third edition, 1991.

[Pay04] T. M. Payne. The effect of scene elevation on the coherence of wide-angle crossing node SAR pairs. *IEEE Transactions on Geoscience and Remote Sensing*, 42(3):520–528, March 2004.

[PGR91] C. Prati, A. M. Guarnieri, and F. Rocca. Spot mode focusing with the $\omega - k$ technique. In *Proceedings of the 1991 IEEE International Geoscience and Remote Sensing Symposium*, volume 2, pages 631–634, 1991.

[PGS01] M. Preiss, D. Gray, and N. J. S. Stacy. The effect of polar format resampling on uncompensated motion phase errors and the phase gradient autofocus algorithm. In *Proceedings of the 2001 IEEE International Geoscience and Remote Sensing Symposium*, volume 3, pages 1442–1444, 2001.

[PGS02a] M. Preiss, D. Gray, and N. J. S. Stacy. Estimating scene coherence in a change detection experiment using the DSTO Ingara SAR. In *Proceedings of 4th European Conference on Synthetic Aperture Radar*, pages 225–228, 2002.

[PGS02b] M. Preiss, D. Gray, and N. J. S. Stacy. Space variant filtering of polar format spotlight sar images for wavefront curvature correlation and interferometric processing. In *Proceedings of the 2002 IEEE International Geoscience and Remote Sensing Symposium*, volume 1, pages 179–181, 2002.

[PGS03a] M. Preiss, D. Gray, and N. J. S. Stacy. Change detection in repeat pass interferometric synthetic aperture radar. In *Proceedings of the 2003 International Conference on Radar*, 2003.

[PGS03b] M. Preiss, D. Gray, and N. J. S. Stacy. A change detection statistic for repeat pass interferometric SAR. In *Proceedings of the 2003 IEEE Internation Conference on Acoustics, Speech and Signal Processing*, pages 241–244, 2003.

[PGS03c] M. Preiss, D. Gray, and N. J. S. Stacy. A change detection technique for repeat pass interferometric SAR. In *Proceedings of the 2003 IEEE International Geoscience and Remote Sensing Symposium*, volume 2, pages 938–940, 2003.

[PMIM76] L. J. Porcello, N. G. Massey, R. B. Innes, and J. M. Mark. Speckle reduction in synthetic aperture radars. *Journal of the Optical Society of America*, 66:1305–1311, 1976.

[PRM+02] A. Potsis, A. Reigber, A. Moreira, L. Ferro-Famil, and N. Uzunoglou. Comparison of chirp scaling and wavenumber domain algorithms for airborne low frequency SAR data processing. In *Proceedings of fourth European conference on Synthetic Aperture Radar*, pages 69–73, 2002.

[PTVF94] W. H. Press, S. A. Teukolsky, W. T. Vetterling, and B. P. Flannery. *Numerical recipes in C*. Cambridge University Press, 1994.

[QR95] S. Quegan and I. Rhodes. Statistical models for polarimetric data: Consequences, testing and validity. *International Journal of Remote Sensing*, 16(7):1183–1210, 1995.

[Ree62] I. S. Reed. On a moment theorem for complex Gaussian processes. *IRE Transactions on Information Theory*, pages 194–195, 1962.

[Rei00] A. Reigber. *Airborne SAR Tomography*. PhD thesis, University of Stuttgart, 2000.

[RHJ+00] P. A. Rosen, S. Hensley, I. R. Joughin, F. K. Li, S. N. Madsen, E. Rodriguez, and R. M. Goldstein. Synthetic aperture radar interferometry. *Proceedings of the IEEE*, 88(3):333–382, 2000.

[RM92] E. Rodriguez and J. M. Martin. Theory and design of interferometric synthetic aperture radars. *IEE Proceedings-F*, 139(2):147–159, April 1992.

[RM00] A. Reigber and A. Moreira. First demonstration of airborne SAR tomography using multibaseline L-band data. *IEEE Transactions on Geoscience and Remote Sensing*, 38(5):2142–2152, 2000.

[RN01] N. J. Redding and G. N. Newsam. Inverting the circular Radon transform. Technical report, Defence Science and Technology Organisation, 2001.

[RP03] N. J. Redding and T. M. Payne. Inverting the spherical Radon transform for 3D SAR image formation. In *Proceedings of the 2003 International Conference on Radar*, 2003.

[RRB+92] R. K. Raney, H. Runge, R. Bamler, I. Cumming, and F. Wong. Precision SAR processing without interpolation for range cell migration correction. *IEEE Transactions on Geoscience and Remote Sensing*, 13(5):991–998, 1992.

[RS02] A. Reigber and R. Scheiber. Differential SAR interferometry using an airborne platform. In *Proceedings 4th European Conference on Synthetic Aperture Radar*, pages 373–376, 2002.

[RvZ93] E. J. M. Rignot and J. J. van Zyl. Change detection techniques for ERS-1 SAR data. *IEEE Transactions on Geoscience and Remote Sensing*, 31(4):896 – 906, July 1993.

[RZT+03] B. Rosich, M. Zink, R. Torres, J. Closa, and C. Buck. ASAR instrument performance and product quality status. In *Proceedings of the 2003 IEEE International Geoscience and Remote Sensing Symposium*, volume 2, pages 1109–1111, 2003.

[SB94] N. J. S. Stacy and M. P. Burgess. Ingara: The Australian airborne imaging radar system. In *Proceedings of the 1994 IEEE International Geoscience and Remote Sensing Symposium*, volume 4, pages 2240–2242, 1994.

[SBG+03] N. J. S. Stacy, D. P. Badger, A. S. Goh, M. Preiss, and M. L. Williams. The DSTO Ingara airborne X-band SAR polarimetric upgrade: First results. In *Proceedings of the 2003 IEEE International Geoscience and Remote Sensing Symposium*, 2003.

[SBMS96] N. J. S. Stacy, M. P. Burgess, M. R. Muller, and R. Smith. Ingara: An integrated airborne imaging radar system. In *Proceedings of the 1996 IEEE International Geoscience and Remote Sensing Symposium*, volume 3, pages 1618–1620, 1996.

[SES+95] E. R. Stofan, D. L. Evans, C. Schmullius, B. Holt, J. J. Plaut, J. van Zyl, S. D. Wall, and J. Way. Overview of results of spaceborne imaging radar-C, X-band synthetic aperture radar. *IEEE Transactions on Geoscience and Remote Sensing*, 33(4):817–827, July 1995.

[She00] Z. She. *Array Processing Methods for Calibrating Inverse Synthetic Aperture Radar and Multiple Pass Synthetic Aperture Radar*. PhD thesis, Department of Electrical and Electronic Engineering, The University of Adelaide, 2000.

[Sin89] A. Singh. Digital change detection techniques using remotely sensed data. *International Journal of Remote Sensing*, 10:989–1003, 1989.

[SJW96] F. Stuhr, R. Jordan, and M. Werner. SIR-C/X-SAR: An advanced radar. In *Proceedings of the Aerospace Applications Conference*, volume 2, pages 5–16, 1996.

[SM00] R. Scheiber and A. Moreira. Co-registration of interferometric SAR images using spectral diversity. *IEEE Transactions on Geoscience and Remote Sensing*, 38(5):2179–2191, 2000.

[SRU+99] R. Scheiber, A. Reigber, A. Ulbricht, K. P. Papathanassiou, R. Horn, S. Buckreuss, and A. Moreira. Overview of interferometic data acquisition and processing modes of the experimental airborne SAR system of DLR. In *Proceedings of the 1999 IEEE International Geoscience and Remote Sensing Symposium*, volume 1, pages 35–37, 1999.

[SSL94] D. Sheen, C. Strawitch, and T. Lewis. UHF wideband SAR design and preliminary results. In *Proceedings of the 1994 IEEE International Geoscience and Remote Sensing Symposium*, pages 289–291, 1994.

[Ste88] B. D. Steinberg. Microwave imaging of aircraft. *Proceedings of the IEEE*, 76(12):1578–1592, 1988.

[Sto78] R. H. Stolt. Migration by Fourier transform. *Geophysics*, 43:23–48, 1978.

[SZR+72] I. I. Shapiro, S. H. Zisk, A. E. E. Rogers, M. A. Slade, and T. W. Thompson. Lunar topography: Global determination by radar. *Science*, 178:939–948, 1972.

[TBQ95] R. J. A. Tough, D. Blacknell, and S. Quegan. A statistical description of polarimetric and interferometric synthetic aperture radar data. *Proceedings of the Royal Society of London Series A - Mathematical and Physical Sciences*, 449(1937):567–589, June 1995.

[TL96] R. Touzi and A. Lopes. Statistics of the stokes parameters and of the complex coherence parameters in one-look and multilook speckle fields. *IEEE transactions on Geoscience and Remote Scensing*, 34(2):519–531, 1996.

[TLB88] R. Touzi, A. Lopes, and P. Bousquet. A statistical and geometrical edge detector for SAR images. *IEEE transactions on Geoscience and Remote Scensing*, 26(4):764–773, 1988.

[TLBV99] R. Touzi, A. Lopes, J. Bruniquel, and P. W. Vachon. Coherence estimation for SAR imagery. *IEEE transactions on Geoscience and Remote Scensing*, 37(1):135–149, 1999.

[TPS+99] S. I. Tsunoda, F. Pace, J. Stence, M. Woodring, W. H. Hensley, A. W. Doerry, and B. C. Walker. Lynx: A high-resolution synthetic aperture radar. *Proceedings of the SPIE*, 3704:20–27, 1999.

[UHS03] L. M. H. Ulander, H. Hellsten, and G. Stenstrom. Synthetic-aperture radar processing using fast factorised backprojection. *IEEE transactions on Aerospace and Electronic Systems*, 39(3):760–776, 2003.

[Wal80] J. L. Walker. Range-doppler imaging of rotating objects. *IEEE Transactions on Aerospace and Electronic Systems*, 16(1):23–52, January 1980.

[War81] K. D. Ward. Compound representation of high resolution sea clutter. *Electronics Letters*, 17:561–565, 1981.

[Wea98] D. D. Weatherington. U-2 ASARS-2 improvement program. In *Proceedings of SPIE*, volume 3070, pages 2–9, 1998.

[WEGJ94] D. E. Wahl, P. H. Eichel, D. C. Ghiglia, and C. V. Jakowatz Jr. Phase gradient autofocus - A robust tool for high resolution SAR phase correction. *IEEE Transactions on Aerospace and Electronic Systems*, 30(3):827–834, 1994.

[WGDF95] H. Wu, D. Grenier, G. Y. Delisle, and D. G. Fang. Translational motion compensation in ISAR image processing. *IEEE Transactions on Image Processing*, 14(11):1561–1571, 1995.

[Whi95] R. G. White. A simulated annealing algorithm for radar cross section estimation and segmentation. *SPIE International Conference on Applications of Artificial Neural Networks*, 2243:231–241, 1995.

[Won89] R. Wong. *Asymptotic Approximations of Integrals*. Academic Press, 1989.

[XC99] W. Xu and I. Cumming. A region-growing algorithm for InSAR phase unwrapping. *IEEE Transactions on Geoscience and Remote Sensing*, 37(1):120–134, 1999.

[YKJ+89] S. H. Yueh, J. A. Kong, J. K. Jao, R. T. Shin, and L. M. Novak. K distribution and polarimetric terrain clutter. *Journal of Electromagnetic Waves and Applications*, 3:747–768, 1989.

[Yoc98] D. A. Yocky. Interferometric SAR coherence classification utility assessment. In *Proceedings of the 1998 IEEE International Geoscience and Remote Sensing Symposium*, volume 4, pages 1784–1786, 1998.

[Zeb00] H. A. Zebker. Studying the earth with interferometric radar. *IEEE Computing in Science and Engineering*, 2(3):52–60, 2000.

[Zel76] J. S. Zelenka. Comparison of continuous and discrete mixed-integrator processors. *Journal of the Optical Society of America*, 66(11):1295–1304, 1976.

[Zis72a] S. H. Zisk. Lunar topography: First radar-interferometer measurements of the alphonsus-ptolemaeus-arzachel region. *Science*, 178:977–980, 1972.

[Zis72b] S. H. Zisk. A new, Earth-based radar technique for the measurement of lunar topography. *The Moon*, 4:296–306, 1972.

[ZV92] H. A. Zebker and J. Villasenor. Decorrelation in interferometric radar echoes. *IEEE Transactions on Geoscience and Remote Sensing*, 30(5):950–959, 1992.